



**HAL**  
open science

# Synthesis of iron oxide nanoparticles and development of magnetic coatings by fluid processing

Marie Darcheville

► **To cite this version:**

Marie Darcheville. Synthesis of iron oxide nanoparticles and development of magnetic coatings by fluid processing. Material chemistry. Université Paris-Saclay, 2021. English. NNT : 2021UPASP005 . tel-03209643

**HAL Id: tel-03209643**

**<https://theses.hal.science/tel-03209643v1>**

Submitted on 27 Apr 2021

**HAL** is a multi-disciplinary open access archive for the deposit and dissemination of scientific research documents, whether they are published or not. The documents may come from teaching and research institutions in France or abroad, or from public or private research centers.

L'archive ouverte pluridisciplinaire **HAL**, est destinée au dépôt et à la diffusion de documents scientifiques de niveau recherche, publiés ou non, émanant des établissements d'enseignement et de recherche français ou étrangers, des laboratoires publics ou privés.

# Synthesis of iron oxide nanoparticles and development of magnetic coatings by fluid processing

**Thèse de doctorat de l'université Paris-Saclay**

École doctorale n°564 : physique de l'Ile-de-France (PIF)

Spécialité de doctorat: Physique

Unité de recherche : Université Paris-Saclay, CNRS, Laboratoire de Physique des  
Solides, 91405, Orsay, France

Référent : Faculté des sciences d'Orsay

**Thèse présentée et soutenue à Orsay, le 29 janvier 2021,  
par**

**Marie DARCHEVILLE**

## Composition du Jury

**Sylvie BEGIN-COLIN**

Professeur, IPCMS, Strasbourg

Présidente

**Michael FARLE**

Professeur, Université Duisburg-Essen, Allemagne

Rapporteur & Examinatrice

**Lise-Marie LACROIX**

Maitre de conférences, HDR, LPCNO Toulouse

Rapporteur & Examineur

**Grégoire de LOUBENS**

Cadre scientifique des EPIC, CEA Paris-Saclay

Examineur

**André THIAVILLE**

Directeur de recherche, LPS Orsay, Université Paris  
Saclay

Directeur de thèse

**Clément SANCHEZ**

Directeur de recherche, UPMC Paris

Co-directeur de thèse

**Anne-Lise ADENOT-ENGELVIN**

Ingénieur, CEA Le Ripault

Co-encadrante de thèse

**Nicolas VUKADINOVIC**

Ingénieur, Dassault-Aviation

Invité



*Ici mon chemin sera long et rempli d'obstacles, mais jamais rien ne pourra égaler  
mon envie de réussir.*





<b>REMERCIEMENTS .....</b>	<b>1</b>
<b>RESUME LONG .....</b>	<b>3</b>
<b>INTRODUCTION.....</b>	<b>9</b>
CHAPTER I. ELABORATION OF IRON OXIDE SPINEL NANOPARTICLES.....	15
I. <i>The iron oxide spinel system .....</i>	<i>15</i>
I.1. Magnetite and maghemite .....	15
I.1.1. Crystal structure .....	15
I.1.2. Magnetism basics .....	17
I.1.2.A. Magnetism at the macroscopic scale .....	17
I.1.2.B. Magnetic domains .....	19
I.1.2.C. Magnetic anisotropy.....	21
I.1.2.C.a. Magnetocrystalline anisotropy .....	21
I.1.2.C.b. Shape anisotropy .....	21
I.1.2.C.c. Surface anisotropy .....	22
I.1.2.C.d. Effective anisotropy constant .....	23
I.1.2.D. Dynamic permeability of magnetic materials.....	23
I.1.2.E. Magnetism at the atomic scale and the molecular field theory .....	25
I.1.3. Iron oxide spinels magnetic and electronic properties .....	27
I.1.3.A. Magnetic order .....	27
I.1.3.B. Electronic properties .....	29
I.2. Choice of the iron oxide spinel composition.....	30
I.2.1. Effect of Zn doping on structural properties.....	30
I.2.2. Physical properties.....	31
I.2.2.A. Magnetic properties .....	31
I.2.2.B. The influence of the spinel inversion degree.....	33
I.2.2.C. Electronic properties .....	34
I.2.3. The selected iron oxide spinel composition.....	35
I.3. Particle size effect on the magnetic properties .....	35
I.3.1. Superparamagnetism, transition single/multi domains.....	35
I.3.2. Shape effect.....	36
I.4. Conclusion .....	38
II. <i>Different elaboration methods: state of the art.....</i>	<i>39</i>
II.1. Different elaboration routes.....	39
II.1.1. Coprecipitation .....	40
II.1.2. Hydrothermal/solvothermal synthesis .....	40
II.1.3. Polyol synthesis .....	41
II.1.4. Microemulsion.....	41
II.1.5. Sol-gel process .....	42
II.1.6. A non-hydrolytic route: the thermal decomposition .....	43
II.1.7. Conclusion .....	44
II.2. The thermal decomposition method and heating processes .....	45
II.2.1. Thermal decomposition mechanisms .....	45
II.2.1.A. Synthesis mechanisms.....	45
II.2.1.B. Control of the nanoparticle size, shape and composition .....	46
II.2.2. Comparison between conventional and microwave heating .....	51
II.2.2.A. General overview .....	51
II.2.2.B. Microwave heating for the elaboration of iron oxide spinel nanoparticles.....	54
II.3. Conclusion .....	55
III. <i>Zn<sub>0.4</sub>Fe<sub>2.6</sub>O<sub>4</sub> synthesis by thermal decomposition .....</i>	<i>56</i>
III.1. Comparison of two heating routes .....	56
III.1.1. Classical thermal decomposition .....	56
III.1.1.A. Experimental protocol.....	56
III.1.1.B. Effect of synthesis parameters.....	57
III.1.1.B.a. ... on the particle size .....	57
III.1.1.B.b. ... on the particle shape .....	59
III.1.1.B.c. Discussion .....	60

III.1.2.	Microwave-assisted thermal decomposition.....	62
III.1.3.	Discussion .....	63
III.1.3.A.	Choice of solvents.....	63
III.1.3.B.	Characterization of the morphology and size of Zn <sub>0.4</sub> Fe <sub>2.6</sub> O <sub>4</sub> nanoparticles.....	64
III.1.3.C.	Theoretical and experimental chemical compositions .....	72
III.1.3.D.	Conclusion .....	73
III.2.	Parametric study of the microwave-assisted thermal decomposition .....	74
III.2.1.	Choice of the zinc precursor .....	74
III.2.2.	Influence of solvents.....	77
III.2.2.A.	Addition of ethylene glycol (EG) .....	77
III.2.2.B.	Influence of the molecular weight of the solvent.....	79
III.2.2.B.a.	An invisible solvent: the TREG .....	80
III.2.2.B.b.	Influence of PEG 6000, alone.....	81
III.2.2.B.c.	Influence of a mixture of EG and PEG .....	82
III.2.2.C.	Conclusion .....	84
III.2.3.	Influence of the thermic cycle .....	85
III.2.4.	Influence of surfactants .....	87
III.2.5.	Conclusion .....	92
III.2.6.	Microstructural characterizations.....	93
III.2.6.A.	Infrared spectroscopy.....	93
III.2.6.B.	Characterization of the inversion degree in the spinel structure .....	95
III.2.6.B.a.	X-ray diffraction analysis.....	96
III.2.6.B.b.	Microstructural observations .....	99
III.2.6.B.c.	Mössbauer spectroscopy .....	102
III.2.7.	Chemical characterizations.....	106
III.2.7.A.	At the global scale .....	106
III.2.7.B.	At the local scale.....	107
III.3.	Conclusion and prospects .....	110
CHAPTER II. DEVELOPMENT OF MAGNETIC COATINGS BY AIRBRUSHING.....		125
I.	<i>Introduction</i> .....	125
II.	<i>Formulation of a dispersion</i> .....	126
II.1.	Particle interactions.....	126
II.1.1.	Van der Waals interactions.....	126
II.1.2.	Electrostatic interactions .....	127
II.1.2.A.	Zeta potential measurement.....	128
II.1.2.B.	DLVO theory .....	130
II.1.3.	Magnetic interactions.....	131
II.1.4.	Steric interactions.....	132
II.1.5.	Mechanisms of stabilization .....	132
II.1.5.A.	General concepts.....	132
II.1.5.B.	State of the art on dispersion of ferrite nanoparticles .....	135
II.2.	Study of the nanoparticle cleaning steps.....	138
II.2.1.	Centrifugation sequences .....	138
II.2.2.	Alternatives.....	141
II.2.2.A.	Simple cleaning process by reflux method .....	141
II.2.2.B.	Esterification.....	142
II.2.2.C.	Soxhlet method.....	145
II.2.3.	Conclusion .....	147
II.3.	Dispersion strategies .....	147
II.3.1.	Dispersion in polar media .....	147
II.3.1.A.	Disperbyk 180.....	147
II.3.1.B.	TMAOH .....	149
II.3.1.C.	An overview .....	152
II.3.2.	Dispersion in organic solvents .....	153
II.3.2.A.	Method of dispersion .....	153
II.3.2.B.	Influence of the number of cleanings.....	155
II.3.3.	Transfer in aqueous media .....	158
II.4.	Conclusion .....	161

III.	<i>Elaboration of coatings by airbrushing</i> .....	163
III.1.	The airbrushing process .....	163
III.2.	Thermal treatment of coatings .....	164
III.2.1.	State of the art: thermal treatment of iron oxide spinel coatings .....	164
III.2.2.	Choice of the annealing atmosphere .....	167
III.2.3.	Study of the thermal decomposition of surfactants and nanoparticles .....	168
III.2.3.A.	Decomposition of OAm and OA.....	168
III.2.3.B.	Decomposition of SP(F)M and FM .....	169
III.2.3.C.	Composition of the organic shell around particles .....	171
III.2.3.D.	Estimation of the thickness of the organic shell around particles.....	174
III.2.4.	Optimization of the debinding .....	175
III.2.4.A.	Experimental protocol .....	176
III.2.4.B.	Influence of the debinding on the surface condition and chemical composition of coatings .....	177
III.2.5.	Study of sintering .....	179
III.2.5.A.	Temperature of sintering .....	179
III.2.5.B.	Influence of the sintering on the surface condition and density of coatings.....	181
III.2.5.C.	Alternatives to enhance the coating density .....	184
III.2.5.D.	Influence of the annealing on the coating microstructure .....	193
III.3.	Feasibility of patterned films .....	197
III.4.	Conclusion .....	199
CHAPTER III. PROCESS TRANSFER FOR THE ELABORATION OF FILMS BY INKJET PRINTING .....		207
I.	<i>Introduction</i> .....	207
II.	<i>Formulation of an ink</i> .....	208
II.1.	Compatibility with the inkjet printer .....	208
II.1.1.	The process of inkjet printing .....	208
II.1.2.	Requirements for inks.....	209
II.2.	Development of hexane-based inks with Zn <sub>0.4</sub> Fe <sub>2.6</sub> O <sub>4</sub> nanoparticles.....	210
II.2.1.	Polymers and solvents-based formulations.....	211
II.2.1.A.	Choice of formulations .....	211
II.2.1.B.	Approach for developing a formulation.....	212
II.2.2.	Comparison between polymers and solvents-based formulations .....	214
II.2.3.	Rheological behavior of PF and SF formulations with nanoparticles .....	216
II.3.	Conclusion .....	219
III.	<i>Printing</i> .....	221
III.1.	The inkjet printer and printing parameters .....	221
III.1.1.	Working principle.....	221
III.1.2.	Operating protocol .....	222
III.1.3.	Printing parameters .....	226
III.2.	Zn <sub>0.4</sub> Fe <sub>2.6</sub> O <sub>4</sub> patterned coatings .....	227
III.2.1.	Effect of the ink formulation on the ejection .....	228
III.2.2.	Effect of the ink formulation on coatings .....	229
III.2.2.A.	PF formulation .....	229
III.2.2.A.a.	Splat .....	229
III.2.2.A.b.	Patterns .....	230
III.2.2.B.	SF formulation .....	233
III.2.2.B.a.	Drying of splats .....	233
III.2.2.B.b.	Patterns .....	236
III.2.2.C.	Conclusion .....	238
III.2.3.	Printing with 8 wt% of SP(F)M particles.....	239
III.3.	Conclusion .....	241
CHAPTER IV. MAGNETIC CHARACTERIZATIONS AT DIFFERENT SCALES.....		248
I.	<i>Introduction</i> .....	248
II.	<i>Static magnetic characterizations</i> .....	249
II.1.	Experimental techniques .....	249
II.2.	Static magnetic properties of nanoparticles .....	250
II.2.1.	FM and SP(F)M particles .....	250
II.2.2.	Comparison with the literature .....	254
II.2.3.	Effect of the inversion degree in the spinel structure .....	257

II.2.4.	Effect of the thermal treatment .....	258
II.2.5.	Molecular fields models applied to Zn substituted magnetite .....	261
II.2.5.A.	Choice of a molecular field model .....	261
II.2.5.A.a.	The Néel model.....	261
II.2.5.A.b.	The random localized canting model of Bercoff .....	262
II.2.5.A.c.	The generalized Dionne model of superexchange dilution .....	264
II.2.5.A.d.	Comparison of these molecular fields models .....	266
II.2.5.B.	Modeling the magnetic moment of Zn substituted maghemite with the help of the Bercoff molecular field data.....	266
II.2.5.B.a.	Ni <sub>(1-z)</sub> Zn <sub>z</sub> Fe <sub>2</sub> O <sub>4</sub> ferrites .....	266
II.2.5.B.b.	Application to Zn substituted magnetite .....	268
II.2.5.B.c.	Extension to Zn fraction in both tetrahedral and octahedral sites.....	270
II.2.5.B.d.	From magnetite to maghemite magnetic moment .....	272
II.2.5.B.e.	Interpretation of measured magnetic moments of SP(F)M and FM nanoparticles .....	274
II.2.6.	Conclusion .....	279
II.3.	Static magnetic properties of continuous coatings.....	281
II.3.1.	Influence of the number of particle cleanings .....	281
II.3.2.	Effect of the thermal treatment .....	282
II.3.3.	Conclusion .....	286
III.	<i>Dynamic magnetic and dielectric characterizations</i> .....	287
III.1.	Experimental techniques .....	287
III.2.	At the nanoparticle scale .....	288
III.2.1.	At room temperature .....	288
III.2.1.A.	Permittivity measurements .....	288
III.2.1.B.	Permeability measurements.....	289
III.2.1.B.a.	Different compositions .....	290
III.2.1.B.b.	FM and SP(F)M particles.....	292
III.2.1.C.	Conclusion .....	293
III.2.2.	Study of the permeability at various temperatures.....	293
III.2.2.A.	FM particles .....	294
III.2.2.B.	SP(F)M particles .....	294
III.2.3.	Interpretation through a dynamic susceptibility model .....	296
III.2.3.A.	Value of the anisotropy constant K .....	297
III.2.3.B.	Influence of $\sigma$ : the ratio between the magnetic anisotropy energy and the thermal energy .....	301
III.2.3.C.	Influence of the damping parameter $\alpha$ .....	302
III.2.3.D.	Effect of the size distribution .....	303
III.2.3.E.	Effect of the anisotropy constant K and the saturation magnetization M <sub>s</sub> .....	306
III.2.3.E.a.	K and M <sub>s</sub> independent of the temperature.....	306
III.2.3.E.b.	Temperature dependence of K and M <sub>s</sub> .....	307
III.2.3.F.	Conclusion.....	309
III.3.	Continuous coatings .....	309
IV.	<i>Conclusion</i> .....	311
<b>GENERAL CONCLUSION .....</b>		<b>320</b>
<b>TABLE OF FIGURES.....</b>		<b>325</b>



# Remerciements

Je tiens tout d'abord à remercier Lise-Marie Lacroix et Michael Farle de l'honneur qu'ils m'ont fait en acceptant de rapporter ce travail de thèse. Je remercie également Sylvie Bégin, Grégoire de Loubens et Nicolas Vukadinovic d'avoir bien voulu faire partie de ce jury de thèse.

J'adresse mes remerciements à mes deux Directeurs de thèse, André Thiaville et Clément Sanchez. Merci pour tous les conseils donnés au fil de ces trois années. Vos expertises dans vos domaines respectifs ont été très complémentaires et m'ont apporté beaucoup.

Je remercie la Direction du CEA Le Ripault de m'avoir accueilli au sein de ses unités pendant ces trois années de thèse.

Mes remerciements vont également au chef de laboratoire, ainsi qu'au chef de service qui m'ont accueilli à l'échelle du laboratoire et du service.

Je tiens tout particulièrement à exprimer ma reconnaissance à Anne-Lise Adenot-Engelvin, qui a encadré mes travaux de thèse. Merci pour ton implication et ton soutien sans faille pendant ces trois ans. Je tiens aussi à remercier Christophe Boscher pour toute l'aide apportée sur le terrain. Tu as toujours été là quand j'en avais besoin.

J'exprime aussi ma gratitude envers Christophe Lefevre, Jean-Marc Grenèche, Jose Maria Gonzalez Calbet, et Maria Luisa Ruiz Gonzalez qui ont chacun réalisé des caractérisations microstructurales sur mes échantillons. Ces collaborations ont apporté énormément pour la compréhension du matériau synthétisé.

Merci aussi à Jean-Louis Longuet, Matthieu Junca, et Thierry Piquerot pour le temps que vous m'avez consacré pour me former sur les différents appareils (Microscopie Electronique en Transmission, Microscopie à Balayage, Diffraction des Rayons X, four tubulaire sous argon).

Enfin, je suis reconnaissante envers toutes les personnes ayant collaboré à mes travaux de thèse ainsi qu'à l'ensemble du personnel du laboratoire pour leur accueil, leur aide, leur disponibilité et leur sympathie. Une pensée pour toi, Catherine, que j'ai beaucoup sollicité pour les démarches administratives. Merci de ta patience.

Merci Karim, Karine et Jean-Hugues pour les mesures hyperfréquences. Ce fut agréable de travailler à vos côtés.

Mes profonds remerciements vont à Yves, Charlotte, Luc, Sébastien, Frédéric, Joffrey, Michaël, Olivier, Hervé et Jean-Luc. Vous avez illuminé ces trois années. Merci pour votre soutien, votre dynamisme, vos conseils, pour tous ces moments passés à vos côtés,

professionnellement, sportivement et personnellement. C'est une réelle chance que de vous avoir rencontré et je la mesure.

Un grand merci aux stagiaires qui m'ont aidé à achever mes travaux : Tom Rapeau, Tom Rautureau et Julie. Grâce à vous j'ai pu me centrer pleinement sur la rédaction du manuscrit ces derniers mois.

Ces trois ans ont aussi été marqués de belles rencontres : Agathe, Alexis, Amira, Audrey, Colin, Geoffroy, Marjorie, Jérémy, Jean-Louis, Julien, Juliette, Louis, Marc, Maxime, Samy, Thomas, Vincent F, Vincent G... Merci à tous pour les bons moments partagés au travail et en dehors. Je vous souhaite le meilleur pour la suite et bon courage aux prochains thésards. Je sais que vous ferez des choses incroyables.

Mymy, Jérémy, et Alex, merci d'avoir été présents durant cette épreuve.

Enfin, j'adresse mes plus sincères remerciements à ma famille pour son soutien indéfectible durant toute ma scolarité. Maman, Papa, Manon, Thibaud, Brieux, j'ai enfin réussi et j'espère que vous serez fiers.

Une reconnaissance toute particulière à toi aussi, Ismaïl. Merci pour ton soutien, ta patience et ton aide dans la gestion du quotidien pendant ces mois de rédaction.

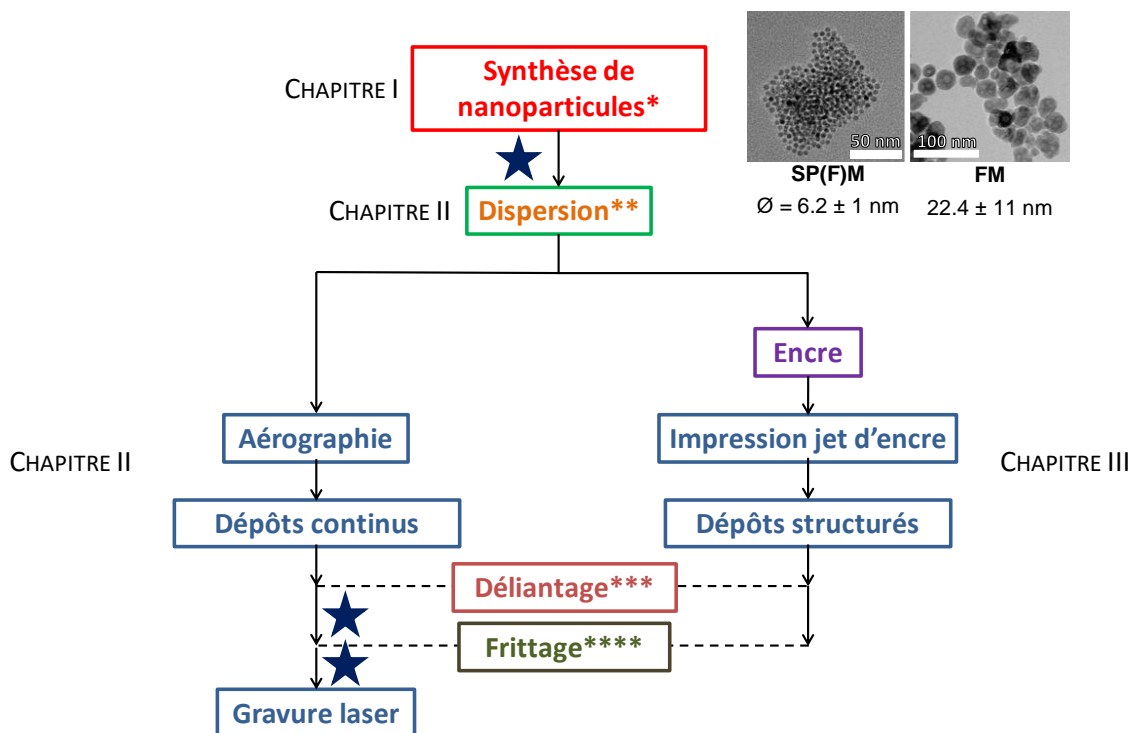
Une pensée aussi à mon grand-père, décédé en début d'année et qui je pense, aurait été fier.



# Résumé long

L'objectif de ces travaux de thèse est la réalisation de nouveaux matériaux aux propriétés magnétiques parfaitement contrôlées pour des applications électromagnétiques de types antennes RFID, stockage de données, transmission de puissance sans fil, absorbants radars... Le contrôle des pertes magnétiques de ces matériaux à des fréquences d'intérêt passe par l'élaboration de réseaux de micro-motifs d'oxydes magnétiques par voie liquide. Le principe repose sur l'élaboration d'une structure organisée en motifs ou domaines magnétiques définie par des caractéristiques géométriques (taille des motifs, rapport de forme, distance entre motifs). La réponse magnétique en perméabilité de tels matériaux est strictement liée aux contributions des domaines et des parois formés, donnant naissance à un matériau dit « multi-bandes » au regard des pics distincts et séparés observés sur son spectre de perméabilité. L'objectif est ainsi de pouvoir piloter les pertes magnétiques d'un matériau via sa structuration en motifs et leurs caractéristiques géométriques.

Deux techniques de réalisation de dépôts structurés à partir d'une dispersion de particules magnétiques sont étudiées : en premier lieu le dépôt d'une couche continue à l'aérographe nécessitant une gravure laser pour l'obtention des motifs, et dans un second temps le dépôt de motifs par impression jet d'encre. Les différentes étapes de mise en œuvre de ces dépôts sont résumées dans le schéma ci-dessous :



\*Décomposition thermique au micro-ondes : tailles et morphologies contrôlées

\*\*Dispersion organique dans l'hexane

\*\*\*Élimination des organiques résiduels

\*\*\*\* Densification, réduction de la porosité

★ Caractérisations magnétiques (CHAPTER IV)

La famille de matériaux sélectionnée pour la synthèse de nanoparticules est un ferrite spinelle de zinc. La composition du matériau est fixée à  $Zn_{0.4}Fe_{2.6}O_4$  afin de combiner à la fois une aimantation à saturation forte, mais aussi une permittivité diélectrique faible pour permettre une bonne pénétration de l'onde électromagnétique dans le dépôt final. Deux gammes de tailles de nanoparticules sont principalement visées dans le but d'analyser leur influence sur la structure et sur les propriétés magnétiques du dépôt. Ainsi, des nanoparticules superparamagnétiques de diamètre inférieur à 20 nm, la limite superparamagnétique, sont synthétisées ainsi que des particules de taille supérieure à la limite superparamagnétique (diamètre compris entre 20 et 1  $\mu\text{m}$ ).

Les nanoparticules sont synthétisées en milieu organique par décomposition thermique. Deux alternatives possibles de chauffage pour cette synthèse sont comparées : d'un côté la voie classique en chauffage conventionnel en chauffe-ballon, et de l'autre côté la voie micro-ondes. La voie conventionnelle permet d'obtenir des nanoparticules avec des morphologies variées (cubes, octaèdres) par un ajustement des paramètres de synthèse tels que les rampes de température, les durées de palier, les ratios entre précurseurs et surfactants. Néanmoins, cette technique de chauffe génère des gradients de température au sein même du mélange réactionnel, ce qui induit une grande polydispersité des particules au niveau de la taille et de la morphologie. Face à ces difficultés, la voie micro-ondes est plus adaptée puisqu'elle permet un chauffage plus homogène et la reproductibilité entre synthèses est améliorée. Cette dernière voie est gardée pour la suite de l'étude avec l'élaboration de nanoparticules superparamagnétiques (notées SP(F)M) sphériques et uniformes de diamètres de  $6.2 \pm 1$  nm, et ferrimagnétiques (notées FM) de diamètres de  $22.4 \pm 11$  nm avec une morphologie atypique de « framboise ». En effet, ces structures « framboises » sont des recolllements de cristallites plus petites avec une continuité entre plans cristallins d'une cristallite à une autre. Ces particules présentent une distribution en taille beaucoup plus large que les particules SP(F)M due à leur morphologie particulière.

Une étude paramétrique de la décomposition thermique en voie micro-ondes est effectuée afin de déterminer le rôle et l'influence de chacun des réactifs dans la synthèse. Ainsi, deux surfactants sont utilisés, l'oleylamine (OAm) et l'acide oléique (OA), avec des rôles bien distincts. L'OA favorise la croissance des particules selon un axe préférentiel tandis que l'OAm l'inhibe. Il est donc possible de contrôler la morphologie des particules en jouant sur le ratio OAm/OA. Des particules sphériques sont obtenues avec un ratio proche de un. L'octadecène (ODE) sert à homogénéiser le mélange. L'éthylène glycol (EG) fait croître les particules dans une certaine limite. En effet, au-dessus d'une certaine quantité d'EG, la tendance s'inverse et la taille des particules diminue avec la formation d'impuretés.

La microstructure des particules est caractérisée par spectroscopie infrarouge (FTIR), diffraction des rayons X (DRX) affinée avec une analyse Rietveld, microscopie à très haute résolution (HAADF-STEM), et spectroscopie Mössbauer. Ces analyses sont réalisées sur les particules SP(F)M ainsi que sur deux échantillons de particules FM avec deux taux de zinc différents : 0.2, et 0.4. Le recoupement de ces diverses techniques met en évidence une oxydation des particules, plus conséquente pour les particules SP(F)M que FM. Par conséquent, les particules peuvent être assimilées à des structures de type cœur/coquille avec un cœur constitué de ferrite spinelle de zinc et une surface oxydée de maghémite substituée au zinc.

Cette hypothèse est nécessaire à la bonne interprétation des propriétés magnétiques des particules. De plus, la DRX couplée à la spectroscopie Mössbauer a permis de détecter une proportion de zinc sur les sites octaédriques de la maille spinelle, appelée plus communément degré d'inversion du spinelle, ce qui impacte aussi les propriétés magnétiques des particules.

Par ailleurs, la composition chimique des particules est homogène à grande échelle (ICP-AES), mais aussi localement (SEM-EDX).

Des dispersions stables à partir de ces nanoparticules sont ensuite mises au point : soit par formulation dans un solvant organique, soit dans un solvant aqueux. Après synthèse et préalablement à la dispersion, les particules passent par un processus de lavage qui vise à éliminer les organiques résiduels provenant de la synthèse. En effet, une fois synthétisées, les particules sont recouvertes d'une pellicule d'organique en surface due à l'utilisation de surfactants organiques (OAm et OA). Une dualité s'inscrit autour de cette couche d'organique. En effet, elle se révèle particulièrement utile pour stabiliser les nanoparticules dans un milieu adéquat en les empêchant de s'agréger entre elles ou de sédimenter. A l'inverse, cette couche étant non magnétique, elle inhibera fortement les propriétés magnétiques des particules et par la suite des dépôts. Il est donc nécessaire de trouver un compromis lors des lavages afin de réduire cette couche d'organique pour apporter une aimantation suffisante aux particules, mais aussi afin de permettre leur dispersion en milieu liquide. Différentes méthodes de lavages sont étudiées : les lavages par centrifugation, reflux, estérification, et par montage Soxhlet. Les lavages par centrifugation sont retenus par rapport à leur efficacité et rapidité d'exécution.

Une fois lavées, les particules sont dispersées directement en milieu organique dans l'hexane. La dispersion est rendue possible par encombrement stérique grâce aux chaînes hydrocarbonées non polaires de l'OA qui ont une bonne affinité avec l'hexane et qui sont adsorbées à la surface des particules par l'intermédiaire d'une tête carboxylique. Quant au rôle de l'OAm, ce surfactant agit comme une base de Lewis et régule le pH du milieu par absorption des protons générés par le greffage de l'OA à la surface de la particule. La surface de la particule serait alors uniquement recouverte par les groupements de l'OA et son épaisseur est estimée à approximativement une couche de carboxylates. Des dispersions stables sont réalisées avec 8 %m de particules SP(F)M, et FM, séparément. Un transfert de la dispersion organique en milieu aqueux s'est avéré concluant avec les particules SP(F)M par le biais d'un agent de transfert : l'oléate de sodium. Néanmoins, la dispersion aqueuse est écartée pour la suite de l'étude, car l'agent utilisé pour la dispersion mousse beaucoup, ce qui risque de perturber la mise en œuvre des dépôts que ce soit par aérographie ou impression jet d'encre. D'autre part, elle reste difficile à adapter sur les plus grosses particules (FM).

Des dépôts continus sont dans un premier temps réalisés par aérographie à partir des dispersions de particules SP(F)M et FM dans l'hexane. Cette technique de mise en œuvre repose sur la nébulisation d'un liquide à travers une buse sous l'impulsion d'air comprimé. Elle est assimilée à du spray.

Une fois mis en forme, les dépôts sont traités thermiquement sous argon à travers deux étapes. Le traitement sous argon se révèle essentiel pour éviter l'oxydation des couches sous air. Les dépôts sont d'abord déliantés à 450 °C pour éliminer les organiques résiduels provenant de la dispersion des particules dans l'hexane. Puis, ils sont frittés dans un second temps à 770

°C, l'objectif étant de diminuer la porosité du matériau final en resserrant les grains après départ des organiques au déliantage, et en densifiant la couche. Ce traitement thermique génère d'importantes contraintes dans les films déposés. Les dépôts réalisés à partir de particules SP(F)M fissurent et se décollent complètement du substrat par endroits dès déliantage, tandis que ceux constitués de particules FM fissurent au moment du frittage. Pour comprendre ces mécanismes de fissuration, une étude de la dégradation des organiques en température est menée par des analyses thermogravimétriques couplées à de la spectrométrie de masse sur les particules et par de la DRX en température sur particules et dépôts.

Ces analyses mettent en évidence un départ des organiques à partir de 300 °C et jusqu'à 600 °C. Les groupements de l'OAm se dégradent en premier dès 300 °C. L'OA se décompose en deux temps avec un départ de sa chaîne hydrocarbonée à 300 °C puis de son groupement carboxylique à 350 °C. Le groupement carboxylique est plus difficile à éliminer car il est chimiquement adsorbé à la surface de la particule. De plus, la dégradation thermique des résidus carbonés à la surface de la particule engendre leur réduction à plus haute température lors du frittage. Une phase de wüstite dopée au zinc est déterminée aux rayons X. L'hypothèse de particules constituées d'une phase spinelle d'oxyde de fer et de zinc à cœur et d'une couche de wüstite de zinc en surface est établie.

La dégradation progressive des organiques, ainsi que l'apparition de cette phase secondaire de wüstite de zinc occasionnent des contraintes dans les dépôts et provoquent donc de la fissuration et /ou perte de matière dans certains cas. Différentes stratégies pour réduire ces effets de fissuration sont examinées sans qu'aucune n'ait apporté d'amélioration.

Le meilleur dépôt fritté avec des particules FM présente un taux de porosité de 50 %. Néanmoins, un test de faisabilité de gravure laser de motifs sur une couche déliantée et sur une couche frittée est mis en œuvre. Il s'avère que la gravure doit impérativement se faire sur couches frittées afin de garder une bonne adhérence de la couche sur le substrat après gravure.

Le procédé d'aérogographie est transféré et adapté pour de l'élaboration de motifs directement par voie jet d'encre. Il s'agit d'un procédé innovant qui permet la réalisation de motifs 2D ou 3D par éjection de gouttes successives via des buses piézoélectriques. L'avantage de cette technique est qu'elle ne nécessite pas de traitement post dépôt pour générer des motifs. En revanche, la dispersion de particules préalablement stabilisées dans l'hexane doit être reformulée dans le but d'obtenir une encre éjectable et compatible avec les spécificités requises par la machine d'impression jet d'encre. Ainsi, la viscosité et la tension de surface du mélange doivent respecter des gammes imposées par la machine. Le rapport d'éjection, fonction de la viscosité et de la tension de surface, est un facteur adimensionnel prépondérant qui définit le caractère éjectable d'une encre. Il doit être compris entre 1 et 10.

Deux encres organiques respectant ces prérequis sont élaborées à partir des particules SP(F)M : une encre à base de polymères avec un mélange de poly(1-decene) et d'hexane, et une encre à base de solvants avec un mélange d'octanol et d'hexane.

Les deux encres sont éjectables et permettent la réalisation de motifs carrés de 500 µm de largeur. La solution à base de polymères est désavantageuse du fait de sa formulation qui présente une tension de surface et une viscosité plus basse que celles de la formulation à base de solvants. Elle induit donc un fort nappage de la plaque à buses qui déstabilise l'éjection de l'encre pendant l'impression et pourrait amener à l'obtention de motifs de moins bonne qualité.

D'autre part, cette encre est constituée d'une majorité de polymère en comparaison avec la quantité d'hexane, ce qui nécessite un recuit à haute température post dépôt différent de celui optimisé pour l'aérogaphie, et qui générera d'autant plus de porosité dans la couche. Pour ces raisons, l'encre à base de solvants est plus adaptée même si la qualité des motifs finaux n'est pas meilleure. En effet, cette formulation a l'avantage de sécher très rapidement sur le substrat, au détriment de phénomènes parasites tel que l'effet « coffee-ring ». Si les résultats sont encourageants et démontrent la faisabilité du procédé, cette dernière formulation peut encore être améliorée pour palier à cet effet.

Cependant, des étapes de déliantage et de frittage similaires aux dépôts réalisés par aérogaphie sont requises pour les dépôts jet d'encre afin d'éliminer les éventuels organiques et de densifier les motifs. Les mêmes problématiques de fissuration seront donc rencontrées. Des voies d'amélioration au niveau du procédé de mise en œuvre des films ainsi que du traitement thermique sont discutées et pourraient être envisagées. Par exemple, l'élaboration de films en partant d'une technique de spray de solutions de précurseurs sur un spinner chauffant ou par voie jet d'encre avec un plateau chauffant, la fabrication de films denses par voie micro-ondes sans post traitement thermique requis, et le frittage laser de dépôts (aérogaphie ou jet d'encre) pour de la fissuration contrôlée.

Les propriétés magnétiques des particules et des dépôts réalisés par aérogaphie sont étudiées. Le lien est établi entre la microstructure du matériau et ses propriétés magnétiques.

Tout d'abord, l'étude des cycles d'aimantation des particules en fonction du champ appliqué souligne des différences au niveau du comportement magnétique des particules SP(F)M et FM. La courbe d'aimantation des particules SP(F)M ne sature pas sous fort champ alors qu'au contraire elle sature dans le cas des particules FM, ce qui confirme bien le caractère superparamagnétique des particules SP(F)M. Par ailleurs, les aimantations à saturation des particules SP(F)M (85.6 emu/g ou A.m<sup>2</sup>/kg) et FM (80.6 emu/g ou A.m<sup>2</sup>/kg) sont inférieures à celle du massif pour la même composition recensée dans la littérature (98.8 emu/g ou A.m<sup>2</sup>/kg). La réduction de l'aimantation à saturation peut provenir de plusieurs causes : une oxydation de surface des particules, un degré d'inversion de la structure spinelle, du spin-canting à la surface des particules. De plus, les cycles d'aimantation des particules FM recuites à différentes températures sont inspectés. L'aimantation à saturation de ces particules diminue entre 300 et 770 °C. Cette baisse est causée par la formation de wüstite substituée au zinc, préalablement identifiée.

Un modèle de Bercoff corrigé basé sur la théorie du champ moléculaire permet de remonter aux moments magnétiques des particules SP(F)M et FM avec les deux taux de zinc différents (0.2 et 0.4) en faisant différentes hypothèses concernant la microstructure des particules : de l'oxydation de surface, un degré d'inversion de la spinelle et du spin-canting de surface.

A l'échelle des dépôts, l'évolution de l'aimantation à saturation en fonction de la température de recuit est différente de celle observée dans le cas des particules. L'écart se justifie par une différence de réactivité au niveau des poudres et des dépôts lors du traitement thermique. La phase secondaire de wüstite de zinc se forme très rapidement dans le cas d'une poudre non mise en forme, alors qu'elle survient à plus haute température dans le cas d'un dépôt de l'ordre de 6 µm d'épaisseur. Par ailleurs, l'aimantation à saturation d'un dépôt fritté de

particules FM est de 76 emu/g ( $A.m^2/kg$ ), ce qui est prometteur d'autant plus que le dépôt est à 50 % poreux.

La permittivité et perméabilité des particules sont caractérisées et comparées à des poudres commerciales de  $Fe_3O_4$ ,  $CoFe_2O_4$  et  $NiZnFe_2O_4$ . L'introduction de zinc dans la composition du matériau permet bien de réduire sa permittivité en comparaison avec la poudre commerciale de  $Fe_3O_4$ , ce qui renforce le choix de la composition puisque les particules combinent bien une faible permittivité avec une forte aimantation à saturation non loin de celle du bulk.

Les niveaux de perméabilité imaginaire sont affectés par la taille des particules, les particules FM induisant des niveaux de perméabilité beaucoup plus élevés que les particules SP(F)M. Un modèle de Raikher sur la susceptibilité dynamique est appliqué et reproduit avec succès le spectre de perméabilité des particules SP(F)M, de même que la dépendance en température des mesures dynamiques. Pour ce dernier point, le modèle prend en compte la dépendance en température du champ d'anisotropie des particules. Les tendances observées au niveau expérimental sont parfaitement reproduites par le modèle, à savoir : un décalage de la fréquence de résonance vers les hautes fréquences ainsi qu'une hausse des niveaux de perméabilité lors de la diminution en température, de même qu'une diminution de la largeur à mi-hauteur du pic de résonance pour les températures décroissantes. Cette dernière observation doit faire l'objet d'une étude plus approfondie.

Les perméabilités imaginaires des dépôts continus déliantés et frittés avec des particules FM présentent des niveaux trop bas pour pouvoir espérer obtenir un comportement « multi-bandes » après structuration, les dépôts étant fissurés. L'obtention de ce type de spectre de perméabilité requiert l'élaboration d'un dépôt le plus dense possible, qui pourrait être réalisé en prenant en compte les perspectives précédemment énoncées sur de nouveaux procédés de mise en œuvre de dépôts en partant de solutions de précurseurs et/ou une autre technique de frittage.

# Introduction

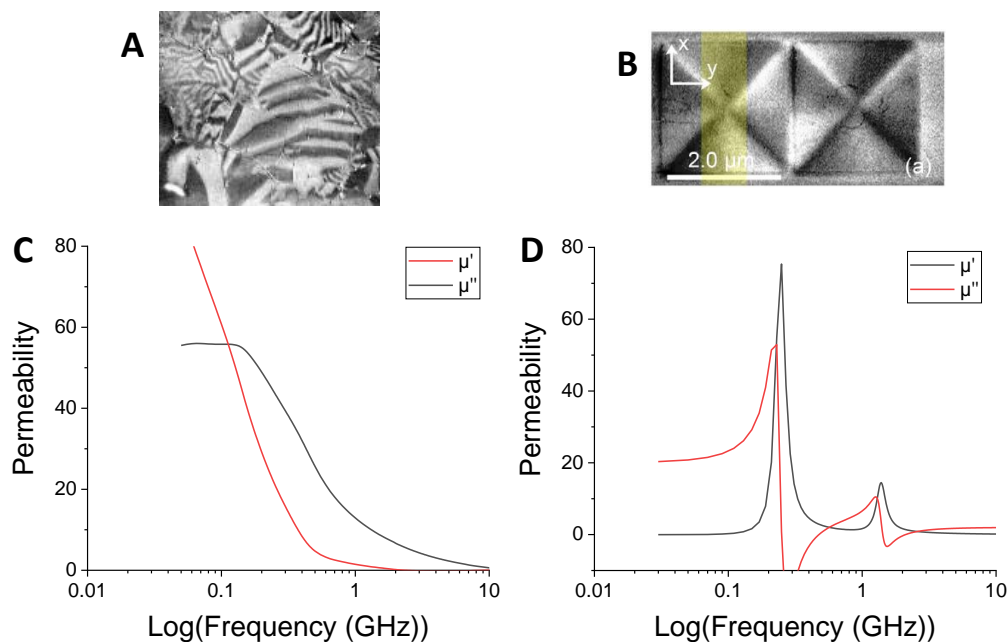
Magnetic iron oxide nanoparticles are employed in a wide range of applications. They are commonly studied for **biomedical applications** like markers for Magnetic Resonance Imaging (MRI), new nanosystems for hyperthermia, or drug delivery carriers due to their low toxicity, and biocompatibility [1]. Their tunable sizes make them perfect candidates to observe or interact locally with entities at the cell scale without damaging healthy tissues [2]. In the case of magnetic hyperthermia, the application of an oscillating magnetic field to the nanoparticles allow them to generate local heat for cancer cells destruction which occurs above 42 °C. The radio-frequency range is usually required to penetrate the tissues in respect of the body. For magnetic hyperthermia, some requirements need to be filled. The particles have to be superparamagnetic with a zero coercivity to avoid the formation of aggregates and thus clots in the venous system. The saturation magnetization should be high enough to allow a sufficient heat of the particles under the applied field [3].

Besides biomedicine, such particles have demonstrated plenty interest in many fields: in **electronics** through magnetic storage media, printed electronics, spintronics, nanowires, quantum dots, carbon nanotubes, nanoelectromechanical systems, and permanent magnets; in **energy** with solar cells, heat distribution through ceramic-like materials, photovoltaic film coatings, fuel cells and batteries; in **defense and aerospace** through nanocomposites, nanocoatings, energy devices, and smart materials; in **environmental remediation** with pollution sensors, water treatment through membrane filtration, permeable barriers; in **construction** with the use of pigments for coloring concrete, tiles, bricks, nanocomposites; and even in **agriculture** through food packaging, nanofertilizers, nanopesticides [4] [5] [6].

Among all of these areas, the present study focuses on **electronics applications**. A high saturation magnetization combined with a high electrical resistivity, low electrical losses and a good chemical stability make iron oxide nanoparticles suitable for designing new magnetic materials for electromagnetic applications, like integrated circuitry, power handling, permanent magnets or magnetic recording. Due to the large panel of possibilities, these applications can be divided in four subgroups: inductors, high frequency, power, and electromagnetic interference suppression applications [7].

**Inductors** consist of low-noise amplifiers, filters, voltage-controlled oscillators, magnetic field sensors in electronic circuits. Multilayered iron oxide materials show a particular interest in the miniaturization and integration of circuits. Some processing methods are adopted to provide a high density and high permeability to the films: sputtering, pulsed laser deposition, tape casting, or a less costly sol-gel technique followed by spin-coating [7]. **High Frequency applications** refer to telecommunications (antennas, circulators in mobile phone) and radars. A complete penetration of the electromagnetic field is required. Non-conductive iron oxide films are more adapted in comparison with metals ones, due to the skin thickness which prevent the total penetration [8]. The third category is about **power applications** for computers, TV, video systems. At last, **electromagnetic interference suppressors** are particularly useful these days with the boom of the number of users of wireless communication devices [7].

The absorption of microwaves in ferrite generate **magnetic losses**. Typically, the **magnetic signature** of a **bulk polycrystalline** ferrite is **wide band** on its permeability spectrum due to its dispersed domain structure affected by the material defects (porosity, grain size distribution, precipitates, grain orientation). This behavior is illustrated in Figure 1.C for a polycrystalline bulk of  $\text{Ni}_{0.5}\text{Zn}_{0.5}\text{Fe}_2\text{O}_4$  composition (Figure 1.C). In this context, the **aim** of this work is to **develop novel materials with perfectly controlled magnetic properties** for the previously described electromagnetic applications. Permeability losses and resonance frequency dependence will define the suitability of a material for an application. The objective is to **tune the magnetic losses of the materials at desired frequencies through the realization of patterned networks of magnetic oxides**. Therefore, it lies on the development of an organized framework in patterns forming magnetic domains, characterized by their geometry, namely pattern size, shape, spacing. The magnetic response of such structures is directly linked to the respective contributions of domains and domain walls. It can be also called “**a multiband**” **magnetic behavior** due to the separate peaks observed on the permeability spectrum. This behavior is exhibited for a metallic alloy structured in magnetic square domains after patterning in Figure 1.D. The magnetic losses are represented by separate absorption bands at different resonance frequencies of vortex, magnetic walls and domains. The magnetic texture is tuned by the geometric parameters of the patterns. The goal is to achieve this kind of behavior with magnetic oxides.



**Figure 1. Examples of a wide band type magnetic behavior of a polycrystalline ferrite (A [9], C), and a multiband one (D) in the case of a structure constituted of squares of permalloy (B) [10]. Permeability versus Log(Frequency) for a polycrystalline bulk  $\text{Ni}_{0.5}\text{Zn}_{0.5}\text{Fe}_2\text{O}_4$  (C) and a perfect square of permalloy ( $150 \times 150 \mu\text{m}^2$ ) (D) [11].**

The system of **zinc iron oxide spinel** is selected for the study. The zinc doping **enhances the saturation magnetization** of ferrite films until a certain amount, and it also provides **insulating properties** to the material, allowing a **good penetration of the electromagnetic wave** in the material, suitable for electromagnetic applications [12].



The ferromagnetic squares of permalloy displayed in Figure 1.B have been realized from a thermal evaporated metallic coating which has been going through an electron-beam lithography technique followed by a lift-off processing. The processes studied in this work are completely different as they are **adapted to oxides**, and **start from the synthesis of nanoparticles**, which will be the material for the elaboration of films by further **fluid processing**. Working with coating processes adapted to oxides has some advantages in comparison with the ones adapted to metals, as these processes are generally low-cost and more easily transferable to large scale.

The **dynamic magnetic response** strictly **depends on the coupling** between particles and on the **particle size**. As a consequence, the range of size of the nanoparticles will be limited to a certain value. Indeed, the transition between magnetic single domain and multi-domain in a particle is linked to the particle size. Above a critical value, the particle is divided in several magnetic domains which display characteristic resonance peaks in the permeability spectrum of the material. These parasitic peaks will disturb the response of the textured material at a larger scale: the scale of pattern. In this case, it will be difficult to control the magnetic losses of the material if it is disturbed by contributions at the particle scale. To avoid the presence of resonance peaks coming from the nanoparticles walls and domains, it is better working with **monodomain particles**. This **limit in size** is fixed at 1  $\mu\text{m}$  considering different critical diameters of particles with compositions close to the desired one: 60 nm for  $\text{Zn}_{0.4}\text{Fe}_{2.6}\text{O}_4$  [13], 80 nm for  $\text{Fe}_3\text{O}_4$  [14], and 3  $\mu\text{m}$  for  $\text{Ni}_{0.49}\text{Zn}_{0.49}\text{Co}_{0.02}\text{Fe}_{1.90}\text{O}_{3.85}$  [15]. Two particular ranges of size will be selected: **superparamagnetic particles** with a diameter **below 20 nm** and **ferrimagnetic ones above 20 nm**.

The manuscript focuses on a **processing method departing from the synthesis of particles to the development of continuous or textured coatings** in order to be able to tune the magnetic losses of coatings through their structuration. The work is divided in **four chapters**:

- The **chapter I** details the context of the study with the **choice of the material** composition and size, and all the magnetism concepts required for the understanding of the study. Different synthesis methods of oxides nanoparticles are described. The **chapter I** also deals with the **synthesis of zinc iron oxide nanoparticles** with a selected route, ensuring a good control of composition, shape and structural properties. The **morphology, chemical composition and microstructure** of these nanoparticles will be deeply investigated through a wide variety of characterization techniques: X-ray diffraction analysis, high resolution microscopy, Mössbauer spectroscopy...
- The **chapter II** focuses on the **stabilization** of the previously synthesized magnetic particles in a **suitable liquid medium**, and on the **development of continuous coatings** through a **spray-like technique**: the airbrushing. The thermal treatment and resultant microstructure of coatings is investigated. The feasibility of patterning through laser etching is examined.

- A technologic **transfer** of the airbrushing to a more innovative and automatized process, the **inkjet printing**, is described in **chapter III**. The **formulation of compatible inks** from a particle dispersion is studied. A previous work has shown the interest of inkjet printing for **elaborating well-controlled patterned coatings for electromagnetic applications** [16].
- At last, the **chapter IV** exposes the **static and dynamic magnetic characterizations** at the nanoparticle and coating scale. Different models are studied in order to retrieve the experimental results and to understand the **link between microstructure and magnetic properties**. This last chapter allows to **conclude about the choice of the overall process** for the obtention of a multiband material.

## Introduction references:

- [1] Y. Xiao and J. Du, "Superparamagnetic nanoparticles for biomedical applications," *J. Mater. Chem. B*, vol. 8, no. 3, pp. 354–367, 2020, doi: 10.1039/C9TB01955C.
- [2] Gubin, *Magnetic Nanoparticles*, Wiley-VCH. 2009.
- [3] M. Bañobre-López, A. Teijeiro, and J. Rivas, "Magnetic nanoparticle-based hyperthermia for cancer treatment," *Rep. Pract. Oncol. Radiother.*, vol. 18, no. 6, pp. 397–400, Nov. 2013, doi: 10.1016/j.rpor.2013.09.011.
- [4] N. Ajinkya, X. Yu, P. Kaithal, H. Luo, P. Somani, and S. Ramakrishna, "Magnetic Iron Oxide Nanoparticle (IONP) Synthesis to Applications: Present and Future," *Materials*, vol. 13, no. 20, p. 4644, Oct. 2020, doi: 10.3390/ma13204644.
- [5] A. Ali *et al.*, "Synthesis, characterization, applications, and challenges of iron oxide nanoparticles," *Nanotechnol. Sci. Appl.*, vol. Volume 9, pp. 49–67, Aug. 2016, doi: 10.2147/NSA.S99986.
- [6] A. S. Teja and P.-Y. Koh, "Synthesis, properties, and applications of magnetic iron oxide nanoparticles," *Prog. Cryst. Growth Charact. Mater.*, vol. 55, no. 1–2, pp. 22–45, Mar. 2009, doi: 10.1016/j.pcrysgrow.2008.08.003.
- [7] R. Valenzuela, "Novel Applications of Ferrites," *Phys. Res. Int.*, vol. 2012, pp. 1–9, 2012, doi: 10.1155/2012/591839.
- [8] M. Pardavi-Horvath, "Microwave applications of soft ferrites," *J. Magn. Magn. Mater.*, vol. 215–216, pp. 171–183, Jun. 2000, doi: 10.1016/S0304-8853(00)00106-2.
- [9] A. Hubert and R. Schäfer, *Magnetic domains: the analysis of magnetic microstructures*. 1998.
- [10] A. Vogel *et al.*, "Coupled Vortex Oscillations in Spatially Separated Permalloy Squares," *Phys. Rev. Lett.*, vol. 106, no. 13, p. 137201, Mar. 2011, doi: 10.1103/PhysRevLett.106.137201.
- [11] J. Neige, "Élaboration, caractérisation et modélisation d'un composite à base de pétales ferromagnétiques pour des applications hyperfréquences," Thesis, Tours, 2013.
- [12] A. Fujiwara, M. Tada, T. Nakagawa, and M. Abe, "Permeability and electric resistivity of spin-sprayed Zn ferrite films for high-frequency device applications," *J. Magn. Magn. Mater.*, vol. 320, no. 8, pp. L67–L69, Apr. 2008, doi: 10.1016/j.jmmm.2007.11.026.
- [13] S. Noh *et al.*, "Nanoscale Magnetism Control via Surface and Exchange Anisotropy for Optimized Ferrimagnetic Hysteresis," *Nano Lett.*, vol. 12, no. 7, pp. 3716–3721, Jul. 2012, doi: 10.1021/nl301499u.
- [14] Q. Li, C. W. Kartikowati, S. Horie, T. Ogi, T. Iwaki, and K. Okuyama, "Correlation between particle size/domain structure and magnetic properties of highly crystalline Fe<sub>3</sub>O<sub>4</sub> nanoparticles," *Sci. Rep.*, vol. 7, no. 1, p. 9894, Dec. 2017, doi: 10.1038/s41598-017-09897-5.
- [15] P. J. van der Zaag, P. J. van der Valk, and M. Th. Rekveldt, "A domain size effect in the magnetic hysteresis of NiZn-ferrites," *Appl. Phys. Lett.*, vol. 69, no. 19, pp. 2927–2929, Nov. 1996, doi: 10.1063/1.117326.
- [16] E. Saleh *et al.*, "3D inkjet-printed UV-curable inks for multi-functional electromagnetic applications," *Addit. Manuf.*, vol. 13, pp. 143–148, Jan. 2017, doi: 10.1016/j.addma.2016.10.002.



# Chapter I. Elaboration of iron oxide spinel nanoparticles

This chapter deals with the choice of the composition of the iron oxide spinel and the elaboration process of the nanoparticles based on a bibliographic analysis. A comprehensive study of nanoparticles morphology, chemical composition and microstructure is exposed to optimize the elaboration parameters to the needs. A detailed analysis of in-depth structural characterization of the spinel inversion degree of the optimized elaboration method is then performed. The magnetic properties will be described in details in chapter IV.

## I. The iron oxide spinel system

This first part consists in a bibliographical outlook of the two major magnetic oxides spinels to which it will be often referred in results interpretation.

### I.1. Magnetite and maghemite

#### I.1.1. Crystal structure

Magnetite  $\text{Fe}_3\text{O}_4$  and maghemite  $\gamma\text{-Fe}_2\text{O}_3$  possess a spinel structure following the general chemical formula  $\text{AB}_2\text{X}_4$  with A and B the cations and X the anions. These structures crystallize in the cubic system belonging to the space group  $\text{Fd}\bar{3}\text{m}$ . The crystalline cell is constituted of 32 oxygen atoms which arrange in a face-centered cubic (FCC) cell with 64 tetrahedral and 32 octahedral sites partially occupied. Indeed, only one eighth of the tetrahedral sites (A sites) and half of the octahedral one (B sites) are filled in the structure (Figure I-1).

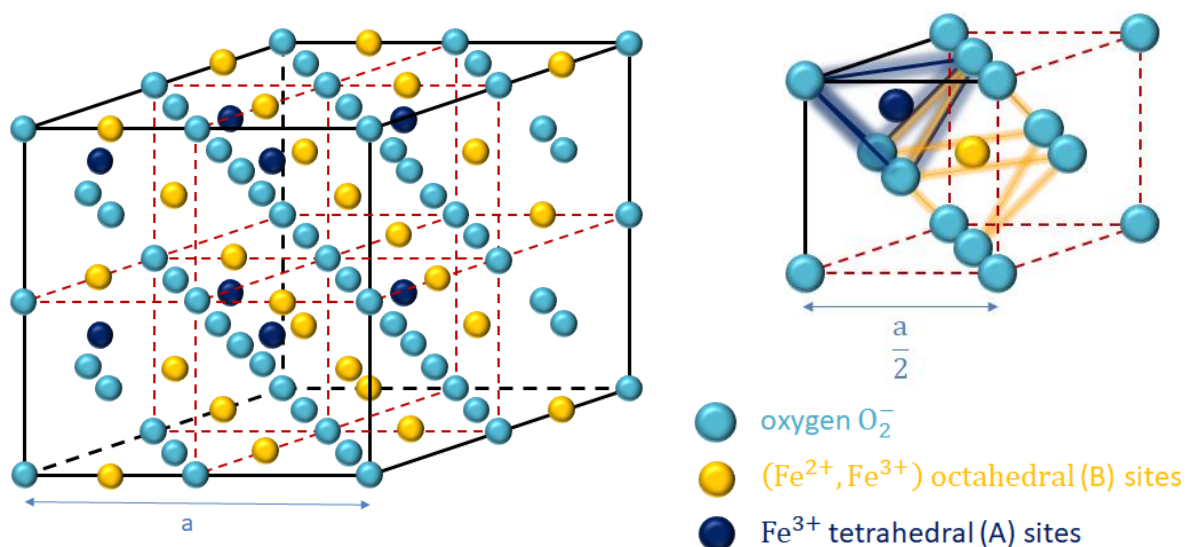
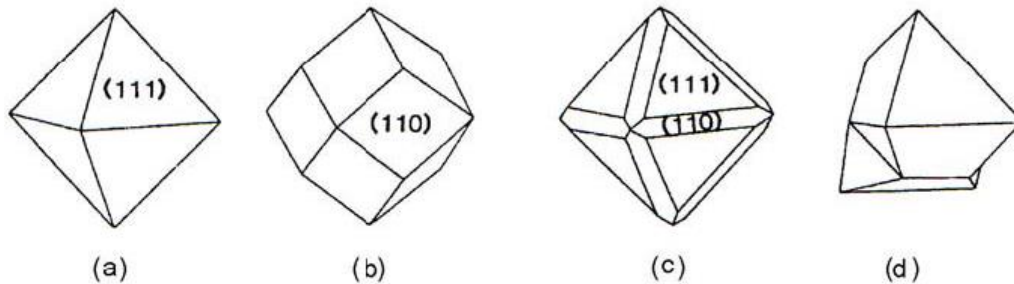


Figure I-1. Basic mesh for the spinel structure [1] [2].

Each octahedron is linked to six other octahedra by the sides and also to six tetrahedra by the tops. In the same way, each tetrahedron is connected to twelve octahedra by its four corners. One oxygen atom sees four iron atoms in its surroundings: one in a tetrahedral site, the three others in octahedra. The most commonly encountered macroscopic shapes of magnetite crystals are presented in Figure I-2 with the crystallographic planes (111) and (110).



**Figure I-2. Most commonly crystal shapes encountered for magnetite phase: octahedral (a-c), and twinned (d) [3].**

There are different spinel configurations depending on the cation distribution on the tetrahedral and octahedral sites. In fact, spinels could arrange in inverse or normal configurations following the general formula below with M for a metallic cation:



with  $\delta$  called the degree of inversion (round and square brackets for tetrahedral and octahedral sites respectively). If  $\delta$  is equal to 0, the spinel is called normal. When  $\delta = 1$ , the spinel is inverse [4].

Magnetite is a mixed oxide comprising  $\text{Fe}^{2+}$  and  $\text{Fe}^{3+}$  with an inverse spinel structure  $(\text{Fe}^{3+})_{\text{Td}}[\text{Fe}^{3+} \text{Fe}^{2+}]_{\text{Oc}}\text{O}_4$  [5]. Tetrahedral sites are only filled with half of trivalent cations whereas the octahedral sites are occupied by the remaining trivalent cations and all of the divalent one [6]. Magnetite possesses a lattice parameter of about 8.393 Å (PDF sheet 04-009-2284) at room temperature.

In the case of maghemite  $\gamma\text{-Fe}_2\text{O}_3$  which is the oxidized form of magnetite, all of the iron cations are in the trivalent oxidation state. Thus, this iron oxide phase shows cationic vacancies in the octahedral sites noted  $\square$  which can organize in three different manners:

- at first with a randomly distribution without inducing mesh distortion. The space group  $\text{Fd}\bar{3}\text{m}$  is preserved. The new structure follows the formula below:  $(\text{Fe}^{3+})[\text{Fe}^{3+}_{5/3}\square_{1/3}]\text{O}_4^{2-}$ . The occupancy rate is about 5/6 and all of the configurations are similar [7].
- Secondly with a partial order on the octahedral sites [8]. This configuration also doesn't generate distortion in the network. However, the space group changes into  $\text{P}4_1\bar{3}2$ . The structure is therefore written:  $(\text{Fe}_8^{3+})[\text{Fe}_{4/3}^{3+}\square_{8/3}\text{Fe}_{12}^{3+}]\text{O}_{32}^{2-}$ . In fact, it is exactly the case of the  $\text{Li}^+$  cation inside  $(\text{Fe}_8)[\text{Li}_4\text{Fe}_{12}]\text{O}_{32}$  structure.

- And lastly, in a completely ordered way. It leads to the obtention of a tetragonal mesh with a space group  $P4_32_12$ .

Magnetite and maghemite possess close structures which can be distinguished from one another by:

- retrieval of their lattice parameter from XRD diffractometer: 8.393 Å (PDF sheet 04-009-2284) for magnetite and 8.351 Å (PDF sheet 00-039-1346) for maghemite).
- infrared spectroscopy since, magnetite and maghemite have different responses at specified wavenumber bands. More precisely, pure magnetite exhibits a single band between 580 and 590  $\text{cm}^{-1}$ . On the contrary, multiple bands have been found for the maghemite phase between 500 and 800  $\text{cm}^{-1}$  [9] [2].
- Mössbauer spectroscopy through the isomeric shift [10]. This technique is sensitive to the oxidation degree of iron atoms, and also to the ratio between  $\text{Fe}^{2+}$  and  $\text{Fe}^{3+}$ .
- Raman spectroscopy.

The next two paragraphs will introduce some basic principles in the field of magnetism and then focus on the magnetic properties applied to magnetite and maghemite.

### I.1.2. Magnetism basics

The basic concepts described in this part introduce notions of both macroscopic static and dynamic properties used in chapter IV in which experimental magnetic characterizations will be analyzed at the particle and thin film scale (macroscopic scale). The link between the macroscopic properties with the atomic scale magnetism is presented since it is relevant to understand the effects of chemical composition and structural disorder.

#### I.1.2.A. Magnetism at the macroscopic scale

The elementary unit of magnetism is defined by a magnetic dipole with a moment  $m$  ( $\text{A}\cdot\text{m}^2$ ) called the magnetic moment [11]. This vector quantity reflects the alignment of a solid body subjected to a magnetic field. It is linked to the angular momentum as detailed in section I.1.2.E. In the case of a solid body constituted of atoms, the attributed magnetization  $\vec{M}$  ( $\text{A}/\text{m}$ ) is written  $\frac{1}{V}\sum \vec{m}$ , defined as the addition of the magnetic moments per unit volume inside the material.

Therefore, to align all of the magnetic dipoles in a solid body, a magnetic field  $H$  ( $\text{A}/\text{m}$ ) could be applied. Thus, the magnetization  $M$  is considered as a result of this dipole alignment, and gives birth to the magnetic susceptibility  $\chi_m = \frac{M}{H}$  which is the ability of a material to magnetize when subjected to a magnetic field.

At this stage, the global magnetic field  $B$  ( $T$ ) also called the magnetic induction could be described as the vector sum of the contributions of the magnetic field  $H$  and the magnetization  $M$ , as follows:  $B = \mu_0(H + M)$  with  $\mu_0$  the permeability of free space equal to  $4\pi \times 10^{-7} \text{ Wb}/\text{Am}$ .

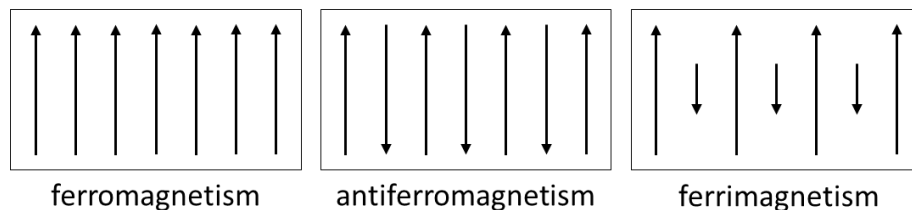
$\mu_0 H$  and  $\mu_0 M$  are the magnetic induction in free space and the part of induction coming from the material magnetization respectively [12].

The concept of bulk susceptibility allows classifying the materials into two categories: materials with a magnetic order below a specified temperature and those without magnetic order.

On the one hand, considering the last category, the interactions between atoms inside the crystalline network are weak. There is no long distance interaction, which results in materials without magnetic order. No spontaneous magnetization is displayed at a macroscopic level, its value is equal to zero without the application of a magnetic field and also even with temperature variation [13]. Two groups of materials match this category:

- Diamagnetic materials with a low and negative susceptibility  $\chi \approx -10^{-5}$ . The magnetization is opposed to the applied magnetic field. For example, it is the case of copper, gold [12]...
- Paramagnetic materials with a low and positive susceptibility  $\chi$  in the range  $10^{-3}$ - $10^{-5}$ . The weak generated magnetization is aligned with the applied magnetic field. For example, aluminum, manganese [12]...

On the other hand, the second category of materials display a long-range ordering of magnetic dipoles which is due to the quantum-mechanical exchange forces [13]. Magnetic moments are ordered in different manners (Figure I-3).



**Figure I-3. Arrangements of magnetic moments for materials with magnetic order**

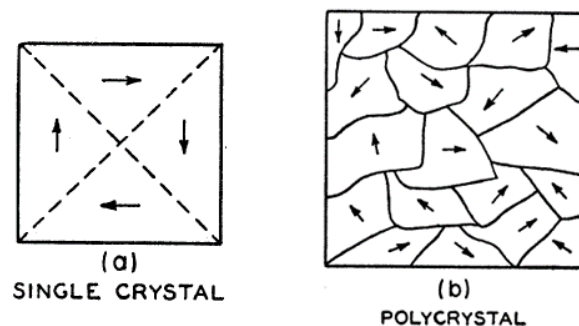
Ferromagnetic materials possess a unique lattice with parallel magnetic moments oriented in the direction of the applied field. Ferrimagnetic and antiferromagnetic materials exhibit an antiparallel configuration of their magnetic moments in two different sublattices. In the case of antiferromagnetism, there is a compensation between the magnetic moments in the sublattices which generate a total magnetization equal to zero. On the contrary, magnetic moments of ferrimagnetic materials are unequal from one lattice to the other, thus leading to non-zero magnetization.

Spontaneous magnetization of materials with magnetic order occurs at zero magnetic field below a specified temperature namely the Curie ( $T_C$ ) or Néel ( $T_N$ ) temperature for ferromagnetic and ferrimagnetic material respectively. Above these temperatures, the material loses its magnetic order and becomes paramagnetic.



### I.1.2.B. Magnetic domains

As mentioned in the last part, above the Curie temperature, the magnetic moments of a ferromagnetic material are randomly distributed. When the temperature decreases, the disordered magnetic moments tend to align until a perfect arrangement is reached below  $T_C$ . This arrangement contains multiple areas or regions in which magnetic moments are parallel and in the same direction. These areas are called magnetic domains or Weiss domains and possess different directions of magnetization to guarantee a global magnetization of the material equal to zero [12], which can be observed on Figure I-4.

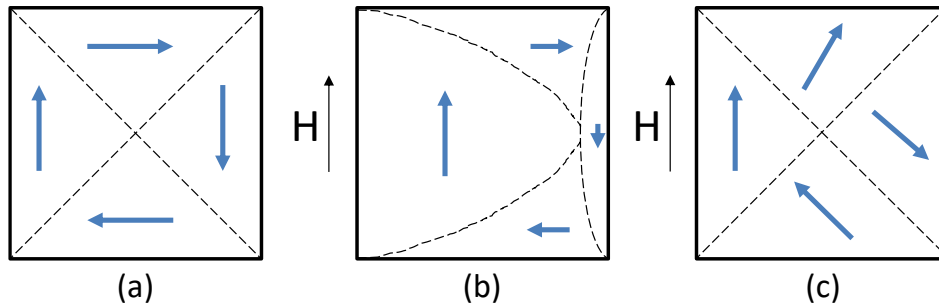


**Figure I-4.** Sketch of the magnetic domains arrangement in a single crystal (a) and in a polycrystal (b) [14].

To simplify the scheme, the crystallites in the polycrystal are represented as if they contain only single domains while it is not typically the case.

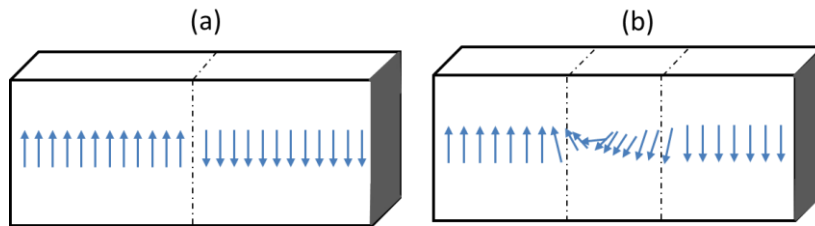
As an explanation, different interactions between magnetic moments have to be considered. Dipolar magnetic interactions between spins have to be taken into account considering a large amount of spins in a material. Indeed, they can be preponderant in front of the exchange interactions which are short distance interactions [15]. In this respect, a configuration of spins all oriented in the same direction is energy-consuming regarding these interactions. To lower these dipolar interactions, the material is divided in domains uniformly magnetized with different orientations from one to the other.

Under the application of the magnetic field, the domains could reorganize in two different manners: by the growth of domains oriented in the applied field direction to the detriment of the others, and by rotation of the magnetic moments in the domains to align with the external applied field (Figure I-5).



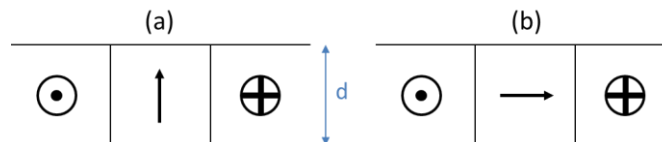
**Figure I-5. Reorganization of the magnetic domains under magnetic field. Arrangements without applied field (a), domains growth under field (b) and domains rotations under field (c) [14].**

Generally, for samples with few defects, the response to weak magnetic fields comes from the displacement of domain boundaries inducing the domain growth whereas the rotation of domains occurs mainly under the application of strong magnetic fields [14]. The domain boundaries are termed the domain walls or Bloch walls. In fact, these boundaries are rather areas of transition between domains than thin walls. In these areas, the magnetization direction rotates from one side to the other between domains [16] (Figure I-6). In fact, an abrupt transition of the magnetic domains (Figure I-6.a) is expensive in exchange energy. A progressive transition of the magnetic moments inside the wall allows to reduce the surface energy in a Bloch wall [15].



**Figure I-6. Transition area between two domains: sharply configuration which never happens (a) and progressively configuration which is called a Bloch wall (b).**

Another type of walls is observed in thin films: the Néel walls [17]. The difference with the Bloch walls lies in the magnetic moment orientation which rotates in parallel to the plane of the film and not in the plane of the wall anymore (Figure I-7). The type of walls will depend on the coating thickness. There is a critical thickness  $D_c$ , approximately equal to  $500 \text{ \AA}$  in the case of permalloy above which Bloch walls are less energy-consuming than Néel walls [17].



**Figure I-7. Bloch wall (a) and Néel wall (b) within a film thickness  $d$ .**

The magnetization direction inside a domain also depends on the crystalline anisotropy which is described in the next part with other important forms of anisotropy.

### I.1.2.C. Magnetic anisotropy

Magnetic anisotropy is an important parameter since it has a real impact on the material magnetization whether at the nanoparticle scale or at the coating level. Four mechanisms are identified: magnetocrystalline, shape, surface and effective anisotropy.

#### I.1.2.C.a. Magnetocrystalline anisotropy

At first, in ferromagnetic materials, the magnetic moments are oriented in the same direction in each Weiss domain below the Curie temperature. The orientation of the spins depends on the magnetocrystalline anisotropy which varies from a material to the other. Indeed, the magnetic moments will tend to align along preferential crystallographic axes [12], that explains why the magnetic moment orientation relies on the crystal structure of the material. This phenomenon comes from the spin-orbit and orbit-lattice coupling which are responsible of a reduction of the material energy along preferential axes. These preferential axes are called directions of easy magnetization [13]. In this respect, magnetization measurement results will differ from a crystallographic axis to the other [18]. In the case of a cubic system like magnetite, the density of magnetocrystalline energy is written using the following formula [19]:

$$E_a^{cubic} = K_1(\alpha_1^2\alpha_2^2 + \alpha_2^2\alpha_3^2 + \alpha_3^2\alpha_1^2) + K_2\alpha_1^2\alpha_2^2\alpha_3^2 + \dots \quad \text{I-2}$$

where  $K_1$  and  $K_2$  the constants of magnetocrystalline anisotropy and  $\alpha_1, \alpha_2, \alpha_3$  the cosines of the angles between the magnetization direction and the crystallographic axes. Also,  $\alpha_1 = \sin\theta\cos\phi$ ,  $\alpha_2 = \sin\theta\sin\phi$  and  $\alpha_3 = \cos\theta$  with  $\theta$  polar and  $\phi$  azimuthal angles. The directions of easy magnetization are determined through  $K_1$  sign and  $\frac{K_2}{|K_1|}$ .  $\text{Fe}_3\text{O}_4$  has one direction of easy magnetization along [111] at room temperature [20] and its anisotropy coefficients are the following:  $K_1 = 1.35 \cdot 10^4 \text{ J}\cdot\text{m}^{-3}$  and  $K_2 = -0.28 \cdot 10^4 \text{ J}\cdot\text{m}^{-3}$  [21].

In the case of maghemite, the direction of easy magnetization is along [110] [22] and  $K_1 = -4.65 \cdot 10^3 \text{ J}\cdot\text{m}^{-3}$  with  $K_2$  negligible [21].

Considering a single-domain nanoparticle with uniaxial anisotry,  $K_2$  becomes negligible and the magnetocrystalline anisotropy energy follows equation I-3:

$$E_a^{uni} = KV\sin^2\theta \quad \text{I-3}$$

with  $K$  the effective uniaxial anisotropy constant.

#### I.1.2.C.b. Shape anisotropy

The shape of a sample also generates anisotropy in a magnetic structure. When a material is subjected to a magnetic field  $H$ , magnetic poles are created on its surface which allow the penetration of magnetic flux lines. The sample could be correlated to a dipole which generates an external magnetic field. In this manner, to counter this external field, the material creates its

own internal demagnetizing field  $H_D$  oppositely directed to the magnetization  $M$ , with the resulting equation:

$$B = \mu_0(H + M) = \mu_0(H + M + H_D) \quad \text{I-4}$$

where  $H_D = -N_D M$  with  $N_D$  the effective demagnetizing factor. This last dimensionless factor is comprised between 0 and 1 and depends on the sample geometry [11]. The dipolar energy  $E_D$  is the result of the interaction between the demagnetizing field and the distribution of magnetic moments inside the material. The demagnetizing field is linked to the orientation of the magnetization with respect to the shape of the sample. This is referred to the shape anisotropy.

For a single-domain spherical sample with uniform magnetization, there is no shape anisotropy due to the isotropic behavior of the demagnetizing field in all directions. Otherwise, concerning non-spherical samples, the magnetization direction would prefer to align in the longest axis for which the demagnetizing field is lower.

The energy of shape anisotropy is expressed by equation I-5 [19]:

$$E_a^{shape} = \frac{1}{2} \mu_0 V (N_x M_x^2 + N_y M_y^2 + N_z M_z^2) \quad \text{I-5}$$

where  $\mu_0$  is the vacuum permeability,  $V$  the sample volume,  $N_x, N_y, N_z$  and  $M_x, M_y, M_z$  the components of the demagnetizing factors and of magnetization in  $(x, y, z)$  directions, respectively. The normalization is respected:  $N_x + N_y + N_z = 1$ . In the case of a spherical nanoparticle,  $N_x = N_y = N_z = \frac{1}{3}$ .

### *1.1.2.C.c. Surface anisotropy*

The origin of surface anisotropy comes from breaking of symmetry and decrease of the coordination of the nearest neighbors at the surface [19]. Considering a material layer, the associated energy is written:

$$E_a^{surf} = K_S V \sin^2 \alpha \quad \text{I-6}$$

with  $K_S$  the effective surface anisotropy constant and  $\alpha$  the angle between magnetization and the surface normal. In the case of nanoparticles, the surface anisotropy is a preponderant factor. Indeed, it increases with the reduction of the particle size due to the enhancement of the surface-to-volume ratio. The surface anisotropy has a predominant impact on the total anisotropy. A phenomenon of “spin-canting” can occur at the particle surface, which means that the spins are inclined at a certain angle with their normal axis [23]. This source of anisotropy induces a decrease in the global magnetization [24] of the particle and is obviously emphasized for nanosized particles. Furthermore, the canting effect could also be observed in the particle core due the amount of vacancies available [23] [25]. Mössbauer spectroscopy is a characterization method which could be useful to determine the amount of canted spins.

### I.1.2.C.d. Effective anisotropy constant

In reality, the different types of anisotropies are tough to discriminate of each other. Thus, an effective anisotropy constant  $K_{eff}$  is employed which includes both surface  $K_S$  and volume  $K_V$  anisotropies. In the case of a spherical particle,  $K_{eff}$  is written (Equation I-7):

$$K_{eff} = K_V + \frac{S}{V} K_S = K_V + \frac{6}{d} K_S \quad \text{I-7}$$

with  $S$  and  $V$  the particle surface and volume, respectively.  $d$  is the particle diameter. Consequently, the anisotropy increases when the particle size decreases [26] [27].

### I.1.2.D. Dynamic permeability of magnetic materials

High frequency and microwave applications of magnetic materials cover a wide range from non-resonant devices, rod antennas, read/write heads for digital tape [28], power transformers in electronic and telecommunications [29] like inductors for power transformers for example [30], information storage [31], and electromagnetic radiation absorption suitable for example for radar absorption [32] [28] of electromagnetic noise suppressor up to wireless power transmission. MnZn or NiZn ferrites are widely used for these applications since they combine a high electrical resistivity hence allowing a good electromagnetic wave propagation and soft magnetic properties. The permeability  $\mu$  defined by  $B = \mu H = \mu_0(H + M)$  is a tensor quantity which links the magnetic induction  $B$  to the magnetic field  $H$  in a material:

$$\mu = \mu' - i\mu'' \quad \text{with} \quad \mu = \mu_0\mu_r \quad \text{I-8}$$

with  $\mu'$  the real part,  $\mu''$  the imaginary part,  $\mu_0$  the permeability of free space and  $\mu_r$  the relative permeability. The magnetization dynamics is described by the nonlinear Landau-Lifshitz-Gilbert (LLG) model [11]:

$$\left(\frac{d\vec{M}}{dt}\right) = \gamma_0(\vec{M} \times \vec{H}) + \frac{\alpha}{M_S} \left(\vec{M} \times \frac{d\vec{M}}{dt}\right) \quad \text{I-9}$$

where  $M_S$  is the saturation magnetization,  $\gamma_0 = \gamma\mu_0$  with  $\gamma$  the gyromagnetic constant,  $H$  the magnetic field, and  $\alpha$  the damping parameter.

An expression of permeability in the case of a small amplitude propagating magnetic field expressed as  $H = \exp(j\omega t)$  could be deduced from equation I-9 [11] with the following real and imaginary parts  $\mu'$  and  $\mu''$ :

$$\mu' = 1 + \omega_M \frac{\omega_r[\omega_r^2 - \omega^2(1 - \alpha^2)]}{[\omega_r^2 - \omega^2(1 + \alpha^2)]^2 + 4\omega_r^2\omega^2\alpha^2} \quad \text{I-10}$$

$$\mu'' = \omega_M \frac{\omega\alpha[\omega_r^2 + \omega^2(1 + \alpha^2)]}{[\omega_r^2 - \omega^2(1 + \alpha^2)]^2 + 4\omega_r^2\omega^2\alpha^2} \quad \text{I-11}$$

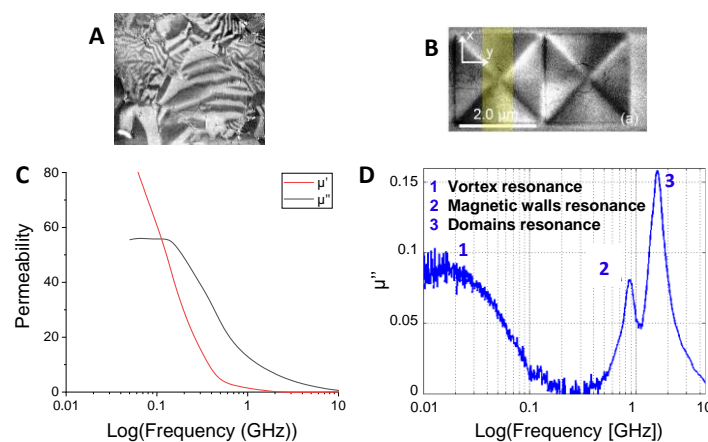
where  $\omega_M = \gamma_0 M_S$  is the angular frequency,  $\gamma_0 = \gamma \mu_0$  with  $\gamma$  the gyromagnetic constant,  $M_S$  the saturation magnetization,  $\omega_r = \gamma_0 H_r$  the resonance frequency,  $H_r$  the effective magnetic field for resonance including the contributions of the anisotropy field, the demagnetizing field and the external field, and then  $\alpha$  the damping parameter. Some of the variables introduced here will be detailed in Chapter IV.

The permeability losses ( $\mu''$ ) and especially the resonance frequency dependence will predict the suitability of a material for an application or another.

The magnetic resonance frequency depends on the local effective field experienced by the magnetic moments, which is not uniform: the local magnetic field in a domain wall has a demagnetization and exchange energy component very different from the volume magnetic domain. Then, the permeability spectrum of bulk polycrystalline ferrites is wide band due to its dispersed domain structure affected by the material microstructure namely the porosity, precipitates, grain size and orientation, and grain size dispersion.

The main idea of this project is to create a multiband behavior in ferrites by a patterning to create a regular domain structure. To illustrate these ideas, two materials with different magnetic textures are compared in Figure I-8. The permeability spectra in panel-C corresponding to the behavior of a polycrystalline bulk  $\text{Ni}_{0.5}\text{Zn}_{0.5}\text{Fe}_2\text{O}_4$  displays a large band regarding the magnetic losses  $\mu''$ . This comportment is attributed to the fact the polycrystalline bulk ferrite possesses a dispersed magnetic structure which depends on the size/orientation of the grains. Hence, the resonances of the different magnetic contributions (magnetic walls, domains) are not dissociated in separate bands.

In the case of a textured film of permalloy in square shapes (Figure I-8.B), the magnetic texture could be controlled by the geometric parameters of the patterns. Indeed, Figure I-8.D represents the expected behavior with separated absorption bands at the resonance frequencies of vortex, magnetic walls, and domains in the case of a perfect square of permalloy [33]. **The dynamic magnetic properties are governed by the pattern, the interest being to obtain a frequency-selective material by managing the losses frequency through the pattern shape.**



**Figure I-8. Pictures of a polycrystalline ferrite (A) [34] and squares of permalloy ( $2 \times 2 \mu\text{m}^2$ ) (B) [35]. Difference of permeability behavior between a wide band (C) and a multiband material (D). Permeability versus Log(Frequency) for a polycrystalline bulk  $\text{Ni}_{0.5}\text{Zn}_{0.5}\text{Fe}_2\text{O}_4$  (C) and a perfect square of permalloy ( $150 \times 150 \mu\text{m}^2$ ) (D) [33].**

### I.1.2.E. Magnetism at the atomic scale and the molecular field theory

At the atomic scale, the magnetic moment  $\vec{\mu}_j$  of a charged particle is equal to  $-g\mu_B\vec{J}$  with  $g$  the Landé factor,  $\mu_B$  the Bohr magneton, and  $\vec{J}$  the angular momentum of the particle. Considering one electron, two contributions to the angular momentum are distinguished: the orbital angular momentum  $\vec{l}$  attributed to the orbit around the nucleus, and the intrinsic angular momentum  $\vec{s}$  corresponding to the electron spin.

$\vec{L}$  and  $\vec{S}$  are the total orbital momentum and spin momentum of the atom, calculated by adding all of the electrons contributions. At each angular momentum is associated a magnetic moment. Indeed, an orbital magnetic moment  $\vec{\mu}_l$  is associated to the orbital angular momentum  $\vec{l}$  and reciprocally for  $\vec{s}$ . The Landé factor is equal to 1 for the orbital momentum and 2 for the spin one.

The link between these atomic quantities which can be computed by quantum mechanics and the macroscopic magnetic quantities of paragraphs I.1.2.A, I.1.2.B and I.1.2.C was made historically in oxides by the molecular field theory. New approaches based on the Density Functional Theory (DFT) calculations are currently under development.

The interactions concerning the spins alignment in ferromagnetic materials have been represented by Weiss in 1907. He introduced in its theory an internal field  $H_m$  called the molecular field, in addition to the external magnetic field  $H$ . According to the theory, the internal field  $H_m$  is arising from the interactions between the magnetic moments in relation to each other. It gives an explanation to the origin of the existence of a spontaneous magnetization of the material, without external magnetic field.

A few years after Weiss, Heisenberg (1928) has described the exchange energy  $E_{ex}$  between two adjacent spins  $S_1$  and  $S_2$  by an electrostatic interaction in the following form:

$$E_{ex} = -J \cdot \vec{S}_1 \cdot \vec{S}_2 = -J \cdot S_1 \cdot S_2 \cdot \cos \phi \quad \text{I-12}$$

where  $J$  is the exchange integral, and  $\phi$  the angle between the spins  $S_1$  and  $S_2$ .

The sign of  $J$  determines the magnetic order. For  $J > 0$ , the parallel arrangement is favored (ferromagnetic arrangement) and for  $J < 0$ , the antiparallel configuration is privileged (antiferromagnetic or ferrimagnetic).

Similarly, the exchange energy  $E_{ex}$  per unit volume is written:

$$E_{ex} = \frac{-\mu_0}{2} \sum_{i,j \neq i} n_{ij} m_i m_j = \frac{-\mu_0}{2} \sum_i m_i H_i \quad \text{I-13}$$

with  $H_i = \sum_{j \neq i} n_{ij} m_j$ ,  $m_i$  and  $m_j$  the magnetic moments of two adjacent atoms,  $n_{ij}$  a coefficient positive (parallel) or negative (antiparallel) as a function of the orientation of the magnetic moments.

$H_i$  is considered as a local field on the moment  $m_i$ . Regarding the Weiss molecular field theory, the variation of  $H_i$  should be neglected and only its average should be regarded as a function of the temperature:

$$\langle E_{ex} \rangle_T = -\mu_0 \sum_i \langle m_i \rangle_T \langle H_i \rangle_T \quad \text{I-14}$$

$$\langle H_i \rangle_T = H_m = \sum_{j \neq i} n_{ij} \langle m_j \rangle_T \quad \text{I-15}$$

The molecular field  $H_m$  is thus introduced in Equation I-15.

According to the quantum theory of paramagnetism, the magnetization of an individual sublattice is written as follows [11]:

$$M_i = n_i g \mu_B S_i B_{S_i} \left( \frac{g J \mu_B \mu_0 H}{k_B T} \right) \quad \text{I-16}$$

with  $n_i$  the volume density of spins  $S_i$ ,  $g$  the Landé factor,  $\mu_B$  the Bohr magneton,  $J$  the total angular momentum, and  $B_{S_i}(x)$  the Brillouin function (Equation I-17).

$$B_{S_i}(x) = \left[ \frac{(2J+1)}{2J} \right] \coth \left[ \frac{(2J+1)x}{2J} \right] - \left( \frac{1}{2J} \right) \coth \left( \frac{x}{2J} \right) \quad \text{I-17}$$

The magnetization reaching zero at the Curie temperature  $T_C$ , its value can be obtained by linearizing the Brillouin function. Applying the molecular field theory to a ferrimagnetic material, the magnetization in each opposite sublattice could be stated as follows:

$$M_i = \frac{C_i}{T} (H + N_{ii} M_i + N_{ij} M_j) \quad C_i = \frac{n_i g_i^2 \mu_B^2 S_i (S_i + 1)}{3k} \quad \text{I-18}$$

$$M_j = \frac{C_j}{T} (H + N_{ji} M_i + N_{jj} M_j) \quad C_j = \frac{n_j g_j^2 \mu_B^2 S_j (S_j + 1)}{3k} \quad \text{I-19}$$

where  $N_{ii}$  ( $N_{jj}$ ) and  $N_{ij}$  ( $N_{ji}$ ) are the molecular field coefficients in each sublattice and between sublattices respectively, with  $M_i$  and  $M_j$  the magnetization inside each sublattice.  $C_i$  and  $C_j$  are called the Curie coefficients.

With a zero applied field  $H$ , the Curie temperature  $T_C$  (Equation I-20) derives from the previous system of two linear equations (Equations I-18 and I-19) with  $M_i \neq M_j \neq 0$  by calculating the determinant of the system:

$$T_C = \frac{1}{2} (C_i N_{ii} + C_j N_{jj}) + \frac{1}{2} \sqrt{(C_i N_{ii} - C_j N_{jj})^2 + 4 C_i C_j N_{ij}^2} \quad \text{I-20}$$



The molecular field theory also predicts the global magnetization as a function of the temperature in a material with opposite sublattices (Equation I-21).

$$M = |M_i - M_j| \quad \text{I-21}$$

After applying the Brillouin-Weiss function to each sublattice, the expression of the magnetization inside each sublattice as a function of the temperature is determined:

$$M_i(T) = M_i(0)B_{S_i}(a_i) \quad \text{I-22}$$

$$M_j(T) = M_j(0)B_{S_j}(a_j) \quad \text{I-23}$$

with  $B_{S_i}(a_i)$  and  $B_{S_j}(a_j)$  the Brillouin functions.  $a_i$  and  $a_j$  are expressed as a function of the temperature (Equations I-24 and I-25).

$$a_i(T) = \frac{m_i H_m^{(i)}}{kT} = \frac{g_i \mu_B S_i}{kT} (N_{ii} M_i + N_{ij} M_j) \quad \text{I-24}$$

$$a_j(T) = \frac{m_j H_m^{(j)}}{kT} = \frac{g_j \mu_B S_j}{kT} (N_{ji} M_i + N_{jj} M_j) \quad \text{I-25}$$

The corresponding molecular field coefficients are displayed in Equation I-26.

$$\begin{aligned} M_i(0) &= n_i g_i \mu_B S_i & M_j(0) &= n_j g_j \mu_B S_j \\ N_{ii} &= \frac{z_{ii}}{n_i} \frac{2J_{ii}}{g_i^2 \mu_B^2} & N_{jj} &= \frac{z_{jj}}{n_j} \frac{2J_{jj}}{g_j^2 \mu_B^2} \\ N_{ij} &= \frac{z_{ij}}{n_j} \frac{2J_{ij}}{g_i g_j \mu_B^2} & N_{ji} &= \frac{z_{ji}}{n_i} \frac{2J_{ji}}{g_j g_i \mu_B^2} \end{aligned} \quad \text{I-26}$$

with  $n_i$ ,  $n_j$  the numbers of magnetic atoms in each sublattice per unit volume and  $z_{ij}$  the number of  $S_j$  nearest neighbors of spin  $S_i$ .

Among the other macroscopic properties introduced in paragraph I.1.2.C.a, magnetocrystalline anisotropy can be understood as a consequence of effective “one-ion” or “two-ions” contributions arising from spin-orbit coupling.

### I.1.3. Iron oxide spinels magnetic and electronic properties

#### I.1.3.A. Magnetic order

Magnetite and maghemite are ferrimagnetic materials. Three different exchange interactions rule the cations magnetic order: exchange interactions between tetrahedral sites

(AA), between octahedral sites (BB) and between the two different types of sites (AB).  $Fe^{3+}$  and  $Fe^{2+}$  ions possess spin magnetic moments of  $5 \mu_B$  and  $4 \mu_B$  respectively.

In the case of magnetite, the magnetic moments are ferromagnetic inside the tetrahedral and octahedral sublattices (AA and BB interactions) which are in antiferromagnetic configuration in relation to each other (AB interactions) [36]. Thus, the spin magnetic moments follow the sketch on Figure I-9.

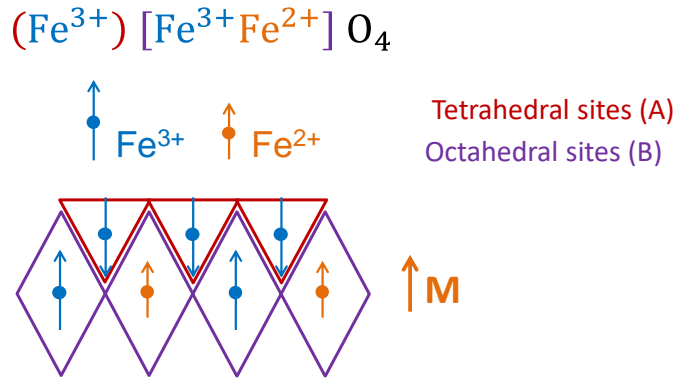


Figure I-9. Organization of magnetic moments in A and B sublattices for magnetite case.

Magnetic moments of ferric ions  $Fe(III)$  cancel each other out. The global magnetization is thus only due to the magnetic moments of ferrous ions  $Fe(II)$  (configuration  $d^6$ ). Theoretically, the resultant of the magnetic moments is equal to  $4 \mu_B$  in a reduced mesh, corresponding to  $32 \mu_B$  due to the presence of 8  $Fe^{2+}$  ions per unit cell [3] [37]. A saturation magnetization of bulk magnetite of  $92 \text{ emu/g}$  ( $A.m^2/kg$ ) has been previously reported [38] [39]. This value is close to  **$98 \text{ emu/g}$**  ( $A.m^2/kg$ ) which is calculated from the theoretical value of  $32 \mu_B$  for the magnetic moment and  $8.393 \text{ \AA}$  as the lattice parameter of massive magnetite through the following expression to convert Bohr magnetons in  $\text{emu/g}$ :

$$M_S(\text{emu/g}) = \frac{n_B(\mu_B)N_A\mu_B}{M} \tag{I-27}$$

with  $n_B(\mu_B)$  the magnetic moment per formula unit in Bohr magnetons,  $N_A$  the Avogadro's number ( $\text{mol}^{-1}$ ),  $\mu_B$  the Bohr magneton equal to  $9.274 \times 10^{-21} \text{ emu}$  and  $M$  the molar mass ( $\text{g.mol}^{-1}$ ). If the spinel was normal, the magnetic moment of a reduced mesh would have been equal to  $(2 \times 5 - 4) \mu_B = 6 \mu_B$ .

For the maghemite, considering the expression  $(Fe^{3+})[Fe^{3+}_{5/3}O_{1/3}]O_4^{2-}$  given at the part I.1.1 [7] for the space group  $Fd3m$ , the magnetization is given by  $(5/3 - 1) \times 5 \mu_B = 10/3 \mu_B$  in a reduced mesh. The saturation magnetization  $M_S$  of bulk maghemite corresponds to  $87 \text{ emu/g}$  ( $A.m^2/kg$ ) (Equation I-27) which is close to the value of  $74 \text{ emu/g}$  ( $A.m^2/kg$ ) reported in the literature [40] [41].

The magnetization is linked to the amount of lone pair electrons per unit mesh. Figure I-10 summarizes the number of lone pair electrons, the theoretical and experimental spin moments and also the bulk saturation magnetization for each structure, magnetite and maghemite.

	Number of lone pair electrons per f.u	Theoretical moment ( $\mu_B/f.u$ )	Experimental moment ( $\mu_B/f.u$ )	Bulk saturation magnetization ( $M_s$ ) (emu/g)
<b>Fe<sub>3</sub>O<sub>4</sub></b>	14	4	4.2	92
<b><math>\gamma</math>-Fe<sub>2</sub>O<sub>3</sub></b>	13.33	3.33	3.15	74

**Figure I-10. Summary table of the general information (per formula unit), about spin magnetic moment and magnetization of magnetite and maghemite, from Dunlop *et al.* [21] [42].  $M_s$  is about 95 emu/g ( $A \cdot m^2/kg$ ) for Fe<sub>3</sub>O<sub>4</sub> above the Verwey temperature.**

### I.1.3.B. Electronic properties

In the spinel ferrite system, the conduction occurs by means of electrons hopping between Fe<sup>3+</sup> and Fe<sup>2+</sup> ions [43] located on the neighboring octahedral sites. In this way, the probability of electronic displacement is higher in Fe<sub>3</sub>O<sub>4</sub> due to the same number of Fe<sup>3+</sup> and Fe<sup>2+</sup> ions placed on octahedral sites. In comparison, the probability is zero for  $\gamma$ -Fe<sub>2</sub>O<sub>3</sub> because the structure does not contain any Fe<sup>2+</sup> ions (except at their surface because of defects).

At room temperature, for bulk materials, the resistivity is around  $10^{-2} \Omega \cdot cm$  for magnetite and of  $10^{19} \Omega \cdot cm$  for the maghemite which possesses insulating properties [44]. A gap of 0.14 eV is observed between occupied and empty states in the electronic structure of Fe<sub>3</sub>O<sub>4</sub> [45] and maghemite is a semiconductor which exhibits a 2.03 eV band gap [46].

Magnetite is therefore considered as a semiconductor with good conductivity properties. Indeed, its structure displays a high conductivity comprised between  $10^3$  and  $2.5 \times 10^4 \Omega^{-1} m^{-1}$  according to Verwey *et al* [43] [47]. However, a phase change occurs around  $T = 120$  K in the magnetite structure with alterations of its properties. The conductivity is drastically reduced and a decrease of the magnetization is also observed [47] [48]. This reaction induces a specific heat peak around 114 K which confirms the phase change [49]. It is called the Verwey transition with the corresponding Verwey temperature  $T_V$ . This phenomenon is not fully understood. Some hypotheses have been made. At first, an electronic exchange occurs between Fe<sup>3+</sup> and Fe<sup>2+</sup> ions above  $T_V$  and suddenly disappears below  $T_V$ . The disappearance of the electrons hopping in octahedral sites might be due to a charge ordering below  $T_V$  which explains the metal-insulator transition [50] [51]. A crystal structure change which induces a modification of the electronic properties is also an explanation [52].

The Verwey temperature  $T_V$  is influenced by the stoichiometry and in other words by the inversion degree in the spinel structure  $\delta$ , but also by the surface oxidation of particles [53] [54]. In this way,  $T_V$  also depends on the particle size, and Bohra *et al.* observed it completely vanishes for magnetite particles with diameters below 20 nm [51] which could be due to the fact that tiny nanoparticles are more sensitive to the surface oxidation [55]. Similarly,  $T_V$  decreases with the reduction of the particle size and shifts to low temperature with the introduction of cations in the structure (Zn, Ti...) until the transition is not anymore observed above a certain amount of cations [51].

As previously mentioned, the insertion of cations in the spinel structure generates serious changes in the microstructural, chemical and physical properties of the material. The introduction of zinc in the structure has a particular interest for our study. The next paragraphs will introduce and explain the choice of the composition in agreement with our final application which is to develop magnetic coatings combining a high saturation magnetization with insulating properties. A compromise between these two parameters is made. The difference with magnetic properties of magnetite will be highlighted.

## I.2. Choice of the iron oxide spinel composition

Nonmagnetic 3d ion addition in ferrites ( $Al^{3+}$ ,  $Zn^{2+}$ ) has proven to paradoxically enhance their magnetic properties. This effect is reviewed for the well-known case of Zn and explained in the frame of the two sublattices model of ferrimagnetism.

### I.2.1. Effect of Zn doping on structural properties

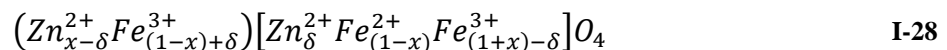
As seen in the previous part, magnetite possesses an inverse cubic spinel structure with oxygen in FCC configuration. The cations are divided between tetrahedral and octahedral sites. The insertion of other cations impacts  $Fe^{2+}$  and  $Fe^{3+}$  arrangement in the structure. They will occupy one or both sites according to their ionic radius, charge and coordination number [24]. Several possibilities are observed in Figure I-11.

	$Fe^{3+}$					$Fe^{2+}$				$Zn^{2+}$			
<b>Ionic radius (pm)</b>	49	58	55	64.5	78	63	61	78	92	60	68	74	90
<b>Spin state</b>	HS	LS	HS	HS	HS	HS	LS	HS	HS				
<b>Coordination</b>	IV	V	VI		VIII	IV	VI		VIII	IV	V	VI	VIII
<b>Charge</b>	+3					+2				+2			

Figure I-11. General data about  $Fe^{3+}$ ,  $Fe^{2+}$  and  $Zn^{2+}$  ions. High spin noted HS and low spin LS. Information from R.D. Shannon [56].

In maghemite, the  $Fe^{3+}$  in tetrahedral sites (coordination IV) have a radius of 49 pm which is smaller than  $Zn^{2+}$  in the same site. The addition of Zn in the structure will expand the lattice parameter.

$Zn^{2+}$  ions rather prefer to occupy tetrahedral sites [57]. In this case, Zn-doped magnetite adopts the following formula:



where  $x$  is the molar quantity of  $Zn^{2+}$  ions in  $Zn_xFe_{3-x}O_4$  composition and  $\delta$  the degree of inversion in the spinel structure. The structure is designated as “normal” when all of the Zn cations are localized on the tetrahedral sites (A) and as an “inverse” framework when they lie on the octahedral one (B). At some point, it occurs that the Zn cations could be retrieved on both sites and the spinel structure starts to reverse. Thus, cation organization in A and B sites

strongly influences the magnetic properties of the material and especially its global magnetization, its Curie temperature as inferred from the molecular field theory... Synthesis conditions clearly impact the inversion degree  $\delta$  [58] as well as its dependence with the temperature. Therefore, a good control of the synthesis and its parameters is required for the elaboration of nanoparticles with adjustable magnetic properties.

## I.2.2. Physical properties

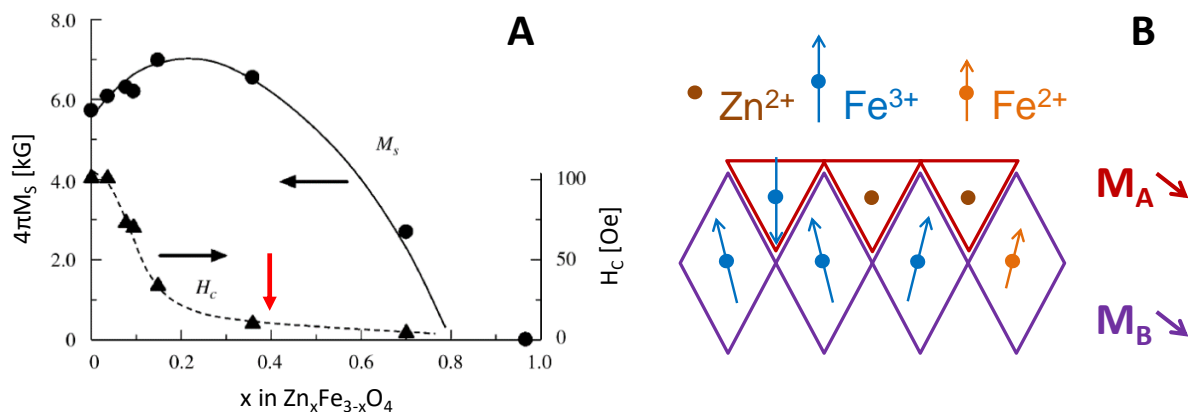
### I.2.2.A. Magnetic properties

Starting from the normal formula  $(Zn_x^{2+}Fe_{1-x}^{3+})[Fe_{1+x}^{3+}Fe_{1-x}^{2+}]$ , the theoretical global magnetization of the structure can be calculated. It comes from the difference between the total magnetic moments at B and A sites [59] expressed in  $\mu_B$ :

$$M_A = (1 - x) \times 5\mu_B \quad M_B = (1 + x) \times 5\mu_B + (1 - x) \times 4\mu_B \quad \text{I-29}$$

$$M = M_B - M_A = (4 + 6x) \times \mu_B$$

Accordingly, the magnetization is clearly dependent on the Zn content  $x$  in the structure. The evolution of the saturation magnetization  $M_S$  and of the coercive field  $H_C$  with the increase of Zn content in the structure is depicted on Figure I-12.A in the case of  $Zn_xFe_{3-x}O_4$  films obtained by spin-spray plating (SSP) [30]. The same trend is observed for  $Zn_xFe_{3-x}O_4$  coatings prepared by dipping the substrate in a solution containing nitrate precursors in DMAB as a solvent [60].



**Figure I-12.** Measurements of  $M_S$  and  $H_C$  as a function of the Zn amount in  $Zn_xFe_{3-x}O_4$  films [30] (A) (the red arrow points the interesting composition for the study) and a scheme of the Yafet-Kittel-type canting effect (B).

The dependence of the saturation magnetization at room temperature on Zn content exhibited on Figure I-12.A results from both decrease of Curie temperature with zinc content and changes in intrinsic magnetic moment at 0 K which is shown on Figure I-13 [42].

An attempt of a quantitative interpretation of this trend in the frame of the molecular field theory is presented in chapter IV.

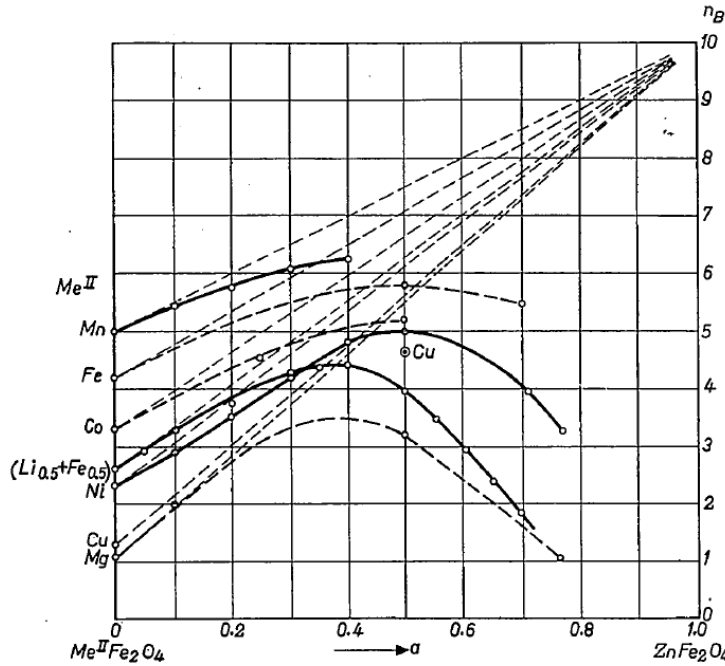


Figure I-13. Saturation magnetic moment in  $\mu_B$  of various ferrites with Zn content, including  $Zn_xFe_{3-x}O_4$ . From Gorter [42].

In the case of low Zn concentrations ( $0 < x < 0.5$ ) (Figure I-13),  $Fe^{2+}$  ion content decreases with the increase of  $Zn^{2+}$ .  $Fe^{3+}$  ions are still positioned on both sites. The structure follows a model of collinear ferrimagnetism with an antiparallel configuration between A and B sites because of prevalency of superexchange interaction A-O-B over B-O-B interactions. The magnetization at 0 K is equal to  $(4+6x) \times \mu_B$  as described above (Equation I-29).

For higher Zn concentrations ( $0.5 < x < 1$ ) (Figure I-13), the addition of  $Zn^{2+}$  in the structure induces a gradual replacement of  $Fe^{3+}$  ions with  $Zn^{2+}$  in A sites. A-O-B interactions are not prevailing anymore and B-O-B interactions become dominant. The octahedral sites (B) then splits into two sublattices where each part possesses a magnetic moment of the same amplitude but oriented at opposite angles [61]. This phenomenon is represented in a sketch on Figure I-12-B and is called the Yafet-Kittel-type canting. The global magnetization  $M$  becomes:

$$M = M_B \cos \alpha_{YK} - M_A \tag{I-30}$$

with  $\alpha_{YK}$  the canting angle between the magnetic moment with the direction of the global magnetization in the octahedral sites, also called the Yafet-Kittel angle [60],  $M_A$  and  $M_B$  the total magnetization at the tetrahedral and octahedral sites, respectively. The Yafet-Kittel-type canting causes a decrease of  $M_B$  which explains the general diminution of the global magnetization for a certain amount of zinc.

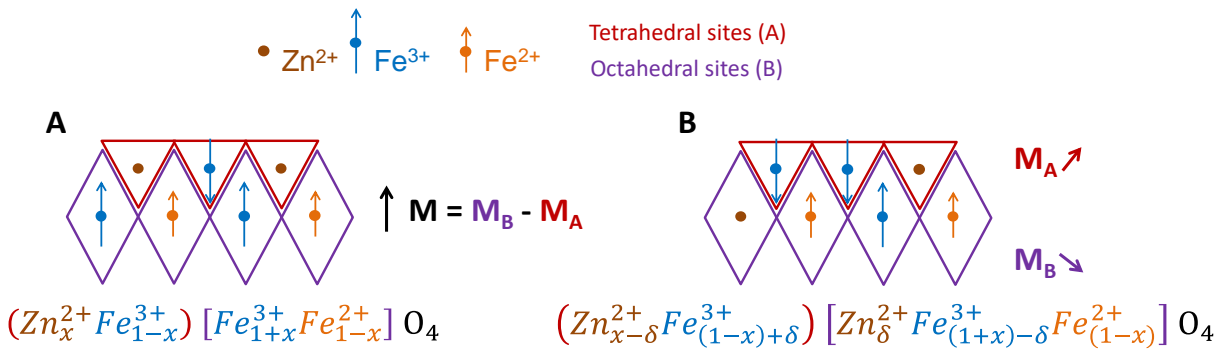
Concerning the coercive field  $H_C$  which is linked to the magnetic anisotropy, a sharp decrease with the Zn amount until approximately 0.2 is noticed (Figure I-12-A), which seems to be the border between a semi-hard magnetic material to a soft one. A smoother drop is then observed for  $x$  between 0.2 and 1 until it reaches zero around  $x \approx 0.8$ . Such a trend could be interpreted by the decrease of the  $Fe^{2+}$  content, which has an effective one ion contribution to magnetic anisotropy greater than  $Fe^{3+}$  (for which  $L = 0$ ). At  $x \approx 0.8$ , the Curie temperature may

be lower than room temperature which is the case for  $\text{Ni}_{1-x}\text{Zn}_x\text{Fe}_2\text{O}_4$  with a  $T_C$  below room temperature for  $x = 0.8$  [62].

For the sake of simplicity, the degree of inversion  $\delta$  in the spinel structure has not initially been taken into account in this explanation. The next paragraph focuses on the way  $\delta$  could impact the magnetization properties of the material, separately from the Zn content.

### I.2.2.B. The influence of the spinel inversion degree

As previously mentioned (I.2.1), the magnetic properties of  $\text{Zn}_x\text{Fe}_{3-x}\text{O}_4$  depend on the organization of cations on the tetrahedral (A) and octahedral (B) sites. It has been clearly demonstrated in some similar compositions with for example  $\text{Mn}_{1-x}\text{Zn}_x\text{Fe}_2\text{O}_4$  [63]. This concept is described in the following schemes (Figure I-14).



**Figure I-14.** Cation distribution on A and B sites for  $\text{Zn}_x\text{Fe}_{3-x}\text{O}_4$  composition in a “normal” (A) and “inverse” (B) spinel structure.

In the case of the “normal” configuration (Figure I-14.A), all of the Zn cations are located on the A sites.  $\text{Fe}^{3+}$  cations are divided between B sites and the available positions in A sites. Finally,  $\text{Fe}^{2+}$  cations lie only on the B sites. Otherwise, when the spinel starts to reverse, an exchange between  $\text{Zn}^{2+}$  on A sites and  $\text{Fe}^{3+}$  on B sites occurs. Hence,  $\text{Zn}^{2+}$  cations could be found at the octahedral positions (Figure I-14.B) resulting in a decrease of  $M_B$  and then of the global magnetization  $M$ .

The inversion of the spinel could appear for any Zn amount. Indeed, it has been examined for  $\text{ZnFe}_2\text{O}_4$ ,  $\text{MnFe}_2\text{O}_4$ ,  $\text{CoFe}_2\text{O}_4$  composition and sometimes with a spin canting effect at the octahedral sites [25].

Franklinite ( $\text{ZnFe}_2\text{O}_4$ ) has all of its A sites filled with  $\text{Zn}^{2+}$  cations in the “normal” organization. B sites only contain  $\text{Fe}^{3+}$  cations for this composition. Since  $\text{Zn}^{2+}$  cations are non-magnetic, there is only a B-O-B exchange interaction and the magnetic moments are settled in an antiferromagnetic configuration in the octahedral sites (Figure I-15-A). Consequently, the global magnetization of the material is equal to zero. Bulk franklinite is paramagnetic above 10 K ( $T_N$ ) [32] [64].

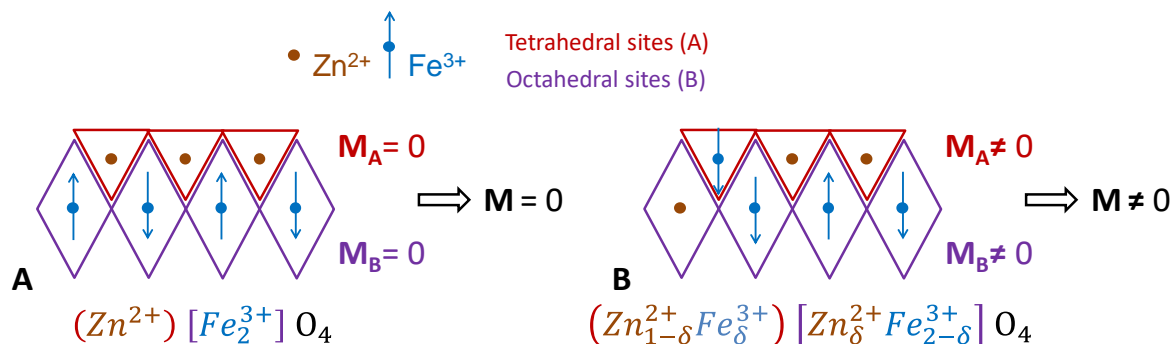


Figure I-15. Cation distribution on A and B sites for  $ZnFe_2O_4$  composition in a “normal” (A) and “inverse” (B) spinel structure.

The inversion of the spinel proceeds in the same way as for the general  $Zn_xFe_{3-x}O_4$  formula. Indeed, some  $Zn^{2+}$  and  $Fe^{3+}$  are exchanged and are found at the octahedral (B) and tetrahedral (A) positions, respectively. The inversion gives to the material a magnetization at room temperature. The structure becomes ferrimagnetic at the nanoscale due to the predominance of A-O-B interactions [32].

### 1.2.2.C. Electronic properties

The resistivity  $\rho$  increases with  $x$  on a logarithmic scale (Figure I-16). Indeed, the electron hopping between  $Fe^{2+}$  and  $Fe^{3+}$  in octahedral sites is affected by the insertion of  $Zn^{2+}$  ions in the structure which tends to diminish the proportion of  $Fe^{2+}$  in B sites. **The conductivity is then reduced [30]. Above a Zn concentration of 0.15, the resistivity exceeds a value of 50  $\Omega\cdot\text{cm}$  above which a material is considered as a perfect insulator for application in high-frequency devices.** It is thus a good indicator on which to rely on for the choice of the nanoparticles composition.

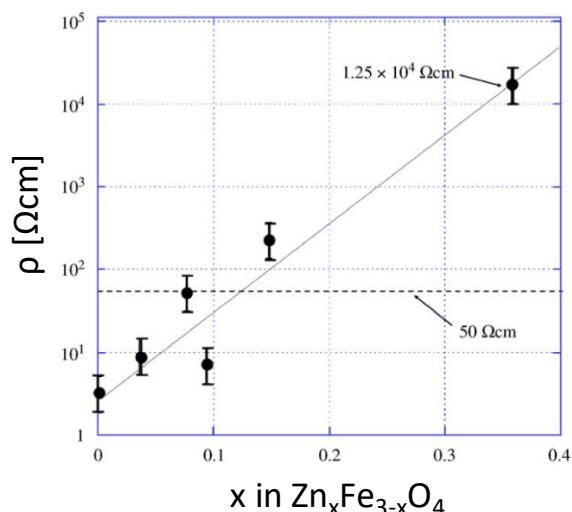


Figure I-16. Evolution of the resistivity versus the Zn content in  $Zn_xFe_{3-x}O_4$  films [30].



### I.2.3. The selected iron oxide spinel composition

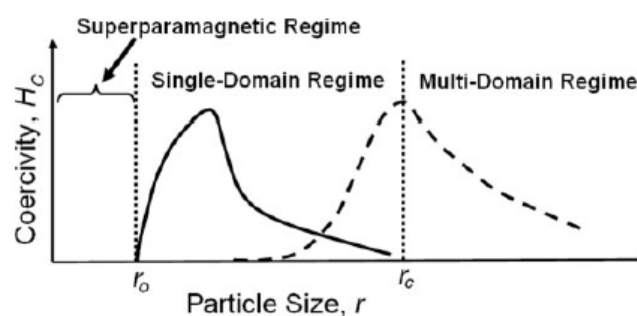
*To summarize, the Zn-doping ferrite system is selected to obtain an insulating mixed-oxide and allow a good penetration of the electromagnetic wave in the material. Good insulating properties are noticed from  $x$  above 0.15, as well as a high saturation magnetization and weak coercive field for  $x$  below 0.5 (Figure I-12). For all of these reasons, the composition is fixed at  $Zn_{0.4}Fe_{2.6}O_4$  in the overall study.*

## I.3. Particle size effect on the magnetic properties

### I.3.1. Superparamagnetism, transition single/multi domains

At the particle scale, the size strongly influences the magnetic properties. The magnetization curve may exhibit if anisotropy is low enough a superparamagnetic behavior at room temperature, characterized by a non-saturating signal under high magnetic field. Indeed, below a certain limit of size  $r_0$  (20 nm according to S. Noh *et al.* [65]), the thermal energy becomes sufficient to overcome the energy barrier responsible of the change of magnetization direction of a particle. Thus, in the case of a non-interacting particles set, at zero applied field, the magnetization direction of each nanoparticle fluctuates over time and results in a zero global magnetization for a measured time above the reversal time of the spins [66] as well as a coercive field which tends towards zero (Figure I-17). However, when an external magnetic field is applied, the superparamagnetic particles magnetize in the direction of the field [67].

Another parameter relative to superparamagnetic particles is the blocking temperature  $T_B$ , the temperature at which the thermal energy becomes strong enough to compete with the energy barrier of spins flipping and relative to the measurement time. Further details will be provided in Chapter IV.



**Figure I-17.** Relation between the coercive field and the particle size (solid and dashed lines for particles without and with interactions, respectively). From U. Jeong *et al.* [67].

Under a critical size value  $r_C$  and above  $r_0$ , the particle moves from a multi-domain regime where multiple magnetic domains coexist to a single one. In fact, below  $r_C$ , the domains become unstable and the configuration of lower energy is a single domain with all of the magnetic moments oriented in the same direction. The critical radius  $r_C$  follows Equation I-31 [68] [69]:

$$r_c = \frac{9\gamma_w}{\mu_0 M_S^2} \quad \text{I-31}$$

where  $\gamma_w = (AK)^{\frac{1}{2}}$  is the surface energy of a Bloch wall,  $A$  is the exchange constant,  $K$  the anisotropy constant,  $\mu_0$  the vacuum permeability and  $M_S$  the saturation magnetization.

The transition between a polydomain and a monodomain particle depends on the material composition. Indeed,  $d_c = 2r_c$  defined as the critical diameter has been determined experimentally as the maximum of the curve representing  $H_C$  as a function of the diameter of nanoparticles (Figure I-17).  $d_c$  is about 80 nm in the case of  $\text{Fe}_3\text{O}_4$  particles [12] [70] and 60 nm for  $\text{Zn}_{0.4}\text{Fe}_{2.6}\text{O}_4$  particles [65]. In the case of a polycrystalline material, this diameter is considerably increased due to the particle interactions which stabilize the monodomain structure. An experimental study by a neutron depolarization technique has shown that this diameter is about 3  $\mu\text{m}$  for  $\text{Ni}_{0.49}\text{Zn}_{0.49}\text{Co}_{0.02}\text{Fe}_{1.90}\text{O}_{3.85}$  particles [71]. The size of the grain governing the domain wall creation, this parameter will intervene in the dynamic behavior of the material.

Consequently, considering a set of particles in a film, the dynamic magnetic response will depend on the coupling between grains and also on the particle size. When the particle size exceeds the critical value of approximately 3  $\mu\text{m}$  for the  $\text{Ni}_{0.49}\text{Zn}_{0.49}\text{Co}_{0.02}\text{Fe}_{1.90}\text{O}_{3.85}$  composition, the permeability spectra will display resonance peaks for domain walls and domains. On the contrary, for diameters below 3  $\mu\text{m}$ , no resonance peak of walls and domains remains.

Hence, the interest of the project is to manage the magnetic losses by avoiding the parasitic signals of particle walls and domains. For this purpose, we would like to pilot the magnetic walls through the elaboration of patterns by the pattern geometry and not imposed by the particle size. This prerequisite imposes to work only with single-domain particles and thus to respect a condition on the nanoparticle size: the diameter should be below 1  $\mu\text{m}$  by taking into account the particle interactions.

As a consequence, two ranges of size of nanoparticles are selected for the present project, one below 20 nm [65] to study the superparamagnetic influence and one comprised between 20 and 1  $\mu\text{m}$  with ferrimagnetic particles.

### I.3.2. Shape effect

Added to the particle size effect, the magnetic properties could also be influenced by the particle morphology.

Noh *et al.* [65] have noticed a difference of 50 emu/g ( $\text{A}\cdot\text{m}^2/\text{kg}$ ) in the saturation magnetization  $M_S$  of  $\text{Zn}_{0.4}\text{Fe}_{2.6}\text{O}_4$  cubic and spherical particles with a diameter of about 20 nm. The highest value is obtained for the cubic shape. It might be due to the fact the curved surface of round-shape particles includes multiple facets which generate an increase of spins disorder

at the surface. In comparison, the cube has flat low energy faces and thus displays a smaller surface anisotropy.

The coercive field  $H_C$  could be impacted by the particle shape too. At same particle sizes of around 100 nm, Li *et al.* [70] highlight a higher  $H_C$  in the case of a  $\text{Fe}_3\text{O}_4$  cube in comparison with a sphere of the same material but with same values of  $M_S$ . The difference would be attributed to the multiple orientations of easy axis in the sphere influenced by the polycrystals in its multi-domain structure.

The control of the nanoparticle morphology through the synthesis is hence a major issue.

## I.4. Conclusion

*Part I gives a detailed view of the state of the art and the basic concepts required for the understanding of the study. Globally, it concerns the material choice and its physical properties resumed as follows:*

- *At first, notions of magnetism are presented: the different magnetic behaviors encountered in a material (paramagnetic, ferro-, ferri-, antiferro-...magnetic), the definition of a magnetic domain, the notion and types of anisotropy, and the dynamic magnetic properties.*
- *The introduction to the family of iron oxides incorporating the crystal structure, magnetic and electronic properties.*
- *The Zn-doping of iron oxide  $Zn_xFe_{3-x}O_4$  with the influence on the doping on: the crystal structure, magnetic and electronic properties, and the phenomenon of inversion degree in the spinel structure. The inversion degree will be discussed all along this manuscript.*
- *The presentation of the superparamagnetism, described deeply in Chapter IV. The size effect on the magnetic properties of nanoparticles is introduced with the notion of the critical size for the transition between a single to multi domains, and then the incidence of the particle shape on the magnetic properties.*
- *To end, the choice of the particle composition and size for the study is justified. The selected composition is  $Zn_{0.4}Fe_{2.6}O_4$  to combine a high value of the saturation magnetization with an electrical resistivity sufficient to ensure the penetration of the electromagnetic wave. Two preferred ranges of size are: below 20 nm with a superparamagnetic behavior, and ferrimagnetic between 20 and 1  $\mu m$ .*

*Such a material finds many applications in high frequency devices like non-resonant devices, rod antennas, read/write heads for digital tape, power transformers in electronic and telecommunications, information storage, radar absorption... or even for wireless power transfer (WPT) [72].*

*Magnetic and electronic properties of iron oxide spinel nanoparticles are influenced by their size and shape.*

*Therefore, the nanoparticles elaboration method should be chosen from:*

- *The homogeneity of the chemical composition  $Zn_{0.4}Fe_{2.6}O_4$  and crystal phase.*
- *The versatility of the method to elaborate two sizes of nanoparticles with a narrow dispersion for magnetic properties homogeneity: below 20 nm and above 20 nm.*
- *The shape which has to be isotropic to avoid shape anisotropy or porosity in the coating.*
- *The compatibility with the further step of the coating process.*

*The next part will focus on the choice of the elaboration method.*

## II. Different elaboration methods: state of the art

There are many ways to elaborate iron oxide spinel nanoparticles.

Many researches demonstrate the interest of magnetic nanoparticles for applications in magnetic hyperthermia, or in recuperation of waste or soft matter based compounds. In this context, Lacroix *et al.* [73] have studied the synthesis of monodisperse FeCo nanoparticles with a 14 nm diameter through the decomposition of organometallic precursors under H<sub>2</sub> atmosphere [74]. Salgueirino-Maceira *et al.* have demonstrated the benefit of a core/shell particle framework sliced in three layers: an iron oxide core, a gold shell on the outer and a silica intermediate layer to isolate the magnetic core from the gold coating. Such a structure is interesting in order to combine imaging and therapy for cancer treatment, as well as controlling the particle pathway towards the infected cells in the body through the application of an external magnetic field. Uniform particles in size and shape are required and have been synthesized by a coprecipitation method for the magnetic core [75]. Similarly, the elaboration of Fe<sub>3</sub>O<sub>4</sub> particles by coprecipitation and their arrangement in chains embedded in a gel matrix have been investigated by Myrovali *et al.* in order to improve the hyperthermia efficiency. Two ranges of size (10 and 40 nm) have been examined. The increase of particle diameter has been done by changing the precursor nature and especially by replacing chlorides with sulfates [76].

Magnetic nanoparticles possess many more potential applications like magnetic data storage or permanent magnets for example. Cobalt nanodisks with controlled dimensions (diameter of 21 nm and thickness of 12 nm) have been evaluated for this purpose [77].

We would like to focus on the most commonly used elaboration methods and describe the advantages and drawbacks. The difficulty lies in the development of pure nanoparticles with perfectly controlled size and shape, with a high crystallinity and above all homogeneous regarding the chemical composition.

### II.1. Different elaboration routes

All of the existing synthesis methods are divided into two main categories called the top-down and bottom-up approaches. On the one hand, the top-down approach deals with the mechanic reduction or fragmentation of a massive material in small particles with sizes of up to the nanometer range. This process is carried out by means of grinding, ball-milling and even ultrasonication [78] [79]. Even though, these mechanic techniques generally induce a broad size distribution, very long reaction times, low yields, and impurities [78]. This is not the best way for a size and morphology control of pure nanoparticles. Another physical method could also be mentioned: an evaporation/sputtering process based on the principle of the Physical Vapor Deposition (PVD). A target constituted of the material of interest is vaporized by ion bombardment. An inert gas flow carries out the evaporated material onto the substrate where steps of nucleation/growth occur during condensation and allow the particle formation [80]. This last technique is expensive and is only applicable to metallic nanoparticles [81] [82].

On the other hand, the bottom-up approach concerns the synthesis of nanoparticles starting from the assembling of atoms and molecules and resulting from condensations reactions or molecule decomposition. The particles are synthesized directly through chemical synthesis. The nanoparticle size and shape can be controlled by the synthesis parameters, with for example the temperature profile, the reaction duration, the chemical products, the stirring process, the ratio between surfactant and precursors, the pH... Some examples of the most common synthesis methods are described in the parts below: coprecipitation, thermal decomposition, hydrothermal/solvothermal synthesis, polyol synthesis, microemulsion, sol-gel process and oxidation/reduction. The technique used for the doped zinc ferrite nanoparticles synthesis has been chosen from the comparison between these different chemical methods considering the advantages and disadvantages in each case.

### II.1.1. Coprecipitation

The coprecipitation is the most commonly used method to synthesize ferrite nanoparticles [78]. It has the advantage to be simple because it is carried out in water and it allows obtaining good reaction yields, what makes this synthesis eco-friendly. It has also the possibility to be developed on a large scale through automatized systems.

Iron oxides nanoparticles ( $\text{Fe}_3\text{O}_4$ ,  $\gamma\text{-Fe}_2\text{O}_3$ ) could be synthesized from divalent and trivalent iron salts which precipitate by adding a base [83] [84] [10] [85] [86] [87] [88]. Some examples of salts used in this context are sulphates, chlorides, nitrate [89] [84]... The pH of the reaction media will have an important effect on the nanoparticles formation, that is why this parameter has to be controlled. It can be tuned by addition of a sodium hydroxide solution for example [78]. After the introduction of all the reactants, the reaction can occur under intense stirring and sometimes can be initiated by heat [78].

Nanoparticles with sizes comprised between 2 and 50 nm could be elaborated [89]. However, this method entails a certain number of drawbacks. The size is tough to control, that is why the synthesis is heterogeneous in terms of size [79]. Then, the nanoparticles from this synthesis don't have a high crystallinity. Consequently, this method requires a heating post-treatment to enhance the degree of crystallinity [78]. Moreover, the coprecipitation process does not require a specific ligand in the reaction media, which is frequently used in organic synthesis to control the nanoparticles size and shape. Thus, it can generate the aggregation of nanoparticles which are difficult to separate after the synthesis [79].

Other synthesis methods have been studied in order to obtain a better control of nanoparticles size and morphology.

### II.1.2. Hydrothermal/solvothermal synthesis

The hydrothermal synthesis is close to the coprecipitation process except that it occurs in an autoclave in high temperature and pressure conditions. These supercritical conditions allow attaining a higher control of the nanoparticles size and morphology [79]. In fact, it affords to

monitor the Ostwald ripening through the hydrolysis kinetics which are considerably facilitated due to a better dissolution of the ionic species in the reactor [79]. Divalent and trivalent metal salts are dissolved in water or water-miscible organic solvents including ethanol or ethylene glycol [78]. The obtained solution is then introduced in an autoclave under high pressure. The applied temperature depends on the solvent used in the system. For example, Co-Zn ferrite nanoparticles with sizes ranging from 5.5 and 9 nm have been synthesized with the hydrothermal method [79] [90].  $\text{Co}^{2+}$ ,  $\text{Zn}^{2+}$  and  $\text{Fe}^{2+}$  ions were precipitated at room temperature in aqueous media with a NaOH base. The solution is afterwards inserted in the autoclave with pressure and temperature conditions of about 103 kPa and 105 °C, respectively. Nanoparticle sizes are governed in this case by two important parameters: the pH and the reaction time.

This synthesis method is suitable for nanoparticles production on a large scale [78] [84]. Morphology, size and size distribution can be well controlled by adjusting the pH, reaction time, temperature and pressure inside the autoclave and with the choice of adequate solvents. The primary drawback seems to be the low obtained yields [78].

The hydrothermal synthesis takes place in aqueous media whereas the solvothermal one is its equivalent in organic solvents.

### II.1.3. Polyol synthesis

The polyol route is a common synthesis used for the elaboration of monodisperse colloidal magnetic ferrite nanoparticles with high crystallinity. It deals with the use of polyols such as ethylene glycol, diethylene glycol, poly(ethylene glycol) and so on [91]... These solvents possess multiple roles in the synthesis and act as high-boiling point solvents, complexing agents, surfactants, reducing agents and amphiprotic solvents [78] [91]. This process is based on the reduction of metal salts in non-agglomerated particles. The choice of the polyol (molecular weight, polarity) has an effect on the nanoparticle shape, solubility and state of aggregation [79] [91]. The obtained nanoparticles could be easily spread out in polar solvents due to the presence of a hydrophilic layer around the particle coming from the polyol during synthesis [91].

Tiny nanoparticles with sizes ranging approximately from 5 to 15 nm could be synthesized with a narrow size distribution [89] [91]. This method is also appropriate for the synthesis of mixed oxides ferrites nanoparticles [78] with for example zinc nickel ferrite  $\text{Zn}_{0.7}\text{Ni}_{0.3}\text{Fe}_2\text{O}_4$  [91] or manganese zinc ferrite  $\text{Mn}_{0.48}\text{Zn}_{0.12}\text{Fe}_{2.4}\text{O}_4$  [93] nanoparticles.

### II.1.4. Microemulsion

The microemulsion method involves the use of micelles as nanoreactors. A microemulsion is a thermodynamically stable dispersion of two originally immiscible phases, which is made possible by the addition of an amphiphilic molecule called a surfactant [78]. The dispersion process falls into two categories: an oil-in-water emulsion called normal and a water-in-oil emulsion called the reverse one. The emulsion nature is linked to the ratio between the two phases (oil and water) and also the hydrophilic or lipophilic character of the surfactant at the

interfaces between water and oil phases [79]. The polar head of the surfactant is hydrophilic and therefore compatible with the water phase, whereas the non-polar tail is hydrophobic and will instead move in the oil phase. The dispersed droplets are between 2 and 100 nm.

The mixture of two microemulsions of the same nature and containing the suitable reagents allows the precipitation of the nanoparticles inside the nanoreactors. The obtained nanoparticles can be recovered by adding ethanol to the system and with centrifugations or filtrations.

The advantages of this method are: the synthesis of stable nanoparticles with different shapes and sizes by changing the type of surfactant, the ratio between the two phases and the reaction conditions [79]. It is also important to precise that it takes place at low temperature and that it can be used at the industrial scale. Indeed, most of the used solvents and surfactants can be recycled for many batches, in order to limit the production costs [78]. For example,  $\text{MnFe}_2\text{O}_4$  nanoparticles with sizes ranging from 4 to 15 nm were synthesized by the reverse emulsion technique with water-in-toluene micelles and sodium dodecylbenzenesulfonate as a wetting agent [94].

This synthesis is complicated to set-up and implies low yields of products. In addition, the produced nanoparticles are not well crystallized and often polydisperse [84].

#### II.1.5. Sol-gel process

The sol-gel synthesis is carried out in two stages: the hydrolysis and condensation of precursors and especially metal alkoxides  $\text{M}(\text{OR})_n$  with M for a metal and R for an organic alkyl group [78]. The obtained sol (a stable colloidal dispersion) may then be transformed into gel by further condensation reactions, still at room temperature. The solvent is here trapped in a solid network. There are two types of sol-gel reactions: a hydrolytic and a non-hydrolytic one [95]. The hydrolytic route involves the use of metallic salts in aqueous media. It allows the development of hydrogels which are gels consisting in hydrated oxides particles. Whereas this is the less expensive way, it is difficult to control the nanoparticle sizes. In this way, the non-hydrolytic way which employs metal alkoxides in organic solvents leads to a better control of the nanoparticle monodispersity.

This method is beneficial because the reactions occur at low temperatures (between 25 and 200°C) with good control of nanoparticle size distribution and shape, and obviously it is simple in terms of equipment and process. The composition, size and shape can be monitored through sol concentration, annealing temperature, stirring velocity [78]. As an example, iron oxide nanoparticles with sizes ranging from 10 to 16 nm were synthesized by the polymeric sol-gel route with a high crystallinity [96].

Heating post treatments are required to remove the residual solvents, reaction by-products and obtain the pure crystalline nanoparticles [78].



### II.1.6. A non-hydrolytic route: the thermal decomposition

The thermal decomposition method is one of the easiest ways for the ferrite nanoparticles synthesis. It has been inspired from the synthesis of superconductor nanoparticles established in the 1990s [84] [97] and then employed for metallic and oxide nanoparticles synthesis. The obtained nanoparticles are monodisperse with a narrow size distribution, possess homogeneous morphologies and are highly crystalline. It consists in a thermal decomposition of organometallic precursors in organic media with the addition of a surfactant [78]. If we focus on the synthesis of iron oxide nanoparticles, the organometallic precursors are often metal acetylacetonates  $M(\text{acac})_n$  with  $M = \text{Fe, Mn, Co, Ni, Zn}$ , carbonyls, metal cupferronates ( $\text{Cup} = \text{C}_6\text{H}_5\text{N}(\text{NO})\text{O}^-$ ), oleates and chlorides [84] [2]. A number of studies suggest that the purity of the precursors is an important factor for obtaining reproducible and pure nanoparticles, that is why the precursors are synthesized in a preliminary step [98] [99]. The surfactants commonly used are fatty acids, oleic acid, and a mixture of oleylamine and oleic acid. In more detail, the reactive media usually consists of the metal precursor, an adapted surfactant, and a hydrocarbon solvent.

The synthesis temperature will depend on the decomposition temperature of the precursors. In general, it occurs at high temperature, that is why this method requires the use of solvents with high boiling points (between 270 and 350°C), for example alkenes and ethers. This synthesis allows a good control of the nanoparticle size and morphology through the tuning of the decomposition temperature, the ratio between precursors and surfactant, the choice of solvent, precursors and surfactant, the heating rate, and the reaction time [79] [84]. It is well adapted for large-scale production [78].

In comparison with the above mentioned methods like co-precipitation which are suitable for the obtention of high yields but not for monodisperse nanoparticles, this method allows a better control of the nanoparticle uniformity in terms of size and shape even if it is not convenient for large amount production [79].

The method is convenient for the elaboration of mixed-oxide ferrite nanoparticles and consequently, it seems to be adapted in our case with the synthesis of zinc ferrite nanoparticles. For example,  $M\text{Fe}_2\text{O}_4$  nanoparticles synthesis with  $M = \text{Co, Ni or Mn}$  by thermal decomposition of acetylacetonates and carboxylate precursors in organic media have been mentioned [100] [101] [102] [31].

Moreover, due to the use of organic surfactants in the synthesis media, the obtained nanoparticles are often coated with an organic layer at the end of the process, and therefore are hydrophobic. Consequently, this synthesis method is appropriate to obtain a stable dispersion of the nanoparticles in organic solvents such as hexane, toluene or chloroform. K. Butter's group has studied the dispersion of iron-based colloids synthesized by thermal decomposition of iron carbonyl with different surfactants [103].

## II.1.7. Conclusion

*The main advantages and drawbacks of the most used synthesis methods for the elaboration of iron oxide nanoparticles have been detailed in the previous part. We can summarize these information in Figure I-18.*

Methods	Set-up	Solvent	Surfactant	T (°C)	Reaction time	Size (nm)	Shape control	Yield
Coprecipitation	very simple	<ul style="list-style-type: none"> <li>aqueous</li> <li>acids and bases added (NaOH, KOH...)</li> </ul>		20 - 90	minutes	3 - 20 broad/non monodispersed	difficult	high/scalable
Hydrothermal/ solvothermal	simple/ supercritical conditions	<ul style="list-style-type: none"> <li>aqueous</li> <li>ethanol</li> <li>organic for the solvothermal method</li> </ul>		>200	hours	<1000 narrow	very good	medium
Polyol	very simple	polyols	polyols	>180	minutes	5 - 15 narrow	very good	medium/scalable
Microemulsion	difficult	aqueous/organic	amphiphilic molecules	20 - 50	hours	<50 narrow	good	low
Sol-gel process	simple	aqueous/organic		25 - 200	hours	10 - 30 narrow	good	high
Thermal decomposition	difficult	organic	fatty acids, oleic acid...	200 - 350	hours	<40 very narrow	very good	high/scalable

**Figure I-18. Comparison between the different chemical synthesis methods to elaborate magnetic nanoparticles [2] [78] [84] [104].**

*In the context of our research, we have chosen the thermal decomposition process to synthesize zinc iron oxide nanoparticles. Indeed, this method allows obtaining nanoparticles with a very narrow size distribution, a good control of the particle morphology, with an homogeneous chemical composition and with high yields (Figure I-18). Moreover, the nanoparticles are functionalized in-situ with the surfactants used in the reaction media. Thus, it looks easier to formulate stable dispersions after this kind of synthesis and we will detail this concept in the next chapter. Another suitable synthesis could have been the polyol synthesis. However, though this method is simple and fast, it is limited in terms of particle size. The literature suggests it is difficult to exceed a particle diameter of 15 nm.*

*Additionally, another explanation could be added to justify the fact the polyol synthesis is not the best option. Actually, non-hydrolytic processes possess a lot of advantages in comparison with the hydrolytic ones. If the hydrolytic chemistry allows working at low temperatures between 20 and 100 °C and respecting the environment (concept of a green chemistry), there are a lot of disadvantages like the elaboration of systems with low crystallinity, and particles with hydroxides on the surface which require a post-functionalization step to obtain stable dispersions. Likewise, homocondensation M-O-M (M = metal, O = oxygen) is favored in these systems. In contrast, non-hydrolytic systems are more adapted to mixed oxides and enhance heterocondensation M-O-M'. The obtained systems are mono and multicationic oxides well-crystallized in the nanometer range. The presence of organic molecules at the surface makes the nanoparticles hydrophobic and a transfer in organic media is eased [105] [106] [107] [108] [109] [110] [111] [112]. All of these benefits convinced us to select an organic synthesis and especially the thermal decomposition method regarding the Figure I-18.*

*In this project, we elaborate zinc iron oxide nanoparticles by thermal decomposition of iron and zinc acetylacetonates in different chemical media which are described and compared in the part III. The mechanisms driving the thermal decomposition are described more precisely in the next section (part II.2), as well as different methods to perform the heating.*

## II.2. The thermal decomposition method and heating processes

Two different heating routes are studied for the thermal decomposition of zinc iron oxide nanoparticles: a conventional way in a heating mantle and a microwave heating. In this part, the thermal decomposition synthesis will be described regarding the reaction mechanism and the two different methods of heating will be introduced and then compared specifically in the case of the synthesis of iron oxide nanoparticles.

### II.2.1. Thermal decomposition mechanisms

As previously detailed, the thermal decomposition is a suitable synthesis for the elaboration of mixed cubic ferrites  $M_xFe_{3-x}O_4$  in comparison with other synthesis routes [113]. The particle formation occurs through the thermal decomposition of organometallic precursors in organic media with the addition of surfactants. The produced particles possess some advantages like a good control of their diameter, size distribution, and morphology through the tuning of the decomposition temperature, the ratio between precursors and surfactant, the choice of solvent, precursors and surfactant, the heating rate, and the reaction time. The LaMer's theory is a pedagogical model commonly used to explain the thermal decomposition mechanisms which are in fact close to the seed-mediated growth [84].

#### II.2.1.A. Synthesis mechanisms

The nucleation/growth theory, otherwise known as the LaMer's theory allows depicting the mechanisms of the thermal decomposition synthesis from the precursor decomposition to the formation of nanoparticles. Following the theory [114], the nanoparticle formation is described in three steps: the production of monomers or the pre-nucleation step, the nucleation from a supersaturated solution which occurs from a critical concentration of nuclei and then, the growth of the formed nuclei (Figure I-19).

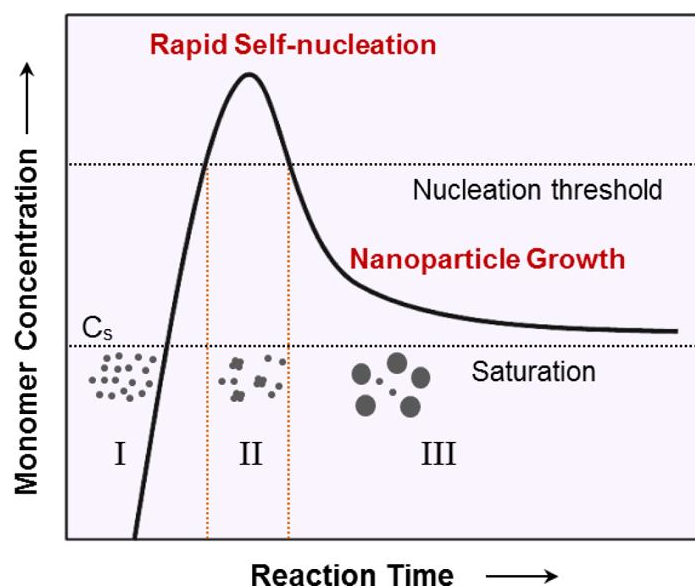


Figure I-19. LaMer's diagram: monomer concentration versus time of reaction [114]. From L. Wu *et al.* [115].

During the pre-nucleation step, the starting point is the supersaturated solution which is initiated by the dissolution and decomposition of precursors in the solvents, leading to the release of ions in solution. The concentration of reactive species in solution increases until solubility limit is reached. Then, at the critical concentration, the nucleation spontaneously occurs which further reduces the ion concentration below the nucleation limit. Hence the nucleation step is fast, giving rise to the growth of the formed nuclei in a last step. The growth is governed by a diffusion of the solute towards the particle surface and lasts until all the reagents are used up.

In this way, the synthesis is governed by the decomposition of the precursors. During heating, the reagents are heated up to the boiling point of the used solvent. When the decomposition temperature of the precursors is reached, the precursors start to decompose, initiating the release of species in the solution. When the critical concentration is attained, the nuclei become stable in solution and nucleation/growth steps can occur.

The nanoparticle size distribution can be monitored through the nucleation and growth steps, with a precise control of the supersaturation conditions. To obtain monodisperse nanoparticles with a narrow size distribution, it is necessary to separate these steps. Indeed, if nucleation and growth could occur at the same time, it means that new nuclei will be created during the growth of nuclei previously formed. Thus, it will induce the formation of heterogeneous nanoparticles in terms of size and this is clearly what should be avoided [114].

Moreover, coalescence between particles could appear during the growth step. To avoid this phenomenon, electrostatic or steric repulsion between particles may be a solution. It can be set up by the introduction of a surfactant in the starting mixture either to create a charged double layer in a polar solvent at the particle surface or to enable steric hindrance with adsorption of molecules from long-chain polymers, both methods leading to the stabilization of particles in solution [116]. It will be described in more details in the chapter II.

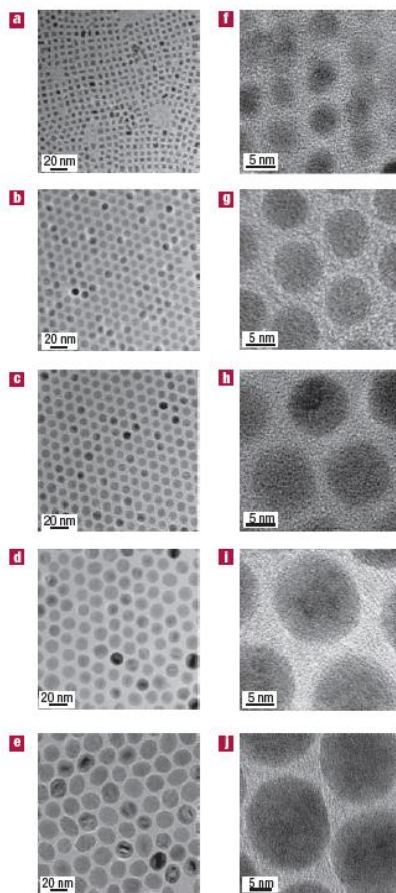
Besides the LaMer's theory, other mechanisms also exist to describe the crystal growth like the oriented attachment. Indeed, in oriented attachment, particles with similar crystallographic orientations clump together forming organized aggregates with bindings of particles at planar interfaces [117].

### *II.2.1.B. Control of the nanoparticle size, shape and composition*

This kind of synthesis method is convenient to control the nanoparticle size, shape and even the chemical composition.

On the one hand, it is possible to control the nanoparticle size by changing the solvent in the reaction mixture and especially by modifying the boiling point of the solvent. For example, J. Park *et al.* have obtained nanoparticles with sizes ranging from 5 to 22 nm by using one different solvent each time: 1-hexadecene, octyl ether, 1-octadecene, 1-eicosene and trioctylamine (Figure I-20) [26]. The nanoparticle diameter increases with the elevation of the

boiling point of the solvent. It is believed to be due to a better reactivity of the iron precursor in solvents with higher boiling points.



**Figure I-20.** (a,f) 5 (b,g) 9 (c,h) 12 (d,i) 16 and (e,j) 22 nm nanoparticles obtained by increasing the boiling point of the solvent. From J. Park *et al.* [26].

At the same time, nanoparticles sizes can be more finely tuned. In this context, iron oxide nanoparticles with sizes ranging from 6 to 13 nm were synthesized. The purpose was to increase the nanoparticle size by 1 nm by a seed-mediated growth technique with different ratios of iron precursor and oleic acid as a surfactant (Figure I-21) [118]. This study perfectly shows how to adjust the nanoparticle size by controlling the growth step of the thermal decomposition process.

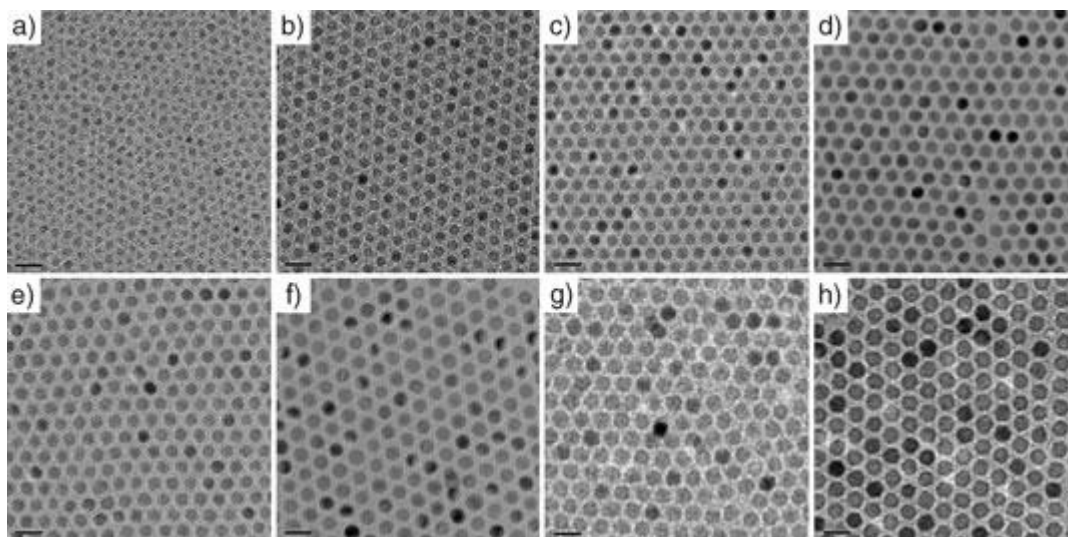


Figure I-21. a) 6 b) 7 c) 8 d) 9 e) 10 f) 11 g) 12 and h) 13 nm nanoparticles obtained by a seed-mediated growth method. From J. Park *et al.* [118].

The two effects previously mentioned had also been studied by Demortière *et al.* (Figure I-22) [27]. Thus, the nanoparticle diameter increases when the ratio between oleic acid and iron oleate rises and with the elevation of solvent boiling point.

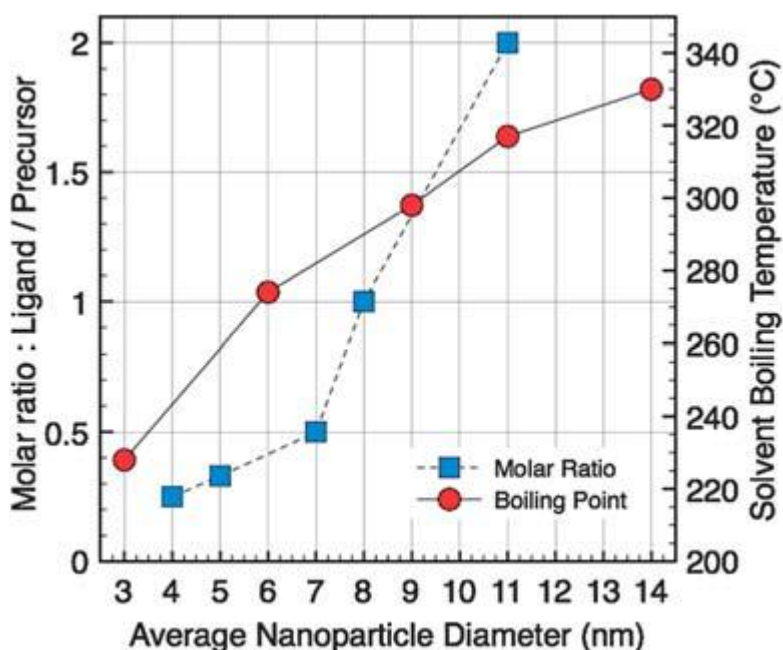


Figure I-22. Effect of the molar ratio between surfactant and precursor and the solvent boiling point on the nanoparticle size. From Demortière *et al.* [27].

In other cases, the nanoparticle sizes could be well adjusted by using a combination of two surfactants. Monodisperse  $\text{Fe}_3\text{O}_4$  nanoparticles were synthesized by thermal decomposition of iron(III) acetylacetonate in 1,2 hydrocarbon-diol as a solvent with a mixture of two surfactants: oleic acid and oleylamine (Figure I-23) [119] [120].

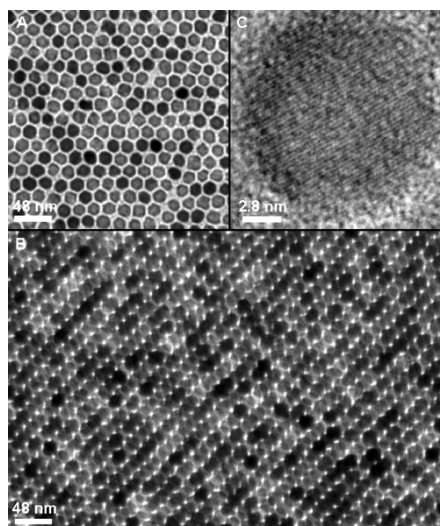


Figure I-23. 16 nm  $\text{Fe}_3\text{O}_4$  nanoparticles (TEM bright field images. From S. Sun and H. Zeng [119].

Moreover, as with the control of the nanoparticle size, a lot of studies were performed about how to tune the nanoparticle shapes. One of the parameters although not mentioned in this section is the reactivity of precursors which can be tuned to control the nanoparticles size and shape during synthesis. Indeed it can be controlled by the chain length and concentration of the surfactant. The speed and efficiency of the reaction will increase with short chain length.

The change of ratio between iron oleate as a precursor and oleic acid as a surfactant, through the study of the reaction temperature, have resulted in the elaboration of  $\gamma\text{-Fe}_2\text{O}_3$  nanoparticles with cubic and spherical shapes in a controlled way (Figure I-24) [121].

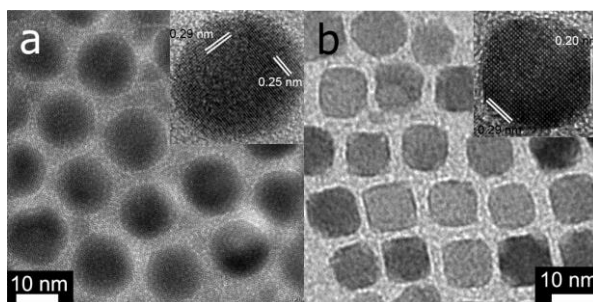


Figure I-24. TEM images of a) spherical and b) cubic  $\gamma\text{-Fe}_2\text{O}_3$  nanoparticles. From G. Salazar-Alvarez *et al.* [121].

Following the same strategy,  $\text{Fe}_3\text{O}_4$  nanoparticles with controlled shapes and sizes between 8 and 50 nm were obtained by thermal decomposition of iron oleate in octadecene [122]. The nanoparticle sizes were monitored by changing the ratio between the precursor and acid oleic, the surfactant in this case. Different shapes were obtained: cubic and then spherical when the reaction time was increased (Figure I-25).



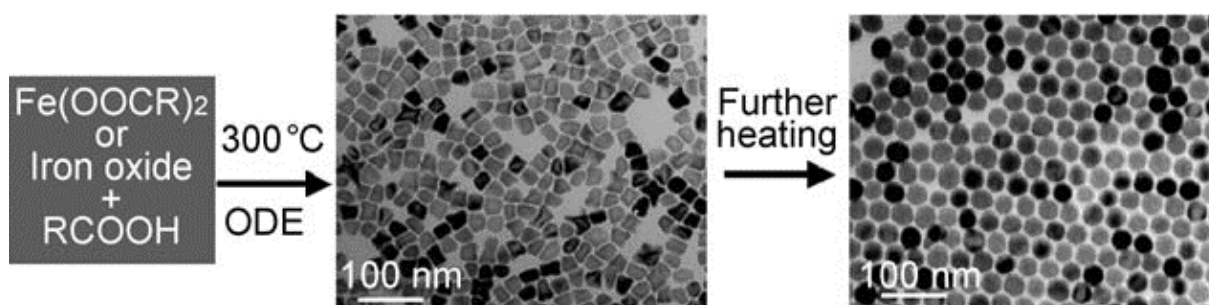


Figure I-25.  $\text{Fe}_3\text{O}_4$  nanoparticles synthesis by thermal decomposition in octadecene. From N. R. Jana's group [122]

Furthermore, W. Baaziz *et al.* had investigated the synthesis of cubic iron oxide nanoparticles in a mixture of a homemade iron oleate precursor, octadecene as a solvent and a mixture of two surfactants: oleic acid and sodium oleate (Figure I-26) [123].

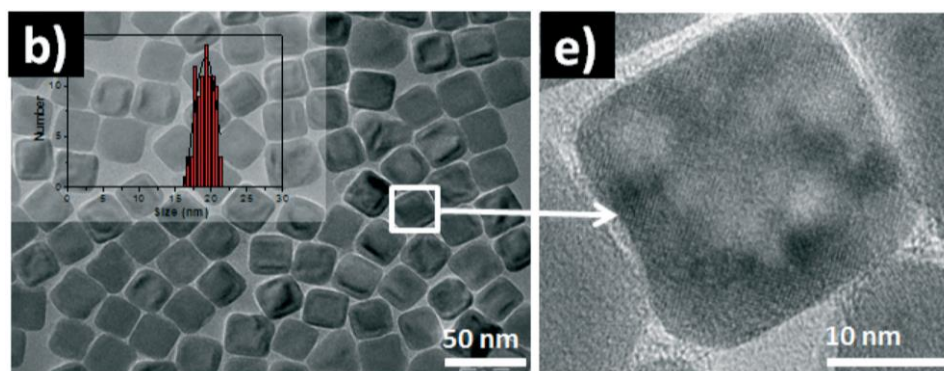


Figure I-26. b) TEM image and e) HRTEM micrograph of 19 nm nanoparticles with cubic shape. From W. Baaziz *et al.* [123].

On the other hand, the tuning of nanoparticle chemical composition has been explored. The choice of the type of precursor has a predominant role in the chemical composition homogeneity of nanoparticles. Mixed-oxide nanoparticles  $\text{M}_x\text{Fe}_{3-x}\text{O}_4$  could be synthesized by mixing several metallic precursors ( $\text{M} = \text{Zn}, \text{Co}, \text{Ni}, \text{Mn} \dots$ ) [31] [102] [105] [124]. Acetylacetonate  $\text{M}(\text{acac})$  metal salts are often used [31] [102] [105] [119] [125]. Otherwise, the chemical composition is not so simple to control. In most of the cases, heterogeneity of composition was noticed and it is often caused by the difference between the decomposition temperatures of the used precursors. Using precursors with decomposition temperature close allows obtaining nanoparticles with an homogeneous chemical composition [105].

Additionally, in the case of magnetite nanoparticles, the chemical composition can vary with the nanoparticle size. Some studies have highlighted the formation of a thin oxidized layer at the surface of the particle like a core-shell framework with the magnetite phase as a core. This phenomenon has been observed for nanoparticles with sizes above a dozen nanometers. Under this indicated size, the nanoparticles seem to be constituted of maghemite [27] [2].



## II.2.2. Comparison between conventional and microwave heating

In the classical way, the heating is achieved with a heating mantle into contact with a hot plate. The energy is transferred through mechanisms of convection, conduction and radiation of heat between the plate and the surface of the mantle [115], which generate inevitable thermal gradients in the solution. The difficulty also relies on the way to maintain a constant temperature, especially at large scale [116]. Microwave heating has been developed to solve these issues. Indeed, it allows to generate heat through the interactions between the molecules in the reaction vessel and the electromagnetic field, resulting in a more homogeneous temperature. The next part will focus on the advent of the microwave oven in chemistry and also its interest in comparison with the conventional heating.

### II.2.2.A. General overview

The first experiments of material synthesis by microwave heating emerged in 1986 [126]. This recent process is used as an aid to classical chemical synthesis like the hydrothermal or thermal decomposition method. Indeed, the microwave route offers short heating times, high heating rates, a homogeneous thermal transmission [127], fast reaction kinetics, and the formation of less by-products of reaction [127] [128]. Similarly, it provides a better reproducibility between experiments, quantitative yields, even if lower than with co-precipitation, hydrothermal or thermal decomposition [78] and it is also scalable [127].

The microwave heating technique occurs through two mechanisms: dipolar polarization and ionic conduction. The permanent dielectric dipolar moment of a molecule aligns with the electric field of the microwave excitation by orientating the molecule parallel to the field. Mechanical losses (which can be seen as frictions between molecules) are transformed into heat. The ionic conduction refers to charged chemical species which will move into the media under the electrical force  $F = qE$  with  $q$  the charge and  $E$  the electrical field. The viscosity of the medium will convert this kinetic energy into heat.

Three indicators quantify the suitability of a solvent for microwave heating:

- the dielectric constant  $\epsilon'$  which predicts the ability of a material to be polarized by an external electric field. It can be assimilated to a measure of the microwave energy density.
- the dielectric loss  $\epsilon''$  namely the loss factor which defines the efficiency of conversion of electromagnetic energy in heat.
- the loss tangent  $\tan \delta = \epsilon'' / \epsilon'$  which corresponds to the ratio between dissipative and capacitive behavior of a material. A high value indicates the efficiency of production of heat through microwave irradiation.

The choice of solvent is important in microwave reaction. In such synthesis, the thermal decomposition is less governed by the boiling temperature of solvents than their dielectric constant. What mattered is to select a mixture of solvents capable of coupling with the applied

microwave field [129]. Polar solvents are hence more convenient than nonpolar ones for a better coupling with the microwave. A compromise has to be done because too polar solvents like DMSO (dielectric constant  $\epsilon' = 47$ ) initiate too much pressure in the microwave reactor (due to a too high loss tangent) activating the system security and the shutdown of the device. Non polar solvents with a too low dielectric constant produce in general paramagnetic particles. It is the case for the experiments performed by Brollo *et al.* who synthesized superparamagnetic  $\text{Fe}_3\text{O}_4$  particles with octadecene (ODE) [129].

The nanoparticle growth is sensitive to reaction conditions. Microwave devices are well adapted to this kind of synthesis because they enable to control different parameters like the temperature, the pressure and temperature rates [128]. In general, these systems can heat up until 300 °C and the most used frequency is about 2 450 MHz for microwave magnetrons with a power from 600 to 1000 W [130]. The temperature can be monitored inside the reactor with an optical fiber probe and an external infrared sensor. Sometimes some devices present a camera for the observation of stirring (Figure I-27) [128]. The overpressure inside the reactor due to the evaporation of constituent of the reaction medium can be evacuated thanks to a drain at the surface of the vessel [78].

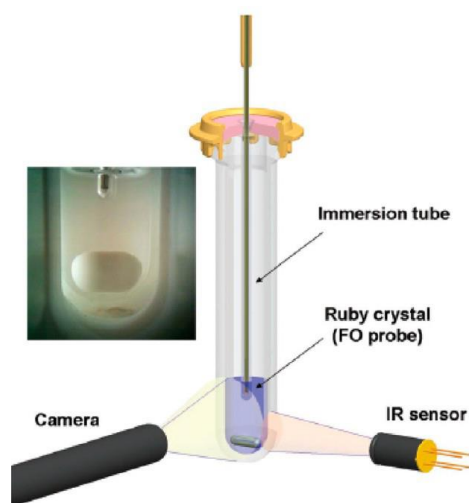


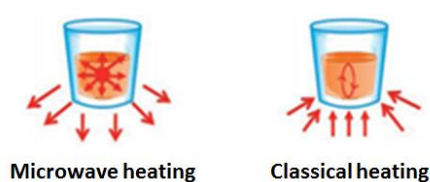
Figure I-27. Scheme of a microwave reactor with a temperature probe. From Gawande *et al.* [128].

One of the major assets is that the microwave heating enables to produce more homogeneous nanoparticles in terms of size in comparison with the classical heating [127]. This phenomenon is due to two different facts.

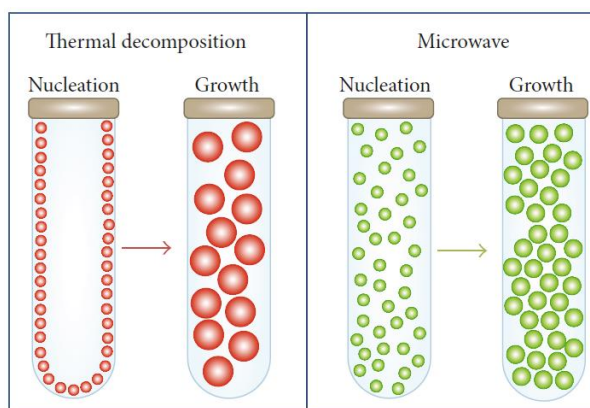
On the one hand, the delivering of a more uniform heat inside the reactor has an impact on the nanoparticle homogeneity. In classical heating, the heat transfer is performed from the external surface of the glass container to the interior of the container (Figure I-28). This type of heat transfer could generate temperature gradients inside the solution volume, hence the heat heterogeneity. On the contrary, in microwave heating, the heating process starts in the solution and spreads to the reactor walls. There is a heat release from the inside of the container to the exterior (Figure I-28) [130], which explains the uniform heating.

On the other hand, a homogeneous nucleation and a shorter crystallization time under microwave irradiation are responsible for the production of monodisperse nanoparticles.

Indeed, in microwave heating, the dipoles tend to align in the direction of the applied electric field and the generated energy losses are dissipated as heat due to dielectric losses and molecular friction. This point explains why the heating starts at the heart of the solution with multiple nucleation. Thus, competitive growth is also induced inside the solution which means that there will have a slight decrease of the nanoparticle mean size whereas in classical way, the nucleation operates on the glassware walls which gives somewhat bigger nanoparticles (Figure I-29) [129].



**Figure I-28. Mechanisms of heating for microwave and classical configurations. From Perino *et al.* [130].**



**Figure I-29. Difference of reactional mechanism for the particle formation for classical and microwave thermal decomposition. From Brollo *et al.* [129].**

For an optimal efficiency of the heating, the mixture must possess a suitable high dielectric constant  $\epsilon'$  to allow microwave absorption [131]. Figure I-30 depicts the loss tangent  $\delta$  which quantify the heating efficiency of solvents. When this value is above 0.5, the solvent is considered as efficient for microwave heating. When the value is comprised between 0.1 and 0.5, it is acceptable and then below 0.1, the solvent is inefficient [128].

solvent	$\tan \delta$	solvent	$\tan \delta$
ethylene glycol (EG)	1.350	1,2-dichloroethane	0.127
ethanol	0.941	water	0.123
dimethyl sulfoxide (DMSO)	0.825	chloroform	0.091
methanol	0.659	acetonitrile	0.062
1,2-dichlorobenzene	0.280	tetrahydrofuran	0.047
<i>N</i> -methyl-2-pyrrolidone (NMP)	0.275	dichloromethane	0.042
acetic acid	0.174	toluene	0.040
dimethylformamide (DMF)	0.161	hexane	0.020

**Figure I-30. Loss tangent  $\delta$  for the most common solvents (2.45 GHz, 20°C). From Gawande *et al.* [128].**

As an example, dibenzyl ether seems to be a promising candidate to elaborate homogeneous magnetite nanoparticles with sizes around 6 nm by a thermal decomposition method [119]. However, dibenzyl ether possesses a low dielectric constant  $\epsilon'$  of 3.86, that makes it not suitable for microwave-assisted thermal decomposition. An alternative in this case could be the use of room temperature ionic liquids (RTIL) with for example [bmim] [BF<sub>4</sub>] which can be used to improve the polarity of solvents, as a microwave absorbing agent [132].

### *II.2.2.B. Microwave heating for the elaboration of iron oxide spinel nanoparticles*

Firstly, M. E. F. Brollo *et al.* have compared a thermal decomposition synthesis with and without the use of microwave heating [129] for the development of iron oxide magnetic nanoparticles. Iron oleate has been used as a precursor, oleic acid as a surfactant. Solvents with different dielectric constants have been tested like dibenzyl ether, octadecene, benzyl alcohol, and dimethyl sulfoxide DMSO. The influence of the solvents has been studied and the results are in agreement with the previous part II.2.2.A. DMSO has a high dielectric loss tangent (Figure I-30). The conversion of microwave energy into heat is enhanced and the temperature rises close to the boiling point of the solvent. The ascent of pressure is then generated into the reaction vessel resulting in the stop of the reaction for safety requirements. It is therefore not the case for solvents with a lower loss tangent like octadecene.

Other parameters have been investigated: the heating ramp, the reaction time and the precursor concentration. At first, the more rapid the heating ramp, the smaller the particles will be. Next, a long reaction time will grow bigger particles until precursor depletion. And finally, a high precursor concentration will tend to produce smaller particles [129].

A. Makridis *et al.* have performed the synthesis of manganese and cobalt ferrite nanoparticles through microwave-assisted hydrothermal method [133]. Nanoparticles with sizes below 14 nm have been synthesized in a mixture of metal acetylacetonates and octadecylamine. The microwave-assisted method results in best yields and times of reaction 24 times shorter compared to the classical hydrothermal process [134].

In the same way, Fe<sub>3</sub>O<sub>4</sub> nanoparticles have been synthesized through microwave-assisted hydrothermal method [135]. A. Rizzuti *et al.* have studied the addition of different surfactants (polyvinylpyrrolidone, oleic acid) on the control of nanoparticle shape and growth.

Some other authors have investigated the microwave heating and reported the elaboration of nanoparticles with high purity and crystallinity. M. Sertkol *et al.* have set up a microwave-assisted combustion method to develop 20 nm Zn<sub>x</sub>Ni<sub>1-x</sub>Fe<sub>2</sub>O<sub>4</sub> nanoparticles [136]. C. Sciancalepore *et al.* have reported a microwave-assisted thermal synthesis of magnetite nanoparticles with sizes ranging from 4 to 8 nm [137].

All of the previously mentioned synthesis assisted by microwave have been realized in the single mode. Otherwise, it is possible to scale-up by upgrading towards the multi-mode microwave-assisted synthesis. The synthesis operates in the same manner, the difference being that the system consists of a multiple vessels rotor for simultaneous batches. This novel configuration has been tested by L. Gonzalez-Moragas *et al.* with the production of 3 g of superparamagnetic Fe<sub>2</sub>O<sub>3</sub> nanoparticles in less than 1 h in one time. To have a better idea of what it represents, only 22 mg of the same nanoparticles could be obtained in one batch with the single mode. In both methods, the nanoparticles hold the same characteristics in terms of size, stability, and magnetic properties [138].

### II.3. Conclusion

*Different synthesis routes employed for the elaboration of mixed cubic ferrites  $M_xFe_{3-x}O_4$  have been detailed and summarized (coprecipitation, hydrothermal/solvothermal, polyol, microemulsion, sol-gel, and thermal decomposition). The advantages and drawbacks of the methods have guided the choice of the synthesis to a non-hydrolytic synthesis: the thermal decomposition.*

*Among the assets, the particles synthesized by thermal decomposition evidence a good control of their diameter, size distribution, and morphology through the tuning of the decomposition temperature, the ratio between precursors and surfactant, the choice of solvent, precursors and surfactant, the heating rate, and the reaction time. In addition, this approach favors a homogeneous chemical composition and high yields.*

*Moreover, the nanoparticles are also functionalized directly in-situ with the surfactants used in the reaction media, which will ease the stabilization of particles in solution. This particularity is a major strength to the next step of the project: the formulation of a stable dispersion of nanoparticles (Chapter II). Indeed, the synthesis choice has to take into account the overall process of the study, the final goal being to produce a stable ink for inkjet printing.*

*The reactional mechanisms of the selected synthesis method have been detailed through the LaMer's theory, comparable to the seed-mediated growth.*

*Two ways have been explored and compared for the heating process: a classical way in a heating mantle and a microwave one. The microwave option has been retained for the study. This reproducible route allows combining a homogeneous heating directly inside the reactor, eliminating the issues of thermal gradients engendered by the conventional heating, as well as a production of uniform particles in terms of size and shape.*

*Thus, the microwave assisted thermal decomposition is well adapted for the present study: the synthesis of zinc iron oxide nanoparticles.*

### III. $\text{Zn}_{0.4}\text{Fe}_{2.6}\text{O}_4$ synthesis by thermal decomposition

#### III.1. Comparison of two heating routes

The nanoparticles are synthesized by thermal decomposition with organic solvents. Two different ways of heating are employed derived from the literature: the conventional one in a heating mantle which has been carried out by Audrey Delots during a 6 month internship and the other one in a microwave oven. These two different processing methods are compared to determine the most appropriate way to control the size and the morphology spread of the obtained nanoparticles. A good control of the particle size of  $\text{Fe}_3\text{O}_4$  through the addition of ethylene glycol has been reported [139]. Other studies have used this work to synthesize core-shell  $\text{Fe}_3\text{O}_4$  nanoparticles [140] [141]. We applied this technique to mixed oxides of  $\text{Zn}_x\text{Fe}_{3-x}\text{O}_4$ , in order to tune the magnetic and dielectric properties by the ratio Zn/Fe [142] (Part I.2.).

This chapter will only focus on the nanoparticles synthesis and their microstructural and chemical properties. The two different experimental protocols are described in the next parts and then compared.

##### III.1.1. Classical thermal decomposition

###### III.1.1.A. Experimental protocol

A first method for  $\text{Zn}_x\text{Fe}_{3-x}\text{O}_4$  synthesis is inspired and adapted from Y. Yang *et al.* group [32]. The setup is described on Figure I-31.A.

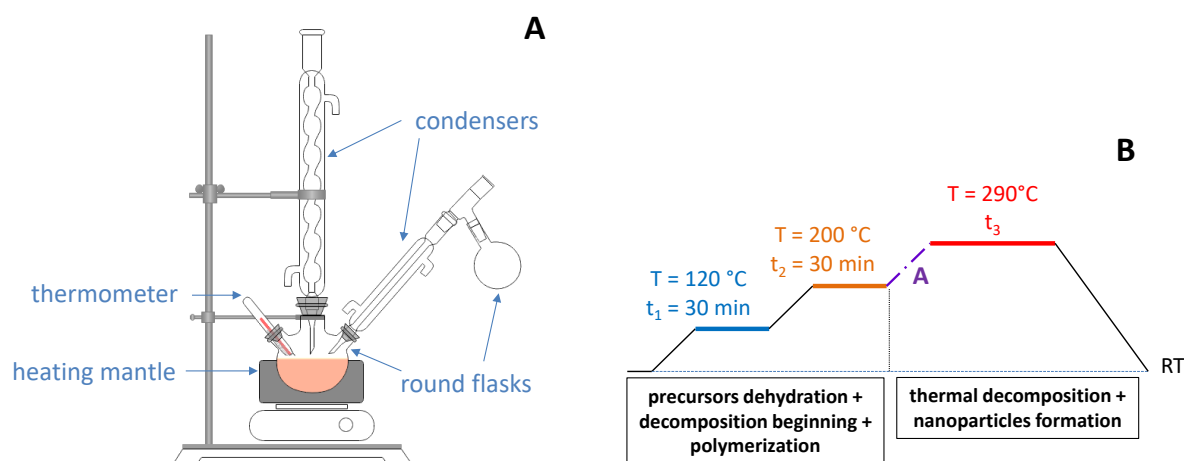


Figure I-31. Setup sketch (A) and temperature profile (B) for classical thermal decomposition.

The quantities of precursors which includes iron, zinc acetylacetonates ( $\text{Fe}(\text{acac})_3$  and  $\text{Zn}(\text{acac})_2$ ) and oleic acid (OA) are dispersed in benzyl ether. The obtained mixture is stirred during 10 min to homogenize the solution and then heated up to 120 °C during 30 min to dehydrate the precursors (Figure I-31.B). After the dehydration stage, the solution is reheated to 200 °C during 30 min to remove a portion of oleic acid from the main flask, which goes

directly in the second round flask in Figure I-31.A. At this temperature, the precursors start to decompose. Indeed, oleic acid begins its decomposition around 200 °C (Figure I-32), Fe(acac)<sub>3</sub> around 195 °C [143] and Zn(acac)<sub>2</sub> around 136 °C [144]. It initiates a condensation reaction.

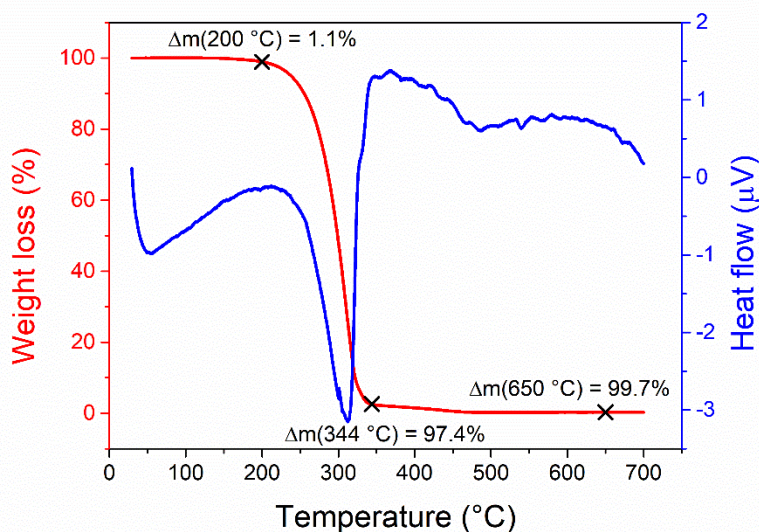


Figure I-32. TG-DTA curves of acid oleic (90% purity)

Thereafter, the second flask in the set-up is removed and the temperature is increased to the boiling temperature of benzyl ether (290 °C) at a certain rate A (°C/min) for refluxing during a time  $t_3$  (Figure I-31-B). This step allows to pursue the decomposition of the precursors and thus to induce the nucleation/growth of nanoparticles. The system is finally cooled down to room temperature. The variation of A and  $t_3$  has an impact on the nanoparticle shape and size. These parameters finally drive the nanoparticle morphology. The next part introduces the results obtained through this synthesis, the aim being to obtain nanoparticles homogeneous in terms of shape and size and which meet the requirements defined in part I.4. Indeed, it needs to be borne in mind that two ranges of size are researched in the interest of this study: superparamagnetic particles with a diameter below 20 nm and ferrimagnetic particles with diameters comprised between 30 and 60 nm.

### III.1.1.B. Effect of synthesis parameters...

#### III.1.1.B.a. ... on the particle size

Five different experiments are described in this section on Figure I-33. The influence of the content of zinc, solvent, surfactant and even the temperature rate A with the duration time  $t_3$  have been briefly examined. A short comparison with Audrey Delots' results will be summarized at the end of the part. The goal was to handle and verify the reproducibility of the synthesis, as well as the main observed conclusions.

	$\frac{Zn}{Fe}$	$\frac{solvent}{Fe}$	$\frac{surfactant}{Fe}$	$\frac{solvent}{surfactant}$	A (°C/min)	$t_3$ (h)	Theoretical composition	Size (nm)	
								TEM	DRX
1	0.10	18	5		20	0.5	Zn <sub>0,27</sub> Fe <sub>2,73</sub> O <sub>4</sub>	40 - 80	39.8
2	0.19	9	2	4	6	2.5	Zn <sub>0,48</sub> Fe <sub>2,52</sub> O <sub>4</sub>	50 - 100	57.1
3	0.19	9	2		10	2	Zn <sub>0,48</sub> Fe <sub>2,52</sub> O <sub>4</sub>	80 - 400	64.7
4	0.60	11	3		6	2	Zn <sub>1,13</sub> Fe <sub>1,87</sub> O <sub>4</sub>	100	60.4
5	0.60	11	1	9	10	1.5	Zn <sub>1,13</sub> Fe <sub>1,87</sub> O <sub>4</sub>	25 - 50	

**Figure I-33. Summary table of the experiments with variation of some parameters: molar ratios of Zn, solvent and surfactant compared to Fe, molar ratio of solvent versus surfactant, and also A and  $t_3$ .**

An analysis of the different parameters on the nanoparticles size and shape can be drawn from these results (Figure I-33). The nanoparticle size is compared through TEM observations (Figure I-35) and X-ray diffraction (XRD) patterns (Figure I-34). The TEM pictures give a simple idea of the range of size while XRD allows to calculate the size more precisely with the Debye-Scherrer formula [145] as follows:

$$d = \frac{K \lambda}{\beta \cos(\theta)} \quad \text{I-32}$$

with  $d$  the crystallite diameter,  $K$  a shape factor (equal to 0.89 is the case of spherical particles),  $\lambda$  the wavelength of the X-ray source,  $\beta$  the full-width at half maximum (FWHM) and  $\theta$  the peak position. Each peak is fitted with a Lorentzian function as follows:

$$y = y_0 + \frac{2 \times A}{\pi} \times \frac{\beta}{4 \times (x - x_c)^2 + \beta^2} \quad \text{I-33}$$

where  $y$  is the intensity,  $y_0$  the offset,  $A = \frac{H \times \pi \times \beta}{2}$  the area under the curve with  $H$  the maximum peak intensity,  $x$  the angle in theta degree and  $x_c$  the position of the peak.

The values of diameters in Figure I-33 are the average of the calculated sizes corresponding to the main peaks displayed in Figure I-34.



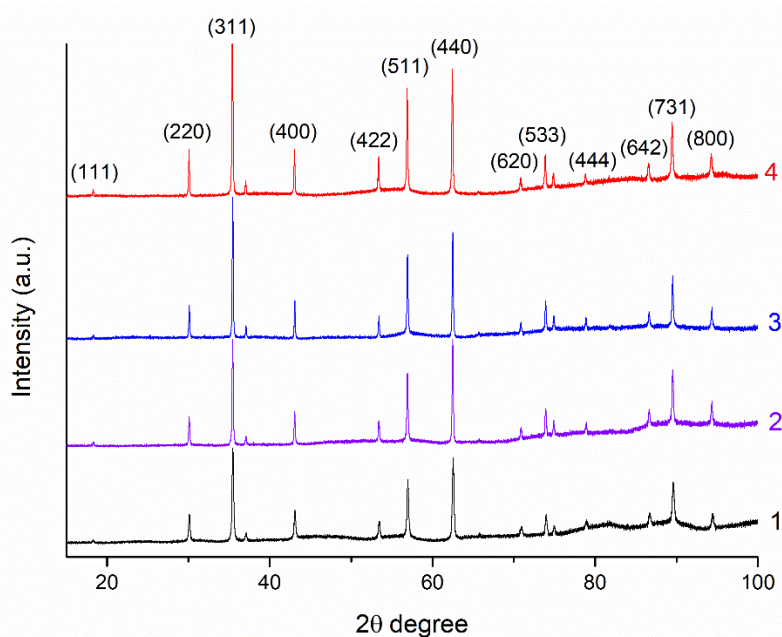


Figure I-34. X-ray diffraction patterns for the experiments 1 to 4 summarized in Figure I-33.

As we previously mentioned (III.1.1.A), the protocol parameters clearly influence the particle synthesis. Indeed, the duration of the step at 290 °C  $t_3$  has a direct impact on the particle size. Experiments 1 and 5 have been performed with the shortest temperature stages and they also show the smallest particle sizes of the campaign. Hence, the longer  $t_3$  is, the bigger the nanoparticles are.

In the same manner, the sloped ramp  $A$  to attain the stage at 290 °C affects the particle growth. In general, a slow heating rate gives to the particles more time to form and develop [146]. The particles should acquire bigger diameters with slower heating rates. However, it is not confirmed by these experiments, especially regarding the samples 2 and 3 in the table (Figure I-33).

After the protocol parameters, the proportions between solvents, surfactants and precursors have their own effect. The surfactant, oleic acid, is used to control the particle growth. Indeed, the increase of the molar ratio between surfactant and Fe makes the particle diameters grow. It is shown with experiments 2 and 4. Likewise, the quantity of solvent is also important. It seems that a large volume of solvent compared to the surfactant induces a decrease of the particle size. It may be due to the dilution of the surfactant. This could be the case for the samples 3 and 5 with at the same time the effect of a shorter duration time at 290 °C.

### III.1.1.B.b. ... on the particle shape

The molar ratio of surfactant versus precursors is also known to master the particle morphology. In their work [32], Y. Yang *et al.* highlight more specifically the incidence of the molar ratio of Zn with surfactant on the particle shape. Indeed, they conclude that if the Zn content is in large excess compared to the surfactant one, the obtained particle morphologies are irregular and less defined. In their study, the particles display octahedral forms for a ratio below 0.58, polyhedral between 0.6 and 0.75 and disparate above 0.75.

Building on this insight, all of the five samples possess ratios below 0.58. Therefore, according to Y. Yang et al. [32] the particles should be octahedral which is clearly not the case (Figure I-35).

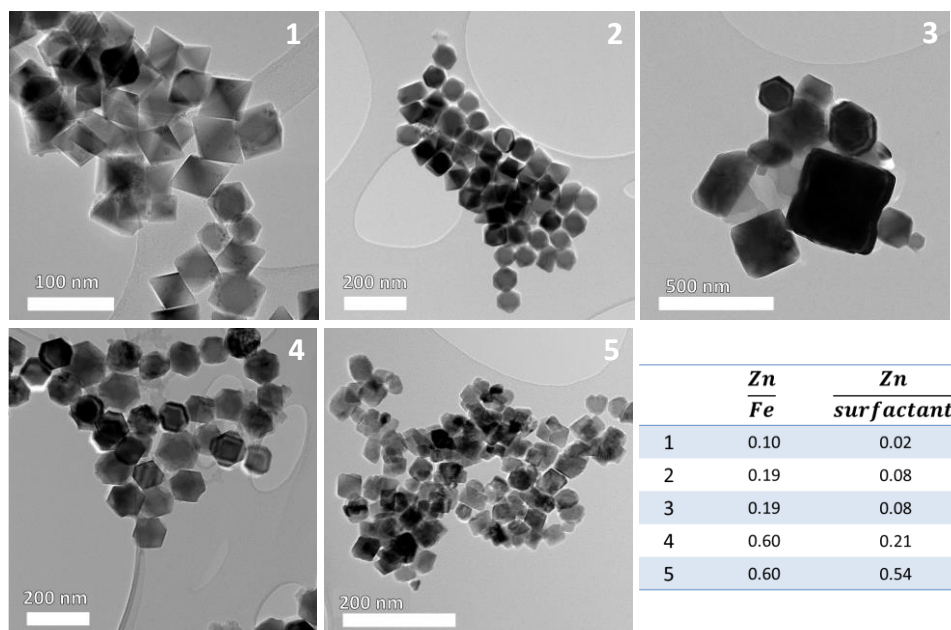


Figure I-35. TEM pictures for the experiments 1 to 5 summarized in Figure I-33.

Instead, the nanoparticles exhibit polyhedral shapes with a huge polydispersity whether in terms of size or morphology in each batch. The only exception is for the sample 4 for which the particles look uniform with hexagonal shapes (truncated octahedron) of approximately 80 nm, which is in agreement with XRD analysis (Figure I-33 and Figure I-34). Considering the sample 5 with a value of 0.54 is close to the limit under which particles should be octahedral and above which they must be polyhedral, it could match with the literature. However, the global trend observed in the literature is not observed.

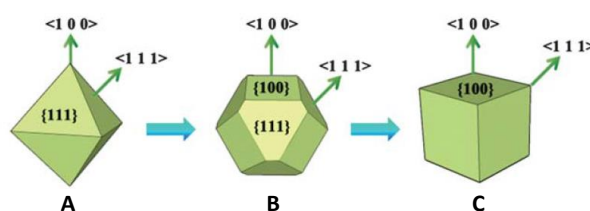
### III.1.1.B.c. Discussion

Nonetheless, some similarities with what Audrey Delots has noticed during her internship are verified. On the one hand, regarding the protocol parameters, the duration  $t_3$  of the heating stage at 290 °C controls the nanoparticle growth. A long time  $t_3$  improves the formation of bigger particles. A compromise has to be made because too long duration time could induce heterogeneities in the system due to the generation of new nuclei with a delayed growth, and thus polydispersity.

The shape and size monodispersity of particles is also enhanced with fast heating rates. The homogeneous nucleation is made possible due to a simultaneous growth of nuclei. This point is not evidenced with our particles.

On the other hand, Audrey Delots has also pointed the surfactant and precursors effect. Indeed, the particle size increases with the ratio Zn on surfactant (samples 2 and 4). An

explanation could be that the nucleus growth is easier in an environment with a surfactant content reduced. Four types of morphologies have been discovered by varying the molar ratio between Zn and Fe, and which also differ from the literature [32]. Below 0.17, the particles should be spherical, between 0.17 and 0.33 octahedral, cubic between 0.33 and 0.67, and then polyhedral above 0.67. This tendency is not exhibited in this case either. Anyhow, it is true that the surfactant versus Zn content has an impact on the particle shape. The surfactant binds preferentially onto crystallographic planes and thus inhibits the growth in the normal of this direction [147]. Indeed, the surfactant is used to reside on the faces with lower energies and especially in the planes (111), (110) and (100) [148]. Hence, the surfactant fixes on these planes and, octahedral, polyhedral or cubic shapes are preferred depending on the quantity added (Figure I-36).



**Figure I-36. Octahedral (A), polyhedral (truncated octahedral) (B) and cubic (C) morphology with a precursor/surfactant ratio below 0.58 (A), between 0.58 and 0.72 (B) and between 0.72 and 0.78 (C). At higher ratio, irregular particles are formed. From Y. Yang *et al.* [32].**

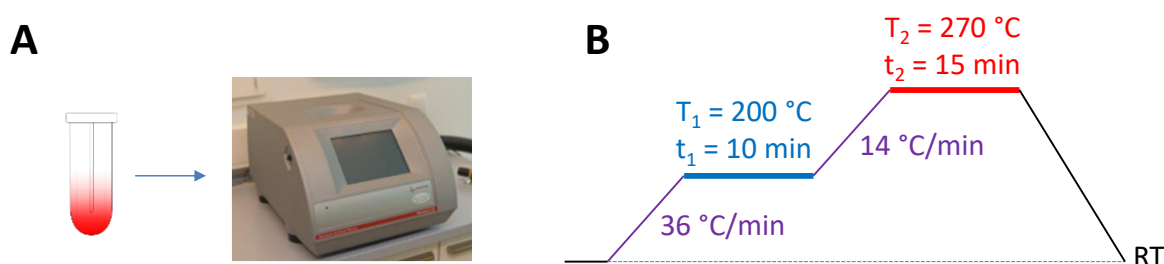
The presence of large nanoparticles of about 300-400 nm of diameters, also called mesocrystals (sample 3) may originate from secondary reactions due to non-hydrolytic coupling at high temperature. They would come from aggregation caused by nanoparticles embedded in an organic framework emerging from the surfactant. The formation of organic shells at the particle surrounding occurs during the synthesis and will be described in details in Chapter II.

As a conclusion, the uniformity of particle size and shape is closely related to the protocol parameters (heating rate  $A$  and duration time  $t_3$ ) and also to the solvent, surfactant and precursors contents. A competition between these two types of criteria is observed.

A global polydispersity in size and shape is noticed in the samples. The synthesis conditions are difficult to pilot with a basic chemical set-up. It is thus delicate to draw conclusions when a lot of parameters vary at the same time, without the possibility to set one of them. Especially, the heating rate  $A$  is conditioned by the heating mantle used. A solution is to modify the set-up and to precisely pilot the temperature rate with a heating mantle directly connected to a temperature controller. In this way, an experimental procedure could be performed by keeping the heating rate constant and modifying the other parameters and back again. In this manner, it could be easier to discriminate the effect of a parameter with another one. Finally, the key of a well-controlled synthesis lies in the operating protocol. In view of the major problems encountered and to improve the reproducibility between experiments, the thermal decomposition in a microwave oven is investigated.

### III.1.2. Microwave-assisted thermal decomposition

The second synthesis method of  $Zn_xFe_{3-x}O_4$  particles is based on the work of Y-J. Liang *et al.* who have performed the synthesis of  $Fe_3O_4$  nanoparticles through microwave-assisted thermal decomposition [139]. In this method, the molar quantities of  $Fe(acac)_3$  and  $Zn(acac)_2$  are added to a homogeneous mixture of oleylamine (OAm), oleic acid (OA) and octadecene (ODE). A volume of ethylene glycol (EG) is introduced only to make the nanoparticles grow. The obtained solution is kept under ultrasound during 10 minutes before introduction in the microwave reactor monowave 300 (Anton-Paar, Figure I-37.A). The mixture is at first heated up to 200 °C in 5 min and maintained at this temperature for 10 min. Then, the temperature is increased from 200 °C to 270 °C in 5 min and stays constant for 15 min. The reactor is finally cooled down to 60 °C (Figure I-37.B).



**Figure I-37. Setup sketch (A) and temperature profile (B) for microwave-assisted thermal decomposition.**

The effect of each solvent (OAm, OA, ODE, EG) is not clearly described in the publication [139], except for EG which is used to increase the particle sizes. OAm and OA are employed as surfactants. An experimental campaign has provided many answers considering the incidence of each solvent in the synthesis. It is described in part III.2.

In this manuscript, the word “surfactant” is used to qualify oleylamine and oleic acid to ease the explanation. Indeed, they are much more than surfactants. These multifunctional reactants are employed in the synthesis of multiple nanoparticle systems as surfactants, solvents, stabilizers, or reducing agents. They combine several functions at the same time, depending on the precursors and other reactants used in the synthesis. Oleylamine alone can also complex with metal ions, forming intermediate precursors decomposed in a controllable way to elaborate nanoparticles [149].

As previously described, oleylamine is often used as a cosolvent with oleic acid. In the study, the reaction medium has a reductive effect due to the amine functions of oleylamine, which contribute to the reduction of  $Fe^{3+}$  in  $Fe^{2+}$  ions. The combination of oleylamine with oleic acid also enables to tune the particle morphology by changing their proportion, these two reagents binding differently onto the crystal planes of the particle [149]. The present chapter focus on the influence of oleylamine and oleic acid on the particle morphology, other functions are investigated in chapter II.

After both synthesis methods, the nanoparticles are recovered and washed six times by centrifugation processes with addition of a mixture of 73 %<sub>v</sub> of ethyl acetate and the rest of ethanol. Once all of the organics are removed, the nanoparticles are dried naturally under air.

The monowave 300 microwave allows to work with small containers of a maximum of 20 mL per reactor. Only between 50 and 100 mg of particles are collected per reactor. A synthesis transfer in reactors of 500 mL capacity is made possible with another system: the Masterwave BTR. The procedure has been adapted. The second temperature increase  $T_2$  (Figure I-37-B) occurs at 250 °C, not at 270 °C. The reproducibility between the two devices has been verified. The set-up at larger scale raises productivity 10 to 20 times compared with the monowave 300.

### III.1.3. Discussion

#### III.1.3.A. Choice of solvents

Liang *et al.* [139] have used two different mixtures of solvents. On the one hand, the first mixture is constituted of three solvents with low dielectric constants, dielectric losses and loss tangents: OAm, OA and ODE (Figure I-38). Contrary to Brollo *et al.* [129], they have succeeded to synthesize non superparamagnetic particles with diameters of 4 and 20 nm with only ODE as a solvent.

In the second mixture, a quantity of ethylene glycol (EG) is added. EG is a polar solvent with a high dielectric constant (Figure I-38), making it a suitable candidate for microwave heating. The addition of such solvent allows at the same time enhancing the heating efficiency of the solvent and increasing the particle diameter to 50 and 200 nm depending on the added ratios.

	benzyl ether	OAm	OA	ODE	EG
Boiling temperature (°C)	298	> 300	194	315	197
Dielectric constant $\epsilon'$ from literature (20-25 °C)	3.86	2.13	2.46	2.25	37
Mesured dielectric constant $\epsilon'$	3.74	2.68	2.18	2.00	14.40
Mesured dielectric loss $\epsilon''$	0.58	0.10	0.06	0.04	14.41
Mesured loss tangent $\tan \delta$	0.16	0.04	0.03	0.02	1.00

**Figure I-38.** Boiling point (from the safety data sheets) and the measured dielectric constant, loss and loss tangent at 2.45 GHz of the solvents used. Comparison of the dielectric constants with the literature [150] [151] [152].

According to the different results obtained with octadecene in the literature, it is worth questioning this solvent efficiency in microwave heating. Octadecene is not a good microwave absorber due to its small loss tangent, it looks thus not well adapted for microwave synthesis. A rapid heating is favored by solvents with higher loss tangents.

A hypothesis for the elaboration of particles with octadecene through microwave irradiation is that considering a mixture of precursors in a solvent, the precursors could have higher loss tangents than the liquid media, thus engendering a selective heating in the reactor [153] [154]. It explains why nanoparticles could be synthesized even in solvent with a low dielectric constant.

Conversely, a mixture of precursors in a solvent with a high loss tangent will favor the absorption of the microwave by the solvent with a short penetration length of the microwave due to the reactivity of the solvent. In this case the heating is fast and effective.

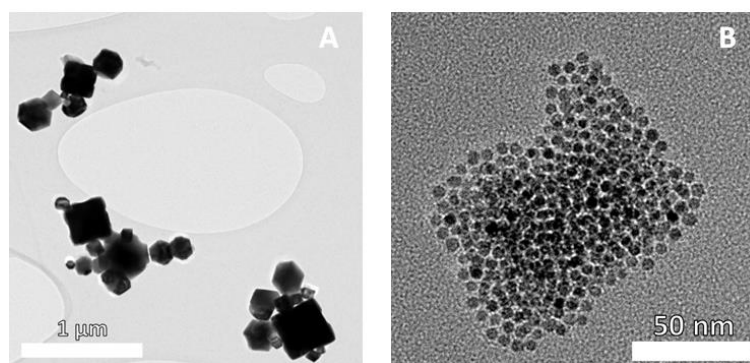
In the case of a solvent with a low loss tangent, the microwaves will penetrate deeply in the reactor until reaching a constituent with a higher loss tangent which will allow a slower heating of the solution [155]. Furthermore, it is important to keep in mind that the dielectric properties depend on the frequency and also the temperature [156] [157].

As in the case of benzyl ether mentioned in part II.2.2.A (Figure I-38), an ionic liquid could be added to the reaction media to enhance the heating efficiency through microwave coupling.

Hence, ODE could be used as a solvent in microwave reactor as it leads to the elaboration of homogeneous particles even with a less efficient heating.

### III.1.3.B. Characterization of the morphology and size of $Zn_{0.4}Fe_{2.6}O_4$ nanoparticles

As explained in part I.2.2, we will focus on  $Zn_{0.4}Fe_{2.6}O_4$  nanoparticles with the composition of interest for the study. On the one hand, the two different heating processes for the thermal decomposition could be compared through the nanoparticle morphologies. The conventional way in a heating mantle allows obtaining various morphologies: cubes, octahedra (III.1.1.B)... However, it induces heterogeneity in terms of size and shape in a batch, due to insufficient monitoring of the temperature and gradients during the reaction, which is clearly observed in Figure I-39-A.

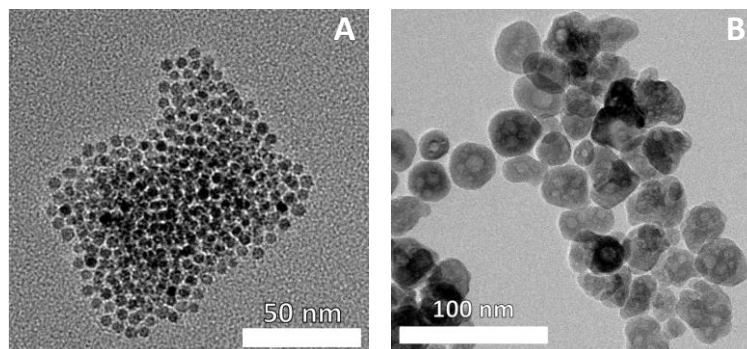


**Figure I-39. Nanoparticles obtained by thermal decomposition. (A) classical and (B) microwave heating.**

On the contrary, it is easier to control the temperature rates with the microwave-assisted thermal decomposition. Indeed, it enables a fast and more uniform heating, leading to nanoparticles with homogeneous size and shape, and also reproducible (Figure I-39.B).

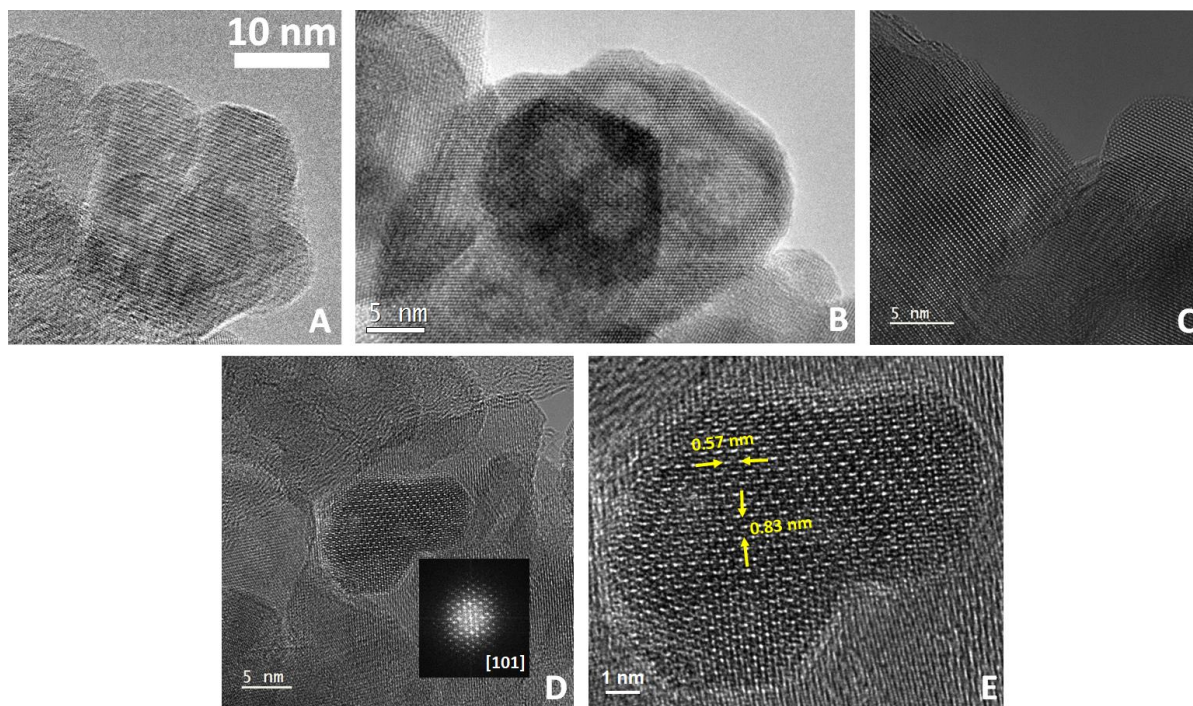


Moreover, in addition to enabling homogeneity in terms of nanoparticles size and morphology, the two ranges of size mentioned in part I.4 are attainable and controllable (Figure I-40). Indeed, particles with sizes below the superparamagnetic limit [65] are obtained in Figure I-40.A with a diameter close to 5 nm (written SP(F)M for superparamagnetic particles within the document), and then diameters above this limit are also achievable with sizes around 35 nm at first glance (Figure I-40.B, written FM for ferrimagnetic particles). The nanoparticle growth occurs with the addition of ethylene glycol in the reactor. The effect of each solvent used in the microwave synthesis will be detailed in part 0.



**Figure I-40.**  $\text{Zn}_{0.4}\text{Fe}_{2.6}\text{O}_4$  microwave heating. (A) SP(F)M and (B) FM particles.

If the SP(F)M nanoparticles (Figure I-40.A) are spherical in shape, the morphologies displayed in Figure I-40-B look like “raspberry” frameworks. This structure could be assimilated to a binding between crystallites (Figure I-41.A) and the continuity of the crystal planes in one raspberry structure is confirmed thanks to a close observation of the structure with high-resolution transmission electron microscopy (HRTEM in GRAND ARM, Figure I-41.B-E) performed at the Spanish National Center for Electron Microscopy (ICTS) in Complutense University in Madrid in Spain. This shape type has already been observed in previous studies, in particular in the case of iron oxide [158] with nanostructures of about 250 nm.



**Figure I-41.** (A) TEM and (B-E) HRTEM in GRAND ARM images of the “raspberry” structure (FM particles).

In respect of the atypical morphology of the FM particles, the pore diameters of the nanoparticles have been estimated according to the BET (Brunauer-Emmett-Teller) method. The BET analysis allows measuring the surface area and pore volume of a material by nitrogen adsorption/desorption. Furthermore, it is crucial to verify that the synthesized material is not too porous, its density being important regarding its magnetic properties. Figure I-42 summarizes the specific surfaces, cumulative volume to desorption and the mean diameter of the pores in the case of three experiments with a classical heating and one microwave-assisted. In general, the pore diameters are comprised between 10 and 30 Å (Figure I-43). The pore size decreases with the specific surface of the particle. Thus, larger particles tend to display broader pores than smaller particles. In parallel, the increase of the desorption volume with the specific surface (Figure I-43) evidences the presence of more pores in the small particles, but with smaller diameters. This result is in agreement with the raspberry-like shape of the FM particles which should present more pores as a result of its framework. These informations indicate that the SP(F)M particles might possess tiny pores due to their huge specific area and also that the classical heating does not provide particles less porous than the microwave heating.

In addition, the specific surfaces analyzed by the BET technique are in agreement with the theoretical ones for the sample 5 and FM particles (Figure I-42). On the contrary, a large gap is noticed for samples 2 and 4. It means that a lot of developed surface of particles is lost in the case of samples 2 and 4, due to closed porosity. It is consistent with the desorption volume. FM particles are finally less porous and the developed surface is more accessible.



	Heating	$\langle D \rangle$ (nm)		Specific surface (m <sup>2</sup> /g)		Cumulative volume (desorption) (cm <sup>3</sup> /g)	Mean porous diameter (Å)
		TEM	XRD	BET	Theo		
2	classical	50 - 100	57.1	5.6	15.3	0.041	19.3
4		100	60.4	0.7	11.5	0.049	26.2
5		25 - 50	-	31.9	30.5	0.122	12.1
FM	MW	27.4 ± 4.0	19.1	37.3	41.8	0.144	10.4

Figure I-42. Values of specific surfaces, cumulative volume to desorption and pore diameters estimated by BET for nanoparticles obtained by classical and microwave heating.

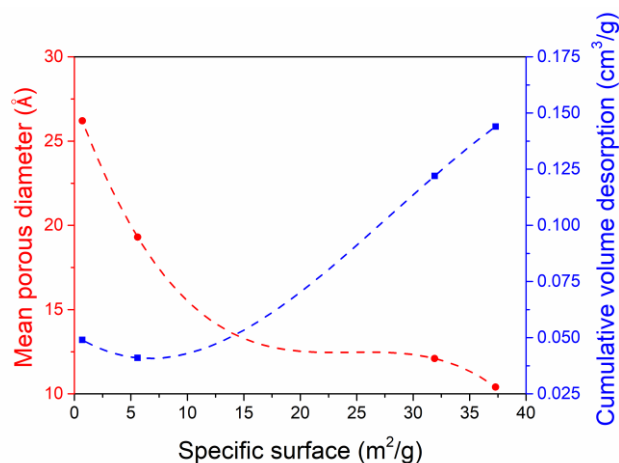
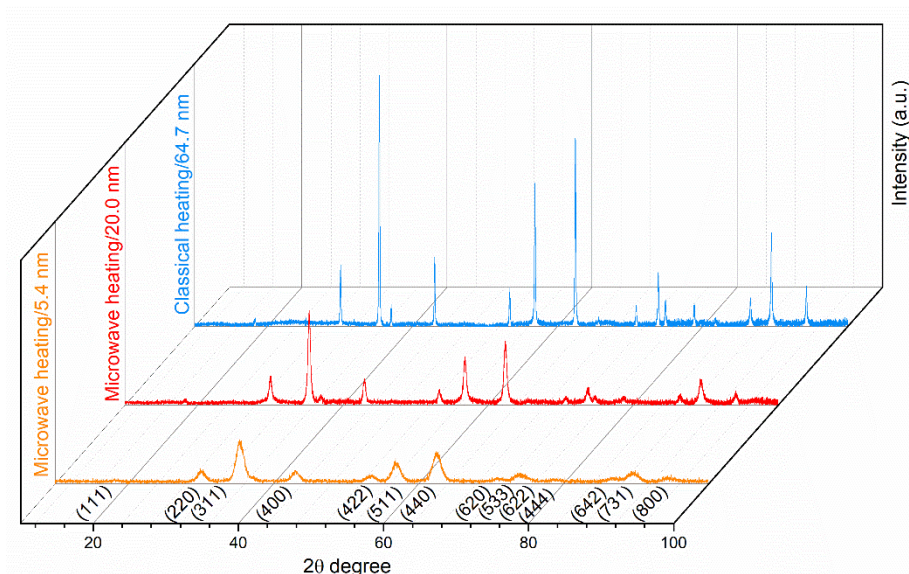


Figure I-43. Evolution of pore diameters and cumulative volume to desorption versus the specific surface for classical and microwave samples (Figure I-42). Dashed lines are just guides for eyes.

The phase purity of the obtained nanoparticles is also demonstrated with X-ray diffraction patterns (Figure I-44). All of the patterns match with the PDF 04-021-5090 which corresponds to pure Zn<sub>0.35</sub>Fe<sub>2.65</sub>O<sub>4</sub> magnetite with a cubic structure and Fd-3m space group. The main peaks are indexed in Figure I-44. In the case of the microwave heating, according to the Scherrer formula (Equation I-32), the crystallite size is equal to 5.4 nm for the SP(F)M particles which is in agreement with TEM (Figure I-40.A). The FM particles possess crystallites with a 20.0 nm diameter which corroborates the hypothesis of a “raspberry” structure constituted of several crystallites (Figure I-40.B).



**Figure I-44. X-ray diffraction patterns of  $\text{Zn}_{0.48}\text{Fe}_{2.52}\text{O}_4$  (blue curve) and  $\text{Zn}_{0.4}\text{Fe}_{2.6}\text{O}_4$  nanoparticles (FM in red and SP(F)M in orange) for classical and microwave heating respectively.**

To complete the X-ray diffraction results, the samples are observed by TEM and the diameters are deduced from the pictures with the software ImageJ.

At first, the diameter values are counted from image processing with ImageJ. Figure I-45 and Figure I-46 exhibit the frequency distribution in percentage of the diameters observed in several experiments for SP(F)M and FM particles respectively. 150 to 750 particles are recorded per sample. Each distribution is fitted with a log normal distribution with the following formula [159]:

$$f(D) = \frac{1}{\sqrt{2\pi}\sigma D} e^{-\frac{\ln^2\left(\frac{D}{D_0}\right)}{2\sigma^2}} \quad \text{I-34}$$

with  $D$  the particle diameter,  $D_0$  the median diameter and  $\sigma$  the degree of polydispersion.  $D_0$  and  $\sigma$  are displayed on each graph. The mean diameter  $\langle D \rangle$  and the standard deviation  $\sigma_D$  are then calculated as follows:

$$\langle D \rangle = D_0 e^{\sigma^2/2} \quad \text{I-35}$$

$$\sigma_D = \langle D \rangle \sqrt{e^{\sigma^2} - 1} \quad \text{I-36}$$

The results are classified in the charts in Figure I-45 and Figure I-46. Then, the sizes are averaged through 5 to 7 samples originating from different synthesis batches. The final average is calculated from 1000 to 2500 particles.

Concerning SP(F)M nanoparticles (Figure I-45), the mean diameter is of  $6.3 \pm 1.1$  nm based on seven experiments (Figure I-49). The crystallite diameter calculated with the Scherrer formula is compared to the one obtained through the log normal distribution with TEM images

for four of the samples. A good correlation between those values is noticed even if the crystallite size is always smaller than the diameter observed in TEM. It could be due to a lack of accuracy during image treatment. Moreover, the narrow distributions confirm the homogeneity of the particle sizes and also the good reproducibility of the experiments.

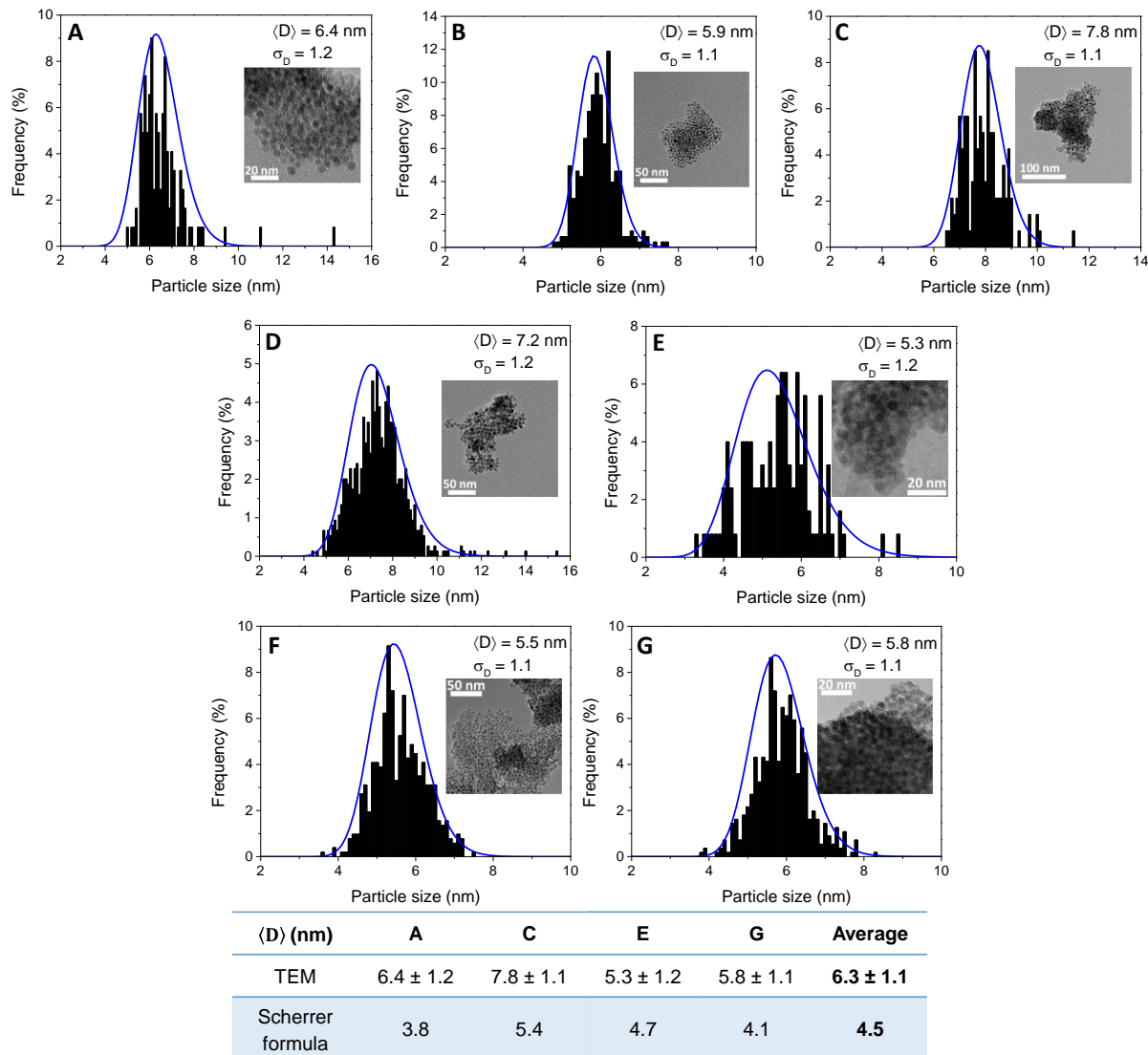


Figure I-45. Frequency distribution in percentage of the diameters of 7 samples of SP(F)M nanoparticles.

As the FM particles are not perfect spheres and due to the “raspberry” morphology, the contours of a single particle are difficult to distinguish. Indeed, some confusion could occur between the “raspberry” as the particle entity, and crystallites. Thus, the uncertainties are greater in this case. Large distributions of particle size which are in fact the addition of two subdistributions corresponding to two populations of size are displayed in Figure I-46. This tendency is emphasized in Figure I-47 with the clear evidence of two distributions, one around 16.5 nm and the second around 44.6 nm. The first population around 16.5 nm might correspond to unit crystallites whereas the second one should be assimilated to the “raspberry” particles, considered as collections of many crystallites arranged in bunch. The crystallite size (16.5 nm) in Figure I-47 is consistent with the values calculated with the Scherrer formula in Figure I-46. The mean diameter considering the five experiments is equal to  $21.6 \pm 1.5 \text{ nm}$ . Therefore,

broadly speaking, in view of the complexity of the morphology, the experiments are reproducible.

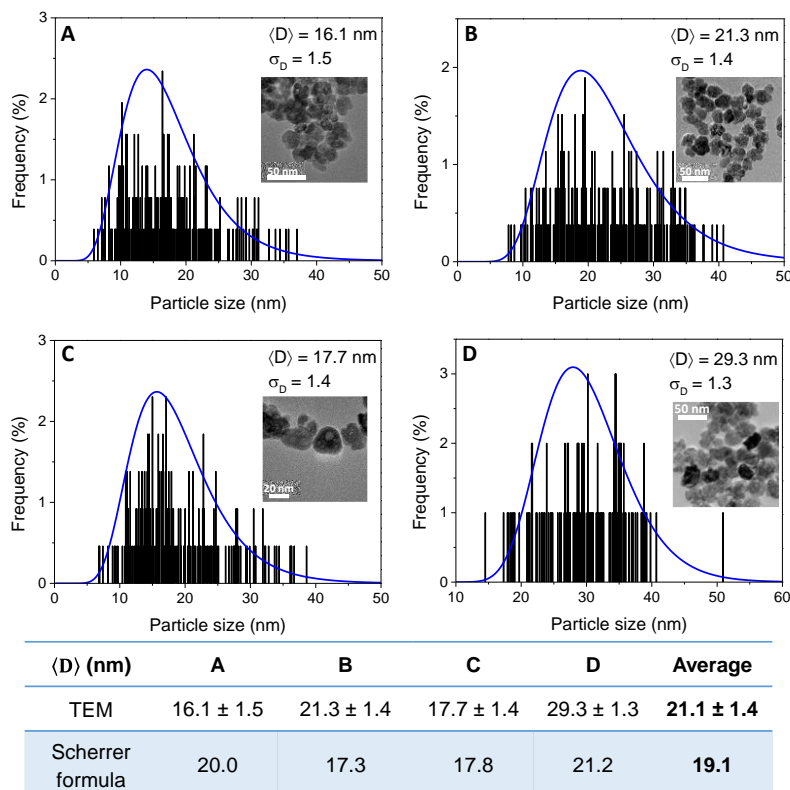


Figure I-46. Frequency distribution in percentage of the diameters of 4 samples of FM nanoparticles.

Taking into account the two populations of size, Figure I-47 exhibits the homogeneity of the particles if we consider the first peak ( $D_0 = 16.5 \text{ nm}$ ) with the crystallites only. The second peak ( $D_0 = 44.6 \text{ nm}$ ) displays a broader distribution due to the fact that “raspberry” particles are difficult to discriminate and to separate from each other.

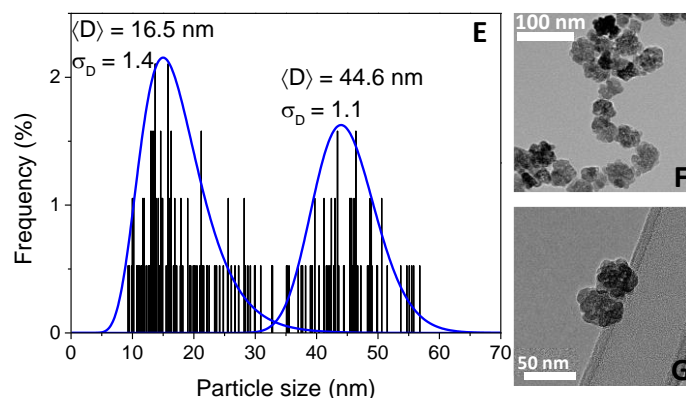


Figure I-47. Highlighting of two populations of size in the frequency distribution of diameters for FM particles.

To summarize all of these histogram distributions, the partition criteria of the Sturges method [160] is taken into account to slice the particles in a number of size categories. The larger of one category or the bin-width ( $W$ ) is expressed as follows:

$$W = \frac{D_{max} - D_{min}}{k} \quad \text{I-37}$$

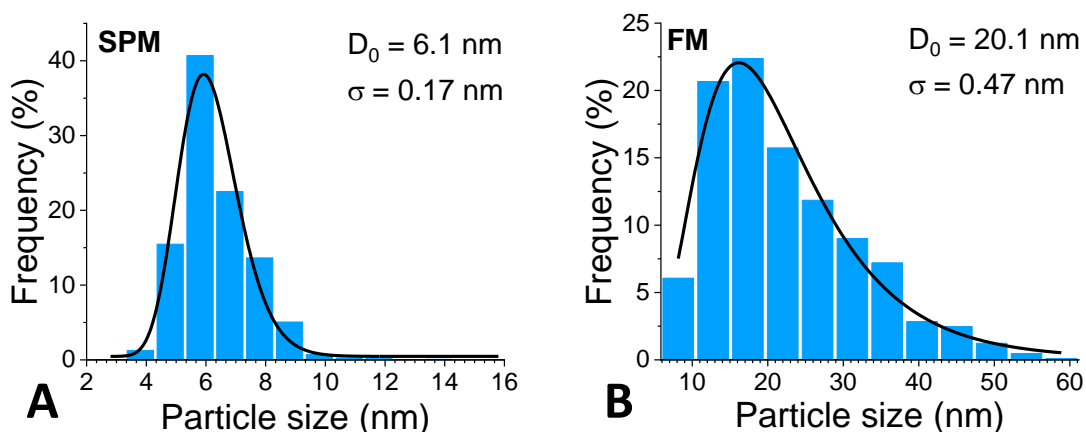
$$\text{with } k = 1 + 3.322 \times \log(N)$$

where  $D_{max}$  and  $D_{min}$  are the maximum and minimum diameters,  $k$  the total number of classes and  $N$  the number of assessed particles. The total number of classes  $k$  is equal to 13 for SP(F)M and 12 for FM particles. Figure I-48 shows the final distributions fitted with a lognormal function: SP(F)M particles with a mean diameter of  $6.2 \pm 1$  nm and FM particles with a  $22.4 \pm 11$  nm diameter.

The average crystallite size for SP(F)M (resp. FM) computed from XRD patterns: 4.5 nm (resp. 19.1 nm) is reduced compared to the TEM one:  $6.2 \pm 1$  nm (resp.  $22.4 \pm 11$  nm) (Figure I-45 and Figure I-46), as found for  $\text{Fe}_3\text{O}_4$  nanoparticles [161]. Nevertheless, in the case of FM particles, the Sturge slicing allows to obtain a mean particle diameter closer to the one obtained in XRD which is actually more accurate even if the standard deviation is important due to the large particle size distribution.

Concerning SP(F)M particles, the values are close. The gap between TEM and XRD diameters is not surprising, especially knowing that the Debye-Scherrer method which is an approximate method is used for XRD analysis.

For FM particles, the discrepancies could be due to the nanoparticle morphology (a crystallite assembly in a “raspberry structure”), highlighting the fact it is difficult to distinguish the borders of one particle from another. Moreover, when a particle is constituted of several grains, the diameter calculated by XRD should be below the one estimated by TEM, because the particle is not a single-domain. Also, another explanation lies in the large distribution of particles as inferred from the histograms (Figure I-46 to Figure I-48).



**Figure I-48.** Histogram distributions fitted with a lognormal function in dark lines of  $\text{Zn}_{0.4}\text{Fe}_{2.6}\text{O}_4$  (A) SP(F)M and (B) FM with sizes of  $6.2 \pm 1$  nm and  $22.4 \pm 11$  nm respectively. Statistic made with a set of 1000 to 2500 particles.

As a conclusion, the heating in a microwave oven allows to obtain nanoparticles with the two desired ranges of size, namely **SPM spherical particles with a  $6.2 \pm 1$  nm diameter** and **FM “raspberry” particles with a  $22.4 \pm 11$  nm diameter**. This type of heating enables a good

morphology and size control which lead to homogeneity, and the method is reproducible. On the contrary, even if different morphologies are accessible with the classical way, a few disadvantages are reported. Indeed, the heterogeneity in size and shape is observed and this technique is clearly not easily reproducible (Figure I-49). At the same time, the classical way does not allow to reduce the particle porosity in comparison with the microwave technique.

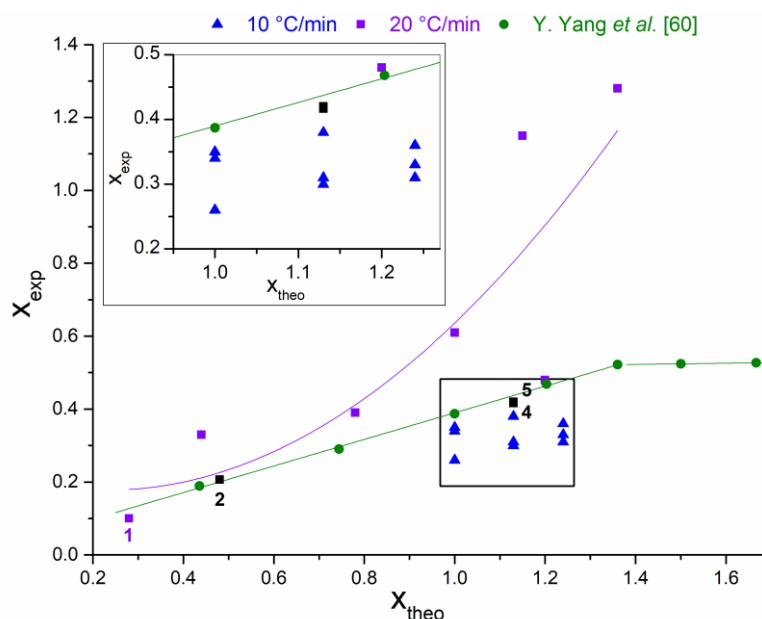
Heating type	Protocol	Precursors	Solvents	Surfactant	$\langle D \rangle$ (nm)		Advantages	Drawbacks
					TEM	XRD		
Classical	290°C 2h	Fe(acac) <sub>3</sub> Zn(acac) <sub>2</sub>	benzyl ether	OA	80 - 400	64.7	• Different morphologies (cubes, octahedra)	• Heterogeneity in size and shape • Problem of reproducibility
Microwave	270°C 15 min				ODE	EG EG		
		22.4 ± 11 (FM)	19.1					

OA = oleic acid, Oam = oleylamine, ODE = octadecene, EG = ethylene glycol

**Figure I-49. Summary table of the two heating ways with advantages and drawbacks.**

### III.1.3.C. Theoretical and experimental chemical compositions

The agreement between theoretical and experimental chemical compositions has to be checked to ensure that the magnetic properties are homogeneous and reproducible. Figure I-50 exhibits the gaps between the theoretical and experimental chemical compositions analyzed by ICP-AES in the case of classical thermal decomposition. At first, Audrey Delots' experiments are confronted to the literature. Indeed, three types of experiments are displayed, synthesis with 10 °C/min as the heating ramp (A, Figure I-31) (blue points), another with 20 °C/min (violet points) and the comparison with the trend obtained in the literature [32] (green points).



**Figure I-50. Discrepancies between theoretical and experimental chemical composition for classical thermal decomposition.  $x$  given for the molar quantity of Zn in the formula  $Zn_xFe_{3-x}O_4$ . Samples 1, 2, 4, 5 added (Figure I-33).**

Regarding the blue points, one can conclude that the experiments are not reproducible. Indeed, three theoretical compositions were reproduced and resulted with three different experimental chemical compositions. Thus, no clear tendency could emerge from these results.

Considering the experiments with 20°C/min for the temperature ramp, a possible trend could be evidenced which highlights the existence of a discrepancy between theoretical and experimental compositions. As the theoretical molar quantity of Zn is more important than the experimental one, it is clearly proved that zinc enters hardly inside the spinel structure and in an inhomogeneous manner. This fact could be due to the nature of the zinc precursor and especially to the difference between the decomposition temperature of iron and zinc precursors [162] [163]. Moreover, Y. Yang *et al.* [32] demonstrate a linear trend for the same interval of theoretical compositions (between 0.4 and 1.4 for  $x$ ) which clearly underlines the difficulty to reproduce the classical synthesis by changing operator and/or experimental setup. Furthermore, it appears that from a certain molar quantity of zinc (1.4), the experimental chemical composition stays the same. The system seems to reach a chemical saturation for a certain amount of zinc, which is clearly not exhibited with our assays (violet points).

Figure I-51 introduces the theoretical and experimental chemical compositions of some classical samples displayed in Figure I-33 and samples obtained through microwave heating. Samples 1 to 5 resulting from classical heating are also placed on the graph in Figure I-50. This seems to follow the trend observed in the literature (green curve) and the chemical composition looks reproducible considering sample 4 and 5.

In the case of microwave heating, the experimental compositions are close to the theoretical one and also reproducible, making this method more controllable.

		Theoretical composition	Experimental composition			Nanoparticle size	
			1	2	3	nm (TEM)	nm (XRD)
Classical heating	1	$Zn_{0.27}Fe_{2.73}O_4$	$Zn_{0.10}Fe_{2.90}O_4$	-	-	40 - 80	39.8
	2	$Zn_{0.48}Fe_{2.52}O_4$	$Zn_{0.20}Fe_{2.80}O_4$	$Zn_{0.21}Fe_{2.79}O_4$	$Zn_{0.21}Fe_{2.79}O_4$	50 - 100	57.1
	4	$Zn_{1.13}Fe_{1.87}O_4$	$Zn_{0.42}Fe_{2.58}O_4$	$Zn_{0.42}Fe_{2.58}O_4$	$Zn_{0.41}Fe_{2.59}O_4$	100	60.4
	5		$Zn_{0.42}Fe_{2.58}O_4$	$Zn_{0.42}Fe_{2.58}O_4$	$Zn_{0.42}Fe_{2.58}O_4$	25 - 50	-
Microwave heating	without EG	$Zn_{0.4}Fe_{2.6}O_4$	$Zn_{0.38}Fe_{2.62}O_4$	-	-	$6.2 \pm 1$	4.5
	with EG		$Zn_{0.31}Fe_{2.69}O_4$	$Zn_{0.31}Fe_{2.69}O_4$	-	$22.4 \pm 11$	19.1

**Figure I-51. Summary of the theoretical and experimental chemical compositions for classical and microwave-assisted thermal decomposition. The three experimental compositions corresponds to three measures realized in the same batch.**

#### III.1.3.D. Conclusion

*To conclude, to counter the various disadvantages encountered with the classical heating (heterogeneity in size and shape, non-reproducibility), the microwave-assisted thermal decomposition is selected as the convenient method in this study to synthesize uniform*



*spherical nanoparticles with a reproducible chemical composition. The next part III.2 will focus on a parametric study of the microwave synthesis to allow a better understanding of the reaction mechanisms and of the influence of each solvent/surfactant.*

### III.2. Parametric study of the microwave-assisted thermal decomposition

This parametric study is intended to optimize the reaction parameters: the Zn precursor, the solvents and surfactants proportions and the temperature ramp in order to check the sensibility of the synthesis to these parameters. The incidence of one parameter on the chemical composition through XRD, the morphology by TEM and size of crystallites by the Scherrer method is investigated.

#### III.2.1. Choice of the zinc precursor

The synthesis of mixed oxides  $Zn_xFe_{3-x}O_4$  requires the use of two precursors: one for the iron, the other for the zinc. A difference between the reactivity of each precursor could occur and favor the insertion of an element at the expense of another. Hence, it could generate gradient of chemical composition within the nanoparticles and also an important gap between the theoretical and experimental compositions. The point in this case is to avoid any heterogeneity of composition.

In the case of the use of two acetylacetonates, as  $Fe(acac)_3$  decomposition occurs around 195 °C [143] and  $Zn(acac)_2$  decomposition around 136 °C [144], a large difference between these two temperatures is noticed. It should then induce heterogeneity in terms of chemical composition according to the literature [162] [163] with the formation of secondary products of reaction for example. Indeed, as stated by E. Solano *et al.* [162] in the case of  $CuFe_2O_4$  nanoparticles the synthesis is governed by the decomposition of the two acetylacetonates. The gap between the decomposition temperatures creates a two-speed reaction with the generation of a temperature gradient. In this case, the formation of a secondary phase (metallic copper) due to the difference between decomposition temperatures of  $Fe(acac)_3$  (180 °C) and  $Cu(acac)_2$  (280 °C) has been observed [162]. A better outcome is demonstrated by replacing  $Zn(acac)_2$  with  $ZnCl_2$ .

Actually, mixing an acetylacetonate with a chloride allows controlling the reaction only with the decomposition of the iron precursor.  $ZnCl_2$  is an ionic salt and just incorporates directly in the particle structure when dissolving in TREG [163]. The use of  $ZnCl_2$  should enhance the reaction with  $Fe(acac)_3$  allowing a direct incorporation of zinc and thus pure products with a chemical homogenization.

To check all of these informations and to choose the most appropriate Zn precursor in the synthesis, the use of a Zn acetylacetonate and a Zn chloride are compared in similar conditions. The use of  $ZnCl_2$  requires a polar organic media. Thus the reaction media has been adapted for this experiment with the use of triethylene glycol (TREG) which possesses a dual role namely a solvent and a capping agent. This kind of synthesis does not require the addition of a



surfactant. To be sure of evidencing the impact of the precursor change, the two trials have been executed in the same exact conditions with a heating mantle.

ZnFe<sub>2</sub>O<sub>4</sub> nanoparticles have been synthesized. First, the particles obtained in the case of ZnCl<sub>2</sub> as the precursor are larger in comparison with those achieved with Zn(acac)<sub>2</sub> (Figure I-52). The analysis of the X-ray diffraction patterns is in agreement with TEM pictures (Figure I-53). The particle diameters calculated with the Scherrer formula (Equation I-32) are of 13.1 nm and 6.5 nm for ZnCl<sub>2</sub> and Zn(acac)<sub>2</sub> precursors respectively (Figure I-54).

Secondly, the experimental chemical compositions displayed in Figure I-54 are surprising in view of the literature. Indeed, the use of Zn(acac)<sub>3</sub> allows to produce nanoparticles with chemical compositions close to the theoretical ones whereas ZnCl<sub>2</sub> is responsible of an important gap between theory and experiment. These experiments significantly contradict the literature.

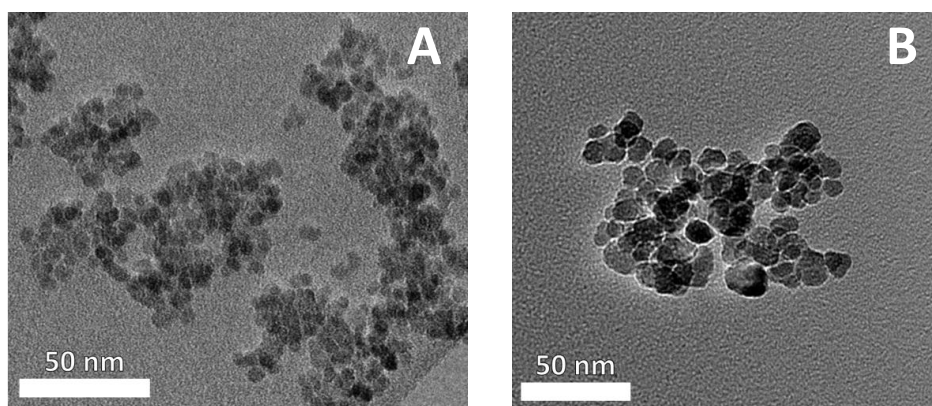


Figure I-52. Microwave-assisted thermal decomposition with change of Zn precursor: (A) Zn(acac)<sub>2</sub> and (B) ZnCl<sub>2</sub>.

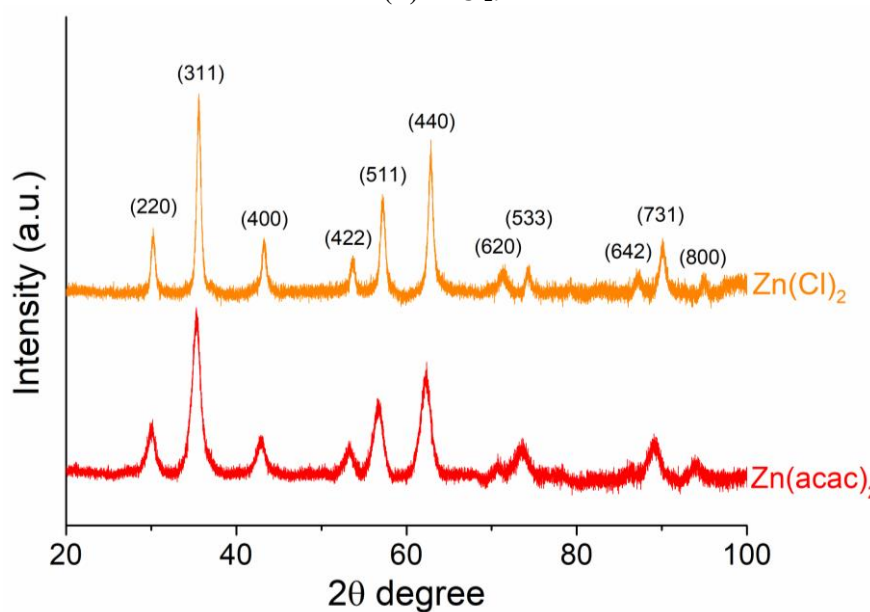


Figure I-53. X-ray diffraction patterns of two dissociated experiments realized with Zn(acac)<sub>2</sub> and ZnCl<sub>2</sub>.

Precursor	Theoretical composition	Experimental composition		Nanoparticle size nm
		1	2	
Zn(acac) <sub>2</sub>	ZnFe <sub>2</sub> O <sub>4</sub>	Zn <sub>0.97</sub> Fe <sub>2.03</sub> O <sub>4</sub>	Zn <sub>0.98</sub> Fe <sub>2.02</sub> O <sub>4</sub>	6.5
ZnCl <sub>2</sub>		Zn <sub>0.13</sub> Fe <sub>2.87</sub> O <sub>4</sub>	Zn <sub>0.13</sub> Fe <sub>2.87</sub> O <sub>4</sub>	13.1

**Figure I-54.** Comparison of chemical compositions from ICP-AES and nanoparticle sizes with the change of Zn precursor.

Despite this gap in the chemical compositions, none of the precursors introduces impurities in the system (Figure I-53) since no secondary phases is noticed. Hence, this particular behavior can be due to a difficulty of Zn to enter into the lattice. At some point, if we consider that ZnCl<sub>2</sub>, as an ionic salt, dissolves rapidly in the media, there is a certain amount of time before the start of the decomposition of Fe(acac)<sub>3</sub>. Finally, maybe we should consider it is better to have two precursors with decomposition temperatures not so far away considering the case of Fe(acac)<sub>3</sub> (180 °C) and Cu(acac)<sub>2</sub> (280 °C) [162] than using two different families of precursors with one them available too soon before the other. A second option could be to introduce ZnCl<sub>2</sub> in the mantle at the time the decomposition of Fe(acac)<sub>3</sub> starts.

Lastly, ZnCl<sub>2</sub> is not relevant for the nanoparticles synthesis in our case. This short study about Zn precursor in a solvothermal synthesis highlights the fact that a combination of two acetylacetonates will be the best way to achieve nanoparticles homogeneous in terms of chemical composition and with an experimental composition close to the ratio introduced at the beginning of the experiment. The interest is thus to combine these advantages with the microwave heating which conducts to a monodisperse distribution. After discussing about precursors, the influence of the solvents has also to be underlined.

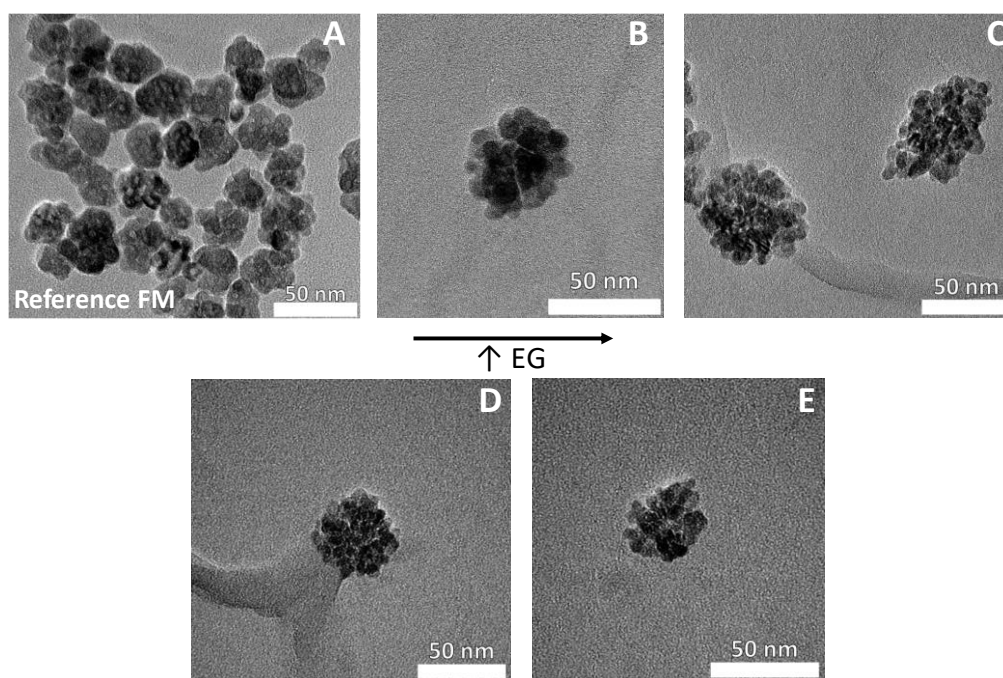
### III.2.2. Influence of solvents

The microwave-assisted thermal decomposition described in part III.1.2 employs two different solvents: octadecene (ODE) and ethylene glycol (EG). The effect of the addition of EG in the experiment is examined in the following part. By adding the ethylene glycol (EG) quantity, the synthesis route is close to a polyol process rather than a thermal decomposition one.

#### III.2.2.A. Addition of ethylene glycol (EG)

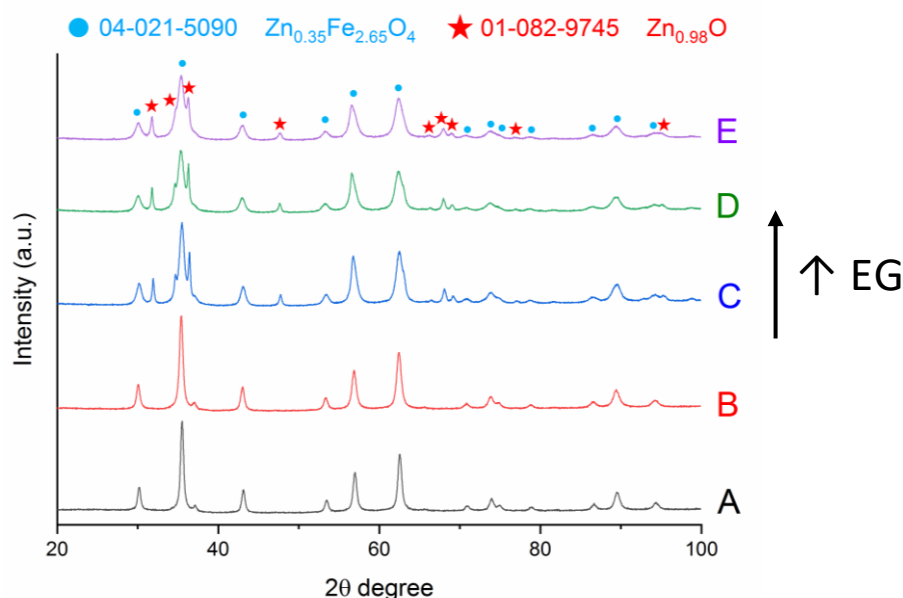
A first observation has been made in part III.1.1.B.c about the introduction of EG in the reaction media. Indeed, according to Figure I-40, the EG is responsible for an increase of the particle size from  $6.2 \pm 1$  nm (without EG) to  $22.4 \pm 11$  nm with addition of EG (respectively SP(F)M and FM particles). Four other experiments have been conducted by increasing the EG quantity inside the microwave reactor, departing from the synthesis with the FM particles (part III.1.1.B.c) taken in the study as a reference. The idea is to analyze which particle diameter is attainable by increasing EG quantity. The expectation was to obtain larger particles by increasing the EG volume due to the bond of more crystallites together in the "raspberry" structure.

The "raspberry"-like morphology depicted in III.1.3.B and typical to the addition of EG is recovered in these experiments (Figure I-55). The EG quantity increases from test A to E with A corresponding to the FM particles. TEM pictures (Figure I-55) only allows to define the nanoparticles morphologies. Due to the intriguing particle shape and to the chains they form on the picture, X-ray data are required to determine the particle size and thus to conclude if EG quantity has an influence on the particle size.



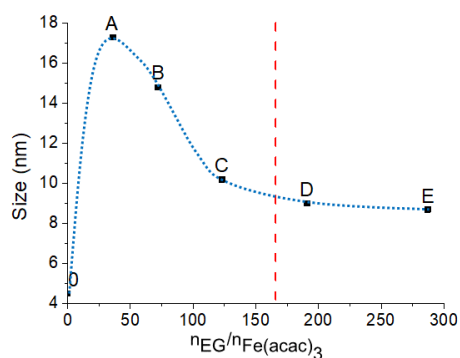
**Figure I-55.** Effect of ethylene glycol quantity in the microwave synthesis:  $n(\text{EG})/n(\text{Fe}(\text{acac})_3) = 36$  (A), 72 (B), 123 (C), 191 (D) and 287 (E). A is the reference corresponding to FM particles.

On the one hand, the presence of a secondary phase is clearly demonstrated in Figure I-56 with the presence of  $Zn_{0.98}O$  (PDF 01-082-9745) from a certain quantity of EG (test C,  $n_{EG}/n_{Fe(acac)_3}=123$ , Figure I-58). An excess of EG in the system might affect the homogenization of the precursors inside the reactor which leads to the emergence of impurities and especially zinc oxide. All of the zinc has not been able to react with the iron.



**Figure I-56. X-ray diffraction patterns evidencing the influence of EG addition through A to E experiments.**

On the other hand, the nanoparticle diameters decrease with the increase of EG quantity in the reaction media (Figure I-57 and Figure I-58). This behavior is the exact opposite of what we were expecting for. The particle size decreases up to a certain limit of EG quantity, from which it stabilizes (test D, Figure I-58). Consequently, the FM nanoparticles with a diameter of  $27.4 \pm 4.0$  nm (test A) are the ones with the largest sizes. The addition of EG does not allow to exceed this size. Indeed, for high quantity, ethylene glycol might act as a complexing agent with metallic precursors and prevent them to react together, conducting to smaller particles [164]. Moreover, under heating, this polyol solvent might become more reductive than oleylamine with oleic acid.



**Figure I-57. Evolution of the particle diameter with the increase of EG content (derived from XRD) The blue dashed line is just a guide for the eyes.**

	0	A	B	C	D	E
$n(\text{EG})/n(\text{Fe}(\text{acac})_3)$	0	36	72	123	191	287
Size (nm)	4.5	17.3	14.8	10.2	9.0	8.7

**Figure I-58. Overview of the particle size (from XRD) in relation to the EG amount.**

In order to understand the synthesis mechanisms, the influence of solvents with higher molecular weight is also tested. A first assumption was that it could increase the particle diameters.

### III.2.2.B. Influence of the molecular weight of the solvent

While still considering the synthesis of FM nanoparticles as a reference, different solvents have been used to replace or in combination with ethylene glycol (EG) in order to state about the influence of the molecular weight of the solvent on the nanoparticle shape and size. For this purpose, triethylene glycol (TREG) and polyethylene glycol (PEG) have been employed (Figure I-59).

	EG	TREG	PEG-136
Molecular formula	$\text{C}_2\text{H}_6\text{O}_2$	$\text{C}_6\text{H}_{14}\text{O}_4$	$\text{HO}(\text{C}_2\text{H}_4\text{O})_{136}\text{H}$
Semi-developed formula	$\text{HO}-\text{CH}_2-\text{CH}_2-\text{OH}$	$\text{HO}-\left[\text{CH}_2-\text{CH}_2-\text{O}\right]_3-\text{H}$	$\text{HO}-\left[\text{CH}_2-\text{CH}_2-\text{O}\right]_{136}-\text{H}$
Structural formula			
Molecular weight (g/mol)	62.07	150.17	6000

**Figure I-59. Molecular weight of ethylene glycol (EG), triethylene glycol (TREG) and polyethylene glycol (PEG).**

PEG 6000 is employed (Figure I-59). It can be written PEG-136 with 136 corresponding to the number  $n$  of oxyethylene groups ( $\text{C}_2\text{H}_4\text{O}$ ) calculated as follows:

$$M_w = 2M(\text{H}) + M(\text{O}) + M(\text{C}_2\text{H}_4\text{O}) \times n = 18 + 44n = 6000 \quad \text{I-38}$$

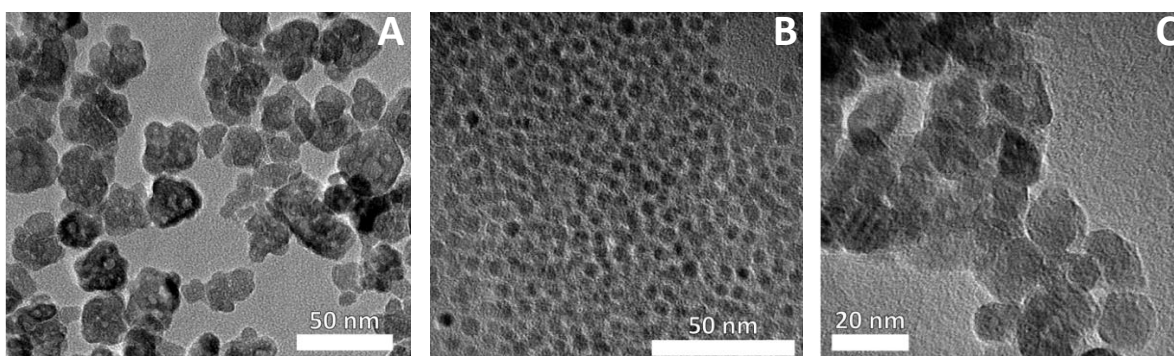
with  $M_w$  the molecular weight (g/mol) and  $M$  the molar mass (g/mol).

### III.2.2.B.a. *An invisible solvent: the TREG*

Three experiments are compared in this section in Figure I-60: the first is the reference namely the FM particles (A), secondly the same assay by replacing the EG quantity with TREG which possesses a higher molecular weight (Figure I-59), and then a last sample with a mix of EG and TREG in the same quantity.

Correlating both the TEM images (Figure I-60) and XRD analysis (Figure I-61 and Figure I-62), the sample (B) exhibits the same morphology and a range of size of the order of the SP(F)M nanoparticles (Figure I-40-A), specifically spherical particles with a 3.9 nm diameter. It results in the nanoparticles obtained only with a mixture of OAm, OA and ODE. Thus, the use of TREG in substitution of EG has no effect on the nanoparticles.

Raspberry-type frameworks are retrieved in the case of the sample (C) with a combination of EG and TREG. Hence, raspberry shapes are the signature of the EG solvent. The slightly smaller diameters observed for these particles in comparison with the reference synthesis (A) might be due to the use of less EG and to the uselessness of the TREG. No impurities are noticed in the experiments (Figure I-62).

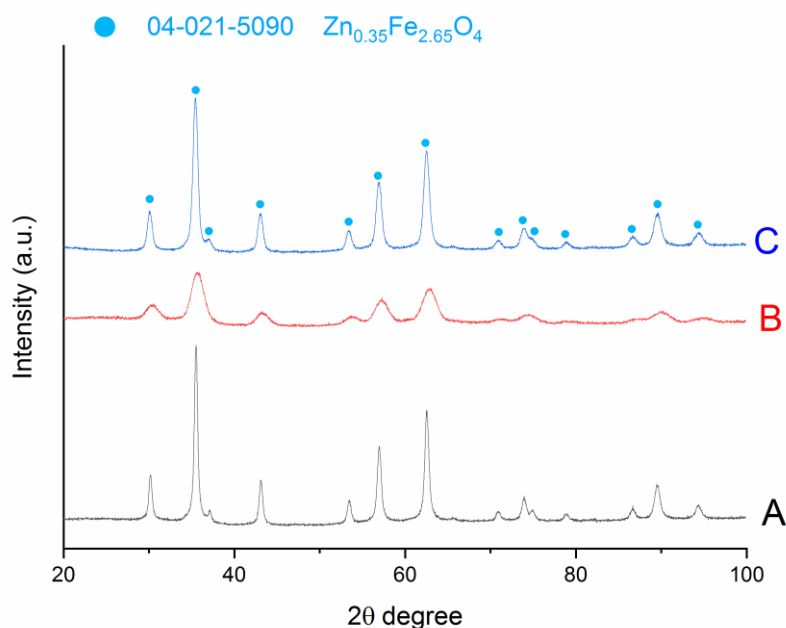


**Figure I-60.** Nanoparticles obtained by microwave-assisted thermal decomposition with EG (A), TREG (B), and a mix of EG and TREG (C). See Figure I-61 for ratios.

		A	B	C
$V_{EG}$	mL	2	-	1
$V_{TREG}$	mL	-	2	1
Size	nm	17.3	3.9	11.5

**Figure I-61.** Volume quantities of solvents and XRD sizes of nanoparticles synthesized with EG (A), TREG (B), and a mix of EG and TREG (C).





**Figure I-62.** X-ray diffraction patterns of nanoparticles synthesized with EG (A), TREG (B), and a mix of EG and TREG (C).

The use of TREG as a solvent with almost three times the molecular weight of the EG has clearly no impact on the synthesis when compared with the SP(F)M particles.

### III.2.2.B.b. Influence of PEG 6000, alone

After the assays with TREG, the EG was replaced with PEG 6000 to increase the molecular weight even more (Figure I-59). Figure I-63 to Figure I-65 compare the characterizations results of the reference FM nanoparticles for the sample (A) and the sample (B) synthesized in the same exact conditions but with introduction of PEG 6000 instead of EG in the microwave reactor. The nanoparticles obtained with PEG 6000 (Figure I-63-B) display an important heterogeneity in terms of size with platelet and triangular morphologies. Indeed, the nanoparticle framework is not spherical and of raspberry-type anymore. On the contrary, the particles tend to stretch out along one or several preferential crystallographic axis and thus show these rectangular or triangular shapes. It is worth noting that the rectangular forms could correspond to a triangle observed from one of its edge.

Regarding the XRD analysis (Figure I-64 and Figure I-65), the introduction of PEG induces an increase of the particle diameters in comparison with the SP(F)M particles, but considerably below the sizes of the FM particles. The particles are also pure regarding the crystalline phase (Figure I-65).

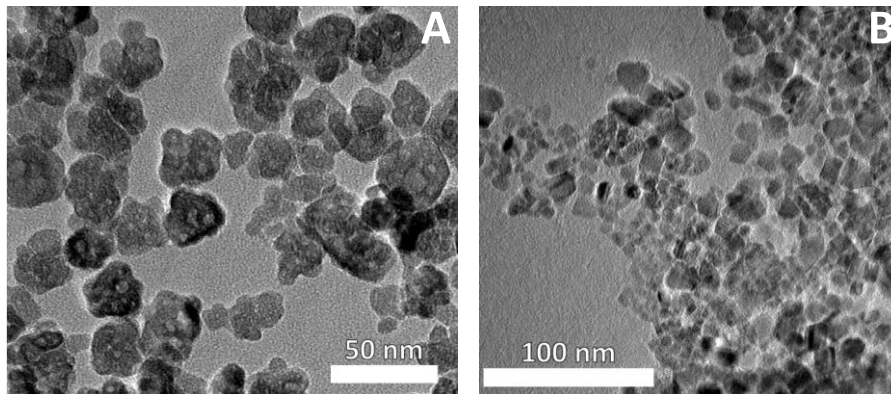


Figure I-63. Nanoparticles obtained by microwave-assisted thermal decomposition with EG (A) and PEG (B). See Figure I-64 for ratios.

		A	B
$V_{EG}$	mL	2	-
$V_{PEG}$		-	2
Size	nm	17.3	6.9

Figure I-64. Volume quantities of solvents and XRD sizes of nanoparticles synthesized with EG (A), and PEG (B).

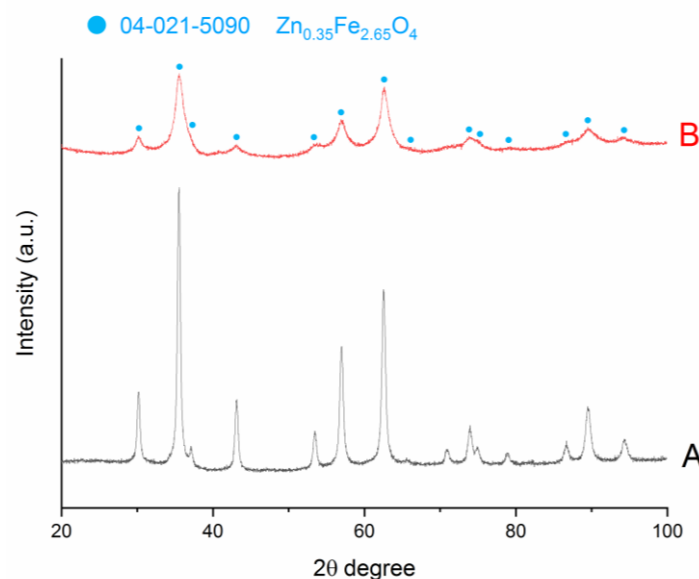


Figure I-65. X-ray diffraction patterns of nanoparticles synthesized with EG (A), and PEG (B).

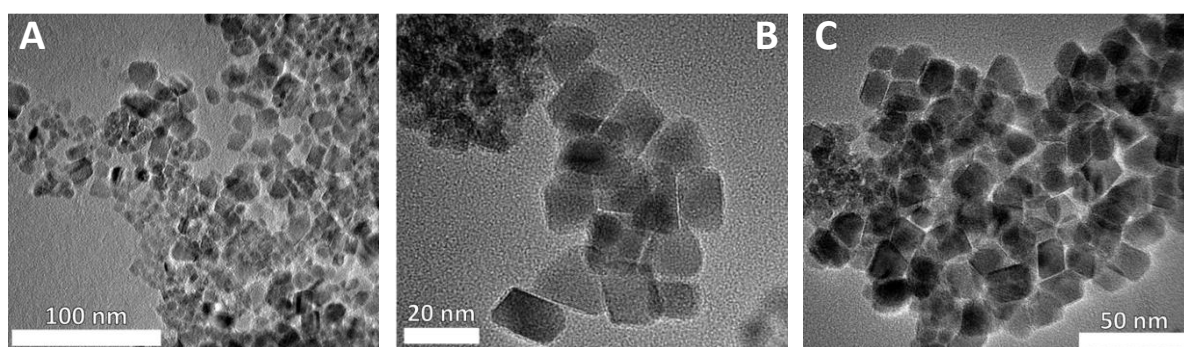
To conclude, the use of a solvent with a higher molecular weight does not improve the nanoparticle sizes, even if it seems that PEG 6000 makes the particles grow which is clearly not the case for TREG. Besides, if TREG allows to keep a certain homogeneity of the particles, the PEG induces a lot of heterogeneity that we try so hard to avoid.

### III.2.2.B.c. Influence of a mixture of EG and PEG

A combination of EG and PEG has also been studied. Three samples are compared in this section: (A) synthesized only with PEG, (B) and (C) with a mixture of PEG and EG, sample

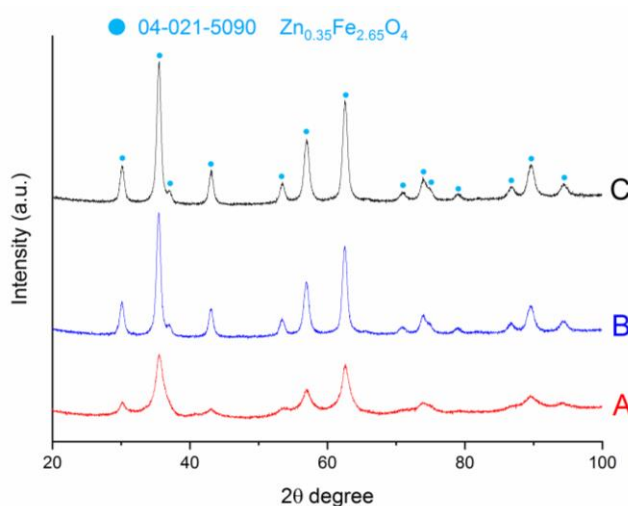


(C) containing the doubled quantities (Figure I-66 and Figure I-68). The typical morphology previously analyzed in the case of PEG and EG used alone is retrieved in TEM pictures (Figure I-66). Indeed, once PEG and EG are mixed together in the reactor (Samples B and C), two populations of nanoparticles are clearly discerned: the first one corresponding to the rectangular and triangular nanoparticles observed only with the use of PEG (Sample A) and the second one attributing to the “raspberry” type morphology of the nanoparticles. It seems that these two solvents play two separated roles in the synthesis, their effect do not unite to make the particle grow in the same manner. They behave exactly like if the synthesis were done separately and then mixed together at the end of the process. These observations completely confirm that EG is the only responsible for the amazing framework of nanoparticles with raspberry-like shapes.



**Figure I-66.** Nanoparticles obtained by microwave-assisted thermal decomposition with PEG (A) and a combination of PEG and EG (B-C). See Figure I-68 for ratios.

X-ray diffraction analysis underscores pure cubic spinel structures for all the samples as in the previous parts (Figure I-67). Sample (B) and (C) display the same particle diameters (Figure I-68), which means that the dilution of the precursors has no incidence on the nanoparticles growth.



**Figure I-67.** X-ray diffraction patterns of nanoparticles synthesized with PEG (A) and a combination of PEG and EG (B-C). See Figure I-68 for ratios.

	A	B	C
$\frac{n_{EG}}{n_{Fe(acac)_3}}$	-	18	36
$\frac{n_{PEG}}{n_{Fe(acac)_3}}$	0.4	0.2	0.4
Size (nm)	6.9	10.2	10.1

Figure I-68. Molar ratio of solvents and XRD sizes of nanoparticles synthesized with PEG (A) and a combination of PEG and EG (B-C).

### III.2.2.C. Conclusion

These experiments establish the role of the EG in the formation of “raspberry” structures. A simple picture could explain how EG addition results in raspberry morphology: the respective  $-OH$  terminations of EG may link together two smaller crystallites during the growth phase. This hypothesis should be checked with comparison of other raspberry morphologies. Figure I-69 compares the raspberry morphology obtained in this study with some similar structures synthesized in other works with EG [158] [165].

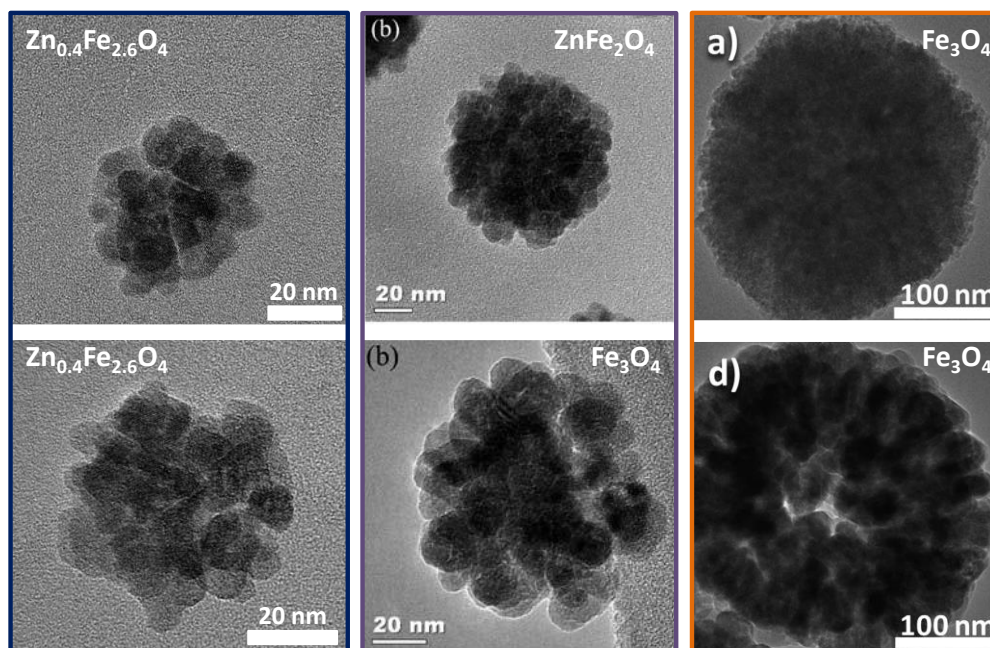


Figure I-69. Comparison of raspberry nanoparticles elaborated in this study (blue box), by Xuan *et al.* [165] (violet box) and by Gerber *et al.* [158] (orange box).

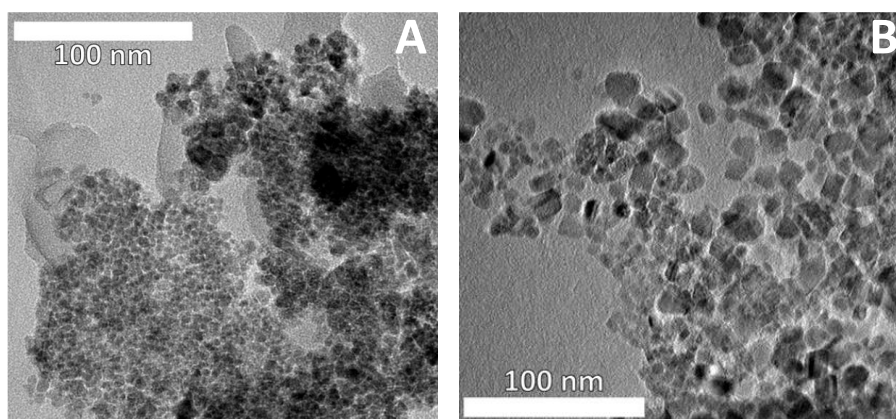
Xuan *et al.* have elaborated ferrite nanospheres with diameters comprised between 100 and 300 nm through a solvothermal method involving chloride salts in a mixture of EG and diethylene glycol (DEG). The particle size is tuned by the ratio between EG and DEG volumes. The particle atypical framework is depicted as an agglomeration of nanocrystals with sizes between 10 and 20 nm, emphasizing the polycrystalline nature of the raspberry particle [165]. Gerber *et al.* have studied the synthesis of raspberry nanostructures of iron oxide by means of a polyol solvothermal method with chloride salts in EG. They define the raspberry structure as an ensemble of aggregated nanocrystals with similar crystallographic orientations. The crystallite size is adjusted between 5 and 60 nm and the overall particle reaches a size of approximately 250 nm [158].

*Further research works also illustrate the synthesis of raspberry-type structure with chloride salts in solvothermal routes performed in EG:  $Fe_3O_4$  particles of 250 nm [166], Zn ferrite hollow nanospheres of 250 nm [167],  $ZnFe_2O_4$  spherical porous structures (between 15 and 90 nm) [168], and nickel ferrite nanoparticles (between 130 and 240 nm) [169].*

### III.2.3. Influence of the thermic cycle

The interest of the temperature ramps in the synthesis protocol is also studied with PEG 6000 in place of EG in the microwave reactor. The nanoparticles (B) in Figure I-70 represent the result obtained with the whole thermal protocol (Figure I-37-B) whereas in the inset (A) only the first heating ramp was performed. The reactor was cooled down to room temperature after being maintained at 200 °C during 10 minutes. The color of the solution gives a valuable insight of the reaction stage. In this way, samples (A) and (B) have showed a brown and dark colors at the end of the synthesis, respectively, which clearly confirms they are not at the same stage of development. Indeed, the temperature ramp at 200 °C and 270 °C has two specific roles.

Considering the nanoparticle size and morphology (Figure I-70), significant differences appear. The particles in the inset (A) are smaller than the ones in the inset (B). Moreover, they look not crystallized, sounding like a mass of amorphous particles with undefined shapes. It is not the case for the sample (B) as mentioned in the previous part (III.2.2.B.b).



**Figure I-70.** Microwave-assisted thermal decomposition completed until the first temperature level ( $T_1, t_1$ , Figure I-37.B) (A) in comparison with the full protocol (B).

X-ray diffraction analysis seems to confirm the previous assumption. Indeed, the sample (A) exhibits very wide peaks in its XRD pattern (Figure I-71), which means the nanoparticles are not well crystallized and contain a significant amorphous quantity. The ratio between the particle diameters of the two samples is almost two (Figure I-72).

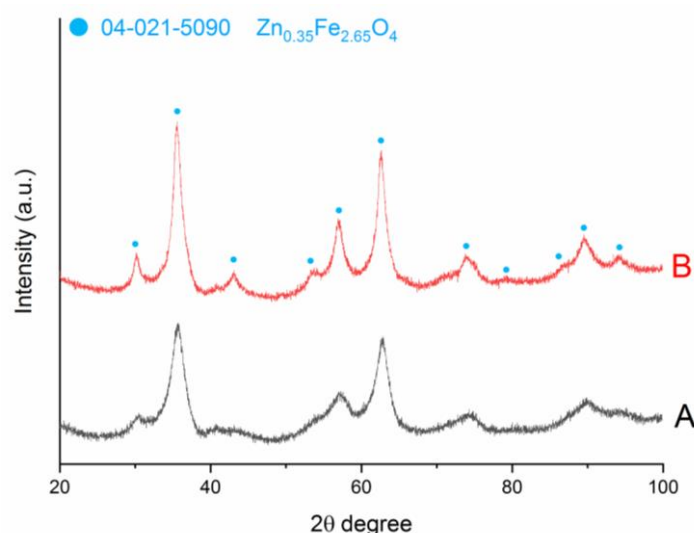


Figure I-71. X-ray diffraction patterns of nanoparticles represented in Figure I-70, synthesized with PEG.

		A	B
$\frac{n_{\text{PEG}}}{n_{\text{Fe}(\text{acac})_3}}$			0.4
Size	nm	4.5	6.9

Figure I-72. Molar ratio of PEG with iron precursor and XRD sizes of nanoparticles (A) and (B) of Figure I-70.

Following these results, we could attribute the function of each temperature ramp in the operating protocol, giving some precisions on the reaction process. At 200 °C, oxolation reactions between cationic complexes coming from precursors seem to occur while the crystallization step and growth require increasing the temperature to 270 °C (Figure I-73). The oxolation consists of a condensation reaction between monomers, leading to the formation of oxo bridges (O=) between cations, and hence to metal-oxygen-metal bridges. Carboxylic groups coming from oleic acid molecules can exchange with the acetylacetonate ligands. Therefore and at the same time, carboxylic acids could lead to esterification reactions with enolic functions existing in the reaction medium (enolic forms of free beta diketones). The esterification reaction generates water in-situ, which is consumed during the oxolation reactions maintaining the medium hydrophobic [170].

In this way, the particles in sample A have not completed their growth and could not be well crystallized. In addition, these experiments highlight an overpressure inside the microwave reactor due to the introduction of PEG, making this solvent not suitable for the synthesis. The overpressure is attributed to a high dielectric constant  $\epsilon'$  and above all a high loss tangent of the aqueous solution of PEG (10 wt%) introduced in the reactor. The value is at least twice the dielectric constant  $\epsilon'$  of EG at this concentration according to Arnold *et al.* [171].

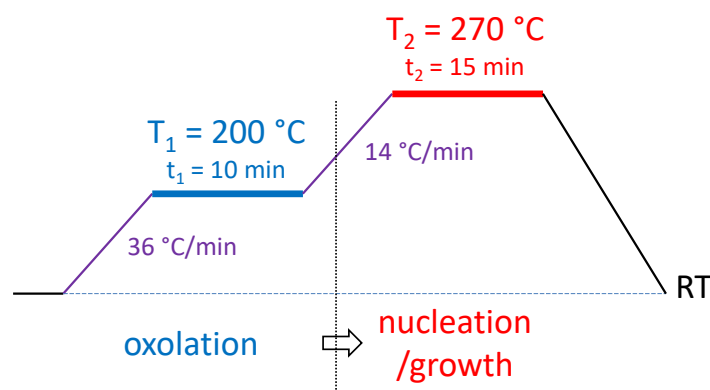


Figure I-73. Reaction steps during thermal procedure.

### III.2.4. Influence of surfactants

The microwave synthesis deals with a mixture of three solvents namely OAm, OA and ODE. ODE is used in the operating protocol to ease the handling and the solubilization of the viscous surfactants in the reactor. As it is only used to homogenize the overall precursors with surfactants, ODE does not influence the particle nucleation/growth and is thus not studied in the section. OAm and OA are the wetting agents of the synthesis which influence the nanoparticle shape and size differently. These surfactants possess two different and complementary functions in the synthesis.

The sample A (Figure I-74) could be easily compared to the SP(F)M spherical particles. Indeed, the nanoparticles have been elaborated with the inverse volumetric proportions (2 mL OAm, 8 mL OA, and 8 mL OAm, 2 mL OA respectively). Elongated particles with cubic, cube-like and tetrahedron shapes with a mean diameter of 18 nm are observed in the sample A (Figure I-74 and Figure I-75), which is clearly an expression of the surfactant ratio. A first assumption is that OA favors the nanoparticles growth along a preferential crystallographic axis.

The nanoparticles of the sample C synthesized with the exact same quantities of OAm and OA in the reactor are spherical in shape and with relatively homogeneous diameters around 8.9 nm (Figure I-74 and Figure I-75). However, the presence of a few cubes or cube-like shapes is noticed. Thus, when introduced in the same proportions, the surfactants' effects cancel each other.

Tiny spherical nanoparticles of about 6.0 nm are obtained with the SP(F)M synthesis ratio divided by 2 (Sample D, Figure I-74 and Figure I-75). The increase of OA does not seem enough to induce a growth of the nanoparticles along a certain crystallographic axis.

Nanoparticles in the sample B synthesized with the inverse proportion of surfactant in comparison with the sample D do not display spherical morphologies (Figure I-74). This observation is in agreement with our first assumption stating that OA induces a particle elongation along a certain axis. The particle sizes are smaller compared to sample A (Figure



I-75). At this stage, a second assumption could be made: OAm would inhibit the nanoparticles growth by complexing the metallic cations.

These four experiments allow to distinguish two potential roles for our surfactants. Indeed, OA stimulates the nanoparticle growth along a preferential axis while OAm slows down its growth. Tuning their compositional ratio yields to a good control of the nanoparticle morphology. Thus, the nanoparticles become spherical in shape using the appropriate ratio between the two surfactants.

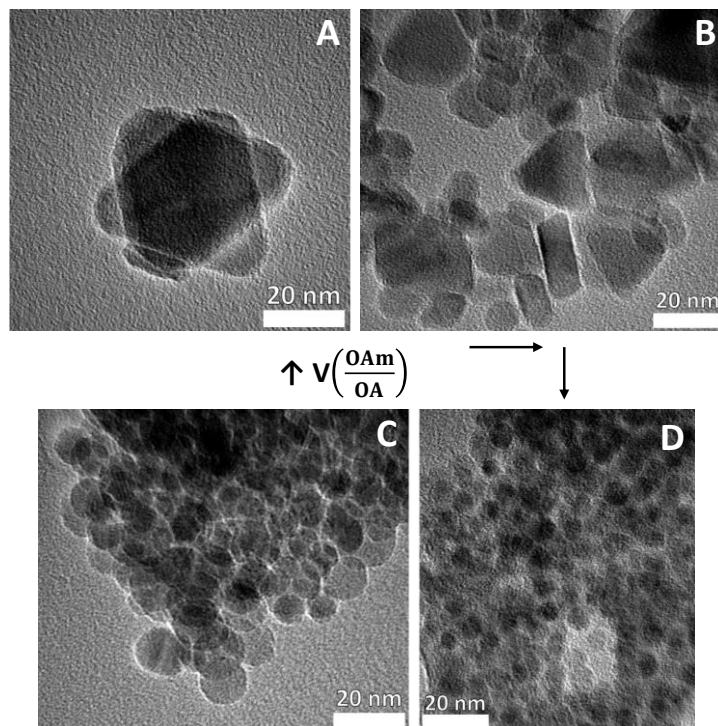
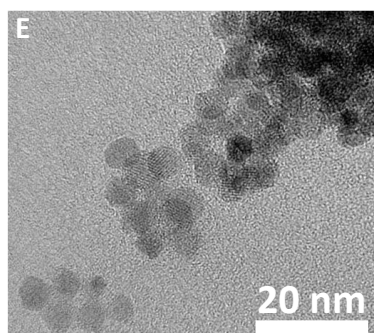


Figure I-74. Influence of the surfactants: oleylamine (OAm) and oleic acid (OA) in the microwave synthesis. Figure I-75 for ratios.

	A	B	C	D
$V\left(\frac{OAm}{OA}\right)$	0.3	0.5	1	2
Size (nm)	18.0	13.1	8.9	6.0
Shape	polyhedrons		spheres	

Figure I-75. Volumetric ratio of OAm versus OA and XRD sizes of nanoparticles (A) to (D) of Figure I-74.

The second assumption is verified with another trial (Sample E, Figure I-76). The OAm quantity is slightly increased compared to sample D and the XRD mean diameter is reduced, which confirms the hypothesis. Moreover, the ODE volume is diminished from 6 to 2 mL at the same time. This quantity may be sufficient to blend and homogenize the surfactants.

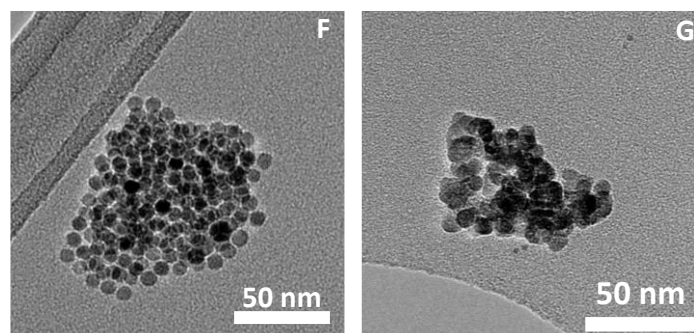


	SPM	FM	E
V(OAm)	8	8	10
V(OA)	2	2	4
V(ODE)	6	6	2
V(EG)	0	2	0
Size (nm)	4.5	19.1	4.9

**Figure I-76. Nanoparticles synthesized with a surfactant volumetric ratio of 2.5 and by decreasing the volume of ODE (2 instead of 6 mL).**

Similarly, the sample F (Figure I-77) has been obtained in the presence of a very large excess of OAm. The produced nanoparticles are spherical and of comparable sizes with SP(F)M reference. Once again, it supports the inhibitor role of OAm in the synthesis.

Moreover, the sample G (Figure I-77) could be compared to the FM reference as the difference lies in the increase of the EG quantity without using ODE to homogenize the precursors. The nanoparticle framework looks different in terms of morphology from the “raspberry” type structure usually observed when using EG in the reactor (part III.2.2.A). In this case, the EG has a double function: it is used both as a binder to group some unit crystallites and as a simple solvent to mix the surfactants uniformly in replacement of ODE. Following the trend in Figure I-57, the nanoparticles should exhibit a diameter of approximately 9-10 nm, which is hard to deduce from TEM images as we already mentioned before.



	SPM	FM	F	G
V(OAm)	8	8	18	8
V(OA)	2	2	0	2
V(ODE)	6	6	0	0
V(EG)	0	2	0	8

Figure I-77. Nanoparticles synthesized without ODE evidencing the influence of OAm and EG.

As a conclusion, OAm and OA are used as complementary surfactants in the synthesis. Their own role is balanced when used in the proper quantities and allow to produce spherical and reproducible nanoparticles. The ODE is only required to homogenize the overall precursors with surfactants. The question of precursor homogenization gives rise to another: are the nanoparticles homogeneous in terms of chemical composition? Does it depend on the nanoparticle shape?

To verify the local chemical composition at the nanoparticle level, the samples were analyzed by STEM coupled with EDX. This technique allows to determine the chemical elements contained in a material up to quantitatively when using reference samples. To ensure the reliability of the method, the Zn/Fe ratios estimated by STEM-EDX of two samples with spherical shapes are compared to the theoretical ones (Figure I-78). It clearly appears that the technique determines a ratio close to the theory and thus differentiates one sample from another through its zinc level. Thus, the method is trustworthy.

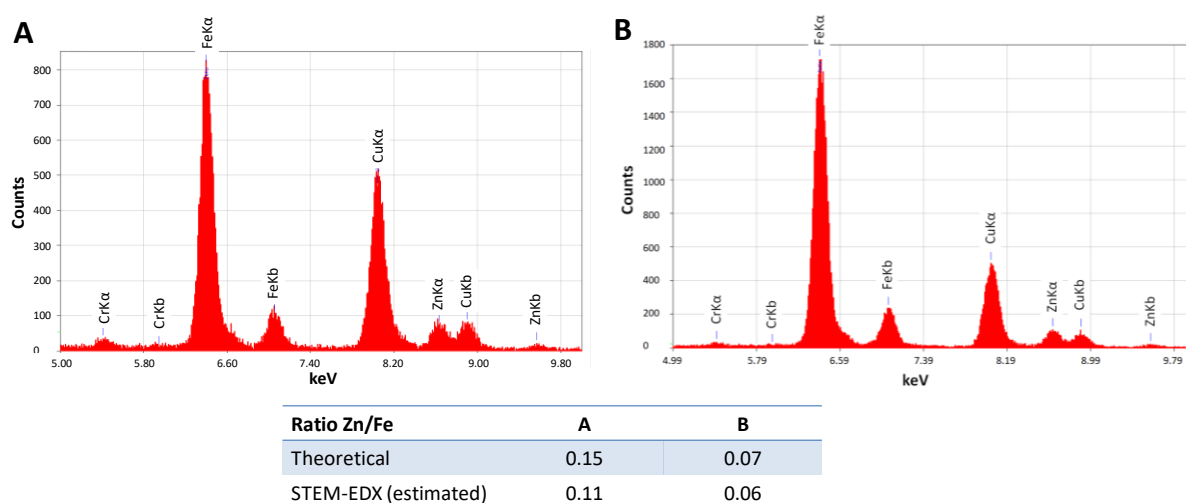


Figure I-78. Comparison of the theoretical Zn/Fe ratio of two samples with the one estimated by STEM-EDX.



The sample A (Figure I-74 and Figure I-75) is examined by STEM-EDS. Four nanoparticles exhibiting rectangular and triangular shapes in 2D view are picked and analyzed (Figure I-79). Iron and zinc quantities are determined in any nanoparticle shape. Therefore, the presence of different morphologies is not induced by a preferential growth of a phase in a different system. Both rectangular and triangular shapes look of the same composition. The Zn/Fe ratios incorporated in the table (Figure I-79) are presented only for information purposes and above all are just qualitative factors. Even if these values do not quantify precisely the amount of iron and zinc in the particles, the zinc is retrieved in low quantity, which means its incorporation is not ideal with the surfactant ratio employed in the experiment. In comparison, the SP(F)M reference synthesis (Figure I-78) exhibits higher Zn/Fe ratios, indicating the proportions of surfactant used are more convenient and favor a better homogenization of the precursors.

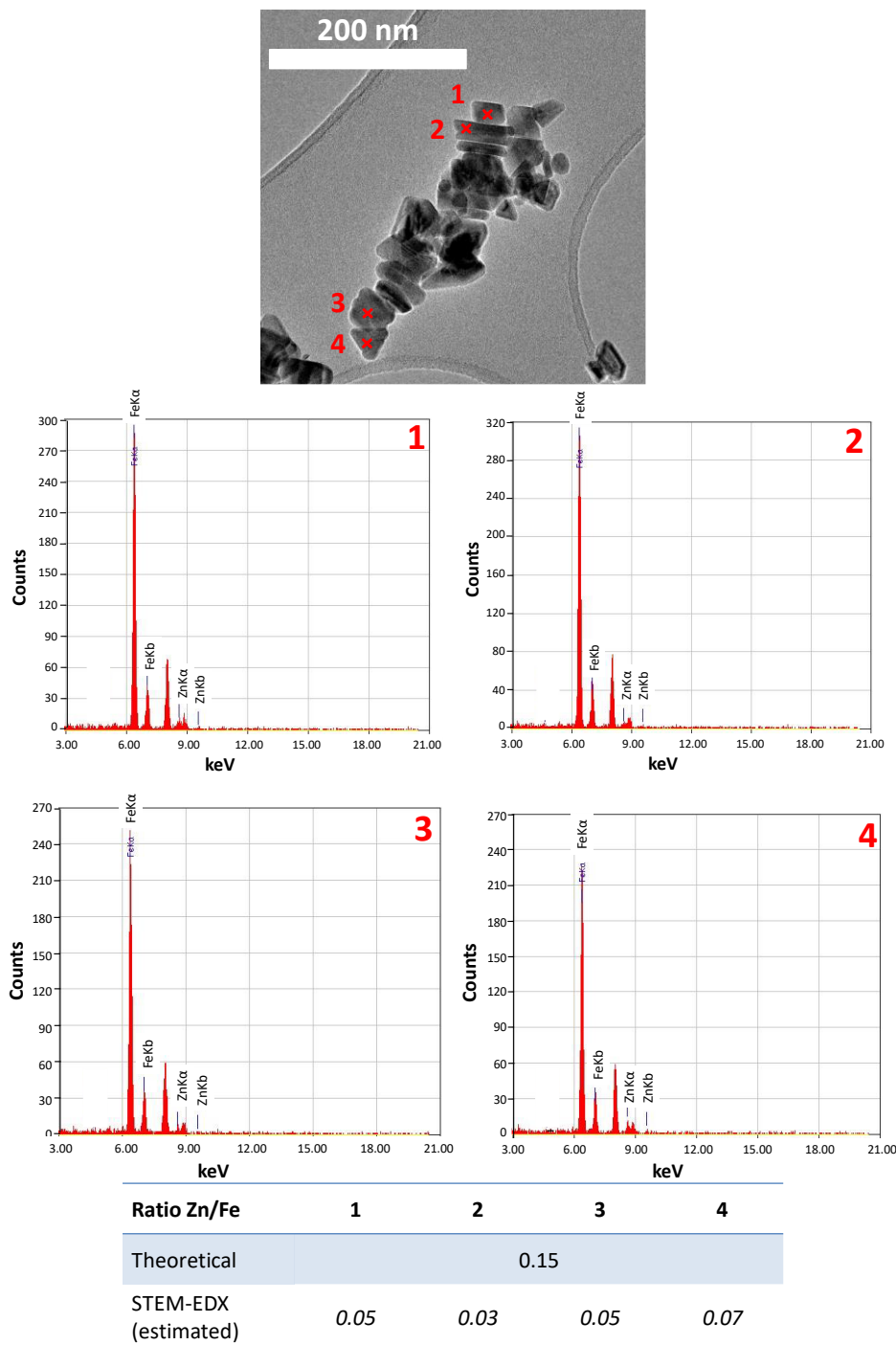


Figure I-79. Estimated Zn/Fe ratios of four different nanoparticles in sample A (Figure I-74, Figure I-75).

### III.2.5. Conclusion

*The previous experimental campaign has enabled to identify the role of each solvent in the synthesis. The choice of the zinc precursor has been justified. The introduction of EG in the reactor allows to increase the particle diameter until a certain quantity, from which the particle size decreases and with the presence of impurities in the system. Regarding the surfactants, OA encourages the particle growth along a preferential axis and OAm inhibits its growth. The nanoparticle morphology could be well-controlled by adjusting the surfactants ratio. The conditions taken for SP(F)M and FM references synthesis are retained*

*due to reproducibility, homogeneity in terms of size, shape and chemical composition reasons.*

### III.2.6. Microstructural characterizations

#### III.2.6.A. Infrared spectroscopy

After synthesis, the nanoparticles are recovered and washed by centrifugation processes with addition of a mixture of ethanol and ethyl acetate. This procedure is required to remove the remaining organics and the surfactants still present at the particle surroundings and surface. The cleaning steps will be described in details in the Chapter II. Once all of the organics are removed, the nanoparticles are dried naturally under air.

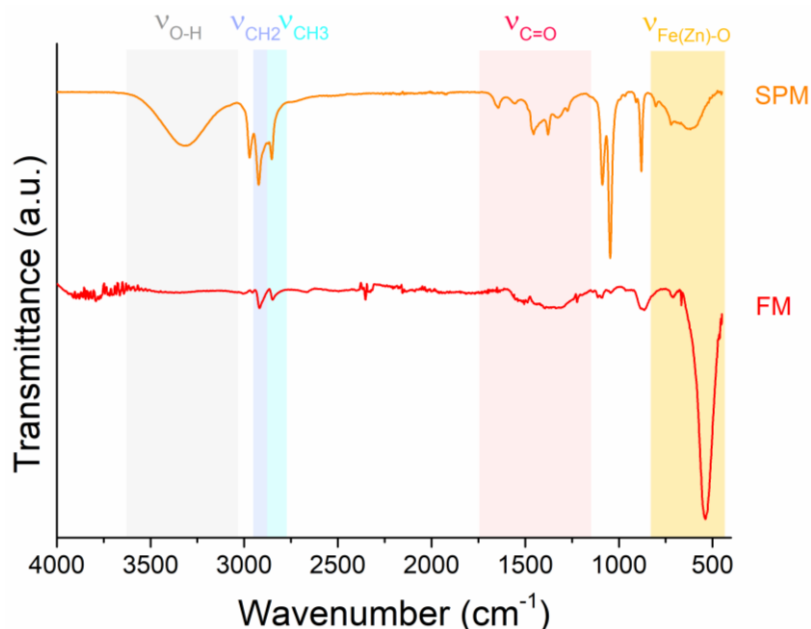
A Fourier Transform Infrared Spectroscopy (FTIR) analysis is performed on the nanoparticles once dried after the cleaning operations. This technique enables to investigate the nanoparticle structure through the vibration modes of the chemical bonds in the iron zinc oxide nanoparticles.

The resolution of these bands will depend on the structural order depicted above and especially on the vacancies [172]. Indeed, a decrease of the number of absorption bands is attributed to an increase of the vacancies disorder. A completely disordered phase with randomly distribution of cations and vacancies involves a band broadening between 500 and 800  $\text{cm}^{-1}$  due to a spreading of the vibrational frequencies which are different from one lattice to the other. An ordered phase shows more absorption bands and also sharper [9]. For example,  $\text{Fe}_3\text{O}_4$  nanoparticles synthesized by a sol-gel technique [173] display two particular peaks in FTIR transmission spectra. A first metal-oxygen band observed at 590  $\text{cm}^{-1}$  represents the stretching vibrations of the metal at tetrahedral sites. A second metal-oxygen band at 445  $\text{cm}^{-1}$  corresponds to the same vibrations except that it is located in octahedral sites. The observation of these two peaks are in agreement with X-ray diffraction analysis which shows that the calculated lattice parameter is comprised between the magnetite and maghemite value. Thus, the obtained phase is not pure magnetite [173].

It could also help to depict the organic layer at the particle surface (Chapter II). This technique does not introduce precisely quantification, and just give a qualitative idea of the proportion of each phase in the synthesized material.

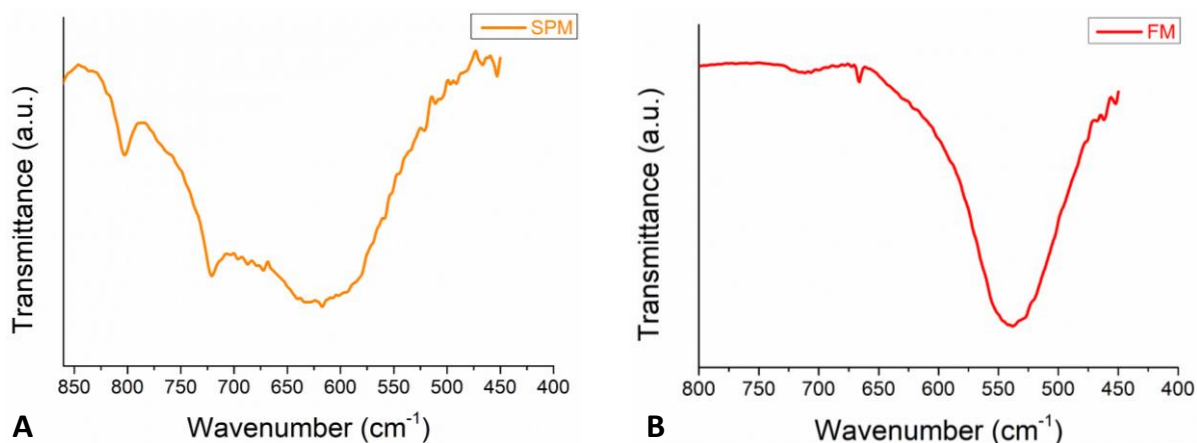
The infrared spectra of the SP(F)M and FM nanoparticles between 4000 and 400  $\text{cm}^{-1}$  are represented in Figure I-80. The nanoparticles have not seen the same cleaning steps. Indeed, the SP(F)M particles have been washed by centrifugation four times while the FM particles have been centrifuged six times. The purpose of this chapter is not to compare the number of washings, since it will be described in Chapter II. The aim is to be able to identify the five separate interesting areas in the infrared spectrum, shown with five distinct color bands in Figure I-80. In ascending order, we find in yellow the Fe-O bond (400-850  $\text{cm}^{-1}$ ) band corresponding to the link between iron and oxygen inside the particles, in pink the carbonyl groups C=O (1200-1800  $\text{cm}^{-1}$ ) at the particle surface, in blue and violet the alkyl chains also at

the particle surface ( $2800\text{--}3000\text{ cm}^{-1}$ ) by dissociating  $\text{CH}_2$  and  $\text{CH}_3$ , and then in gray the hydroxyl O-H groups at the particle surface ( $3000\text{--}3700\text{ cm}^{-1}$ ) depending on the progress on the particle cleaning steps. Overall, the intensity of the last four bands depends entirely on the number of cleaning steps and hence on the organic amount still present around the particles (Chapter II). In this section, we will only focus on the first band (in yellow): the one corresponding to the material.



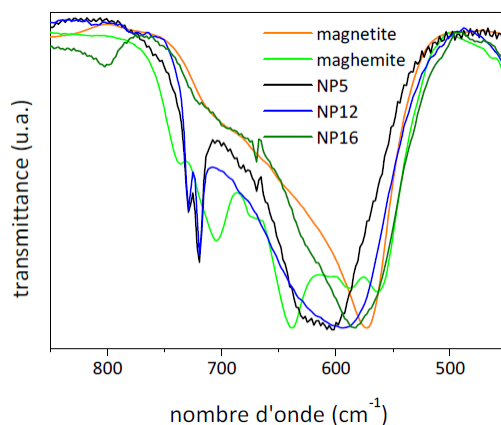
**Figure I-80.** Infrared spectrum of the SP(F)M and FM nanoparticles after 4 and 6 cleaning steps respectively.

The Fe-O bond ( $400\text{--}850\text{ cm}^{-1}$ ) bands for the SP(F)M and FM nanoparticles are displayed in Figure I-81. The layout of the band is clearly affected by the nanoparticle size.



**Figure I-81.** Infrared spectrum of the SP(F)M (4 cleaning steps) (A) and FM (6 cleaning steps) (B) nanoparticles (zoom on the Fe-O vibrational band).

In his thesis, M. Pauly compared the infrared spectrum of iron oxide nanoparticles with 3 different sizes and correlated the trend to the ones obtained for pure magnetite and maghemite (Figure I-82) [2].



**Figure I-82. Infrared spectrum of iron oxide nanoparticles with 5 (NP5), 12 (NP12) and 16 (NP16) nm diameter, correlated to pure magnetite and maghemite. From M. Pauly [2].**

Magnetite and maghemite displays their own particularities regarding this band (Figure I-82) [2]. In the case of pure magnetite, a wide single band is observed around  $580\text{-}590\text{ cm}^{-1}$  with a maximum at  $573\text{ cm}^{-1}$ . The presence of a shoulder at  $700\text{ cm}^{-1}$  due to superficial oxidation is also evidenced [2]. In the case of pure maghemite, several bands at different wavenumbers between  $500$  and  $800\text{ cm}^{-1}$ , close enough from each other, are considered with a major peak at  $640\text{ cm}^{-1}$ .

As the particle size increases, the band becomes closer in shape to the pure magnetite band and at the same time the peak position is moving towards the peak maxima of magnetite [2].

In our case, the FM particles (Figure I-81-B) display a peak with a maximum intensity at  $538\text{ cm}^{-1}$  corresponding to Fe-O stretching vibrations in pure spinel zinc ferrite nanoparticles. The trend of the curve looks similar to the one observed in the case of pure magnetite [2] which means that our FM reference looks pure in phase.

The wide Fe-O stretching vibrations band of SP(F)M particles (Figure I-81-A) is divided in several peaks with different maxima which match the maghemite profile (Figure I-82). It appears that the SP(F)M nanoparticles could be constituted of two phases: the pure  $\text{Zn}_{0.4}\text{Fe}_{2.6}\text{O}_4$  phase and a phase of  $\text{Zn}^{2+}$  substituted maghemite. The assumption is that they exhibit a core/shell structure with the oxidized layer as the shell and the pure phase in the core. This result is usual since M. Pauly [2] evidences the presence of magnetite and maghemite in  $\text{Fe}_3\text{O}_4$  particles with sizes below 16 nm. He also mentions the fact  $\text{Fe}^{2+}$  ions in small particles of magnetite are more sensitive to oxidation. The presence of  $\text{Zn}^{2+}$  substituted maghemite could be confirmed with X-ray diffraction. The value of the lattice constant ( $8.396\text{ \AA}$ ) is close to the one obtained by Mozaffari *et al.*[174] for oxidized  $\text{Zn}_{0.4}\text{Fe}_{2.6}\text{O}_4$ .

### III.2.6.B. Characterization of the inversion degree in the spinel structure

As explained in part I.2.2.B, the inversion degree in the spinel structure influences the physical properties of the material and especially its magnetic properties. The combination of three methods of characterizations, namely X-ray diffraction, high-resolution TEM (HRTEM)

and Mössbauer spectroscopy, will allow determining if the spinel structure of our nanoparticles is normal, inverted or partially inverted. These results have a potential interest in the analysis of the static magnetic properties at the nanoparticle scale in Chapter IV.

Three samples with different chemical compositions and sizes are analyzed:  $\text{Zn}_{0.2}\text{Fe}_{2.8}\text{O}_4$  nanoparticles with a  $22.4 \pm 11$  nm diameter, and  $\text{Zn}_{0.4}\text{Fe}_{2.6}\text{O}_4$  nanoparticles with  $6.2 \pm 1$  (SP(F)M reference) and  $22.4 \pm 11$  nm (FM reference) diameters.

### *III.2.6.B.a. X-ray diffraction analysis*

The X-ray diffraction analysis for the determination of the inversion degree in the spinel structure has been achieved by Christophe Lefevre at the IPCMS in Strasbourg. The X-ray diffractometers are analyzed and refined by the Rietveld method on Fullprof software and give structural information as the unit cell parameter, the particle size, ion coordination and ion occupancy in the framework.

Figure I-83 shows the results obtained for the three samples through the Rietveld refinement. All of the samples present a cubic spinel structure (space group  $\text{Fd}\bar{3}\text{m}$ ) with a single phase. The unit cell  $a$ , the particle diameter  $\langle D \rangle_R$ , and the location of Zn cations at the tetrahedral (Th) and octahedral (Oh) sites are acquired.  $\langle D \rangle_R$  can be correlated to the particle diameters calculated through distribution functions fitted with a log normal law from TEM observations  $\langle D \rangle_{TEM}$ , and with the Debye-Scherrer formula (Equation I-32)  $\langle D \rangle_S$ .

	TEM	Scherrer	Rietveld			
	$\langle D \rangle$	$\langle D \rangle$	a	$\langle D \rangle$	Zn <sub>Th</sub>	Zn <sub>Oh</sub>
	nm	nm	Å	nm	-	
Zn <sub>0.2</sub> Fe <sub>2.8</sub> O <sub>4</sub>	22.4 ± 11	18	8.398	15 ± 1	0.2	0
Zn <sub>0.4</sub> Fe <sub>2.6</sub> O <sub>4</sub>	6.2 ± 1	5	8.396	4 ± 1	0.4	0
Zn <sub>0.4</sub> Fe <sub>2.6</sub> O <sub>4</sub>	22.4 ± 11	20	8.408	17 ± 1	0.26	0.14
			PDF sheet data			
			a	Sheet number		
Fe <sub>2</sub> O <sub>3</sub>	-	-	8.351	00-039-1346		
Fe <sub>3</sub> O <sub>4</sub>	-	-	8.393	04-009-2284		
Zn <sub>0.35</sub> Fe <sub>2.65</sub> O <sub>4</sub>	-	-	8.414	04-021-5090		
ZnFe <sub>2</sub> O <sub>4</sub>	-	-	8.442	01-071-5149		

**Figure I-83. Estimated crystallite size of Zn<sub>x</sub>Fe<sub>3-x</sub>O<sub>4</sub> particles through TEM, Scherrer and Rietveld analysis. Information about Zn cations positions on the tetrahedral and octahedral sites.**

The estimated sizes  $\langle D \rangle_R$  and  $\langle D \rangle_S$  are reduced in comparison with  $\langle D \rangle_{TEM}$  and follow the trend:

$$\langle D \rangle_R < \langle D \rangle_S < \langle D \rangle_{TEM} \quad \text{I-39}$$

The three diameters are in the same order of magnitude. The method on which to rely on for the determination of the size is the Rietveld analysis. Indeed, by contrast with Scherrer which is an approximate method giving just a simple estimation of the size, the Rietveld analysis is a fine method of diffractometer treatment analysis. It takes into account the background signal, the shapes, positions and intensities of the peaks. A progressive refinement is proceeded until achieving a perfect match with the experimental data. One difference with the Scherrer formula is that the instrumental parameters are also considered and the crystallite size is corrected with the device contribution, making this method trustworthy.  $\langle D \rangle_{TEM}$  is an overestimated diameter due to the manual retrieval of particles with ImageJ. Finally, the diameters are classified from highest to lowest accuracy.

The values of the lattice parameter  $a$  coming from the Rietveld treatment (Figure I-83) are consistent with the values found in the reference PDF sheets. Pure Zn<sub>0.35</sub>Fe<sub>2.65</sub>O<sub>4</sub> (PDF 04-021-5090) and ZnFe<sub>2</sub>O<sub>4</sub> (PDF 00-001-1108) with a cubic structure and Fd-3m space group display values of 8.414 Å and 8.442 Å for  $a$ . Considering equal nanoparticle sizes, the unit cell  $a$  tends to increase by rising the Zn content.

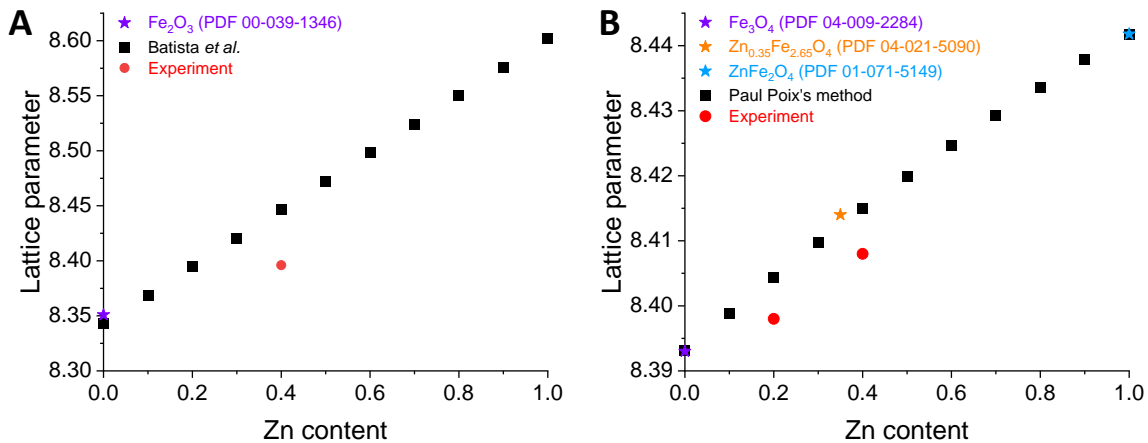
This is consistent with the trend observed using the invariant method of Paul Poix [175] applied to mixed ferrites (Figure I-84). The invariant method of Paul Poix allows to calculate the lattice parameter  $a$  by resolving a second-order equation:

$$\frac{11}{64}\alpha^2 - \frac{5\alpha}{4\sqrt{3}}a + \alpha^2 - \beta^2 = 0 \quad \text{I-40}$$

$$\alpha^2 = 3\alpha^2\left(u - \frac{1}{8}\right)^2, \quad \beta^2 = \alpha^2\left(3u^2 - 2u + \frac{3}{8}\right) \quad \text{I-41}$$

with  $\alpha$  and  $\beta$  the distances between a cation and an oxygen atom at the position  $(u,u,u)$  in a tetrahedral and octahedral sites, respectively. The solution of the equation is given by:

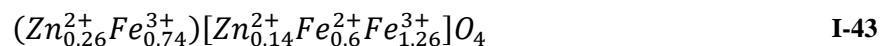
$$a = \frac{40\alpha}{11\sqrt{3}} + \sqrt{\frac{64}{11}\beta^2 - \frac{512}{363}\alpha^2} \quad \text{I-42}$$



**Figure I-84.** Evolution of the experimental lattice parameters as a function of the Zn content in the case of Zn<sup>2+</sup> substituted maghemite (A) and magnetite composition (B). The points are correlated to a fit from Batista *et al.* [176] (A) and with the Paul Poix's method.

The lattice parameter of a mixed oxide (here Zn<sub>x</sub>Fe<sub>3-x</sub>O<sub>4</sub>) follows a linear law in function of  $x$  (Figure I-84), which is consistent with the literature [177] [178]. It can be also understood from Figure I-83 that the ionic radius of Zn<sup>2+</sup> is higher in tetrahedral site than the one of Fe<sup>2+</sup> in octahedral site, so the lattice parameter increases as the Zn content increases.

The inversion degree  $\delta$  in the spinel structure corresponds to the number of Zn cations located at the octahedral (Oh) sites, namely the last column of the table in Figure I-83. Thus, only one sample displays a partial inversion of its structure: the  $22.4 \pm 11$  nm diameter particles with Zn<sub>0.4</sub>Fe<sub>2.6</sub>O<sub>4</sub> composition, also known as the FM reference in this manuscript. The formula I-28 (part I.2.1) can be applied with  $\delta = 0.14$  to describe the detailed structure, with round and square brackets for the tetrahedral (Th) and octahedral (Oh) sites:





Regardless the normal structures of the other samples, it is natural to wonder if the inversion degree occurs only from a specify particle diameter meaning if there is a limit size, or depending on an amount of zinc in the structure. Kotsikau *et al.* [179] have assessed inversion degrees in  $Zn_xFe_{3-x}O_4$  particles with a 10 nm diameter and relatively similar zinc quantities [179]. Hence, the inversion could also occur in the SP(F)M particles.

Considering the Zn amount, it depends on the synthesis. Saha *et al.* [180] have reported a start of inversion in the spinel structure from  $x = 0.2$  in the same material.

These results underline the stochastic behavior of the cation distribution in the spinel structure. This phenomenon remains not well controlled and is clearly affected by the synthesis route and conditions. Indeed, it should absolutely be taken into account due to its impact in the magnetic properties of the whole structure, making those systems hard to tune [180] [181] [182] [183].

### III.2.6.B.b. *Microstructural observations*

Thorough microstructural characterizations have been performed by Maria Luisa Ruiz Gonzalez and Jose Maria Gonzalez Calbet in the National Center for Electron Microscopy (ICTS) at the Complutense University of Madrid (UCM). Deeper observations than the ones realized at CEA with a TEM have been realized with a scanning transmission electron microscope (STEM) combined to the high-angle annular dark-field imaging (HAADF) technique. HAADF-STEM allows observing a material until the atomic scale with a very high resolution. It could be coupled to electron energy loss spectroscopy (EELS) to retrace the position of atoms in the crystalline structure, depending on the chemical composition.

The same samples (part III.2.6.B.a) have been analyzed in this section. The observations go into determining the position of iron and zinc cations in the spinel structure of  $Zn_xFe_{3-x}O_4$  nanoparticles and thus defining if the spinel is normal or inversed. An amount of Zn cations at the octahedral positions means that the spinel is inversed with a value of a degree of inversion  $\delta$  comprised between 0 and 1.

Figure I-85 to Figure I-88 only deal with the FM reference sample of  $Zn_{0.4}Fe_{2.6}O_4$  nanoparticles with a  $22.4 \pm 11$  nm diameter. At first, the particles are observed along different crystal planes. The network of crystal planes is clearly seen in Figure I-85 for [211] and [100] directions with the position of atoms in the mesh.

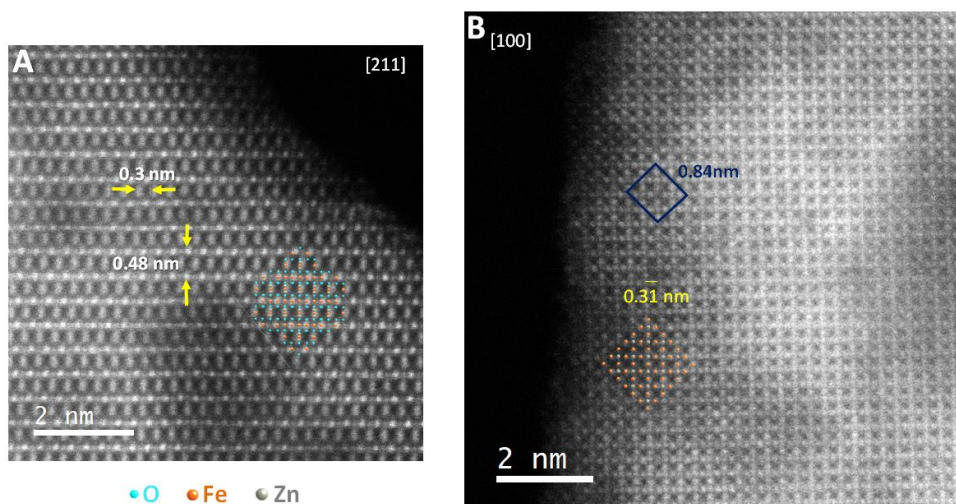


Figure I-85. Typical atomic resolved HAADF images of an area of an orientated particle along [211] (A) and [100] (B).

Direction [101] is chosen as the octahedral and tetrahedral sites are more visible in this axis. Figure I-86.A exhibits the HAADF image of a particle oriented along [101]. A scheme represents the position of iron, zinc and oxygen atoms in the structure with iron and zinc located respectively at the octahedral (Oh) and tetrahedral (Th) sites (Figure I-86.B-C).

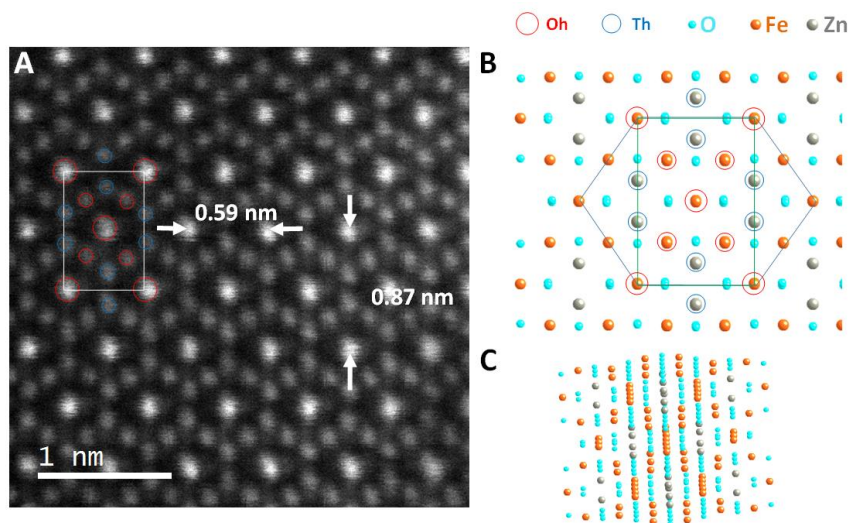
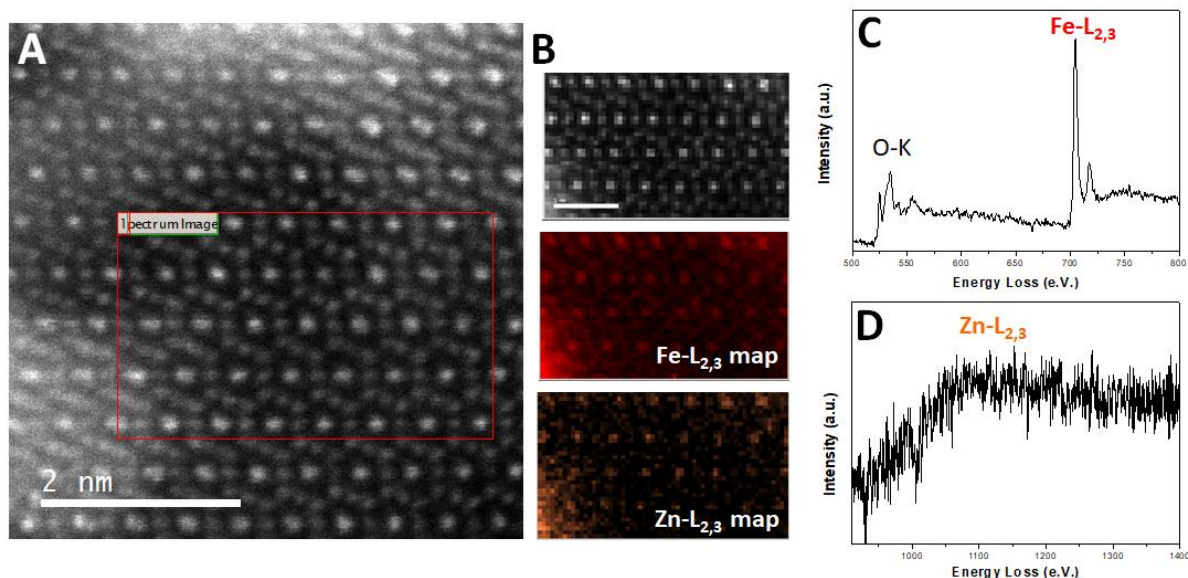


Figure I-86. (A) Typical atomic resolved HAADF image of an area of an orientated particle along [101], (B) Position of Fe and Zn cations in the spinel structure, (C) Spinel structure in 3D.

Once coupled with EELS (Figure I-87 and Figure I-88), atomically resolved chemical mappings are obtained. At the beginning, the detection of Zn was tricky. The Zn-L<sub>2,3</sub> edge was too weak and hard to distinguish in the EELS spectra, making the observation not easy as the starting Zn amount in the particle is low. Finally, the detection of Zn has been possible through some adjustments of the device as the use of two energy windows and at the same time by changing the spot size.

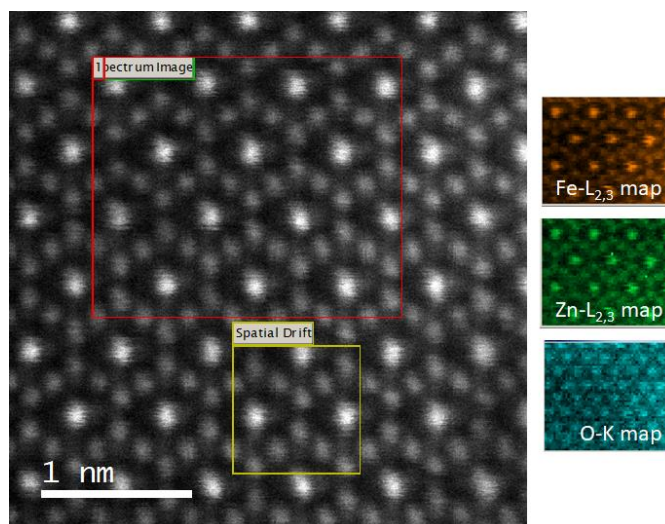
Zn is hence detected even if its signal remains noisy (Figure I-87.D). According to Figure I-87 and Figure I-88, it seems that Zn cations are at least detected on the octahedral positions.

This result is in complete agreement with the Rietveld analysis produced from the X-ray data of the sample (Figure I-83). The FM particles evidence a partially inverted structure. X-ray diffraction analysis and STEM observations point in the same direction.



**Figure I-87.** (A) HAADF image of a particle oriented along [101] with the following HAADF-EELS chemical mapping (B), Fe (C) and Zn (D)  $L_{2,3}$  EELS spectra.

The relative intensity of the peak corresponding to Fe- $L_{2,3}$  edge matches with the one obtained for  $Fe_3O_4$  in the literature [184] ( $Fe^{3+} Fe^{2+}$ ), which depicts the measurement reliability and quality.



**Figure I-88.** HAADF-EELS chemical mappings of a particle oriented along [101].

After microstructural observations, the samples are characterized by Mössbauer spectroscopy to complete and support the outcomes.

### III.2.6.B.c. Mössbauer spectroscopy

The measurements have been carried out by Jean-Marc Grenèche at the Institut des Molécules et Matériaux du Mans (IMMM UMR CNRS 6283) at the Maine University in Le Mans.

Due to its high sensibility to the local atomic environment and the oxidation degree of iron,  $^{57}\text{Fe}$  Mössbauer spectrometry allows to determine the ratio between the concentrations of  $\text{Fe}^{2+}$  and  $\text{Fe}^{3+}$  in a material, their environment, and hence the distribution of each iron species in the tetrahedral and octahedral sites of the iron oxide spinel leading to the inversion cationic degree  $\delta$ .

$^{57}\text{Fe}$  Mössbauer spectra are first realized at 300 and 77 K. The hyperfine structure results essentially in magnetic sextets with asymmetrical and broadened lines for the largest particles but quadrupolar features for the smallest particles. The spectra are fitted using the MOSFIT program with Lorentzian lines according to quadrupole and magnetic contributions. A calibration sample of  $\alpha\text{-Fe}$  is used. The values of the hyperfine parameters are refined: the isomer shift  $\delta_{\text{Fe}}$  (mm/s) which depicts the oxidation degree of iron, the width at half height  $\Gamma$  (mm/s), the quadrupole splitting  $QS$  (mm/s) which is the distance between the lines of the quadrupole doublet reflecting the asymmetry of charges in the iron environment, the quadrupole shift  $2\varepsilon$  (mm/s) which corresponds to the quadrupolar electric interaction in the presence of dipolar magnetic interactions and the hyperfine magnetic field  $B_{\text{hf}}$  (T) which comes from the interaction between the magnetic moment of the nucleus with its magnetic environment [185] [186].

On the one hand, the spectra at 300 K and 77 K obtained on  $\text{Zn}_{0.2}\text{Fe}_{2.6}\text{O}_4$  and FM particles are shown in Figure I-89. The asymmetry of outermost lines at 300 K has to be compared to those typical of maghemite and magnetite: one concludes to the presence of a mixture of Fe magnetic moments in blocked state and suggested to superparamagnetic relaxation phenomena. In addition, the oxidation Fe state is not exclusively 3+. At 77 K, the hyperfine structure exhibits more resolved magnetic sextet attributed mostly to the presence of  $\text{Fe}^{3+}$  species with a magnetic blocked order. In addition, the shoulder of some lines (located at around -3 mm/s) is consistent with the presence of  $\text{Fe}^{2+}$  component, as observed in the case of magnetite.

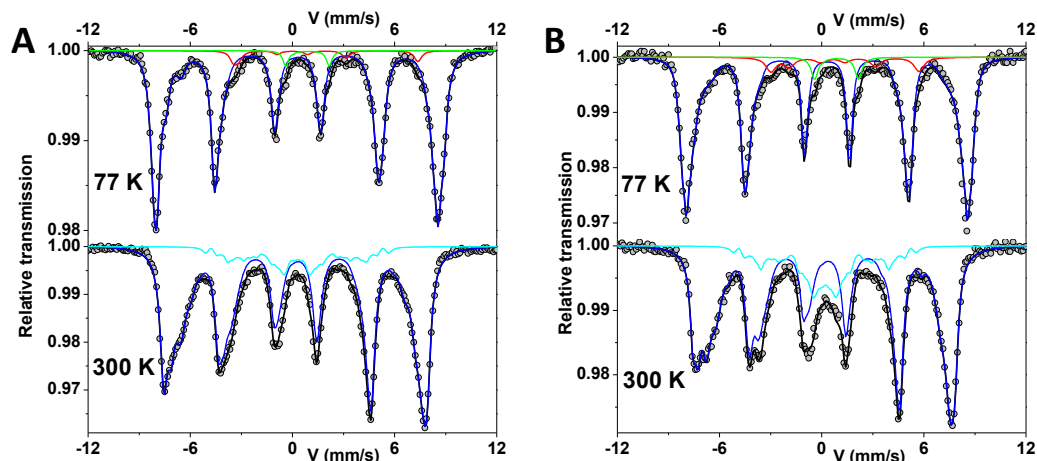


Figure I-89. Mössbauer spectra of  $\text{Zn}_{0.2}\text{Fe}_{2.6}\text{O}_4$  and FM particles at 77 and 300 K.



At 300 K, the fitting model is based on two main components: they consist of (i) a distribution of hyperfine fields linearly correlated to that of isomer shift (dark blue in Figure I-89), attributed to the biggest nanoparticles containing Fe species different oxidation states ranged from 3+ to 2+ and (ii) a distribution of only hyperfine fields (cyan in Figure I-89) attributed to the smallest particles containing only Fe<sup>3+</sup> species. At 77 K, the best physical description consists in three components: a distribution of hyperfine fields linearly correlated to that of isomer shift (dark blue in Figure I-89), attributed to the biggest particles containing Fe species with oxidation states rather close to 3+, (ii) a magnetic component (red in Figure I-89), attributed to an Fe<sup>2+</sup> magnetic component and (iii) a small quadrupolar doublet assigned to Fe<sup>2+</sup> ions. It is clear that the present fitting models are not unique to describe the broadened lines but the mean values of the hyperfine parameters remain invariant. The mean values of the isomer shift  $\delta_{Fe}$  at 300 K allows calculating the proportion of Zn<sup>2+</sup> substituted maghemite and magnetite (Figure I-90) from the isomer shift values of pure maghemite and magnetite at room temperature of 0.32 mm/s and 0.53 mm/s, respectively [187]. As a conclusion, Zn<sub>0.2</sub>Fe<sub>2.6</sub>O<sub>4</sub> and FM particles are partially oxidized. The particles present core-shell structures with Zn<sup>2+</sup> substituted magnetite at the inner and Zn<sup>2+</sup> substituted maghemite at the outer. FM particles are constituted of approximately 55 % of Zn<sup>2+</sup> substituted maghemite making them less oxidized than Zn<sub>0.2</sub>Fe<sub>2.6</sub>O<sub>4</sub> ones (Figure I-90).

	Temperature	Isomer shift	Zn <sup>2+</sup> substituted magnetite	Zn <sup>2+</sup> substituted maghemite
	K	mm/s ±0.005	% ±2	% ±2
Zn <sub>0.2</sub> Fe <sub>2.6</sub> O <sub>4</sub>	300	<0.424>	49.5	50.5
FM	300	<0.435>	54.8	45.2

**Figure I-90.** Mean values of isomer shift and the corresponding proportions of Zn<sup>2+</sup> substituted magnetite and maghemite for Zn<sub>0.2</sub>Fe<sub>2.6</sub>O<sub>4</sub> and FM particles.

On the other hand, the Mössbauer spectra of SP(F)M particles are also recorded at the same temperatures (Figure I-91). Their hyperfine structures are different: indeed, one observes at 300 K a rather well resolved quadrupolar doublet and a second component resulting in wide and symmetrical wings, which can be well described using a large single component. But the 77 K spectrum appears as a very large single line component: its symmetry is also consistent with a unique oxidation state, i.e. Fe<sup>3+</sup> species according to the value of the isomer shift: this result is in perfect agreement with the one observed at 300 K. In fact, the hyperfine magnetic field is equal to zero over time due to the relaxation of the magnetic moments of particles during the measurement time. These spectra illustrate the effect of very fast superparamagnetic relaxation in SP(F)M particles, which confirms the superparamagnetic behavior of these smallest particles, compared to previous ones. Two contributions are displayed at 300 K meaning there are two different times of relaxation which could be ascribed to a distribution of particle size due to aggregation, or to the existence of interactions between particles.

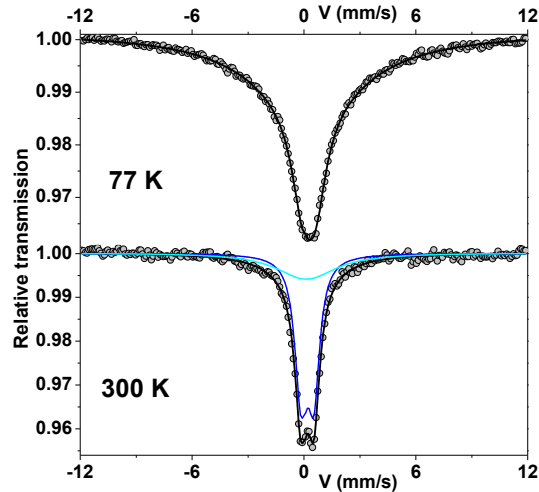


Figure I-91. Mössbauer spectra of SP(F)M particles at 77 and 300 K.

The mean value of isomer shift of 0.32 mm/s evidences clearly the presence of only  $\text{Fe}^{3+}$  ions. Thus, SP(F)M particles seems completely oxidized (Figure I-92).

<i>Temperature</i>	<i>Isomer shift</i>
<i>K</i>	<i>mm/s</i>
	$\pm 0.05$
300	0.32

Figure I-92. Mean value of isomer shift of SP(F)M particles at 300 K.

At this stage, a second important question to better understand the magnetic properties results in the location of the different cationic species in the tetrahedral and octahedral sites in the one hand and in the estimation of the canting angle of these respective magnetic moments and of the thickness of the superficial canted layer, on the other hand. It is clear that the lack of resolution of the hyperfine structure observed on the classical Mössbauer spectra prevents from a clear discrimination of the two Fe species and thus an accurate quantitative description, as is generally concluded in most studies on ferrites and nanoferrites.

To get around this difficulty, in-field Mössbauer experiments are required. Indeed, one can follow the action of the external magnetic field from the intensities of the intermediate lines of the sextet and the evolution of the magnetic splitting which corresponds to the effective magnetic field at the  $^{57}\text{Fe}$  nucleus, equivalent to the vectorial sum of the hyperfine field and the external magnetic field. In the case of a ferrimagnetic sample, one expects a splitting into two magnetic components describing the parallel and anti-parallel magnetic Fe moments respect to the external magnetic field, providing a sufficiently large external field of at least 6-7 T. It is also important to mention that in the case of the Fe oxides, the hyperfine field is anti-parallel to the magnetic moment, resulting in the large negative contact term contribution: this sign cannot be obtained from classical Mössbauer experiments but from in-field Mössbauer experiments. Consequently, the analysis of the in-field spectrum gives rise to the values of the effective field  $B_{\text{eff}}$  of the different Fe sites and their respective angle  $\theta$  defined by the directions of the  $\gamma$ -beam and Fe magnetic moment, in addition to their isomer shift and quadrupole shift. One can then estimate the values of the hyperfine field according to the following expression:

$$B_{hf}^2 = B_{eff}^2 + B_{app}^2 - 2B_{eff}B_{app}\cos\theta \quad \text{I-44}$$

when the applied magnetic field  $B_{app}$  is oriented parallel to the  $\gamma$ -beam.

In the present study, Mössbauer spectra were recorded on the three samples at 14 K under a magnetic field of 8 T using the cryomagnetic device where the external magnetic field is oriented parallel to the  $\gamma$ -beam. They are illustrated in Figure I-94 while the values of the different hyperfine parameters are given in Figure I-93.

In the case of SP(F)M nanoparticles, the in-field spectrum consists of two magnetic sextets characterized by four well resolved lines, as the two intermediate lines are very low, in agreement with a weakly canted ferrimagnetic structure. The fitting model requires at least 2 sub-components to adequately describe each sextet: the values of isomer shift allow to assign clearly the two components to  $\text{Fe}^{3+}$  species located in tetrahedral and octahedral sites, as confirmed by the two values of hyperfine field while the relative proportions are estimated at 35.6 and 64.4 %, respectively. In addition, one can discuss the canting of these two types of Fe magnetic moments.

As the size of these particles is very small, one can assume that this canting results from a pure surface effect resulting in a symmetry breaking. The description can be thus done with a perfect ferrimagnetic core surrounded by a canted spin surface layer. The thickness can be estimated by using the relation  $e = r/2 \sin^2\theta$ , where  $r$  corresponds to the mean radius of the nanoparticles.

The in-field Mössbauer spectra of  $\text{Zn}_{0.2}\text{Fe}_{2.6}\text{O}_4$  and FM samples are compared to that of SP(F)M nanoparticles in Figure I-94. The hyperfine structures consist also of two well resolved sextets composed of 4 lines but significantly different in the range -5 - -6 mm/s and around +7 mm/s with the presence of a “shoulder”. Contrary to the first spectrum, the fitting model requires at least three sub-components to well describe the experimental spectra. Since the first two components give rise to similar values of hyperfine parameters, the third one has to be assigned to the presence of  $\text{Fe}^{2+}$  component: this tendency is fairly consistent with that observed in zero-field spectra. The refined values of the different parameters are listed in Figure I-93. The isomer shift values are unambiguously attributed to  $\text{Fe}^{3+}$  species which are located in tetrahedral and octahedral sites, as expected and to  $\text{Fe}^{2+}$  in the blocked electronic state for the larger nanoparticles. It confirms the oxidation of the smallest nanoparticles into only pure  $\text{Fe}^{3+}$  states, in agreement with previous studies giving rise to a ferric shell with a thickness estimated at about 3 nm [10]. Surprisingly, no significant canting is observed in the smallest nanoparticles contrarily to the largest ones. It could be ascribed to the atypical morphology of FM particles which are of “raspberry” type with many tiny particles binding together. Perhaps these kind of structures enhances the surface spin-canting.

Another point is the absence of canting for the tetrahedral Fe moments: as the surface is magnetically canted, this suggests that it results probably in a large majority of  $\text{Fe}^{3+}$  at octahedral positions, as concluded in the case of hollow nanoparticles [188].

Additionally, the proportions of  $\text{Fe}^{3+}$  at tetrahedral and octahedral locations allow to compute the inversion degree of  $\text{Zn}_{0.2}\text{Fe}_{2.6}\text{O}_4$  and FM particles from formula I-28 (section I.2.1),

which are respectively of 0 and 0.1. The values are close to the ones determined through the Rietveld analysis (section III.2.6.B.a).

Sample	Fe site	$\delta$	$2\epsilon$	$B_{\text{eff}}$	$\theta$	$B_{\text{hf}}$	Absorption area	e
		mm/s $\pm 0.05$	mm/s $\pm 0.05$	T $\pm 0.5$	$^{\circ}$ $\pm 5$	T $\pm 0.5$		
SP(F)M	Fe <sup>3+</sup> A	0.37	0.00	60.3	2	52.3	35.6	0
	Fe <sup>3+</sup> B	0.53	0.00	45.5	15	53.3	64.4	0.10
Zn <sub>0.2</sub> Fe <sub>2.6</sub> O <sub>4</sub>	Fe <sup>3+</sup> A	0.38	-0.03	60.1	0	52.1	32.5	0
	Fe <sup>3+</sup> B	0.56	0.00	45.2	15	53.0	49.1	0.38
	Fe <sup>2+</sup>	1.15	-0.71	39.5	27	32.6	18.4	-
FM	Fe <sup>3+</sup> A	0.38	0.00	59.8	0	51.7	29.4	0
	Fe <sup>3+</sup> B	0.54	0.00	44.8	19	52.4	59.7	0.60
	Fe <sup>2+</sup>	1.15	-0.15	37.9	6	30.0	10.9	-

Figure I-93. Refined values of the hyperfine parameters estimated from the in-field Mössbauer spectra (see Figure I-94) obtained on SP(F)M, Zn<sub>0.2</sub>Fe<sub>2.6</sub>O<sub>4</sub> and FM particles.

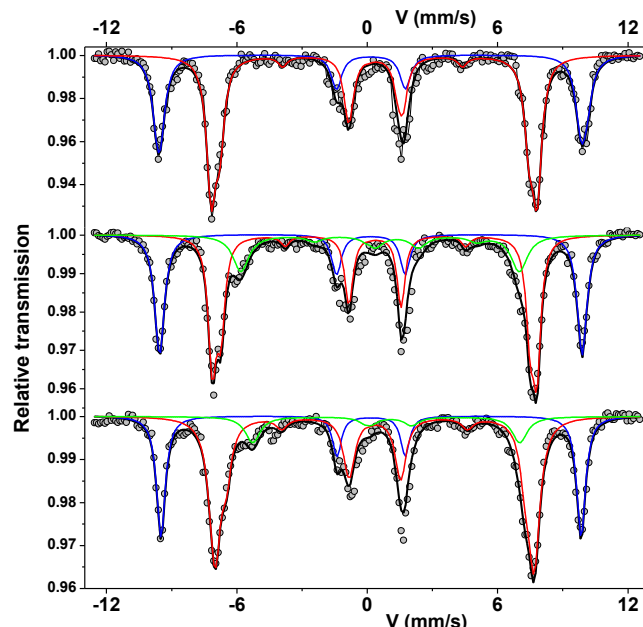


Figure I-94. Mössbauer spectra of SP(F)M (top), Zn<sub>0.2</sub>Fe<sub>2.6</sub>O<sub>4</sub> (middle) and FM (bottom) particles at 14K under an external magnetic field of 8T applied parallel to the  $\gamma$ -beam.

### III.2.7. Chemical characterizations

The chemical homogenization of the sample is investigated at global and local scales. The interest is to verify that the local composition is in agreement with the global one and to avoid chemical heterogeneities.

#### III.2.7.A. At the global scale

On the one hand, the chemical composition of a nanoparticle batch of powder of SP(F)M and FM references is evaluated by inductively coupled plasma atomic emission spectrometry



(ICP-AES) (Figure I-95). This characterization technique is used to analyze the chemical elements of a sample. A good agreement between theory and experiment is noticed at the global scale on the SP(F)M and FM particles (Figure I-95).

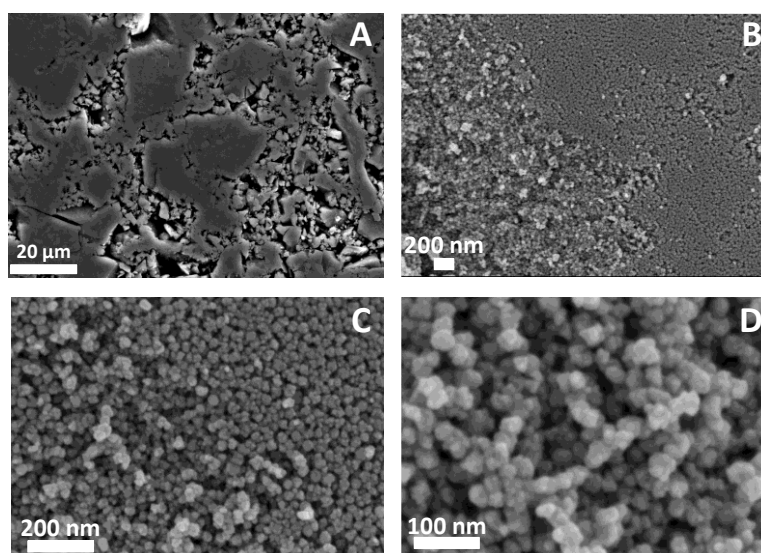
Ratio Zn/Fe	6.2 ± 1 nm	22.4 ± 11 nm
Theoretical		0.15
ICP-AES	0.15	0.12

**Figure I-95. Comparison between theoretical chemical composition and the one determined by ICP-AES at the global scale.**

However, a chemical composition close to the theoretical one at the global scale does not mean that all of the nanoparticles are homogeneous in composition. The chemical composition has to be controlled more locally.

### III.2.7.B. *At the local scale*

On the other hand, another technique is employed to define specific chemical compositions at different areas of a sample: chemical mappings realized through EDX coupled with SEM. These analyzes have been conducted with a SEM-FEG. This device allows getting a higher resolution compared to a tungsten filament SEM. The nanoparticle images obtained through this technique enable to observe the “raspberry” structure more precisely (Figure I-96.B-D), the SP(F)M particles being still too small regarding the device resolution (Figure I-96.A). Indeed, this method provides morphology information in 3D while TEM gives 2D nanoparticle images. Hence it confirms the idea of a “raspberry” type shape with the presence of bunches of grapes which were suspected on the TEM pictures.



**Figure I-96. SEM-FEG of SP(F)M (A) and FM particles (B-D) pressed in pellets.**

Chemical mappings of the SP(F)M reference have been achieved through SEM-EDX (Figure I-97). In the top left corner, the area of the nanoparticles pellet selected for the analysis is showed. Then, Fe, O and Zn elements have been analyzed in this area. The quantitative results

concerning these atomic elements are exposed in Figure I-98. The resulting Zn/Fe ratio is of 0.14 (Figure I-101) which is in agreement with the chemical composition at the global scale and also with the theoretical one.

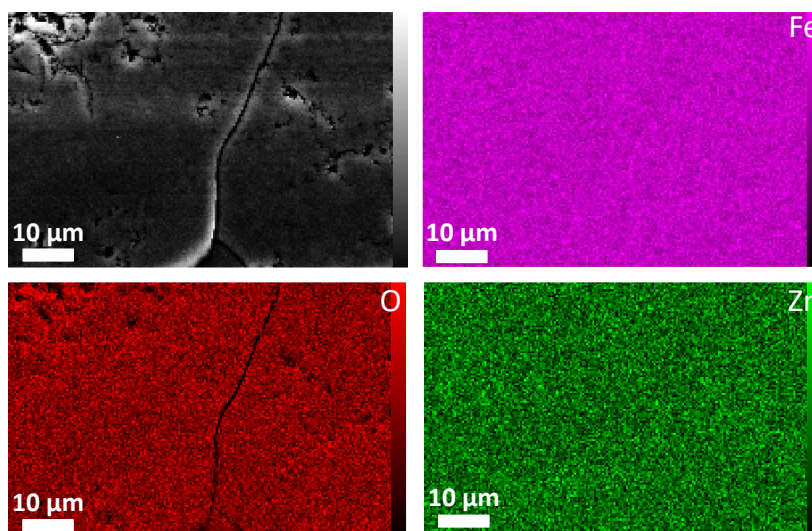


Figure I-97. Chemical mapping of SP(F)M particles.

Elt	A%
C	33.24
O	29.13
Si	0.52
Fe	32.47
Zn	4.65
	100.00

Figure I-98. Chemical composition details of SP(F)M particles at the local scale (Figure I-97).

Regarding the FM nanoparticles, an example of chemical mapping is exhibited in Figure I-99. Fe, Zn and O atomic elements look well spread in the area of interest. Two chemical compositions are detailed in Figure I-100, corresponding to two different areas of the pellet. The Zn/Fe ratios are equal to 0.13 (Figure I-101) for the two situations which is also in line with the theory and with the global composition.

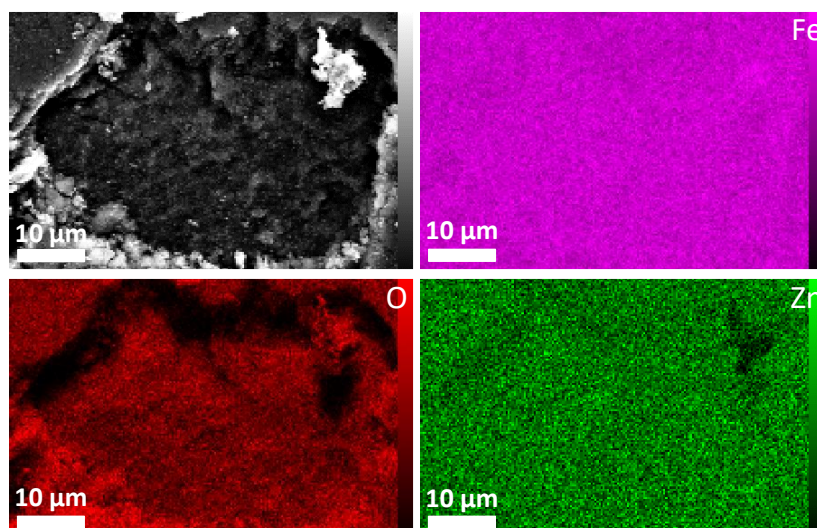


Figure I-99. Chemical mapping of FM particles.

Elt	A%	Elt	A%
C	15.79	C	11.24
O	37.38	O	37.15
Fe	41.61	Fe	45.86
Zn	5.22	Zn	5.74
<b>(a)</b>	100.00	<b>(b)</b>	100.00

Figure I-100. Chemical composition details of FM particles at the local scale in two different areas.

The chart in Figure I-101 is a summary of the Zn/Fe ratios for the SP(F)M and FM nanoparticles references. The agreement between theoretical, global and local composition is demonstrated. The nanoparticles display a good homogeneity in terms of chemical composition which is sufficient for the intended application.

Ratio Zn/Fe	6.2 ± 1 nm	22.4 ± 11 nm
Theoretical	0.15	
ICP-AES	0.15	0.12
SEM-EDX	0.14	0.13

Figure I-101. Summary table of the global and local chemical composition for SP(F)M and FM particles.

In this chapter, iron and zinc quantities are only considered. At this stage, the concern is to make sure of the particle composition. This does not mean the particles are free of organics. A significant amount of carbon is otherwise detected by SEM-EDX (Figure I-98 and Figure I-100). The presence of other elements will be discussed elsewhere in chapter II.

### III.3. Conclusion and prospects

*The thermal decomposition synthesis of  $Zn_{0.4}Fe_{2.6}O_4$  nanoparticles through two different heating processes was studied: the classical and microwave routes. In both cases, the synthesis was executed with organic solvents. On the one hand, the conventional way in a heating mantle results in the following conclusions:*

- *Some parameters influence the particle size and shape, as well as their uniformity: the protocol parameters such as the heating rate and the duration time, and also the ratios between solvent, precursors and surfactant.*
- *The increase of oleic acid content, employed as a surfactant, induces the particle growth. This surfactant also governs the particle shape. Various morphologies are achievable: cubes, octahedra...*
- *The synthesized nanoparticles exhibit a huge polydispersity in size and shape.*
- *This route is difficult to manage due to the set-up which does not allow to monitor precisely the temperature rate. The experiments are thus not reproducible.*
- *Discrepancies between theoretical and experimental chemical composition are noticed and it is difficult to predict a relationship between those values due to the non-reproducible behavior of the method.*

*To improve the temperature control of the set-up and to avoid temperature gradients in the reactor, the microwave way was explored:*

- *A fast and more uniform heating is completed, leading to nanoparticles with homogeneous size and shape, and also reproducible.*
- *The experimental chemical compositions coincide with the theoretical ones and are also reproducible. All of the precursors react in the solution in an homogeneous manner.*
- *The major drawback is that this method is selective in terms of solvent. It requires a solvent with a high dielectric constant and loss tangent. However, some studies show successful synthesis using solvent with a low dielectric constant.*
- *One of the goal exposed in part I.4 is carried out. The synthesis of nanoparticles with the two specified ranges of size is realized: superparamagnetic particles (SP(F)M reference) and ferrimagnetic ones (FM reference).*
- *SP(F)M particles are spherical in shape with a mean diameter of  $6.2 \pm 1$  nm. The narrow size distributions confirm the uniformity of the particle sizes and also the good reproducibility of the experiments. The size computed from XRD patterns is of 4.5 nm.*
- *FM particles are compared to “raspberry” frameworks, constituted of a binding between crystallites with continuity between the crystal planes. The mean size of such a structure is of  $22.4 \pm 11$  nm with a corresponding diameter of 19.1 nm from XRD analysis. Large distributions of particle size are noticed due to the atypical morphology. The experiments are quite reproducible.*

*All these advantages and results convince to select the microwave route for the synthesis of uniform spherical nanoparticles with a reproducible chemical composition. A deeper study of the method is performed through a parametric study which underlines the influence of the mixture of solvents used in the synthesis, composed of oleylamine (OAm), oleic acid (OA), octadecene (ODE) and ethylene glycol (EG):*

- *OAm and OA are used as surfactants, and ODE as a solvent. EG is introduced to increase the particle diameter, allowing to generate FM particles.*
- *The choice of zinc precursor is justified. Zn(acac)<sub>2</sub> is chosen due to its best reactivity with Fe(acac)<sub>3</sub>, compared to ZnCl<sub>2</sub>.*
- *The addition of EG in the reaction mixture induces the decrease of the particle size above a critical volume. Beyond a certain quantity of EG, the presence of impurities is detected in the chemical composition of the particle. The maximum diameter attainable is the one of the FM reference (27.4 ± 4.0 nm).*
- *The use of solvents with a higher molecular weight (TREG, PEG 6000) in replacement of EG does not increase the nanoparticle sizes. The “raspberry” shape of nanoparticles disappears by using other solvents, meaning the EG is the only one to create these structures.*
- *OAm and OA are complementary surfactants and act differently on the particle morphology. OA favors the particle growth along a preferential axis and OAm inhibits its growth. In equal quantities, they produce spherical and reproducible nanoparticles. The nanoparticle morphology is well-controlled by tuning the surfactants ratio. The ODE homogenizes the precursors with the surfactants.*
- *The temperature protocol is well understood. At 200 °C, oxolation reactions seem to occur while the crystallization step requires to increase the temperature to 270 °C.*

*The microstructure and chemical composition of SP(F)M and FM particles have been analyzed:*

- *A Fourier Transform Infrared Spectroscopy (FTIR) analysis evidences a potential core/shell structure for SP(F)M particles due to oxidation of the particle surface, exhibiting Zn<sup>2+</sup> substituted maghemite at the core.*
- *A partial inversion of the spinel structure for FM particles is demonstrated through three means of characterization: X-ray diffraction with a Rietveld analysis, HAADF-STEM coupled to EELS, and Mössbauer spectroscopy.*
- *Mössbauer spectroscopy evidences the presence of volume oxidation of SP(F)M and FM particles near the surface. SP(F)M particles appear completely oxidized.*
- *A layer of surface spin-canted for SP(F)M and FM particles is estimated by Mössbauer spectroscopy, with a higher thickness for larger particles.*
- *The chemical composition is homogeneous at global (ICP-AES) and local scales (SEM-EDX) and are in agreement with the theoretical one.*

*For these ranges of size, the particles are very sensitive to oxidation once synthesized. The samples being not handled in a glovebox, it is necessary to pay attention to the fact the particle oxidation certainly evolves over time.*

*The microwave route is suitable in this study for the synthesis of uniform  $Zn_{0.4}Fe_{2.6}O_4$  nanoparticles with the two desired ranges of size. In this work, the chemical composition has been restricted to doped zinc iron oxide spinel particles and avoid dealing with precursors with different decomposition temperatures. Nevertheless, the microwave route could be adapted for the synthesis of other interesting composition, like  $(ZnMn)Fe_2O_4$  or  $(NiZn)Fe_2O_4$ , with the addition of another acetylacetonates for example. A procedure of synthesis of  $Ni_{0.5}Zn_{0.5}Fe_2O_4$  ferrite nanoparticles through microwave assisted thermal combustion of oxides precursors has been described by Peng et al. [185]. Hence, the idea of a microwave assisted thermal decomposition by adding another metallic precursor may be considered thereafter. Indeed, the addition of ions in the structure of the ferrite might potentially be attractive to tune the electrical and magnetic properties of the material due to cation distribution. The material behavior will differ with responses on different frequency ranges, leading to different types of applications [142] [190] [191] [192] [193] [194] [195] [196].*

*The inversion degree of the spinel can be tuned by post processing rapid thermal annealing (RTA) as demonstrated by R. Sai et al. [197], which opens the opportunities of optimizing magnetic properties through Zn position in the spinel [198].*

*There are obviously limits to the microwave route. The use of a suitable solvent with a high dielectric constant and loss tangent to cause heating under the microwave field restricts the possibilities. In the same way, the obtained yields are low compared to the volume of solvents introduced in the reactor. If some improvements could be done like working with the multiple vessel configuration or the possible transfer at large scale, the method remains solvent-wasting and time-consuming, which is not part of an ecological approach.*

*This chapter recalls the magnetism basis, the choice of the material with some applications, as well as the selected synthesis method. Uniform  $Zn_{0.4}Fe_{2.6}O_4$  nanoparticles with the two desired ranges are synthesized ( $6.2 \pm 1$  and  $22.4 \pm 11$  nm). The microstructure and chemical composition are confirmed.*

*The next chapter (Chapter II) will focus on the dispersion of  $Zn_{0.4}Fe_{2.6}O_4$  nanoparticles and on the elaboration of coatings through a first investigated process.*

## Chapter I references:

- [1] S. Mornet, "Synthèse et modification chimique de la surface de nanoparticules de maghémite à des fins d'applications biomédicales," p. 222.
- [2] M. Pauly, "Structuration de nanoparticules magnétiques d'oxyde de fer en films et étude de leurs propriétés magnétiques et de magnéto-transport," Thesis, 2010.
- [3] R. M. Cornell and U. Schwertmann, *The iron oxides: structure, properties, reactions, occurrences and uses*, Weinheim, New York, VCH. 1996.
- [4] G. Kh. Rozenberg *et al.*, "Structural characterization of temperature- and pressure-induced inverse  $\leftrightarrow$  normal spinel transformation in magnetite," *Phys. Rev. B*, vol. 75, no. 2, p. 020102, Jan. 2007, doi: 10.1103/PhysRevB.75.020102.
- [5] O. ur Rahman, S. C. Mohapatra, and S. Ahmad, "Fe<sub>3</sub>O<sub>4</sub> inverse spinal super paramagnetic nanoparticles," *Mater. Chem. Phys.*, vol. 132, no. 1, pp. 196–202, Jan. 2012, doi: 10.1016/j.matchemphys.2011.11.032.
- [6] G. V. Lewis, C. R. A. Catlow, and A. N. Cormack, "Defect structure and migration in Fe<sub>3</sub>O<sub>4</sub>," *J. Phys. Chem. Solids*, vol. 46, pp. 1227–1233, 1985.
- [7] M. P. Morales, C. Pecharroman, T. Gonzalez Carreno, and C. J. Serna, "Structural Characteristics of Uniform  $\gamma$ -Fe<sub>2</sub>O<sub>3</sub> particles with different axial (length/width) ratios," *J. Solid State Chem*, vol. 108, pp. 158–163, 1994.
- [8] A. N. Shmakov, G. N. Kryukova, S. V. Tsybulya, A. L. Chuvilin, and L. P. Solovyeva, "Vacancy Ordering in  $\gamma$ -Fe<sub>2</sub>O<sub>3</sub>: Synchrotron X-ray Powder Diffraction and High-Resolution Electron Microscopy Studies," *J. Appl. Crystallogr.*, vol. 28, no. 2, pp. 141–145, Apr. 1995, doi: 10.1107/S0021889894010113.
- [9] P. Tartaj, M. a del P. Morales, S. Veintemillas-Verdaguer, T. Gonz lez-Carre o, and C. J. Serna, "The preparation of magnetic nanoparticles for applications in biomedicine," *J. Phys. Appl. Phys.*, vol. 36, no. 13, pp. R182–R197, Jul. 2003, doi: 10.1088/0022-3727/36/13/202.
- [10] T. J. Daou *et al.*, "Hydrothermal Synthesis of Monodisperse Magnetite Nanoparticles," *Chem. Mater.*, vol. 18, no. 18, pp. 4399–4404, Sep. 2006, doi: 10.1021/cm060805r.
- [11] G. F. Dionne, *Magnetic Oxides*, Springer. 2009.
- [12] D. Jiles, *Introduction to magnetism and magnetic materials*, CRC Press. 2016.
- [13] Gubin, *Magnetic Nanoparticles*, Wiley-VCH. 2009.
- [14] C. Kittel, "Physical Theory of Ferromagnetic Domains," *Rev. Mod. Phys.*, vol. 21, no. 4, pp. 541–583, Oct. 1949, doi: 10.1103/RevModPhys.21.541.
- [15] N. W. Ashcroft and N. D. Mermin, *Physique des Solides*, EDP Sciences. 2002.
- [16] L. Néel, "Some theoretical aspects of rock-magnetism," *Advances in physics*, 1955.
- [17] M. Louis NÉEL, "PAROIS DANS LES FILMS MINCES," *J. Phys. Colloq.*, vol. 29, no. C2, pp. C2-87-C2-94, Feb. 1968, doi: 10.1051/jphyscol:1968215.
- [18] T. Thomson, "Magnetic properties of metallic thin films," in *Metallic Films for Electronic, Optical and Magnetic Applications*, Elsevier, 2014, pp. 454–546.
- [19] S. Bedanta and W. Kleemann, "Supermagnetism," *J. Phys. Appl. Phys.*, vol. 42, no. 1, p. 013001, Jan. 2009, doi: 10.1088/0022-3727/42/1/013001.
- [20] V. Skumryev, H. J. Blythe, J. Cullen, and J. M. D. Coey, "AC susceptibility of a magnetite crystal," *J. Magn. Magn. Mater.*, vol. 196–197, pp. 515–517, May 1999, doi: 10.1016/S0304-8853(98)00863-4.
- [21] D. J. Dunlop and Ö. Özdemir, *Rock Magnetism: Fundamentals and Frontiers*, vol. 3. Cambridge University Press: Cambridge, 1997.
- [22] E. P. Valstyn, J. P. Hanton, and A. H. Morrish, "Ferromagnetic Resonance of Single-Domain Particles," *Phys. Rev.*, vol. 128, no. 5, pp. 2078–2087, Dec. 1962, doi: 10.1103/PhysRev.128.2078.
- [23] J. M. D. Coey, "Noncollinear Spin Arrangement in Ultrafine Ferrimagnetic Crystallites," *Physical Review Letters*, vol. 27, no. 17, 1971.



- [24] M. Srivastava, S. K. Alla, S. S. Meena, N. Gupta, R. K. Mandal, and N. K. Prasad, "Zn<sub>x</sub>Fe<sub>3-x</sub>O<sub>4</sub> (0.01 ≤ x ≤ 0.8) nanoparticles for controlled magnetic hyperthermia application," *New J. Chem.*, vol. 42, no. 9, pp. 7144–7153, 2018, doi: 10.1039/C8NJ00547H.
- [25] J. Marx, H. Huang, K. S. M. Salih, W. R. Thiel, and V. Schünemann, "Spin canting in ferrite nanoparticles," *Hyperfine Interact.*, vol. 237, no. 1, p. 41, Dec. 2016, doi: 10.1007/s10751-016-1241-5.
- [26] J. Park *et al.*, "Ultra-large-scale syntheses of monodisperse nanocrystals," *Nat. Mater.*, vol. 3, no. 12, pp. 891–895, Dec. 2004, doi: 10.1038/nmat1251.
- [27] A. Demortière *et al.*, "Size-dependent properties of magnetic iron oxidenanocrystals," *Nanoscale*, vol. 3, no. 1, pp. 225–232, 2011, doi: 10.1039/C0NR00521E.
- [28] S. A. Popescu, P. Vlazan, and P. V. No, "ELECTROMAGNETIC BEHAVIOR OF ZINC FERRITES OBTAINED BY A COPRECIPITATION TECHNIQUE," *UPB Sci Bull*, vol. 73, no. 4, p. 10, 2011.
- [29] W. Yan, Q. Li, H. Zhong, and Z. Zhong, "Characterization and low-temperature sintering of Ni<sub>0.5</sub>Zn<sub>0.5</sub>Fe<sub>2</sub>O<sub>4</sub> nano-powders prepared by refluxing method," *Powder Technol.*, vol. 192, no. 1, pp. 23–26, May 2009, doi: 10.1016/j.powtec.2008.11.010.
- [30] A. Fujiwara, M. Tada, T. Nakagawa, and M. Abe, "Permeability and electric resistivity of spin-sprayed Zn ferrite films for high-frequency device applications," *J. Magn. Magn. Mater.*, vol. 320, no. 8, pp. L67–L69, Apr. 2008, doi: 10.1016/j.jmmm.2007.11.026.
- [31] Q. Song and Z. J. Zhang, "Shape Control and Associated Magnetic Properties of Spinel Cobalt Ferrite Nanocrystals," *J. Am. Chem. Soc.*, vol. 126, no. 19, pp. 6164–6168, May 2004, doi: 10.1021/ja049931r.
- [32] Y. Yang *et al.*, "Synthesis of nonstoichiometric zinc ferrite nanoparticles with extraordinary room temperature magnetism and their diverse applications," *J. Mater. Chem. C*, vol. 1, no. 16, p. 2875, 2013, doi: 10.1039/c3tc00790a.
- [33] J. Neige, "Élaboration, caractérisation et modélisation d'un composite à base de pétales ferromagnétiques pour des applications hyperfréquences," 2013.
- [34] A. Hubert and R. Schäfer, *Magnetic domains: the analysis of magnetic microstructures*. 1998.
- [35] A. Vogel *et al.*, "Coupled Vortex Oscillations in Spatially Separated Permalloy Squares," *Phys. Rev. Lett.*, vol. 106, no. 13, p. 137201, Mar. 2011, doi: 10.1103/PhysRevLett.106.137201.
- [36] Z. Zhang and S. Satpathy, "Electron states, magnetism, and the Verwey transition in magnetite," *Physical Review B*, vol. 44, no. 24, 1991.
- [37] R. Baladi and K. Gheisari, "Structural, Magnetic and Dielectric Properties of Nanocrystalline (M = Li and Mg) Ferrites Synthesized via EDTA/EG Assisted Sol-Gel Method," *Trans. Indian Ceram. Soc.*, vol. 78, no. 4, pp. 195–203, Oct. 2019, doi: 10.1080/0371750X.2019.1671901.
- [38] D. H. Han, J. P. Wang, and H. L. Luo, "Crystallite size effect on saturation magnetization of fine ferrimagnetic particles," *J. Magn. Magn. Mater.*, vol. 136, no. 1–2, pp. 176–182, Sep. 1994, doi: 10.1016/0304-8853(94)90462-6.
- [39] R. N. Panda, N. S. Gajbhiye, and G. Balaji, "Magnetic properties of interacting single domain Fe<sub>3</sub>O<sub>4</sub> particles," *J. Alloys Compd.*, vol. 326, no. 1–2, pp. 50–53, Aug. 2001, doi: 10.1016/S0925-8388(01)01225-7.
- [40] H. Shokrollahi, "A review of the magnetic properties, synthesis methods and applications of maghemite," *J. Magn. Magn. Mater.*, vol. 426, pp. 74–81, Mar. 2017, doi: 10.1016/j.jmmm.2016.11.033.
- [41] S. Yoon, "Preparation and Physical Characterizations of Superparamagnetic Maghemite Nanoparticles," *J. Magn.*, vol. 19, no. 4, pp. 323–326, Dec. 2014, doi: 10.4283/JMAG.2014.19.4.323.
- [42] E. W. Gorter, "Philips Research Reports," vol. 9, pp. 295–321, 1954.
- [43] E. J. Verwey, P. W. Haayman, and F. C. Romeijn, "Physical Properties and Cation Arrangement of Oxides with Spinel Structures II. Electronic Conductivity," *J. Chem. Phys.*, vol. 15, no. 4, pp. 181–187, Apr. 1947, doi: 10.1063/1.1746466.
- [44] J. Smit and H. P. J. Wijn, *Ferrites: Physical properties of ferromagnetic oxides in relation to their technical applications*. Philips Tech. Lib., 1959.



- [45] V. N. Antonov, B. N. Harmon, V. P. Antropov, A. Ya. Perlov, and A. N. Yaresko, "Electronic structure and magneto-optical Kerr effect of  $\text{Fe}_3\text{O}_4$  and  $\text{Mg}^{2+}$ - or  $\text{Al}^{3+}$ -substituted  $\text{Fe}_3\text{O}_4$ ," *Phys. Rev. B*, vol. 64, no. 13, p. 134410, Sep. 2001, doi: 10.1103/PhysRevB.64.134410.
- [46] A. Cabot *et al.*, "Vacancy Coalescence during Oxidation of Iron Nanoparticles," *J. Am. Chem. Soc.*, vol. 129, no. 34, pp. 10358–10360, Aug. 2007, doi: 10.1021/ja072574a.
- [47] F. Walz, "The Verwey transition - a topical review," *J. Phys. Condens. Matter*, vol. 14, no. 12, pp. R285–R340, Apr. 2002, doi: 10.1088/0953-8984/14/12/203.
- [48] P. Weiss and R. Forrer, "La saturation absolue des ferromagnétiques et les lois d'approche en fonction du champ et de la température," *Ann. Phys.*, vol. 10, no. 12, pp. 279–372, 1929, doi: 10.1051/anphys/192910120279.
- [49] R. W. Millar, "THE HEAT CAPACITIES AT LOW TEMPERATURES OF 'FERROUS OXIDE,' MAGNETITE AND CUPROUS AND CUPRIC OXIDES <sup>1</sup>," *J. Am. Chem. Soc.*, vol. 51, no. 1, pp. 215–222, Jan. 1929, doi: 10.1021/ja01376a026.
- [50] N. Mott, "Festkörperprobleme 19: Hopping conduction and the Coulomb gap; applications to  $\text{Fe}_3\text{O}_4$ ,  $\text{Ti}_4\text{O}_7$  and impurity conduction in  $\text{Si:P}$ ," *Adv. S. S. Phys.*, pp. 331–361, 1979.
- [51] M. Bohra, N. Agarwal, and V. Singh, "A Short Review on Verwey Transition in Nanostructured  $\text{Fe}_3\text{O}_4$  Materials," *J. Nanomater.*, vol. 2019, pp. 1–18, Mar. 2019, doi: 10.1155/2019/8457383.
- [52] G. Kh. Rozenberg *et al.*, "Origin of the Verwey Transition in Magnetite," *Phys. Rev. Lett.*, vol. 96, no. 4, p. 045705, Feb. 2006, doi: 10.1103/PhysRevLett.96.045705.
- [53] W. B. Mi, E. Y. Jiang, and H. L. Bai, " $\text{Fe}^{3+}/\text{Fe}^{2+}$  ratio controlled magnetic and electrical transport properties of polycrystalline  $\text{Fe}_{3(1-\delta)}\text{O}_4$  films," *J. Phys. Appl. Phys.*, vol. 42, no. 10, 2009, doi: 10.1088/0022-3727/42/10/105007.
- [54] Ö. Özdemir, D. J. Dunlop, and B. M. Moskowitz, "The effect of oxidation on the Verwey transition in magnetite," *Geophys. Res. Lett.*, vol. 20, no. 16, pp. 1671–1674, Aug. 1993, doi: 10.1029/93GL01483.
- [55] W. Baaziz *et al.*, "Magnetic Iron Oxide Nanoparticles: Reproducible Tuning of the Size and Nanosized-Dependent Composition, Defects, and Spin Canting," *J. Phys. Chem. C*, vol. 118, no. 7, pp. 3795–3810, Feb. 2014, doi: 10.1021/jp411481p.
- [56] R. D. Shannon, "Revised Effective Ionic Radii and Systematic Studies of Interatomic Distances in Halides and Chalcogenides," *Acta Crystallographica A32*, pp. 751–767, 1976.
- [57] A. Verma, T. C. Goel, R. G. Mendiratta, and P. Kishan, "Magnetic properties of nickel-zinc ferrites prepared by the citrate precursor method," *J. Magn. Magn. Mater.*, vol. 208, no. 13, 2000.
- [58] C. Upadhyay, H. C. Verma, and S. Anand, "Cation distribution in nanosized Ni–Zn ferrites," *J. Appl. Phys.*, vol. 95, no. 10, pp. 5746–5751, May 2004, doi: 10.1063/1.1699501.
- [59] S. Singhal and K. Chandra, "Cation distribution and magnetic properties in chromium-substituted nickel ferrites prepared using aerosol route," *J. Solid State Chem.*, vol. 180, no. 1, pp. 296–300, Jan. 2007, doi: 10.1016/j.jssc.2006.10.010.
- [60] Q. Tian, Q. Wang, Q. Xie, and J. Li, "Aqueous Solution Preparation, Structure, and Magnetic Properties of Nano-Granular  $\text{Zn}_x\text{Fe}_{3-x}\text{O}_4$  Ferrite Films," *Nanoscale Res. Lett.*, vol. 5, no. 9, pp. 1518–1523, Sep. 2010, doi: 10.1007/s11671-010-9672-4.
- [61] G. Alvarez, H. Montiel, J. F. Barron, M. P. Gutierrez, and R. Zamorano, "Yafet–Kittel-type magnetic ordering in  $\text{Ni}_{0.35}\text{Zn}_{0.65}\text{Fe}_2\text{O}_4$  ferrite detected by magnetosensitive microwave absorption measurements," *J. Magn. Magn. Mater.*, vol. 322, no. 3, pp. 348–352, Feb. 2010, doi: 10.1016/j.jmmm.2009.09.056.
- [62] R. Pauthenet, "Aimantation spontanée des ferrites," *Ann. Phys.*, vol. 12, no. 7, pp. 710–747, 1952, doi: 10.1051/anphys/195212070710.
- [63] Z. Beji *et al.*, "Magnetic properties of Zn-substituted  $\text{MnFe}_2\text{O}_4$  nanoparticles synthesized in polyol as potential heating agents for hyperthermia. Evaluation of their toxicity on Endothelial cells," *Chem. Mater.*, vol. 22, no. 19, pp. 5420–5429, Oct. 2010, doi: 10.1021/cm1001708.
- [64] V. Blanco-Gutiérrez, M. J. Torralvo-Fernández, and R. Sáez-Puche, "Magnetic Behavior of  $\text{ZnFe}_2\text{O}_4$  Nanoparticles: Effects of a Solid Matrix and the Particle Size," *J. Phys. Chem. C*, vol. 114, no. 4, pp. 1789–1795, Feb. 2010, doi: 10.1021/jp908395v.

- [65] S. Noh *et al.*, "Nanoscale Magnetism Control via Surface and Exchange Anisotropy for Optimized Ferrimagnetic Hysteresis," *Nano Lett.*, vol. 12, no. 7, pp. 3716–3721, Jul. 2012, doi: 10.1021/nl301499u.
- [66] J. L. Dormann, "Le phénomène de superparamagnétisme," *Rev. Phys. Appliquée*, vol. 16, no. 6, pp. 275–301, 1981, doi: 10.1051/rphysap:01981001606027500.
- [67] U. Jeong, X. Teng, Y. Wang, H. Yang, and Y. Xia, "Superparamagnetic Colloids: Controlled Synthesis and Niche Applications," *Adv. Mater.*, vol. 19, no. 1, pp. 33–60, Jan. 2007, doi: 10.1002/adma.200600674.
- [68] R. C. O'Handley, *Modern magnetic materials: Principles and application*. USA, 2000.
- [69] B. Barbara, "Single-particle nanomagnetism," *Solid State Sci.*, vol. 7, no. 6, pp. 668–681, Jun. 2005, doi: 10.1016/j.solidstatesciences.2004.11.013.
- [70] Q. Li, C. W. Kartikowati, S. Horie, T. Ogi, T. Iwaki, and K. Okuyama, "Correlation between particle size/domain structure and magnetic properties of highly crystalline Fe<sub>3</sub>O<sub>4</sub> nanoparticles," *Sci. Rep.*, vol. 7, no. 1, p. 9894, Dec. 2017, doi: 10.1038/s41598-017-09897-5.
- [71] P. J. van der Zaag, P. J. van der Valk, and M. Th. Rekveldt, "A domain size effect in the magnetic hysteresis of NiZn-ferrites," *Appl. Phys. Lett.*, vol. 69, no. 19, pp. 2927–2929, Nov. 1996, doi: 10.1063/1.117326.
- [72] M. Bissannagari, W. Lee, W. Y. Lee, J. H. Jeong, and J. Kim, "Fully-Inkjet-Printed Ag-Coil/NiZn-Ferrite for Flexible Wireless Power Transfer Module: Rigid Sintered Ceramic Body into Flexible Form," *Adv. Funct. Mater.*, vol. 27, no. 31, p. 1701766, Aug. 2017, doi: 10.1002/adfm.201701766.
- [73] L.-M. Lacroix *et al.*, "Magnetic hyperthermia in single-domain monodisperse FeCo nanoparticles: Evidences for Stoner–Wohlfarth behavior and large losses," *J. Appl. Phys.*, vol. 105, no. 2, p. 023911, Jan. 2009, doi: 10.1063/1.3068195.
- [74] C. Desvaux *et al.*, "Multimillimetre-large superlattices of air-stable iron–cobalt nanoparticles," *Nat. Mater.*, vol. 4, no. 10, pp. 750–753, Oct. 2005, doi: 10.1038/nmat1480.
- [75] V. Salgueiriño-Maceira, M. A. Correa-Duarte, M. Farle, A. López-Quintela, K. Sieradzki, and R. Diaz, "Bifunctional Gold-Coated Magnetic Silica Spheres," *Chem. Mater.*, vol. 18, no. 11, pp. 2701–2706, May 2006, doi: 10.1021/cm0603001.
- [76] E. Myrovali *et al.*, "Arrangement at the nanoscale: Effect on magnetic particle hyperthermia," *Sci. Rep.*, vol. 6, no. 1, p. 37934, Dec. 2016, doi: 10.1038/srep37934.
- [77] M. Comesana-Hermo *et al.*, "Stable single domain Co nanodisks: synthesis, structure and magnetism," *J. Mater. Chem.*, vol. 22, no. 16, pp. 8043–8047, 2012.
- [78] K. K. Kefeni, T. A. M. Msagati, and B. B. Mamba, "Ferrite nanoparticles: Synthesis, characterisation and applications in electronic device," *Mater. Sci. Eng. B*, vol. 215, pp. 37–55, Jan. 2017, doi: 10.1016/j.mseb.2016.11.002.
- [79] A. Joseph and S. Mathew, "Ferrofluids: Synthetic Strategies, Stabilization, Physicochemical Features, Characterization, and Applications," *ChemPlusChem*, vol. 79, no. 10, pp. 1382–1420, Oct. 2014, doi: 10.1002/cplu.201402202.
- [80] C. Dhand *et al.*, "Methods and strategies for the synthesis of diverse nanoparticles and their applications: a comprehensive overview," *RSC Adv.*, vol. 5, no. 127, pp. 105003–105037, 2015, doi: 10.1039/C5RA19388E.
- [81] O. Dmitrieva *et al.*, "Enhancement of L1<sub>0</sub> phase formation in FePt nanoparticles by nitrogenization," *J. Phys. Appl. Phys.*, vol. 39, no. 22, pp. 4741–4745, Nov. 2006, doi: 10.1088/0022-3727/39/22/001.
- [82] M. Maicu, R. Schmittgens, D. Hecker, D. Glöß, P. Frach, and G. Gerlach, "Synthesis and deposition of metal nanoparticles by gas condensation process," *J Vac Sci Technol A*, vol. 32, no. 2, p. 10, 2014.
- [83] R. Massart and V. Cabuil, "Synthèse en milieu alcalin de magnétite colloïdale : contrôle du rendement et de la taille des particules," *J. Chim. Phys.*, vol. 84, pp. 967–973, 1987, doi: 10.1051/jcp/1987840967.
- [84] A.-H. Lu, E. L. Salabas, and F. Schüth, "Magnetic Nanoparticles: Synthesis, Protection, Functionalization, and Application," *Angew. Chem. Int. Ed.*, vol. 46, no. 8, pp. 1222–1244, Feb. 2007, doi: 10.1002/anie.200602866.

- [85] T. J. Daou *et al.*, "Coupling Agent Effect on Magnetic Properties of Functionalized Magnetite-Based Nanoparticles," *Chem. Mater.*, vol. 20, no. 18, pp. 5869–5875, Sep. 2008, doi: 10.1021/cm801405n.
- [86] T. J. Daou, "Synthèse et fonctionnalisation de nanoparticules d'oxydes de fer magnétiques," 2007.
- [87] B. Basly *et al.*, "Effect of the nanoparticle synthesis method on dendronized iron oxides as MRI contrast agents," *Dalton Trans*, vol. 42, no. 6, pp. 2146–2157, 2013, doi: 10.1039/C2DT31788E.
- [88] T. J. Daou *et al.*, "Phosphate Adsorption Properties of Magnetite-Based Nanoparticles," *Chem. Mater.*, vol. 19, no. 18, pp. 4494–4505, Sep. 2007, doi: 10.1021/cm071046v.
- [89] D. Toulemon, "Stratégies d'assemblage par chimie 'click' de nanoparticules magnétiques sur des surfaces fonctionnalisées," 2013.
- [90] P. Acharya, R. Desai, V. K. Aswal, and R. V. Upadhyay, "Structure of Co-Zn ferrite ferrofluid: A small angle neutron scattering analysis," *Pramana*, vol. 71, no. 5, pp. 1069–1074, Nov. 2008, doi: 10.1007/s12043-008-0225-7.
- [91] B. I. Kharisov, H. V. R. Dias, O. V. Kharissova, A. Vázquez, Y. Peña, and I. Gómez, "Solubilization, dispersion and stabilization of magnetic nanoparticles in water and non-aqueous solvents: recent trends," *RSC Adv*, vol. 4, no. 85, pp. 45354–45381, 2014, doi: 10.1039/C4RA06902A.
- [92] Y. Flores-Arias, G. Vázquez-Victorio, R. Ortega-Zempoalteca, U. Acevedo-Salas, S. Ammar, and R. Valenzuela, "Magnetic phase transitions in ferrite nanoparticles characterized by electron spin resonance," *J. Appl. Phys.*, vol. 117, no. 17, p. 17A503, May 2015, doi: 10.1063/1.4916935.
- [93] T. Gaudisson, Z. Beji, F. Herbst, S. Nowak, S. Ammar, and R. Valenzuela, "Ultrafine grained high density manganese zinc ferrite produced using polyol process assisted by Spark Plasma Sintering," *J. Magn. Magn. Mater.*, vol. 387, pp. 90–95, Aug. 2015, doi: 10.1016/j.jmmm.2015.03.045.
- [94] C. Liu, B. Zou, A. J. Rondinone, and Z. J. Zhang, "Reverse Micelle Synthesis and Characterization of Superparamagnetic  $\text{MnFe}_2\text{O}_4$  Spinel Ferrite Nanocrystallites," *J. Phys. Chem. B*, vol. 104, no. 6, pp. 1141–1145, Feb. 2000, doi: 10.1021/jp993552g.
- [95] M. Niederberger, "Nonaqueous Sol–Gel Routes to Metal Oxide Nanoparticles," *Acc. Chem. Res.*, vol. 40, no. 9, pp. 793–800, Sep. 2007, doi: 10.1021/ar600035e.
- [96] I.-C. Masthoff *et al.*, "Study of the growth process of magnetic nanoparticles obtained via the non-aqueous sol–gel method," *J. Mater. Sci.*, vol. 49, no. 14, pp. 4705–4714, Jul. 2014, doi: 10.1007/s10853-014-8160-0.
- [97] C. B. Murray, D. J. Norris, and M. G. Bawendi, "Synthesis and characterization of nearly monodisperse CdE (E = sulfur, selenium, tellurium) semiconductor nanocrystallites," *J. Am. Chem. Soc.*, vol. 115, no. 19, pp. 8706–8715, Sep. 1993, doi: 10.1021/ja00072a025.
- [98] B. P. Pichon *et al.*, "Microstructural and Magnetic Investigations of Wüstite-Spinel Core-Shell Cubic-Shaped Nanoparticles," *Chem. Mater.*, vol. 23, no. 11, pp. 2886–2900, Jun. 2011, doi: 10.1021/cm2003319.
- [99] M. V. Kovalenko, M. I. Bodnarchuk, R. T. Lechner, G. Hesser, F. Schäffler, and W. Heiss, "Fatty Acid Salts as Stabilizers in Size- and Shape-Controlled Nanocrystal Synthesis: The Case of Inverse Spinel Iron Oxide," *J. Am. Chem. Soc.*, vol. 129, no. 20, pp. 6352–6353, May 2007, doi: 10.1021/ja0692478.
- [100] J.-H. Lee *et al.*, "Artificially engineered magnetic nanoparticles for ultra-sensitive molecular imaging," *Nat. Med.*, vol. 13, no. 1, pp. 95–99, Jan. 2007, doi: 10.1038/nm1467.
- [101] A. Shavel, "Shape control of iron oxide nanoparticles," p. 7, 2009.
- [102] H. Zeng, P. M. Rice, S. X. Wang, and S. Sun, "Shape-Controlled Synthesis and Shape-Induced Texture of  $\text{MnFe}_2\text{O}_4$  Nanoparticles," *J. Am. Chem. Soc.*, vol. 126, no. 37, pp. 11458–11459, Sep. 2004, doi: 10.1021/ja045911d.
- [103] K. Butter, K. Kassapidou, G. J. Vroege, and A. P. Philipse, "Preparation and properties of colloidal iron dispersions," *J. Colloid Interface Sci.*, vol. 287, no. 2, pp. 485–495, Jul. 2005, doi: 10.1016/j.jcis.2005.02.014.
- [104] S. Esposito, "'Traditional' Sol-Gel Chemistry as a Powerful Tool for the Preparation of Supported Metal and Metal Oxide Catalysts," *Materials*, vol. 12, no. 4, p. 668, Feb. 2019, doi: 10.3390/ma12040668.

- [105] S. Sun *et al.*, "Monodisperse  $MFe_2O_4$  ( $M = Fe, Co, Mn$ ) Nanoparticles," *J. Am. Chem. Soc.*, vol. 126, no. 1, pp. 273–279, Jan. 2004, doi: 10.1021/ja0380852.
- [106] M. Niederberger, G. Garnweitner, N. Pinna, and G. Neri, "Non-aqueous routes to crystalline metal oxide nanoparticles: Formation mechanisms and applications," *Prog. Solid State Chem.*, vol. 33, no. 2–4, pp. 59–70, Jan. 2005, doi: 10.1016/j.progsolidstchem.2005.11.032.
- [107] J.-P. Jolivet, C. Chanéac, and E. Tronc, "Iron oxide chemistry. From molecular clusters to extended solid networks," *Chem Commun*, no. 5, pp. 477–483, 2004, doi: 10.1039/B304532N.
- [108] A. P. Wilkinson, C. Lind, and S. Pattanaik, "A New Polymorph of  $ZrW_2O_8$  Prepared Using Nonhydrolytic Sol–Gel Chemistry," *Chem. Mater.*, vol. 11, no. 1, pp. 101–108, Jan. 1999, doi: 10.1021/cm9805065.
- [109] J. N. Hay and H. M. Raval, "Synthesis of Organic–Inorganic Hybrids via the Non-hydrolytic Sol–Gel Process," *Chem. Mater.*, vol. 13, no. 10, pp. 3396–3403, Oct. 2001, doi: 10.1021/cm011024n.
- [110] P. H. Mutin and A. Vioux, "Nonhydrolytic Processing of Oxide-Based Materials: Simple Routes to Control Homogeneity, Morphology, and Nanostructure," *Chem. Mater.*, vol. 21, no. 4, pp. 582–596, Feb. 2009, doi: 10.1021/cm802348c.
- [111] M. Niederberger, G. Garnweitner, J. Buha, J. Polleux, J. Ba, and N. Pinna, "Nonaqueous synthesis of metal oxide nanoparticles: Review and indium oxide as case study for the dependence of particle morphology on precursors and solvents," *J. Sol-Gel Sci. Technol.*, vol. 40, no. 2–3, pp. 259–266, Dec. 2006, doi: 10.1007/s10971-006-6668-8.
- [112] J. Livage and C. Sanchez, "Sol-gel chemistry," *J. Non-Cryst. Solids*, vol. 145, pp. 11–19, Jan. 1992, doi: 10.1016/S0022-3093(05)80422-3.
- [113] M. S. Pessoa, P. S. Moscon, R. S. Melo, A. Franco, and P. C. Morais, "A comprehensive study of  $Co_{1-x}Ni_xFe_2O_4$  nanoparticles fabricated via three different synthetic methods," *Mater. Res. Express*, vol. 6, no. 12, p. 125068, Nov. 2019, doi: 10.1088/2053-1591/ab597c.
- [114] V. K. LaMer and R. H. Dinegar, "Theory, Production and Mechanism of Formation of Monodispersed Hydrosols," *J. Am. Chem. Soc.*, vol. 72, no. 11, pp. 4847–4854, Nov. 1950, doi: 10.1021/ja01167a001.
- [115] L. Wu, A. Mendoza-Garcia, Q. Li, and S. Sun, "Organic Phase Syntheses of Magnetic Nanoparticles and Their Applications," *Chem. Rev.*, vol. 116, no. 18, pp. 10473–10512, Sep. 2016, doi: 10.1021/acs.chemrev.5b00687.
- [116] A. Delattre, "Synthèses chimiques, transformation de phase et étude des propriétés magnétiques des nanoparticules de FePt et FePd," p. 202.
- [117] H. Cölfen and M. Antonietti, *Mesocrystals and Nonclassical Crystallization*, John Wiley & Sons, Ltd. 2008.
- [118] J. Park *et al.*, "One-Nanometer-Scale Size-Controlled Synthesis of Monodisperse Magnetic Iron Oxide Nanoparticles," *Angew. Chem. Int. Ed.*, vol. 44, no. 19, pp. 2872–2877, May 2005, doi: 10.1002/anie.200461665.
- [119] S. Sun and H. Zeng, "Size-Controlled Synthesis of Magnetite Nanoparticles," *J. Am. Chem. Soc.*, vol. 124, no. 28, pp. 8204–8205, Jul. 2002, doi: 10.1021/ja026501x.
- [120] C. Xu and S. Sun, "Superparamagnetic nanoparticles as targeted probes for diagnostic and therapeutic applications," *Dalton Trans.*, no. 29, p. 5583, 2009, doi: 10.1039/b900272n.
- [121] G. Salazar-Alvarez *et al.*, "Cubic versus Spherical Magnetic Nanoparticles: The Role of Surface Anisotropy," *J. Am. Chem. Soc.*, vol. 130, no. 40, pp. 13234–13239, Oct. 2008, doi: 10.1021/ja0768744.
- [122] N. R. Jana, Y. Chen, and X. Peng, "Size- and Shape-Controlled Magnetic (Cr, Mn, Fe, Co, Ni) Oxide Nanocrystals via a Simple and General Approach," *Chem. Mater.*, vol. 16, no. 20, pp. 3931–3935, Oct. 2004, doi: 10.1021/cm049221k.
- [123] W. Baaziz, B. P. Pichon, J.-M. Grenèche, and S. Begin-Colin, "Effect of reaction environment and *in situ* formation of the precursor on the composition and shape of iron oxide nanoparticles synthesized by the thermal decomposition method," *CrystEngComm*, vol. 20, no. 44, pp. 7206–7220, 2018, doi: 10.1039/C8CE00875B.

- [124] N. Bao, L. Shen, W. An, P. Padhan, C. Heath Turner, and A. Gupta, "Formation Mechanism and Shape Control of Monodisperse Magnetic  $\text{CoFe}_2\text{O}_4$  Nanocrystals," *Chem. Mater.*, vol. 21, no. 14, pp. 3458–3468, Jul. 2009, doi: 10.1021/cm901033m.
- [125] F. X. Redl *et al.*, "Magnetic, Electronic, and Structural Characterization of Nonstoichiometric Iron Oxides at the Nanoscale," *J. Am. Chem. Soc.*, vol. 126, no. 44, pp. 14583–14599, Nov. 2004, doi: 10.1021/ja046808r.
- [126] S. F. Hasany, I. Ahmed, R. J. and A. Rehman, "Systematic Review of the Preparation Techniques of Iron Oxide Magnetic Nanoparticles," *Nanosci. Nanotechnol.*, vol. 2, no. 6, pp. 148–158, Jan. 2013, doi: 10.5923/j.nn.20120206.01.
- [127] A. Kumar Mondal, S. Chen, D. Su, K. Kretschmer, H. Liu, and G. Wang, "Microwave synthesis of  $\alpha\text{-Fe}_2\text{O}_3$  nanoparticles and their lithium storage properties A comparative study.pdf," *J. Alloys Compd.*, vol. 648, pp. 732–739, 2015.
- [128] M. B. Gawande, S. N. Shelke, R. Zboril, and R. S. Varma, "Microwave-Assisted Chemistry: Synthetic Applications for Rapid Assembly of Nanomaterials and Organics," *Acc. Chem. Res.*, vol. 47, no. 4, pp. 1338–1348, Apr. 2014, doi: 10.1021/ar400309b.
- [129] M. E. F. Brollo, S. Veintemillas-Verdaguer, C. M. Salván, and M. del P. Morales, "Key Parameters on the Microwave Assisted Synthesis of Magnetic Nanoparticles for MRI Contrast Agents," *Contrast Media Mol. Imaging*, vol. 2017, pp. 1–13, 2017, doi: 10.1155/2017/8902424.
- [130] S. Perino and F. Chemat, "Chauffage micro-ondes comme éco-procédé en industrie agroalimentaire," p. 24, 2015.
- [131] H. Hu *et al.*, "Unique role of ionic liquid in microwave-assisted synthesis of monodisperse magnetite nanoparticles," *Chem. Commun.*, vol. 46, no. 22, p. 3866, 2010, doi: 10.1039/b927321b.
- [132] N. E. Leadbeater and H. M. Torenius, "A Study of the Ionic Liquid Mediated Microwave Heating of Organic Solvents," *J. Org. Chem.*, vol. 67, no. 9, pp. 3145–3148, May 2002, doi: 10.1021/jo016297g.
- [133] A. Makridis, I. Chatzitheodorou, K. Topouridou, M. P. Yavropoulou, M. Angelakeris, and C. Dendrinou-Samara, "A facile microwave synthetic route for ferrite nanoparticles with direct impact in magnetic particle hyperthermia," *Mater. Sci. Eng. C*, vol. 63, pp. 663–670, Jun. 2016, doi: 10.1016/j.msec.2016.03.033.
- [134] V. Georgiadou, V. Tangoulis, I. Arvanitidis, O. Kalogirou, and C. Dendrinou-Samara, "Unveiling the Physicochemical Features of  $\text{CoFe}_2\text{O}_4$  Nanoparticles Synthesized via a Variant Hydrothermal Method: NMR Relaxometric Properties," *J. Phys. Chem. C*, vol. 119, no. 15, pp. 8336–8348, Apr. 2015, doi: 10.1021/acs.jpcc.5b00717.
- [135] A. Rizzuti *et al.*, "Shape-control by microwave-assisted hydrothermal method for the synthesis of magnetite nanoparticles using organic additives," *J. Nanoparticle Res.*, vol. 17, no. 10, Oct. 2015, doi: 10.1007/s11051-015-3213-0.
- [136] M. Sertkol, Y. Köseoğlu, A. Baykal, H. Kavas, A. Bozkurt, and M. S. Toprak, "Microwave synthesis and characterization of Zn-doped nickel ferrite nanoparticles," *J. Alloys Compd.*, vol. 486, no. 1–2, pp. 325–329, Nov. 2009, doi: 10.1016/j.jallcom.2009.06.128.
- [137] C. Sciancalepore, R. Rosa, G. Barrera, P. Tiberto, P. Allia, and F. Bondioli, "Microwave-assisted nonaqueous sol–gel synthesis of highly crystalline magnetite nanocrystals," *Mater. Chem. Phys.*, vol. 148, no. 1–2, pp. 117–124, Nov. 2014, doi: 10.1016/j.matchemphys.2014.07.020.
- [138] L. Gonzalez-Moragas, S.-M. Yu, N. Murillo-Cremaes, A. Laromaine, and A. Roig, "Scale-up synthesis of iron oxide nanoparticles by microwave-assisted thermal decomposition," *Chem. Eng. J.*, vol. 281, pp. 87–95, Dec. 2015, doi: 10.1016/j.cej.2015.06.066.
- [139] Y.-J. Liang *et al.*, "Size-dependent electromagnetic properties and the related simulations of  $\text{Fe}_3\text{O}_4$  nanoparticles made by microwave-assisted thermal decomposition," *Colloids Surf. Physicochem. Eng. Asp.*, vol. 530, pp. 191–199, Oct. 2017, doi: 10.1016/j.colsurfa.2017.06.059.
- [140] L. Chen *et al.*, "Precise Study on Size-Dependent Properties of Magnetic Iron Oxide Nanoparticles for *In Vivo* Magnetic Resonance Imaging," *J. Nanomater.*, vol. 2018, pp. 1–9, May 2018, doi: 10.1155/2018/3743164.

- [141] Y.-J. Liang *et al.*, "High-Performance Poly(lactic-co-glycolic acid)-Magnetic Microspheres Prepared by Rotating Membrane Emulsification for Transcatheter Arterial Embolization and Magnetic Ablation in VX<sub>2</sub> Liver Tumors," *ACS Appl. Mater. Interfaces*, vol. 9, no. 50, pp. 43478–43489, Dec. 2017, doi: 10.1021/acsami.7b14330.
- [142] A. Fujiwara, M. Tada, T. Nakagawa, and M. Abe, "Permeability and electric resistivity of spin-sprayed Zn ferrite films for high-frequency device applications," *J. Magn. Magn. Mater.*, vol. 320, no. 8, pp. L67–L69, Apr. 2008, doi: 10.1016/j.jmmm.2007.11.026.
- [143] B. Pal and M. Sharon, "Preparation of iron oxide thin film by metal organic deposition from Fe<sup>3+</sup>-acetylacetonate: a study of photocatalytic properties," p. 6, 2000.
- [144] S. Brahma and S. A. Shivashankar, "Zinc acetylacetonate hydrate adducted with nitrogen donor ligands: Synthesis, spectroscopic characterization, and thermal analysis," *J. Mol. Struct.*, vol. 1101, pp. 41–49, Dec. 2015, doi: 10.1016/j.molstruc.2015.07.075.
- [145] U. Holzwarth and N. Gibson, "The Scherrer equation versus the 'Debye-Scherrer equation,'" *Nat. Nanotechnol.*, vol. 6, no. 9, pp. 534–534, Sep. 2011, doi: 10.1038/nnano.2011.145.
- [146] J. L. Hernández-Pinero *et al.*, "Effect of heating rate and plant species on the size and uniformity of silver nanoparticles synthesized using aromatic plant extracts," *Appl. Nanosci.*, vol. 6, no. 8, pp. 1183–1190, Nov. 2016, doi: 10.1007/s13204-016-0532-0.
- [147] Z. L. Wang, "Transmission Electron Microscopy of Shape-Controlled Nanocrystals and Their Assemblies," *J. Phys. Chem. B*, vol. 104, no. 6, pp. 1153–1175, Feb. 2000, doi: 10.1021/jp993593c.
- [148] Y. Hou, Z. Xu, and S. Sun, "Controlled Synthesis and Chemical Conversions of FeO Nanoparticles," *Angew. Chem. Int. Ed.*, vol. 46, no. 33, pp. 6329–6332, Aug. 2007, doi: 10.1002/anie.200701694.
- [149] S. Mourdikoudis and L. M. Liz-Marzán, "Oleylamine in Nanoparticle Synthesis," *Chem. Mater.*, vol. 25, no. 9, pp. 1465–1476, May 2013, doi: 10.1021/cm4000476.
- [150] E. R. Smith, "Table of Dielectric Constants of Pure Liquids," p. 52.
- [151] V. V. Vodnik, D. K. Božanić, N. Bibić, Z. V. Šaponjić, and J. M. Nedeljković, "Optical Properties of Shaped Silver Nanoparticles," *J. Nanosci. Nanotechnol.*, vol. 8, no. 7, pp. 3511–3515, Jul. 2008, doi: 10.1166/jnn.2008.144.
- [152] M. V. Dover and W. A. Hensley, "Properties of 1-Octadecene, n-Octadecane, and Di-m-tolylethane," *Ind. Eng. Chem.*, vol. 27, no. 3, pp. 337–339, Mar. 1935, doi: 10.1021/ie50303a023.
- [153] A. L. Washington II and G. F. Strouse, "Microwave Synthesis of CdSe and CdTe Nanocrystals in Nonabsorbing Alkanes," *J. Am. Chem. Soc.*, vol. 130, no. 28, pp. 8916–8922, Jul. 2008, doi: 10.1021/ja711115r.
- [154] M. Baghbanzadeh, L. Carbone, P. D. Cozzoli, and C. O. Kappe, "Microwave-Assisted Synthesis of Colloidal Inorganic Nanocrystals," *Angew. Chem. Int. Ed.*, vol. 50, no. 48, pp. 11312–11359, Nov. 2011, doi: 10.1002/anie.201101274.
- [155] V. Chikan and E. McLaurin, "Rapid Nanoparticle Synthesis by Magnetic and Microwave Heating," *Nanomaterials*, vol. 6, no. 5, p. 85, May 2016, doi: 10.3390/nano6050085.
- [156] F. Chemat and G. Cravotto, Eds., *Microwave-assisted Extraction for Bioactive Compounds*. Boston, MA: Springer US, 2013.
- [157] Y.-J. Zhu and F. Chen, "Microwave-Assisted Preparation of Inorganic Nanostructures in Liquid Phase," *Chem. Rev.*, vol. 114, no. 12, pp. 6462–6555, Jun. 2014, doi: 10.1021/cr400366s.
- [158] O. Gerber *et al.*, "Low Oxidation State and Enhanced Magnetic Properties Induced by Raspberry Shaped Nanostructures of Iron Oxide," *J. Phys. Chem. C*, vol. 119, no. 43, pp. 24665–24673, Oct. 2015, doi: 10.1021/acs.jpcc.5b08164.
- [159] L. León-Félix *et al.*, "Synthesis and characterization of uncoated and gold-coated magnetite nanoparticles," *Hyperfine Interact.*, vol. 224, no. 1–3, pp. 179–188, Jan. 2014, doi: 10.1007/s10751-013-0857-y.
- [160] F. H. Aragón *et al.*, "Evolution of the doping regimes in the Al-doped SnO<sub>2</sub> nanoparticles prepared by a polymer precursor method," *J. Phys. Condens. Matter*, vol. 27, no. 9, p. 095301, Mar. 2015, doi: 10.1088/0953-8984/27/9/095301.

- [161] E. Lima, A. L. Brandl, A. D. Arelaro, and G. F. Goya, "Spin disorder and magnetic anisotropy in Fe<sub>3</sub>O<sub>4</sub> nanoparticles," *J. Appl. Phys.*, vol. 99, no. 8, p. 083908, Apr. 2006, doi: 10.1063/1.2191471.
- [162] E. Solano *et al.*, "Facile and efficient one-pot solvothermal and microwave-assisted synthesis of stable colloidal solutions of MFe<sub>2</sub>O<sub>4</sub> spinel magnetic nanoparticles," *J. Nanoparticle Res.*, vol. 14, no. 8, Aug. 2012, doi: 10.1007/s11051-012-1034-y.
- [163] E. Solano, R. Yáñez, S. Ricart, and J. Ros, "New approach towards the polyol route to fabricate MFe<sub>2</sub>O<sub>4</sub> magnetic nanoparticles: The use of MCl<sub>2</sub> and Fe(acac)<sub>3</sub> as chemical precursors," *J. Magn. Magn. Mater.*, vol. 382, pp. 380–385, May 2015, doi: 10.1016/j.jmmm.2015.02.002.
- [164] R. M. Freire *et al.*, "Effect of solvent composition on the structural and magnetic properties of MnZn ferrite nanoparticles obtained by hydrothermal synthesis," *Microfluid. Nanofluidics*, vol. 17, no. 1, pp. 233–244, Jul. 2014, doi: 10.1007/s10404-013-1290-x.
- [165] S. Xuan, F. Wang, Y.-X. J. Wang, J. C. Yu, and K. C.-F. Leung, "Facile synthesis of size-controllable monodispersed ferrite nanospheres," *J. Mater. Chem.*, vol. 20, no. 24, p. 5086, 2010, doi: 10.1039/c0jm00159g.
- [166] S.-W. Cao, Y.-J. Zhu, and J. Chang, "Fe<sub>3</sub>O<sub>4</sub> polyhedral nanoparticles with a high magnetization synthesized in mixed solvent ethylene glycol–water system," *New J. Chem.*, vol. 32, no. 9, p. 1526, 2008, doi: 10.1039/b719436f.
- [167] A. Yan, X. Liu, R. Yi, R. Shi, N. Zhang, and G. Qiu, "Selective Synthesis and Properties of Monodisperse Zn Ferrite Hollow Nanospheres and Nanosheets," *J. Phys. Chem. C*, vol. 112, no. 23, pp. 8558–8563, Jun. 2008, doi: 10.1021/jp800997z.
- [168] J. Kurian and M. J. Mathew, "Structural, optical and magnetic studies of CuFe<sub>2</sub>O<sub>4</sub>, MgFe<sub>2</sub>O<sub>4</sub> and ZnFe<sub>2</sub>O<sub>4</sub> nanoparticles prepared by hydrothermal/solvothermal method," *J. Magn. Magn. Mater.*, vol. 451, pp. 121–130, Apr. 2018, doi: 10.1016/j.jmmm.2017.10.124.
- [169] J. Wang, F. Ren, R. Yi, A. Yan, G. Qiu, and X. Liu, "Solvothermal synthesis and magnetic properties of size-controlled nickel ferrite nanoparticles," *J. Alloys Compd.*, vol. 479, no. 1–2, pp. 791–796, Jun. 2009, doi: 10.1016/j.jallcom.2009.01.059.
- [170] J.-P. Jolivet, *De la solution à l'oxyde*. EDP Sciences, 2015.
- [171] K. Arnold, A. Herrmann, L. Pratsch, and K. Gawrisch, "The dielectric properties of aqueous solutions of poly(ethylene glycol) and their influence on membrane structure," *Biochim. Biophys. Acta BBA - Biomembr.*, vol. 815, no. 3, pp. 515–518, May 1985, doi: 10.1016/0005-2736(85)90381-5.
- [172] M. P. Morales *et al.*, "Surface and Internal Spin Canting in  $\gamma$ -Fe<sub>2</sub>O<sub>3</sub> Nanoparticles," *Chem. Mater.*, vol. 11, no. 11, pp. 3058–3064, Nov. 1999, doi: 10.1021/cm991018f.
- [173] T. Ozkaya, M. S. Toprak, A. Baykal, H. Kavas, Y. Köseoğlu, and B. Aktaş, "Synthesis of Fe<sub>3</sub>O<sub>4</sub> nanoparticles at 100°C and its magnetic characterization," *J. Alloys Compd.*, vol. 472, no. 1–2, pp. 18–23, Mar. 2009, doi: 10.1016/j.jallcom.2008.04.101.
- [174] M. Mozaffari *et al.*, "Synthesis of Zn<sup>2+</sup> substituted maghemite nanoparticles and investigation of their structural and magnetic properties," *J. Magn. Magn. Mater.*, vol. 382, pp. 366–375, May 2015, doi: 10.1016/j.jmmm.2015.01.087.
- [175] C. Lefevre, "Relation structure-propriétés de différents oxydes pour l'électronique de spin.," HDR, 2014.
- [176] M. A. Batista, "CRISTALLOCHEMICAL CHARACTERIZATION OF SYNTHETIC Zn-SUBSTITUTED," p. 8, 2008.
- [177] C. M. Srivastava, S. N. Shringi, R. G. Srivastava, and N. G. Nanadikar, "Magnetic ordering and domain-wall relaxation in zinc-ferrous ferrites," *Phys. Rev. B*, vol. 14, no. 5, pp. 2032–2040, 1976, doi: 10.1103/PhysRevB.14.2032.
- [178] K. Shinoda, K. Sugiyama, C. Reynales, Y. Waseda, and T. Jacob, "An Improved X-ray Structural Analysis for Determining Cation Distribution in ZnFe<sub>2</sub>O<sub>4</sub> and ZnFe<sub>2</sub>O<sub>4</sub> - Fe<sub>3</sub>O<sub>4</sub> Solid Solutions," *Shigen--Sozai*, pp. 801–806, 1995.
- [179] D. Kotsikau, V. Pankov, E. Petrova, V. Natarov, D. Filimonov, and K. Pokholok, "Structural, magnetic and hyperfine characterization of Zn<sub>x</sub>Fe<sub>3-x</sub>O<sub>4</sub> nanoparticles prepared by sol-gel

- approach via inorganic precursors," *J. Phys. Chem. Solids*, vol. 114, pp. 64–70, Mar. 2018, doi: 10.1016/j.jpcs.2017.11.004.
- [180] P. Saha, R. Rakshit, M. Alam, and K. Mandal, "Magnetic and Electronic Properties of Zn -Doped Fe<sub>3</sub>O<sub>4</sub> Hollow Nanospheres," *Phys. Rev. Appl.*, vol. 11, no. 2, p. 024059, Feb. 2019, doi: 10.1103/PhysRevApplied.11.024059.
- [181] F. Nakagomi *et al.*, "Cation distribution of Zn Co<sub>1</sub>-Fe<sub>2</sub>O<sub>4</sub> nanoparticles: A resonant X-ray diffraction study," *J. Alloys Compd.*, vol. 842, p. 155751, Nov. 2020, doi: 10.1016/j.jallcom.2020.155751.
- [182] D. Carta *et al.*, "A Structural and Magnetic Investigation of the Inversion Degree in Ferrite Nanocrystals MFe<sub>2</sub>O<sub>4</sub> (M = Mn, Co, Ni)," *J. Phys. Chem. C*, vol. 113, no. 20, pp. 8606–8615, May 2009, doi: 10.1021/jp901077c.
- [183] E. Petrova, D. Kotsikau, and V. Pankov, "Structural characterization and magnetic properties of sol-gel derived Zn<sub>x</sub>Fe<sub>3-x</sub>O<sub>4</sub> nanoparticles," *J. Magn. Magn. Mater.*, vol. 378, pp. 429–435, Mar. 2015, doi: 10.1016/j.jmmm.2014.11.076.
- [184] C. Colliex, T. Manoubi, and C. Ortiz, "Electron-energy-loss-spectroscopy near-edge fine structures in the iron-oxygen system," *Phys. Rev. B*, vol. 44, no. 20, pp. 11402–11411, Nov. 1991, doi: 10.1103/PhysRevB.44.11402.
- [185] Y. Yoshida and G. Langouche, Eds., *Mössbauer Spectroscopy*. Berlin, Heidelberg: Springer Berlin Heidelberg, 2013.
- [186] Y. E. Mendili, "Etude des propriétés structurales et magnétiques de nanoparticules de maghémite dispersées dans une matrice de silice," Thesis, Université du Maine, 2011.
- [187] J. Fock *et al.*, "On the 'centre of gravity' method for measuring the composition of magnetite/maghemite mixtures, or the stoichiometry of magnetite-maghemite solid solutions, via <sup>57</sup>Fe Mössbauer spectroscopy," *J. Phys. Appl. Phys.*, vol. 50, no. 26, p. 265005, Jul. 2017, doi: 10.1088/1361-6463/aa73fa.
- [188] F. Sayed *et al.*, "Surface Effects in Ultrathin Iron Oxide Hollow Nanoparticles: Exploring Magnetic Disorder at the Nanoscale," *J. Phys. Chem. C*, vol. 122, no. 13, pp. 7516–7524, Apr. 2018, doi: 10.1021/acs.jpcc.8b00300.
- [189] Y. Peng, J. Nie, W. Zhang, C. Bao, J. Ma, and Y. Cao, "Preparation of soft magnetic composites for Fe particles coated with (NiZn)Fe<sub>2</sub>O<sub>4</sub> via microwave treatment," *J. Magn. Magn. Mater.*, vol. 395, pp. 245–250, Dec. 2015, doi: 10.1016/j.jmmm.2015.07.071.
- [190] K. Kondo *et al.*, "Conducted noise suppression up to GHz range by spin-sprayed Ni<sub>0.2</sub>Zn<sub>x</sub>Fe<sub>2.8-x</sub>O<sub>4</sub> (x = 0, 0.6) films having different natural resonance frequencies," *J. Magn. Magn. Mater.*, vol. 301, no. 1, pp. 107–111, Jun. 2006, doi: 10.1016/j.jmmm.2005.06.021.
- [191] A. M. M. Farea, S. Kumar, K. M. Batoor, A. Yousef, C. G. Lee, and Alimuddin, "Influence of the doping of Ti<sup>4+</sup> ions on electrical and magnetic properties of Mn<sub>1+x</sub>Fe<sub>2-2x</sub>Ti<sub>x</sub>O<sub>4</sub> ferrite," *J. Alloys Compd.*, vol. 469, no. 1–2, pp. 451–457, Feb. 2009, doi: 10.1016/j.jallcom.2008.01.139.
- [192] L. Nalbandian, A. Delimitis, V. T. Zaspalis, E. A. Deliyanni, D. N. Bakoyannakis, and E. N. Peleka, "Hydrothermally prepared nanocrystalline Mn–Zn ferrites: Synthesis and characterization," *Microporous Mesoporous Mater.*, vol. 114, no. 1–3, pp. 465–473, Sep. 2008, doi: 10.1016/j.micromeso.2008.01.034.
- [193] K. Jalaiah and K. Vijaya Babu, "Structural, magnetic and electrical properties of nickel doped Mn–Zn spinel ferrite synthesized by sol-gel method," *J. Magn. Magn. Mater.*, vol. 423, pp. 275–280, Feb. 2017, doi: 10.1016/j.jmmm.2016.09.114.
- [194] H. Kavas, A. Baykal, M. S. Toprak, Y. Köseoğlu, M. Sertkol, and B. Aktaş, "Cation distribution and magnetic properties of Zn doped NiFe<sub>2</sub>O<sub>4</sub> nanoparticles synthesized by PEG-assisted hydrothermal route," *J. Alloys Compd.*, vol. 479, no. 1–2, pp. 49–55, Jun. 2009, doi: 10.1016/j.jallcom.2009.01.014.
- [195] K. Kondo *et al.*, "Conducted noise suppression effect up to 3 GHz by NiZn ferrite film plated at 90 °C directly onto printed circuit board," *J. Appl. Phys.*, vol. 93, no. 10, pp. 7130–7132, May 2003, doi: 10.1063/1.1555362.



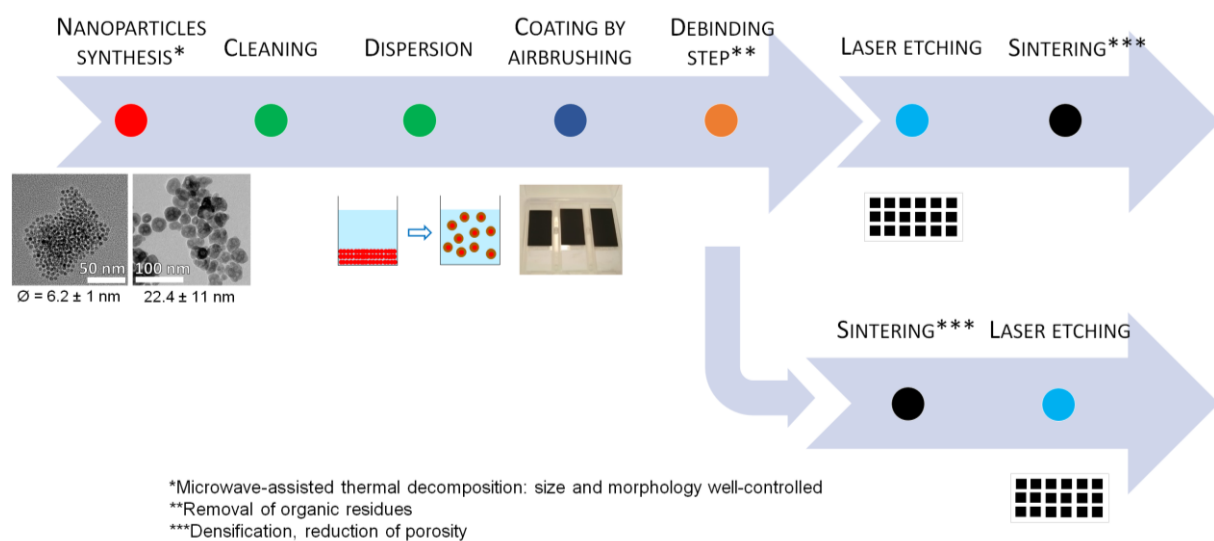
- [196] R. R. Kahmei, R. Sai, S. Arackal, S. A. Shivashankar, and N. Bhat, "Nanostructured Zn-Substituted Nickel Ferrite Thin Films: CMOS-Compatible Deposition and Excellent Soft Magnetic Properties," *IEEE Magn. Lett.*, vol. 10, pp. 1–5, 2019, doi: 10.1109/LMAG.2019.2941427.
- [197] R. Sai, S. D. Kulkarni, S. S. M. Bhat, N. G. Sundaram, N. Bhat, and S. A. Shivashankar, "Controlled inversion and surface disorder in zinc ferrite nanocrystallites and their effects on magnetic properties," *RSC Adv.*, vol. 5, no. 14, pp. 10267–10274, 2015.
- [198] V. G. Harris and V. Šepelák, "Mechanochemically processed zinc ferrite nanoparticles: Evolution of structure and impact of induced cation inversion," *J. Magn. Magn. Mater.*, vol. 465, pp. 603–610, Nov. 2018, doi: 10.1016/j.jmmm.2018.05.100.



# Chapter II. Development of magnetic coatings by airbrushing

## I. Introduction

Once the material is synthesized, the development of dense layers could be studied. A quick way to elaborate these coatings from the nanoparticles is the airbrushing process. It deals with the atomization of a stable dispersion of nanoparticles in a liquid media on a desired substrate (Figure II-1). In this way, the particles follow cleaning and dispersion steps after synthesis. After coating, annealing steps are required in order to remove the organic residues contained in the layer and also to ensure a sufficient mechanical resistance of the coating. The thermal treatment is split in two stages: a debinding step to decompose the organic residues, and a sintering one to densify the layer after the organics removal. A good adherence of the film on the substrate is needed to pattern it by laser etching. Hence, two options will be studied: the laser etching directly after the debinding and just after sintering.



**Figure II-1. Elaboration of coatings through airbrushing and thermal treatments.**

Through these different steps, the goal is to increase the density of coatings. A first target is to attain 70% of the bulk density after the sintering step. A decrease of the intra-layer porosity will enhance the magnetic properties of coatings, and conversely, too much porosity between grains will considerably reduce the magnetization of coatings. Thus, the thermal treatment has to be adjusted to increase the coating density with the aim of enhancing particle couplings, as well as the magnetic properties of coatings. The magnetic behavior of the coatings will be characterized in Chapter IV.

This chapter focuses on the cleaning of particles previously synthesized (Chapter I), the formulation of a stable dispersion, the development of continuous and patterned coatings by

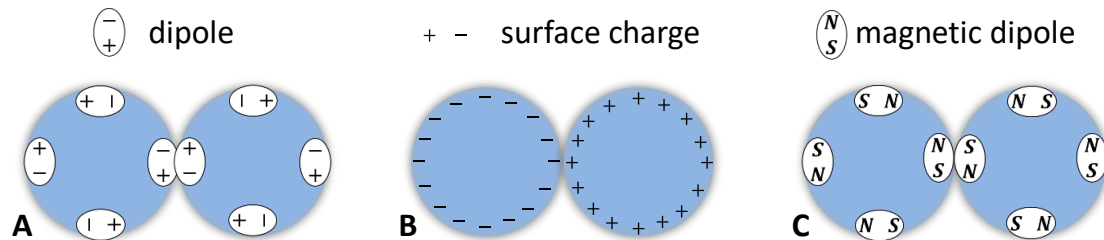
airbrushing, and finally the optimization of the thermal treatment. In this chapter, the coatings are elaborated with SP(F)M and FM particles.

## II. Formulation of a dispersion

From the nanoparticles previously synthesized to thick coatings, there is just one step: the formulation of a stable dispersion. The purpose is to sustain the nanoparticles in suspension in a suitable liquid by avoiding aggregation and sedimentation. Indeed, some particle-particle interactions exist and favor the nanoparticles agglomeration. An important part of the project is to work on different methods to counter these interactions and thus elaborate a proper stable dispersion of nanoparticles. Four major particle interactions are encountered: electrostatic, Van der Waals, steric and magnetic interactions.

### II.1. Particle interactions

When experiencing the dispersion of nanoparticles, different types of particle interactions have to be taken into account since they could cause particle attraction and induce aggregation and/or sedimentation of the particles. They are schematized in Figure II-2 and include attractive forces and especially Van der Waals forces, repulsive forces namely the electrostatic forces, and also magnetic attraction dedicated to the specific case of particles displaying a magnetization  $M$ .



**Figure II-2. Sketches of particle attraction interactions: Van der Waals forces (A), electrostatic forces (B) and magnetic forces (C) [1].**

The listed interactions are depicted in the following parts.

#### II.1.1. Van der Waals interactions

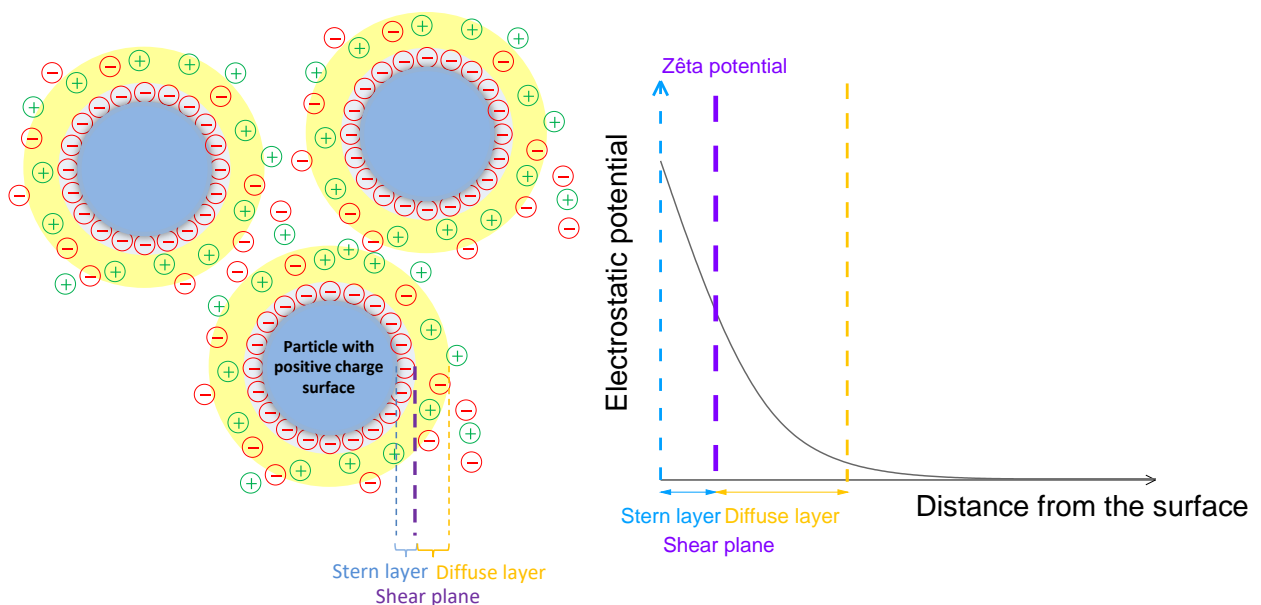
The Van der Waals interactions result in attractive forces between two particles which behave like electrostatic dipoles positively and negatively charged. These interactions derive from variations of dipolar interactions at the molecular scale with a potential energy of interaction which decreases according to a law  $r^{-6}$  with  $r$  the distance between two dipoles. These interactions are significant in front of  $kT$  (in order to hundred times) [2]. The Van der Waals interaction is one of the main causes of particle aggregation and sedimentation in a solution. It can be tuned by adding specific ligands at the particle surroundings creating electrostatic or steric stabilization, as appropriate (part II.1.5).

### II.1.2. Electrostatic interactions

Electrostatic interactions are of repulsive nature between two particles with the same sign of potential. These interactions could naturally counter particle aggregation, it is hence a useful tool to stabilize the particles in solution by means of counterions located at the particle surface (concentration, ion size) or even just within the solvent (dielectric constant) [2]. Moreover, the particle functionalization with ionic species (addition of an acid or a base) could be a solution in the case of particles not naturally charged to counter the Van der Waals interactions and prevent aggregation [3].

The particles could be modeled as in Figure II-3. The particles are surrounded by different layers of charges, forming a charges cloud around the particle and protecting them from aggregation. The electrical double-layer model defined by Stern (Figure II-3) describes the way the particles repel each other. The charges cloud is divided into three zones: the Stern layer which corresponds to the layer of adsorbed counterions on the particle surface, the diffuse layer constituted of free ions not directly bound on the surface, and the shear or slipping plane which is the boundary between the Stern and diffuse layer. The hydrodynamic size of particles is measured at the slipping plane and its surface potential corresponds to the zeta potential.

Indeed, the surface charges at the particle surface are considered as a capacitor. The electrostatic potential finally decreases as a function of the distance from the surface. The decrease is linear in the Stern layer and exponential in the diffuse zone.



**Figure II-3. Scheme of the electrical double layer (particles with positive charge surfaces) and relation between electrostatic potential and distance from the surface proposed by Stern [4].**

The depth of the electrostatic interactions is given by the thickness of the diffuse layer  $\kappa^{-1}$  (the Debye length) neglecting the thickness of the Stern layer  $\delta$  ( $\delta \ll \kappa^{-1}$ ) (Equation II-1).

$$\kappa^{-1} = \sqrt{\frac{\varepsilon_0 \varepsilon_r k_B T}{2 N_A C_0 e^2 z^2}} \quad \text{II-1}$$

with  $\varepsilon_0$  the vacuum permittivity (F/m),  $\varepsilon_r$  the dielectric constant of the solvent,  $k_B$  the Boltzmann constant (J/K),  $T$  the temperature (K),  $N_A$  the Avogadro's number,  $C_0$  the electrolyte concentration (mol/m<sup>3</sup>),  $e$  the elementary charge (C), and  $z$  the valency of the electrolyte.

Thus, the quality of the dispersion can be controlled by the choice of the electrolyte species, the dielectric constant of the solvent and the ionic strength.

#### II.1.2.A. Zeta potential measurement

The charge surface of a particle assembly in a solution can be estimated through its zeta potential measurement which is an indicator of the stability of the dispersion. It allows to quantify the electrostatic interactions between particles and thus to determine if the repulsion forces are strong enough to maintain the particles away from each other. The electrophoretic mobility  $\mu$  of particles, which is in fact the velocity of particles normalized by the applied electric field, can be correlated to the zeta potential through the Henry equation (Equation II-2) [5]. The zeta potential is obtained by light scattering measurement from the values of electrophoretic mobility  $\mu$ .

$$\mu = \frac{\zeta \varepsilon_0 \varepsilon_r}{\eta} f(\kappa^{-1} a) \quad \text{II-2}$$

where  $\zeta$  is the zeta potential (mV),  $\eta$  the solvent viscosity (Pa.s), and  $f(\kappa^{-1} a)$  a function of the Debye length  $\kappa^{-1}$  (nm) and of the particle radius  $a$  (nm).

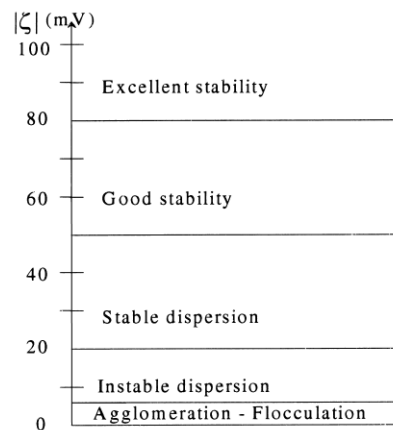
When the particle size is small compared to the thickness of the double layer ( $a \ll \kappa^{-1}$ ), the Hückel approach is applied to determine the value of  $f(\kappa^{-1} a)$  and conversely the Smoluchowski approach becomes effective in the case of larger particles ( $a \gg \kappa^{-1}$ ) [5] (Figure II-4).

	$f(\kappa a)$	$\mu$
Hückel ( $a \ll \kappa^{-1}$ )	$2/3$	$\frac{\zeta \varepsilon_0 \varepsilon_r}{1.5 \eta}$
Smoluchowski ( $a \gg \kappa^{-1}$ )	$1$	$\frac{\zeta \varepsilon_0 \varepsilon_r}{\eta}$

**Figure II-4. Influence of Hückel and Smoluchowski approach in the electrophoretic mobility  $\mu$  of particles.**

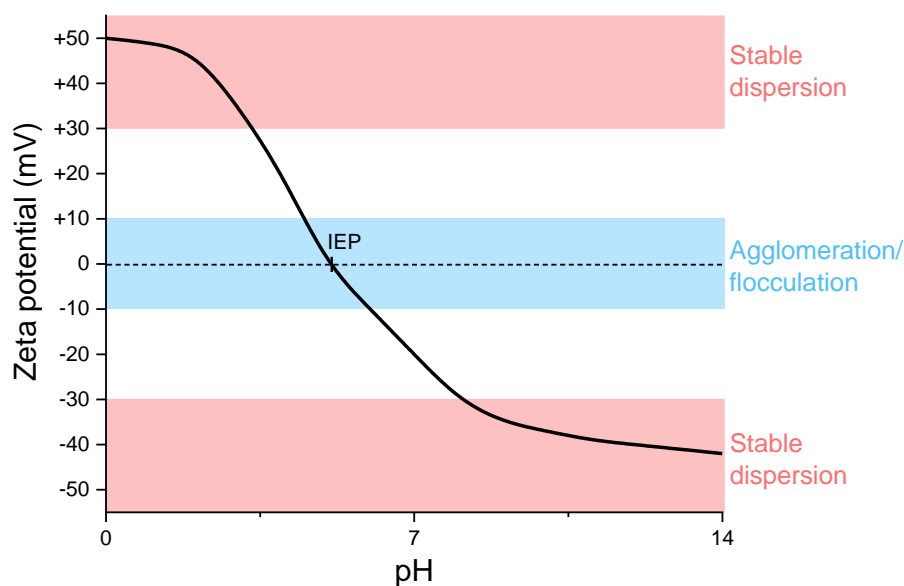
For similar values of zeta potential, the particles behave differently according to the dielectric constant and viscosity of the solvent. A solvent with a low dielectric constant and/or a moderate viscosity favors a slowdown of the particles displacements inside the solution, such as ethanol and toluene. In contrast, rapid mobility of particles is encouraged by solvents with higher dielectric constant and/or lower viscosities like water [5].

A dispersion is considered stable for absolute values of zeta potential  $|\zeta|$  above 30 mV and the highest values give the best dispersions (Figure II-5). This basic principle has been verified in a lot of studies: the dispersion of carbon black in aqueous and organic media [6], the dispersion of different oxides ( $ZrO_2$ ,  $TiO_2$ ...) in water with the elaboration of oxides-based slurries [7],  $SiO_2$  nanospheres in water [8], carbon nanotubes in water [9], silica in water [10] and even with magnetite [11] [12] [13]...



**Figure II-5. Indication of the dispersion stability as a function of the zeta potential. From Vallar et al. [7].**

Furthermore, the zeta potential strictly depends on the pH of the solution (Figure II-6). An important value has to be taken into account when studying dispersion: the Isoelectric Point (IEP). The IEP is the pH near which the zeta potential is equal to 0 meaning the complete flocculation of particles. It should not be confused with the Point of Zero Charge (PZC) which corresponds to a zero surface charge of particles and slightly differs from the IEP due to the fact that the zeta potential is measured at the shear plane between the Stern layer and the diffuse one. In this manuscript, IEP will only be considered.



**Figure II-6. Zeta potential behavior as a function of pH.**

According to Figure II-6, a good dispersion is obtained for pH far from the range of IEP values. The dispersion remains unstable for absolute zeta potential values around 10 mV. A preliminary test to ensure a stable colloidal solution is to proceed to a shift of the pH value to 2 or 3 points from the IEP. Moreover, the IEP gives the information on the acidic or basic character of the particle surface: acid for IEP below 7 and basic above 7. It helps for the selection of adapted ionic species and solvents, suitable for a stable dispersion. The IEP of magnetite is comprised between 6 and 6.8 [14] [15] [16], and between 6 and 8 for  $\text{ZnFe}_2\text{O}_4$  [17] [18] [19]. Hence, both acidic and basic media could be tested with  $\text{Zn}_{0.4}\text{Fe}_{2.6}\text{O}_4$  nanoparticles.

### II.1.2.B. DLVO theory

The Derjaguin Landau Verwey Overbeek (DLVO) theory is used to describe the stability of charged particles in a polar solvent. It deals with two additional forces which intervene between particles in solution: the attractive Van der Waals and repulsive electrostatic interactions.

The total potential energy ( $V_T$ ) is the sum of the contributions of the attractive ( $V_A$ ) and repulsive energies ( $V_R$ ). Figure II-7 shows the total potential energy of interaction as a function of the distance  $d$  between two particles.

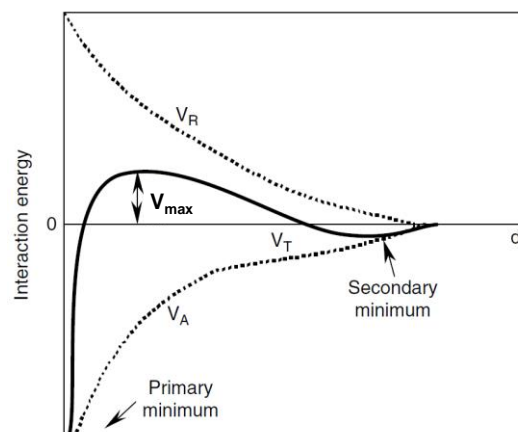


Figure II-7. Total potential energy as a function of the distance following the DLVO theory. From Dickerson *et al.* [5].

Three different areas are distinguished:

- A primary minimum with particles in the agglomerated state. At this stage, the attractive forces prevail.
- An energy barrier to overcome particle aggregation ( $V_{max}$ ). The dispersion is stable.
- In the case of highly charged surfaces with an important concentration of electrolyte, a secondary minimum is present. The flocculation is avoided due to the formation of a gel between particles [5] [20]. In this situation, the aggregates could easily be redispersed by stirring.



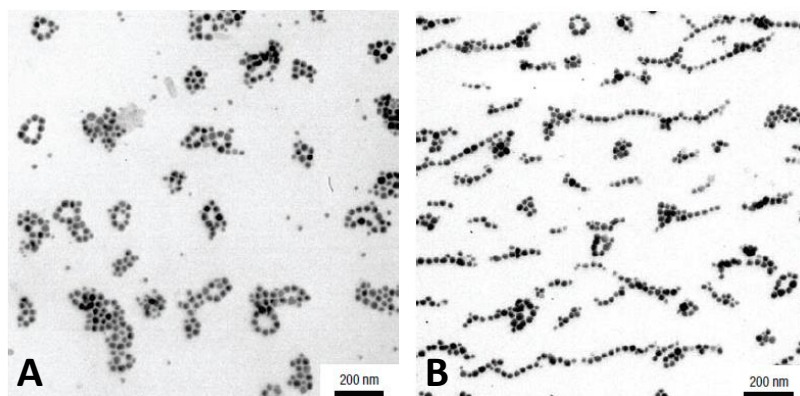
When the energy barrier decreases ( $V_{max}$ ), the aggregation is promoted and the system becomes unstable. In some cases due to the energy barrier drop, stationary states are created due to an energy balance between aggregation and dispersion. Aggregates are formed and stabilized in a state which never completely flocculates. It is called a kinetically limited aggregation [20].

The formulation of a stable dispersion lies in the compensation, and not suppression, of charges at the particle surface by addition of a suitable electrolyte localized at the particle surrounding. As a consequence, the particles keep their spheres of solvation and are maintained separate at least by the thickness of their Stern layers. The direct contact has to be avoided to prevent the Van der Waals interactions and the possible reactions of condensation between oxygens groups at the particle surface [20].

The size of the electrolyte introduced in the dispersion strictly influences the particle surface charge and thus the stabilization of the dispersion. The smaller the molecule, the better it affects the particle charge surface and acts as a charged screen surrounding the particle [21].

### II.1.3. Magnetic interactions

Magnetic interactions occur between magnetic particles. This attraction is made possible due to the orientation of their magnetic dipoles following the magnetic dipole-dipole interaction. In the presence of an external magnetic field, the dipoles turn in the direction of the field generating a short and long-range order [3]. Indeed, Figure II-8 exhibits Co nanoparticles dispersed in toluene which arrange in rings without application of a magnetic field (short-range order Figure II-8-A) and in strings under an external field (long-range order Figure II-8-B).

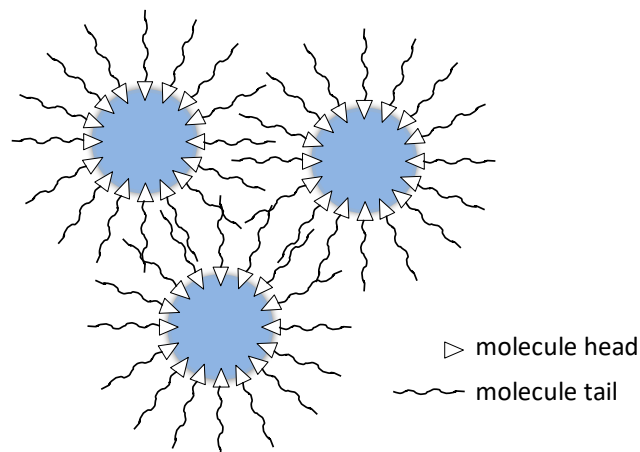


**Figure II-8. Short and long range arrangements of Co nanoparticles without (A) and with (B) external field. From Tripp *et al.* [22].**

In the case of iron oxide particles stabilized with oleic acid in hexane, the magnetic forces dominate over the Van der Waals ones and the phenomenon is amplified with the particle diameter [23]. These interactions will have a major impact on the stabilization of the dispersion. The formulation of dispersion will differ depending on the range of sizes of particles, namely SP(F)M with a  $6.2 \pm 1$  nm diameter and FM ( $22.4 \pm 11$  nm). As the direction of magnetization in the SP(F)M particles fluctuates over time, no strong magnetic interactions are expected to take place.

### II.1.4. Steric interactions

Another category of interactions, not listed above, could also occur. Steric interactions or repulsion by steric hindrance depict the specific interactions between particles embedded or surrounded by uncharged molecules anchored at their surface. A corona of molecules is formed at the particle surface and creates a protective shell which prevents particles from aggregating. Only the shells touch each other and intertwine which stabilizes the system (Figure II-9). Thus, the effects of Van der Waals or electrostatic interactions are completely cancelled. The suitable molecules used are polymers and surfactants with specific heads and tails which respectively exhibit a good affinity with the particle surface and solvent to ensure an ideal grafting.



**Figure II-9. Steric hindrance principle.**

The depth of the steric interactions is intimately linked to the thickness of the shell and can be measured through the radius of gyration of the polymer  $R_g$  (m) with the following formula:

$$R_g = l \sqrt{\frac{N}{6}} \quad \text{II-3}$$

where  $l$  is the length of a monomer (m) and  $N$  the number of monomers. The previous equation (Equation II-3) is relevant assuming the polymer chains spread in the form of a coil with  $R_g$  as the radius of gyration.

The dispersion of particles is strongly affected by their interactions: Van der Waals, electrostatic, steric and magnetic ones. A sol could be stabilized in different manners depending on these interactions. The different methods to counter the nanoparticle aggregation are described in the next section (part II.1.5).

### II.1.5. Mechanisms of stabilization

#### II.1.5.A. General concepts

Two major approaches are employed for nanoparticle dispersion: non-ionic and ionic stabilizations. Each method induces special interactions between particles, previously

mentioned, or counters the existing forces between particles. Indeed, the non-ionic stabilization allows a good dispersion through the steric effect (II.1.4) or depletion, whereas the ionic one introduces electrostatic (II.1.2) or electrosteric interactions between particles (Figure II-10).

Non-ionic stabilization	Ionic stabilization
Steric hindrance	Electrostatic effect
Depletion	Electrosteric effect

Figure II-10. Summary of the effect engendered by the stabilization methods.

The steric hindrance results from the grafting of polymers at the nanoparticle surface, which maintain the particles spaced apart. In the case of a stable dispersion, the polymer acts as a surfactant composed of a tail compatible with the dispersion media and a head, adsorbed on the particle surface. This effect is achievable in aqueous and organic media.

The depletion looks like the steric hindrance, the only difference being that the polymer is not adsorbed on the particle surface. The polymer chains are unattached and completely free in the solution [5]. A stable dispersion is allowed thanks to the hindrance of the chains which are located around the particles and prevent contacts between them.

The electrostatic effect is most of the time performed in aqueous media. The charge at the particle surface is modified by the introduction of ionic species which inserts electrostatic repulsive forces between the particles. The creation of an electrical double-layer (section II.1.2) around particles enables the elaboration of a stable dispersion.

The use of charged polymers like polyelectrolytes combines both electrostatic and steric effects. Indeed, polyelectrolytes are polymers with ionized species. The charged polymer releases counterions in solution. This association gives what we call the electrosteric effect. Examples of polyelectrolytes are polyacrylic acid (PAA) and polystyrene sulfonate [24].

Figure II-11 summarizes the advantages and issues of the commonly encountered effects: electrostatic and steric stabilizations.

Electrostatic stabilization	Steric stabilization
Aqueous medium	Aqueous and non-aqueous media
Irreversible flocculation	Reversible flocculation
Destabilization by pH change	Stabilization not subjected to pH change
DLVO theory	No theory

Figure II-11. Advantages and drawbacks of electrostatic and steric stabilization. From Hunter *et al.* [25].

The chemical compounds used to obtain stable dispersions are commonly called surfactants, causing steric or electrosteric effect depending on the nature of the molecule. A surfactant is a specific amphiphilic molecule constituted of a polar head with a hydrophilic behavior and a hydrophobic tail (Figure II-12). The tail is often an alkyl chain with 8 to 18 C atoms.

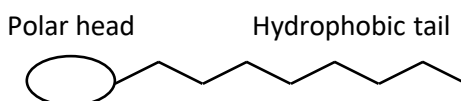


Figure II-12. Scheme of a surfactant molecule.

There are four groups of surfactants according to the nature of the hydrophilic head [26]:

- Anionic surfactants with a polar head negatively charged
- Cationic surfactants with a polar head positively charged
- Amphoteric surfactants with at least one positive and negative charge on the polar head
- Non-ionic surfactants with no charge

A surfactant possesses multiple properties and can be used as a detergent, as well as a wetting, dispersing, and solubilizing agent. It confers a change of the surface tension between two interfaces and it is also used to stabilize a system with two immiscible phases, creating an emulsion.

In water, when introduced in small concentration, the surfactant molecules are adsorbed at the air/liquid interface to avoid contact between their hydrophobic tails with water and keep their hydrophilic heads in water, resulting in a decrease of the surface tension at the liquid surface (Figure II-13. area 1 to 2). This decrease allows the dispersion of a phase in another one. This phenomenon favors the production of foam at the interface.

Above a certain concentration of surfactant called the Critical Micellar Concentration (CMC), the surfactant arranges in micelles with a polar shell constituted of the hydrophilic heads directly in contact with water and the tails grouped at the core of the framework (Figure II-13. area 3). Above the CMC, the surface tension is constant, meaning the surfactant does not influence the surface tension anymore. This is the ideal concentration required to meet a complete efficiency of the surfactant, enough to form micelles in solution and not too much to avoid a saturation of the solution.

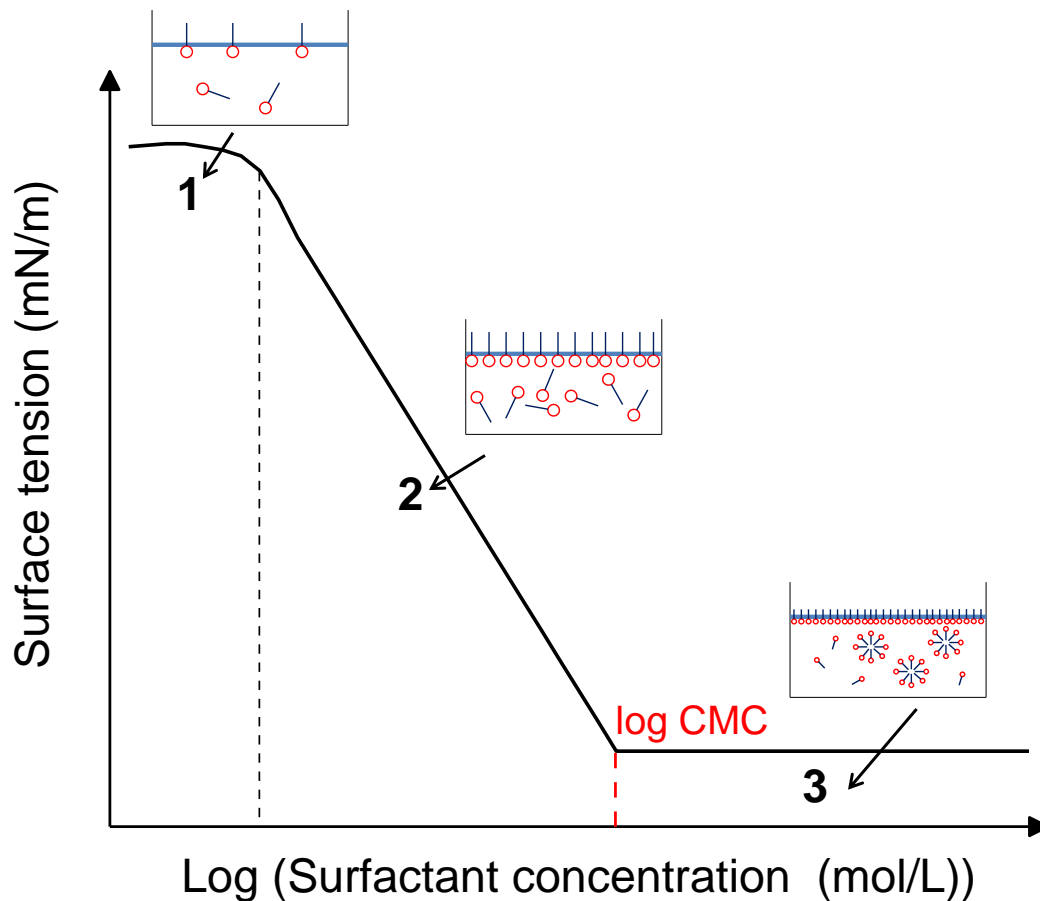


Figure II-13. Surface tension as a function of the surfactant concentration in logarithmic scale.

In oily media, the process is similar excepted that the micelles are inversed due to the fact that the hydrophobic tails are compatible with oils while the polar heads are not. In the case of a biphasic solution with both oil and water, heads and tails are oriented in their preferential media. The formation of an oil-in-water (O/W) emulsion requires a surfactant with a hydrophilic nature and, conversely, a more hydrophobic one for water-in-oil (W/O) emulsions [27]. The Hydrophilic Lipophilic Balance (HLB) value classifies the surfactants from less hydrophilic to more. Some formulae calculate the HLB through the chemical composition of surfactants and a scale of values between 0 and 20 quantifies their hydrophilic behavior [28] [29]. Thus, a surfactant with a high HLB value (near 20) will favor an O/W emulsion.

As a conclusion, non-ionic and ionic strategies could be used to disperse nanoparticles. The next part focuses on the dispersion of ferrite particles with different solvents and surfactants that can be applied to the nanoparticles previously synthesized (Chapter I).

#### II.1.5.B. State of the art on dispersion of ferrite nanoparticles

Figure II-14 reviews some examples of dispersion of ferrite particles. The particles have been synthesized by thermal decomposition with similar precursors and solvents used in the previous synthesis (Chapter I): namely acetylacetonates for iron and zinc precursors, oleylamine and oleic acid as synthesis surfactants. The interest is to learn from other experiences having the same starting material, with particle sizes below 50 nm.

Material	Size (nm)	Synthesis	Dispersion media		Surfactant	Stabilization	References		
NiZn ferrite	50	commercial	organic	hexane	commercial dispersing agent BYK111	Steric	[30]		
MFe <sub>2</sub> O <sub>4</sub> (M = Fe, Mn, Co)	7 - 20	Thermal decomposition: oleates, oleic acid, octadecene					[31]		
Fe <sub>3</sub> O <sub>4</sub>	4 - 14	Thermal decomposition: Fe(acac) <sub>3</sub> , oleic acid, oleylamine, organic solvents					[32]		
Fe <sub>3</sub> O <sub>4</sub>	4 - 14	Thermal decomposition: Fe(acac) <sub>3</sub> , oleic acid, oleylamine, organic solvents	aqueous	water	DMSA	Electrostatic	[32]		
MFe <sub>2</sub> O <sub>4</sub> (M = Fe, Mn, Co)	7 - 20	Thermal decomposition: oleates, oleic acid, octadecene					[31]		
NiFe <sub>2</sub> O <sub>4</sub>	9 - 11.7	Solvothermal route: Fe(acac) <sub>3</sub> , Ni(acac) <sub>2</sub> , oleylamine					[33]		
Fe <sub>3</sub> O <sub>4</sub>	7 - 12	Thermal decomposition: Fe(acac) <sub>3</sub> , oleic acid, oleylamine, 1,2-dodecanediol, octadecene					[34]		
NiFe <sub>2</sub> O <sub>4</sub>	9 - 11.7	Solvothermal route: Fe(acac) <sub>3</sub> , Ni(acac) <sub>2</sub> , oleylamine					CTAB	Electrostatic	[33]
Fe <sub>3</sub> O <sub>4</sub>	4 - 15	Thermal decomposition: FeOOH, oleic acid, octadecene					sodium oleate	Steric	[35]

Figure II-14. Dispersion of ferrite particles synthesized by thermal decomposition in organic solvents.

The table is divided in two parts: the organic (in orange) and aqueous (in blue) dispersions (Figure II-14). The nanoparticles being synthesized in organic media, their surface nature is hydrophobic. Thus, an organic dispersion in adapted solvents like hexane, toluene or chloroform could be obtained directly after synthesis. The aqueous dispersions are obtained only after transferring the previous organic dispersion through transferring agents in water.

On the one hand, two steric stabilizations in organic media are described. A commercial dispersant known as DISPERBYK 111 allows the dispersion of 50 nm commercial particles in a mixture of N,N dimethylformamide and alpha-terpineol. The molecule is a copolymer with acidic groups composed of a phosphoric acid polyester. The second one is a dispersion in hexane through oleic acid groups. Oleic acid is a fatty acid of 18 carbon chain with a C=C bond.

Its carboxylic group (-COOH) is chemically absorbed on the particle surface and its nonpolar hydrocarbon tail lies in the organic solvent, resulting in a good hindrance around particles.

On the second hand, three different surfactants seem suitable for an aqueous dispersion. Dimercaptosuccinic acid (DMSA) and cetyltrimethylammonium bromide (CTAB) enable the dispersion of ferrite particles with a range of sizes between 4 and 20 nm and through the electrostatic interactions. DMSA introduces repulsive charges between particles due to the deprotonation of one of its carboxylic groups at pH = 10 into a carboxylate bond (COO<sup>-</sup>). CTAB is a cationic surfactant and induces the adsorption of its cationic headgroup CTA<sup>+</sup> on the negative particle surface. Repulsive forces are then created between particles due to the presence of counter ions Br<sup>-</sup> at the end of the CTAB tail. In both cases, the particle surfaces are hydrophilic and allow dispersion in water.

The third case is a steric stabilization with sodium oleate as a dispersant. Sodium oleate is constituted of a hydrocarbon tail (hydrophobic) and a carboxylate head (hydrophilic). The hydrophobic tail is grafted on the particle surface due to its affinity with the hydrocarbon tail of oleic acid coming from the synthesis. The dispersion in water is made possible through the presence of the carboxylate groups, yielding an hydrophilic behavior of the particle.

All of these successful tests of dispersion in the literature give an anchor point for the nanoparticles previously synthesized (Chapter I). A dispersed medium is a system in which two originally incompatible or immiscible phases are finally made stable through the dispersion of a phase in another one, achieved through the addition of one or many ingredients (especially surfactant). In the following sections, the dispersed phase will be constituted of the zinc ferrite oxide nanoparticles previously synthesized (Chapter I) and the continuous phase will be an adapted solvent, inspired from the literature (Figure II-14). Different methods and formulations will be described in the part II.3.

However, before being dispersed, the nanoparticles have to be cleaned (Figure II-1) to remove most of the organic species coming from the synthesis. Indeed, a too large amount of organics at the nanoparticle surrounding will considerably reduce the magnetic properties after the elaboration of coatings. With these considerations in mind, different ways of cleaning are studied in the following part.

## II.2. Study of the nanoparticle cleaning steps

Here, several methods are investigated to clean the particles with the following assessment grid:

- the decrease of the organic/inorganic ratio,
- the efficiency through time and numbers of steps in the cleaning process.

### II.2.1. Centrifugation sequences

After synthesis, the nanoparticles are recovered and washed. Different cleaning methods are studied.

At first, the nanoparticles are washed by centrifugation processes with addition of a mixture of ethanol and ethyl acetate. The supernatant is discarded between each centrifugation. The goal is to remove the remaining organics coming from the synthesis and the surfactants still present at the particle surroundings and surface. Oleylamine ( $C_{18}H_{37}N$ ) and oleic acid ( $C_{18}H_{34}O_2$ ) create organic bonds at the particle surface. These bonds are detected by Fourier Transform Infrared Spectroscopy (FTIR) (Chapter I).

The interesting bands in the infrared spectrum are represented in Figure II-15: the Fe-O ( $400-850\text{ cm}^{-1}$ ), C=O ( $1200-1800\text{ cm}^{-1}$ ), and  $CH_2$  and  $CH_3$  ( $2800-3000\text{ cm}^{-1}$ ) bonds. The C=O and  $CH_2$  and  $CH_3$  in red and violet allow quantifying qualitatively the presence of oleylamine and oleic acid at the particle surrounding. The contribution of each surfactant is not dissociated.

In this section, the cleanings are only described in the case of FM particles. Similar results and trends are observed for SP(F)M particles (Chapter III). FM particles are washed 4 times by centrifugation. The cleaning solvents are eliminated between each washing operation. Figure II-15 shows the infrared curves obtained after a first centrifugation operation in ethanol to recover the particles after synthesis, and also after each cleaning centrifugation in the mixture of ethanol and ethyl acetate. This technique gives a qualitative idea of the amount of organics if compared with the Fe-O bond, characteristic of the material. The intensity of the bands depends on the number of cleanings. The cleaning method efficiency is estimated through the ratio between the Area Under Curve (AUC) of C=O and  $CH_2$  and  $CH_3$  bands with the material one. The smaller the ratios are, the more efficient the cleanings are, see Figure II-16.



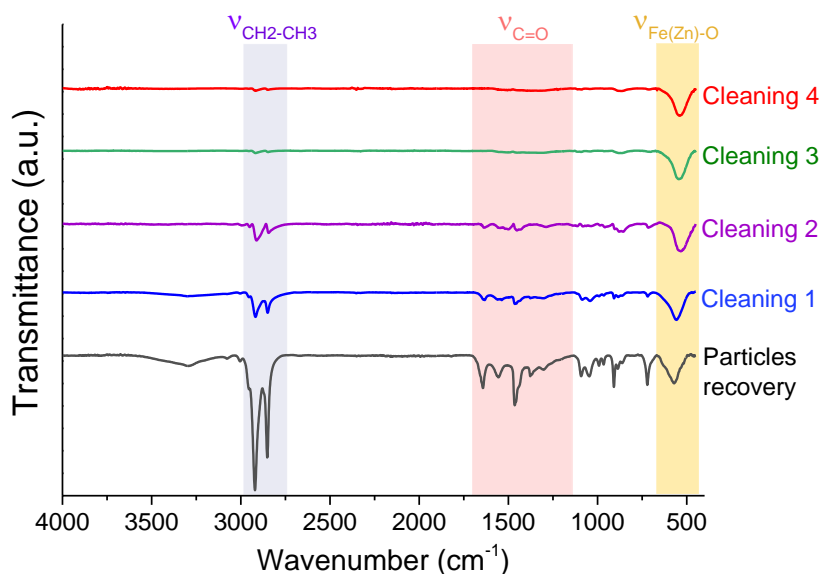


Figure II-15. Infrared spectrum of the evolution of nanoparticle cleanings by centrifugation.

Number of centrifugation	Step	Cleaning media	AUC $\nu_{CH_2-\nu_{CH_3}}$	AUC $\nu_{C=O}$	AUC $\nu_{Fe(Zn)-O}$	AUC ratio $\nu_{CH_2-\nu_{CH_3}}/\nu_{Fe(Zn)-O}$	AUC ratio $\nu_{C=O}/\nu_{Fe(Zn)-O}$
1	Particles recovery	EtOH	3078.8	2525.5	773	3.98	3.27
2	Cleaning 1	EtOH/ethyl acetate (1:1)	4328.2	4991.3	4871.7	0.89	1.03
3	Cleaning 2		1862.6	1670.7	3595.2	0.52	0.47
4	Cleaning 3		248.0	1111.9	4900.7	0.05	0.23
5	Cleaning 4		304.2	1375.8	5545.7	0.06	0.25

Figure II-16. Area Under Curve (AUC) of the characteristic bands observed by FTIR (Figure II-15) during cleanings by centrifugation. AUC are calculated with Origin.

The cleaning operations are effective from the first one with a sharp decrease of the ratios of AUC for the two bands characteristic of organics normalized in relation to the material band (Figure II-17). After the first cleaning, a slightly lower decrease is observed until the third washing cycle. The fourth washing is clearly not useful.

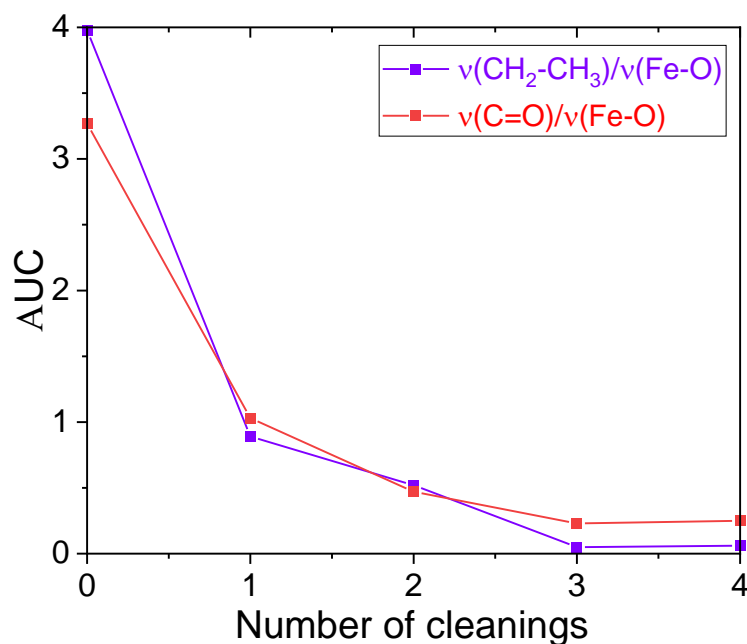


Figure II-17. Ratios of the AUC of the bands characteristic of the organics to the one of the material as a function of the number of cleanings.

Knowing the AUC method is unprecise and gives just a qualitative trend of the efficiency of cleanings, a chemical characterization of a sample washed 2 and 6 times has been performed through ICP-AES. The results are compared in Figure II-18.

	Concentration (wt%)	
	2 cleanings	6 cleanings
Fe	57±3	59.3±0.9
Zn	7.4±0.4	7.5±0.2
<b>Zn/Fe</b>	<b>0.13</b>	<b>0.13</b>
C	3.9±0.4	4.1±0.4
N	0.201±0.007	0.195±0.04

Figure II-18. Concentrations (wt%) in Fe, Zn, C and N in FM particles, washed 2 and 6 times.

On the one hand, the zinc to iron ratios are close to the theoretical one: 0.13 versus 0.15 for the theory. Thus, the stoichiometry is respected. C and N elements quantify the amount of oleylamine ( $\text{C}_{18}\text{H}_{37}\text{N}$ ) and oleic acid ( $\text{C}_{18}\text{H}_{34}\text{O}_2$ ) in the samples. The concentrations of C and N are not impacted by the number of cleanings above 2 cycles. This observation complements the trend observed in Figure II-17. FTIR being inaccurate, ICP-AES allows to determine that above 2 cycles, the cleanings look inefficient. This assumption will be further investigated in part II.3.2.B.

In order to further reduce the organic amounts at the particle surface as well as optimize the washing yields, other cleaning routes are examined.

## II.2.2. Alternatives

## II.2.2.A. Simple cleaning process by reflux method

An alternative to the centrifugation operations is the reflux method. The nanoparticles are recovered from synthesis by one centrifugation in ethanol and are then introduced in a heating mantle under reflux with ethanol. The mixture is mechanically stirred and subjected to a low heating at 80 °C to initiate the disbonding of the organic species from the particles (Figure II-19).

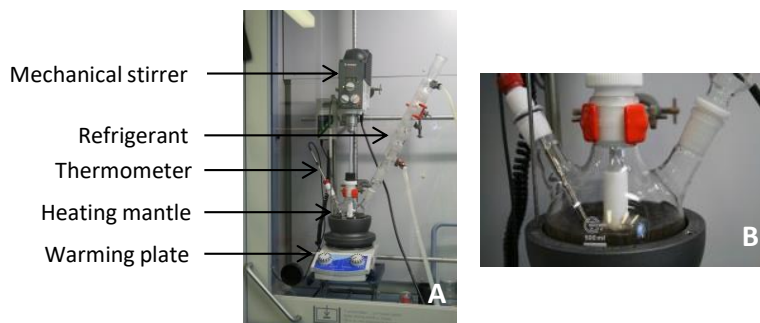


Figure II-19. Set-up for cleaning in a heating mantle.

The procedure for the qualitative assessment of the organic amount exemplified in the case of the cleanings by centrifugation (II.2.1) is reproduced for each alternative method.

A sample of the supernatant is analyzed by FTIR at different times of the cleaning procedure (Figure II-20). The AUC are summarized in Figure II-21 and the ratios of the AUC of the interesting bands ( $\text{CH}_2\text{-CH}_3$  and  $\text{C=O}$ ) to the AUC of the material ( $\text{Fe-O}$ ) are represented in Figure II-22 as a function of the reflux time.

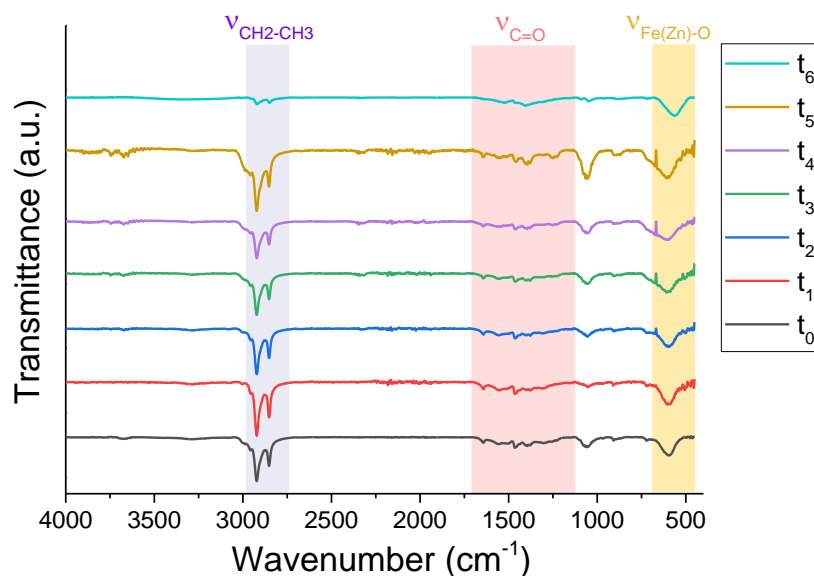


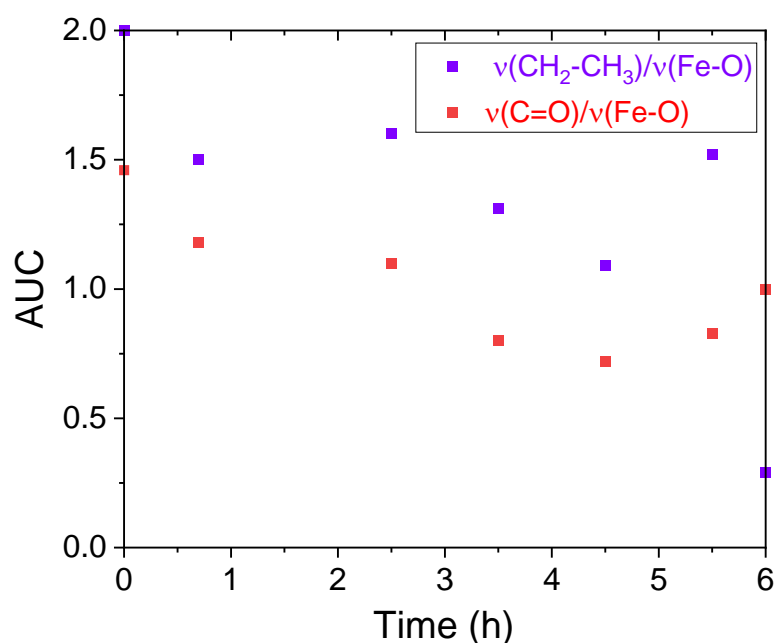
Figure II-20. Infrared spectrum of the evolution of nanoparticle cleaning by reflux.

The infrared spectrum at  $t_6$  corresponds to dried power obtained at the end of the reflux after centrifugation of all of the solution in the heating mantle, which explains the difference of intensities between the vibrational bands in comparison with the other spectra.

	Time (h)	AUC $\nu_{CH_2-\nu_{CH_3}}$	AUC $\nu_{C=O}$	AUC $\nu_{Fe(Zn)-O}$	AUC ratio $\nu_{CH_2-\nu_{CH_3}}/\nu_{Fe(Zn)-O}$	AUC ratio $\nu_{C=O}/\nu_{Fe(Zn)-O}$
$t_0$	0	549.0	403.2	275.6	2.00	1.46
$t_1$	0.7	115.8	90.5	77.0	1.50	1.18
$t_2$	2.5	139.7	96.5	87.5	1.60	1.10
$t_3$	3.5	118.9	72.9	90.7	1.31	0.80
$t_4$	4.5	181.7	119.9	167.1	1.09	0.72
$t_5$	5.5	176.4	96.3	116.1	1.52	0.83
$t_6$	end	833.1	2835.1	2845.7	0.29	1.00

AUC: Area Under Curve

**Figure II-21.** Area Under Curve (AUC) of the characteristic bands observed by FTIR (Figure II-20) during cleaning by reflux. AUC are calculated with Origin.



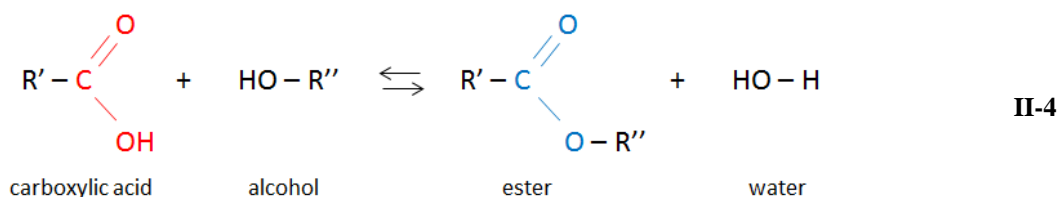
**Figure II-22.** Ratios of the AUC of the bands characteristic of the organics to the one of the material as a function of the reflux duration.

The ratios of AUC for the two bands characteristic of organics versus the material band stagnate and the points in Figure II-22 does not display a net decrease. The reflux method is not efficient even after 6 hours of reflux. This option is thus discarded.

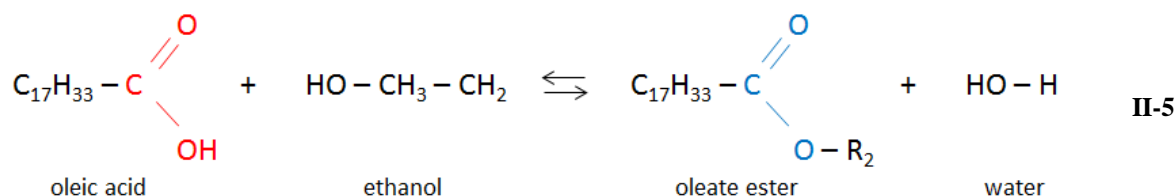
### II.2.2.B. Esterification

The esterification reaction is also studied as another alternative method to cleanings by centrifugation. The principle of the method is based on the condensation of a carboxylic acid with an alcohol which generates an ester and water (Equation II-4). The esterification could be

applied to the nanoparticles previously synthesized in Chapter I due to the presence of carboxylic groups (-COOH) at the particle surface coming from oleic acid during synthesis.



The esterification reaction of oleic acid is written in Equation II-5 with the carboxyl groups in red and the ester function in blue. At the same time as the esterification reaction of the oleic acid groups which takes place in the alcoholic medium, the extraction of the ester occurs by the better chemical affinity of the ester with the toluene. This is expected to overcome the balance of the reaction which is given by the ratio of the products to the reactant and to achieve a better yield. The reaction has to be catalyzed by an acid.



For this purpose, an emulsion constituted of two phases is prepared: a phase with toluene (1/3) and another with particles in a mix of ethanol (2/3) and sulfuric acid (1 vol. %). The mixture is heated at 80 °C under mechanical stirring during 30 minutes. The ester extraction is expected due to the special affinity of the oleate ester with toluene. The emulsion would favor the transfer of oleate ester in the toluene phase. The process is completed with the SPM particles for a preliminary study before application to the FM ones.

At the beginning of the reaction, a rust-colored homogeneous mix is observed (Figure II-23). The color of the solution reminds the one of the precursors when introduced in the microwave reactor before synthesis.



Figure II-23. Mixture of particles with toluene and ethanol.

As the mixture is normally black after synthesis, the hypothesis of the dissolution of the particles in the medium is investigated by Dynamic Light Scattering (DLS). Particles with a mean diameter of 5 nm are retrieved (Figure II-24), which is in agreement with the diameter of

the SPM particles ( $6.2 \pm 1$  nm). The result contradicts the previous hypothesis. The particles are thus not dissolved in the mixture.

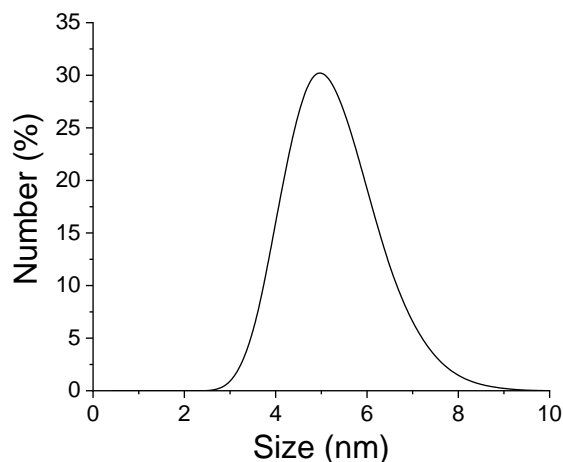
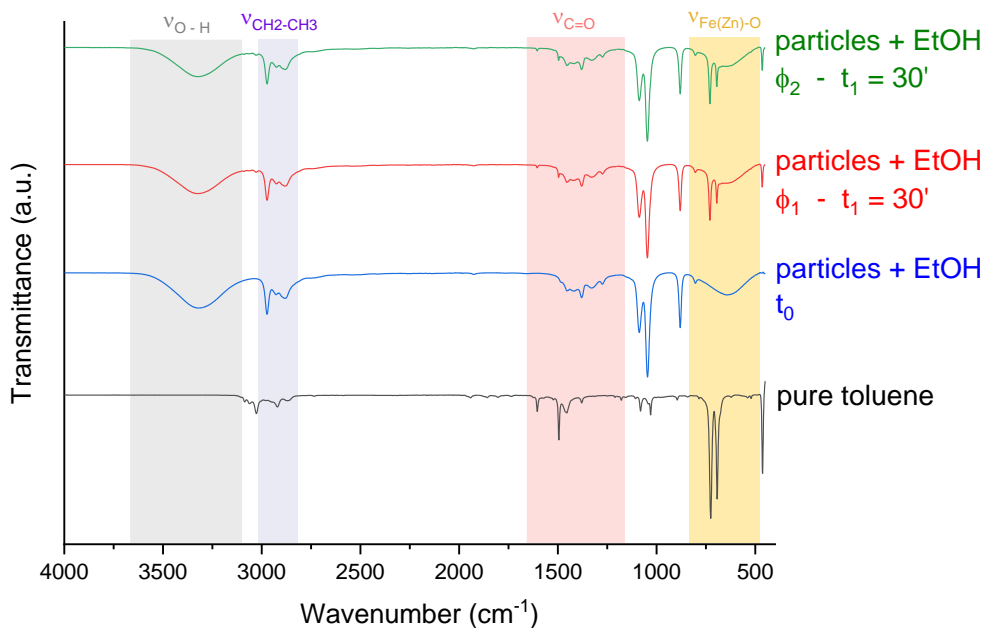


Figure II-24. Size distribution in number by DLS.

Figure II-25 displays the infrared signatures of: pure toluene, the homogeneous mixture at the beginning of the reaction at  $t_0$ , and the surface (written  $\phi_1$ ) and the bottom ( $\phi_2$ ) of the mixture after 30 minutes. The same infrared spectra are identified at the surface and bottom of the flask after 30 minutes (red and green curves), showing the uniformity of the mixture. The phase separation is not observed by decanting.

When the signatures at the beginning and end of the reaction are compared (blue and red curves), several observations can be done. The presence of additional peaks at  $t_1$  is noticed and is attributed to pure toluene, meaning that the mixture was more heterogeneous at the beginning of the reaction contrary to the end of the reaction. Hence, at the beginning, the solution was split in two phases which tend to homogenize under vigorous stirring and heating.

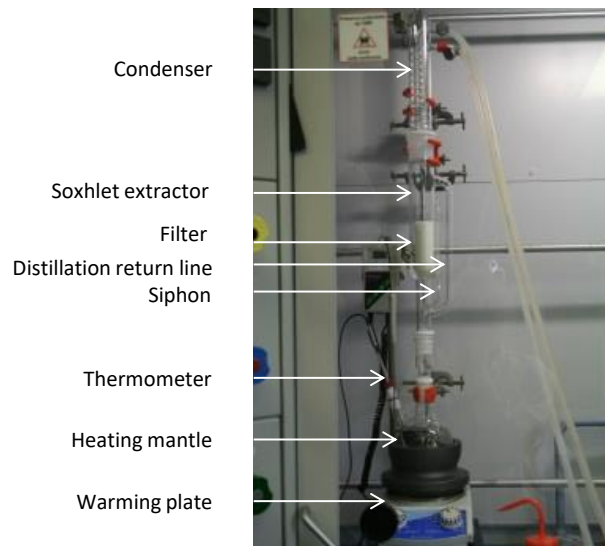
Above all, the intensities of the bands corresponding to  $\text{CH}_2\text{-CH}_3$  and  $\text{C=O}$  bonds are not attenuated compared to the inorganic one. The carboxylic groups are still at the particle surface and no IR signature of the ester has been evidenced. Thus, the esterification reaction has not occurred and the particles have not been cleaned. This second alternative method is abandoned too since it may need an extensive study to achieve it.



**Figure II-25. Infrared spectrum of the evolution of nanoparticle cleaning by esterification.**

### *II.2.2.C. Soxhlet method*

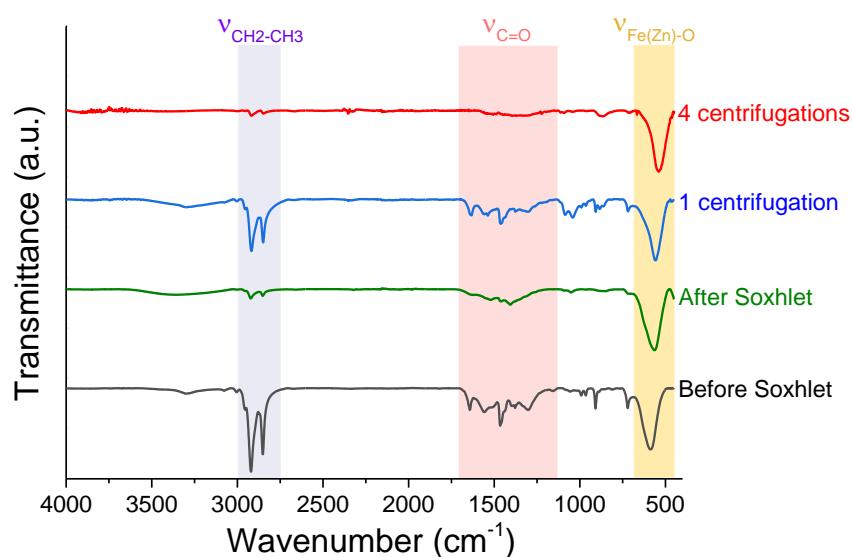
Another idea to enhance the nanoparticle cleaning is through the Soxhlet method. The set-up described in Figure II-26 is constituted of a heating mantle filled with ethanol to which a Soxhlet column following by a condenser is fixed. The particles are recovered after synthesis through one step of centrifugation. They are then introduced inside a filter maintained in the Soxhlet extractor. The Soxhlet column is maintained under reflux at the boiling temperature of ethanol. Once the temperature reached the boiling point of ethanol, the ethanol vapors condensate inside the condenser and liquefy directly in the Soxhlet extractor. The process repeats itself until the Soxhlet container is completely full. As a consequence, the siphon is triggered and the Soxhlet column empties through the distillation return line directly in the heating mantle. The nanoparticles cleaning proceeds by cycles of filling/draining solvent inside the filter indefinitely. The advantage of the method is the continuous renewal of solvent in the filter while recycling the same volume of ethanol without adding more solvent. This technique is hence less solvent consuming than the centrifugations.



**Figure II-26. Soxhlet extraction set-up.**

One cycle is defined by one filling of the extractor following by its complete draining. Six cleaning sequences are operated in two hours. The process is longer than the centrifugation one which requires only 10 minutes by cycle. Otherwise, another asset is that the washings run automatically once settled. It is not the case with the centrifugations.

After six cycles, the characteristic bands of organics ( $\text{CH}_2\text{-CH}_3$  and  $\text{C=O}$ ) are considerably reduced compared to the material band ( $\text{Fe-O}$ ) (Figure II-27 and Figure II-28). The Soxhlet method is an efficient cleaning method. Considering the AUC calculated with the FTIR data (Figure II-28), it seems however qualitatively less productive in comparison with centrifugations. Moreover, in addition to the longer time of achievement, the particles are difficult to extract from the filter, the losses are indeed significant. These reasons explain why the centrifugation method is finally selected for the nanoparticles cleaning.



**Figure II-27. Comparison between the centrifugations and the Soxhlet method by FTIR.**



	AUC $\nu_{CH_2-\nu_{CH_3}}$	AUC $\nu_{C=O}$	AUC $\nu_{Fe(Zn)-O}$	AUC ratio $\nu_{CH_2-\nu_{CH_3}}/\nu_{Fe(Zn)-O}$	AUC ratio $\nu_{C=O}/\nu_{Fe(Zn)-O}$
Before Soxhlet (1 centrifugation)	3328.3	4126.8	3426.4	<b>0.97</b>	<b>1.20</b>
1 centrifugation	4278.3	5008.2	5981.8	<b>0.72</b>	<b>0.84</b>
After Soxhlet (6 sequences)	295.4	1634.0	3025.6	<b>0.10</b>	<b>0.54</b>
4 centrifugations	304.2	1375.8	5545.7	<b>0.06</b>	<b>0.25</b>

**Figure II-28.** Area Under Curve (AUC) of the characteristic bands observed by FTIR (Figure II-27) with the Soxhlet method. AUC are calculated with Origin.

### II.2.3. Conclusion

*In this part, several cleaning methods have been investigated and are summarized in Figure II-29:*

Method		AUC ratio $\nu_{C=O}/\nu_{Fe-O}$	Time (min)	Efficiency (AUC < 1)	Comments
<b>Centrifugations</b>	2 cycles	0.47	20	from 2 cycles	fast and efficient low particle losses
	4 cycles	0.25	40		
<b>Reflux method</b>		1.00	360	inefficient	not working
<b>Esterification</b>		-	30	-	failure need further study
<b>Soxhlet</b>		0.54	120	moderate	high particle losses

**Figure II-29.** Overview of the different cleanings methods tested with the corresponding organic/inorganic ratios and the cleaning efficiency.

*The centrifugation with 4 cycles is the more efficient method and becomes the reference technique of cleaning for the study. Furthermore, the centrifugation method has been employed by M. Pauly in his thesis with the requirement of three cycles of 10 minutes for the washing of iron oxide particles surrounded by a layer of oleic acid as a surfactant [36].*

## II.3. Dispersion strategies

### II.3.1. Dispersion in polar media

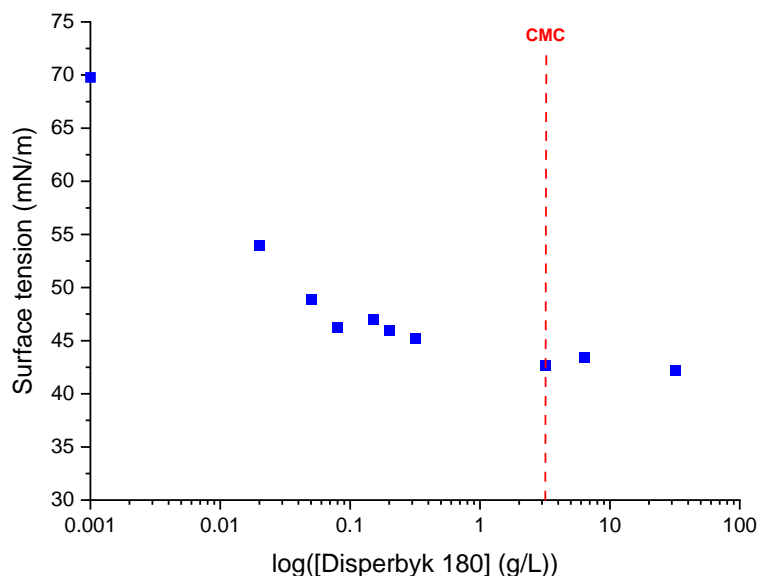
#### II.3.1.A. Disperbyk 180

Once cleaned through a centrifugation procedure (part II.2.1), a suitable solvent and surfactant have to be found to stabilize the nanoparticles in solution. A first approach is to study the dispersion of nanoparticles in polar solvents. As seen in part II.1.5.B, electrostatic dispersions in aqueous media is achievable.

A commercial surfactant, Disperbyk 180, suitable for aqueous media is tested for the dispersion of commercial NiZnFeO particles with a size below 100 nm (supplier information). Disperbyk 180 is an alkylolammonium salt of a copolymer with acidic group. Preliminary tests are done with commercial powders to determine the Critical Micellar Concentration (CMC) of

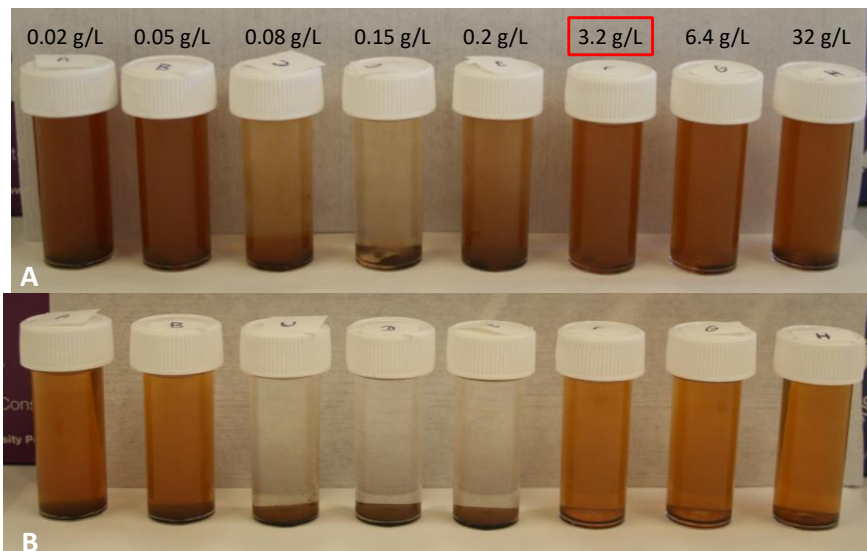
the surfactant without wasting too much synthesized particles due to the low yields in microwave oven.

Figure II-30 exhibits the evolution of the surface tension by increasing the amount of Disperbyk 180 in water. The surface tension smoothly decreases until a concentration of 3.2 g/L of surfactant. From this value, the surface tension remains constant with addition of Disperbyk 180. The CMC is determined at the slope break of the curve. The point at 3.2 g/L is hence called the CMC and it corresponds to the ideal concentration at which the surfactant forms micelles. This is supposed to be a suitable concentration for particle dispersion.



**Figure II-30. Surface tension versus the concentration of Disperbyk 180 in logarithmic scale.**

From the previous curve (Figure II-30), 10 mg of a NiZnFeO commercial powder are introduced in eight aqueous solutions of Disperbyk 180 with different concentrations (Figure II-31-A). After a few minutes, partial sedimentation is observed for concentrations of Disperbyk 180 between 0.02 to 0.05 g/L, as well as a complete sedimentation between 0.05 to 0.2 g/L (Figure II-31.B). From 3.2 g/L, a slight sedimentation is noticed but the particles look well stabilized in water. However, once applied to higher amounts of powder, the sedimentation becomes unavoidable even at 3.2 g/L. As a consequence, another surfactant is studied in order to obtain a better stabilization of the particles in water: tetramethylammonium hydroxide (TMAOH).

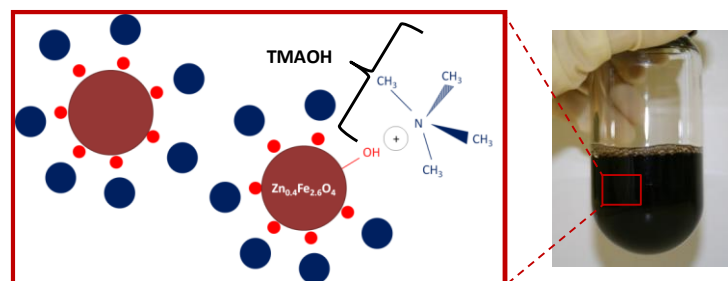


**Figure II-31.** Dispersion tests with a NiZnFeO commercial powder, (A) after ultrasonication (B) after being left for a few minutes.

### II.3.1.B. TMAOH

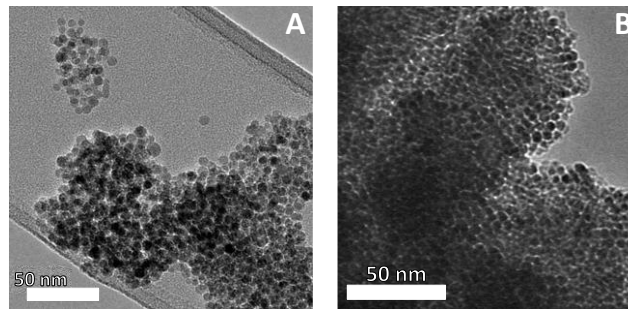
TMAOH is a good candidate for the dispersion of  $Zn_{0.4}Fe_{2.6}O_4$  nanoparticles [37]. Indeed, as the particles display a negative surface charge at pH above the IEP (between 6 and 8 for  $ZnFe_2O_4$  [17] [18] [19]),  $[N(CH_3)_4]^+$  cations in the TMAOH molecule adsorb on the negative surface charge of particles. Repulsive electrostatic forces are thus induced between particles (Figure II-32).

An aqueous dispersion of the SP(F)M particles with TMAOH is studied following the same procedure as Andrade *et al.* [21] for the alkalization of magnetite with TMAOH. An aqueous solution of TMAOH (25 wt%) is gradually added until attaining a pH of 10 in an aqueous solution with the SP(F)M particles. The pH is fixed at 10 as a preliminary test to be placed at 2 to 3 points from the IEP and thus increasing the particle stability in the medium. Only 3 wt% of particles is introduced at a first time. The obtained dispersion is shown in Figure II-32. No sedimentation is observed.



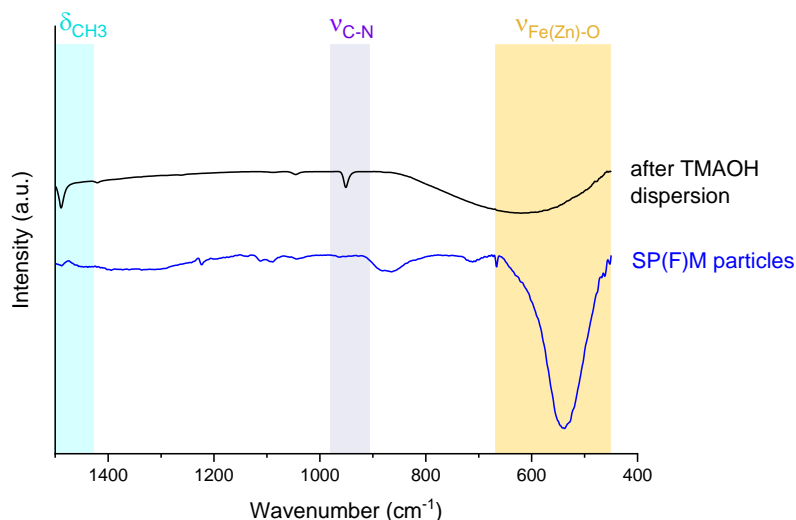
**Figure II-32.** Aqueous dispersion of SP(F)M particles (3 wt%) with TMAOH.

The particles are characterized before and after dispersion in order to determine if the TMAOH molecule is well grafted on the particle surface. Figure II-33 compares the morphology and sizes of particles before and after dispersion by TEM observations of dried powder. The particles are still uniform with spherical shapes and a mean size around 6 nm.



**Figure II-33. SP(F)M particles before (A) and after (B) aqueous dispersion with TMAOH.**

FTIR spectroscopy of the SP(F)M particles before and after dispersion is presented in Figure II-34. Two new bands have appeared on the infrared spectrum of the dispersion. These bands are specific to TMAOH. The first band located at  $950\text{ cm}^{-1}$  corresponds to the asymmetric elongation mode of C-N bond ( $\nu_{\text{asym}}(\text{C-N})$ ) and the second one at  $1490\text{ cm}^{-1}$  is attributed to the asymmetric  $\text{CH}_3$  deformation mode ( $\delta_{\text{asym}}(\text{CH}_3)$ ) [21]. It reflects the grafting of the TMAOH molecule at the particle surface after dispersion.



**Figure II-34. FTIR spectra of the SP(F)M particles before and after dispersion with TMAOH.**

The dispersion being successful, its thermal behavior is analyzed in order to determine at which temperature the surfactant is removed from the particles. This characterization gives an idea of the temperature required to anneal the coatings once elaborated. Figure II-35 displays the DTA-TGA analysis of the dispersion between room temperature and  $450\text{ }^{\circ}\text{C}$ . Two weight losses are revealed: a first one around  $100\text{ }^{\circ}\text{C}$  corresponding to the departure of water (87.3 wt%) and a second one around  $171\text{ }^{\circ}\text{C}$  (9.3 wt%) attributed to the TMAOH removal. The residual percentage is in agreement with the concentration of particles in the dispersion given at the beginning (around 3 wt%). The coatings could then be annealed at  $200\text{ }^{\circ}\text{C}$  to make sure of the complete removal of surfactant inside the layers, which has benefits in staying in mild conditions for the thermal treatment of coatings.

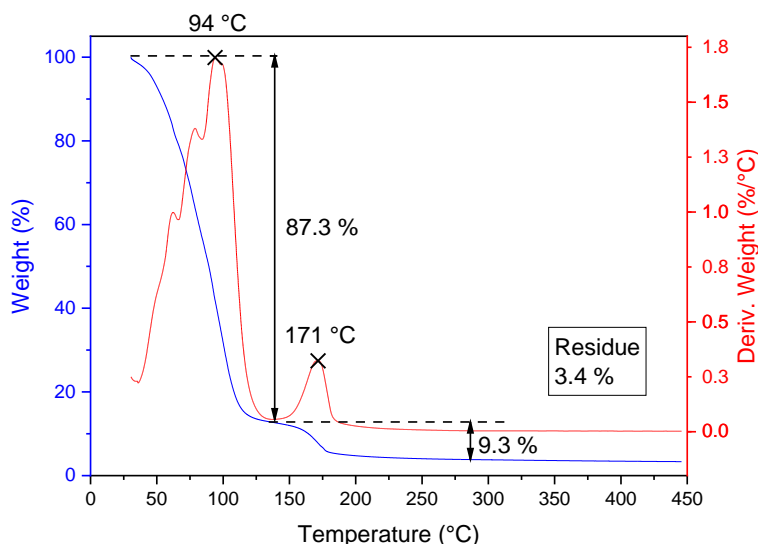


Figure II-35. DTA-TGA of an aqueous dispersion of SP(F)M particles (3 wt%) with TMAOH.

However, the X-ray diffraction pattern of the particles after dispersion and annealing at 200 °C exhibits larger peaks combined with a decrease in intensity. The pattern is also very noisy (Figure II-36). Indeed, the thermal treatment at 200 °C under air clearly affects the crystallinity of the particles after dispersion. The nanoparticles are poorly crystalline and they display reduced sizes compared with the SP(F)M particles before dispersion. A poor crystallinity will considerably impact the magnetic properties of the particle and especially reduce the magnetization of the particles. Hence, the TMAOH dispersion route is set aside, the goal being to stabilize the particles with a surfactant which will not alter the crystallinity of particles after thermal treatment. The link between TMAOH, reduction of particle crystallinity and size through thermal treatment has not been deeply investigated. Other dispersion routes have been studied to avoid this problem.

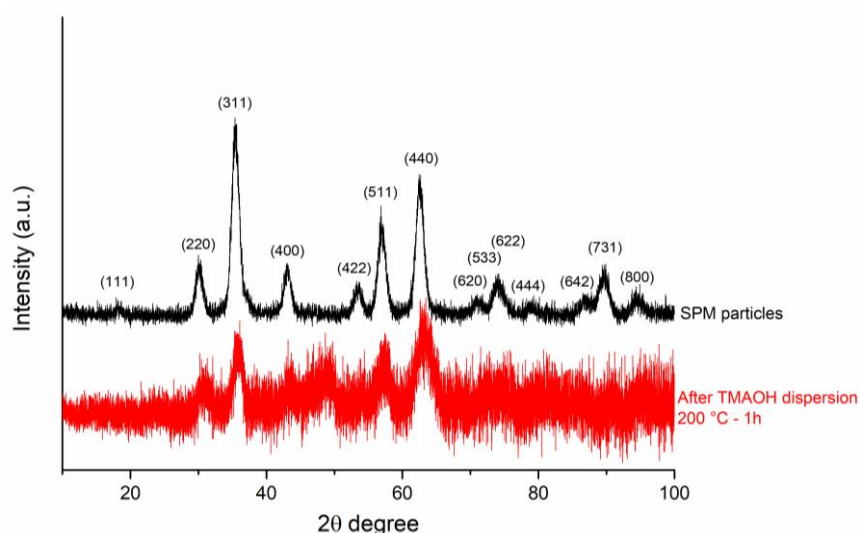


Figure II-36. X-ray diffraction pattern of SP(F)M particles before dispersion and annealed at 200 °C after dispersion.

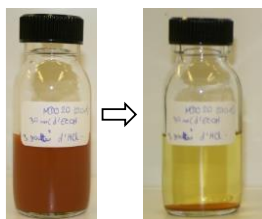
### II.3.1.C. An overview

Figure II-37 summarizes the dispersion tests of commercial and synthesized nanoparticles in polar solvents and especially in water, ethanol, ethylene glycol, and glycerol.

Particle type	Particle size	Environment	
Commercial $\text{Fe}_3\text{O}_4$	50 - 100 nm	basic medium	water TMAOH
Commercial NiZnFeO	< 100 nm (supplier information)	-	water Disperbyk 180
$\text{Zn}_{0.4}\text{Fe}_{2.6}\text{O}_4$	$6.2 \pm 1$ nm (SP(F)M)	acid medium	water
			PAA
			EtOH
	basic medium	HCl	
		EtOH	
		acetic acid	
$22.4 \pm 11$ nm (FM)	acid medium	EG	
		HCl	
		water	
basic medium	-	TMAOH	
		water	
		soda	
acid medium	-	EtOH	
		EtOH/EG	
		water/citric acid [34]	
basic medium	-	water	
		PAA	
		water	
acid medium	-	TMAOH	
		glycerol	
		glycerol	

Figure II-37. Summary of the dispersion tests in polar media.

The stabilization of large particles being more difficult due to their strong magnetic interactions, most of the tests were performed on the SP(F)M particles. To conclude, all of the tests result in sedimentation, excepted the one in TMAOH (part II.3.1.B). Figure II-38 is an example of the sedimentation observed in the case of a test with SP(F)M particles in ethanol with hydrochloric acid (HCl). The sedimentation is even noticed in solvents with higher viscosities like ethylene glycol (EG,  $\eta = 19.8$  mPa.s at 20 °C [38]) or glycerol ( $\eta = 1.49$  Pa.s at 20 °C [39]).



**Figure II-38. Test of peptization of SP(F)M particles in ethanol with HCl.**

The mechanism of dispersion by electrostatic stabilization in polar solvents is complicated, and even more with FM particles. Two of them are otherwise detailed in the previous sections (parts II.3.1.A and II.3.1.B). As a consequence, the direct dispersion of particles in polar solvents after synthesis is not adapted. Due to the organic nature of the particle synthesis, the idea is to disperse the particles directly in an organic solvent after synthesis. An aqueous dispersion could be performed by transferring the organic dispersion in water through the addition of a transferring agent. The new strategies are summarized in Figure II-39 and will be the subject of parts II.3.2 and II.3.3.

transfer	media	surfactant	dispersion
organic → organic	hexane	oleic acid	steric [32] [36]
organic → aqueous	water	sodium oleate	electrosteric [35]

**Figure II-39. New strategies of dispersion.**

## II.3.2. Dispersion in organic solvents

### II.3.2.A. Method of dispersion

The particles are synthesized with two surfactants: oleylamine (OAm) and oleic acid (OA). The carboxylic group (-COOH) of oleic acid is chemically absorbed on the particle surface, which means the dispersion of these nanoparticles requires the use of an organic solvent compatible with the nonpolar hydrocarbon tail of oleic acid to stabilize the particle by steric hindrance. Thus, after the synthesis and the cleaning operations, the nanoparticles could be dispersed in an organic solvent like toluene, hexane [32] or chloroform.

Figure II-40 illustrates a dispersion of SP(F)M particles in hexane through the oleic acid groups. The overall procedure of dispersion is described in the scheme in Figure II-41.



**Figure II-40. Dispersion of SP(F)M particles in hexane.**

At first, the particles are recovered from the synthesis medium by a cycle of centrifugation in ethanol. They are then cleaned through a number of centrifugations in a mixture of ethyl acetate and ethanol. Finally, after removal of the last supernatant of centrifugation, the particles are directly suspended in hexane and ultrasonicated during one hour. The obtained dispersion



of SP(F)M particles do not sedimentate and are stable for hours. A zeta potential measurement performed on a Zetasizer (DLS device) gives a value of -66.7 mV (averaged over three points), which indicates the dispersion has a good stability (Figure II-5). Nevertheless, the dispersion is always maintained under agitation on mechanical rolls. In the case of FM particles, the dispersion is fairly stable, a slight sedimentation is noticed.

	<b>SYNTHESIS</b>	<b>RECOVERY</b>	<b>CLEANINGS</b>	<b>DISPERSION</b>
	Microwave	1 <sup>st</sup> centrifugation	N centrifugations	ultrasound
<i>Duration</i>	50'	10'	N x 10'	60'
<i>Media</i>	OAm, OA, ODE, EG	EtOH	ethyl acetate (2/3) EtOH (1/3)	hexane

**Figure II-41. Process of dispersion in hexane starting from the synthesis.**

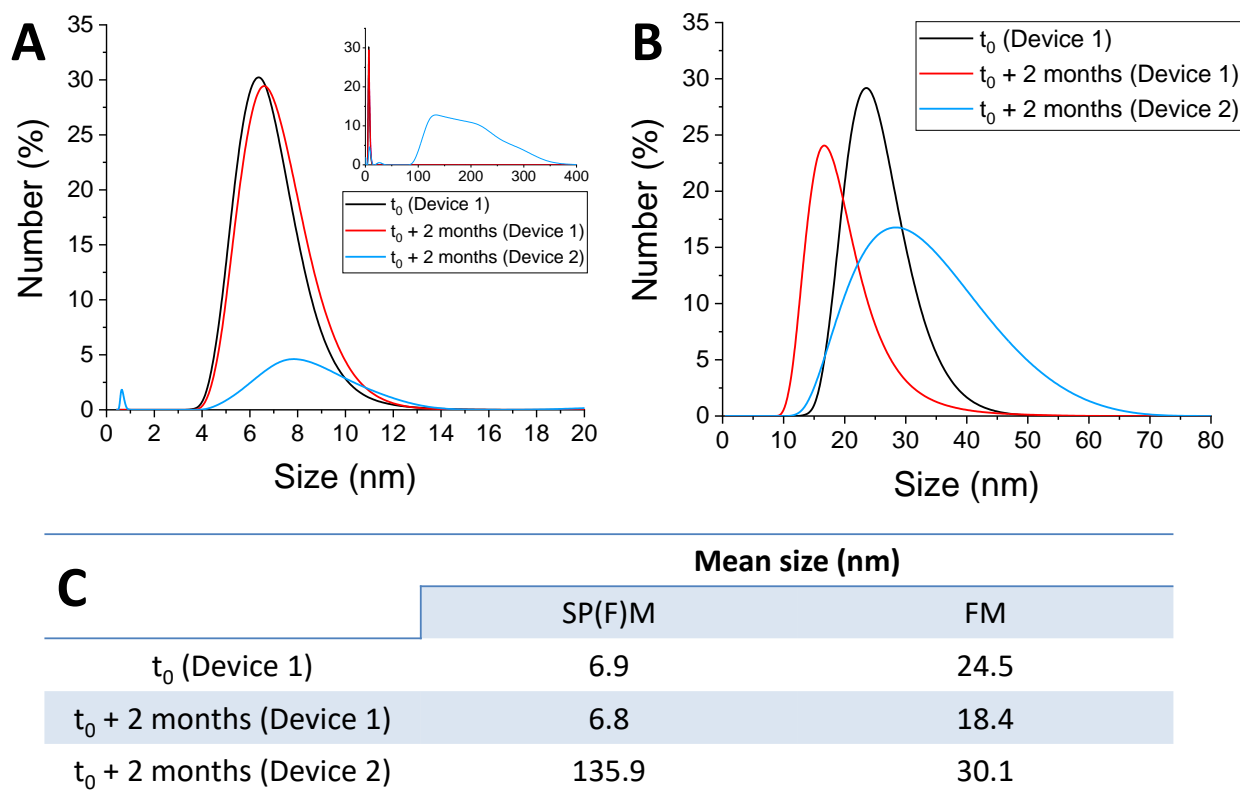
The particle concentration is estimated by dry extract  $DE_{wt}$  which is the percentage of dry mass in relation to the total mass. The particle concentration is settled at 8 wt%.

Furthermore, the size distributions of SP(F)M and FM particles are characterized by DLS from their dispersions in hexane (Figure II-42). In order to test the reliability of the measurement, three curves are compared in both cases: one executed at CEA with a Device 1, the same analysis two months later at CEA, and at Paris-Diderot University with a Device 2. Device 1 and 2 are a similar Zetasizer Nano ZS (Malvern Instruments).

In the case of SP(F)M particles, the two measurements carried out with the device 1 within two months of each other are reproducible and indicate a mean size of around 7 nm (Figure II-42.A-C), which is consistent with the particle diameter ( $6.2 \pm 1$  nm). The data obtained by DLS is normally an overestimation of the diameter because the DLS measures the hydrodynamic size. The measurement done with the device 2 is different from the reproducible ones obtained with the Device 1. A less intense peak is observed around 8 nm and a large distribution is detected at large diameters between 100 and 350 nm. The assumption is that the dispersion has been destabilized, inducing the formation of large aggregates with sizes between 100 and 350 nm. As the distribution is in number, the presence of large aggregates considerably reduces the intensity of the peak at 8 nm which corresponds to the unit particles non-aggregated.

Regarding FM particles, the three measurements are located around the same range of sizes with mean diameters between 18 and 30 nm. It is thus in agreement with the particle diameter of  $22.4 \pm 11$  nm. A weak ageing of the dispersion with time is noticed for the measurement with the device 2 due to the distribution broadening and decrease in intensity (Figure II-42.B-C).





**Figure II-42.** Size distributions in number by DLS for SP(F)M (A) and FM (B) particles. Table related to the mean size calculated from DLS measurements (C).

DLS is a trustworthy method to examine particle distributions from stable dispersions. However, it is important to correlate the results with another technique like TEM. The difficulty of the method is to properly manage dilutions which have to be reproducible between two measurements and also suitable for the dynamic light scattering (for which a minimum of light transmission is needed) without destabilizing the dispersion. Moreover, the diameters are often overestimated, the measurement taking into account the overall solvation sphere.

Stable dispersions of hydrophobic particles in hexane are successful. The influence of the number of cleanings  $N$  (Figure II-41) is also studied. As seen in a previous part (section II.2.1), the number of washing affects the quantity of organic species at the particle surface. These molecules are required to obtain stable dispersions, and at the same time they are avoided because a too large amount of organics inhibits the magnetic properties of particles and prevents them from coupling. The goal is to determine the ideal balance between these two criteria, and thus to define a suitable number of cleanings  $N$  to obtain the best configuration, namely a stable dispersion with as little organics as possible in order to induce good interactions between particles and thus a high magnetization of coatings. Even if it has been concluded in part II.2.1 that above 2 cycles the cleanings are inefficient, the influence of the number of cleanings has to be verified at the coating scale.

### II.3.2.B. Influence of the number of cleanings

Three dispersions with different  $N$  cycles of centrifugation are studied. SP(F)M particles are cleaned once, six and twelve times before dispersing in hexane.

The remaining organics are estimated in the final three dispersions through ATR-FTIR spectra (Figure II-43). The intensity of the characteristic bands of organics ( $\text{CH}_2\text{-CH}_3$  and  $\text{C=O}$ ) decreases with the number of cleanings  $N$  when compared to the material band ( $\text{Fe-O}$ ) (Figure II-43). Considering the AUC calculated with the FTIR data (Figure II-44 and Figure II-45), the downward trend is confirmed for the  $\text{CH}_2\text{-CH}_3$  bond with a sharp drop of the AUC ratio. In the case of  $\text{C=O}$  bond, the decrease is smooth and occurs from twelve cleanings. Thus, the higher the number of cleanings  $N$  is, the more it reduces the organic shell around particles. The washings are more effective with twelve cleanings.

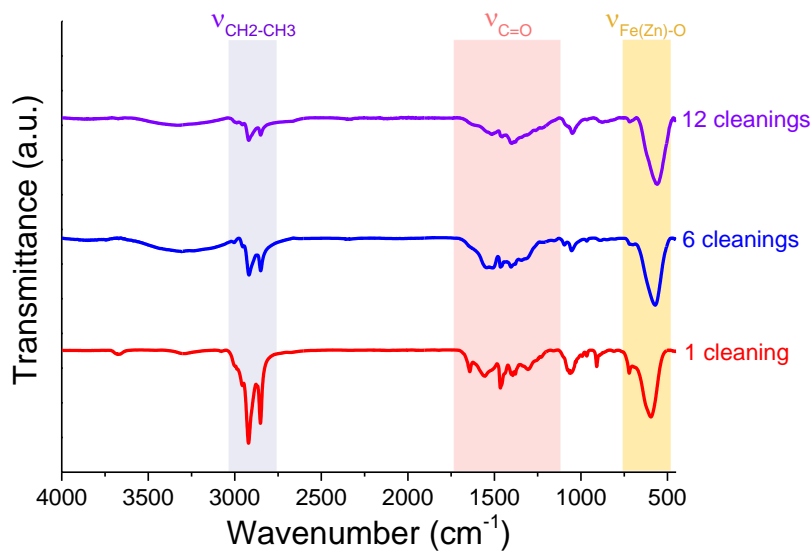
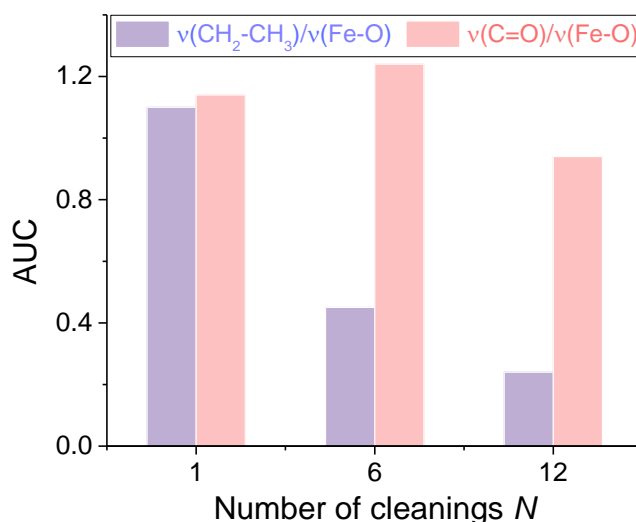


Figure II-43. Influence of the number of cleaning  $N$  on the presence of organics around particles by FTIR.

Number of cleaning	AUC $\nu_{\text{CH}_2-\text{CH}_3}$	AUC $\nu_{\text{C=O}}$	AUC $\nu_{\text{Fe(Zn)-O}}$	AUC ratio $\nu_{\text{CH}_2-\text{CH}_3} / \nu_{\text{Fe(Zn)-O}}$	AUC ratio $\nu_{\text{C=O}} / \nu_{\text{Fe(Zn)-O}}$
1	4414.6	4581.7	4026.7	<b>1.10</b>	<b>1.14</b>
6	2259.4	6270.8	5043.5	<b>0.45</b>	<b>1.24</b>
12	230.4	887.3	947.3	<b>0.24</b>	<b>0.94</b>

Figure II-44. Area Under Curve (AUC) of the characteristic bands observed by FTIR (Figure II-43). AUC are calculated with Origin.



**Figure II-45.** Ratios of the AUC of the bands characteristic of the organics to the one of the material as a function of the number of cleanings  $N$ .

The dispersion obtained with the nanoparticles washed twelve times is the one with the presence of less organics. However, the behavior of each dispersion is also examined once dried on a substrate. Figure II-46 presents three pictures with each dispersion dried on a glass substrate after annealing at 300 °C during 30 minutes under argon atmosphere. The coating process will be described in part III.1. The interest is to observe the influence of the number of cleanings  $N$  on the behavior of coatings after drying. A better washing of particles will allow reducing the organic amount which has to be removed by thermal treatment, inducing less stress inside the coating layer and thus a better mechanical strength of coatings.



**Figure II-46.** Visual appearance of coatings after annealing at 300 °C during 30 minutes under argon atmosphere as a function of the number of cleanings  $N$ .

After one cleaning, the coating has an oily appearance with cracking and debonding of some pieces of material from the substrate. It is probably due to the presence of too much organics which break the layer after decomposing during thermal treatment. The surface of coating looks less oily after six cleanings and a good adherence of the film on the glass substrate is noticed. However, after twelve cleanings, the layer is very powdery and the particles adhere less to the substrate than after six cleanings. Hence, a quantity of organics is required to maintain the adherence between the film and the substrate. The best configuration is the one with 6 cleanings. It is a good bargain allowing to considerably reduce the amount of organics at the particle surface by keeping a good adhesion of the particle layer on a substrate after thermal treatment. Thus, even if above 2 cleanings the washings look not efficient anymore in ICP-AES, the number of cleanings is fixed at 6 in the further project to ensure a good adhesion of the film on

the substrate. As ICP-AES is a measure of the weight fraction of the organic amount, it may be not relevant to deal with surface related mechanisms like adherence and evaporation of the solvent which are more sensitive to area than to volume.

The magnetic properties of these coatings will be analyzed in Chapter IV to discern in which case the magnetic properties are enhanced.

### II.3.3. Transfer in aqueous media

The stabilization of particles in water from the organic dispersion in hexane is schematized in Figure II-47. The protocol is inspired from Mei *et al.* [35].

At first, the SP(F)M particles from the previous dispersion in hexane are precipitated by centrifugating a mixture of the dispersion with half of the volume of ethanol (Step 1). The supernatant is discarded. The particles are recovered and then washed by three centrifugations with addition of ethanol and hexane (Step 2). After cleanings, the obtained powder is dispersed in 15 mL of chloroform (Step 3). A dark brown emulsion is elaborated from the previous dispersion in chloroform with the addition of 8 mL of an aqueous solution of sodium oleate NaOL (0.05 mol/L) (Step 4). The chloroform is at that time evaporated using a rotary evaporator at 35 °C during 15 minutes (Step 5). Finally, after a complete removal of the chloroform, the particles are dispersed in 15 mL of water using ultrasonication (Step 6). The obtained dispersion is stable for hours. A zeta potential measurement performed on a DLS device gives a value of -64.6 mV (averaged over three points), which indicates the good stability of the dispersion (Figure II-5). The dispersion is also kept under agitation on mechanical rolls. The step 5 requires the use of a solvent with a boiling point below the one of water. For example, the replacement of chloroform by tetrachloroethylene with boiling points of 61.2 °C and 121.2 °C respectively leads to the water evaporation before tetrachloroethylene.

	ORGANIC DISPERSION	⇒ RECOVERY	⇒ CLEANINGS	⇒ INTERMEDIARY DISPERSION	⇒ EMULSION	⇒ TRANSFER	⇒ AQUEOUS DISPERSION
	Initial state	Step 1 1 centrifugation	Step 2 3 centrifugations	Step 3 ultrasound	Step 4 ultrasound	Step 5 evaporator	Step 6 ultrasound
Media	hexane	EtOH (1:2)	EtOH (1/2) hexane (1/2)	chloroform	chloroform, NaOL aqueous solution	NaOL aqueous solution	water

**Figure II-47. Transfer of the organic dispersion to an aqueous medium.**

The SP(F)M particles are sterically stabilized through the hydrophilic head of sodium oleate. The hydrophobic tail of sodium oleate is grafted on the particle surface due to its affinity with the hydrocarbon tail of oleic acid coming from the synthesis. In this way, sodium oleate acts as a transferring agent between organic and aqueous media through the formation of a liposomal bilayer.

The size distribution of the SP(F)M particles dispersed in water is characterized by DLS (Figure II-48). The same devices as in Figure II-42.A-B are adopted. The three measurements match with a slight ageing of the solution shown with the Device 2. The mean diameter fluctuates between 114 and 259 nm (Figure II-49). The huge difference with the particle diameter ( $6.2 \pm 1$  nm) could be explained by the fact the DLS measures the hydrodynamic radius of particle, hence including the liposomal bilayer at the particle surrounding. This explanation does not explain the gap between TEM and DLS, the size is indeed multiplied by at least 20. The assumption is that the solution should probably contain massive aggregates of particles stabilized in the medium through the hydrophilic parts of sodium oleate.

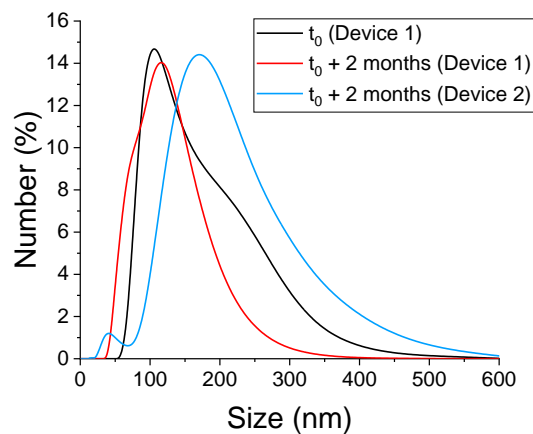


Figure II-48. Size distributions in number by DLS for SP(F)M particles dispersed in water.

	Mean size (nm)
$t_0$ (Device 1)	149.2
$t_0 + 2$ months (Device 1)	114.4
$t_0 + 2$ months (Device 2)	259.1

Figure II-49. Table related to the mean size calculated from DLS measurements (Figure II-48).

Figure II-50 exemplifies a dispersion of SP(F)M particles in water. A large amount of foam is noticed and is induced by the presence of sodium oleate. For this reason, the suspension of particles in water has not been used for the elaboration of coatings, as it can disturb the coating process during spraying or even printing. To manage this issue, less concentrated solutions of sodium oleate could be prepared in order to determine the CMC and stabilize the particles without too much surfactant.



Figure II-50. Dispersion of SP(F)M particles in water.

In the case of FM particles, a slight sedimentation was already observed when dispersed in hexane. The organic dispersion is thus hardly transferrable in water. The diameter of FM particles is at least three times the one of SP(F)M particles. The magnetic interactions are also stronger between the particles, making them harder to stabilize without a significant amount of surfactant. Another strategy should be investigated for the dispersion of FM particles in water with for example polymers with a higher molecular weight like PVA, PMMA, or a polymeric resin. The same compromises and adjustments should be taken into account between dispersion, annealing and magnetic properties.

## II.4. Conclusion

*The first half of this chapter focuses on the cleaning and dispersion steps of the operating protocol (Figure II-1) in order to elaborate dense coatings.*

*First of all, the interactions between particles were reminded and described, namely the Van der Waals, electrostatic, magnetic, and steric interactions.*

*These interactions should be kept in mind when studying the cleanings and of course the dispersion. The particle dispersion depends on these interactions. Two methods were described for the stabilization of particles: non-ionic through steric effects, and ionic ones inducing electrostatic or electrosteric effects.*

*On the one hand, different cleaning methods have been studied:*

- *Cycles of centrifugation which are efficient. Beyond two cycles, the cleanings appear not to have significant effects.*
- *The reflux and esterification methods which were discarded due to their complete inefficiency.*
- *The Soxhlet set-up. The method competes with the centrifugations in terms of efficiency. However, it engenders massive losses of particles.*

*Finally, the centrifugation method was selected for the nanoparticles cleaning.*

*On the other hand, once the cleaning method is selected, different solvents and surfactants were tested to stabilize the particles in a suitable medium. Polar solvents with surfactants like Disperbyk 180 or TMAOH are not successful even though the case of TMAOH is particular. TMAOH provides a stable dispersion of SP(F)M particles. Nevertheless, this route was abandoned due to the TMAOH effect on the particle crystallinity after thermal treatment. Its repercussion on the particle crystallinity and size through thermal treatment might be the subject of another study.*

*The organic dispersion is the only successful route to stabilize the particles without aggregation and sedimentation directly after synthesis. This is due to the organic nature of the particles after synthesis. The nonpolar hydrocarbon tails of oleic acid, adsorbed on the particle surface through its carboxylic head, assure a direct dispersion in organic solvent by steric hindrance. SP(F)M and FM particles were successfully dispersed in hexane, even if a slight sedimentation was noticed in the case of FM particles.*

*The influence of the number of cleanings on the organic dispersion was also studied. The goal is to elaborate a stable dispersion with as little organics as possible to allow good magnetic properties of coatings. Indeed, a lot of organics adsorbed at the particle surface will prevent them from interacting, inducing a low magnetization of coatings. The concept will be detailed in Chapter IV.*

*Moreover, even if only two cleanings looked enough to wash the particles properly from the point of view of a weight amount of organics, a too small number of washings does not allow a good adhesion of the particles on the substrate. Hence, six cleanings seem to be a good compromise to considerably reduce the amount of organics by keeping a good attachment of the particle layer on the substrate after thermal treatment.*

*Lastly, an aqueous dispersion of SP(F)M particles has been formulated by transferring the organic dispersion in water through the addition of a transferring agent: sodium oleate. However, this agent produces a lot of foam which will disturb the selected coating process, either per spraying or printing. For this reason, this route is not suitable and has not been pursued. A solution could be to diminish the concentration of surfactant until finding a good balance between particle dispersion and production of foam, or the addition of an antifoam agent compatible with the ferrite particles.*

*Due to their larger size and stronger magnetic interactions, the stabilization of FM particles in water requires the use of polymers with higher molecular weights (PVA, PMMA) or even polymeric resins. The problem is that these strategies do not match with the goal of the project as this kind of molecules possess high decomposition points and are thus complicated to remove from the coatings. It will damage the magnetic properties of coatings.*

*Thus, after cleaning with six cycles of centrifugation and dispersing directly in hexane, coatings could be elaborated from this previous dispersion with SP(F)M and FM particles.*

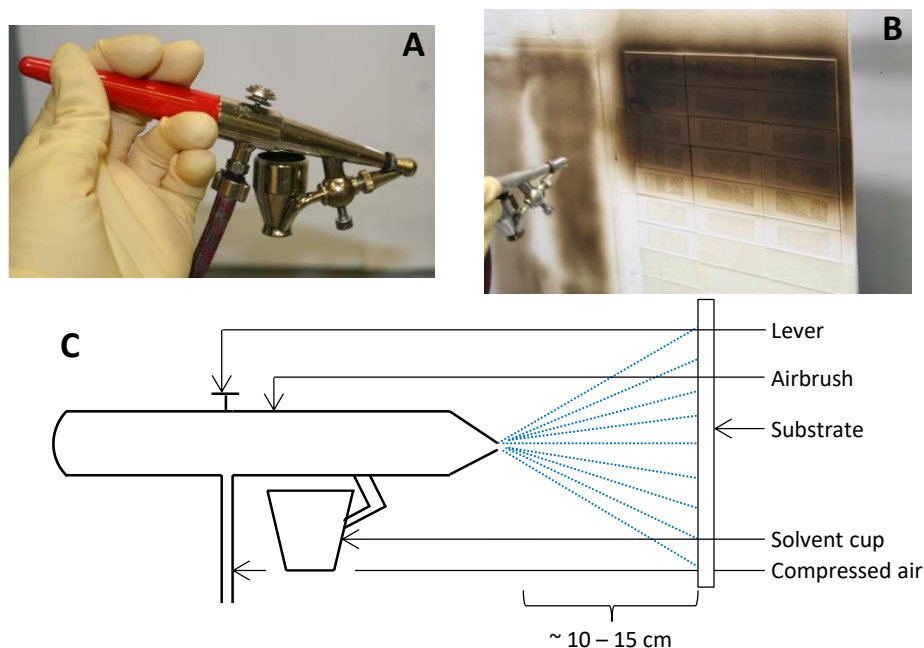


### III. Elaboration of coatings by airbrushing

#### III.1. The airbrushing process

The airbrush is a pneumatic controlled device, similar to the spray technique. It is commonly used as spray gun in the arts field.

The principle is the nebulization of a solution on a substrate under the action of compressed air in a Venturi tube. The liquid is drawn in by the creation of a depression in the narrow part of the tube, induced by the flow of compressed air in the tube. The speed of the air flow allows nebulizing the solution in fine spray particles. The operating pressure is between 20 and 30 PSI. The coatings are vertically elaborated by maintaining the gun horizontally. The device is schemed in Figure II-51.



**Figure II-51. Experimental set-up.**

The liquid vaporization is controlled by the action of a lever (Figure II-51-C). Some parameters influence the coating quality: the nozzle aperture (fixed at 0.55 mm), the pressure at the tube exit, and the working distance between the nozzle and the substrate (between 10 and 15 cm). These parameters have been settled for the overall study. Other criteria are studied to vary the coating thickness or increase its density like the spraying speed and the number of applications. An application is defined as one trip of the airbrush on the substrate from the left to the right, or from the right to the left. The application direction changes every second time. The spraying always begins from the left to the right of the substrate. As an example, a coating elaborated with 2 applications means that the sample has seen one go and return trip of the airbrush with a return at the starting point (at the left of the sample). Some examples of continuous films obtained with airbrushing are displayed with SP(F)M particles on glass slides (Figure II-52) and FM particles on alumina and silicon wafers (Figure II-53).

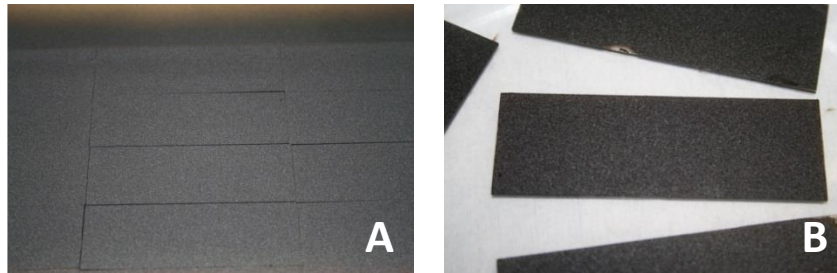


Figure II-52. Coatings obtained with a dispersion of SP(F)M particles in hexane (3 wt%).

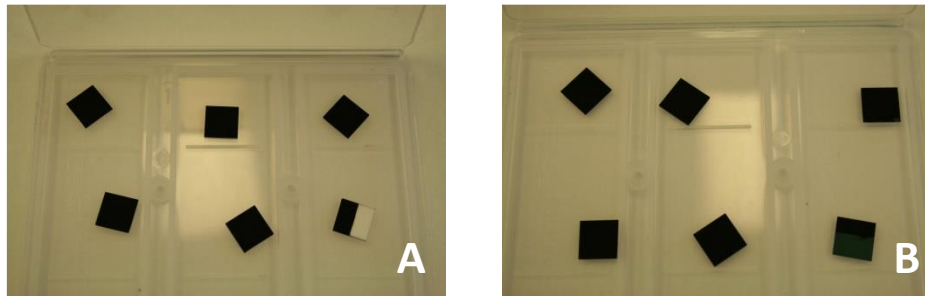


Figure II-53. Coatings with a dispersion of FM particles in hexane (8 wt%) on alumine (A) and silicon wafers (B).

The reproducibility, thickness control of the process could be improved using an automated setup instead of a hand-guided one.

### III.2. Thermal treatment of coatings

After elaboration, the coatings need to be thermally treated first to remove all of the residual organics coming from synthesis and/or dispersion steps which reduce the magnetization of the material and prevent the particles from magnetic interactions, and second to allow a good adhesion of the layer to the substrate with a satisfying density.

#### III.2.1. State of the art: thermal treatment of iron oxide spinel coatings

When studying the thermal treatment of a material, it is necessary to make sure of the stability of the phase under temperature and to have knowledges of the possible phases formed under constraints or atmospheric conditions. In this manner, Figure II-54 presents the iron-oxygen phase diagram. Magnetite ( $\text{Fe}_3\text{O}_4$ ) is stable until high temperature ( $\sim 1600\text{ }^\circ\text{C}$ ). In the case of  $\text{Zn}^{2+}$  substituted magnetite, the fusion temperature depends weakly on the  $\text{Zn}/(\text{Zn}+\text{Fe})$  ratio (Figure II-55). The removal of the organics should proceed without phase change as far as the boiling points of the used organic species are less than  $400\text{ }^\circ\text{C}$  ( $350\text{ }^\circ\text{C}$  for OAm and  $200\text{ }^\circ\text{C}$  for OA).

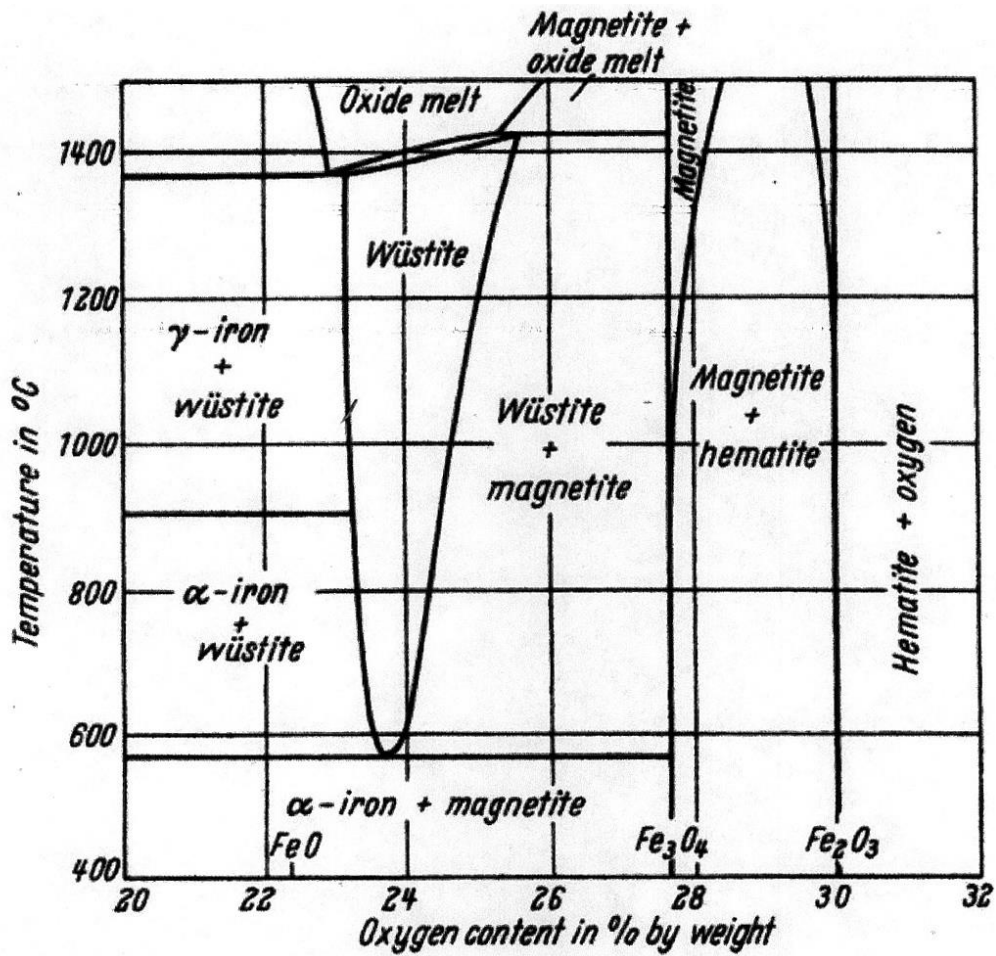


Figure II-54. Fe-O phase diagram with FeO for wüstite and  $\alpha$ -Fe<sub>2</sub>O<sub>3</sub> for hematite. From A. Ranzani da Costa [40] [41] [42].

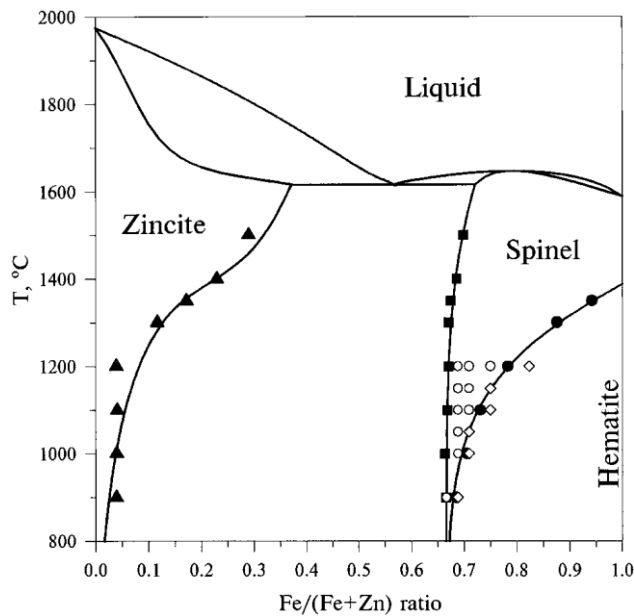


Figure II-55. Zn-Fe-O phase diagram in air. From A. Sergei *et al.* [43].

Once the organics are removed, a lot of porosity is induced in the coatings. Some previous works depict the interest of a sintering step in the thermal treatment protocol of ferrite films in

order to enhance its density, keeping in mind the emergence of a magnetic multi-band behavior requires a good density of coatings.

M. Bissannagari *et al.* have developed inkjet printed NiZn ferrite films with an ink constituted of 30 wt% of particles with a 50 nm diameter [30]. The particle diameter being of the same order of magnitude, their study looks like the present one. After processing, a sintering at temperatures between 600 to 950 °C during 3 hours under air was examined. The relative density (ratio of the measured density to the bulk one) of their films evolves from 61.6 to 95.6 % after sintering at 950 °C (Figure II-56-A). They have demonstrated the interest of the sintering step in the case of Wireless Power Transfer (WPT) applications due to the absence of magnetic losses at the interest frequencies (6.78 and 13.56 MHz) (Figure II-56-B). Moreover, the grains attain a size of 300 nm after sintering at 950 °C. The grain size remains hence less than 3 μm, remembering it corresponds to the critical diameter not to exceed to avoid the formation of domain walls in the permeability spectra (Chapter I). A sintering step is thus perfectly adapted because the particle size will not exceed the critical size imposed by the application.

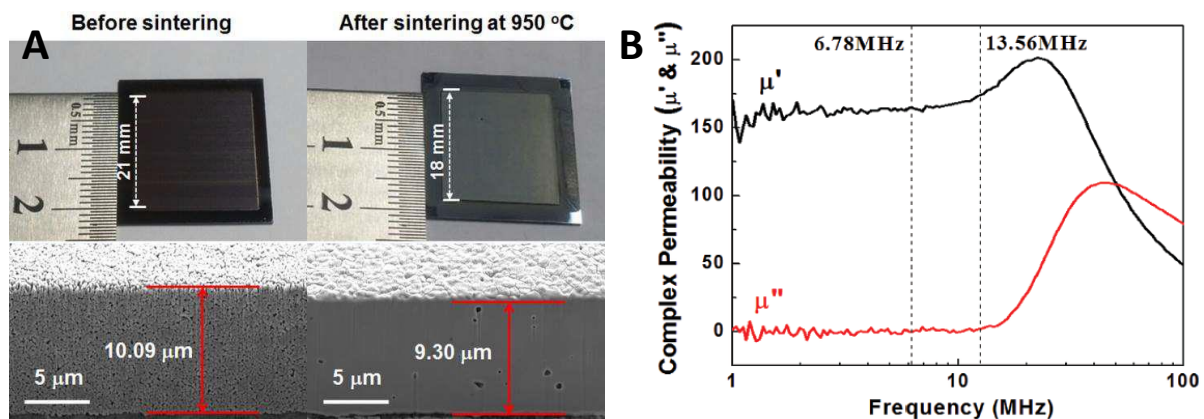


Figure II-56. Effect of a sintering at 950 °C on NiZn ferrite films (A) and its corresponding permeability spectra. From M. Bissannagari *et al.* [30].

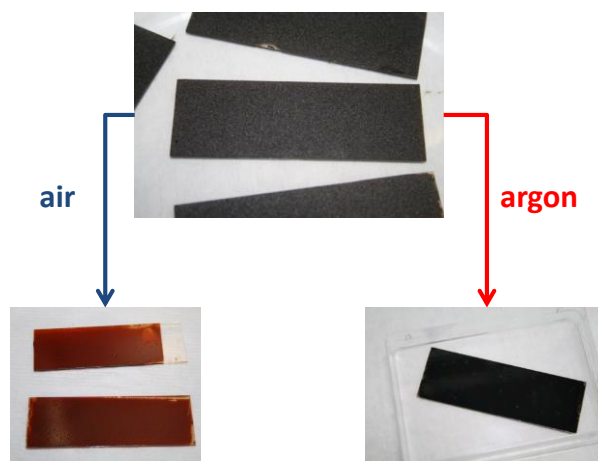
In the same way, Zn doped  $\text{Fe}_3\text{O}_4$  were sintered under argon at 1100 °C during 3 hours [44], and La-doped strontium ferrite films elaborated by a dip-coating and sol-gel method went through a thermal treatment of three steps, namely a drying at 40-50 °C during 2 hours, a pre-sintering at 400 °C during 30 minutes and finally a sintering at 900 °C during 2 hours [45].

The sintering is then required to improve the coating density. According to the literature, the sintering temperature should not exceed 1100 °C which will not induce problems of phase stability at this temperature (Figure II-54). The sintering temperature will be determined with a dilatometry measurement (III.2.5.A).

The thermal treatment procedure will be split in two steps: a debinding to remove all of the organic residues, and a sintering to enhance the coating density and reduce the porosity generated by the first annealing step.

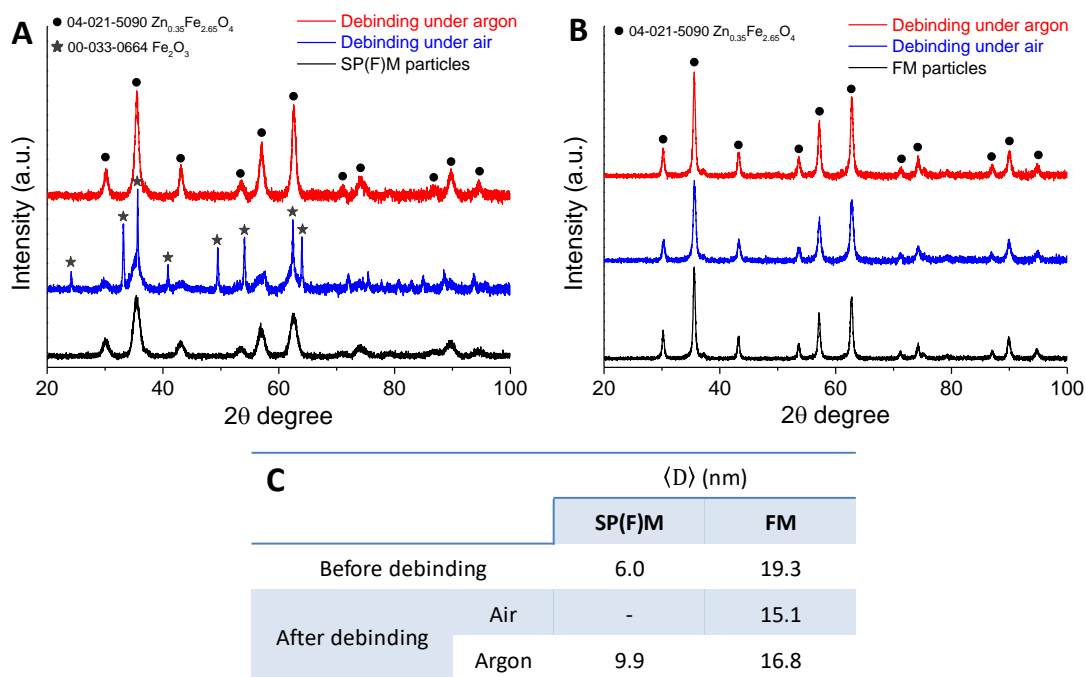
### III.2.2. Choice of the annealing atmosphere

First of all, the annealing atmosphere has an effect on the oxidation of particles, that is why it has to be carefully chosen. The first tests of thermal treatment have been performed under air, and a color change from black to rust has been noticed each time. This color change is not observed under an argon atmosphere (Figure II-57) and could be attributed to the oxidation of the surface of the layer.



**Figure II-57. Observation of a color change between a SP(F)M coating annealed under air and argon atmosphere during 24h at ~100 °C.**

The previous assumption is verified by X-ray diffraction analysis on SP(F)M and FM powders after debinding at 450 °C under air and argon atmospheres (Figure II-58). The transition between magnetite and maghemite is difficult to detect from XRD diffractometers. Nevertheless, the presence of a secondary phase which coincides with a  $\text{Fe}_2\text{O}_3$  phase (PDF sheet 00-033-0664) is discovered in addition of the pure  $\text{Zn}_{0.35}\text{Fe}_{2.65}\text{O}_4$  phase (PDF sheet 04-021-5090) for SP(F)M particles (Figure II-58.A). This supplementary phase is not revealed under argon and is also not observed at all in the case of FM particles (Figure II-58.B).



**Figure II-58.** Effect of the annealing atmosphere on the debinding of SP(F)M (A) and FM (B) powders at 450 °C. The table summarizes the crystallite sizes before and after debinding from Scherrer equation.

The color change and the apparition of a  $\text{Fe}_2\text{O}_3$  phase for SP(F)M particles raise the issue of the particle oxidation under air. Indeed,  $\text{Fe}^{2+}$  ions are sensitive to oxidation, which is consistent with the work of S. Ayyappan *et al.* [46] where they have evidenced the formation of maghemite in the case of thermal treatment of magnetite particles under air between 250 and 350 °C, and even the presence of hematite from 600 °C. As a consequence, all of the annealing cycle is performed under argon. Regarding the particle size (Figure II-58-C), it appears that an annealing under argon at 450 °C does not necessarily make the particle grow, especially for FM powders.

### III.2.3. Study of the thermal decomposition of surfactants and nanoparticles

The thermal degradations of surfactants and nanoparticles were previously studied in order to determine the lower temperature at which all of the organics are removed from the sample (debinding temperature) and to better understand the surfactant removal from coatings at this stage.

#### III.2.3.A. Decomposition of OAm and OA

On the one hand, the thermal decomposition of OAm and OA is analyzed by a Thermogravimetric/Differential Thermal Analyzer (TG-DTA) analysis coupled to mass spectroscopy under an inert atmosphere of helium (Figure II-59).

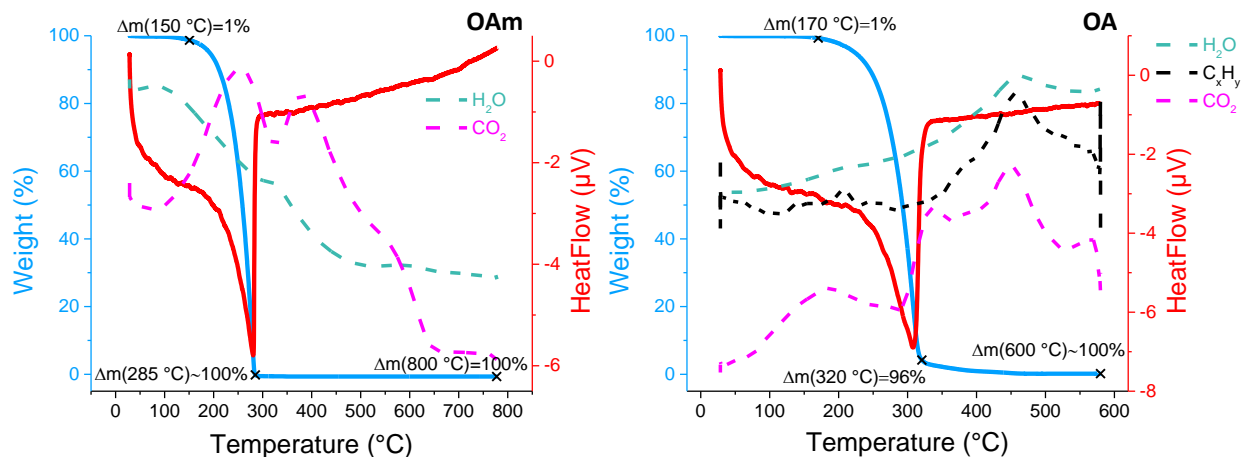


Figure II-59. TG-DTA and mass spectroscopy curves of OAm and OA under helium.

The thermal degradation of OAm is fast and takes place in two phases: a slight dehydration of the molecule at 150 °C with a weight loss of 1% and a massive weight loss of 99% corresponding to an exothermic peak at 285 °C with a departure of CO<sub>2</sub>.

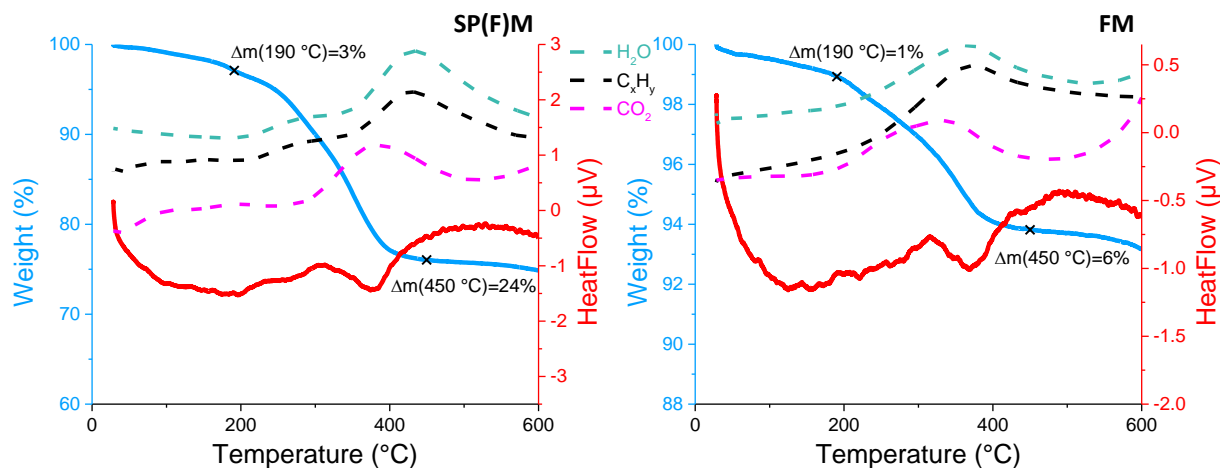
OA is decomposed in three steps. A dehydration step occurs at 170 °C with a weight loss of 1%. The two other weight losses (the first between 170 and 320 °C, the second between 320 and 600 °C) could be attributed to two different kinds of bonds in the molecule which decompose at different temperatures. This assumption is deeply investigated in the next section (III.2.3.B). An exothermic peak at 320 °C with a weight loss of 96% indicates that most of the molecule is decomposed at this temperature.

As a conclusion, the thermal degradation of OAm is faster than OA. OAm groups might be eliminated before OA groups in the study of the particle decomposition. All of the organics are removed at 600 °C. The thermal degradation of SP(F)M and FM are thus examined from room temperature to 600 °C in the following section.

### III.2.3.B. Decomposition of SP(F)M and FM

On the other hand, Figure II-60 displays the thermal decomposition of SP(F)M and FM particles by TG-DTA analysis under helium until 600 °C.





**Figure II-60.** TG-DTA and mass spectroscopy curves of SP(F)M and FM particles under helium until 600 °C.

The same trend is observed for SP(F)M and FM particles. The thermal decomposition occurs in three steps:

- A first loss between 100 and 190 °C attributed to residual water or solvents: weight losses of 3% and 1% for SP(F)M and FM, respectively.

and then the degradation of the organic shell which takes place with a second weight loss between 190 and 450 °C corresponding to 21% and 5% for SP(F)M and FM, respectively. This second weight loss is ascribed to two different contributions:

- A first departure is attributed to the OAm groups due to the lower temperature decomposition of OAm in comparison with OA around 285 °C (Figure II-59). This observation is in agreement with a previous study of a thermo-gravimetric analysis of Mn-Zn nanoparticles coated with OAm with the illustration of the physical absorption of OAm between 280 and 340 °C [47]. The decomposition of OA is divided in two steps with a first one at the same temperature as OAm groups. Indeed, the hydrocarbon chains of OA firstly decomposes because these groups are the weakly physically bound functional groups of the overall molecule [46] [48].
- Hence, the last removal corresponds to the decomposition of the chemically absorbed OA groups above 300 °C.

As an explanation, OA molecules end with a carboxylate group ( $\text{COO}^-$ ) which interferes and grafts onto the particle surface through the metallic ions, namely iron in this case (Figure II-61). As previously mentioned, two kinds of bonds are present: the hydrocarbon chain (C-C and C=C) which decomposes at first and the bond between the headgroup of the molecule and the particle surface which is stronger and requires higher temperatures to degrade. OA behaves as a bilayer structure which explains its two-step thermal decomposition [49].



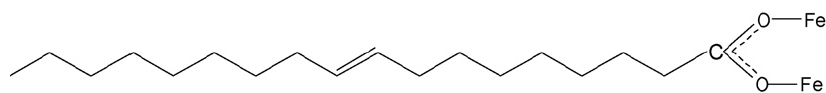


Figure II-61. Scheme of the interaction between carboxylate group and particle surface. From Zhang *et al.* [49].

This behavior is most discernable in Figure II-62 which shows the derivative of the weight loss under helium for SP(F)M and FM particles. Three weight losses are distinguished: one around 190°C for the dehydration of the surfactants, and two other around 280 and 350 °C attributed to the two-step decomposition of the oleic acid and also to the contribution of OAm groups at 280 °C. The same behavior is proposed by L. Zhang *et al.* [49] with oleic acid coated magnetite particles.

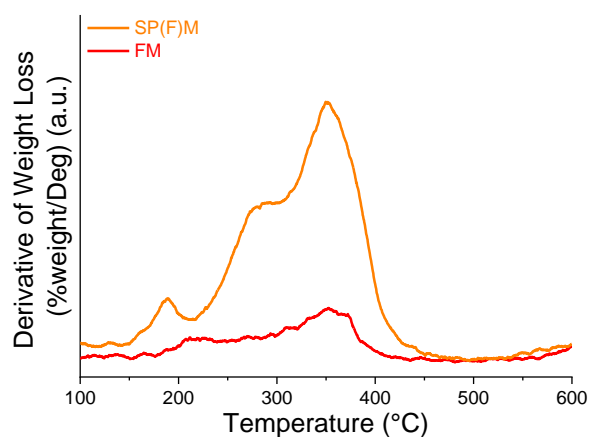


Figure II-62. Derivative of the weight loss for SP(F)M and FM particles under helium.

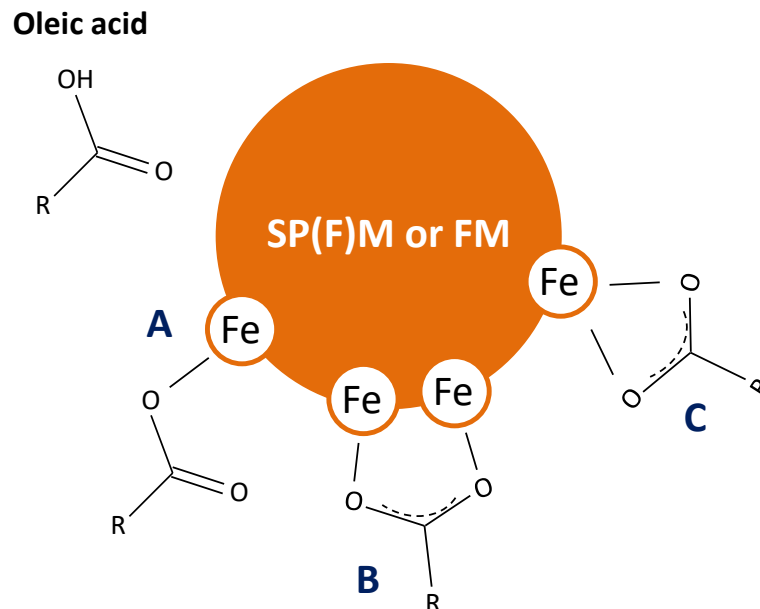
### III.2.3.C. Composition of the organic shell around particles

The thermal degradation of particles does not allow to determine the residual respective amounts of a surfactant from another. The decomposition temperatures of OAm and OA correlated to the ones of the particles enable to clearly identify the two-step decompositions of OA. However, as OAm decomposes at the same temperature as the first OA binding groups, it is hard to determine if OAm groups are bound on the particle surface. This question is justified as some previous researches have demonstrated that OAm groups do not bind with iron during particle synthesis when coupled with oleic acid. A. Sahraneshin *et al.* have not indicated the presence of amine groups onto the particle surface of yttrium aluminum garnet (YAG) particles synthesized in a media with OAm and OA, whereas carboxyl groups from OA are chemically adsorbed on the particle surface. They have also mentioned that OAm could serve as a Lewis base when interacting with OA in the reaction media [242]. Additionally, they have confirmed OAm acts as a growth inhibitor of the particle in some crystallographic directions (Chapter I). J. Luo *et al.* have also exposed the adsorption of OA groups on V and Fe atoms in the elaboration of PtVFe particles while OAm groups only graft with Pt atoms [51].

The action of OAm as a Lewis base is the subject of a recent qualitative model established by R. A. Harris *et al.* in their study of OAm/OA coated particles [52]. The grafting of OA

molecules on an iron oxide spinel particle leads to the deprotonation of its carboxyl groups in  $\text{COO}^-$ , involving the release of a  $\text{H}^+$  in the system.

OA and OAm are considered as two different types of molecules because of the way they could bind to a particle surface. In the case of OA, there are three possibilities for interactions between the head of a carboxylate group and iron atoms: monodentate, bidentate (bridging or chelating) (Figure II-63).



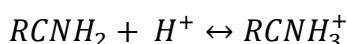
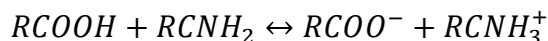
**Figure II-63. Interaction of oleic acid (COOH) with particles through monodentate (A), bridged (B) and chelating (C) configurations.**

The monodentate configuration implies only one oxygen atom bonded to a metallic one. In the case of the involvement of two oxygen atoms (bidentate), the configuration is called “bridged” or “chelating” when the binding is made with two (bridged) or one (chelating) metal atom(s) [53] (Figure II-63).

Following the work of L. Zhang *et al.* [49], the interaction between a carboxylate group and iron atoms should correspond to the chelating bidentate type with the creation of a covalent bond.

However, carboxyl groups have a stronger affinity with iron than amines. Indeed, in the case of OAm with an amine headgroup ( $\text{RNH}_2$ ), supposing the molecule binds on the particle surface, there is only one possibility of coordination to the particle surface: a monodentate one with a single bond (N-Fe) to the surface [53] [54]. Furthermore, the probability of bonding is better for a carboxyl group to bind with  $\text{Fe}^{2+}$  and  $\text{Fe}^{3+}$  atoms at the particle surface than for an amine one due to the higher number of interaction possibilities in the case of OA groups with iron atoms. The mechanism of binding between OAm and the particle surface remains unclear and only one carboxylate bond could be formed by OA with the particle surface at a time, meaning it cannot couple with OAm at the same time [52].

Through dynamic simulations of molecular mechanics, R. A. Harris *et al.* [52] explain that OAm (CNH<sub>2</sub>) and OA (COOH) groups form an acid-base complex in the medium during synthesis. The acid-base formation comes from the generation of free protons during the deprotonation of carboxyl groups of OA in COO<sup>-</sup> when adsorbing onto the particle surface. These free protons are readily absorbed at the same time by OAm groups to form RCNH<sub>3</sub><sup>+</sup>, whence the importance of the pH of the medium (Equation II-6).



An excess of free protons in the media will provoke some desorption of carboxyl groups from particle surfaces, as expected in the cleaning attempt by esterification. Thus, the presence of OAm stabilizes the system by acting as a proton acceptor. A balance has to be found regarding OAm/OA quantity in order to favor carboxyl adsorption and the acid-base formation [52] [55]. Moreover, it appears that the OAm/OA coupling enhances the thermal stability of the particle phase [56] as OAm boosts the grafting of carboxylates groups on the particle surface.

A useful method to verify the assumptions of R. A. Harris *et al.* [50] is to study the FTIR spectra of SP(F)M and FM particles in the 1300-1700 cm<sup>-1</sup> area (Figure II-64).

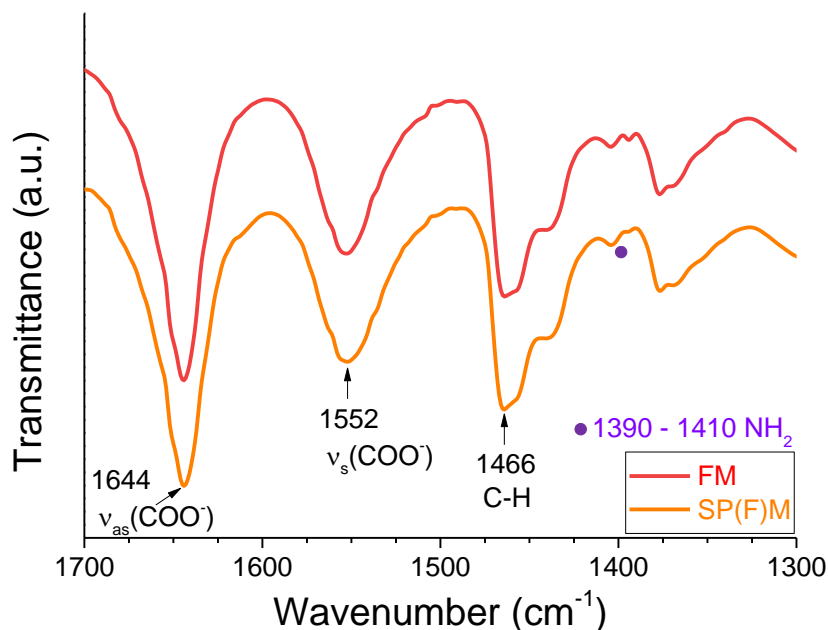


Figure II-64. Focus on the 1300-1700 cm<sup>-1</sup> area of FTIR spectra for SP(F)M and FM particles directly after synthesis.

The peaks characteristic of the OA grafting on the particle surface are displayed at 1466 cm<sup>-1</sup> for the C-H bending ( $\nu_a(\text{CH}_3)$ ,  $\nu(\text{CH}_2)$ ), and at 1552 and 1644 cm<sup>-1</sup> attributed to symmetric and asymmetric COO<sup>-</sup> stretching bands, meaning that the carboxylate binds to the particle

surface through  $\text{Fe}^{3+}$  atoms [57]. The nature of the coordination mode of carboxylate groups can be determined through the spacing between asymmetric and symmetric bands. The value being of  $92\text{ cm}^{-1}$ , the interaction between a carboxylate group and iron atoms corresponds to the chelating bidentate mode [49]. Indeed, if this value is between  $200$  and  $320\text{ cm}^{-1}$ , the coordination type of the carboxylate group is monodentate, between  $140$  and  $190\text{ cm}^{-1}$ , bridging bidentate and below  $110\text{ cm}^{-1}$ , chelating bidentate [49]. A OAm grafting through  $\text{NH}_2$  groups to  $\text{Fe}^{3+}$  atoms should appear at  $1393\text{ cm}^{-1}$  according to J. Vidal-Vidal *et al.* [57]. As a consequence, bands between  $1390$  and  $1410\text{ cm}^{-1}$  are observed and could be attributed to OAm grafting through  $\text{NH}_2$  groups to  $\text{Fe}^{3+}$  [57]. In such a way, the possibility of an OAm grafting cannot be completely ruled out even though the band amplitudes are low. Nevertheless, the mechanism of an acid-base formation seems to prevail.

As a conclusion, the assumption of an organic shell only constituted of OA thanks to their carboxylate head around particles is made.

#### III.2.3.D. Estimation of the thickness of the organic shell around particles

Figure II-65 correlates the weight losses as a function of the temperature until  $600\text{ }^\circ\text{C}$  of OAm, OA, SP(F)M and FM particles. As previously mentioned, all of the organic species are removed at  $600\text{ }^\circ\text{C}$  and the weight losses are of 24 and 6% for SP(F)M and FM particles, respectively.

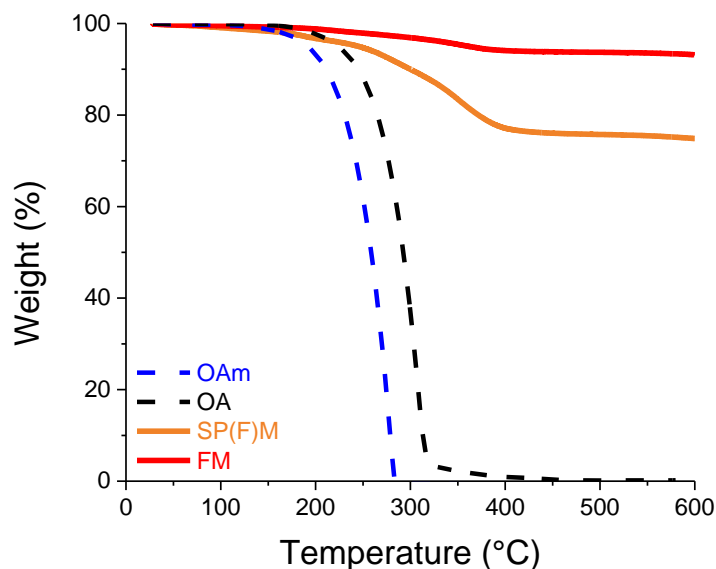


Figure II-65. Comparison of TG curves of OAm, OA, SP(F)M and FM particles under helium.

Considering the particles are only covered of carboxylates and are perfect spheres, some calculations can be performed in order to estimate the thickness of the organic shell at the particle surroundings. According to Zhang *et al.* [49], the carboxylate head has a surface area of  $24\text{ \AA}^2$  and the length of the whole OA molecule (oleate) is  $2\text{ nm}$ , which gives a  $480\text{ \AA}^3$  volume for this molecule approximated as a cylinder.

Figure II-66 summarizes the calculations to evaluate the number of carboxylate layers around particles. The particle surfaces and volumes ( $S_P$ ,  $V_P$ ) are calculated from their radius ( $R_P$ ). The computation of the mass of a single particle ( $m_P$ ) is obtained by using the density of the  $Zn_{0.35}Fe_{2.6}O_4$  composition ( $5.236 \text{ g/cm}^3$ ) in the PDF sheet 04-021-5090. From  $m_P$ , the number of particles per sample ( $N_P$ ) is expressed by removing the organic percentage. Then, the number of OA molecules (oleates) required to form an organic layer covering the overall particle surface ( $N_{OA \text{ molecules/layer}}$ ) derives from  $S_P$  and the surface of a carboxylate head ( $24 \text{ \AA}^2$ ). Finally, the masses of an OA layer ( $m_{OA \text{ layer}}$ ) resulted from  $N_{OA \text{ molecules/layer}}$  and OA density ( $0.898 \text{ g/cm}^3$ ), and the quantity of OA per particle ( $m_{OA/P}$ ) obtained from the weight losses measured by TG-DTA analysis and  $N_P$ , allow to estimate the number of OA (oleate) layers around particles.

	$R_P$	$S_P$	$V_P$	$m_P$	$N_P$	$N_{OA}$ molecules/ layer	Weight loss	$m_{OA/P}$	$m_{OA \text{ layer}}$	$N_{OA}$ layer
	$\text{\AA}$	$\text{\AA}^2$	$\text{\AA}^3$	mg	-	-	%	mg	mg	-
<b>SP(F)M</b>	31	12076	124788	$6.5 \times 10^{-16}$	$1.1 \times 10^{16}$	503	24	$2.1 \times 10^{-16}$	$2.2 \times 10^{-16}$	<b>0.95</b>
<b>FM</b>	112	157633	5884949	$3.1 \times 10^{-14}$	$2.8 \times 10^{14}$	6568	6	$2.0 \times 10^{-15}$	$2.8 \times 10^{-15}$	<b>0.70</b>

**Figure II-66. Calculation of the number of OA layer ( $N_{OA \text{ layer}}$ ) around particles.**

Thus, SP(F)M and FM are surrounded with approximately one layer of oleates. The number of organic layers decreases with the increase of the particle diameter. If SP(F)M particles are almost entirely covered with carboxylates ( $\sim 1$  layer), FM particles possess bare zones (0.70 layer) indicating these particles are less well functionalized.

This trend is consistent with Zhang *et al.* [49] and S. Ayyappan *et al.* [58] who explain that the packing density of organics around particle decreases with increasing particle size. This phenomenon is explained in the literature by the fact that more surfactant is adsorbed on smaller particles to compensate the higher Van Der Waals interactions. It also justifies why the larger particles are more difficult to disperse, besides the existence of magnetic interactions between FM particles and not SP(F)M particles (Chapter I).

In the case of FM particles, the number of oleate layers is quite approximate since they present a “raspberry” morphology of particles instead of perfect spheres assumed in the computation. The estimation of the organic weights through TG curves will enable to correct the error induced on the magnetic measurements due to the unknown proportion of organics around particles (Chapter IV).

### III.2.4. Optimization of the debinding

As previously mentioned, the thermal treatment of coatings is composed of two steps: a debinding and a sintering. The debinding stage is explored in the first instance. Coatings elaborated with SP(F)M particles will be written SP(F)M coatings in the remainder of the study, and similarly with FM particles.

### III.2.4.A. Experimental protocol

The overall annealing requires a tube oven perfectly closed to isolate and confine the samples in a pure argon atmosphere (Figure II-67).

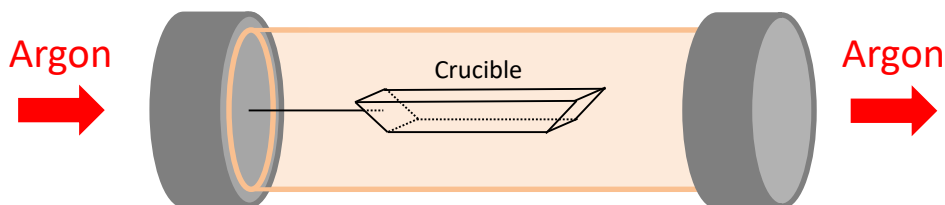


Figure II-67. Experimental scheme of the set-up of the tube oven under an argon flow of 2.5 L/min.

The following temperature profile is optimized after multiple tests (Figure II-68). The debinding lasts approximately 2 days.

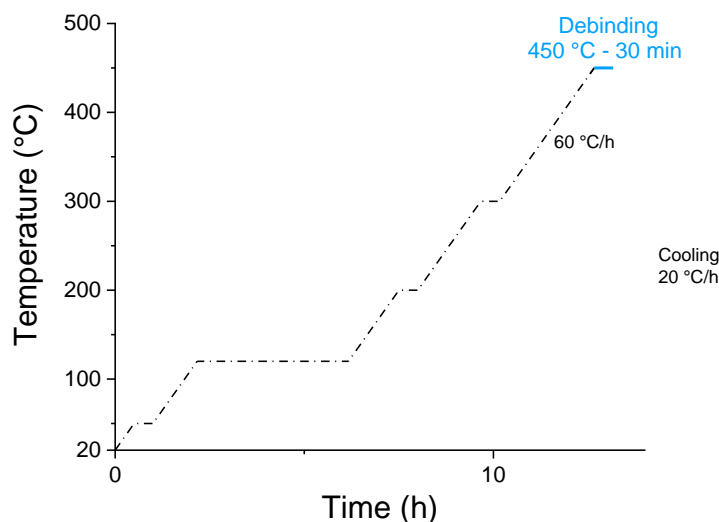
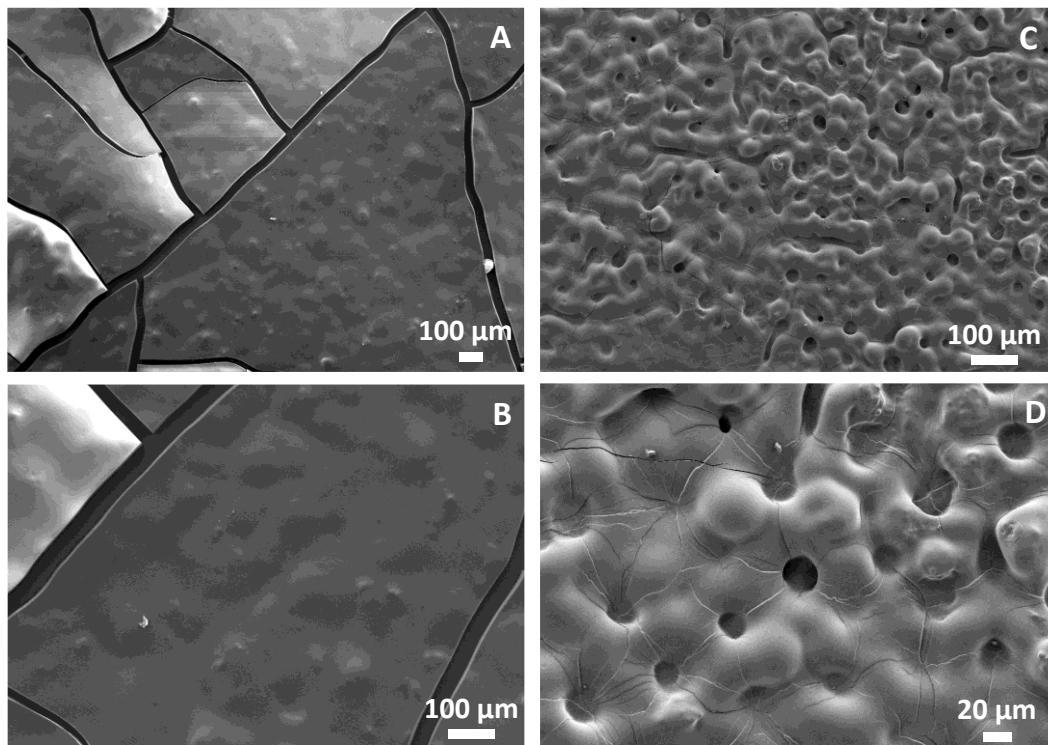


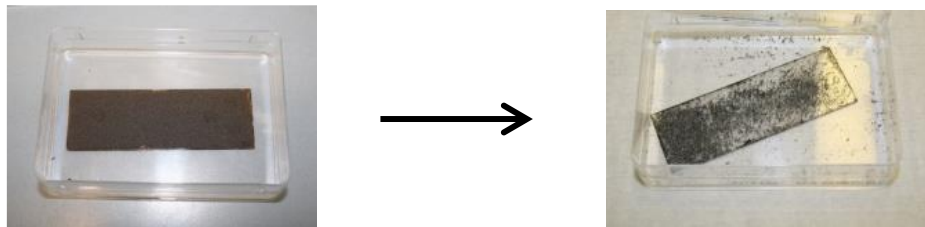
Figure II-68. Temperature profile of the debinding step.

The requirement is to remove the remaining organics from coatings after particle cleanings and dispersion, and to provide at the same time the adherence of the coating on the substrate by avoiding any cracking, bubbling or matter debonding. The bubbling is generated by the removal of organic residues from the coating layers. It can evolve to cracking (Figure II-69).



**Figure II-69.** Examples of cracks (A, B) and bubbling (C, D) at the surface of SP(F)M coatings (SEM-FEG).

Typically, fast temperature ramps induce too harsh conditions of heating, creating material losses with partial debonding of the puzzled film (Figure II-70).



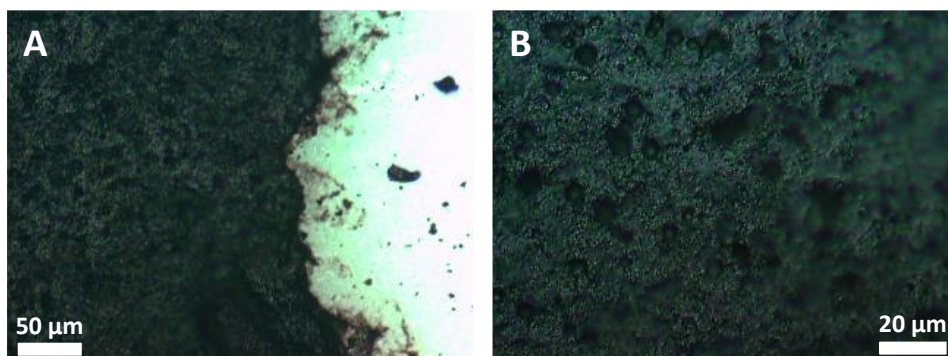
**Figure II-70.** Incidence of a fast temperature ramp (300 °C/h) on coatings.

A slow temperature ramp is needed to keep the integrity of the film, justifying the smooth temperature conditions in Figure II-68.

#### *III.2.4.B. Influence of the debinding on the surface condition and chemical composition of coatings*

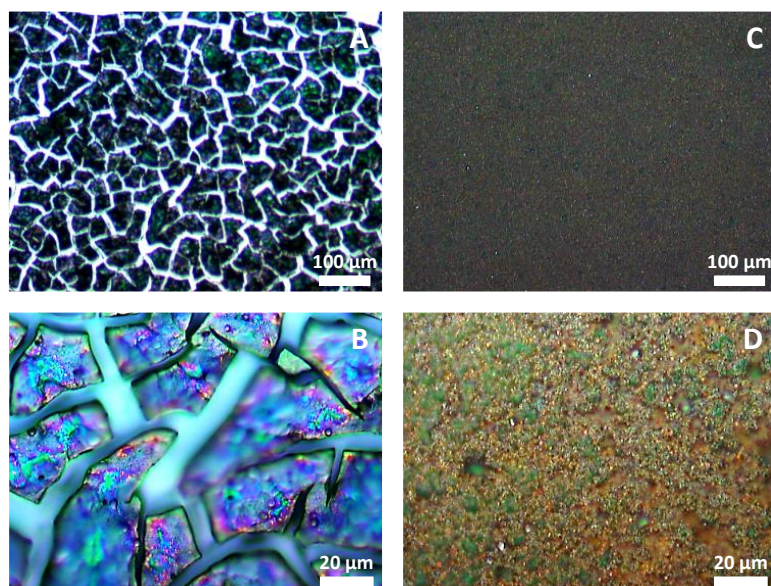
The surface of coatings is observed just after processing and before thermal treatment to detect the surface state. The coatings are wet with several pierced blisters on the surface due to the fast hexane evaporation during and after airbrushing (Figure II-71).





**Figure II-71. Optical microscopy of FM coatings before annealing (4 applications by airbrushing).**

The influence of the debinding at 450 °C with the protocol previously detailed (Figure II-68) on the coating surface is inspected in Figure II-72 by optical microscopy. The coating behavior depends on the particle size used in the dispersion for the airbrushing process. SP(F)M particles induce deep cracks in coatings (Figure II-72.A-B) with matter debonding from the substrate whereas FM particles do not crack coatings (Figure II-72.C-D) during organic removal. The films obtained with FM particles look dense in appearance after debinding.



**Figure II-72. Optical microscopy of SP(F)M (A, B) and FM (C, D) coatings after debinding under argon.**

In addition, chemical mappings of a piece of a SP(F)M coating after debinding is exhibited in Figure II-73 to observe the chemical homogeneity of coatings.



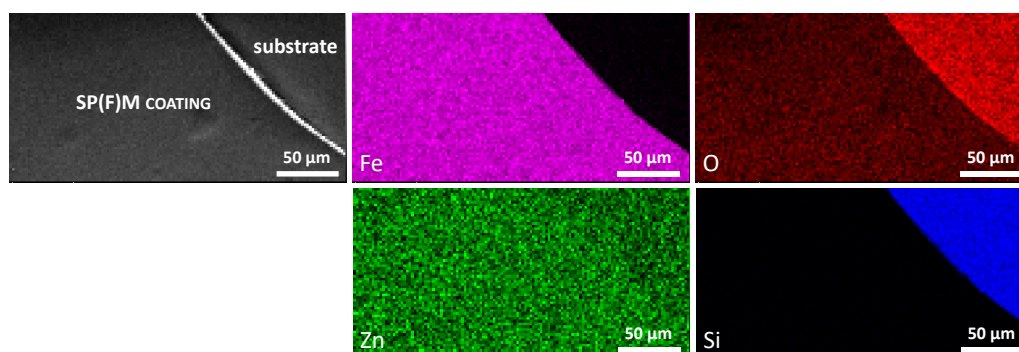


Figure II-73. Chemical mappings of a SP(F)M coating on a glass substrate after debinding.

Iron and zinc are well distributed on the surface. Coatings seem to be homogeneous in terms of chemical composition. The Zn/Fe ratio estimated by STEM-EDX is equal to 0.13 which is close to the theoretical one (0.15).

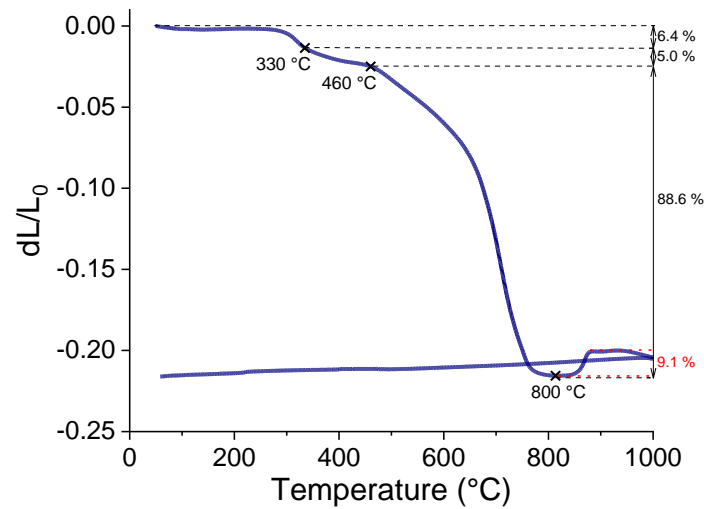
### III.2.5. Study of sintering

Once the organics are removed, the coatings need to be sintered to increase their density.

#### III.2.5.A. Temperature of sintering

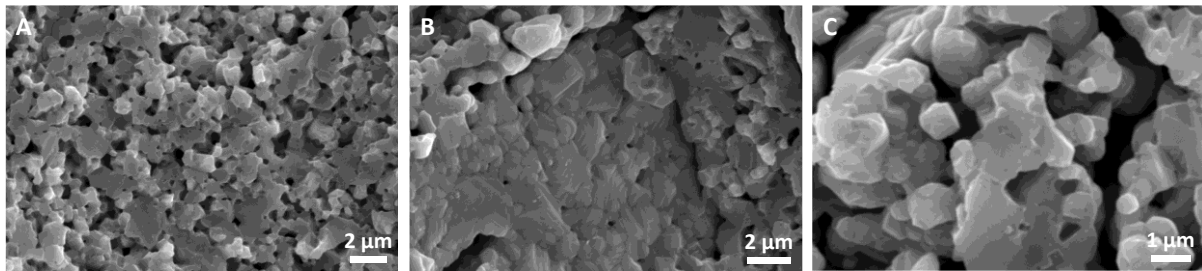
The sintering is a consolidation process of a powdered material under temperature without melting. During the procedure, the microstructure rearranges by matter displacement between grains, engendering grain bonding and a reduction of the porosity inside the material. A shrinkage of the material is characteristic of the sintering. Four processes occur during sintering and not necessarily separated: a consolidation with the formation of bridges between particles, a densification with the porosity reduction and shrinkage of the material, the granular growth and physico-chemical reactions within the material.

The temperature of sintering has to be determined precisely to apply a suitable sintering procedure to the material. A dilatometry measurement of a pellet constituted of FM particles depicts the dimensional variation of the pellet as a function of the temperature (Figure II-74). Three dimensional changes are noticed: the first two assigned to organic departures (50-330 °C and 330-460 °C), and the last one between 460 and 800 °C attributed to the sintering process with grain bonding, porosity reduction. A positive dimensional variation is encountered above 800 °C. This phenomenon might be due to different reasons like a phase change, oxidation or crystallization above 800 °C. As a consequence, the sintering temperature is chosen just below 800 °C, namely at 770 °C. The final phase stays stable during cooling.



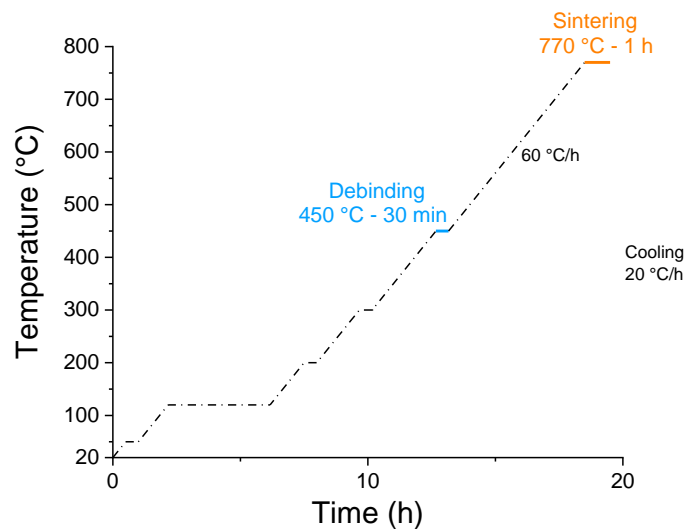
**Figure II-74.** Dilatometry curve of a pellet of FM particles heated from room temperature to 1000 °C under argon.

Figure II-75 exemplifies the sintering principle of a pellet constituted of FM particles through the presence of grain boundaries after mechanism of grain bonding, particle growth and reduction of porosity after sintering at 1000 °C.



**Figure II-75.** SEM images of a pellet of FM particles annealed at 1000 °C.

In the same manner as for the debinding protocol, the sintering step is added with a slow temperature rate of 60 °C/h (Figure II-76). The overall process lasts two and a half days including the cooling. The important factors at this stage are the grain size which does not exceed 3 μm (Chapter I) and the porosity which must be reduced as much as possible.

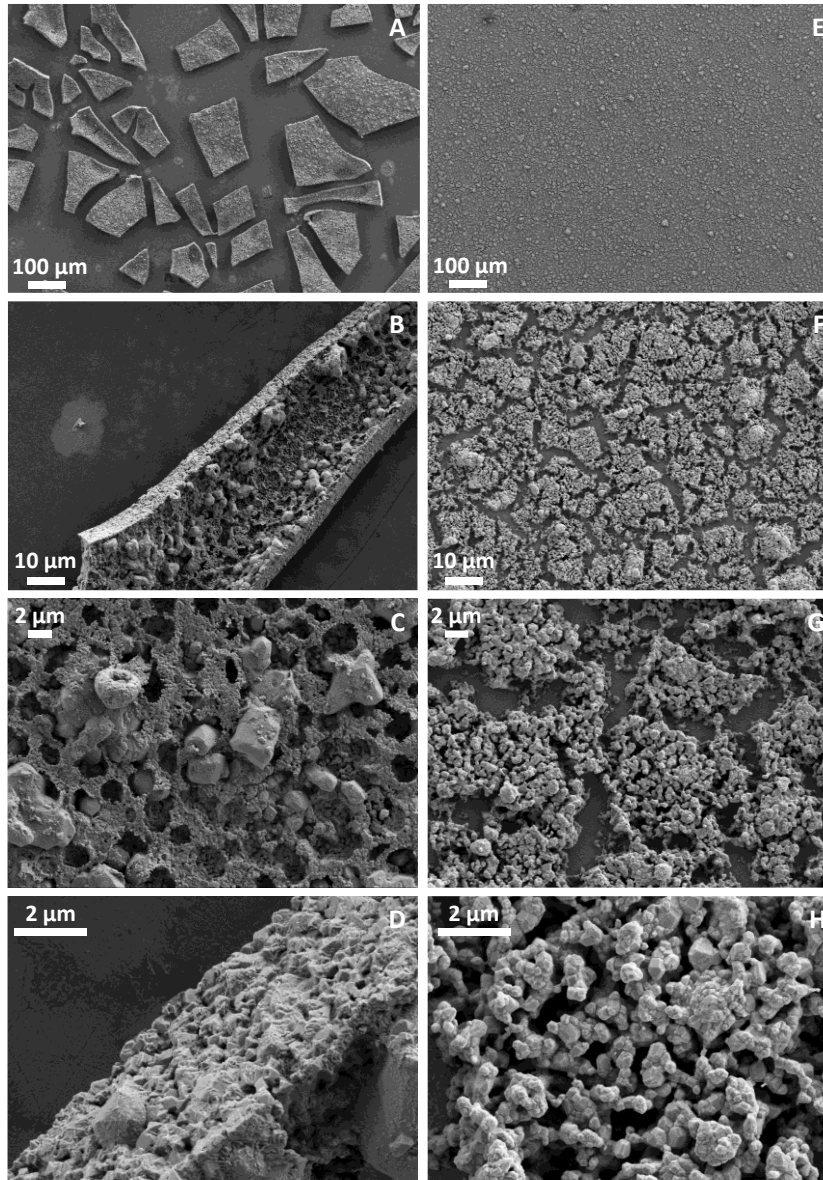


**Figure II-76. Temperature profile of thermal treatments including a debinding and a sintering step.**

### *III.2.5.B. Influence of the sintering on the surface condition and density of coatings*

The sintering at 770 °C is compared for SP(F)M and FM coatings (Figure II-77) elaborated with 10 applications of airbrush, equivalent to 5 go and return trips of the nozzle onto the substrate. Regarding SP(F)M coatings, the films are still cracked (Figure II-77.A-B) with the birth of craters (Figure II-77.C-D) on the surface and in the thickness of the pieces. Cracking is firstly induced by the debinding step and remains at the sintering step. The pieces of the film are too far from each other to induce any consolidation process. SP(F)M particles are not adapted for the elaboration of dense coatings.

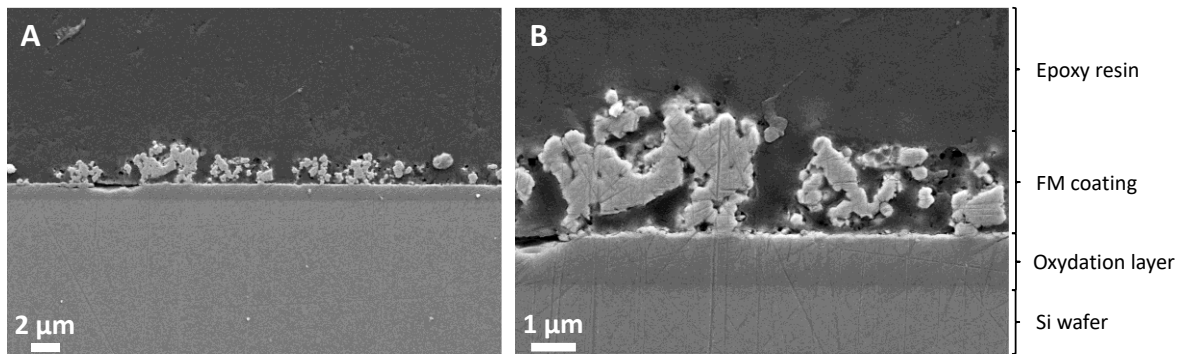
Concerning FM coatings, the surface looks not cracked at long range (Figure II-77.E). However, cracks are undoubtedly distinguished with higher magnifications (Figure II-77.F-G). The coating surface looks similar to a patterned layer with a network of particle clusters separated with cracks with a width of approximately 2  $\mu\text{m}$ . The particles in H-inset look not as sintered as in the case of the pellet at 1000 °C, leading to a large amount of porosity in the films.



**Figure II-77. SEM-FEG at various magnifications of SP(F)M (A-D) and FM (E-H) coatings after sintering under argon.**

This porosity is also observable in the cross-section view of the FM coating embedded in an epoxy resin (Figure II-78). Some loss of material comes from the sample preparation during the polishing cycles of the resin. However, the major proportion of the porosity was present before polishing and is hence attributed to the sintering. The thickness of the film seems to be 4 μm.

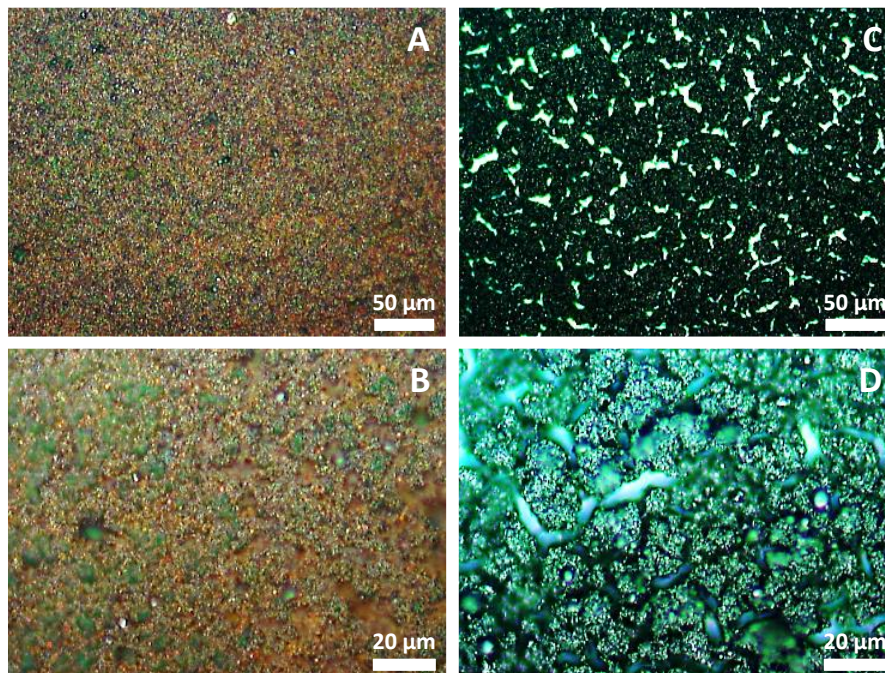




**Figure II-78.** Cross-section view of an epoxy-coated FM film (SEM-FEG).

An estimation of the porosity of coatings through the weight loss of samples before and after thermal treatment indicates a porosity of approximately 50%. The significant porosity will not lead to the desired multiband behavior of coatings (Chapter I).

To conclude, Figure II-79 confronts FM coatings before and after sintering under argon. The sintering step is responsible for the birth of a crack network in the coatings. The cracks could be due to constraints generated by the shrinkage in the film, amplified by the relatively large thickness of 4  $\mu\text{m}$ . Moreover, a color change proceeds between debinding and sintering. Indeed, the coating turns brown to black which means a successful sintering [59].



**Figure II-79.** Comparison of FM coatings on silicon wafers after debinding (A, B) and sintering (C, D) under argon (optical microscopy).

The goal of the study being to obtain the magnetic multiband behavior of coatings through the permeability spectra (Chapter I), different strategies are tested in order to increase the density of FM coatings.

### III.2.5.C. Alternatives to enhance the coating density

Some solutions are experimented to enhance the coating density: the change of substrate, the addition of layers to fill in the holes, the reduction of the coating thickness, the increase of the particle concentration, the decrease of the temperature ramp, and finally the use of two ranges of particle size. In each case, the density is controlled by optical microscopy through a rough visual evaluation of the porosity amount.

#### III.2.5.C.a. Nature of the substrate

In the first instance, two different substrates are adopted: silicon wafer and alumina. FM particles are sprayed onto these substrates and are then subjected to debinding and sintering steps. The coating surfaces are observed and compared in Figure II-80. The surfaces are exactly in the same state with cracks of 2  $\mu\text{m}$  thick. The nature of the substrate does not change the thermal behavior of coatings after sintering.

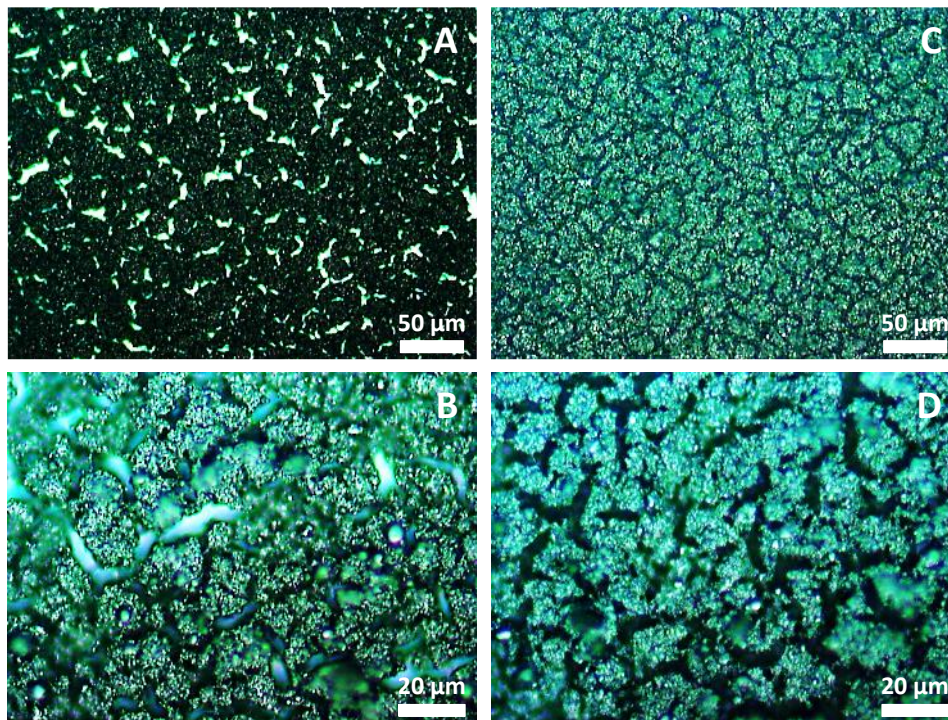


Figure II-80. Comparison between FM particles sprayed on a silicon wafer (A, B) and on alumina (C, D) after sintering under argon (optical microscopy).

#### III.2.5.C.b. Additional layers

The FM coating seen in Figure II-79 is taken as a reference. From this sample, the aim is to fill the cracks with FM particles in order to create bridges between the previous layer with the particles freshly sprayed inside the cracks. The hope is to completely fill in the holes and at the same time to form a continuous film with grain bonding at the crack interface. The goal is to fabricate a compact framework with as few holes as possible. The reference film has been elaborated with 10 applications of airbrush (namely 5 go and return trips) onto the substrate.



The strategy is to spray some FM particle layer onto the actual sintered film in the expectation of plugging the cracks. At first, 4 applications (2 go and return trips) are added to the reference film and then thermal treated. This protocol is repeated twice (Figure II-81). The tests make things worse with the presence of wider cracks with widths of about 10  $\mu\text{m}$  after 14 applications in total. After 18 applications, the cracks are less wide but still present.

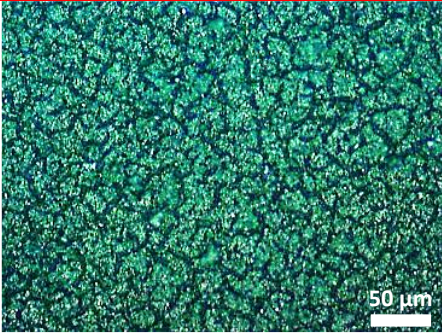
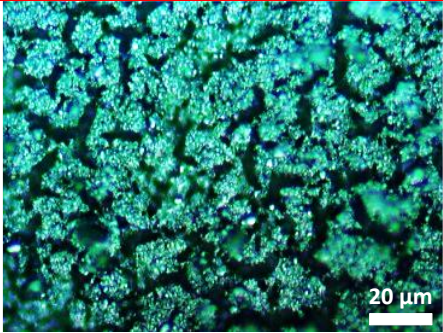
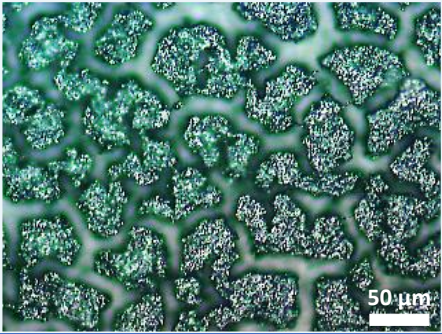
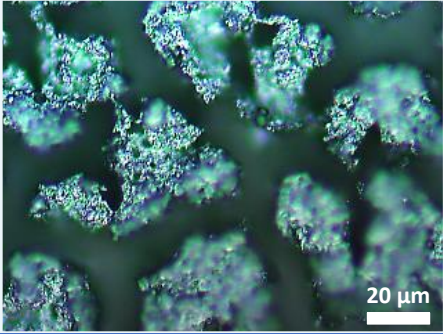
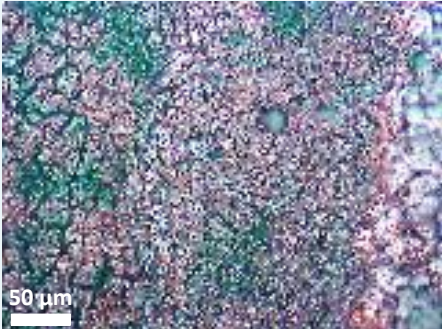
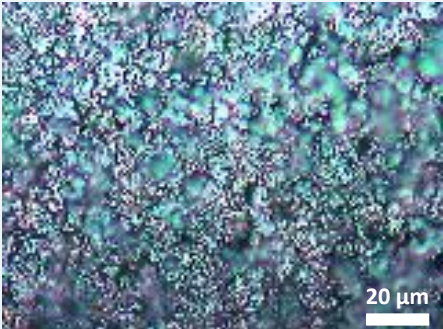
Particle	N	Pictures of optical microscopy	
8 wt% FM	10		
	14	10 passes $\rightarrow$ Thermal treatment	4 passes $\rightarrow$ Thermal treatment
			
18	10 passes $\rightarrow$ Thermal treatment	4 passes $\rightarrow$ Thermal treatment $\rightarrow$ 4 passes $\rightarrow$ Thermal treatment	
			

Figure II-81. Pictures of the coating surface after annealing of additional layers in comparison with the coating reference (red box). N is the number of applications.

It seems difficult to obtain a continuous layer without cracks from a cracked surface in the beginning.

*III.2.5.C.c. Coating thickness*

As a new start, the effect of the coating thickness through the number of applications of the airbrush nozzle onto the substrate is examined and compared to the reference coating (Figure II-82). The reference coating is inside the red box in the Figure II-82.



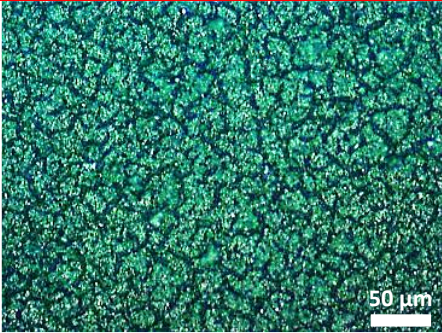
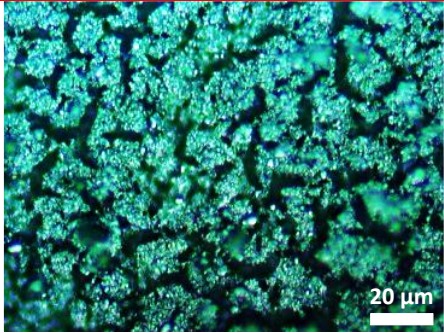

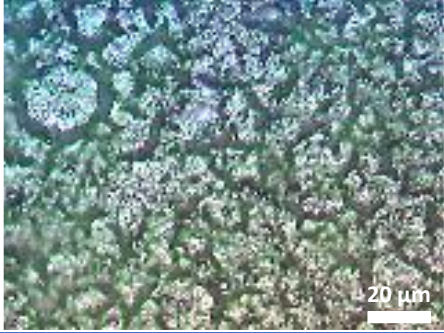
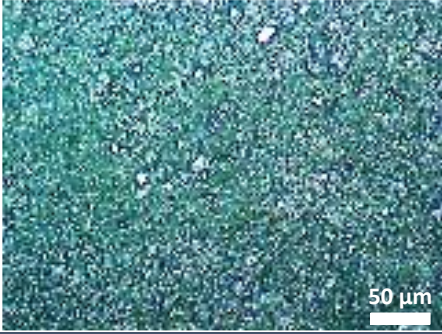
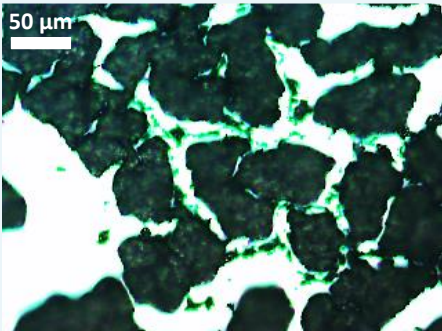
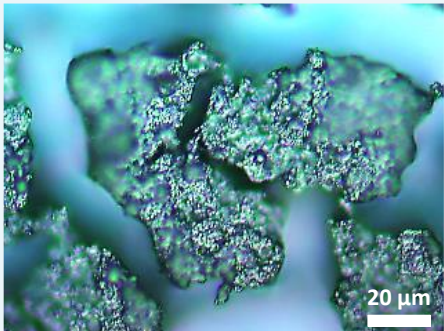
Particle	N	Pictures of optical microscopy	
8 wt% FM	10		
	4		
		8	
8 wt% FM	20		

Figure II-82. Effect of the number of layers on coating surface in comparison with the coating reference (red box). *N* is the number of applications.

In this way, only 4 applications are deposited and annealed (Figure II-82.A). The number is thus reduced from more than twice in comparison with the reference sample. The state of the coating surface after sintering is cracked in exactly the same way as the coating reference

nonetheless. The situation is not better after applying 4 more applications above it (Figure II-82.A).

Moreover, increasing the coating thickness with 20 applications promotes and exacerbates cracking (Figure II-82.B). The cracks are widened to approximately 20  $\mu\text{m}$ .

Additional layers are definitely not a good option to improve the coating density. The porosity of coating is not reduced and is even increased if the coating thickness is too high.

### III.2.5.C.d. Particle concentration

Another alternative is to increase the particle concentration from 8 wt% to 15 wt% in the dispersion media before airbrushing. The number of applications is reduced to 2 and the obtained layer is cracked after sintering (Figure II-83). The increase of the particle concentration before processing worsens the surface cracking of coatings with large cracks of more than 20  $\mu\text{m}$  thick. The assumption is that an increase of the particle concentration in the dispersion will tend to increase the layer thickness, which increases stresses inside coatings when shrinkage occurs during sintering, leading to a worse quality of the film.

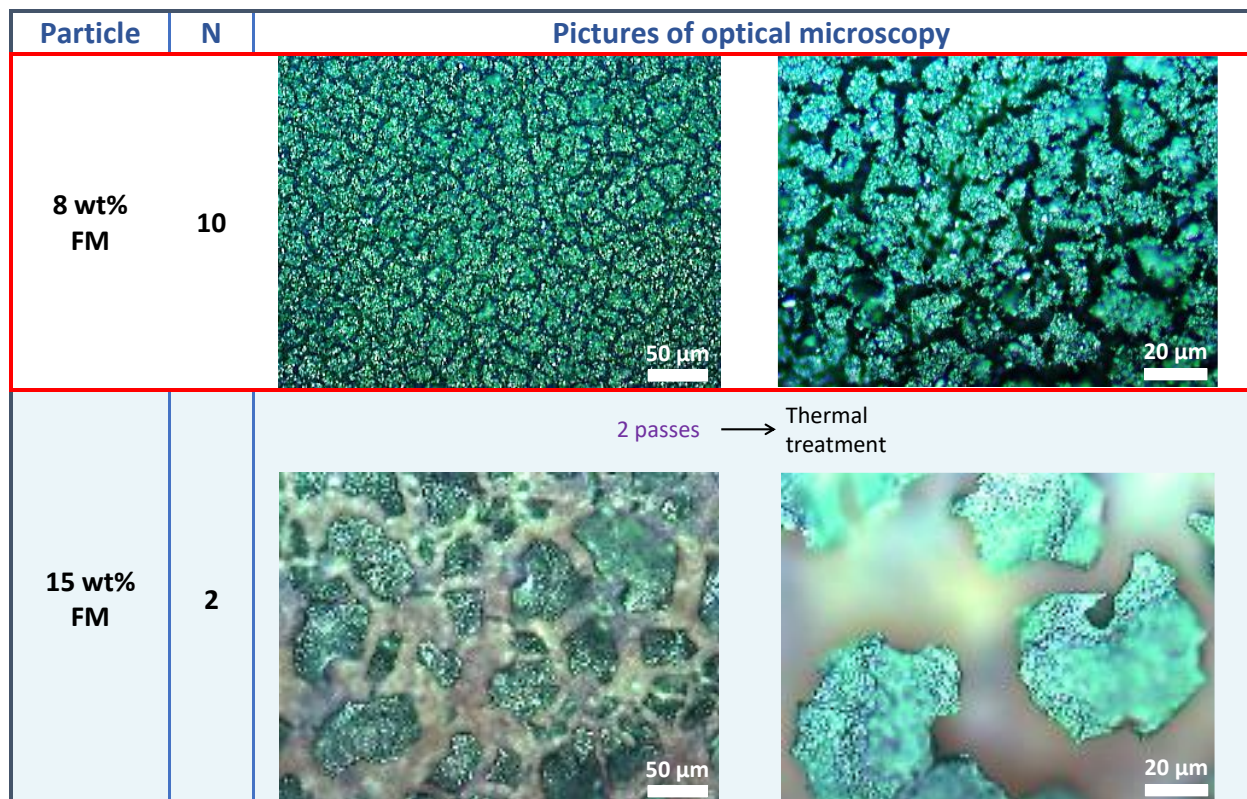


Figure II-83. Effect of the particle concentration on coating surface in comparison with the coating reference (red box).  $N$  is the number of applications.

### III.2.5.C.e. Temperature ramp

After modifying parameters relative to the airbrushing conditions without any sign of reduction of porosity, the thermal procedure is reviewed and especially the temperature ramps.



As previously reported (III.2.4.A), fast temperature ramps easily induce cracking and matter debonding from coatings. As a consequence, the temperature ramp is further slowed from 60 °C/h for the coating reference to 20 °C/h (Figure II-84). The two films in Figure II-84 are elaborated in the same conditions with 10 applications, the only difference lying in the slowdown of the temperature ramp. The coating surface being in the same state, namely with 2 µm width cracks, the decrease of the temperature ramp below 60 °C/h does not seem to impact the coating in any way.

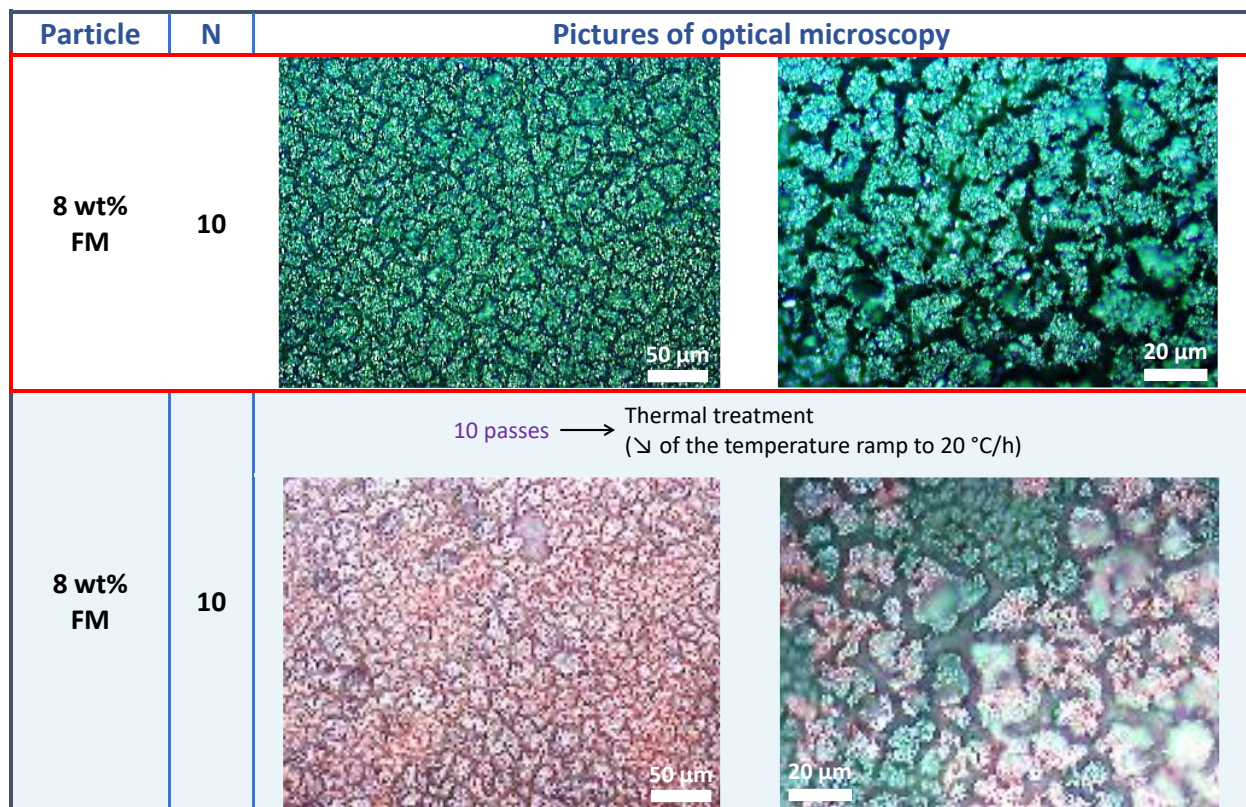


Figure II-84. Effect of a slower temperature ramp on coating surface in comparison with the coating reference (red box). *N* is the number of applications.

### III.2.5.C.f. Use of two ranges of particle size

A last alternative is tested with the use of two ranges of size in the particle dispersion required for spraying. The principle of the method is to mix FM with SP(F)M particles in the airbrushing media in the suitable proportions to increase the packing density up to 80%. According to H. Y. Sohn *et al.* [60], a mixture of 60 wt% of FM particles with 40 wt% of SP(F)M particles, of diameters of  $22.4 \pm 11$  and  $6.2 \pm 1$  nm respectively, is formulated and sprayed on a silicon wafer (Figure II-85).

After the same airbrushing (10 applications) and thermal treatment protocol as for the coating reference, the film displays a lot of cracking at its surface too (Figure II-85). The film looks also a bit more porous than the reference one. This strategy is not working either.

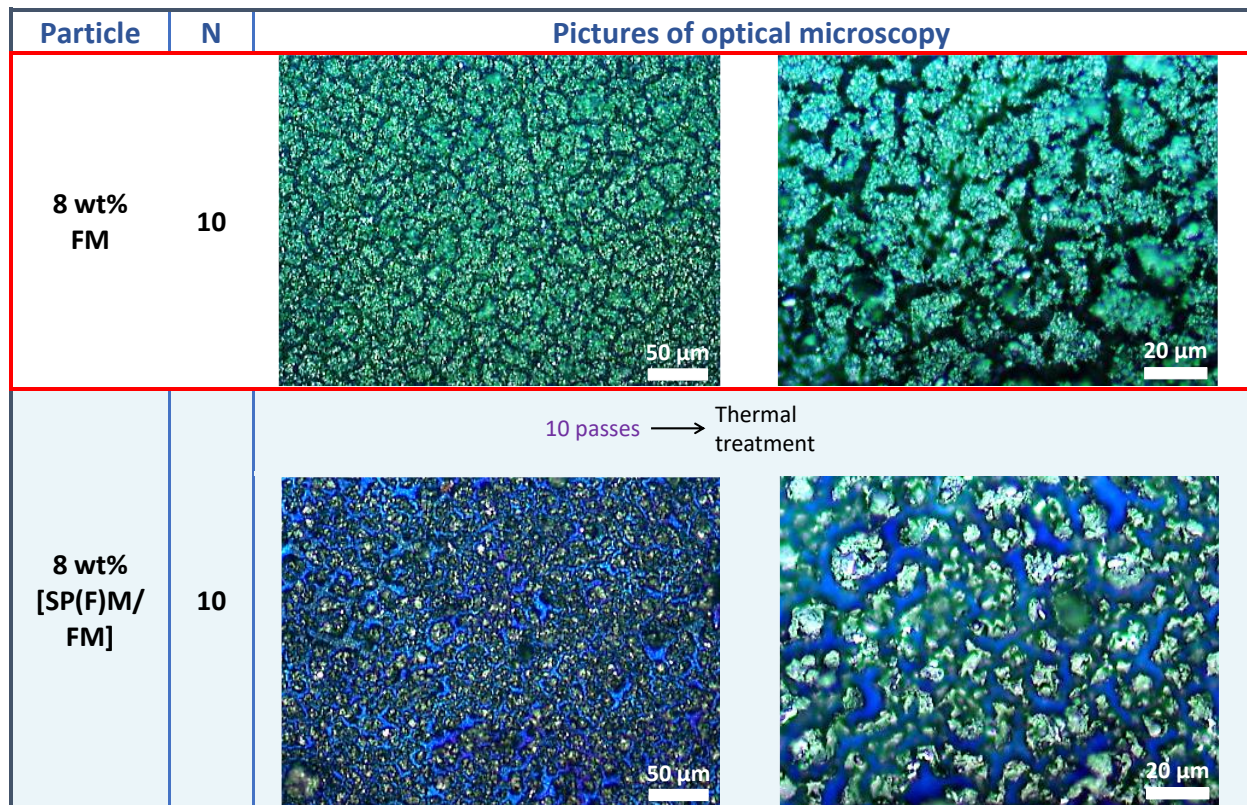


Figure II-85. Effect of the use of two ranges of particle size on coating surface in comparison with the coating reference (red box). N is the number of applications.

### III.2.5.C.g. Conclusion and prospects

All of these approaches including the change of substrate, the addition of layers, the reduction of the coating thickness, the increase of the particle concentration, the decrease of the temperature ramp, and also the use of two ranges of particle size have been unsuccessful. The coating density has not been improved and the best case remains the coating reference with approximately 50% of porosity (Figure II-79).

At the sintering step, it seems that the decrease of volume (of  $3dL/L_0$  from the dilatometric characterization (Figure II-74) meaning 60 % of volume variation) does not take place only through the thickness of the coating, but by the sides of it. As the adherence of the film is good, the shrinkage creates stresses in the film which result in cracking. This has been shown for silica sol gel coating sintering for which a critical thickness of the film of about  $1 \mu\text{m}$  has been computed [61]. M. Bissannagari et al. succeeded to obtain a not cracked sintered NiZn thin film because the thin film has lost the adhesion to the substrate, then allowing to release the stresses [30].

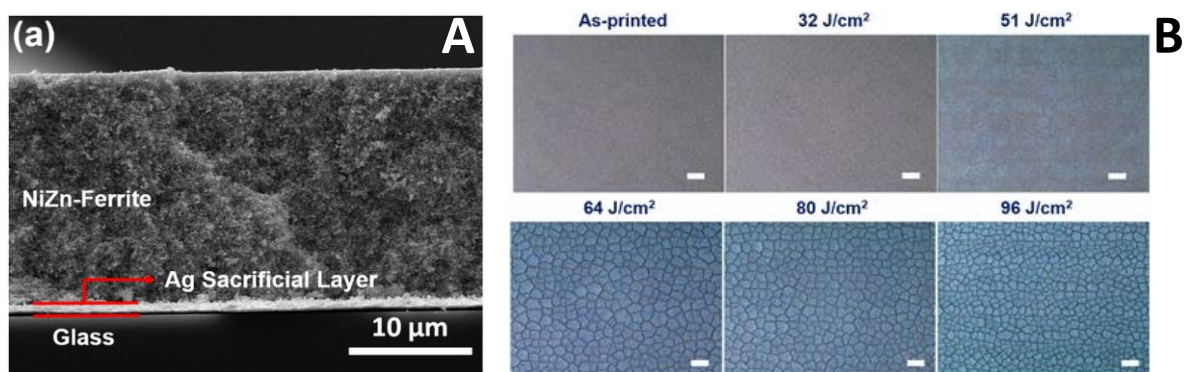
However, in this study, a 50% of density is too low to expect the magnetic multiband behavior of coatings through the permeability spectra (Chapter I). Indeed, this multiband behavior is expected for perfectly controlled network of patterns with magnetic particles and through the control of the magnetic losses by the pattern geometry. Before patterning, some requirements need to be fulfilled with continuous coatings in order to generate this patterned



framework and hence provide a magnetic multiband behavior. As mentioned in the Chapter I, the particle size does not exceed a critical limit of 3  $\mu\text{m}$ . Additionally, the material needs to be dense to enable magnetic interactions as strong as possible between particles. Otherwise, a too high percentage of porosity inside the layers will not favor magnetic couplings between particles and affect the dynamic properties of coatings, making them not suitable to evidence the multiband behavior.

The present strategy was based on a two steps process with at first a preliminary step of particle synthesis, and secondly the elaboration of films constituted of these previous synthesized nanoparticles. The idea was to control the particle size before elaborating the film not to exceed the critical limit imposed by the application. However, this technique appears to be not well adapted to the application due to the poor density of coatings even after sintering. In this respect, thanks to these first coatings, some technological barriers were better identified and lead to the following perspectives intervening at different steps of the procedure (Figure II-1).

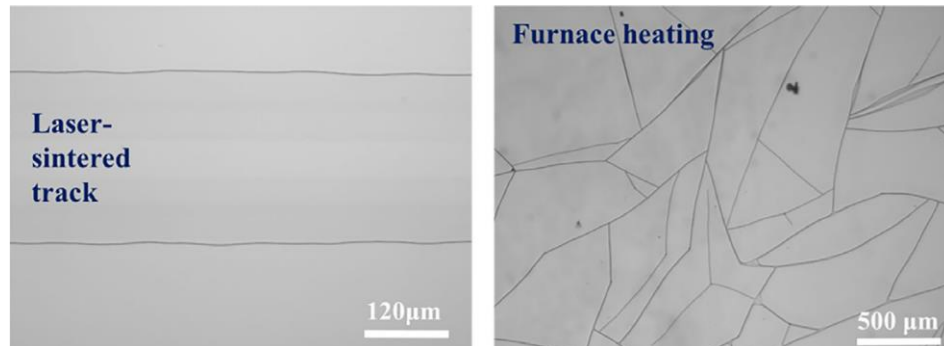
On the one hand, another thermal densification technique of films could be studied and replace the conventional sintering in a furnace: the laser sintering. This sintering method is of special interest. Indeed, it induces local heating through laser irradiation on the coating surface, and hence causes less cracking since stress relief can occur in the non-sintered part of the film. Moreover, the piloting of the cracks to generate a kind of patterned network is also feasible. As an example, NiZn ferrite films elaborated by aerojet-printing with an ink containing 50 nm diameter particles have been densified by laser sintering (Figure II-86.A) to increase the packing density of 48.6 % before sintering [59]. The formation of a network of cracks as a function of the laser fluence is shown in Figure II-86.B. The cracks are generated by a local heating/cooling of the areas touched by the laser spot during sintering. The best sintering conditions are filled with a laser fluence of 64  $\text{J}/\text{cm}^2$  in terms of magnetic properties of the film [59].



**Figure II-86.** Crosssectional view of a NiZn ferrite film aerojet-printed (A) and influence of the laser fluence on the surface conditions of coatings after laser sintering (B). From K. Rajaram [59].

A second example with laser-sintered silica films is displayed in Figure II-87 and compared to a classical heating in a furnace. A  $\text{CO}_2$  laser beam draws tracks on the films during sintering. The cracks are generated along the edge of the tracks whereas the conventional sintering at 1100  $^\circ\text{C}$  provokes a disordered organization of cracks at the surface (Figure II-87). The porosity

can be managed through the laser power. The technique has demonstrated a good reproducibility, allows to obtain smooth and crack free surfaces. In the same manner, designed patterns can be drafted by laser sintering with a laser galvanometer scanner [61]. It could be valuable to study the laser sintering with the FM coatings to fix the issue of porosity.

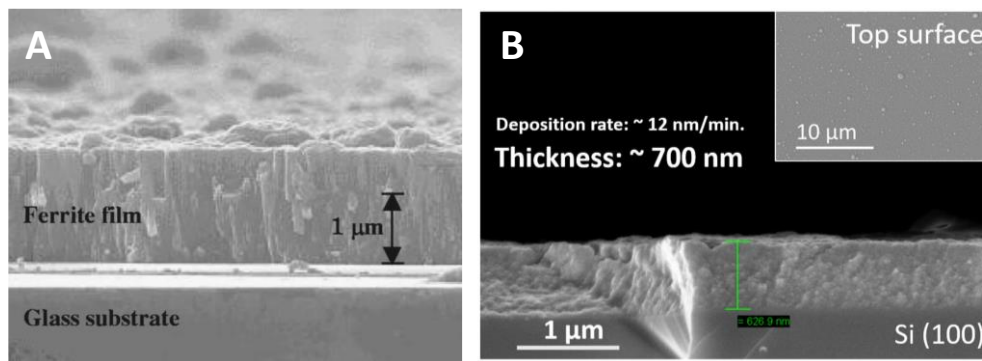


**Figure II-87. Optical images of surfaces of sintered silica films after laser sintering and furnace heating. From J. Lei *et al.* [61].**

On the other hand, the overall process could be reviewed by replacing the two steps in a single one with the direct elaboration of coatings at low temperature through solution of precursors without synthesizing the material independently of the film. For instance, ferrite films have been developed by a spray technique at 90 °C of an aqueous solution of iron chloride onto a heating spinner [62] [63]. The obtained films (Figure II-88.A) are suitable for noise suppressors application in the gigahertz range.

Furthermore, a mixture of nickel, zinc and iron acetylacetonate in ethanol and 1-decanol is used in a microwave oven at a temperature between 120 and 137 °C for the direct growth of a ferrite film onto the substrate inside the reactor [64]. The technique is called low temperature microwave-assisted solvothermal (MAS) method. The films possess crystallites with diameters between 4 and 6 nm and are convenient for soft magnetic or high-frequency applications (Figure II-88.B).

The coatings could be subjected to drying at temperatures below 100 °C but no further postannealing treatment is required to densify the films. In addition, no surfactant is employed which is a considerable advantage meaning the particles are not surrounded by an organic layer and their magnetic properties or interactions are thus not inhibited.



**Figure II-88.** (A) Cross-sectional view of a sprayed ferrite film. From J. Miyasaka *et al.* [62]. And (B) of a microwave-deposited NiFe<sub>2</sub>O<sub>4</sub> film. From R.D. Ralandinliu Kahmei *et al.* [64].

#### III.2.5.D. Influence of the annealing on the coating microstructure

The microstructure of powder and coatings must be examined during thermal treatment to have a complete view about the annealing effect on the evolution of the phase in the material with temperature. Two methods of characterization are correlated: XRD and TG-DTA.

On the one hand, the stability of the phase as a function of the temperature is investigated for FM powder (Figure II-89) and coatings (Figure II-91) under argon atmosphere between 30 and 1000 °C by X-ray diffraction analysis. After heating at 1000 °C, the sample is cooled down to 30 °C and subjected to X-ray diffraction again in order to define the reversibility of the phase. In both cases, the main peaks corresponding to pure spinel Zn<sub>0.35</sub>Fe<sub>2.6</sub>O<sub>4</sub> phase (PDF sheet 04-021-5090) are indexed. A general trend is also observed: higher peak amplitudes with a decrease of the Full Width at Half Maxima (FWHM) with temperature. This phenomenon means that the crystallite size increases with temperature due to crystal growth and particle coalescence during solid-state diffusion with sintering.

In the case of FM powder (Figure II-89), a left shifting of the peaks attributed to Zn<sub>0.35</sub>Fe<sub>2.6</sub>O<sub>4</sub> magnetite with the temperature is noticed from 325 °C, reflecting an increase of the lattice parameter of the material (Figure II-90). This shift is accentuated from 625 °C and generally at high angles. Moreover, additional peaks are also exhibited from 400 °C corresponding to the presence of a secondary phase of Zn<sup>2+</sup> substituted wüstite (Zn<sub>x</sub>Fe<sub>1-x</sub>O phase) with a space group Pn3m and a lattice parameter of 12.862 [65]. These peaks expand until 1000 °C. A similar phase has been previously studied in the development of nanocomposite films of wurtzite (Fe:ZnO) and spinel (Zn:Fe<sub>3</sub>O<sub>4</sub>) phases by pulse laser deposition at 500 °C [66].

The initial phase is retrieved when the powder is cooled down to 30 °C, which implies the reversibility of the spinel phase.

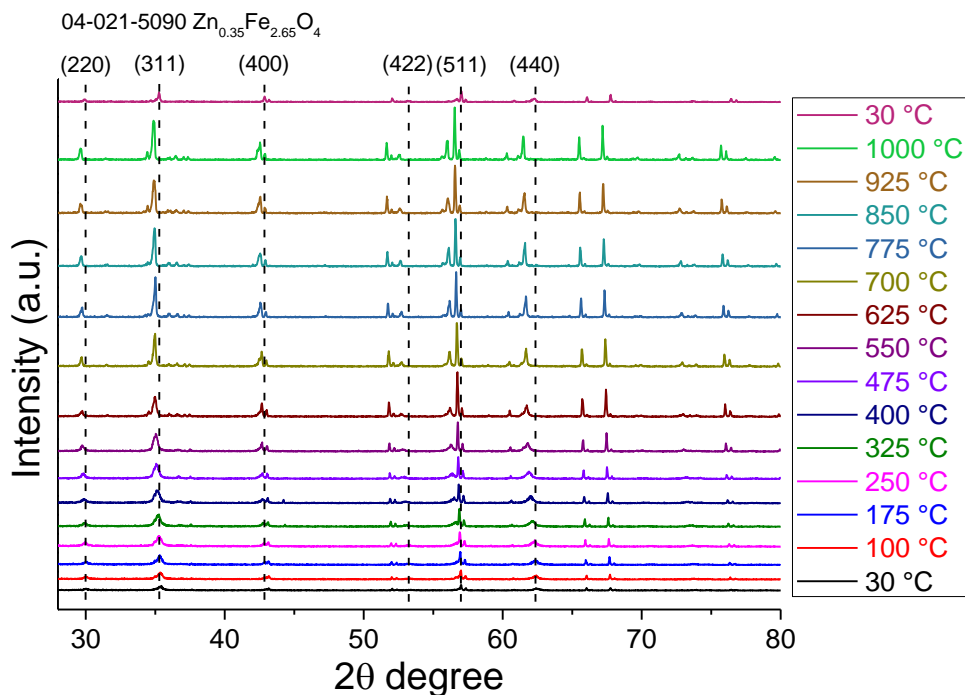


Figure II-89. Effect of the temperature on the X-ray diffraction patterns of FM powder from 30 to 1000 °C under argon.

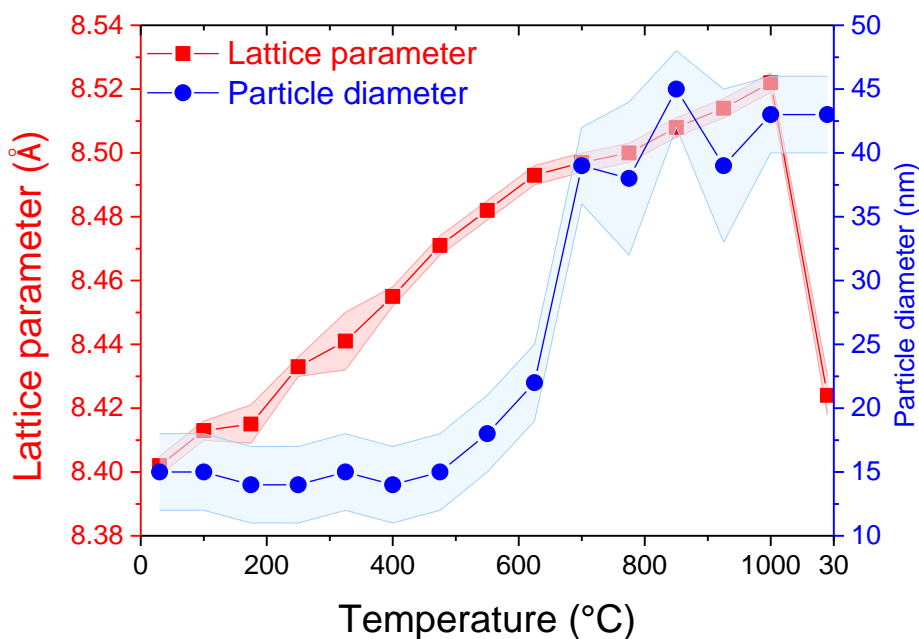


Figure II-90. Variation of the lattice parameter and of the particle diameter as a function of the temperature for the principal phase of zinc iron oxide spinel in the case of powder. Obtained from the diffractometers in Figure II-89. The confidence interval (in light red for the lattice parameter and light blue for the particle diameter) is equal to three times the standard deviation. The last point at 30 °C is measured after decreasing temperature.

Regarding FM coatings (Figure II-91), the shifting of the  $Zn_{0.35}Fe_{2.6}O_4$  phase at low angles when increasing the temperature is also shown from 325 °C. The lattice parameter increases with temperature too. The variation of the lattice parameter and the particle size is not represented for coatings because of the difficulty to deconvolute the peaks from the substrate



contribution. Additional peaks corresponding to the same secondary phase of  $\text{Zn}^{2+}$  substituted wüstite ( $\text{Zn}_x\text{Fe}_{1-x}\text{O}$  phase) [65] appear from 625 °C at higher temperature than for the powder. This distinction could be due to a difference of reactivity between powder and coatings. Furthermore, this additional phase does not completely disappear when returning back to 30 °C.

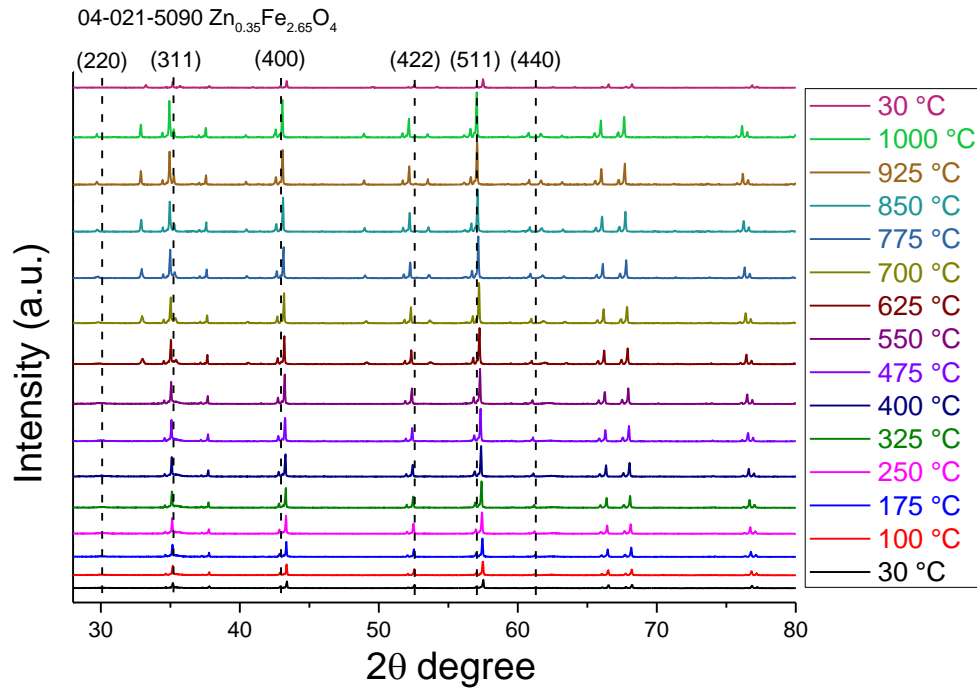


Figure II-91. Effect of the temperature on the X-ray diffraction patterns of FM coatings from 30 to 1000 °C under argon.

On the other hand, the thermal decomposition of SP(F)M and FM particles is completed at higher temperatures until 800 °C under helium (Figure II-92). It adds the portion between 600 and 800 °C to the TG-DTA analysis already mentioned in Figure II-60 in section III.2.3.B, examined for the understanding of the organics departure. In this section, the analysis serves to verify the stability of the phase between 600 and 800 °C.

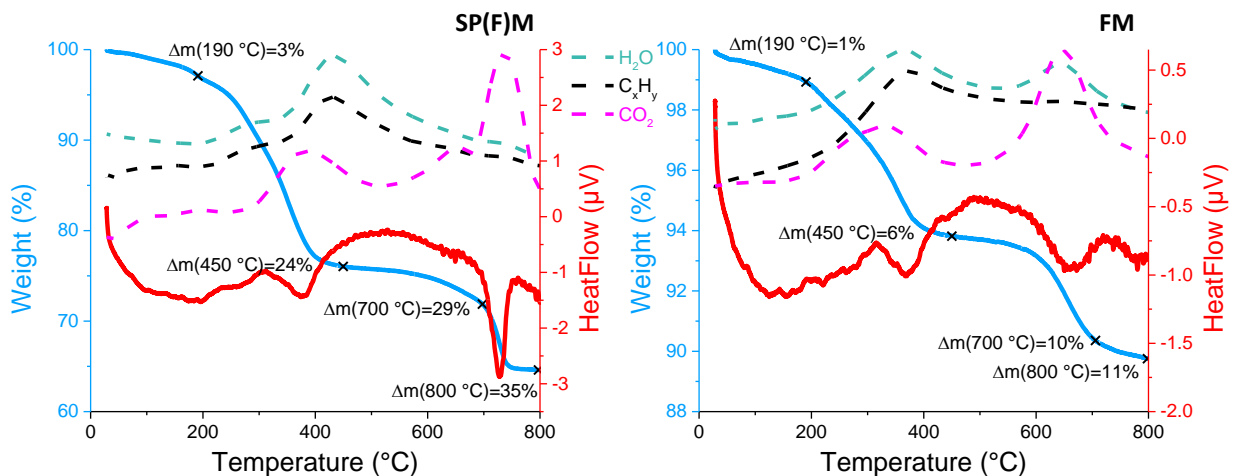
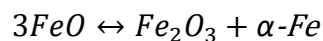
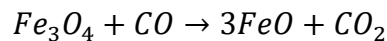


Figure II-92. TG-DTA and mass spectroscopy curves of SP(F)M and FM particles under helium until 800 °C.

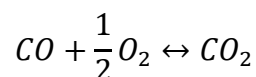
A fourth weight loss occurs between 600 and 800 °C for SP(F)M and FM particles, which could not have been seen in section III.2.3.B. This loss takes place during the sintering step and is equal to 11 % and 5 % for SP(F)M and FM particles, respectively. As all of the organics are removed at 600 °C, this loss could not be attributed to the organic shell around particles.

However, in accordance with the previous X-ray diffraction results, it could correspond to the reduction of the material phase.

According to the literature, the organic shell around particles could induce the reduction of the  $Zn_{0.4}Fe_{2.6}O_4$  phase of nanoparticles during thermal treatment. Indeed, it is the case of oleic acid coated  $Fe_3O_4$  annealed under vacuum [46] [48] [58]. The cubic spinel structure with the  $Fe_3O_4$  phase is stable between room temperature to 500 °C. Between 500 and 700 °C, the phase is decomposed in  $\alpha$ -Fe and  $\gamma$ - $Fe_2O_3$ . Above 700°C, the system evolves with the presence of wüstite FeO and  $\alpha$ -Fe. The indicated temperatures depend on the particles size and correspond to the ones encountered for particle diameter of approximately 10 nm. The reduction mechanism occurs above 600 °C, as follows [46]:



II-7



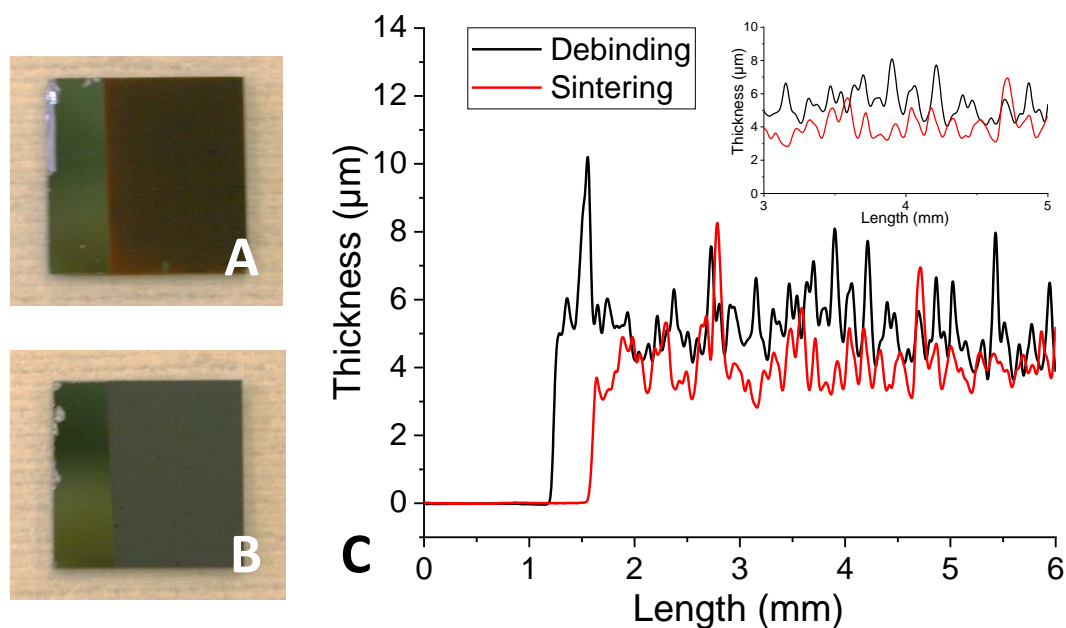
The reduction of the particles is caused by the degradation of the carbon residues coming from the decomposition of the carboxylate head above 500 °C. The reduction is the consequence of a strong chemical adsorption of the surfactant on the particle surface. This phenomenon is expressed on the TG-DTA curves (Figure II-92) with the presence of a  $CO_2$  emission between 700 and 750 °C. A significant amount of oxygen is removed from the material during reduction of  $Zn_{0.4}Fe_{2.6}O_4$  particles in  $Zn^{2+}$  substituted wüstite. The mechanism is faster for FM particles due to the thinner organic layer around FM particles (section 0). The presence of zinc in the particles allows to make the wüstite stable below 600°C [67], which explains why  $\alpha$ -Fe and  $\gamma$ - $Fe_2O_3$  are not formed before the apparition of wüstite, as in the case of annealing of  $Fe_3O_4$  particles.

As a result, the particles could be described as a core/shell structure with  $Zn_{0.4}Fe_{2.6}O_4$  composition at the core and  $Zn^{2+}$  substituted wüstite at the outer. The cracking observed on the surface of FM coatings after sintering could hence be due to the combination of two parameters: the shrinkage induced by the particle coalescence and also by the reduction of the phase.

### III.3. Feasibility of patterned films

Despite the cracked surface of the FM coatings, a feasibility test of laser etching was carried out at the Femto-ST Institute in Besançon by laser micromachining. The coating surface is directly etched by means of a femtosecond laser with a wavelength of 1050 nm and a pulse length of 200 fs. The aim of this feasibility test is to determine at which stage of the process the laser etching has to intervene in order to produce a network of patterns firmly attached to the substrate. In this context, the laser etching is tested on the films after debinding and sintering (Figure II-1).

Figure II-93 exposes two FM coatings after debinding (Figure II-93.A) and after sintering (Figure II-93.B), deposited on  $9 \times 9 \mu\text{m}^2$  silicon wafers with a naked area to enable the thickness measurement of the film with a profilometer. Regarding the evolution of the thickness with the length, the coating surface looks rough because the airbrushing is not automated and due to inhomogeneous stack of particles. The thicknesses are of 6 and  $4 \mu\text{m}$  in the case of the debinded and sintered samples, respectively (Figure II-93.C). The change of color from brown to black previously observed between debinding and sintering is clearly visible (Figure II-93.A-B).

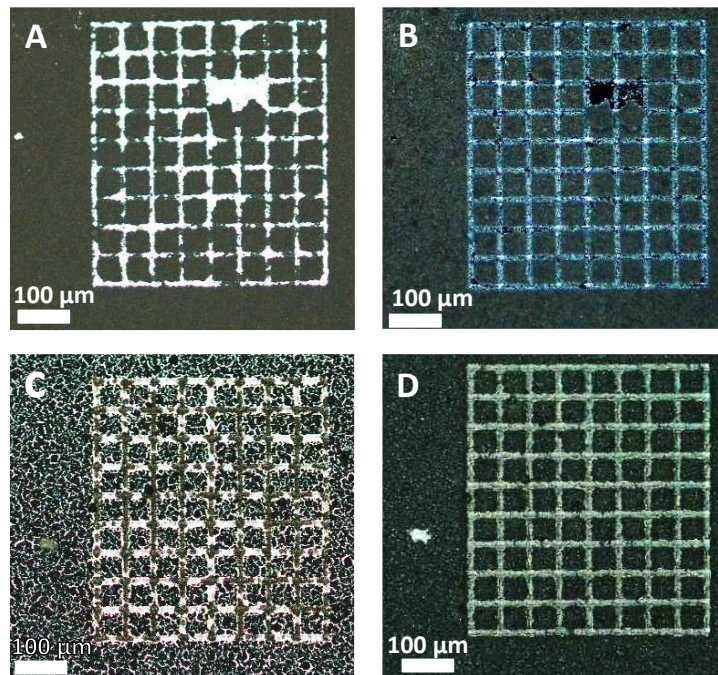


**Figure II-93.** Thickness of the layer versus its length (C), after debinding (A) and sintering (B).

Square patterns with a  $48 \mu\text{m}$  length and spaced of  $11 \mu\text{m}$  were realized onto the debinded and sintered films and their surfaces were observed by optical microscopy after etching (Figure II-94). After debinding, the patterns poorly adhere onto the silicon wafer. A low accuracy of etching and a debonding of patterns is noted (Figure II-94.A-B).

After sintering, a better adherence of patterns appears with a more accurate etching of the pattern borders. No matter debonding is observed (Figure II-94.C-D). The crack network engendered by the sintering does not weaken the mechanical adherence of the layer on the

substrate. Thus, in response to the scheme of the global protocol in Figure II-1, the laser etching needs to be done after sintering, at the end of the procedure.

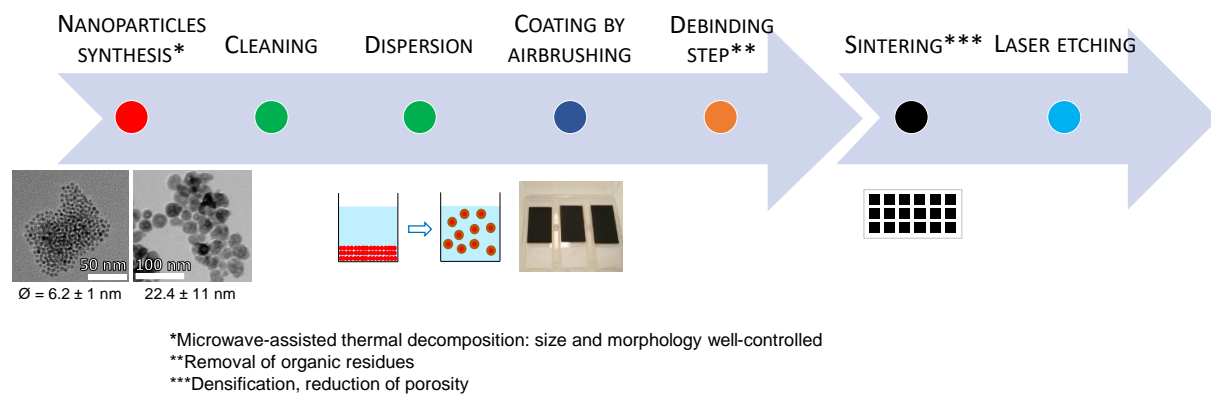


**Figure II-94.** Optical microscopy of patterned coatings after debinding (A in bright field, B in dark field) and after sintering (C in bright field, D in dark field).

### III.4. Conclusion

*In the context of the optimization of magnetic textures of films, the elaboration of a patterned network from continuous coatings of magnetic particles was examined. The aim is to control the magnetic losses of coatings by the pattern geometry at desired frequencies, also called multiband behavior.*

*The development of dense coatings through an airbrushing technique was studied. The technique relies on the atomization of a stable dispersion of nanoparticles in a liquid media on a desired substrate. The different steps of the process are summarized in the final scheme in Figure II-95 from the material synthesis, to the thermal treatment of coatings, ending with a laser etching step to create the patterned films. All along the process, a balance has to be found concerning the organics as they are both required and prohibited. Indeed, the presence of organics is necessary in the particle synthesis for the size and morphology control, as well as in dispersion to limit the particle interactions and stabilize them in a suitable liquid media for airbrushing, whereas it is a restraining factor for the elaboration of dense coatings with strong magnetic interactions between particles. These magnetic interactions are one of the required conditions to obtain the desired magnetic multiband behavior of coatings through permeability measurements, in addition to the critical particle size of 3  $\mu\text{m}$  not to exceed. In this respect, the films must exhibit a high density to enable magnetic interactions as strong as possible between particles. A too high percentage of porosity will be unfavorable to the multiband behavior.*



**Figure II-95. Development of magnetic coatings by airbrushing.**

*From the particle synthesis, each step is explored:*

- *At first, the particle cleaning. After synthesis, the particles need to be washed in order to remove the organic residues. The centrifugation method was selected with six cycles to obtain a good compromise between a reduction of organics and an easy dispersion of particles in the next step.*
- *Then, the dispersion. The organic dispersion is the only way to successfully stabilize the particles without aggregation and sedimentation directly after synthesis. SP(F)M and FM particles are stabilized in hexane through the nonpolar hydrocarbon tails of oleic acid, chemically adsorbed at the particle surface through its carboxylic head.*
- *The elaboration of coatings by airbrushing which can be improved by automatization.*

*After the elaboration of continuous coatings, the films were annealed through two stages to allow a good adhesion of the layer to the substrate with a satisfying density:*

- *A debinding step from room temperature to 450 °C to remove the organic residues from the films. SP(F)M coatings are completely cracked, while the FM ones remain undamaged, which makes SP(F)M particles not suitable for the elaboration of dense coatings. At this stage, the degradation of the organic shell around particles occurs in two steps:*
  - ❖ *A first departure below 300 °C attributed to the grafted amine groups of OAm and to the hydrocarbon chains of OA which decompose before the rest of the OA molecule due to their weak bonding with the particle.*
  - ❖ *A second departure above 300 °C which corresponds to the decomposition of the headgroups of OA (carboxylates groups COO<sup>-</sup>), chemically adsorbed onto the particle surface through iron atoms.*
- *A sintering step at 770 °C to densify the layer after the organic departure, and thus reduce the porosity. Cracking on FM coatings is induced at this stage with a high amount of porosity estimated at approximately 50%. Different unsuccessful solutions have been tried to reduce the coating porosity:*
  - ❖ *the change of substrate,*
  - ❖ *the addition of layers,*
  - ❖ *the reduction of the coating thickness,*
  - ❖ *the increase of the particle concentration,*
  - ❖ *the decrease of the temperature ramp,*
  - ❖ *and finally the use of two ranges of particle size.*

*The thermal treatment is realized under an argon atmosphere to avoid the oxidation of particles due to the high sensitivity of Fe<sup>2+</sup> ions to oxidation. During sintering, the reduction of the particles is caused by the degradation of the carbon residues coming from the strong chemical adsorption of the OA carboxylates groups at the particle surface. The particles are thus assimilated to core/shell frameworks with Zn<sub>0.4</sub>Fe<sub>2.6</sub>O<sub>4</sub> composition at the core and Zn<sup>2+</sup> substituted wüstite at the outer.*

- *The laser etching is the last step of the protocol. A feasibility test allows combining a good adherence of patterns on the substrate with a good accuracy of etching.*

*The chemical composition of the final coatings is homogeneous.*

*As a conclusion, the coating density of the films has not been improved. Three alternatives in order to enhance the coating density are:*

- *The replacement of the conventional sintering by laser sintering. Local heating is induced, generating less cracking. The possibility to create a patterned network by managing the cracks is also feasible.*

- *The elaboration of films through precursor solutions directly on the substrates through low temperature processes like a microwave-assisted solvothermal method (MAS), or the spraying of a solution on a heating spinner. No further post annealing treatment is required to densify the films.*
- *A crack patterning method from the aqueous dispersion of particles. The principle is to control the solvent evaporation to generate periodic cracks in a film deposited by dip-coating [68].*

*Moreover, the study of the thermal treatment of particles has highlighted the effect of the two surfactants in the dispersion media. OA acts as a surfactant and allows the particle dispersion through the grafting of its carboxylates groups  $\text{COO}^-$  on the particle surface and by keeping its hydrocarbon tails in hexane for which they have a good affinity. When used in a mixture with OA, OAm serves as a Lewis base and absorbs the free protons generated by the grafting of OA carboxyl groups at the particle surface. The assumption is that the organic shell around particle is only constituted of OA carboxylates groups. After calculation, SP(F)M and FM particles are surrounded with approximately one layer of carboxylates (0.95 and 0.7 layer, respectively). FM particles are thus less well functionalized, which could explain partially why SP(F)M coatings are already cracked after debinding and not FM coatings.*

*A transfer of the airbrushing towards an innovative and more accurate process, the inkjet printing, is investigated in the next Chapter (Chapter III). This process has a major advantage: the realization of patterned coatings in a single step without post-processing.*



## Chapter II references:

- [1] J. Tomas, "Adhesion of ultrafine particles—A micromechanical approach," *Chem. Eng. Sci.*, vol. 62, no. 7, pp. 1997–2010, Apr. 2007, doi: 10.1016/j.ces.2006.12.055.
- [2] K. J. M. Bishop, C. E. Wilmer, S. Soh, and B. A. Grzybowski, "Nanoscale Forces and Their Uses in Self-Assembly," *Small*, vol. 5, no. 14, pp. 1600–1630, Jul. 2009, doi: 10.1002/smll.200900358.
- [3] Y. Min, M. Akbulut, K. Kristiansen, Y. Golan, and J. Israelachvili, "The role of interparticle and external forces in nanoparticle assembly," *Nat. Mater.*, vol. 7, pp. 527–538, Jul. 2008.
- [4] J. Araki, "Electrostatic or steric? – preparations and characterizations of well-dispersed systems containing rod-like nanowhiskers of crystalline polysaccharides," *Soft Matter*, vol. 9, no. 16, p. 4125, 2013, doi: 10.1039/c3sm27514k.
- [5] J. H. Dickerson and A. R. Boccaccini, Eds., *Electrophoretic Deposition of Nanomaterials*. New York, NY: Springer New York, 2012.
- [6] R. Xu, C. Wu, and H. Xu, "Particle size and zeta potential of carbon black in liquid media," *Carbon*, vol. 45, no. 14, pp. 2806–2809, Nov. 2007, doi: 10.1016/j.carbon.2007.09.010.
- [7] S. Vallar, D. Houivet, J. El Fallah, D. Kervadec, and J.-M. Haussonne, "Oxide slurries stability and powders dispersion: optimization with zeta potential and rheological measurements," *J. Eur. Ceram. Soc.*, vol. 19, no. 6–7, pp. 1017–1021, Jun. 1999, doi: 10.1016/S0955-2219(98)00365-3.
- [8] D. Sun, "Effect of Zeta Potential and Particle Size on the Stability of SiO<sub>2</sub> Nanospheres as Carrier for Ultrasound Imaging Contrast Agents," *Int. J. Electrochem. Sci.*, pp. 8520–8529, Oct. 2016, doi: 10.20964/2016.10.30.
- [9] E. F. de la Cruz, Y. Zheng, E. Torres, W. Li, W. Song, and K. Burugapalli, "Zeta Potential of Modified Multi-walled Carbon Nanotubes in Presence of poly (vinyl alcohol) Hydrogel," *Int J Electrochem Sci*, vol. 7, no. 4, pp. 3577–3590, 2012.
- [10] M. Larsson, A. Hill, and J. Duffy, "Suspension Stability; Why Particle Size, Zeta Potential and Rheology are Important," *Annu. Trans. Nord. Rheol. Soc.*, vol. 20, 2012.
- [11] C. Barrera, A. P. Herrera, and C. Rinaldi, "Colloidal dispersions of monodisperse magnetite nanoparticles modified with poly(ethylene glycol)," *J. Colloid Interface Sci.*, vol. 329, no. 1, pp. 107–113, Jan. 2009, doi: 10.1016/j.jcis.2008.09.071.
- [12] H.-H. Lee, S. Yamaoka, N. Murayama, and J. Shibata, "Dispersion of Fe<sub>3</sub>O<sub>4</sub> suspensions using sodium dodecylbenzene sulphonate as dispersant," *Mater. Lett.*, vol. 61, no. 18, pp. 3974–3977, Jul. 2007, doi: 10.1016/j.matlet.2006.12.091.
- [13] D.-B. Shieh *et al.*, "Aqueous dispersions of magnetite nanoparticles with NH<sub>3</sub><sup>+</sup> surfaces for magnetic manipulations of biomolecules and MRI contrast agents," *Biomaterials*, vol. 26, no. 34, pp. 7183–7191, Dec. 2005, doi: 10.1016/j.biomaterials.2005.05.020.
- [14] Z.-X. Sun, F.-W. Su, W. Forsling, and P.-O. Samskog, "Surface Characteristics of Magnetite in Aqueous Suspension," *J. Colloid Interface Sci.*, vol. 197, no. 1, pp. 151–159, Jan. 1998, doi: 10.1006/jcis.1997.5239.
- [15] J. I. Nieto-Juarez and T. Kohn, "Virus removal and inactivation by iron (hydr)oxide-mediated Fenton-like processes under sunlight and in the dark," *Photochem. Photobiol. Sci.*, vol. 12, no. 9, p. 1596, 2013, doi: 10.1039/c3pp25314g.
- [16] J. L. Viota, F. J. Arroyo, A. V. Delgado, and J. Horno, "Electrokinetic characterization of magnetite nanoparticles functionalized with amino acids," *J. Colloid Interface Sci.*, vol. 344, no. 1, pp. 144–149, Apr. 2010, doi: 10.1016/j.jcis.2009.11.061.
- [17] S. D. Kulkarni, S. Kumbhar, S. G. Menon, K. S. Choudhari, and S. C., "Magnetically separable core-shell ZnFe<sub>2</sub>O<sub>4</sub>@ZnO nanoparticles for visible light photodegradation of methyl orange," *Mater. Res. Bull.*, vol. 77, pp. 70–77, May 2016, doi: 10.1016/j.materresbull.2016.01.022.
- [18] L. Zhang, M. Su, N. Liu, X. Zhou, and P. Kang, "Degradation of malachite green solution using combined microwave and ZnFe<sub>2</sub>O<sub>4</sub> powder," *Water Sci. Technol.*, vol. 60, no. 10, pp. 2563–2569, Nov. 2009, doi: 10.2166/wst.2009.497.

- [19] S. A. Jadhav, S. B. Somvanshi, M. V. Khedkar, S. R. Patade, and K. M. Jadhav, "Magneto-structural and photocatalytic behavior of mixed Ni-Zn nano-spinel ferrites: visible light-enabled active photodegradation of rhodamine B," *J. Mater. Sci. Mater. Electron.*, vol. 31, no. 14, pp. 11352–11365, Jul. 2020, doi: 10.1007/s10854-020-03684-1.
- [20] J.-P. Jolivet, *De la solution à l'oxyde*. EDP Sciences, 2015.
- [21] Â. L. Andrade, J. D. Fabris, J. D. Ardisson, M. A. Valente, and J. M. F. Ferreira, "Effect of Tetramethylammonium Hydroxide on Nucleation, Surface Modification and Growth of Magnetic Nanoparticles," *J. Nanomater.*, vol. 2012, pp. 1–10, 2012, doi: 10.1155/2012/454759.
- [22] S. L. Tripp, S. V. Pusztay, A. E. Ribbe, and A. Wei, "Self-Assembly of Cobalt Nanoparticle Rings," *J. Am. Chem. Soc.*, vol. 124, no. 27, pp. 7914–7915, Jul. 2002, doi: 10.1021/ja0263285.
- [23] B. Faure, "Particle interactions at the nanoscale From colloidal processing to self-assembled arrays," Stockholm University Thesis, Stockholm, 2012.
- [24] A. Dobrynin, "Theory and simulations of charged polymers: From solution properties to polymeric nanomaterials," *Curr. Opin. Colloid Interface Sci.*, vol. 13, no. 6, pp. 376–388, Dec. 2008, doi: 10.1016/j.cocis.2008.03.006.
- [25] R. J. Hunter and L. R. White, *Foundations of Colloid Science*, Oxford University Press., vol. 1. 1987.
- [26] A. Hutin, "Détermination de la Concentration Micellaire Critique d'un tensioactif.," *Petits Savoirs Physicochim.*, 2019, doi: 10.13140/RG.2.2.23594.06089.
- [27] A. Kabalnov and H. Wennerström, "Macroemulsion Stability: The Oriented Wedge Theory Revisited," *Langmuir*, vol. 12, no. 2, pp. 276–292, Jan. 1996, doi: 10.1021/la950359e.
- [28] P. Brochette, "Émulsification - Élaboration et étude des émulsions," *Tech. Ing.*, p. 25, 1999.
- [29] C. Larpent, "Tensioactifs," *Tech. Ing.*, 1995.
- [30] M. Bissannagari, W. Lee, W. Y. Lee, J. H. Jeong, and J. Kim, "Fully-Inkjet-Printed Ag-Coil/NiZn-Ferrite for Flexible Wireless Power Transfer Module: Rigid Sintered Ceramic Body into Flexible Form," *Adv. Funct. Mater.*, vol. 27, no. 31, p. 1701766, Aug. 2017, doi: 10.1002/adfm.201701766.
- [31] L. I. Cabrera, Á. Somoza, J. F. Marco, C. J. Serna, and M. Puerto Morales, "Synthesis and surface modification of uniform MFe<sub>2</sub>O<sub>4</sub> (M = Fe, Mn, and Co) nanoparticles with tunable sizes and functionalities," *J. Nanoparticle Res.*, vol. 14, no. 6, p. 873, Jun. 2012, doi: 10.1007/s11051-012-0873-x.
- [32] A. G. Roca, S. Veintemillas-Verdaguer, M. Port, C. Robic, C. J. Serna, and M. P. Morales, "Effect of Nanoparticle and Aggregate Size on the Relaxometric Properties of MR Contrast Agents Based on High Quality Magnetite Nanoparticles," *J. Phys. Chem. B*, vol. 113, no. 19, pp. 7033–7039, May 2009, doi: 10.1021/jp807820s.
- [33] M. Menelaou, K. Georgoula, K. Simeonidis, and C. Dendrinou-Samara, "Evaluation of nickel ferrite nanoparticles coated with oleylamine by NMR relaxation measurements and magnetic hyperthermia," *Dalton Trans.*, vol. 43, no. 9, p. 3626, 2014, doi: 10.1039/c3dt52860j.
- [34] A. Ruiz *et al.*, "Short-chain PEG molecules strongly bound to magnetic nanoparticle for MRI long circulating agents," *Acta Biomater.*, vol. 9, no. 5, pp. 6421–6430, May 2013, doi: 10.1016/j.actbio.2012.12.032.
- [35] Z. Mei, A. Dhanale, A. Gangaharan, D. K. Sardar, and L. Tang, "Water dispersion of magnetic nanoparticles with selective Biofunctionality for enhanced plasmonic biosensing," *Talanta*, vol. 151, pp. 23–29, May 2016, doi: 10.1016/j.talanta.2016.01.007.
- [36] M. Pauly, "Structuration de nanoparticules magnétiques d'oxyde de fer en films et étude de leurs propriétés magnétiques et de magnéto-transport," Thesis, 2010.
- [37] A. Amirabadizadeh, Z. Salighe, R. Sarhaddi, and Z. Lotfollahi, "Synthesis of ferrofluids based on cobalt ferrite nanoparticles: Influence of reaction time on structural, morphological and magnetic properties," *J. Magn. Magn. Mater.*, vol. 434, pp. 78–85, Jul. 2017, doi: 10.1016/j.jmmm.2017.03.023.
- [38] H. Yue, Y. Zhao, X. Ma, and J. Gong, "Ethylene glycol: properties, synthesis, and applications," *Chem. Soc. Rev.*, vol. 41, no. 11, p. 4218, 2012, doi: 10.1039/c2cs15359a.
- [39] M. L. Sheely, "Glycerol Viscosity Tables," *Ind. Eng. Chem.*, vol. 24, no. 9, pp. 1060–1064, Sep. 1932, doi: 10.1021/ie50273a022.

- [40] A. Ranzani da Costa, "La réduction du minerai de fer par l'hydrogène : étude cinétique, phénomène de collage et modélisation," Thesis, 2011.
- [41] M. Celis, "Transformation de phases et comportement à l'oxydation d'alliages Fe-Al," Thesis, 2007.
- [42] L. S. Darken and R. W. Gurry, "The System Iron—Oxygen. II. Equilibrium and Thermodynamics of Liquid Oxide and Other Phases," *J. Am. Chem. Soc.*, vol. 68, no. 5, pp. 798–816, May 1946, doi: 10.1021/ja01209a030.
- [43] S. A. Degterov, A. D. Pelton, E. Jak, and P. C. Hayes, "Experimental study of phase equilibria and thermodynamic optimization of the Fe-Zn-O system," *Metall. Mater. Trans. B*, vol. 32, no. 4, pp. 643–657, Aug. 2001, doi: 10.1007/s11663-001-0119-2.
- [44] C. T. Lie, P. C. Kuo, W.-C. Hsu, I. J. Chang, and J. W. Chen, "Effect of Zn doping on the magnetoresistance of sintered Fe<sub>3</sub>O<sub>4</sub> ferrites," *J. Magn. Magn. Mater.*, vol. 239, no. 1–3, pp. 160–163, Feb. 2002, doi: 10.1016/S0304-8853(01)00538-8.
- [45] Y. Q. Li, Y. Huang, S. H. Qi, F. F. Niu, and L. Niu, "Preparation, and magnetic and electromagnetic properties of La-doped strontium ferrite films," *J. Magn. Magn. Mater.*, vol. 323, no. 16, pp. 2224–2232, Aug. 2011, doi: 10.1016/j.jmmm.2011.03.040.
- [46] S. Ayyappan, G. Gnanaprakash, G. Panneerselvam, M. P. Antony, and J. Philip, "Effect of Surfactant Monolayer on Reduction of Fe<sub>3</sub>O<sub>4</sub> Nanoparticles under Vacuum," *J. Phys. Chem. C*, vol. 112, no. 47, pp. 18376–18383, Nov. 2008, doi: 10.1021/jp8052899.
- [47] A. H. Monfared, A. Zamanian, M. Beygzadeh, I. Sharifi, and M. Mozafari, "A rapid and efficient thermal decomposition approach for the synthesis of manganese-zinc/oleylamine core/shell ferrite nanoparticles," *J. Alloys Compd.*, vol. 693, pp. 1090–1095, Feb. 2017, doi: 10.1016/j.jallcom.2016.09.253.
- [48] M. Rudolph, J. Erler, and U. A. Peucker, "A TGA–FTIR perspective of fatty acid adsorbed on magnetite nanoparticles—Decomposition steps and magnetite reduction," *Colloids Surf. Physicochem. Eng. Asp.*, vol. 397, pp. 16–23, Mar. 2012, doi: 10.1016/j.colsurfa.2012.01.020.
- [49] L. Zhang, R. He, and H.-C. Gu, "Oleic acid coating on the monodisperse magnetite nanoparticles," *Appl. Surf. Sci.*, vol. 253, no. 5, pp. 2611–2617, Dec. 2006, doi: 10.1016/j.apsusc.2006.05.023.
- [50] A. Sahraneshin, S. Takami, K. Minami, D. Hojo, T. Arita, and T. Adschiri, "Synthesis and morphology control of surface functionalized nanoscale yttrium aluminum garnet particles via supercritical hydrothermal method," *Prog. Cryst. Growth Charact. Mater.*, vol. 58, no. 1, pp. 43–50, Mar. 2012, doi: 10.1016/j.pcrysgrow.2011.10.004.
- [51] J. Luo *et al.*, "Synthesis and Characterization of Monolayer-Capped PtVFe Nanoparticles with Controllable Sizes and Composition," *Chem. Mater.*, vol. 17, no. 21, pp. 5282–5290, Oct. 2005, doi: 10.1021/cm0508219.
- [52] R. A. Harris, P. M. Shumbula, and H. van der Walt, "Analysis of the Interaction of Surfactants Oleic Acid and Oleylamine with Iron Oxide Nanoparticles through Molecular Mechanics Modeling," *Langmuir*, vol. 31, no. 13, pp. 3934–3943, Apr. 2015, doi: 10.1021/acs.langmuir.5b00671.
- [53] A. Weddemann *et al.*, "Review and outlook: from single nanoparticles to self-assembled monolayers and granular GMR sensors," *Beilstein J. Nanotechnol.*, vol. 1, pp. 75–93, Nov. 2010, doi: 10.3762/bjnano.1.10.
- [54] L. A. Wormell Green and N. T. K. Thanh, "High pressure synthesis of FePt nanoparticles with controlled morphology and Fe content," *RSC Adv*, vol. 4, no. 3, pp. 1168–1173, 2014, doi: 10.1039/C3RA45664A.
- [55] M. Klokkenburg, J. Hilhorst, and B. H. Ern e, "Surface analysis of magnetite nanoparticles in cyclohexane solutions of oleic acid and oleylamine," *Vib. Spectrosc.*, vol. 43, no. 1, pp. 243–248, Jan. 2007, doi: 10.1016/j.vibspec.2006.09.008.
- [56] Y. El Mendili, F. Grasset, N. Randrianantoandro, N. Nerambourg, J.-M. Greneche, and J.-F. Bardeau, "Improvement of Thermal Stability of Maghemite Nanoparticles Coated with Oleic Acid and Oleylamine Molecules: Investigations under Laser Irradiation," *J. Phys. Chem. C*, vol. 119, no. 19, pp. 10662–10668, May 2015, doi: 10.1021/acs.jpcc.5b00819.

- [57] J. Vidal-Vidal, J. Rivas, and M. A. López-Quintela, "Synthesis of monodisperse maghemite nanoparticles by the microemulsion method," *Colloids Surf. Physicochem. Eng. Asp.*, vol. 288, no. 1–3, pp. 44–51, Oct. 2006, doi: 10.1016/j.colsurfa.2006.04.027.
- [58] S. Ayyappan *et al.*, "Effect of initial particle size on phase transformation temperature of surfactant capped Fe<sub>3</sub>O<sub>4</sub> nanoparticles," *J. Appl. Phys.*, vol. 109, no. 8, p. 084303, Apr. 2011, doi: 10.1063/1.3564964.
- [59] K. Rajaram and J. Kim, "Flexible wireless power transfer module implemented with aerojet-printing and laser-sintering of rigid NiZn-ferrite ceramic films," *Nano Energy*, vol. 57, pp. 317–326, Mar. 2019, doi: 10.1016/j.nanoen.2018.12.021.
- [60] H. Y. Sohn and C. Moreland, "The effect of particle size distribution on packing density," *Can. J. Chem. Eng.*, vol. 46, no. 3, pp. 162–167, Jun. 1968, doi: 10.1002/cjce.5450460305.
- [61] J. Lei *et al.*, "The effect of laser sintering on the microstructure, relative density, and cracking of sol-gel-derived silica thin films," *J. Am. Ceram. Soc.*, vol. 103, no. 1, pp. 70–81, Jan. 2020, doi: 10.1111/jace.16640.
- [62] J. Miyasaka, M. Tada, M. Abe, and N. Matsushita, "Fe<sub>3</sub>O<sub>4</sub>+ $\delta$  films prepared by 'one-liquid' spin spray ferrite plating for gigahertz-range noise suppressors," *J. Appl. Phys.*, vol. 99, no. 8, p. 08M916, Apr. 2006, doi: 10.1063/1.2177394.
- [63] A. K. Subramani, N. Matsushita, T. Watanabe, M. Tada, M. Abe, and M. Yoshimura, "A simple process for ferrite film preparation from one solution without using hazardous oxidizing agent," *J. Appl. Phys.*, vol. 101, no. 9, p. 09M504, May 2007, doi: 10.1063/1.2709753.
- [64] R. R. Kahmei, R. Sai, S. Arackal, S. A. Shivashankar, and N. Bhat, "Nanostructured Zn-Substituted Nickel Ferrite Thin Films: CMOS-Compatible Deposition and Excellent Soft Magnetic Properties," *IEEE Magn. Lett.*, vol. 10, pp. 1–5, 2019, doi: 10.1109/LMAG.2019.2941427.
- [65] J. M. Claude, M. Zanne, C. Gleitzer, and J. Aubry, "Preparation and study of Zn<sub>x</sub>Fe<sub>0.85-x</sub>O (0.085 < x < 0.170)," *J. Solid State Chem.*, no. 24, pp. 395–400, 1978.
- [66] X. Portier *et al.*, "Microstructure of nanocomposite wurtzite-spinel (Fe:ZnO)-(Zn:Fe<sub>3</sub>O<sub>4</sub>) epitaxial films," *Mater. Chem. Phys.*, vol. 229, pp. 130–138, May 2019, doi: 10.1016/j.matchemphys.2019.02.089.
- [67] T. Sano, "Effect of foreign cation of Zn(II) or Mn(II) ion in FeO-wüstite on its disproportionation reaction below 575°C," *Solid State Ion.*, vol. 104, no. 3–4, pp. 311–317, Dec. 1997, doi: 10.1016/S0167-2738(97)00432-3.
- [68] O. Dalstein *et al.*, "Evaporation-Directed Crack-Patterning of Metal-Organic Framework Colloidal Films and Their Application as Photonic Sensors," *Angew. Chem.*, vol. 129, no. 45, pp. 14199–14203, Nov. 2017, doi: 10.1002/ange.201706745.



# Chapter III. Process transfer for the elaboration of films by inkjet printing

## I. Introduction

The development of coatings directly patterned from a colloidal solution without post-processing for patterns is studied by way of the inkjet printing process. This Chapter deals with a process transfer of the airbrushing detailed in Chapter II towards an innovative and more accurate process, the inkjet printing. The two routes are sketched in Figure III-1.

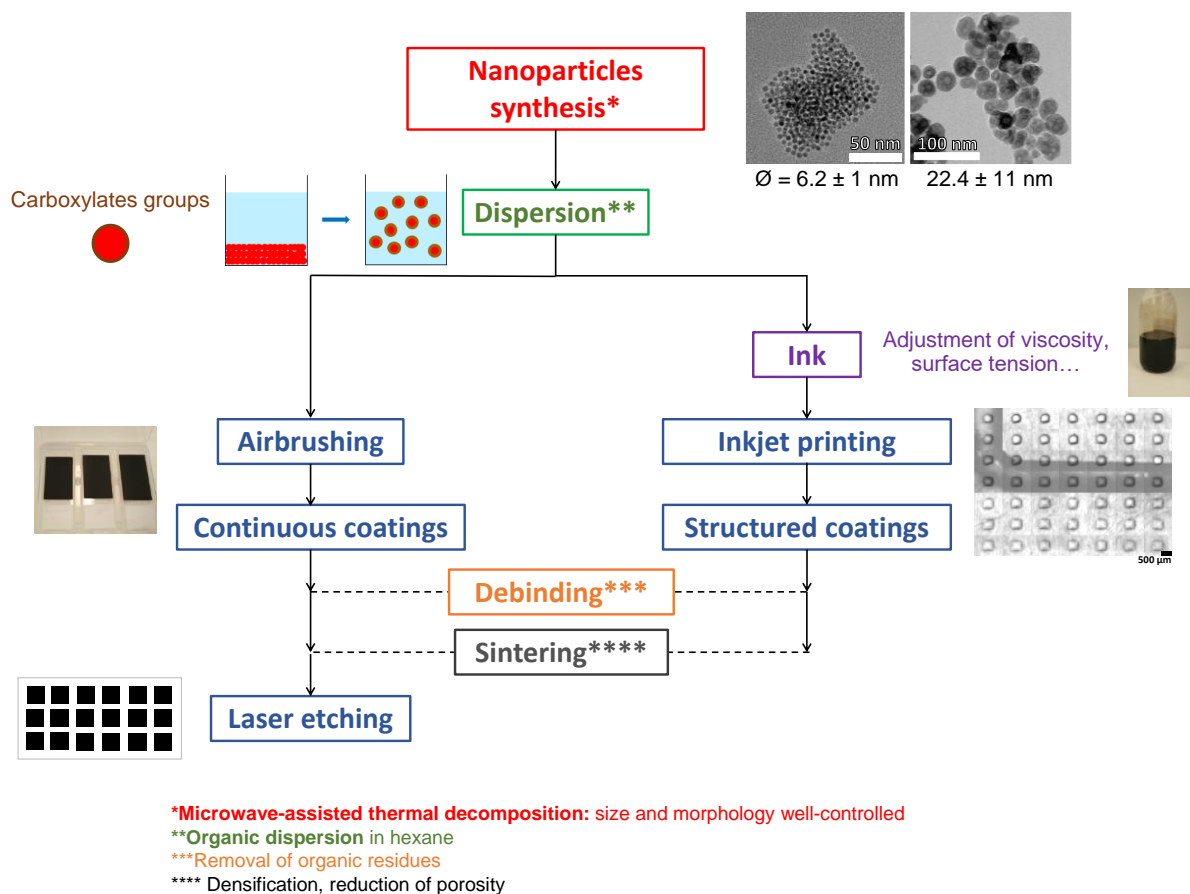


Figure III-1. Transfer of the airbrushing towards the inkjet printing.

The spinel  $\text{Zn}_{0.4}\text{Fe}_{2.6}\text{O}_4$  nanoparticles previously synthesized (Chapter I) are still dispersed in hexane with oleic acid acting as a surfactant (Chapter II). For the elaboration of coatings, a fundamental difference with airbrushing is that the inkjet printing requires the formulation of an ink compatible with the process regarding some physico-chemical characteristics like its viscosity or surface tension (Figure III-1). The patterned coatings are elaborated in a single step in comparison with the airbrushing route which decomposes in two steps: the development of

continuous coatings and then patterning by laser etching. After coating, a thermal treatment divided in a debinding and sintering steps is still required in order to remove the organic residues, densify the coatings and provide a good adherence of the film.

The present chapter focuses on the formulation of an ink compatible with the printer, and the development of patterns with well-defined shapes.

## **II. Formulation of an ink**

The formulation of inks in different media is explored in order to find a composition compatible with the inkjet printer. The first section details the employed equipment and the following physico-chemical requirements to be met by inks.

### **II.1. Compatibility with the inkjet printer**

#### **II.1.1. The process of inkjet printing**

The inkjet printing is an innovative process allowing the elaboration of coatings by successive ejection of droplets through piezoelectric nozzles. Two categories of printers exist: the technology of the Continuous Ink Jet (CIJ) and the Drop On Demand (DOD) system. In the CIJ technology, the ejection of droplets is continuous. The printing takes place as follows: the droplets are charged at the nozzle exit through an electric field and are then deflected under the application of an electrostatic field to the desired areas of the substrate. The unwanted droplets are sent to the ink tank for being ejected again [1].

On the contrary, the Drop On Demand method enables the printing of droplets directly in the locations of interest of the substrate by moving the printhead over the substrate. In this case, the droplets flow is not continuous but perfectly controlled. The droplets are only ejected if required. This last technique is more accurate.

The printer used in this work is from Ceradrop and uses the DOD technology (Figure III-2.A). The process has been developed by Rémi Noguéra in his thesis at SPCTS in Limoges with a patent filing by CNRS [2]. It allows the elaboration of 2D or 3D framework by the stacking of droplets ejected through piezoelectric nozzles (Figure III-2.B). This additive and flexible strategy displays a high precision and a resolution of 0.5  $\mu\text{m}$ . The device can be equipped with three printheads to use three different materials at the same time. In the study, only one printhead is employed (reference: Galaxy JA 256/30 AAA) with a plate of 256 nozzles. Each nozzle has a diameter of 36  $\mu\text{m}$  and the mean volume per droplet is of 28 pL. The working principle is deeply explained in the section III.1.



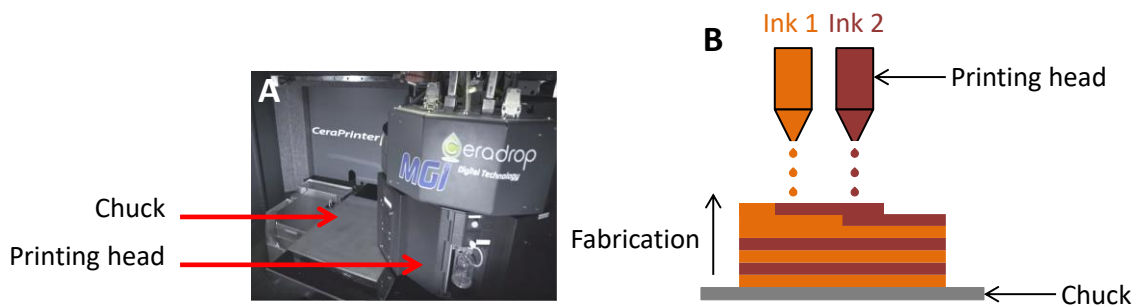


Figure III-2. Picture of the device of inkjet printing developed by Ceradrop (A) and schematic view (B).

### II.1.2. Requirements for inks

The dispersion of particles in hexane serves as a base for the formulation of a compatible ink. Indeed, dispersion of particles is of crucial importance to avoid agglomeration and sedimentation of particles in the printhead which could lead to a clogging of the jetting system.

Usually, the ink is defined as a stable system constituted of several components: the “pigment” which gives the ink its functional properties, here the magnetic powder (the material in the form of nanoparticles), a unique or a mixture of solvent(s), a dispersing agent, a binder, and additional components like additives, surfactants, de-foaming or wetting agents. The formulation of an ink is tricky due to the possible destabilization of the particles previously stabilized in the dispersion by adding other components in the system. As a consequence, a particular attention to the particle stabilization should be paid when adding other constituents to the dispersion in order to formulate an ink.

About the printer, some requirements have to be taken into account to formulate an ink compatible with the printhead, and thus allowing the ejection of the ink through nozzles.

In this respect, several approaches have been investigated in the literature to determine the jet-ability of an ink by inkjet printing. J.E. Fromm (1984) has described a model predicting the compatibility and the jet-ability of an ink from two dimensionless numbers: the Reynolds and Weber numbers [3] [4]. The Reynolds ( $Re$ ) and Weber ( $We$ ) numbers are the ratios of an inertial force to the viscous and the capillary forces, respectively. They are defined as follows:

$$Re = \frac{\rho v r}{\eta}, \quad We = \frac{\rho v^2 r}{\gamma} \quad \text{III-1}$$

with  $\rho$  the fluid density ( $\text{kg}\cdot\text{m}^{-3}$ ),  $v$  the fluid speed ( $\text{m}\cdot\text{s}^{-1}$ ),  $r$  the nozzle radius (m),  $\eta$  the dynamic viscosity of the fluid (Pa.s), and  $\gamma$  the surface tension of the fluid (N/m).

Another parameter is calculated from the Reynolds and Weber number: the ejection ratio  $Z$  or also the inverse of the Ohnesorge number ( $Oh$ ):

$$Z = \frac{Re}{\sqrt{We}} = \frac{\sqrt{\rho r \gamma}}{\eta} = \frac{1}{Oh} \quad \text{III-2}$$

The ejection ratio  $Z$  is a dimensionless number which measures the jet-ability of an ink in the case of Newtonian fluids. According to B. Derby *et al.*, this parameter  $Z$  must be comprised between 1 and 10 to obtain individual and separated droplets in the case of DOD systems [5]. In the case of an ejection ratio  $Z$  below 1, the ink is too viscous to be ejected. On the contrary, in the case of an ejection ratio equal to or above 10, the ejection is flowing continuously, leading to columns of fluid which split in satellite drops, tough to control. The viscosity is hence too low and the jetting is similar as spraying.

The ejection ratio  $Z$  being function of the viscosity and the surface tension of the fluid, these parameters have to be controlled in order to formulate a suitable ink. Moreover, the ink must meet specific criteria in terms of viscosity, surface tension and pH related to the printhead used and recommended by the supplier. These criteria are summarized in Figure III-3 in addition to the interval of the ejection ratio  $Z$ . The parameter  $Z$  is always predominant on the others, meaning an ink is considerable as compatible even if its viscosity and surface tension are slightly out of range as long as  $Z$  is comprised between 1 and 10. The pH of the ink must be fixed between 2 and 14 which is a large range, the only restrictive area being the acidic pH to avoid the degradation of the electronic circuit and of the ink transit through tubes and in the printhead.

	<i>Min value</i>	<i>Max value</i>
<i>Viscosity (mPa.s)</i>	5	20
<i>Surface tension (mN/m)</i>	30	35
<i>pH</i>	2	14
<i>Ejection ratio</i>	1	10

**Figure III-3. Ejection requirements of an ink.**

Another important parameter is the size of the particles dispersed in the ink media. An ideal ratio of 50 has to be considered between the particle size and the nozzle aperture (36  $\mu\text{m}$ ) [4]. Thus, the particle size does not exceed 720 nm. As a consequence, the ink is filtered at 1  $\mu\text{m}$  to prevent clogging of the printing head in case of the presence of aggregates.

A last prerequisite concerns the use of too volatile solvents which has to be avoided due to the fact it generates a fast drying of the ink inside the printhead before or at the beginning of the ejection. It can hence cause nozzle clogging.

## II.2. Development of hexane-based inks with $\text{Zn}_{0.4}\text{Fe}_{2.6}\text{O}_4$ nanoparticles

Different formulations of ink are explored, either with the addition of polymers (polymer-based) or solvents (solvent-based) from the previous dispersion of particles in hexane. A difficulty is the use of components compatible with hexane, which restricts the possibilities.

Indeed, many inks have been historically developed from dispersions in aqueous media (water or alcohol based) with a large choice of solvents and additives whereas formulation of organic based inks is more recent.

Due to the problem of nozzle clogging and possible destabilization of the particle dispersion, the formulations are only elaborated from the dispersion of SP(F)M particles in hexane as this dispersion is more stable than the FM one (Chapter II). The inks are formulated in regard to meet the intervals of viscosity, surface tension and ejection ratio imposed by the process of inkjet printing (Figure III-3).

## II.2.1. Polymers and solvents-based formulations

### II.2.1.A. Choice of formulations

Two types of ink are interesting in this study: aqueous and non-aqueous inks. Aqueous inks have been the first compositions to be developed for inkjet printing. They exhibit low drying on substrate due to the low volatility of solvents, water being commonly mixed with a glycol solvent. And they also have the advantage to be nontoxic [6]. A water based ink with silver nanoparticles constituted of a mixture of ethylene glycol, water, and ethanol has been previously studied and mixtures of ethylene glycol and water have demonstrated a good jet-ability [7].

Despite their more recent advancement, non-aqueous inks (meaning organic ones) are rather employed in some cases in comparison with aqueous ones. For example, an ink of gold and silver nanoparticles in terpineol has been developed for printed electronics, and other solvents like isopropylalcohol, dodecane, toluene, butylbenzene, hexane and cyclohexane have allowed the formulation of stable dispersions of metallic particles adapted for inkjet printing [8] [9].

In the present study, due to the organic nature of the particle dispersion in hexane, organic formulations of inks are preferred in order not to destabilize the dispersion. Polymeric dispersants are useful to provide a good stabilization of particles in inks [10]. Starting from patents reading [11] [12] [13], **two polymers compatible with hexane are selected for formulating polymer-based formulations: poly(1-decene) and polybutene 2300.**

Solvent-based formulations without polymers are also examined because it will provide a fast drying of solvents after printing which will ease the post thermal treatment of coatings. Octane ( $C_8H_{18}$ ) has met a great interest as a solvent in the formulation of some inks in the literature. An hexane in octane mixture with 5 wt% of Ga-doped ZnO particles is handled as an ink for spin casting [14]. In another study, an ink with a mix of octane, hexane and isopropyl alcohol as solvents, paraffin wax as an organic binder and hydroxystearic acid based polyester as a dispersant is elaborated with 14.21 v% of a commercial zirconia powder  $ZrO_2$  [15]. However, despite its lower boiling point, the low viscosity of octane (Figure III-4) is very limiting. Mixtures of octane with hexane might be suitable for spray type jetting with high ejection ratio  $Z$ , and are not adapted for controlled ejection of droplets. In the same family, octanol ( $C_8H_{18}O$ ) is more adapted due to its higher viscosity (Figure III-4) and is selected for a solvent-based formulation. Octanol is a good compromise between a moderate boiling point and a relative high viscosity in comparison to hexane in order to provide a good jet-ability.

	<i>Boiling point</i>	<i>Viscosity</i>	
	°C		mPa.s
<i>Hexane</i>	68	25 °C	0.309
<i>Octane</i>	126		0.515
<i>Octanol</i>	196	20 °C	9.0

**Figure III-4. Comparison of hexane, octane and octanol in terms of boiling point and dynamic viscosity.**

A second solvent is chosen for another solvent-based formulation: terpineol. An ink of gold nanoparticles in a mixture of 10% of hexane and 90 % of terpineol has shown a good jet-ability with a mass loading of 10% [16], close to the 8% of mass loading used with the airbrushing system (Chapter II).

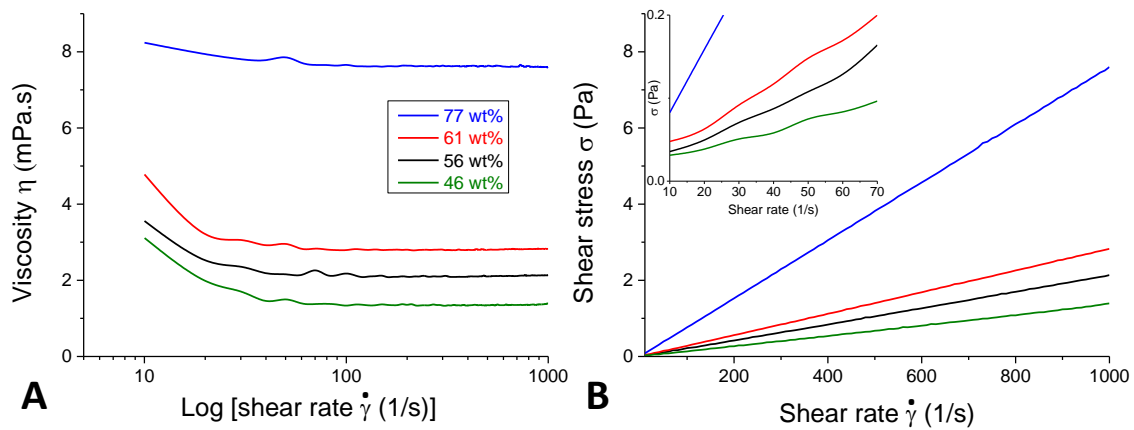
Two solvents are thus chosen to formulate solvent-based formulations: octanol and terpineol.

### *II.2.1.B. Approach for developing a formulation*

The formulations are firstly studied without particles. The followed approach to develop a formulation is described in details for the poly(1-decene).

In the first instance, the viscosity of different mixtures of poly(1-decene) ( $C_{10}H_{20}$ ,  $M_w = 140.268$  mol/g) in hexane is studied with a Couette rotational rheometer [17]. The liquid is inserted in the gap between two coaxial cylinders and is sheared uniformly between two planes through the rotation of the inner cylinder around itself, the outer one being fixed. This rheometer measures the resistance of the liquid through its deformation and flow under the application of an external constraint through the cylinder rotation. The deformation and the flow of the liquid are expressed by two parameters: the dynamic viscosity and the tangential stress, respectively. The analysis is adapted to low viscosities which is specifically useful for the study of ink media in hexane (0.309 mPa.s at 25 °C).

Figure III-5 compares the viscosity (Figure III-5.A) and the shear stress (Figure III-5.B) as a function of the shear rate of mixtures of poly(1-decene) in hexane with 46, 56, 61, and 77 wt% of poly(1-decene).



**Figure III-5.** Variation of the viscosity (A) and the shear stress (B) as a function of the shear rate for different wt% proportion of poly(1-decene) in hexane. The shear rate is in a logarithmic scale in the A inset.

In a Newtonian fluid, the viscosity is constant for all values of shear rate, its viscosity only depends on the temperature and the pressure. In addition, the shear stress applied to the fluid is proportional to the displacement speed of the fluid, with the viscosity as a factor:

$$\sigma = \eta \dot{\gamma} \quad \text{III-3}$$

with  $\sigma$  the shear stress,  $\eta$  the dynamic viscosity and  $\dot{\gamma}$  the shear rate.

In the present study, the mixtures of poly(1-decene) with hexane display the same trend with different magnitudes as a function of the poly(1-decene) proportion. At first, the viscosity decreases for low shear rates between 10 and 70  $\text{s}^{-1}$  and is then constant between 70 and 1000  $\text{s}^{-1}$  (Figure III-5.A). Secondly, a threshold stress is observed for all the mixtures (Figure III-5.B). The evolution of the shear stress versus the shear rate follows a Bingham model:

$$\sigma = \sigma_S + \eta_p \dot{\gamma} \quad \text{III-4}$$

with  $\sigma_S$  the threshold stress and  $\eta_p$  the plastic viscosity.

The Bingham model is typical of a non-Newtonian fluid. Thus, as the viscosity firstly decreases when the shear rate increases (between 10 and 70  $\text{s}^{-1}$ ), the fluid exhibits a shear thinning behavior. The fluid flows only when the threshold stress is overpassed. It is the case of a gel or toothpaste for example. Below this value, the fluid behaves like a solid. For higher shear rates beyond 70  $\text{s}^{-1}$ , the fluid is Newtonian. This portion is only considered to calculate the plastic viscosity.

Another observation is that the viscosity of the different mixtures increases with the poly(1-decene) proportion (Figure III-5).

Figure III-6 compiles the physico-chemical properties of the different mixtures in terms of density, surface tension and dynamic viscosity calculated from the Bingham model (Equation III-4). The ejection ratio  $Z$  is also computed from these values (Equation III-2).

<i>Poly(1-decene)</i>	<i>SP(F)M</i>	$\rho$	<i>Nozzle radius</i>	<i>Surface tension</i>	<i>Viscosity</i>	<i>Ejection ratio Z</i>
wt%	wt%	kg/m <sup>3</sup>	m	mN/m	mPa.s	-
<b>46</b>	-	696	$1.8 \times 10^{-5}$	21	1.3	12
<b>56</b>	-	718		21	2.1	<b>8</b>
<b>61</b>	-	766		22	2.8	<b>6</b>
<b>77</b>	-	794		25	7.6	<b>3</b>

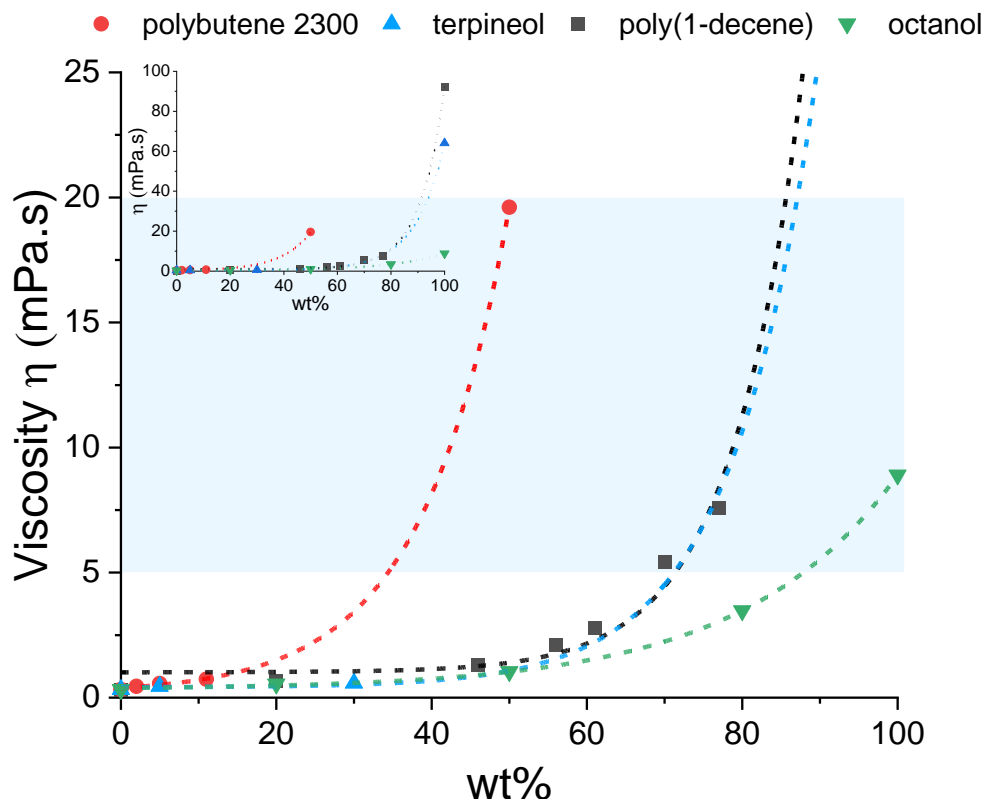
**Figure III-6. Physico-chemical characteristics of ink media with different wt% proportion of poly(1-decene) in hexane.**

Three media possess values between 1 and 10 and are hence compatible with the inkjet printing process following the previous requirements (II.1.2). The surface tension and viscosity are out of range for the majority of the mixtures (Figure III-3). **The mixture with 61 wt% of poly(1-decene) is chosen for printing** because it corresponds to a medium value of 6, the two others being close to the interval limits (3 for 77 wt% and 8 for 56 wt%). In addition, even if the viscosity is better and comprised between 5 and 20 mPa.s in the case of 77 wt% of poly(1-decene), the interest is to introduce as little additive as possible in the dispersion to have less components to remove during thermal treatment of coatings (Figure III-1).

The same approach is then applied to polybutene 2300, octanol and terpineol.

## II.2.2. Comparison between polymers and solvents-based formulations

The viscosity of other polymer or solvent mixtures with hexane is investigated and compared as a function of the proportion of the additional chemical compound in Figure III-7.



**Figure III-7.** Evolution of the viscosity as a function of weight percent of proportion of different polymers or solvents in hexane. The blue box indicates the accepted values for compatibility with the printing device.

The viscosity increases more or less rapidly in all cases with the weight percent of additional component. The more viscous the additional compound is, the faster the global viscosity increases. Indeed, the chemical compounds can be classified in the order of most to least efficient: polybutene 2300 (450 Pa.s at 25 °C [18]), poly(1-decene) (92 mPa.s), terpeneol (64 mPa.s) and octanol (9 mPa.s). All of the points are fitted with an exponential law corresponding to the dotted curves (Figure III-7).

As previously mentioned in section II.1.2, the viscosity must be located between 5 and 20 mPa.s to make the fluid suitable for inkjet printing. The interval of requested viscosity is represented by a blue box in Figure III-7. To attain this range, more than 35 wt% of polybutene 2300, 70 wt% of poly(1-decene) and terpeneol, and 90 wt% of octanol have to be added to hexane to formulate a mixture with a good jet-ability. In this way, the required amount of additives is significant. A compromise has to be found between a solution with a high amount of polymers more difficult to remove by thermal treatment, and an ink constituted of a mixture of solvents easier to dry after printing. Figure III-8 is a table of the boiling points of the different polymers and solvents employed. Octanol is the best candidate due to its faster drying.

	<i>Octanol</i>	<i>Terpeneol</i>	<i>Polybutene 2300</i>	<i>Poly(1-decene)</i>
<i>Boiling point (°C)</i>	196	218	293– 341	> 316

**Figure III-8.** Boiling points of different polymers or solvents used in the ink formulation.



Figure III-9 compares the physico-chemical properties of polybutene 2300 in hexane and octanol in hexane mixtures. The ejection ratio  $Z$  is of 1 and 5 for polybutene 2300 and octanol, respectively. Therefore, despite its high viscosity comprised between 5 and 20 mPa.s, the polybutene 2300 in hexane formulation is defined by a weak ejection ratio  $Z$  at the boundary of the accepted interval. Its viscosity is too high in comparison with the surface tension and the jetting of the ink might necessitated high voltages.

Moreover, besides its high boiling point, polybutene 2300 is a sticky polymer which induces cleaning and handling issues. This is a major problem considering the inkjet printing device in terms of cleaning of ink tank and tubes, as well as possible obstruction and irreversible damages of nozzles due to the polymer. The mixture of 61 wt% of poly-1-decene with hexane is hence chosen as the PF (polymer-based) formulation since the polybutene 2300 has many drawbacks.

<i>Polymer/ solvent</i>	<i>Proportion</i>	$\rho$	<i>Nozzle radius</i>	<i>Surface tension</i>	<i>Viscosity</i>	<i>Ejection ratio Z</i>
-	wt%	kg/m <sup>3</sup>	m	mN/m	mPa.s	-
<i>Polybutene 2300</i>	50	758	$1.8 \times 10^{-5}$	20	19.6	1
<i>octanol</i>	80	769		23	3.5	5

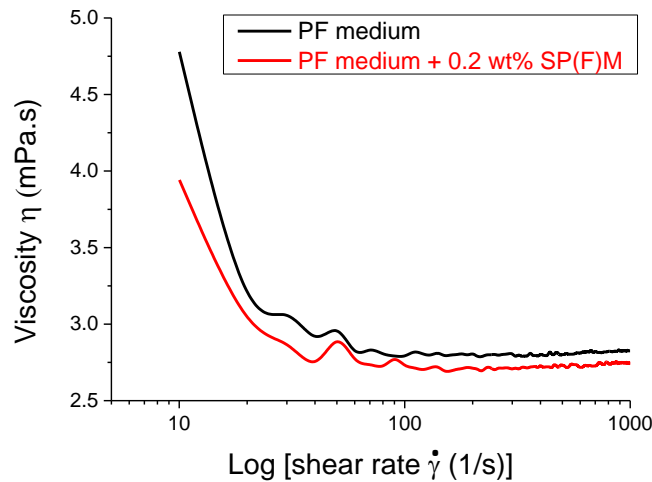
**Figure III-9. Physico-chemical characteristics of ink media with 50 wt% of polybutene 2300 and 80 wt% of octanol in hexane.**

In addition, octanol is chosen for the formulation of a SF (solvent-based) ink due to its low boiling point. A balance between the addition of a low amount of octanol in hexane with a sufficient viscosity to enable a good jetting is found for a proportion of 80 wt% of octanol (Figure III-9), which is, in the following, referred to the SF (solvent-based) formulation.

It will be interesting to confront printings with PF and SF formulations in order to analyze the interest of a media from another in terms of printing jet-ability and quality of coatings.

### II.2.3. Rheological behavior of PF and SF formulations with nanoparticles

A tiny content of SP(F)M particles is introduced in the PF formulation with 61 wt% of poly(1-decene) as a first trial of particle stability in a different medium in comparison with hexane alone. The rheological behavior is not so different from the one without particles (Figure III-10) with a slope slightly less accentuated for the decrease of the viscosity at shear rates below  $70 \text{ s}^{-1}$ , meaning the addition of particles renders the fluid Newtonian on a larger range of shear rate which suits better for an easier study of the ink jetting (II.1.2). The ink is stable for days. This low addition of particles does not change the surface tension either and the ejection ratios are similar (Figure III-11).



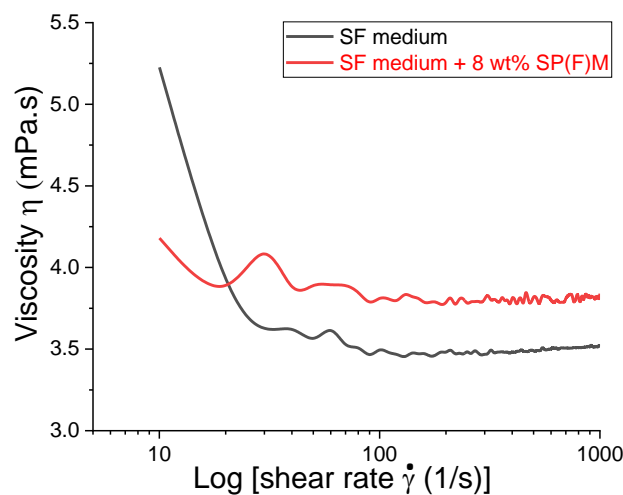
**Figure III-10.** Variation of the viscosity as a function of the shear rate for the PF medium without and with addition of SP(F)M particles in a logarithmic scale.

<i>Poly(1-decene)</i>	<i>SP(F)M</i>	$\rho$	<i>Nozzle radius</i>	<i>Surface tension</i>	<i>Viscosity</i>	<i>Ejection ratio</i>
<i>wt%</i>	<i>wt%</i>	$\text{kg/m}^3$	<i>m</i>	$\text{mN/m}$	$\text{mPa.s}$	-
<i>61</i>	-	766	$1.8 \times 10^{-5}$	22	2.8	<b>6</b>
	0.2	730		22	2.7	<b>6</b>

**Figure III-11.** Physico-chemical characteristics of the PF medium without and with addition of SP(F)M particles.

Figure III-12 shows the evolution of the viscosity versus the shear rate for SF formulations without and with the addition of 8 wt% of SP(F)M particles. The same rheological behavior as for poly(1-decene) in hexane mixtures is observed but with a lower threshold stress at approximately  $30 \text{ s}^{-1}$ , namely a shear-shinning behavior below  $30 \text{ s}^{-1}$  and a Newtonian one beyond this value. Contrary to poly(1-decene)-hexane mixtures the global trend of these dispersions is close to the one of a Newtonian fluid.

Additionally, the introduction of particles converts the rheological properties of the SF medium into the one of an almost perfect Newtonian fluid.



**Figure III-12.** Variation of the viscosity as a function of the shear rate for the SF medium without and with addition of 8 wt% of SP(F)M particles in a logarithmic scale.

The ejection ratio  $Z$  of SF formulations without and with the addition of 8 wt% of SP(F)M particles is of 5 in both cases (Figure III-13), which is excellent for inkjet printing.

<i>Octanol</i>	<i>SP(F)M</i>	$\rho$	<i>Nozzle radius</i>	<i>Surface tension</i>	<i>Viscosity</i>	<i>Ejection ratio</i>
<i>wt%</i>	<i>wt%</i>	$\text{kg/m}^3$	<i>m</i>	$\text{mN/m}$	$\text{mPa.s}$	-
80	-	769	$1.8 \times 10^{-5}$	23	3.5	5
	8	795		23	3.8	5

**Figure III-13. Physico-chemical characteristics of the SF medium without and with addition of 8 wt% of SP(F)M particles.**

### II.3. Conclusion

*The inkjet printing is an innovative and flexible additive technology enabling the elaboration of 2D or 3D frameworks by the ejection of droplets through piezoelectric nozzles. The device chosen for the inkjet printing is a Drop On Demand system from Ceradrop.*

*Specifications in terms of physico-chemical properties of the inks have to be respected in order to formulate a suitable ink, with a good jet-ability and compatible with the printing device. The requirements are the following:*

- *a viscosity between 5 and 20 mPa.s,*
- *a surface tension between 30 and 35 mN/m,*
- *a pH between 2 and 14 to advise against too acidic media which can damage the printing circuit,*

*Viscosity, surface tension and pH are imposed by the type of the printhead and are indicated by the supplier.*

- *the ejection ratio Z which is a dimensionless number predicted by the J.E. Fromm's approach (1984) to quantify the jet-ability of an ink. This number is linked to the viscosity and surface tension of the fluid and must be comprised between 1 and 10. It is a predominant factor over the previous ones. Indeed, the ink can be out of the intervals defined for the viscosity and the surface tension if the ejection ratio Z is respected.*
- *the size of the particles dispersed in the ink media is also important. An ideal ratio of 50 has to be considered between the particle size and the nozzle aperture. Particle aggregation and sedimentation must be avoided by keeping a good stabilization of the particles in the ink medium to prevent the nozzle clogging.*

*Two ink formulations derive from the previous ink prerequisites and are summarized in Figure III-14:*

- *a polymer-based formulation: PF formulation with 60 wt% of poly(1-decene) in hexane.*
- *a solvent-based formulation: SF formulation with 80 wt% of octanol in hexane.*

	Surface tension	Viscosity	Ejection ratio Z
	mN/m	mPa.s	/
<i>Machine compatibility</i>	<b>[30-35]</b>	<b>[5-20]</b>	<b>[1-10]</b>
<b>PF formulation</b>	22	2.7	6
<b>SF formulation</b>	23	3.8	5

Figure III-14. Physico-chemical characteristics of PF and SF formulations of ink with 0.2 and 8 wt% of SP(F)M particles.

*The SF formulation allows increasing the ink viscosity. Likewise, the boiling temperatures of poly(1-decene) and octanol are respectively of 316 and 196 °C. Thus, the*

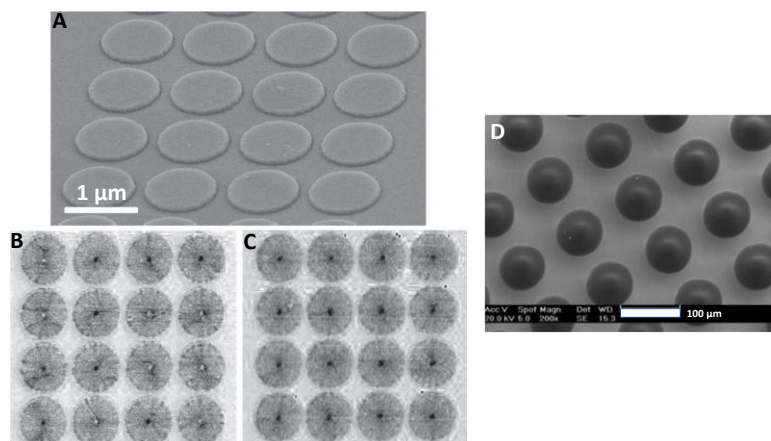
*drying of coatings will be probably enhanced with octanol. A less invasive thermal treatment could be enough to remove solvent and surfactant from the coating with the use of octanol instead of poly(1-decene). The next part focuses on printings and compares the results with PF and SF formulations, highlighting the advantages and drawbacks of one formulation versus the other.*

### III. Printing

Printings with PF and SF formulations are achieved. The first part details the working principle of the inkjet printer with the important parameters to control, and also the different steps from the ink ejection to the coating conception.

#### III.1. The inkjet printer and printing parameters

The aim is to develop a network of perfectly controlled patterns in size and shape with defined spacing to create magnetic networks. This kind of structure is exemplified in Figure III-15. A controlled network of permalloy disks with a 1  $\mu\text{m}$  diameter has been obtained by an electron-beam lithography technique followed by a lift-off processing (Figure III-15.A). Similarly, the presence of vortex inside the permalloy disks under a magnetic field is demonstrated [19] (Figure III-15.B-C). Thanks to the inkjet printing, this two-step process can be converted into a single one to obtain this kind of patterned coatings on magnetic oxides. Figure III-15.D illustrates the ability of the inkjet printing to elaborate oxides network: silica dots have been printed on a silicon wafer with a Ceradrop printing device [20]. The working principle of this last technique is described in the next section (III.1.1).



**Figure III-15.** Permalloy disks with a 500 nm radius on a scanning-electron micrograph (A), and magnetic force micrographs under a field of 0 (B) and 70 mT (C). From A. Vogel *et al.* [19]. SEM image of silica microdots on a silicon wafer obtained by inkjet printing (D). From O. De Los Cobos *et al.* [20].

##### III.1.1. Working principle

The inkjet printing is an innovative process based on the elaboration of coatings by successive ejection of droplets through piezoelectric nozzles.

One printhead is used as the films are constituted of a single material. For example, in the case of a composite material with several overlapped sheets, multiple printheads are required and can be switched easily to rapidly build the material layer after layer. In the study, the employed printhead possesses a plate of 256 nozzles with a diameter of 36  $\mu\text{m}$  and a mean volume per droplet of 28 pL. The system of the printing device is schematized in Figure III-16.

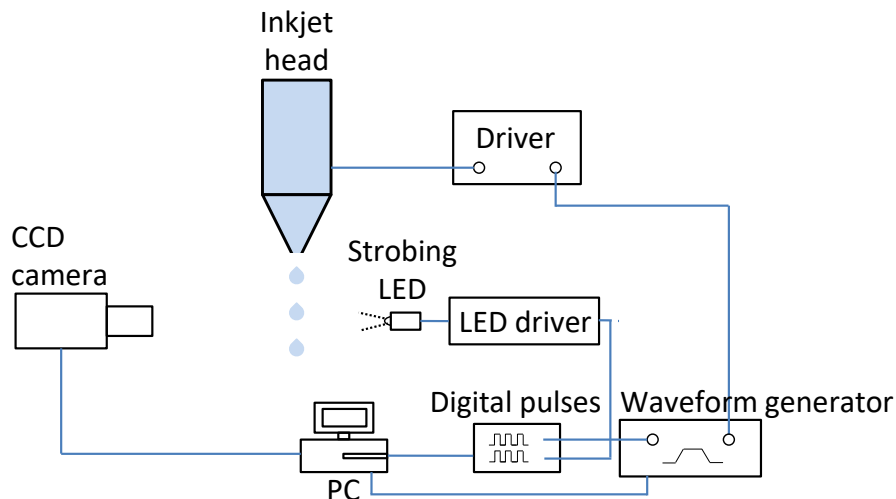


Figure III-16. Principle scheme of working of inkjet printing [1].

The overall system is automatized: the position of the printhead and of the chuck, the printhead with the nozzles, the control of pressure and temperature inside the ink tank and through the nozzles which are fixed during the adjustment of the ejection parameters. The inkjet head is connected to a computer from which the position of nozzles is controlled and synchronized, as well as the droplet ejection. A system of droplet observation through a CCD camera combined to an emitting light source through a diode (LED) allows acquiring images of droplets delayed in time, and getting to distinguish the general pattern of the ejection of droplets.

### III.1.2. Operating protocol

The printing occurs in the same manner through an operating protocol divided in three steps:

- The first step is the formulation of a suitable ink from SP(F)M nanoparticles dispersed in hexane, compatible with the printing head in terms of viscosity and surface tension and displaying a good jet-ability through an ejection ratio comprised between 1 and 10 as described in details in section II.2.
- The second step consists on the control of the ejection of droplets through the piezoelectric nozzles.

Indeed, a piezoelectric membrane is located on one wall of the ink tank (Figure III-17). An electrical pulse is applied to this piezoelectric nozzle through an adapted software connected to the device by a computer. The application of this pulse will generate a deformation of the piezoelectric membrane leading to a reduction of the volume of the tank. It induces the ejection of the ink through nozzles. Thereafter, the membrane returns to its original shape which creates a depression inside the chamber with a refilling of the tank with ink. The ejection through the piezoelectric nozzles is detailed in Figure III-17.



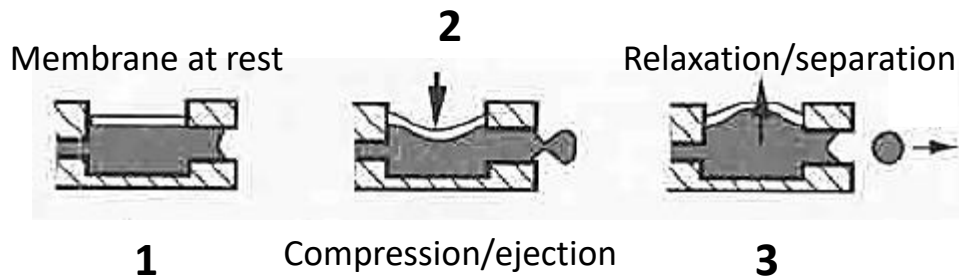


Figure III-17. Scheme of droplet ejection through a piezoelectric nozzle. From J.-J. Eltgen [21].

The electrical pulse applied to the piezoelectric nozzles is characterized by a wave shape split in three stages with three distinct times ( $T_1$ ,  $T_2$  and  $T_3$ ) and a voltage amplitude  $|U|$  (Figure III-18). The modification and control of these four parameters are essential in order to produce ideal and individual droplets stable over time [22]. The pulse is linked to the droplet properties and will thus condition its shape, volume, and speed [23]. It is possible to pilot the droplet characteristics through the pulse, so as to choose the appropriate conditions of jetting for printing.

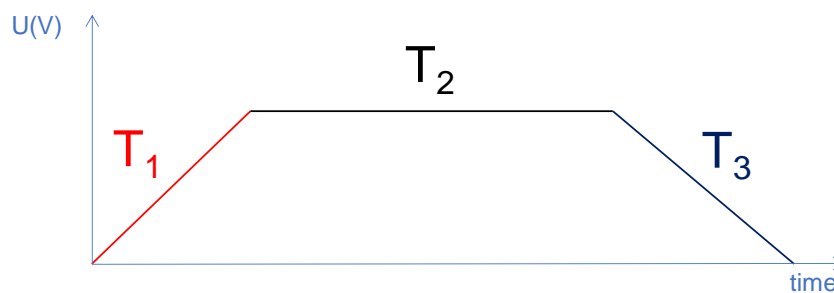
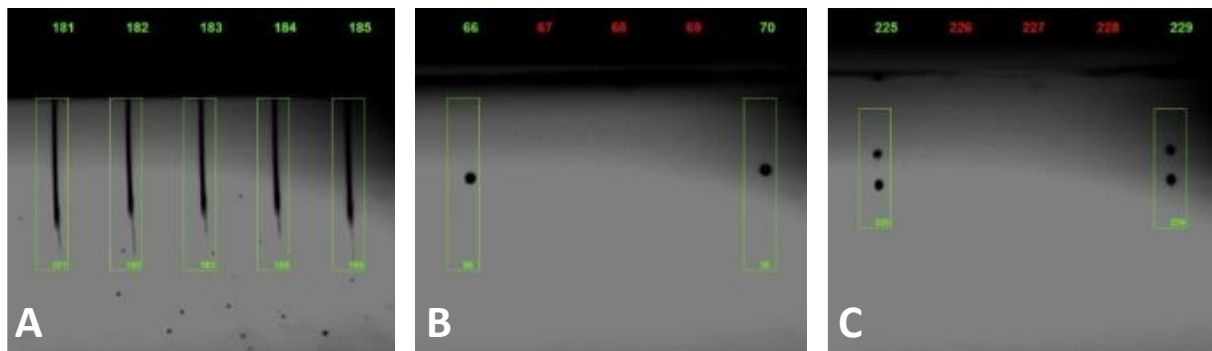


Figure III-18. Electrical pulse applied to piezoelectric nozzles.

In order to determine and adjust the appropriate pulse, the jetting of droplets is observed with a strobe connected to a CCD camera (Figure III-16). All of the droplet path can be acquired from its expulsion at the nozzle exit to its contact with the substrate. The parameters to adjust and control the shape, volume and speed of droplets are the electrical pulse (Figure III-18) and the ejection frequency. From these observations, a window of nozzles adapted for printing can be selected among the 256 nozzles available on the printhead.

At the nozzle exit, the ink goes through two phases before the droplet formation, shown in Figure III-19 with the PF formulation. At first, the ink is ejected in the shape of a liquid column at the nozzle exit. This filament elongates and becomes thinner over time (Figure III-19.A). At this stage, two configurations are possible: on the one hand, during the thinning, the filament does not break and stays continuous. It will then lead to the collapse of the filament in a second step to form a unique and ideal droplet (Figure III-19.B).

On the other hand, the ink flow breaks at different locations of the filament, generating multiple drops after retraction of the filament. These drops are called satellite drops (Figure III-19.C) and are less stable than ideal ones. This kind of ejection induces defects in the printing shape due to the printing of lost drops at undesired areas on the substrate.



**Figure III-19.** Observation by a CCD camera of an ink filament in a columnar shape (A), generating perfect (B), or satellite (C) droplets (PF formulation). (Exposure time = 200  $\mu$ s).

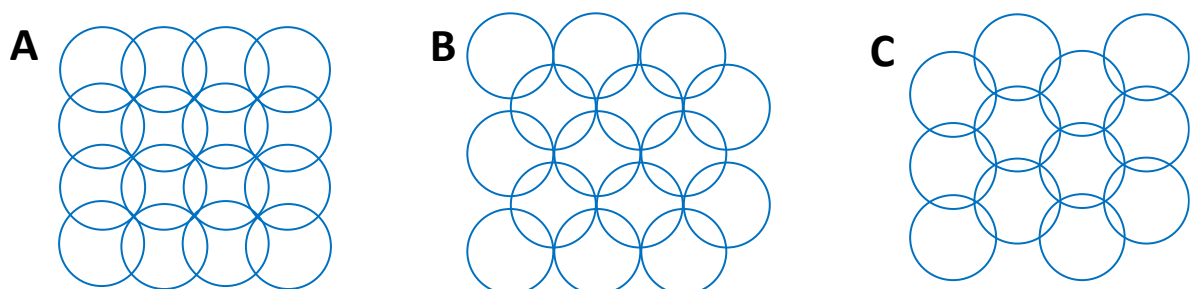
Two ejection types will be compared during the printing study: a columnar and continuous jetting (Figure III-19.A) without forming separated droplets, and ideal droplets (Figure III-19.B).

Two important issues have to be taken into account. The jetting of ink through nozzles is subjected to a destabilization phenomenon when printing during hours. The ejection has to be frequently controlled to verify its quality. Additionally, the ejection of droplets could generate a spreading of the ink on the nozzle plate. In this case, an ink film is formed on the nozzle plate and it will disturb the droplet ejection. Adapted electrical pulses, as well as ejection frequencies have to be selected to avoid this phenomenon.

Therefore, the printings are performed with a limited range of nozzles namely a maximum of about ten nozzles in motion at the same time to keep a good control of the ejection.

- The third step concerns the development of the design of patterns with the Ceraslice software: the “slicing” step.

The Ceraslice software allows to draw the design of the printing area and thus to define its geometric parameters like the pattern shape, the dimensions and the spacing between patterns. Once the object to print is created, a fabrication file divided in rasters and layers is generated. It depicts and simulates the way the object will be printed, hence the “slicing” of the elaboration of the desired object. The patterns being filled with droplets, the filling method is selected at this stage. Different types of mesh exist: square, centered square and hexagonal meshes (Figure III-20).



**Figure III-20.** Square (A), centered square (B) and hexagonal (C) mesh types.

The square mesh is chosen for the overall study. The droplets are thus similarly spaced in X and Y directions. The purpose is to favor a good overlapping of droplets in order to provide a good filling of patterns which improves the resolution and printing quality (Figure III-21).

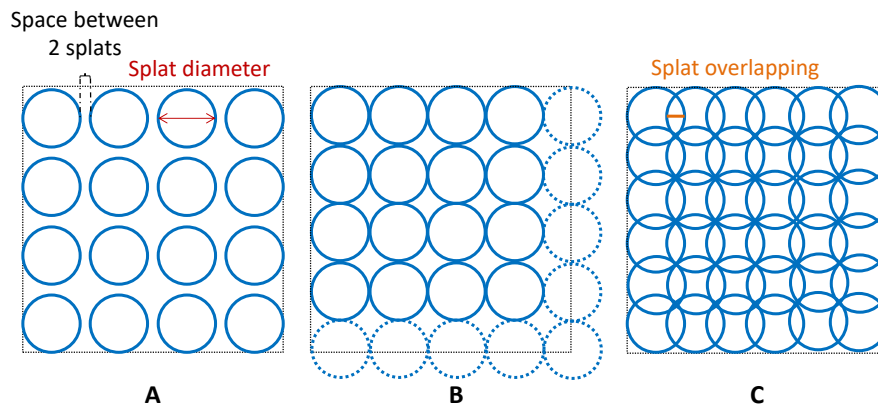


Figure III-21. Filling of a square pattern using a square mesh type with spaced (A), in contact (B) and overlapped (C) splats.

The head moves in the X direction and the chuck along Y. For this purpose, an angle between the nozzle plate and the printing direction is required (Figure III-22). It is also called the “saber angle” [24]. Indeed, if the printing occurs at a  $90^\circ$  angle of the printhead with the direction of printing, the distance between one nozzle from another one (namely  $254\ \mu\text{m}$ ) limits the spacing between the droplets. The nozzle plate needs to be tilted in order to reduce the spacing between droplets and thus enable the partial overlap of droplets. A perfect pattern will display no void in its filling. The more tilted the head is, the better the resolution is.

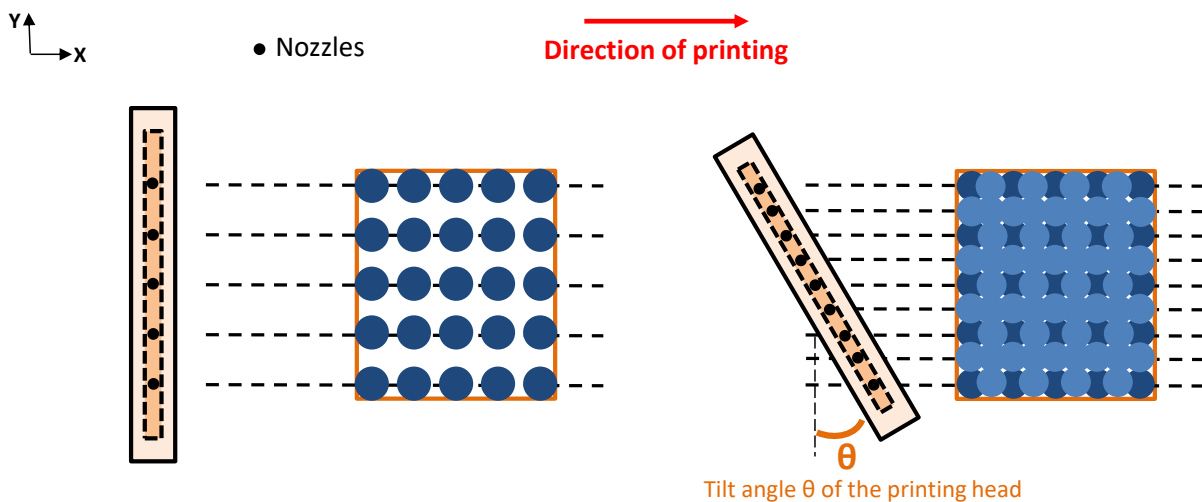


Figure III-22. Inclination of the printhead to allow the overlapping of droplets.

Some parameters are introduced in the fabrication file: the range of nozzles used for the printing, the diameter of a splat which is the name given to a droplet deposited on the substrate, the space between two splats or the overlapping, the layer thickness, and the number of layers. The determination of the splat size for the calculation involves a preliminary test of printing of single and spaced splats.

Through these data, the software computes the printing parameters for an optimal fabrication, depicted in Figure III-23. Indeed, the distance between the centers of two consecutive splats along X axis ( $e_{Fab}$ ) is estimated, as well as along Y axis ( $e_{Shift}$ ). The drop spacing in X ( $e_{Fab}$ ) is intimately linked to the printhead speed and the droplet ejection frequency. The fabrication velocity is deduced from an imposed frequency [22]. Moreover,  $e_{Shift}$  depends on the tilt angle  $\theta$  of the printhead in order to match the nozzle position with the raster to print. A subdivision of  $e_{Fab}$  is also calculated and corresponds to the minimum distance between two consecutive droplets or in other words the printing resolution ( $e_{Trig}$ ) with a minimum value of 5  $\mu\text{m}$ . (Figure III-23).

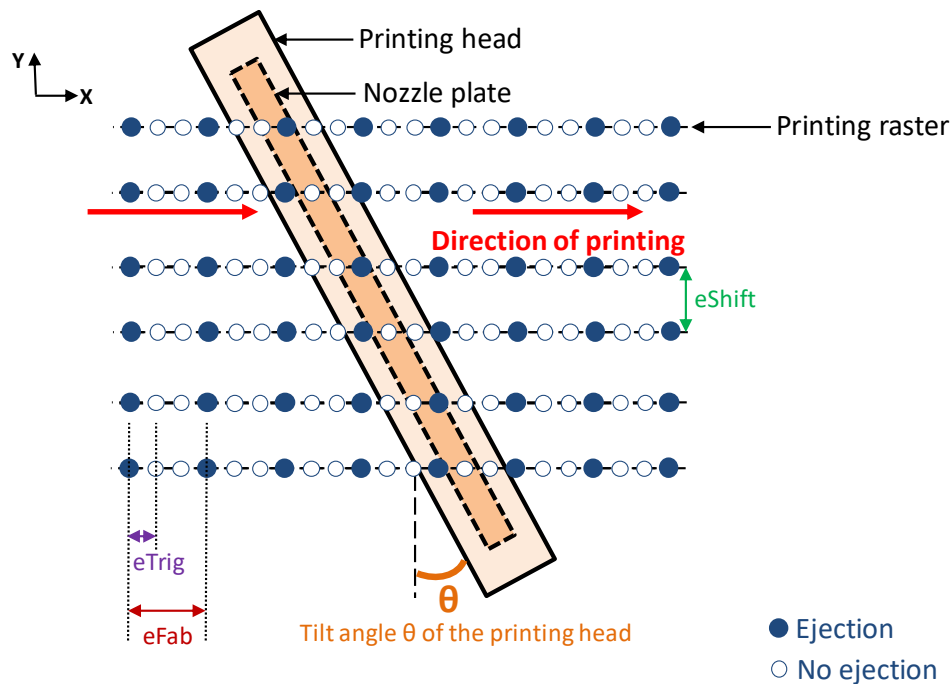


Figure III-23. Top view of the configuration of the printing head during processing with a tilt angle [22].

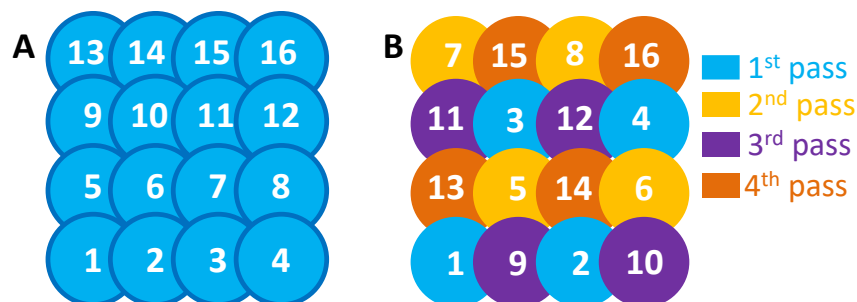
After these steps, the fabrication can be launched.

### III.1.3. Printing parameters

The working process from the ejection of droplets to the elaboration of patterns with a high quality highlights different printing parameters which directly impact the printing quality:

- the working distance between the printing head and the substrate which is taken between 0.5 and 1 mm (0.5 mm in the study).
- the ejection frequency which affects and imposes the displacement speed of the printing head. The frequency does not exceed 1kHz and it is preferably fixed at 200 or 500 Hz.
- the mesh type namely the square one in this study, with the choice of the space between splats to optimize the pattern filling.
- the printing strategy. Two strategies are possible: a free or trapeze mode. The printing strategy gives the printing order of the splats in the chosen mesh.

In the free mode, the splats are printed in an orderly way during the course of the printing head from the left to the right, line by line. During each printhead swath from the right to the left, the nozzle ejection is stopped and restarts when the head moves from the left to the right (Figure III-24.A). In the trapeze mode, the ejection is also only allowed during the movement of the printhead from the left to the right. The splats are printed one time in two and one line of every two (Figure III-24.B). In this last configuration, the filling of the entire mesh requires more printhead swaths. The interest of this method is to ensure a slower and gradual drying of the patterns. It could have an interest to improve the solvent drying and avoid constraint during thermal treatment after processing. The two strategies are tested. That ejection of droplets only allowed from a left to the right pass of the printhead is set by the user.



**Figure III-24. Printing strategies with the square mesh: free (A) and trapeze (B) modes.**

- the coating thickness through the number of layers. The stacking of layers is an alternative to the limitation of the particle concentration in the ink due to clogging issues of the printhead. The trapeze configuration will be interesting in this case to eliminate an accumulation of solvent between layers.

Printing parameters play on the spacing between droplets and the time allowed for drying the droplets. Although coalescence of the droplets seems to be a good thing since it results in a continuous coating, it may affect the precision of the pattern (from square shape to round shape for example) by minimization of surface energy. That is why the drying time of a single droplet is also a critical parameter.

The printings are realized onto glass slides for preliminary trials. Silicon wafers or pure alumina substrates as used with airbrushing will have to be adopted to permit the sample sintering at 770 °C (Chapter II) after processing (Figure III-1).

### III.2. $\text{Zn}_{0.4}\text{Fe}_{2.6}\text{O}_4$ patterned coatings

The elaboration of  $\text{Zn}_{0.4}\text{Fe}_{2.6}\text{O}_4$  patterned coatings follows the previous steps, detailed in section III.1.2. Only SP(F)M (diameter of  $6.2 \pm 1$  nm) particles are printed. The two ink formulations are compared through the overall process. In the first place, the jetting of droplets is assessed.

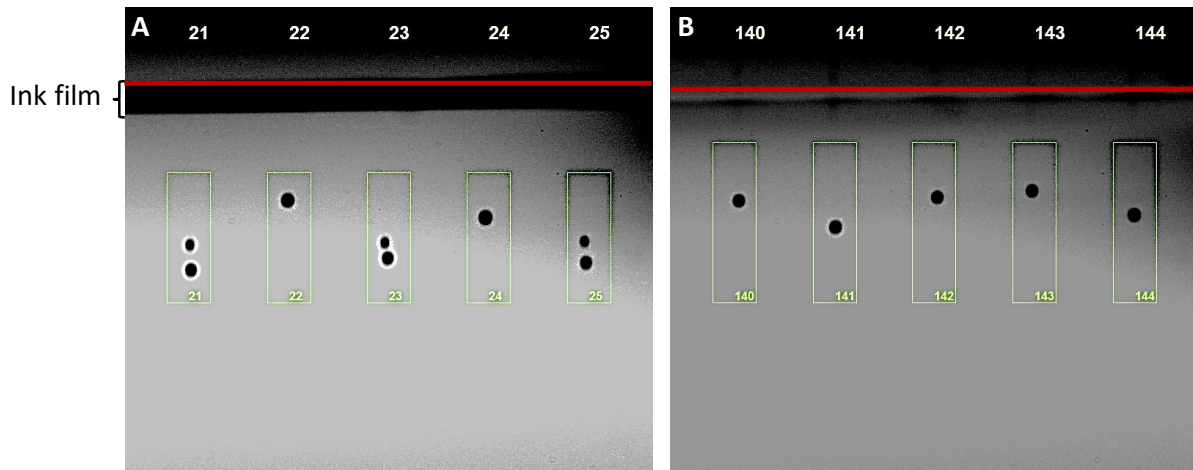
### III.2.1. Effect of the ink formulation on the ejection

The ejection of PF and SF inks through the piezoelectric nozzles is exhibited in Figure III-25. A similar voltage of 60 V is applied in both cases to compare the jetting in the same conditions.

The presence of a layer of ink at the bottom of the nozzle plate is shown in the case of the PF formulation (Figure III-25.A). It leads to the formation of a meniscus during jetting. This massive phenomenon disturbs the jetting, as seen in Figure III-25.A with the formation of satellite droplets. Furthermore, it is applied to the full length of the plate and increases during printing over time. The change of the electrical pulse can slightly reduce the topping but it systematically comes back.

This phenomenon has been observed by M. Mougenot [4] for the ejection of inks in a mixture of ethanol and water displaying a low surface tension of about 23 mN/m. In M. Mougenot's work, the ink possesses a good affinity with the hydrophilic nature of the nozzle plate and completely wets its surface. Inks with a low surface tension are difficult to eject if they are poorly hydrophobic. That is why a small amount of a hydrophobic organosilane (TFTS: tridecafluoro-1,1,2,2-tetrahydrooctyltriethoxysilane) is added to the formulation to allow a better ejection and prevent the formation of an ink film at the bottom of the nozzle plate. In the present study, the mixture of poly(1-decene) and hexane as a medium for the ink is highly hydrophobic and the surface tension is of the same range of values as in M. Mougenot's work (22 mN/m). According to her study, the PF formulation should not exhibit a topping of the nozzle as significant as seen in Figure III-25.A. A possible explanation is the low viscosity of the PF formulation in comparison with M. Mougenot's one, which are of 2.7 and about 5 mPa.s respectively.

Nevertheless, the topping is definitely diminished and barely noticeable with the SF formulation (Figure III-25.B) whereas the mixture of octanol with hexane is also highly hydrophobic. Perfect droplets are observed. For both inks (Figure III-14), the surface tensions are close (22 and 23 mN/m for PF and SF respectively) and are low which tends to induce a good wettability on the nozzle plate. However, the lower viscosity of PF formulation (2.7 versus 3.8 mPa.s for SF) could favor the formation of an ink meniscus on the bottom of the nozzle plate. It is in agreement by comparison with M. Mougenot's work [4]. The particle concentration being similar (around 0.2 wt%) in both cases, it could not be an explanation.



**Figure III-25.** Pictures of the ejection of droplets at 60 V with PF (A) and SF (B) formulations. The red line pinpoints the bottom of the nozzle plate.

As a conclusion, the combination of a low surface tension and viscosity promotes the topping of the ink on the nozzle plate regardless of the hydrophilic or hydrophobic nature of the inks. The SF formulation is hence more adapted.

### III.2.2. Effect of the ink formulation on coatings

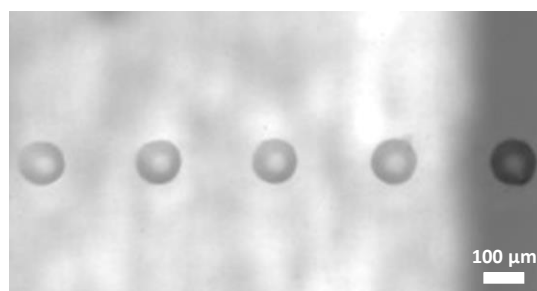
After studying the effect of the ink on the droplet ejection through the piezoelectric nozzles, the effect of each ink on the elaboration of coatings is investigated.

#### III.2.2.A. PF formulation

Firstly, coatings are printed with the PF formulation. The ejection of droplets is often controlled to reduce the topping of the nozzle plate and to allow a correct ejection for printing.

##### III.2.2.A.a. Splat

As previously mentioned in the detailed printing protocol (section III.1.2), the size of a splat needs to be estimated with a first printing of spaced droplets. Reproducible splats with an approximate diameter of 120  $\mu\text{m}$  are obtained with the PF ink (Figure III-26).

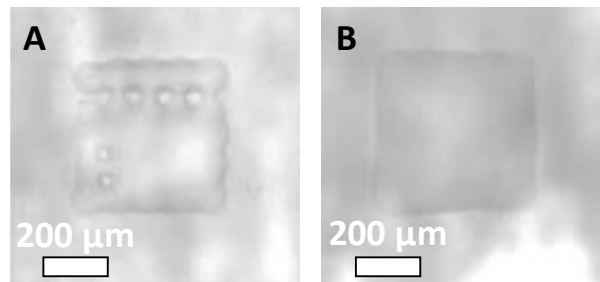


**Figure III-26.** Example of printed splats with the PF formulation with 0.2 wt% of SP(F)M particles.

### III.2.2.A.b. Patterns

The previous diameter of splats is applied in the fabrication file for the printing of square patterns of 500  $\mu\text{m}$ . Three different parameters are analyzed for improvement of the printing quality.

At first, the influence of the type of droplet ejection is examined. Figure III-27 compares the printing of a square pattern with ideal droplets at 60 V in the A inset and with a columnar ejection at 90 V in the B inset. The columnar ejection is the jetting of thin column of fluid which starts to decompose into satellite drops under high voltage while the perfect droplets are unique and round drops ejected under lower voltage. The result is surprising. The square printed with perfect droplets comprises many voids in its structure (Figure III-27.A) whereas no hole is seen in the case of columnar droplets (Figure III-27.B). The quality of patterns is enhanced with the ejection of columnar droplets because there is no time for the jetting to destabilize under a higher voltage.



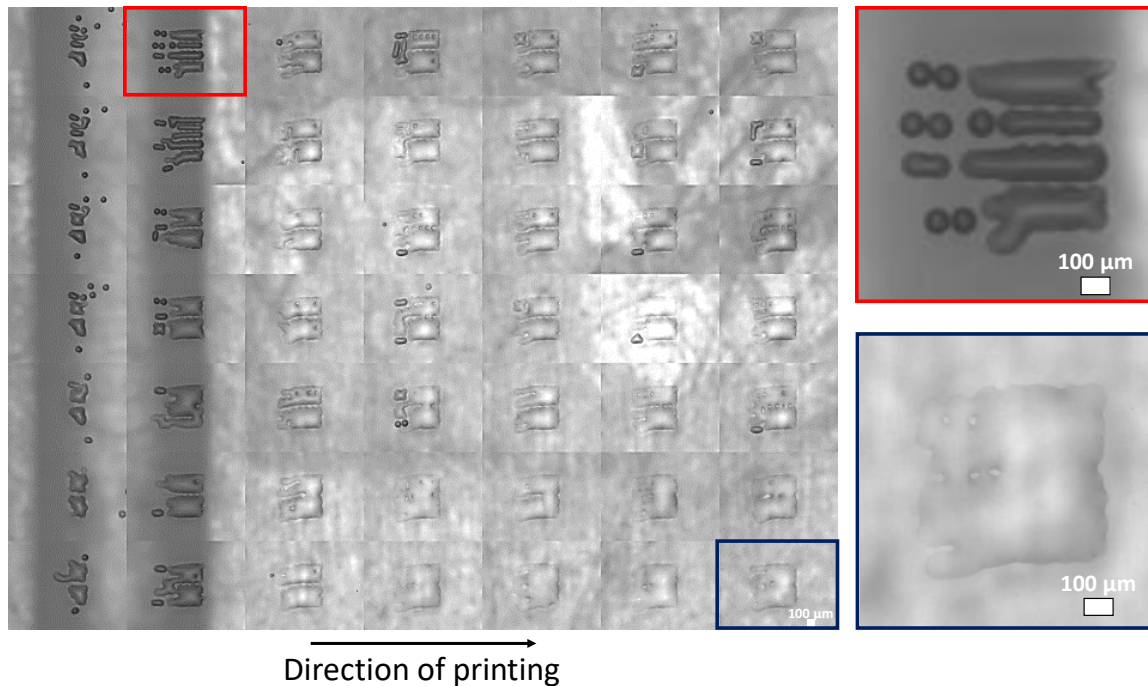
**Figure III-27. Square patterns printed with perfect (A) and columnar (B) droplets with the PF formulation (0.2 wt% particles).**

Indeed, the presence of holes in the pattern printed via an ejection of perfect droplets can be due to the destabilization of the jetting under lower voltage because of the topping of the plate. The ejection being slower, satellite droplets are generated and are destabilized which is detrimental for printing. The jetting is not vertical anymore. Some drops are printed at the wrong places and there is a lack of drops at certain positions, hence the voids in the square. Moreover, the edges of the pattern are not well drawn and the square length is a bit larger than expected (550  $\mu\text{m}$ ) due to the spreading of droplets on the substrate. The quality of printing of the borders of patterns has to be enhanced. Solutions to overcome these problems are discussed in the following paragraphs with two other parameters: the use of a priming zone, and a one in four nozzles strategy.

Another phenomenon is identified during the printing. Figure III-28 shows a network of 49 squares printed seven by seven with perfect droplets. Each raster is printed from the left to the right and line by line from bottom to top. The first patterns printed per line are of poor quality, the shape is not completely filled with inks for at least the first four squares. The quality of patterns is improved throughout the printing when the jetting is not interrupted during a long time. Indeed, all of the first patterns are missed because the ejection is stopped at the end of each line and also during the pass of the printhead from the right to the left to arrive at the beginning of the next line where the jetting will restart. To solve this issue, another factor can



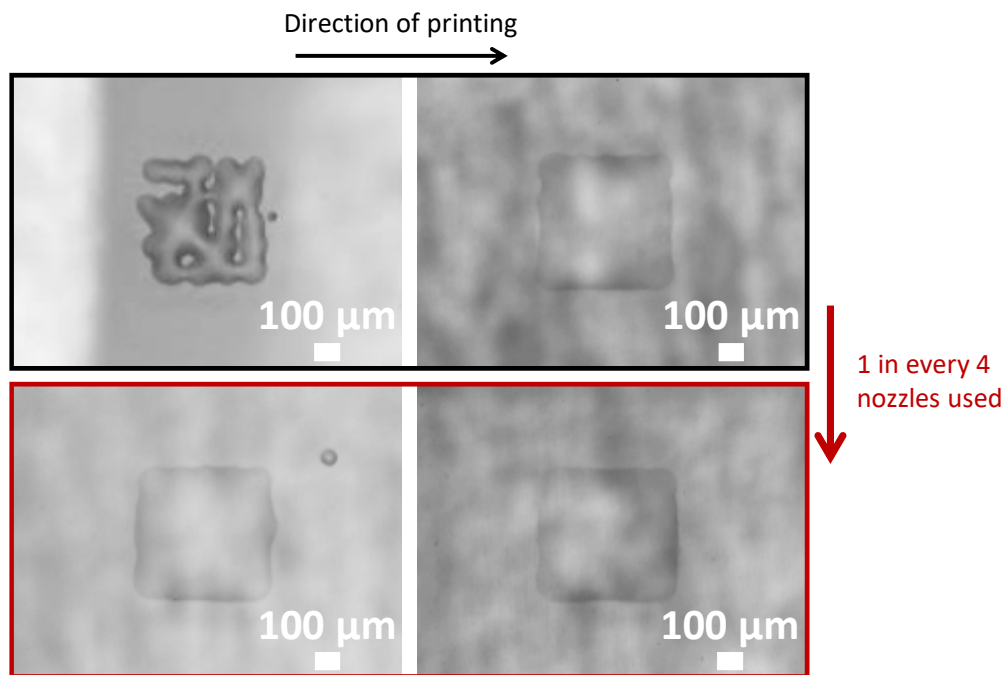
be introduced in the fabrication file: the use of a priming zone. A priming zone is an area on the substrate defined as a test area to launch the jetting in advance before the printing in the interest area. It allows to reach a permanent regime (independent of time) after a transition regime between the no-jetting steps. As a consequence, the quality of the obtained patterns is expected to be improved.



**Figure III-28. Evolution of the design of the squares printed at different locations of the substrate with the PF formulation (0.2 wt% of SP(F)M particles): at the beginning of a line (red box) and at the end of a line (blue box).**

As specified in section III.2.1, the PF formulation induces the topping of the nozzle plate. In this way, the ejection of droplets is perturbed. The jetting becomes difficult to pilot by the electrical pulse and the creation of many satellite droplets is recorded. The ejection of each nozzle is not vertical anymore and intertwines. A way to reduce this topping effect is to use only one in four nozzles for printings. It means that the distance between two selected nozzles is enlarged. As a consequence, the droplets ejected by one nozzle will have less chance to attain and disturb the jetting of another nozzle in the case of a destabilization of the ejection due to the topping.

Figure III-29 illustrates the success of using such a method. The black box represents two squares printed at the beginning and at the end of one raster, representatives of the entire sample. The red box displays similar locations on the substrate but with the strategy of one in four nozzles. The statement is that the quality of patterns is enhanced from the beginning of the raster to the end with the one in every four nozzles strategy of printing.



**Figure III-29. Enhancement of the printing quality by using only one in four nozzles (PF formulation with 0.4 wt% of SP(F)M particles).**

At last, the three enounced parameters are employed at the same time to improve the printing of Swiss crosses (Figure III-30). A columnar ejection, the use of a priming zone, as well as the one in four nozzles strategy are combined. The pattern quality is enhanced with well-defined and regular borders without lost drops. The shapes are also better proportionate with uniform arms of the cross in terms of length and width. Nevertheless, a fringing effect is detected on the pattern edges due to ink accumulation on the borders. This effect could be diminished with the SF formulation.

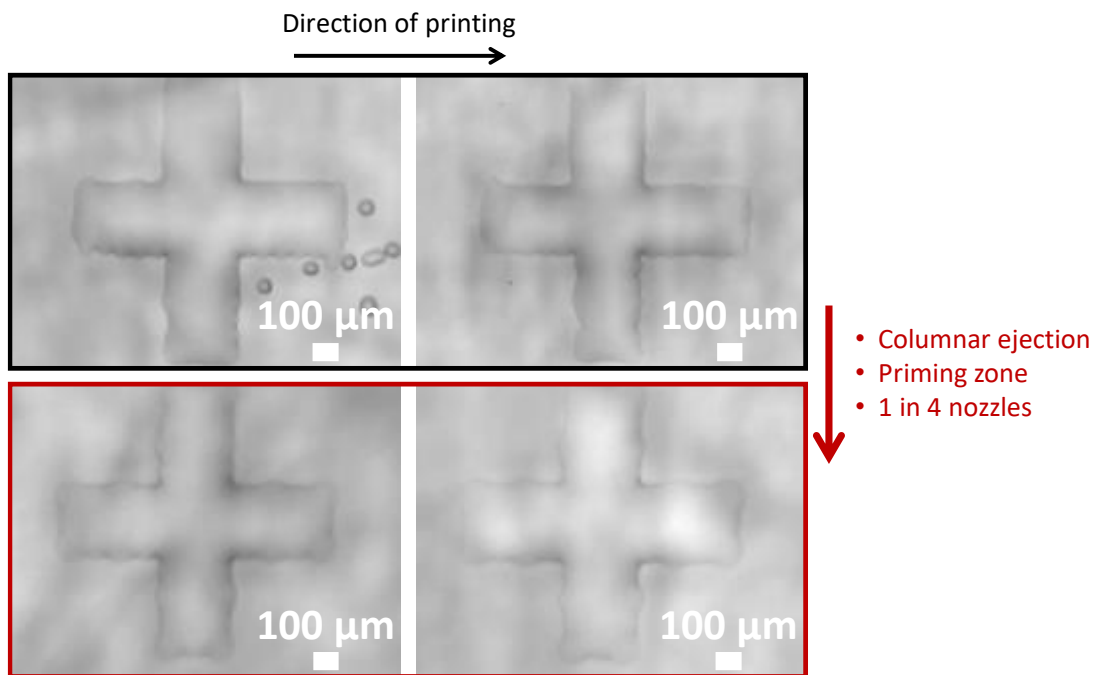


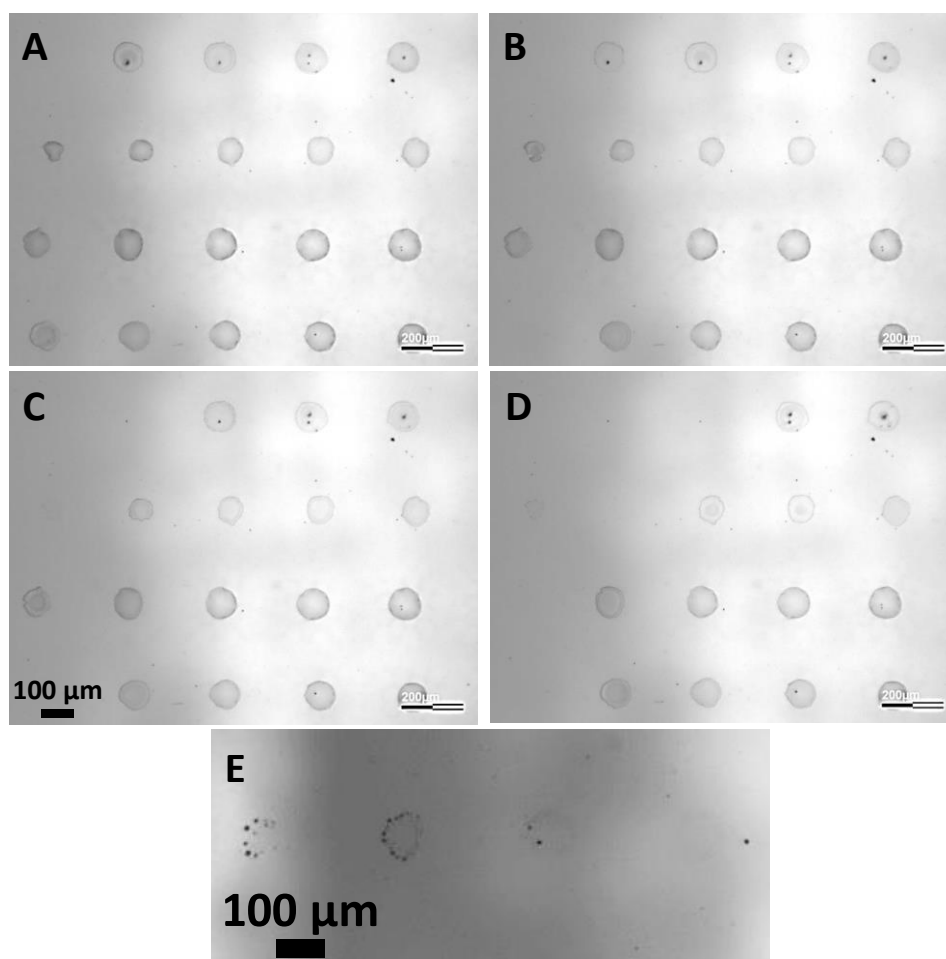
Figure III-30. Enhancement of the printing quality of swiss cross patterns printed with the PF formulation (0.4 %wt particles).

### III.2.2.B. SF formulation

The octanol-based formulation (SF) seems more adapted for printing because of the topping plate reduction (section III.2.1). After the elaboration of coatings with the PF ink, the SF formulation is tested in order to determine if this formulation is more suitable than the PF ink to improve the printing quality.

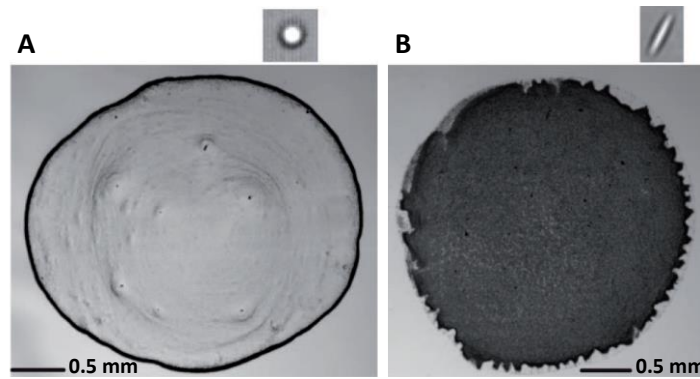
#### III.2.2.B.a. Drying of splats

In a first step, a network of individual and separated splats is printed (Figure III-31). The diameter of a splat is of approximately 110  $\mu\text{m}$  (Figure III-31.A). The SF formulation being constituted of a mixture of solvents with relatively low boiling points, namely octanol (196 °C) and hexane (68°C), the drying of droplets is observed with the naked eye after printing.



**Figure III-31. Observation of the famous “Coffee-ring” effect during the drying of splats with the SF formulation with 0.2 wt% of SP(F)M particles.**

Several pictures are taken every few minutes highlighting the fast drying of droplets with the progressive disappearance of splats over time (Figure III-31.A-D). Figure III-31.E exhibits the presence of a ring of black spots on the outer of the splat at the end of the drying. This wreath is in fact constituted of nanoparticles which migrate from the inner to the outer of the drop during drying. This phenomenon is known as the “Coffee-ring” or halo effect. P. J. Yunker *et al.* describe the drying of droplets of polystyrene in water with the evidence of the “Coffee-ring” effect for nanoparticles with a spherical shape in the A-inset whereas an homogenous drying is exhibited in the case of ellipsoidal particles in the B-inset (Figure III-32). This phenomenon is also observed in non-volatile solvents mixed with a volatile one [25].



**Figure III-32.** « Coffee-ring effect » observed in the case of deposition of spherical particles of polystyrene in water (A) and not with ellipsoidal ones (B). From P. J. Yunker *et al.* [26].

During its drying, the contact angle of the droplet with the substrate diminishes. Different convective fluxes can intervene inside the drop and govern the displacement of matter. In this case, the drying of the splat after jetting relies on the capillary flows inside the droplet. Indeed, during drying, the evaporation of solvents is not homogeneous between the surface and the edges of the drop. It is intensified at the edges in comparison with the center of the drop. As a consequence, a drying gradient is created with the rapid removal of solvents on the edges and low at the center. To compensate this effect, a flux is initiated from the inner to the outer of the drop (Figure III-33.A). This phenomenon is what causes the “Coffee-ring” effect.



**Figure III-33.** Scheme of the effect of capillary flux (A) and Marangoni flux (B) on the drying of a droplet on a substrate.

Marangoni fluxes can be generated inside the drop to reduce or prevent the Coffee-ring effect (Figure III-33.B) by heating the substrate [25] [27]. A surface tension gradient inside the drop will be generated by accelerating the evaporation of the droplet. Indeed, the liquid-air interface is cooler than the inside of the droplet due to the evaporation process. The flow will hence move from the warmer area to the cooler one due to its higher surface tension, which could completely balance the capillary flux and prevent the particles from being expelled to the droplet edges. The heating module of the chuck on which the substrate is put can be used for this purpose. From a certain temperature, the Marangoni fluxes equalize or overcome the capillary one, and the combination of both allows a homogeneous drying [28] [29].

In this study, the mixture of two miscible solvents with one evaporating faster than the other (hexane versus octanol) accentuates the “Coffee-ring” effect due to a gradient of drying inside the deposited layer. The binary phase diagram of the hexane/octanol mixture in Figure III-34 gives a low boiling point for the mixture (80 wt% of octanol with 20 wt% of hexane) at 94 °C, which explains the fast drying of droplets. A solution to slow down the drying could be to increase the boiling point of the mixture by elaborating a ternary system with the addition of a high molecular weight solvent with a higher boiling point [8].

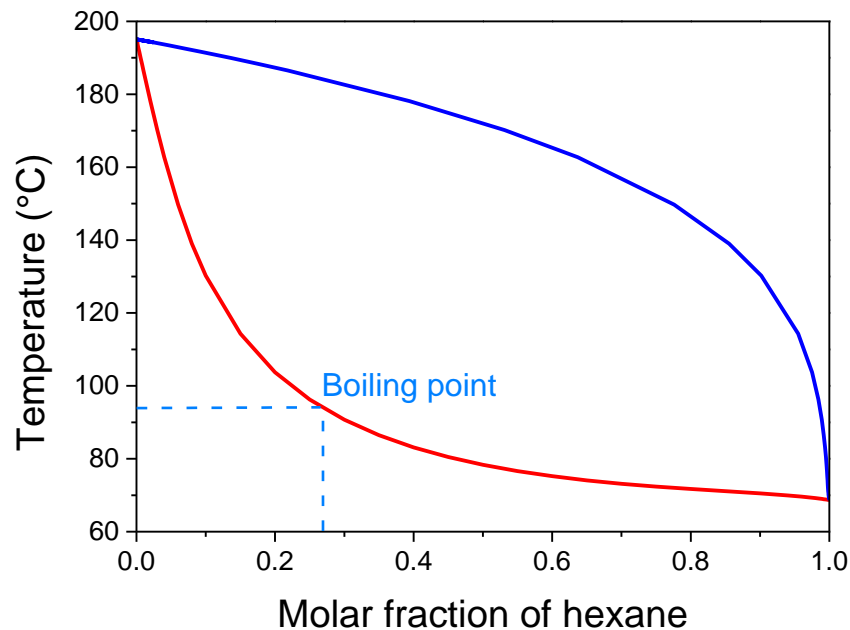


Figure III-34. Binary phase diagram of an hexane in octanol mixture. From [30].

In addition, the fast drying of solvents happens not only in the case of splats meaning with a small amount of solvents but also at the larger scale of patterns (Figure III-35). In this context, a particular attention must be paid to the drying of patterns once filled with an ink more concentrated in particles, the objective still being to develop dense patterns.

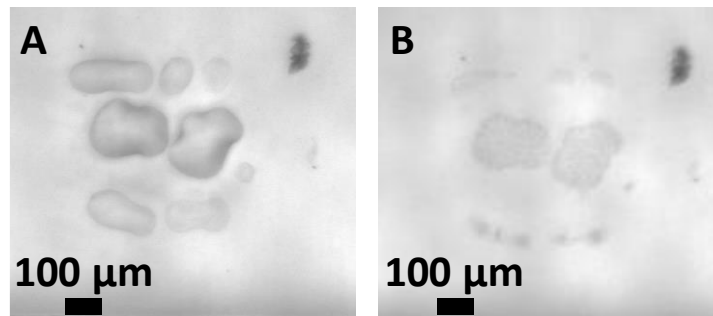
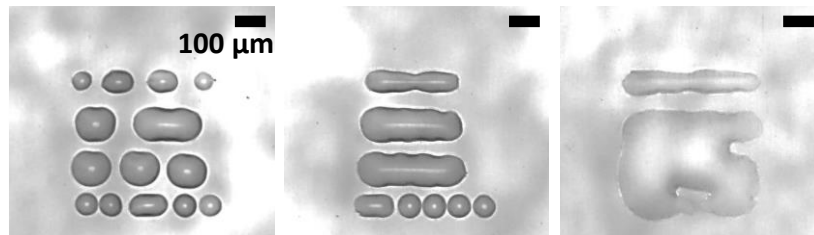


Figure III-35. Drying of a square pattern from A to B printed with the SF Formulation 2 without particles.

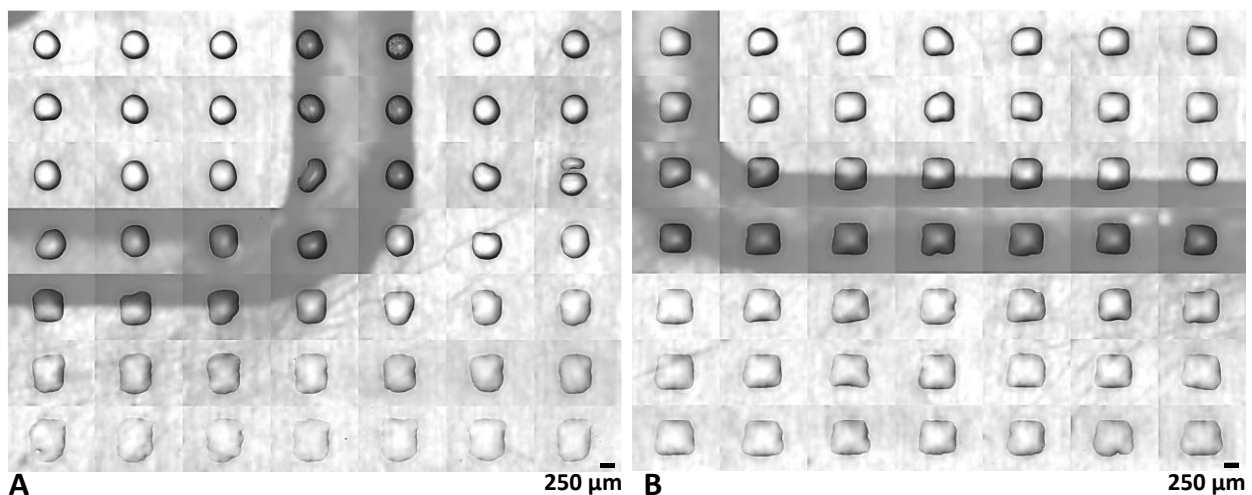
### III.2.2.B.b. Patterns

Square patterns of 500 μm are printed, such as in the study of the PF formulation. First printings are tested with an ideal ejection of unique and separated droplet. Three pictures of square patterns taken at different locations of a network of 49 patterns are shown in Figure III-36. The patterns are collectively all poorly filled. As a result, the significant decrease of the topping of the nozzle plate with the SF formulation does not enhance the printing quality with the ejection of perfect droplets. Nonetheless, the square dimensions are well respected. A length of approximately 470 μm is illustrated in Figure III-36 against 550 μm for the PF ink. The spreading of droplets is attenuated with the SF formulation.



**Figure III-36.** Tests of printing of square patterns with the SF formulation (0.2 wt% of SP(F)M particles).

The parameters responsible of an enhancement of the quality of printings in the case of the PF ink are reused with the SF one. Figure III-37.A is the result of the printing with the association of a columnar ejection with a priming zone, the one in four nozzles strategy being unnecessary due to the stable ejection of the SF ink through the nozzles. The columnar ejection is defined as the separation of the fluid columns into two separated, vertical and stable droplets which are less likely to be destabilized because of the reduction of the topping of the nozzle plate. The obtained patterns are not homogeneous in shape (Figure III-37.A). Indeed, oblongs instead of squares are printed, revealing a problem in the balance of the dimensions of the expected squares. Moreover, even round shapes are produced because for a same volume and at a given thickness the area of a disc is lower than the one of a square, thus minimizing the surface energy.



**Figure III-37.** Improvement of the square shape from A to B by changing the mesh filling in Ceraslice (SF formulation with 0.2 wt% of SP(F)M particles).

Another printing strategy is applied in order to rebalance the dimensions of the shape to obtain squares. Additional drops are manually added in the printing simulator of the software. As the difference of proportions is noticed on the length along X axis, two vertical lines of splats are added in the mesh of patterns on the right edge to balance the square dimensions (Figure III-38). The shape of patterns is considerably improved. They all possess the shape of a square. However, the patterns are not perfectly homogeneous and reproducible and the shape could still be improved.



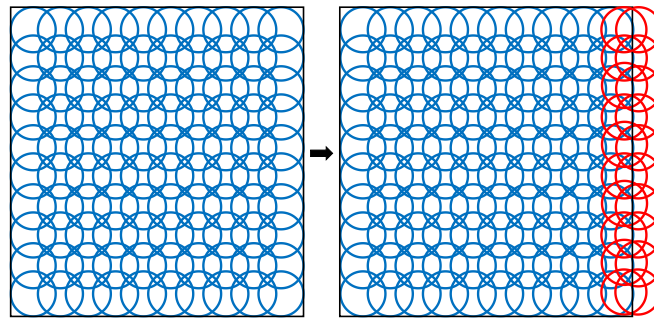


Figure III-38. Addition of drops in the mesh filling of patterns in the simulator in Ceraslice.

If a network of perfect and similar squares is difficult to attain, it is easier to print a network of uniform circular patterns (Figure III-39).

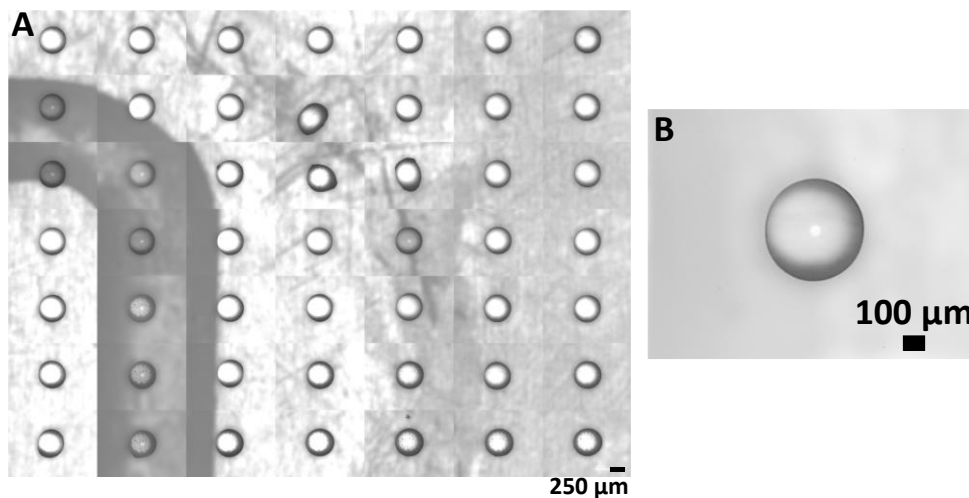


Figure III-39. Network of spherical patterns printed with the SF formulation with 0.2 wt% of SP(F)M particles.

### III.2.2.C. Conclusion

*In conclusion, Figure III-40 compares one square pattern printed with the PF (Figure III-40.A) and SF (Figure III-40.B) inks with the best printing parameters, namely a columnar ejection, a priming zone and also a one in four nozzles strategy in the case of the PF formulation to reduce the topping effect on the nozzle plate. Additional drops are added manually in the mesh in the case of coatings printed with the SF ink. In both cases, the patterns are completely filled and possess the shape of a square. In terms of printing quality, the PF ink displays the best results with the more regular and straighter borders for patterns. However, regarding the aspect of drying, SF formulation is more adapted due to the faster drying of coatings.*



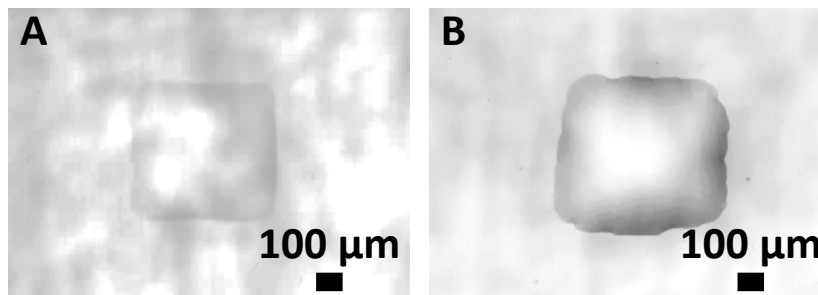
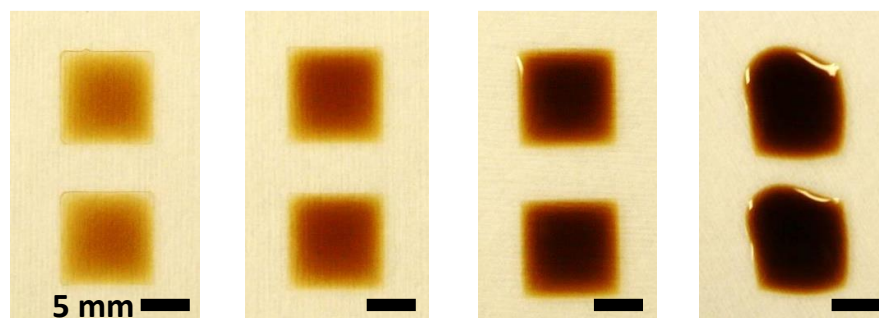


Figure III-40. Comparison of square patterns deposited with the PF (A) and SF (B) formulation with less than 1 wt% of SP(F)M particles.

*As previously investigated in the chapter II, the issues of drying are of paramount importance, that is why the SF formulation is retained. Nonetheless, the pattern aspect has to be improved to at least achieve the quality of coatings printed with the PF formulation.*

### III.2.3. Printing with 8 wt% of SP(F)M particles

With a view of comparing the inkjet printing process with airbrushing, a SF formulation of ink with 8 wt% of SP(F)M particles is ejected and printed on glass slides (Figure III-41). The ejection of perfect droplets enables the elaboration of squares with a surface of 1 cm<sup>2</sup>. The diameter of a splat is of 115 μm in the same range of size as those printed with a solution less concentrated (Figure III-31, section III.2.2.B.a). In these experiments, the trapeze mode (section III.1.2) is tried to ease the evaporation of solvents and the drying of patterns. Implementing this parameter in the fabrication file is even more needed since the number of layers is varied in order to increase the pattern thickness and density. One layer is defined as one complete filling of pattern by the printhead. The splat overlapping is fixed between 15 and 20 μm.



Layer number	1	3	5	10
Splat overlapping (μm)	20	15	15	15

Figure III-41. Printing of square patterns (1x1 cm<sup>2</sup>) with SF formulation (8 wt% SP(F)M particles) as a function of the number of layer et the splat overlapping.

The obtained squares display perfect shapes until 5 layers. The quality of printing is improved due to the change of scale. The results are promising. These conditions of elaboration provide a basis for the printing of smaller patterns of about 500 μm. Beyond 5 layers, the accumulation of ink is such that the ink spreads out of the design. A solution to avoid this

phenomenon could be to stop the printing during a certain amount of time between each layer in order to enable the drying of the layer, and only print on a dried layer.

However, the problem of post thermal treatment to remove the organics and densify the patterns will be encountered as for the airbrushing process. The same type of problem has been encountered in the sintering of inkjet printed yttria stabilized zirconia [31]. A solution could be to choose a substrate that will have the same shrinkage than the ink. In a close approach [32], an Ag ink is deposited before a ferrite ink and during sintering its shrinkage allows to minimize the cracking in the ferrite film since it detaches from the substrate because of its low adherence to it.

Another technique of densification should be used to prevent coatings from cracking like the laser sintering for example (Chapter II).

### III.3. Conclusion

*The airbrushing process detailed in chapter II has been transferred to the inkjet printing. The dispersion of SP(F)M particles in hexane has been adapted to the new process by formulating a compatible ink. The overall process is summarized in Figure III-42. The printer is a Drop On Demand system from Ceradrop.*

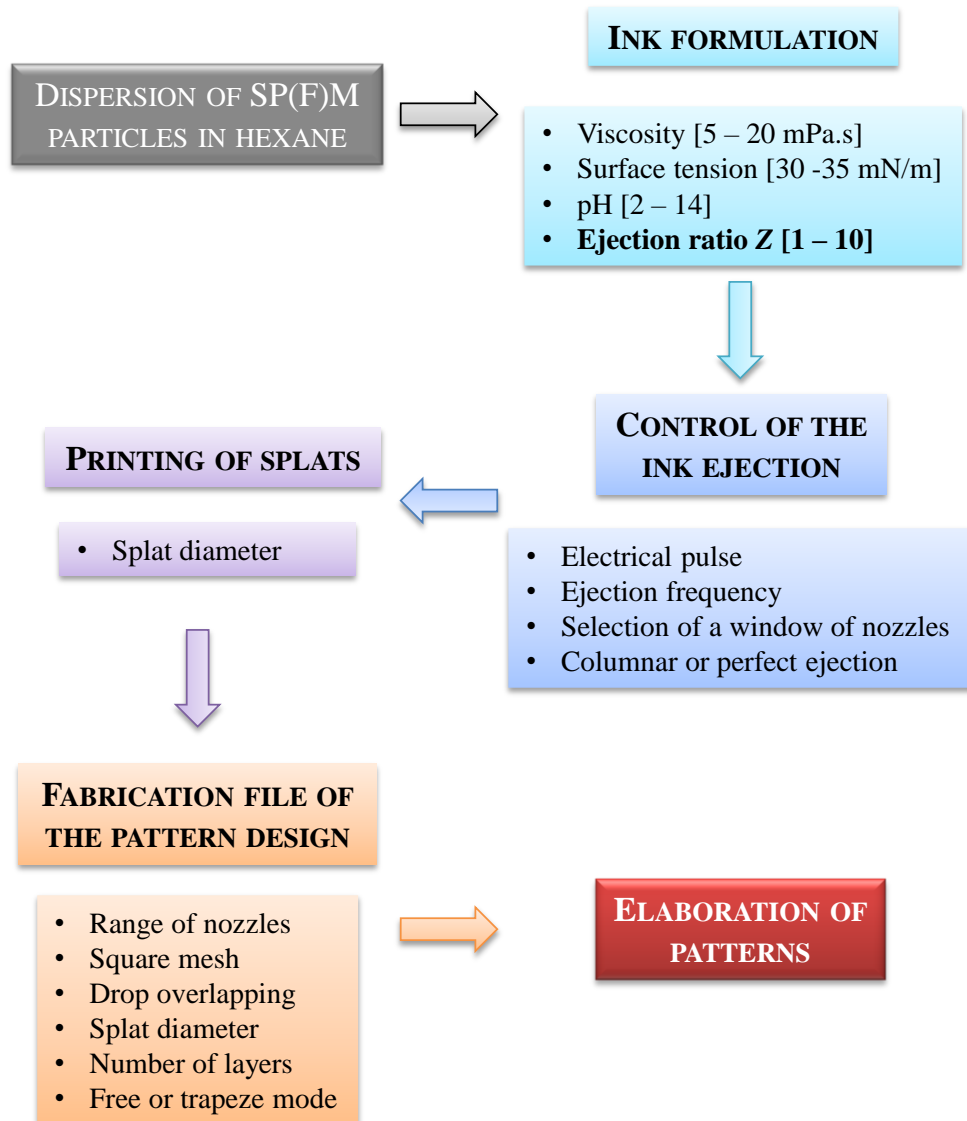


Figure III-42. Different steps of development of network of patterns through the inkjet printing process.

*The protocol is divided in four steps:*

- *The formulation of a suitable ink from SP(F)M nanoparticles (diameter of  $6.2 \pm 1$  nm) dispersed in hexane, compatible with the printing head regarding its viscosity and surface tension. The jet-ability of the ink is determined through a dimensionless ejection ratio comprised between 1 and 10.*

- *The control of the ejection of droplets through the piezoelectric nozzles. The shape, volume and speed of droplets are directly linked to the electrical pulse and the ejection frequency. Two ejection types are encountered: the ejection of perfect, single and stable droplets over time, or the ejection of columns. A columnar ejection induces the formation of satellite droplets which can disturb the printing.*
- *The printing of splats which allows estimating the diameter of a droplet printed on the substrate. The size of a splat is required in the next step to manage the filling of patterns.*
- *The creation of the fabrication file for the pattern design with a software dedicated to the machine. The printing area is drawn and sliced in rasters and layers. Patterns are defined with their geometric parameters, and the method of filling through a meshing. The overlapping of droplets is also computed in order to provide a good filling of patterns and printing quality.*

*Zn<sub>0.4</sub>Fe<sub>2.6</sub>O<sub>4</sub> patterned coatings of approximately 500 μm of length have been elaborated. Two ink formulations have been retained and compared through the previous steps. The formulations have been poorly concentrated (between 0.2 and 0.4 wt%) in particles at the beginning to avoid the printhead clogging and to control the process. Figure III-43 highlights the advantages and drawbacks of each formulation at each step of the process.*

		PF printings	SF printings
<b>Ink formulation</b>	Composition	60 wt% poly(1-decene) in hexane	80 wt% octanol in hexane
		<b>Polymer-based</b>	<b>Solvent-based</b>
<b>Ink ejection</b>	Observations	Topping of the nozzle plate Destabilized ejection Satellite droplets	↳ topping Stable ejection No satellite droplets
	Conclusions	↗ <b>surface tension, viscosity</b>	<b>Suitable ejection</b>
<b>Printing of splats</b>	Observations	Diameter of 120 μm	Diameter of 110 μm
	Conclusions	<b>No drying</b> -	<b>Fast drying</b> « <b>Coffee-ring</b> » effect
<b>Ejection and printing parameters</b>		columnar ejection, priming zone, 1 in 4 nozzles	columnar ejection, priming zone, additional drops
<b>Elaboration of patterns</b>	Square	<b>Good quality</b> regular, straighter borders	<b>Less quality</b> not uniform, not neat edges
	Other shapes	Swiss crosses fringing effect	Circles uniform

Figure III-43. Printing of patterns with PF and SF formulations of ink.

*The polymer-based medium (PF formulation) leads to the elaboration of networks of square patterns with a good printing quality. A major drawback of this formulation is the topping of the nozzle plate which makes the ejection difficult to control. It could be reduced by increasing the surface tension and the viscosity of the ink. Furthermore, this formulation*

*is constituted of a large amount of polymer with a high boiling point which requires the optimization of a thermal treatment at elevated temperature (Chapter II).*

*Due to these two main issues, the solvent-based medium (SF formulation) has been selected for further study. Even if the quality of printing is lower, this formulation has the advantage of a fast drying after printing and a better control of its ejection. In addition, a “Coffee-ring” effect of patterns is observed during drying. This phenomenon could be avoided or reduced by heating the substrate.*

*The pattern quality obtained with the SF ink have been improved with the printing of squares of 1 cm<sup>2</sup>. The particle concentration have been increased to 8 wt% in order to compare the patterns with the ones sprayed by airbrushing (Chapter II). Different parameters have been employed: the ejection of perfect droplets, and the trapeze mode of printing to ease the evaporation of solvent during drying inside and between layers. The obtained squares display perfect shapes until 5 layers. These conditions of elaboration provide a basis for the printing of patterns of about 500 μm with an enhanced quality.*

*This study demonstrates the feasibility of the inkjet printing process for the elaboration of patterns with controlled dimensions. The quality of printing of tiny squares of 500 μm could be improved by further investigation with the SF ink which is a promising candidate to ease the coating drying. Airbrushing and inkjet printing are compared in Figure III-44.*

AIRBRUSHING		INKJET PRINTING	
Advantages	Drawbacks	Advantages	Drawbacks
<ul style="list-style-type: none"> <li>• No further liquid formulation</li> <li>• Easy elaboration</li> </ul>	<ul style="list-style-type: none"> <li>• Two steps (airbrushing + laser etching)</li> <li>• Manual</li> </ul>	<ul style="list-style-type: none"> <li>• A single step (coating + patterns)</li> <li>• Automatized</li> <li>• Module of laser sintering</li> </ul>	<ul style="list-style-type: none"> <li>• Ink formulation</li> <li>• Process handling</li> <li>• “Coffee-ring” effect</li> </ul>

Figure III-44. Comparison between airbrushing and inkjet printing.

*In general, the inkjet printing seems more adapted to the final application due to the possibility to realize the patterned coatings in a single step and in an automatized manner. However, an important disadvantage of the method is the formulation of an ink compatible with the machine. Indeed, it requires the addition of chemical components which have to be removed after printing because they reduce the magnetic properties of coatings. Moreover, the process is limited by the same problem of post thermal treatment required for the coatings elaborated by airbrushing and which cracks the films (Chapter II). A debinding and a sintering steps are necessary to remove the organics from coatings and densify the patterns.*

*Ideas to overcome this issue are:*

- *a laser sintering of coatings after printing. This solution could be studied with the Ceradrop device because there is the possibility to install a module of post-printing treatment in the machine like an IR drying module, according to the need.*
- *a study of more adapted substrate or of an intermediate layer.*
- *the elaboration of a network of patterns from an hydrophobic negative template printed by injet printing which will be then introduced in a microwave oven filled with a precursor solution. It will cause the formation of an adhesive layer from hydrophilic*

*precursors only in the holes of the grid due to the different affinity of the precursors. The microwave synthesis could be inspired from [33] [34]*

- *the transfer of a heating spin coating process starting from a stable solution of precursors developed in [33] [34] to the inkjet printing, with a moderate temperature of 80°C.*

*The next chapter (Chapter IV) will deal with the magnetic properties of the material at the nanoparticle and coating scales. The films obtained by airbrushing will be only discussed.*

### Chapter III references:

- [1] J. G. Korvink, P. J. Smith, and D.-Y. Shin, *Inkjet-based Micromanufacturing*, Wiley-VCH, 2012.
- [2] R. Noguera, M. Lejeune, T. Chartier, and M. Outjedi, "Brevet Ceradrop. Procédé et dispositif de fabrication d'un composant multimatériau tridimensionnel par impression du type jet d'encre.," Brevet Français n°03 10300, 2005.
- [3] J. E. Fromm, "Numerical Calculation of the Fluid Dynamics of Drop-on-Demand Jets," *IBM Journal of Research and Development*, vol. 28, no. 3, pp. 322–333, 1984.
- [4] M. Mougnot, "Réalisation par un procédé d'impression jet d'encre de réseaux de microplots de silice mésoporeuse fonctionnalisée.," thèse Université de Limoges, 2007.
- [5] B. Derby and N. Catarina Reis, "Inkjet printing of highly loaded particulate suspensions.," *MRS Bull.*, vol. 28, no. 11, pp. 815–818.
- [6] E. Svanholm, "Printability and Ink-Coating Interactions in Inkjet Printing," Karlstad University thesis, 2007.
- [7] L. Nayak, "A review on inkjet printing of nanoparticle inks for flexible electronics," *J. Mater. Chem. C*, p. 25, 2019.
- [8] Y. Aleeva and B. Pignataro, "Recent advances in upscalable wet methods and ink formulations for printed electronics," *J Mater Chem C*, vol. 2, no. 32, pp. 6436–6453, 2014, doi: 10.1039/C4TC00618F.
- [9] C. N. Chen *et al.*, "Using nanoparticles as direct-injection printing ink to fabricate conductive silver features on a transparent flexible PET substrate at room temperature," *Acta Mater.*, vol. 60, no. 16, pp. 5914–5924, Sep. 2012, doi: 10.1016/j.actamat.2012.07.034.
- [10] H. J. Spinelli, "Polymeric Dispersants in Ink Jet Technology," *Adv. Mater.*, vol. 10, no. 15, pp. 1215–1218, 1998.
- [11] E. J. Stancik and S. D. Ittel, "INKJET INK FORMULATION," brevet US 2007/0276060 A1, 2007.
- [12] J. Rockenberger, F. Zurcher, S. Haubrich, and N. Sleiman, "Nanoparticle synthesis and the formation of inks therefrom," brevet US 6,878,184 B1.
- [13] W. A. Fessler, G. Ellyn, B. C. Gregory, and O. L. Gerloff, "Printing on olefin polymers and ink compositions therefor," brevet US 3,245,825.
- [14] H. Wei, "Novel Ga-doped ZnO nanocrystal ink: Synthesis and characterization," *Mater. Lett.*, p. 3, 2011.
- [15] X. Zhao, J. R. G. Evans, M. J. Edirisinghe, and J. H. Song, "Formulation of a ceramic ink for a wide-array drop-on-demand ink-jet printer," *Ceram. Int.*, p. 6, 2003.
- [16] H. C. Nallan, J. A. Sadie, R. Kitsomboonloha, S. K. Volkman, and V. Subramanian, "Systematic Design of Jettable Nanoparticle-Based Inkjet Inks: Rheology, Acoustics, and Jettability," *Langmuir*, vol. 30, no. 44, pp. 13470–13477, Nov. 2014, doi: 10.1021/la502903y.
- [17] S. Rodts, F. Bertrand, S. Jarny, P. Poullain, and P. Moucheront, "Développements récents dans l'application de l'IRM à la rhéologie et à la mécanique des fluides," *Comptes Rendus Chim.*, vol. 7, no. 3–4, pp. 275–282, Mar. 2004, doi: 10.1016/j.crci.2003.11.007.
- [18] A. Ponjavic, L. di Mare, and J. S. S. Wong, "The Effect of Pressure on the Flow Behavior of Polybutene," *J. Polym. Sci., Part B: Polym. Phys.* 52, pp. 708–715, 2014.
- [19] A. Vogel, A. Drews, T. Kamionka, M. Bolte, and G. Meier, "Influence of Dipolar Interaction on Vortex Dynamics in Arrays of Ferromagnetic Disks," *Phys. Rev. Lett.*, vol. 105, no. 3, p. 037201, Jul. 2010, doi: 10.1103/PhysRevLett.105.037201.
- [20] O. De Los Cobos *et al.*, "Tunable Multifunctional Mesoporous Silica Microdots Arrays by Combination of Inkjet Printing, EISA, and Click Chemistry," *Chem. Mater.*, vol. 24, no. 22, pp. 4337–4342, Nov. 2012, doi: 10.1021/cm3022769.
- [21] J.-J. Eltgen, "Techniques d'impression d'images numérisées," *Techniques de l'ingénieur*, réf : E5670 V1, p. 37, 1992.
- [22] B. Fousseret, "Fonctionnalisation in-situ de réseaux de microplots de silice mésoporeuse réalisés par un procédé d'impression jet d'encre," thèse Université de Limoges, 2010.

- [23] V. Faure, "Contrôle de la formation de motifs conducteurs par jet d'encre: Maîtrise multi-échelle des transferts de matière dans des suspensions nanométriques," thèse Université Grenoble Alpes, 2017.
- [24] D. Sette, "Functional printing: from the study of printed layers to the prototyping of flexible devices," thèse Université Grenoble Alpes, 2006.
- [25] D. Mampallil and H. B. Eral, "A review on suppression and utilization of the coffee-ring effect," *Adv. Colloid Interface Sci.*, vol. 252, pp. 38–54, Feb. 2018, doi: 10.1016/j.cis.2017.12.008.
- [26] P. J. Yunker, T. Still, M. A. Lohr, and A. G. Yodh, "Suppression of the coffee-ring effect by shape-dependent capillary interactions," *Nature*, vol. 476, no. 7360, pp. 308–311, Aug. 2011, doi: 10.1038/nature10344.
- [27] Y. Lu, S. Theppakuttai, and S. C. Chen, "Marangoni effect in nanosphere-enhanced laser nanopatterning of silicon," *Appl. Phys. Lett.*, vol. 82, no. 23, pp. 4143–4145, Jun. 2003, doi: 10.1063/1.1581387.
- [28] H. Hu and R. G. Larson, "Marangoni Effect Reverses Coffee-Ring Depositions," *J. Phys. Chem. B*, vol. 110, no. 14, pp. 7090–7094, Apr. 2006, doi: 10.1021/jp0609232.
- [29] E. Hendarto and Y. B. Gianchandani, "Size sorting of floating spheres based on Marangoni forces in evaporating droplets," *J. Micromechanics Microengineering*, vol. 23, no. 7, p. 075016, Jul. 2013, doi: 10.1088/0960-1317/23/7/075016.
- [30] "Calculation of vapor-liquid equilibrium (VLE) and drawing of phase diagrams." [http://www.vle-calc.com/phase\\_diagram.html](http://www.vle-calc.com/phase_diagram.html).
- [31] M. Rosa, C. Barou, and V. Esposito, "Zirconia UV-curable colloids for additive manufacturing via hybrid inkjet printing-stereolithography," *Mater. Lett.*, vol. 215, pp. 214–217, Mar. 2018, doi: 10.1016/j.matlet.2017.12.096.
- [32] K. Rajaram and J. Kim, "Flexible wireless power transfer module implemented with aerojet-printing and laser-sintering of rigid NiZn-ferrite ceramic films," *Nano Energy*, vol. 57, pp. 317–326, Mar. 2019, doi: 10.1016/j.nanoen.2018.12.021.
- [33] J. Miyasaka, M. Tada, M. Abe, and N. Matsushita, "Fe<sub>3</sub>O<sub>4</sub>+ $\delta$  films prepared by 'one-liquid' spin spray ferrite plating for gigahertz-range noise suppressors," *J. Appl. Phys.*, vol. 99, no. 8, p. 08M916, Apr. 2006, doi: 10.1063/1.2177394.
- [34] A. K. Subramani, N. Matsushita, T. Watanabe, M. Tada, M. Abe, and M. Yoshimura, "A simple process for ferrite film preparation from one solution without using hazardous oxidizing agent," *J Appl Phys*, vol. 101, 2007.

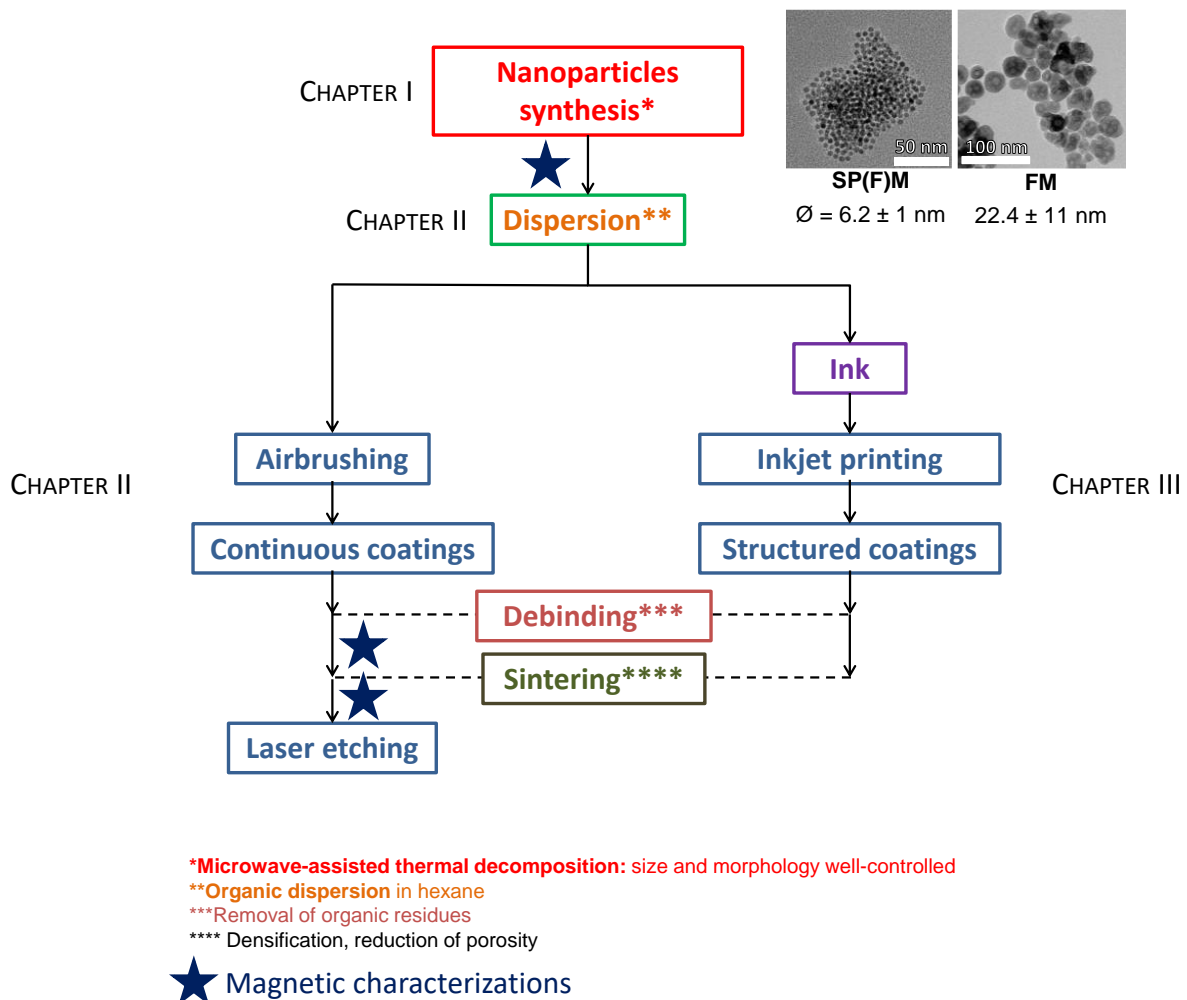




# Chapter IV. Magnetic characterizations at different scales

## I. Introduction

The present chapter focuses on the study of the magnetic properties of the elaborated material at the nanoparticle and coating scales (Figure IV-1).



**Figure IV-1. Scheme of the overall process from the nanoparticle synthesis to the elaboration of coatings through airbrushing and inkjet printing.**

Static and dynamic magnetic characterizations are performed: the static ones to study the magnetic behavior and determine the saturation magnetization  $M_S$  which depends on composition and microstructure, and the dynamic ones which depend on the static one and some features of the mesoscopic scale in order to examine the permittivity and permeability of the samples as a function of the frequency. The objectives are to compare the magnetic properties of SP(F)M and FM nanoparticles and coatings, to establish the link between the microstructure

and the magnetic properties at the nanoparticle and coating scales, to determine if the magnetic properties of continuous FM coatings elaborated by airbrushing are suitable to evidence a magnetic multi-band behavior if patterned, and thus to conclude about the choice of the overall processing method summarized in Figure IV-1.

## II. Static magnetic characterizations

### II.1. Experimental techniques

The static magnetic properties are analyzed using a vibrating sample magnetometer (VSM) (Microsense, model EZ7) at room temperature and also a VSM-SQUID magnetometer (Quantum Design, MPMS) for in-temperature measurements and for evidencing the superparamagnetic state.

With these kind of measurement techniques, curves representing the evolution of the magnetization  $M$  of a material as a function of the intensity of an applied field  $H$  are obtained. Figure IV-2 shows the curve trend in the case of a ferromagnetic material.

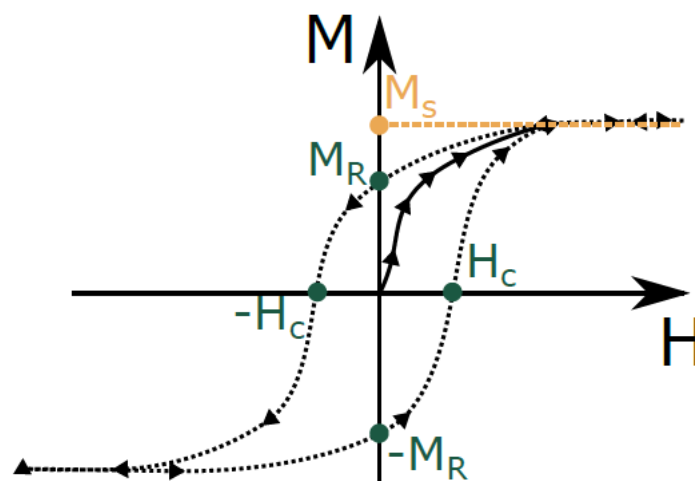


Figure IV-2. Scheme of a magnetization curve with an hysteresis cycle (dashed line) and curve of first magnetization (continuous line). From M. Schott [1].

As previously mentioned in chapter I, without the application of an external field, the material is arranged in domains with magnetic moments oriented in different directions to minimize the system energy. The mean magnetization in this system is then equal to zero. The material is in the demagnetized state.

Under the application of a magnetic field  $H$ , the magnetic moments of each domain will align in the direction of the applied magnetic field  $H$ . The magnetization  $M$  of the material increases as a function of the applied field  $H$ , following the continuous line in Figure IV-2 which corresponds to the curve of first magnetization. Domains with the same magnetization direction expand and grow, giving eventually rise to a single domain structure with magnetic moments oriented in the direction of the applied field  $H$ . This phenomenon leads to the displacement of Bloch walls at the macroscopic scale, which reflects in reality the reversal of

the magnetic moments at the interfaces between several domains (Chapter I). The single domain structure is obtained from a high value of applied field  $H$ , from which the magnetization does not evolve anymore and saturates. The maximum value of magnetization  $M_S$  is called the saturation magnetization (Figure IV-2).

When the applied field  $H$  decreases to zero, the material is progressively split in different magnetic domains again. The displacement of domain walls being an irreversible process, the magnetization deviates from the curve of first magnetization (Figure IV-2). The magnetization  $M$  does not come back to zero at zero applied field and the material possesses a remanent magnetization  $M_R$ , which causes a spontaneous magnetization in the material without application of an external magnetic field. The corresponding field required to cancel the magnetization of a material, previously magnetized, is called the coercive field  $H_C$ .

The magnetization responses are different for ascending or descending values of applied field  $H$  depending on the movement of the Bloch walls inside the material, which leads to the formation of an hysteresis cycle (Figure IV-2).

The shape of the hysteresis cycle depends on the type of the magnetic material, and the sample geometry [2]. Moreover, the area of the hysteresis cycle corresponds to the energy expended by the material in order to orient its magnetic moments inside domains with displacement of Bloch walls.

As a conclusion, the magnetic response of a material to an external field is defined by a couple of characteristic variables: the saturation magnetization  $M_S$ , the remanent magnetization  $M_R$ , and the coercive field  $H_C$ .

## II.2. Static magnetic properties of nanoparticles

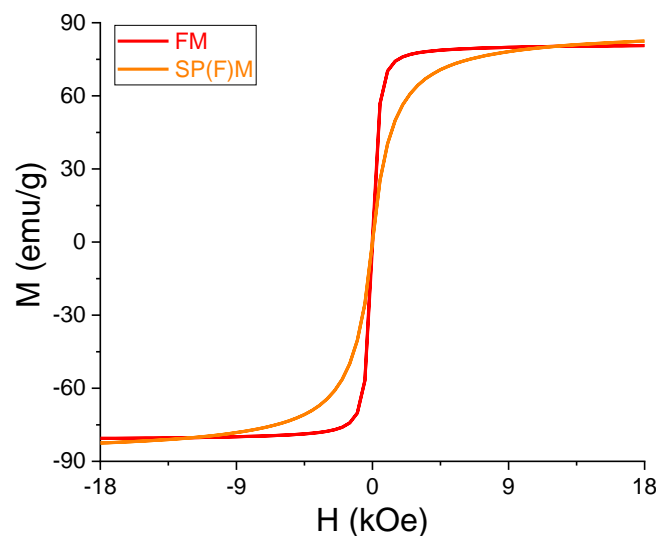
The static magnetic properties of FM and SP(F)M particles are studied through VSM and VSM-SQUID measurements.

### II.2.1. FM and SP(F)M particles

As detailed in chapter II, the particles are surrounded by a significant amount of organics after being synthesized, namely the oleate groups coming from OA. The organics being responsible of a reduction of the magnetization levels, the organic proportion has been subtracted from the weight of particles used for the magnetization measurement. The organic percentage is of 6 wt% for FM particles and 24 wt% for SP(F)M particles. Figure IV-3 provides the resulting magnetization curves of FM and SP(F)M nanoparticles.

Firstly, for both ranges of size, the cycles are very narrow due to the weak coercive fields  $H_C$  of the material, which is in agreement with the soft magnetic behavior determined for the  $Zn_{0.4}Fe_{2.6}O_4$  composition [3] (Chapter I).

The shape of the hysteresis cycles is different depending on the particle size. The magnetization signal of FM particles saturates at 18 kOe ( $18 \times 10^3 / (4\pi)$  kA/m) with a value of 80.6 emu/g ( $\text{A}\cdot\text{m}^2/\text{kg}$ ) for the saturation magnetization  $M_S$  (Figure IV-3). However, this value is lower than the one of the  $\text{Zn}_{0.4}\text{Fe}_{2.6}\text{O}_4$  thin film which is about 98.8 emu/g ( $\text{A}\cdot\text{m}^2/\text{kg}$ ) [3]. This difference can be explained by several reasons. At first, the presence of an amount of  $\text{Zn}^{2+}$  substituted maghemite at the particle surface due to partial oxidation can reduce the saturation magnetization  $M_S$  (Chapter I) because of the smaller value of  $M_S$  for the maghemite bulk (74 emu/g or  $\text{A}\cdot\text{m}^2/\text{kg}$  [4] [5]). It has been previously observed by S. Begin-Colin's group [6]. The magnetization decrease can also be attributed to an inversion degree in the spinel structure [7]. This alternative will be further detailed in section II.2.3. At last, it can be caused by the spin-canting effect at the nanoparticle surface [8] [9]. Indeed, the surface effects are predominant in structures in the nanometric range due to the increase of the surface to volume ratio of the particle. The spin-canting effect can be described as a disordered magnetic layer at the particle surface, comparable to the behavior of a spin-glass [10]. This disordered surface is due to different directions of the surface ions spins in comparison with the volume [11] and can be caused by symmetry breakings, cationic vacancy disorders or crystallinity problems [9]. The SP(F)M particles should be more affected by spin-canting effect than FM ones due to the smaller particle size.



**Figure IV-3. Measured magnetization curves of FM and SP(F)M particles. Mass magnetization versus the applied field.**

On the contrary, in the case of SP(F)M particles, the magnetization curve does not saturate (Figure IV-3). Indeed, when the particle size is below 20 nm [12] (Chapter I), the magnetization curve may exhibit, if anisotropy is low enough, a superparamagnetic behavior at room temperature, characterized by a non-saturating signal under high magnetic field. At zero applied field, for a set of nanoparticles, the magnetization direction of each nanoparticle fluctuates over time and results in a zero global magnetization for a measured time above the reversal time of the spins [13]. When a magnetic field  $H$  is applied and increases, a simple model based on the Langevin function can be used to fit the magnetization curve, as follows:

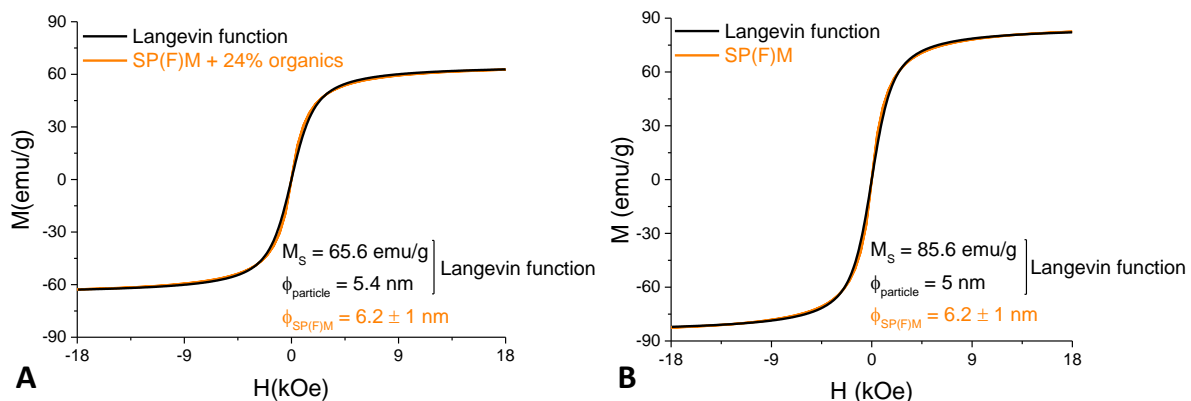
$$\langle M \rangle = M_S L \left( \frac{\mu_0 M_S H V}{k_B T} \right) \quad \text{IV-1}$$

where  $\langle M \rangle$  is the average theoretical magnetization,  $L$  the Langevin function,  $M_S$  the saturation magnetization,  $\mu_0$  the permeability of free space,  $H$  the applied magnetic field,  $V$  the particle volume,  $k_B$  the Boltzmann constant, and  $T$  the temperature [14].

This procedure is well exemplified on SP(F)M particles. Figure IV-4 shows the measured and fitted hysteresis loop for the magnetization of particles including the organic shell at the particle surface (Figure IV-4.A), which reduces the magnetization, and without organics (Figure IV-4.B), at room temperature. Equation IV-1 allows recovering the intrinsic saturation magnetizations and apparent diameters of 5.4 and 5 nm for particles with and without organics, respectively.

The obtained diameters are consistent with the one estimated through TEM images of  $6.2 \pm 1$  nm. Furthermore, the diameter of 5 nm for the particle without the organic shell is close to the crystallite size of 4.5 nm computed from XRD patterns (Chapter I). Thus, there is a good agreement between microstructural and magnetic properties.

The fit of the magnetization curve of SP(F)M particles surrounded by an organic layer will be useful for the dynamic magnetic characterizations (part 0).



**Figure IV-4.** Measured and fitted magnetization curves of SP(F)M particles with (A) and without (B) organics. Mass magnetization  $M$  versus the applied field  $H$ .

The room temperature intrinsic saturation magnetization (85.6 emu/g or  $\text{A}\cdot\text{m}^2/\text{kg}$ , Figure IV-4.B) from the model is in good agreement with the one determined at 2 K with a VSM-SQUID (85 emu/g or  $\text{A}\cdot\text{m}^2/\text{kg}$ , Figure IV-5). The Langevin function is not used at 2 K because the nanoparticles are not superparamagnetic anymore at this temperature (Figure IV-5). The saturation magnetization  $M_S$  of SP(F)M particles (85.6 emu/g or  $\text{A}\cdot\text{m}^2/\text{kg}$ ) is close to the one of FM particles (80.6 emu/g or  $\text{A}\cdot\text{m}^2/\text{kg}$ ), and even larger.

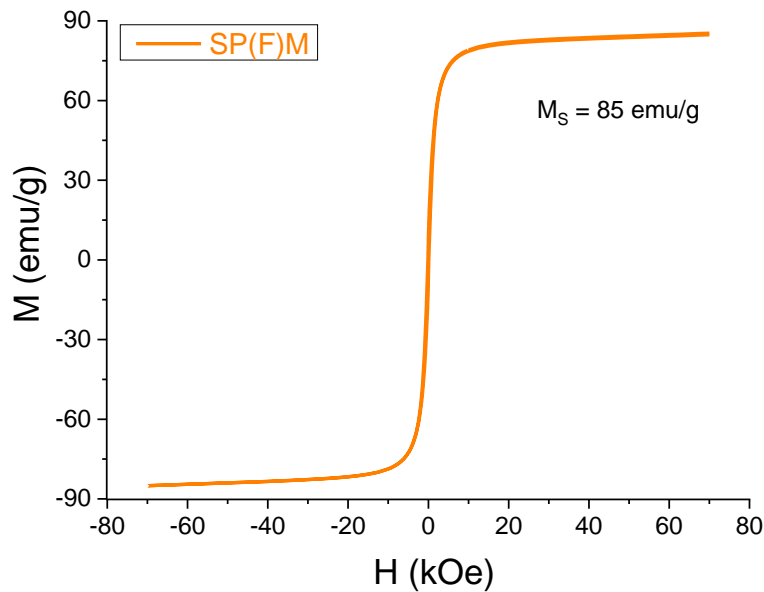


Figure IV-5. Hysteresis loop at 2 K of SP(F)M particles. Mass magnetization  $M$  versus the applied field  $H$ .

Moreover, the superparamagnetic state for SP(F)M particles is also exhibited by the zero-field cooling/field cooling (ZFC/FC) curve measured with a VSM-SQUID magnetometer as displayed in (Figure IV-6.B).

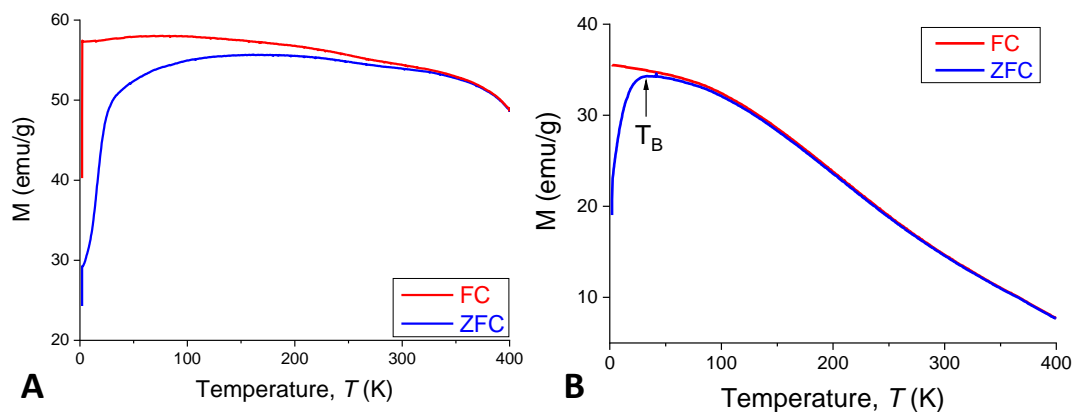


Figure IV-6. ZFC/FC measurements for FM (A) and SP(F)M (B) particles.

The nanoparticles are firstly cooled from room temperature to 2 K at zero field. They are then subjected to a moderate applied field of 500 Oe ( $500 \times 10^3 / (4\pi)$  A/m) and the magnetization is measured during the increase of temperature up to 300 K (ZFC curve). The same process is done by decreasing the temperature to 2K (FC curve) under the same field. It is observed that SP(F)M particles change from the blocked state to the superparamagnetic one at approximately 33 K (blocking temperature  $T_B$ ), determined from the maximum of the ZFC curve (Figure IV-6.B). Moreover, the FC curve is not constant below  $T_B$ , which means that dipolar interactions can be neglected in this case [15]. An estimate of the effective anisotropy constant  $K$  of nanoparticles can be determined from the ZFC curve. In an uniaxial approximation, the effective anisotropy constant reads [16]:

$$K = Ln \left( \frac{\tau_m}{\tau_0} \right) \left( \frac{k_B T_B}{V} \right) \quad \text{IV-2}$$

where  $\tau_m$  is the measuring time ( $\tau_m = 2\text{s}$  in our case) and  $\tau_0 \sim 1 \times 10^{-9}$  s (case of  $\text{MnFe}_2\text{O}_4$  nanoparticles) [17]. This leads to  $K \sim 1.2 \times 10^5$  J/m<sup>3</sup> at  $T_B = 33$  K for nanoparticles with a 5.4 nm diameter.

For the same composition but with FM particles, the superparamagnetic state is clearly not exhibited at room temperature, as seen on the ZFC/FC curve (Figure IV-6.A).

## II.2.2. Comparison with the literature

The saturation magnetizations  $M_S$  of FM and SP(F)M particles measured at room temperature with a VSM are compared to some values found in the literature with nanoparticles of close chemical compositions (Figure IV-7).

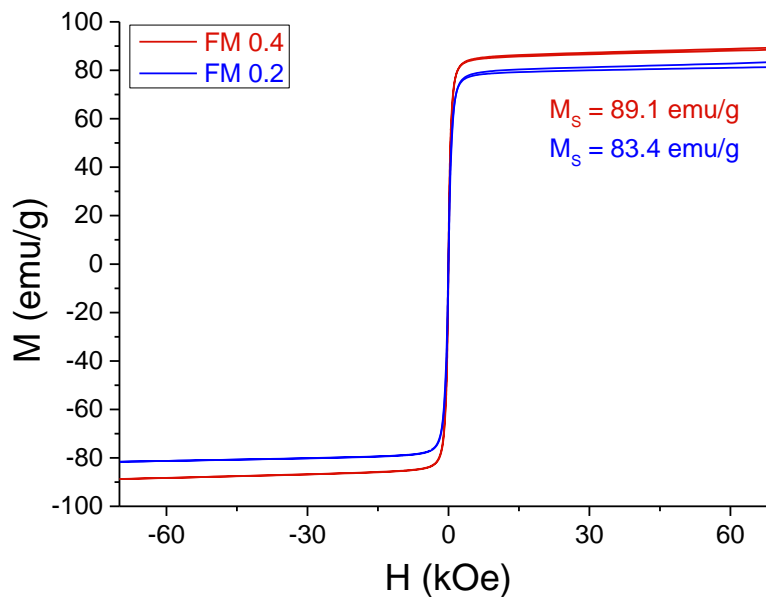
	Theoretical composition	Experimental composition	Size	$M_S$
	-	-	nm	emu/g
[18]	-	$\text{Fe}_3\text{O}_4$	20	81
SP(F)M	$\text{Zn}_{0.4}\text{Fe}_{2.6}\text{O}_4$	$\text{Zn}_{0.38}\text{Fe}_{2.62}\text{O}_4$	$6.2 \pm 1$	85.6
FM		$\text{Zn}_{0.31}\text{Fe}_{2.69}\text{O}_4$	$22.4 \pm 11$	80.6
[19]	-	$\text{Zn}_{0.387}\text{Fe}_{2.613}\text{O}_4$	13.4	30
			26.5	56
			102.2	107.2
[20]	-	$\text{Zn}_{0.27}\text{Fe}_{2.73}\text{O}_4$	$10.2 \pm 0.7$	$55 \pm 3$
[21]	-	$\text{Zn}_{0.4}\text{Fe}_{2.6}\text{O}_4$	15	161
[22]	-	$\text{Zn}_{0.4}\text{Fe}_{2.6}\text{O}_4$	$19.1 \pm 1$	125.7

Figure IV-7. Saturation magnetizations  $M_S$  of zinc iron oxide nanoparticles with a composition close to the one of FM and SP(F)M particles.

On the one hand, the magnetic properties of FM and SP(F)M particles are compared to  $\text{Fe}_3\text{O}_4$  particles with a diameter of 20 nm synthesized from the same synthesis [18]. The saturation magnetization  $M_S$  of  $\text{Fe}_3\text{O}_4$  particles is close to the FM ones with the same particle diameters. The influence of zinc in FM particles ( $22.4 \pm 11$  nm) is studied through VSM-SQUID measurements (Figure IV-8). The saturation magnetization  $M_S$  increases with increasing Zn amount, at least until a Zn molar quantity of 0.4. The same trend has been observed in the literature for nanoparticles until 0.5 [19] and in the case of films [3]. Moreover, the saturation magnetization  $M_S$  of FM particles ( $\text{Zn}_{0.4}\text{Fe}_{2.6}\text{O}_4$ ) is slightly higher than the one reported in Figure IV-7 through VSM analysis. The value of saturation magnetization  $M_S$  measured with VSM-SQUID at 70 kOe ( $70 \times 10^3 / (4\pi)$  kA/m) (89.1 emu/g or A.m<sup>2</sup>/kg) is larger than the one deduced from VSM measurements up to 18 kOe ( $18 \times 10^3 / (4\pi)$  kA/m) (80.6 emu/g or A.m<sup>2</sup>/kg) and also from VSM-SQUID at 17.5 kOe ( $17.5 \times 10^3 / (4\pi)$  kA/m) (86.5 emu/g or A.m<sup>2</sup>/kg) because the “saturation magnetization” is not really taken at the saturation. The magnetization



still increases with field because of the decrease of the canting angle of the canted spins (in volume due to non-magnetic substitution or in surface).



**Figure IV-8.** Hysteresis loop at 300 K of FM particles with different compositions:  $\text{Zn}_{0.2}\text{Fe}_{2.8}\text{O}_4$  and  $\text{Zn}_{0.4}\text{Fe}_{2.6}\text{O}_4$  measured with a VSM-SQUID magnetometer. Mass magnetization  $M$  versus the applied field  $H$ .

On the other hand, nanoparticles with a composition close to  $\text{Zn}_{0.4}\text{Fe}_{2.6}\text{O}_4$  elaborated through similar synthesis of thermal decomposition display values of saturation magnetization  $M_S$  between 30 and 161 emu/g ( $\text{A}\cdot\text{m}^2/\text{kg}$ ) [18] [19] [20] [21]. This large gap can be caused by the reasons previously exposed, namely problems of phase purity, cationic redistribution in the sublattices of the spinel, and spin-canting effect. Indeed, the differences of magnetization have been explained by the increase of the spin disorder as the particle size decreases [19] or even by a gradient of doping inside the particle when the size decreases [20].

Nevertheless, another consideration has to be taken into account: the influence of the synthesis route on the microstructure of the particles. Some synthesis parameters have an effect on the magnetic properties of particles with the choice of precursors, surfactants, and even the nanoparticle cleanings because the magnetization can be reduced by the presence of an organic layer at the particle surface. For example, it has been exemplified by F. Perton [20], who has demonstrated that a higher magnetization than the one summarized in Figure IV-7 is obtained by using a zinc octanoate in squalane instead of a zinc acetate dehydrate in octadecene as a precursor ( $17 \pm 2$  nm,  $85 \pm 3$  emu/g or  $\text{A}\cdot\text{m}^2/\text{kg}$ ). Indeed, some reactants or mixtures can favor the presence of impurities, problem of crystallinity, cationic redistribution in the structure, or even the shape of the nano-object, which will cause modifications of the saturation magnetization  $M_S$ . Thus, as the synthesis parameters directly influence the microstructure of particles, they have a direct impact on the magnetic properties of the final product.

The next part will focus on the influence of the cationic distribution in the spinel sites on the magnetic properties of particles.



### II.2.3. Effect of the inversion degree in the spinel structure

Spherical  $\text{ZnFe}_2\text{O}_4$  particles with diameters between 5 and 7 nm (Figure IV-9) are synthesized by microwave assisted thermal decomposition, the same route as for SP(F)M particles but with different ratios of precursors and surfactants (Figure IV-10).

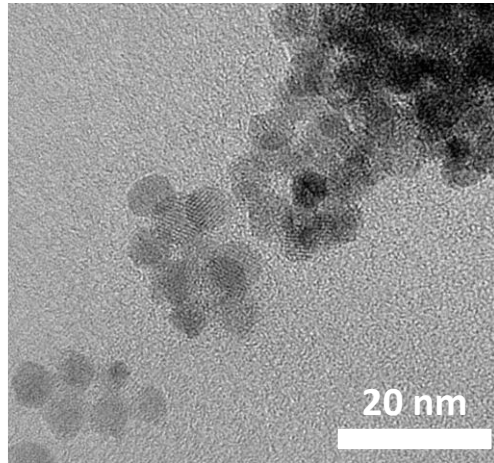


Figure IV-9. TEM pictures of  $\text{ZnFe}_2\text{O}_4$  spherical particles with diameters comprised between 5 and 7 nm.

Molar ratios	$\frac{\text{Zn}}{\text{Fe}}$	$\frac{\text{OAm}}{\text{OA}}$	$\frac{\text{ODE}}{\text{Fe}}$	$\frac{\text{OAm}}{\text{Fe}}$	$\frac{\text{OA}}{\text{Fe}}$
SP(F)M	0.15	4	19	24	6
$\text{ZnFe}_2\text{O}_4$	0.5	2	6	30	13

Figure IV-10. Chemical proportions between reactants for the synthesis of SP(F)M and  $\text{ZnFe}_2\text{O}_4$  particles.

Figure IV-11 represents the corresponding magnetization curve of  $\text{ZnFe}_2\text{O}_4$  particles, fitted by using the Langevin function (Equation IV-1) due to the superparamagnetic behavior of particles. The chemical ratios of reactants being different than for SP(F)M synthesis, the organic amount forming a layer at the particle surrounding is unknown and thus not subtracted from the experimental data. The magnetization is hence slightly reduced due to the presence of an organic layer around particles.

The bulk  $\text{ZnFe}_2\text{O}_4$  composition is antiferromagnetic at the Néel temperature (10 K) with all the diamagnetic  $\text{Zn}^{2+}$  ions at the tetrahedral sites and  $\text{Fe}^{3+}$  ions at the octahedral ones, which means the material is paramagnetic at room temperature [23] [24]. However,  $\text{ZnFe}_2\text{O}_4$  nanoparticles show a superparamagnetic behavior once submitted to a magnetic field (Figure IV-11) with an estimated magnetization saturation of 40.1 emu/g ( $\text{A}\cdot\text{m}^2/\text{kg}$ ). This magnetization can be attributed to a cationic rearrangement of  $\text{Zn}^{2+}$  and  $\text{Fe}^{3+}$  between the tetrahedral and octahedral sites (Figure IV-12). This phenomenon has been previously encountered [23]. The amount of  $\text{Zn}^{2+}$  ions at the octahedral site is called the degree of inversion  $\delta$ .

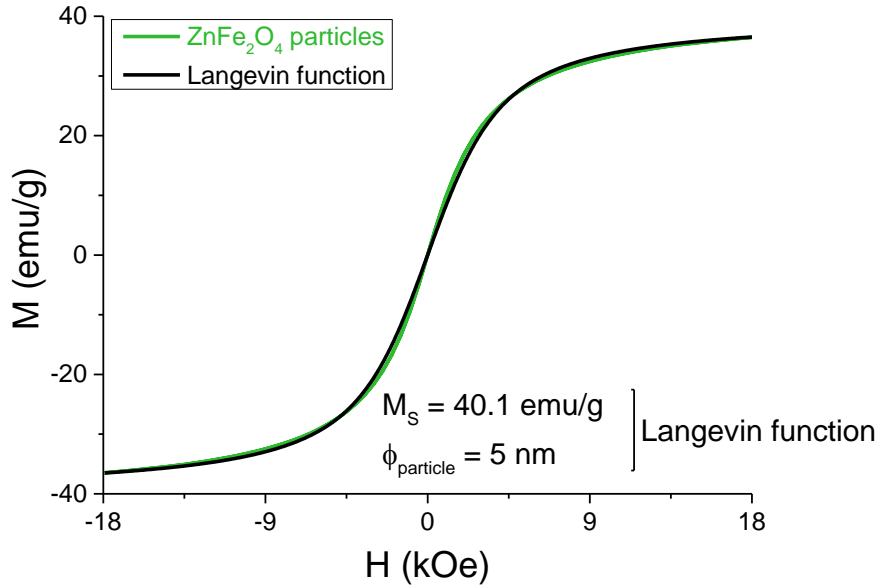


Figure IV-11. Measured and fitted magnetization curves of  $\text{ZnFe}_2\text{O}_4$  particles with diameters comprised between 5 and 7 nm. Mass magnetization  $M$  versus the applied field  $H$ .

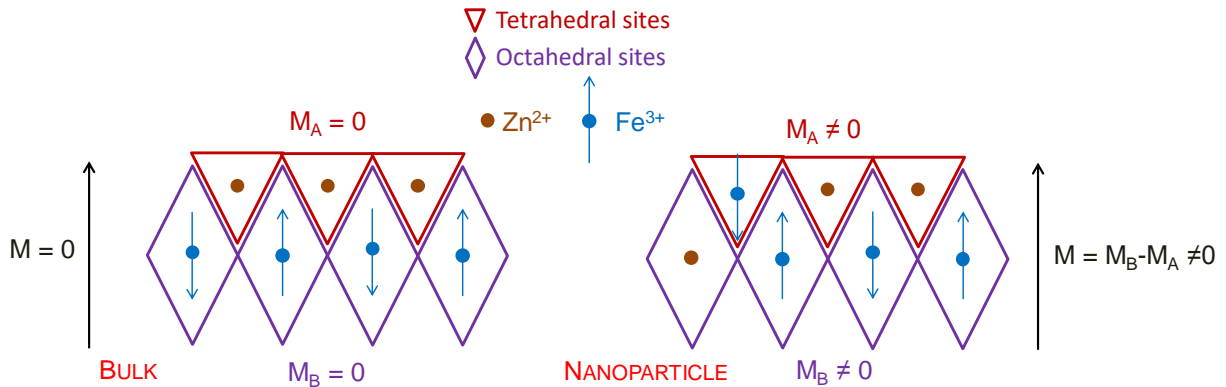


Figure IV-12. Cation distribution on tetrahedral and octahedral sites for  $\text{ZnFe}_2\text{O}_4$  composition at the bulk (left) and nanoparticle (right) scale.

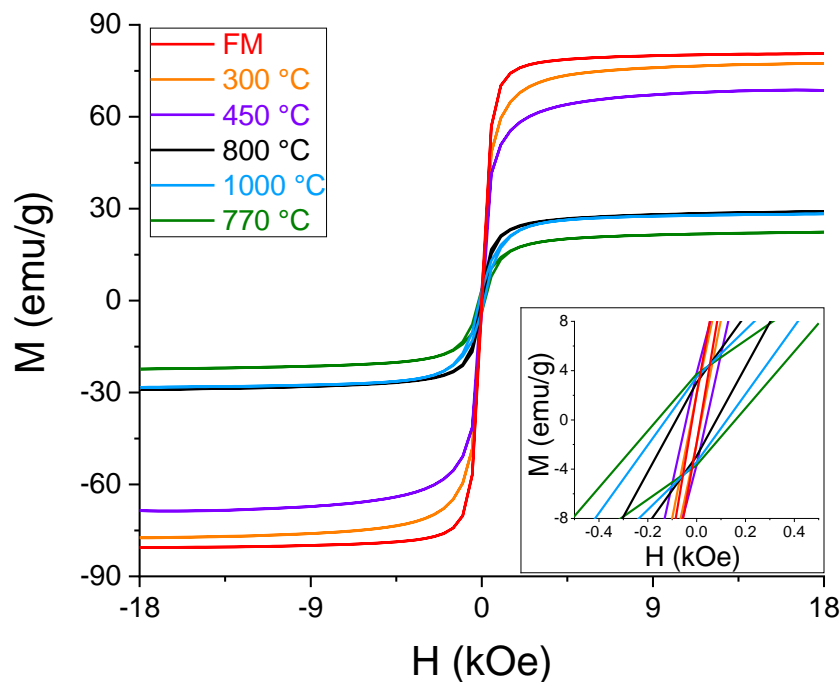
As a conclusion, the effect of the inversion degree on the magnetic properties of nanoparticles is evidenced. The cationic distribution in  $\text{Zn}_x\text{Fe}_{3-x}\text{O}_4$  spinel structure has been discussed in multiple studies [25] and the inversion of the spinel has been demonstrated when studying the evolution of the saturation magnetization  $M_S$  with the increase of the Zn doping ion. The usual trend is an increase of  $M_S$  until a certain amount of zinc (0.2 [26] [27] [28], 0.45 [29], 0.5 [30] [31]) due to the drop of  $\text{Fe}^{3+}$  ions at tetrahedral sites, replaced by  $\text{Zn}^{2+}$  [29]. For higher Zn content,  $M_S$  decreases [26] [27] [28] [30]. The  $\text{Zn}^{2+}$  ions having a preference for an occupancy of the tetrahedral sites [32], this decreases can be attributed to the replacement of  $\text{Fe}^{2+}$  by  $\text{Zn}^{2+}$  ions at the octahedral sites [27] [30] [32] [33].

#### II.2.4. Effect of the thermal treatment

The static magnetic properties of annealed FM particles under argon are investigated in order to better understand the magnetic behavior of coatings (section II.3). Figure IV-13 represents the magnetization curves of FM particles after being submitted to thermal treatments

of 300, 450, 770, 800 and 1000 °C. The curves are compared with the magnetization of untreated FM particles. The hysteresis loop at 300 °C, as well as the FM one have been deprived from their corresponding organic amounts (TG-DTA, Chapter II). Hence, the observations will be not the consequence of the organic layers departure.

The coercive field  $H_C$  values are low and increase with the annealing temperature (Figure IV-13). These low values of coercivity are due to the low magnetocrystalline anisotropy when doping with nonmagnetic  $Zn^{2+}$  [33].



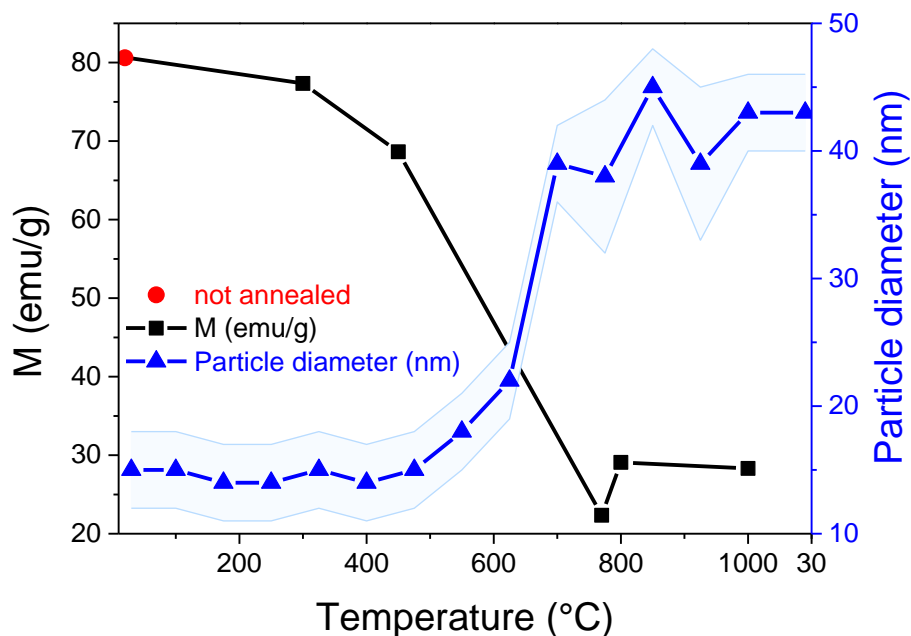
**Figure IV-13.** Measured magnetization curves of FM particles annealed at different temperatures. Mass magnetization  $M$  versus the applied field  $H$ .

The variation of the saturation magnetization  $M_S$  of FM particles is plotted in Figure IV-14 as a function of the annealing temperature, and correlated to the evolution of the particle size with temperature. The thermal treatment of the particles induces a sharp decrease of the saturation magnetization  $M_S$  until 770 °C, the sintering temperature. Beyond 770 °C, the saturation magnetization  $M_S$  slightly increases at 800 °C and remains almost constant until 1000 °C.

The decrease in magnetization is explained by the presence of a secondary phase of  $Zn^{2+}$  substituted wüstite ( $Zn_xFe_{1-x}O$  phase) in the XRD diffractograms of FM particles, emerging at 400 °C, because of the paramagnetic behavior of wüstite at room temperature [34] [35]. The presence of zinc in the material allows to make the wüstite stable below 600°C [36]. When not doped with zinc, wüstite is not stable below 600 °C and is found in the form of a mixture of  $Fe_3O_4$  and  $\alpha$ -Fe (Chapter II).

As detailed in chapter II, the particle size of the main spinel phase stays constant around 20 nm until approximately 600 °C. Beyond 600 °C, the size increases up to 40 nm at the sintering

temperature of 770 °C and no further increase is noticed until 1000 °C (Figure IV-14). The slight increase of the saturation magnetization  $M_S$  above 770 °C (Figure IV-14) could be attributed to the sintering mechanism when the reduction of the material is over. The hypothesis is that between 300 and 770 °C, there is a competition between the material reduction into  $Zn_xFe_{1-x}O$ , which reduces the magnetization, and the long process of sintering, starting after the removal of the organics from the particle and inducing the growth/coalescence of particles with a reduction of porosity. The phenomenon of reduction seems to be predominant until all of the organics are removed around 600 °C and is stopped after 600 °C because all of the organics responsible of the reductive atmosphere are consumed.



**Figure IV-14.** Evolution of the saturation magnetization  $M_S$  and of the particle diameter of FM particles as a function of the temperature.

The decrease of the saturation magnetization  $M_S$  with the temperature can come from other effects, which can occur in addition to the emergence of a secondary phase. Indeed, the increase of the annealing temperature can generate a  $Zn^{2+}$  redistribution in the spinel sites, inducing a decrease of the magnetization. For example, M. A. Cobos *et al.* [37] have shown a decrease of the inversion degree of 0.57 to 0.18 for  $ZnFe_2O_4$  particles with a 11 nm diameter with an increase of the annealing temperature from 300 to 600 °C. They have also demonstrated the link between the magnetization and the inversion degree in the spinel and that a decrease of the inversion tends to reduce the magnetization. In the same way, R. Sai *et al.* [31] have investigated the possibility of tuning the inversion degree by the control of the annealing. A fast temperature ramp slows the decrease of the inversion degree observed with temperature and allows to maintain a high value of inversion, and thus suitable magnetic properties.

Then, the decrease of magnetization with temperature can be assigned to a small contribution of spin-canting [33] [26] [38]. The increase of annealing temperature could enlarge the thickness of the spin disorder at the particle surface. Nevertheless, as seen in chapter I, the contribution of spin-canting is minor. Another hypothesis could be that the annealing

temperature could change the ratio between  $\text{Zn}^{2+}$  substituted maghemite and magnetite in particles before the apparition of wüstite. It should be verified with Mössbauer spectroscopy.

Different models are studied in the next section in order to retrieve the saturation magnetization  $M_S$  of FM and SP(F)M particles as a function of different contributions: cationic ordering with volume spin canting, oxidation from magnetite to maghemite, and surface spin-canting.

## II.2.5. Molecular fields models applied to Zn substituted magnetite

The aim of this part is to link the measured magnetic moments to the composition on tetrahedral and octahedral sub-lattices of the synthesized materials. Despite the progress of DMFT-DFT techniques, the molecular model remains the only quickly available tool to predict the magnetic moment from the composition. As explained in chapter I, the molecular field theory is aimed at predicting the magnetic characteristics like the saturation magnetization  $M_S$ , and the Curie temperature of a given magnetic material, starting from its chemical composition and semi-empirical parameters. After a review and a comparison of some molecular field models, the magnetic moment of  $\text{ZnFe}_{3-x}\text{O}_4$  is predicted and compared to published experimental values as well as values obtained by E.W. Gorter [39].

### II.2.5.A. Choice of a molecular field model

#### II.2.5.A.a. The Néel model

In the case of a spinel ferrite, the simplest molecular field model is given by Néel and expresses the magnetization of a ferrimagnetic spinel as the difference of magnetization between two sublattices  $A$  and  $B$  standing for tetrahedral and octahedral sites (Chapter I):

$$M = |M_i - M_j| = n_i g_i S_i \mu_B - n_j g_j S_j \mu_B \quad \text{IV-3}$$

with  $i$  and  $j$  two opposite sublattices,  $n_i$  the number of magnetic ion per formula of spins  $S_i$ ,  $g$  the Landé factor and  $\mu_B$  the Bohr magneton.

It results from an antiferromagnetic exchange interaction  $J_{AB}$  by neglecting  $J_{AA}$  and  $J_{BB}$  interactions.

The addition of a non-magnetic ion is expressed by the dilution of the magnetic moment of the sublattice affected by the non-magnetic substitution.

In the above molecular field theory, the magnetization depends on:

- the number of magnetic ions in the sublattice  $i$  or  $j$  noted  $q_i$  (or  $n_i$  by the authors),
- the number of nearest magnetic neighbors of the sublattice  $j$  of an ion located in the sublattice  $i$ :  $n_{ij}$  (or  $z_{ij}$ ),

- the magnetic parameters (the spin  $S$ , the Landé factor  $g$ ) of the considered ions,
- the exchange integrals  $J_{AA}$ ,  $J_{AB}$  and  $J_{BB}$  for each magnetic species determined experimentally from thermomagnetization data, or calculated by molecular orbital theory.

### II.2.5.A.b. The random localized canting model of Bercoff

When the composition is substituted with a high proportion ( $> 0.3$ ) of a non-magnetic cation, the Néel model assumption of two antiferromagnetically coupled sublattices becomes less true since  $J_{AB}$  diminishes and  $J_{BB}$  cannot be further neglected ( $J_{AA}$  is still considered by many authors as negligible following Anderson theory of superexchange [40]). To describe the magnetic properties dependence of the composition at high level of non-magnetic substitution, Yafet and Kittel have introduced a splitting of the lattice  $A$  and  $B$  into oppositely and uniformly canted sublattices  $A'$ ,  $A''$ , and  $B'$ ,  $B''$  [41]. To compute the canting angle, Yafet and Kittel have proposed to determine it from the temperature dependence of magnetization, but it does not lead to a quantitative prediction of experimental data [42].

This idea has been further developed by considering local random canting. C.E. Patton and Y-H. Liu [41] have proposed a way to compute by iterations the converged canting angle with introducing a probability expressed by a binomial law for the number of canted magnetic neighbors in the canted sublattice site opposite to the substituted sublattice. In the case of Li-Zn ferrite, they have computed (Figure IV-15) the magnetic moment in function of the assumed ratio of exchange integral  $J_{AB}/J_{BB}$ . However, the ratio that matches the experimental data differs from those experimentally determined.

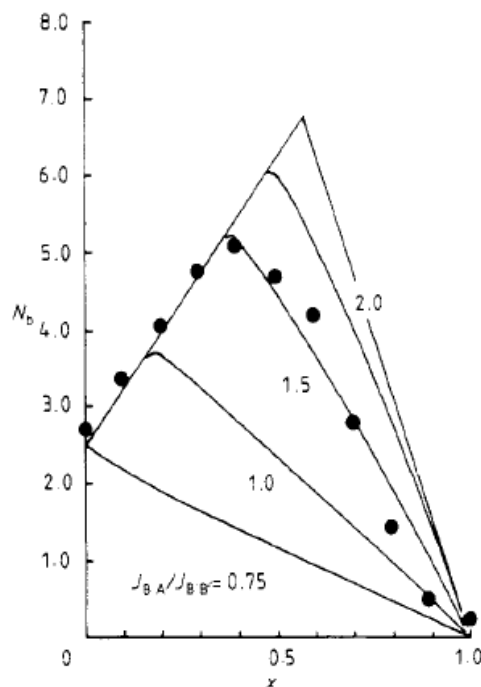


Figure IV-15. Moment  $N_B$  per formula unit as a function of the molar quantity  $x$  in the following formula  $(Zn_x Fe_{1-x})[Li_{0.5-x/2} Fe_{1.5-x/2}]O_4$  and comparison with theoretical predictions. From C. E. Patton and Y-H. Liu [41].



Moreover, they have evidenced that the molecular field approach is not valid in Li-Zn ferrites at high non-magnetic substitution level of  $x > 0.5$ , the assumption of a linear dependence of the effective  $J_{AB}$  and  $J_{BB}$  interactions being no more accurate.

On this basis, P.G. Bercoff and H.R. Bertorello [40] have written a model for  $\text{NiFe}_2\text{O}_4$  spinel substituted by Zn in the tetrahedral sublattices. The octahedral sublattice is then split into a  $B$  sublattice (not canted) and a  $B'$  sublattice (canted) (Figure IV-16).

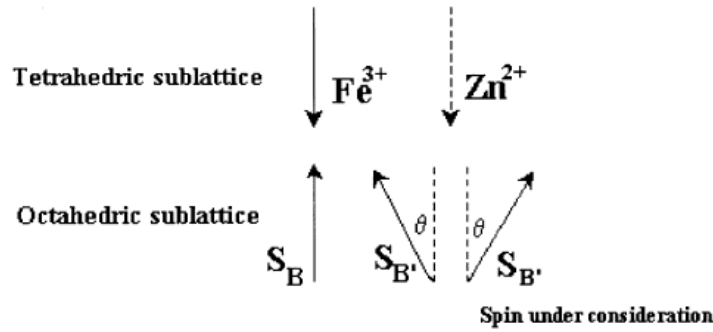


Figure IV-16. Scheme of the configurations of spins in Zn substituted ferrites. From P.G. Bercoff and H.R. Bertorello [40].

When  $\text{Fe}^{3+}$  and  $\text{Ni}^{2+}$  ions are located at the  $B'$  sublattice, the canting angle  $\theta_L$  of the  $B'$  sublattice is determined by minimizing the exchange energy. A simplified (not iterative) way as in [41] is used, due to the fact that in the former frame the spin configuration can be seen as a probability law at two levels on the  $B$  site: canted ( $B'$ ) or not canted ( $B$ ):

$$\cos\theta_L = \frac{-a}{4b} \quad \text{IV-4}$$

$$\text{where } a = -|J_{AB'}|S_A S_{B'}(q_A n_{AB'} + q_{B'} n_{B'A}) + -|J_{BB'}|S_B S_{B'}(q_B n_{BB'} + q_{B'} n_{B'B}) \quad \text{IV-5}$$

$$\text{and } b = 2|J_{B'B'}|S_{B'}^2 q_{B'} n_{B'B'}$$

with  $q_i$  the number of magnetic ion on a sublattice and  $n_{ij}$  the number of  $j$  magnetic neighbors of an  $i$  ion.

There is an error in the expression of  $b$  published by P.G. Bercoff and H.R. Bertorello [40] where a factor 2 is missing in comparison to the correct formula established by C.E. Patton and Y-H. Liu [41].

The magnetization at a given temperature  $T$  is:

$$M_T(T) = M_B(T) + M_{B'}(T)\cos\theta_L - M_A(T) \quad \text{IV-6}$$

and becomes at 0 K:

$$\left(\frac{q_B}{2} + \frac{q_{B'}}{2} \cos\theta_L\right) [g^{Fe^{3+}} S^{Fe^{3+}} (1+z) + g^{Ni^{2+}} S^{Ni^{2+}} (1-z)] - q_A g^{Fe^{3+}} S^{Fe^{3+}} \quad \text{IV-7}$$

In this model, the number of magnetic ions and of the magnetic neighbors is assumed to be not linear and allows to fit the experimental magnetic data over a wide composition range as seen on Figure IV-17.

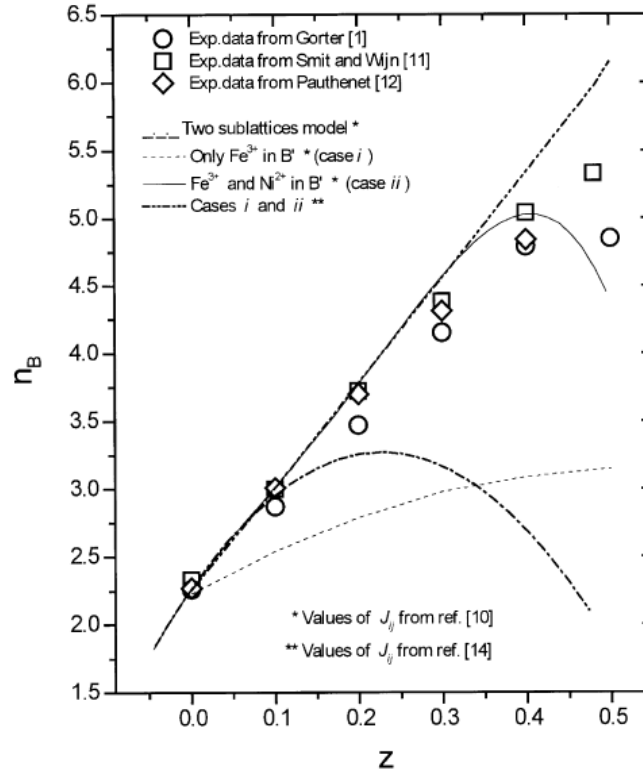


Figure IV-17. Moment  $N_B$  per formula unit as a function of the Zn molar quantity  $x$ . Comparison between model and experiments. From P.G. Bercoff and H.R. Bertorello [40].

### II.2.5.A.c. The generalized Dionne model of superexchange dilution

In this work [42], G.F. Dionne has considered the effect of non-magnetic substitution on both A and B sites taking into account:

- the direct reduction of the exchange field, which stands for the dilution of the magnetic moments,
- the intersublattice canting,
- and the intrasublattice canting.

These effects are expressed through the probability of the two spin-canting possibilities by binomial laws in a high level of generality:

- the canting probability fraction of  $B$  ions is written  $c_A$  for the  $B$  sublattice (resulting from a  $k_A$  non-magnetic substitution level on the A sublattice) for the inter sublattice canting (Figure IV-18, red arrows),

- and  $q_{BA}$  for the intra sublattice canting describing the canting of  $A$  sites caused by the canting of their  $B$  neighbors following the non-magnetic  $A$  substitution.

It has to be noticed that the use of a binominal law for the canting probability for a range of 0 to  $z_{max}$  neighbors implies that high degree of polynoms (up to 6) may be used to describe the effect of canting.

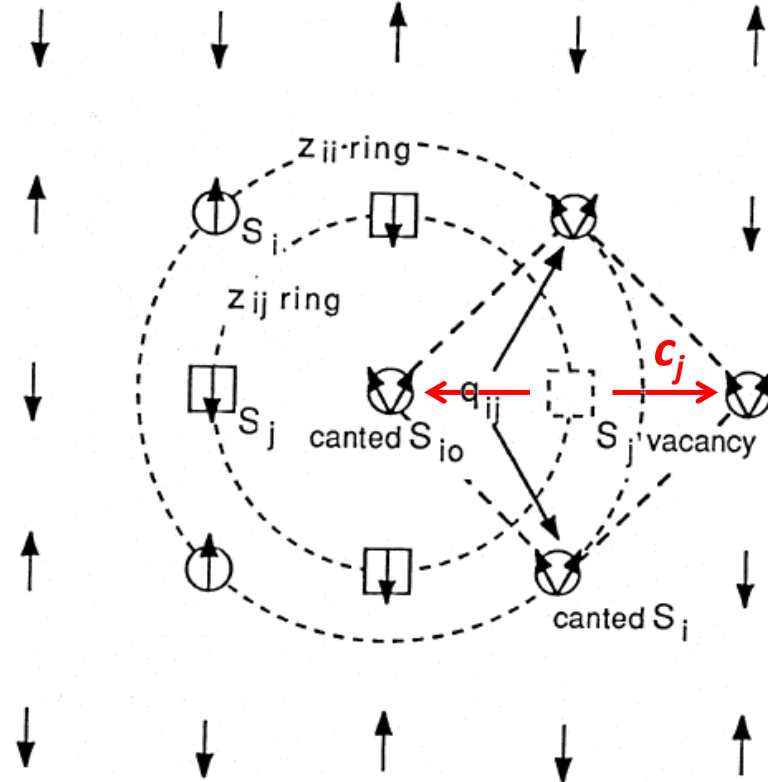


Figure IV-18. Scheme of the spin-canting of  $i$  sites surrounding a vacancy in a  $j$  site. From G.F. Dionne [42].

However, applying this general model is not easy because  $c_{ij}$  is not explicit even in the linearized case for computing the canting probability [42]:

$$c_j \propto \left| \frac{z_{ij}^0 J_{ij} S_j (1 - k_j)}{z_{ii}^0 J_{ii} S_i (1 - z_{ii}^0 q_{ij} c_j k_j) + z_{ij}^0 J_{ij} S_j (1 - k_j)} \right| \quad \text{IV-8}$$

To model the magnetic moment of garnets, G.F. Dionne has introduced in his approach the use of fitted high order polynoms as exemplified by the following equations [42]:

$$\begin{aligned} \mathcal{M}_d(0) &= 3g_d m_B S_d N_A (1 - k_d) (1 - 0.1k_d) \\ \mathcal{M}_a(0) &= 2g_a m_B S_a N_A (1 - k_a) (1 - k_a^{5.4}) \end{aligned} \quad \text{IV-9}$$

### II.2.5.A.d. Comparison of these molecular fields models

The main conclusions of the three described approaches are summed up in Figure IV-19.

	<i>Patton</i>	<i>Bercoff</i>	<i>Dionne</i>
<i>Approach</i>	Random localized canting	Random localized canting	Superexchange dilution
<i>Canting description</i>	Iteratively solved canting angle from the inter sublattice and intra sublattice exchange energy of canted moments	Two (0 or $\theta$ ) canting situations and minimization of energy from the inter sublattice and intra sublattice exchange energy of canted moments	Intersublattice and intrasublattice canting probabilities not explicitly determined
<i>High substitution limit</i>	Limited at substitution $> 0.5$ on Li-Zn ferrites	3 <sup>rd</sup> order polynomial law introduced in spinel allowing extension of the prediction to high substitution level	High order polynomial law introduced in garnets allowing extension of the prediction to high substitution level
<i>Exchange integrals</i>	Taken from literature	Given from thermomagnetic data and molecular orbital theory [43]	Calculated from thermomagnetic data [44]
<i>Application to Ni-Zn ferrites</i>	Restricted to Li-Zn ferrites	Good agreement between predicted magnetic moment with the data for Ni-Zn ferrites [40]	No comparison of predicted magnetic moment with the data for Ni-Zn ferrites [44]
<i>Application to Zn ferrites</i>		Using the exchange energy given for Fe <sup>2+</sup> [43]	

**Figure IV-19. Comparison of the three molecular fields of C.E. Patton and Y-H. Liu, P.G. Bercoff and H.R. Bertorello, and G.F. Dionne.**

The chosen approach is the Bercoff one because it gives for Zn-NiFe<sub>2</sub>O<sub>4</sub> spinels a good agreement with experimental data.

### II.2.5.B. Modeling the magnetic moment of Zn substituted maghemite with the help of the Bercoff molecular field data

#### II.2.5.B.a. Ni<sub>(1-z)</sub>Zn<sub>z</sub>Fe<sub>2</sub>O<sub>4</sub> ferrites

To be sure that the implemented model is correct, the first step is to retrieve the results produced by P.G. Bercoff and H.R. Bertorello for the well documented Ni<sub>(1-z)</sub>Zn<sub>z</sub>Fe<sub>2</sub>O<sub>4</sub> ferrites and to compare it with experimental data.

Since the publication is not free of errors, here are the corrections that are done to the model:

- a. The energy  $b$  of intra sublattice canted interaction for which a factor 2 is lacking.
- b. A constraint has to be set in computing  $\cos(\theta_L) \leq 1$  at low volume fraction. Indeed, at high volume fraction, this inter and intrasublattice canting energy ratio is not anymore constrained.
- c. The expression of  $S_B$  from an average between the number of  $\text{Fe}^{3+}$  moments on site  $B$  and  $\text{Ni}^{2+}$  moments on site  $B$ :

$$\frac{1}{2}(2.5 \times (1 + z) + (1 - z)) \quad \text{IV-10}$$

The following modifications are added in Figure IV-20, with  $q_i$  the number of magnetic ion on a sublattice and  $n_{ij}$  the number of  $j$  magnetic neighbors of an  $i$  ion.

Approach	$q_A$	$q_{B'}$	$q_B$	$n_{AB'}$	$n_{BB'}$	$n_{B'A}$	$n_{B'B'}$	$n_{B'B}$
Bercoff	$1-z$	$2(z-2z^2+2.5z^3)$	$2-q_{B'}$	$12z$	$6z$	$5(1-z)$	$2(1-z^2)$	$6-n_{B'B'}$
corrected		$2(z-2z^2+1.5z^3)$				$6(1-z)$		

Figure IV-20. Corrections of the Bercoff model.

The predicted moment from the Bercoff model with the above corrections **b** and **c** is compared to the experimental data from E.W. Gorter [39], the basic Néel model and the corrected model in Figure IV-21.

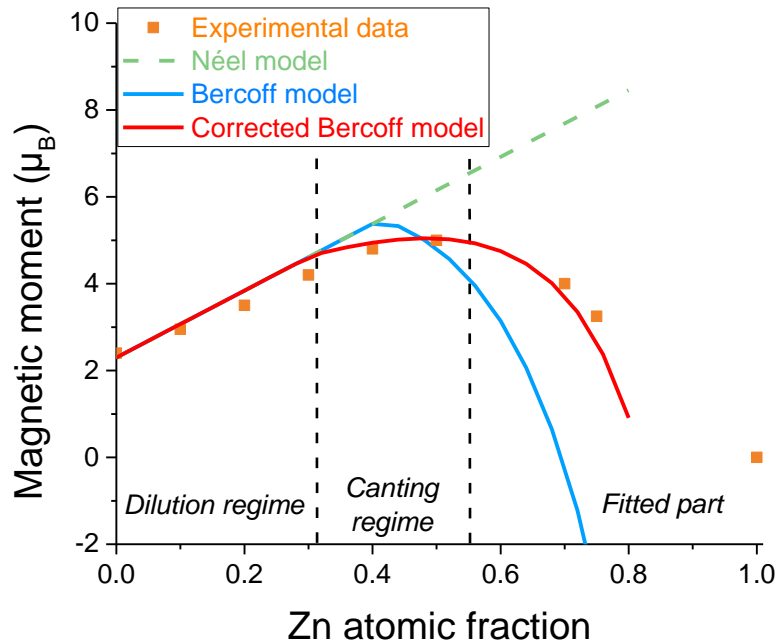


Figure IV-21. Fit of the experimental data for  $\text{Ni}_{(1-z)}\text{Zn}_z\text{Fe}_2\text{O}_4$  ferrite from E.W. Gorter [39] with the uncorrected and corrected Bercoff model and comparison with the Néel model.

In the dilution regime up to approximately 0.3 Zn atomic fraction (Figure IV-21), the Néel model predicts accurately the magnetic moment. From 0.3 up to 0.56 Zn content, the corrected model with a physical value of  $\cos(\theta_L)$  between 0 and 1 describes the canting zone. For Zn atomic fraction larger than 0.56,  $\cos(\theta_L)$  goes below 0 which makes the corrected model not physical anymore, and just an adjustment of the experimental data (fitted part in Figure IV-21).

### II.2.5.B.b. Application to Zn substituted magnetite

As a good agreement is obtained for the corrected model, it can be then applied to our composition for  $(Zn_z^{2+}Fe_{1-z}^{3+})[Fe_{1+z}^{3+}Fe_{1-z}^{2+}]$  (round and square brackets for tetrahedral and octahedral sites respectively) with  $Fe^{2+}$  characterized by  $S = 2$  and  $g = 2.1$ , and with the exchanges energies given in Figure IV-22 [43].

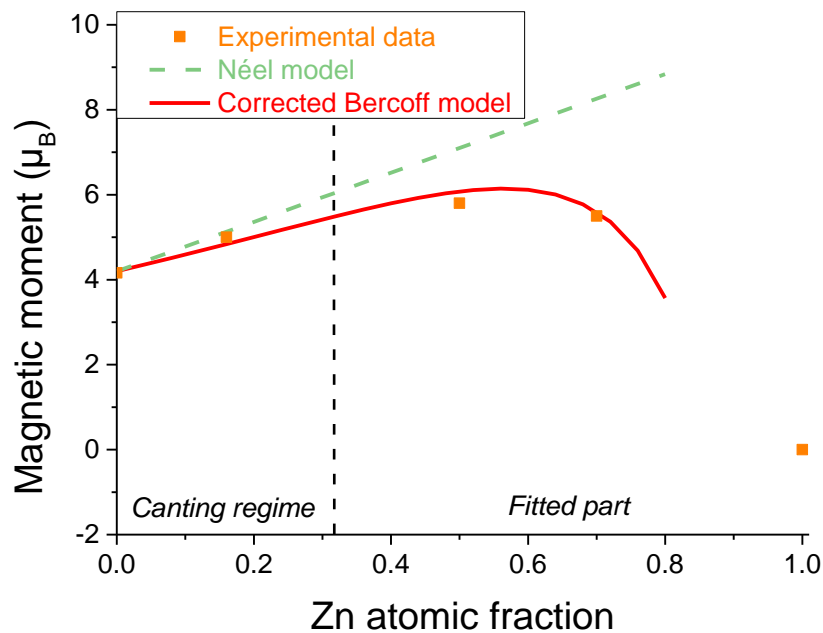
A	Ferrite	n	$J_{AA}$ (K) ( $d^5-d^5$ )		$J_{AB}$ (K) ( $d^5-d^5$ )		$J_{AB}$ (K) ( $d^5-d^n$ )	
			This work	Ref. [6]	This work	Ref. [6]	This work	Ref. [6]
	$Fe_3O_4$	6	0	-14.0	-12.0	-28.0	-17.4	-20.2
	$CoFe_2O_4$	7	0	-14.0	-12.0	-28.0	-20.7	-22.7
	$NiFe_2O_4$	8	0	-14.0	-12.0	-28.0	-29.8	-27.4
	$CuFe_2O_4$	9	0	-14.0	-12.0	-28.0	-29.0	-27.0
B	Ferrite	n	$J_{BB}$ (K) ( $d^5-d^5$ )		$J_{BB}$ (K) ( $d^5-d^n$ )		$J_{BB}$ (K) ( $d^n-d^n$ )	
			This work	Ref. [6]	This work	Ref. [6]	This work	Ref. [6]
	$Fe_3O_4$	6	-8.8	-9.0	-11.4	-11.0	-15.2	+44.0
	$CoFe_2O_4$	7	-8.8	-9.0	-12.2	-10.0	-13.3	+46.0
	$NiFe_2O_4$	8	-8.8	-9.0	-13.6	-10.0	+0.8	+29.0
	$CuFe_2O_4$	9	-8.8	-9.0	-13.6	-10.0	+0.4	+29.0

**Figure IV-22. Values of exchange constants for various interactions of cations. From P.G. Bercoff and H.R. Bertorello [43].**

The comparison between the corrected model defined by the calculated parameters in Figure IV-23, the Néel model and experimental data for Zn substituted ferrites from E.W. Gorter [39] is shown in Figure IV-24.

Parameters	Values
$S_A$	2.5
$S_B$	$\frac{1}{2}(2.5 \times (1+z) + 2 \times (1-z))$
$S_{B'}$	$S_B$
$q_A$	$(1-z)$
$q_B$	$2 - q_{B'}$
$q_{B'}$	$2 \times (0.5z - z^2 + 0.3z^3)$
$n_{AB'}$	as in corrected model
$n_{BB'}$	as in corrected model
$n_{B'A}$	as in corrected model
$n_{B'B'}$	as in corrected model
$n_{B'B}$	as in corrected model
$J_{AB'}$	$\frac{1}{2}((1+z) \times (-12) + (1-z) \times (-17.4))$
$J_{BB'}$	$\frac{1}{4}((1+z)^2 \times (-8.8) + 2 \times (1-z) \times (1+z) \times (-11.4) + (1-z)^2 \times (-15.2))$
$J_{B'B'}$	$J_{BB'}$

**Figure IV-23. Parameters used in the corrected fit plotted in Figure IV-24.**



**Figure IV-24.** Fit of the experimental data for  $\text{Zn}_z\text{Fe}_{3-z}\text{O}_4$  ferrite from E.W. Gorter [39] with the corrected Bercoff model and comparison with the Néel model (all of the zinc is located at the tetrahedral sites).

In this case, the pure dilution regime is not observed as the computed canting angle is different from 0 at low volume fractions up to 0.32 atomic fraction of Zn (Figure IV-24). This comes from the difference of chemical composition in the  $B$  sublattice, since the  $A$  sublattice composition ( $\text{Fe}^{3+}$  and  $\text{Zn}^{2+}$ ) stays the same. As  $\text{Fe}^{2+}$  has a stronger magnetic spin (2) than  $\text{Ni}^{2+}$  (1), the increase of the magnetic moment of the octahedral sublattice comes from the substitution of a  $\text{Fe}^{2+}$  by a  $\text{Fe}^{3+}$  ( $S = 2.5$ ): this effect is less important than in the case of  $\text{Ni}^{2+}$  and the dilution regime is rapidly overcome by the canting regime.

Moreover, Figure IV-25 exhibits the values of the exchange constants  $J_{AB'}$  and  $J_{BB'}$ , computed for the inter and intrasublattice interactions in the case of the NiZn and FeZn compositions. The difference of the exchange energies in the case of the NiZn composition (red and black curves) is greater than for the FeZn composition (green and blue curves), which explains that the canting regime coming from the competition of these interactions takes place at lower volume fraction in the FeZn composition than in the NiZn one.

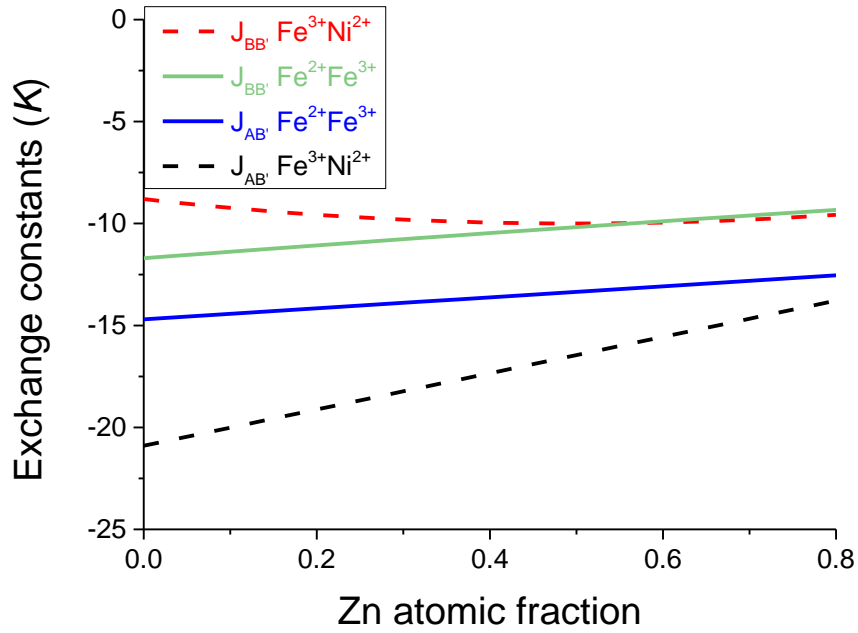


Figure IV-25. Exchange constants  $J_{AB'}$  and  $J_{BB'}$  for the inter and intrasublattice interactions in the case of the NiZn and FeZn compositions.

#### II.2.5.B.c. Extension to Zn fraction in both tetrahedral and octahedral sites

In the most general case, a canting of magnetic moments of  $\text{Fe}^{3+}$  in the tetrahedral sublattice should be considered. However, since the overall Zn substitution of our compositions are 0.2 and 0.4, with a limited volume fraction of Zn in octahedral sites up to 0.14 (Chapter I), the dilution model should be sufficient to describe this dilution effect in the  $B$  sublattice. In this case, the number of canted  $B'$  moments remains dependent of  $z_A$ , the level of substitution on  $A$  sites, whereas the total number of magnetic ions on  $B$  site is reduced by the  $z_B$  substitution.

In the model, the parameters are then described by:



Parameters	Values
$z$	total Zn fraction on A and B sites: 0.2 or 0.4 (FM particles)
$1-z$	Fe <sup>2+</sup> fraction on B site
$z_B$	Zn fraction on B site
$z_A$	Zn fraction on A site = $z-z_B$
$1-z_A$	Fe <sup>3+</sup> fraction on A site
$1+z_A$	Fe <sup>3+</sup> fraction on B site
$S_A$	2.5
$S_B$	$\frac{1}{2}(2.5 \times (1 + z_A) + 2 \times (1 - z))$
$S_{B'}$	$S_B$
$q_A$	$(1 - z_A)$
$q_B$	$2 - z_B - q_{B'}$
$q_{B'}$	$(2 - z_B) \times (0.5z_A - z_A^2 + 0.3z_A^3)$
$n_{AB'}$	$12(1 - z_B)z_A$
$n_{BB'}$	$6(1 - z_B)z_A$
$n_{B'A}$	$6(1 - z_B)(1 - z_A)$
$n_{B'B'}$	$(2 - z_B)(1 - z_A^2)$
$n_{B'B}$	$6(1 - z_B) - n_{B'B'}$
$J_{AB'}$	$\frac{1}{2}((1 + z_A) \times (-12) + (1 - z) \times (-17.4))$
$J_{BB'}$	$\frac{1}{4}((1 + z_A)^2 \times (-8.8) + 2(1 - z) \times (1 + z_A) \times (-11.4) + (1 - z)^2 \times (-15.2))$
$J_{B'B'}$	$J_{BB'}$

Figure IV-26. Parameters used in the corrected fit plotted in Figure IV-27.

In both cases, the Néel model overestimates slightly the magnetic moment because it neglects canting of  $B$  sublattice at low fraction of Zn in  $B$  sublattice (Figure IV-27).

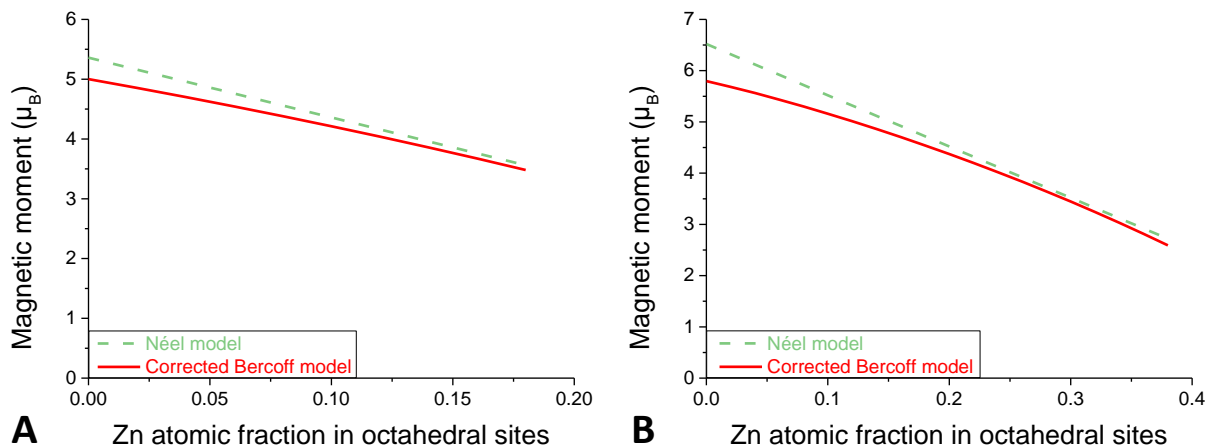


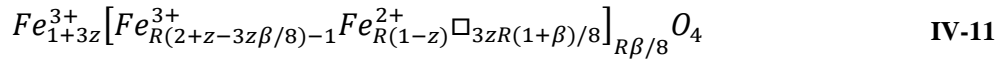
Figure IV-27. Comparison between Néel and Bercoff models as a function of the Zn atomic fraction in octahedral sites for a Zn total content of 0.2 (A) and 0.4 (B).

In both cases and with both models, what is predicted is a decrease of the magnetic moment with the increase of Zn atomic fraction in octahedral sites.

### II.2.5.B.d. From magnetite to maghemite magnetic moment

As the SP(F)M nanoparticles are strongly oxidized following the Mössbauer results (Chapter I), the magnetic moment of maghemite and  $Zn^{2+}$  substituted maghemite has to be estimated.

Maghemite can be described starting from magnetite and introducing vacancies in the octahedral site with the formula  $(Fe^{3+})[Fe^{3+}_{5/3}\square_{1/3}]O_4^-$ . In this case, the magnetic moment is predicted to be  $3.33 \mu_B$  [45] whereas at 0 K the measured value is  $3.11 \mu_B$  [42]. Various assumptions have been proposed by C.J. Goss to explain this difference, and the more efficient is the one of an excess of  $Fe^{3+}$   $\beta$  in tetrahedral site [46]:



with  $R = 8/(8+z)$ ,  $z$  the ratio of  $Fe^{2+}$  to describe various degrees of oxidization from 0 (magnetite) to 1 (maghemite).

To retrieve the experimental value for maghemite, the atomic fraction of Fe in tetrahedral site has to be increased from 1 to 1.02.

For substituted maghemite, several authors have pointed out that the Zn substitution takes place not necessarily in the octahedral sites as it does for the non-oxidized phase [47]. In order to interpret the magnetizations measured for Zn substituted maghemites, Y. Khan and E. Kneller [47] have concluded that a random substitution on both tetrahedral and octahedral sites is the best assumption. This effect overcomes the small correction proposed by C.J. Goss [46] which is then not taken into account to describe the substitution effect of Zn.

To preserve the charge balance, for one  $Zn^{2+}$  added,  $\frac{2}{3} Fe^{3+}$  and  $\frac{1}{3} \square$  are removed.

Three cases are then considered with different magnetization expressions plotted in Figure IV-28:

- The classical substitution of tetrahedral site with  $Fe^{3+}$  transferred from the A site to the B site expressed as  $(Fe_{1-z}^{3+} Zn_z^{2+})_A [Fe_{(5/3)+z-(2/3)z}^{3+} \square_{(1/3)(1-z)}]_B O_4$ :

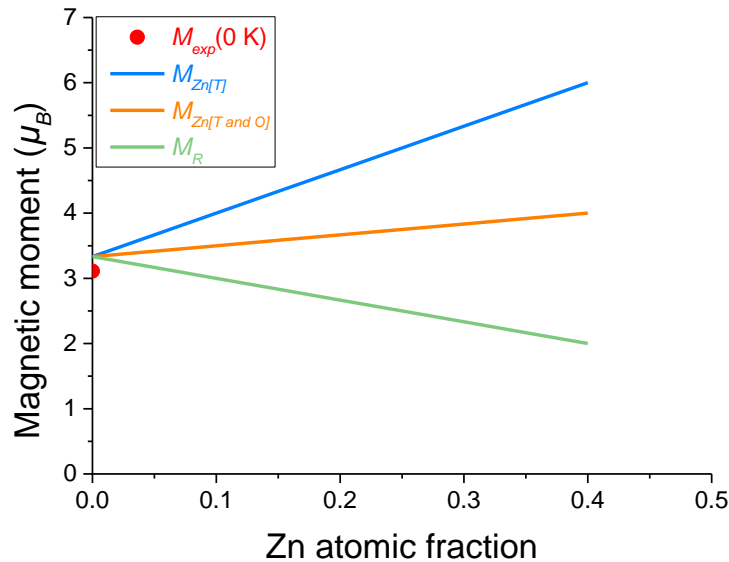
$$M_{Zn[T]} = g_{Fe3+} S_{Fe3+} \left( \frac{5}{3} + z - \frac{2}{3} z \right) - g_{Fe3+} S_{Fe3+} (1 - z) \quad \text{IV-12}$$

- The substitution of  $Zn^{2+}$  on both A and B sites in equal proportion with a transfer of  $Fe^{3+}$  from A to B site expressed as  $(Fe_{1-(z/2)}^{3+} Zn_{(z/2)}^{2+})_A [Fe_{(5/3)+(z/2)-(2/3)z}^{3+} Zn_{(z/2)}^{2+} \square_{(1/3)(1-z)}]_B O_4$ :

$$M_{Zn[T \text{ and } O]} = g_{Fe3+} S_{Fe3+} \left( \frac{5}{3} + \frac{z}{2} - \frac{2}{3} z \right) - g_{Fe3+} S_{Fe3+} \left( 1 - \frac{z}{2} \right) \quad \text{IV-13}$$

- And the random repartition of cations on sites *A* and *B* with no transfer of Fe from *A* to *B* site:

$$M_R = g_{Fe^{3+}} S_{Fe^{3+}} \left( \frac{5}{3} - \frac{2}{3} z \right) - g_{Fe^{3+}} S_{Fe^{3+}} (1) \quad \text{IV-14}$$



**Figure IV-28.** Magnetic moment as a function of zinc atomic fraction with three different configurations depending on the location of iron and zinc in maghemite. Comparison with the experimental point at 0 K.

The corresponding cases are shown in Figure IV-29. Following Y. Khan and E. Kneller [47], the experimental values depends on the synthesis (curve labeled  $\gamma[L]$ ) and post processing of the crystals ( $\gamma[I]$ : heating at high temperature and slow cooling,  $\gamma[H]$ : heating at high temperature and quenching). The curves are located in the area between the lines delimiting a normal maghemite with all zinc at tetrahedral sites and a maghemite with a statistical or random distribution of zinc in the structure.

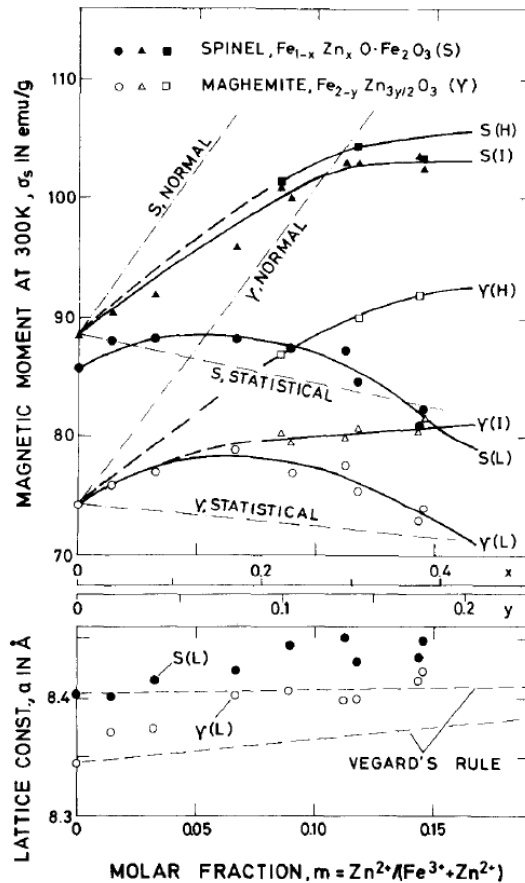


Figure IV-29. Magnetic moment and lattice constant of zinc substituted spinel and maghemite as a function of the zinc molar fraction. From Y. Khan and E. Kneller [47].

In this model, non-canting has been introduced since it would require more experimental data (at 0 K) to be correctly adjusted.

The results are summed up in the following table (Figure IV-30):

Repartition	Predicted moment FM (0.2)	Predicted moment FM (0.4)
Zn[T]	4.66	6
Zn[T and O]	3.67	4
random	2.66	2

Figure IV-30. Predicted magnetic moments for FM particles with different Zn contents (0.2 and 0.4).

II.2.5.B.e. Interpretation of measured magnetic moments of SP(F)M and FM nanoparticles

The measured magnetic moments at 2 K of the magnetic oxides are given in Figure IV-31:

Particle	SP(F)M	FM (0.2)	FM (0.4)
Measured magnetic moment ( $\mu_B$ )	3.59	2.62	3.94

Figure IV-31. Measured magnetic moments at 2 K of SP(F)M and FM particles with different Zn contents (0.2 and 0.4).

First of all, as in the case of Fe<sub>3</sub>O<sub>4</sub> nanoparticles synthesized by thermal decomposition [15], the presence of a magnetic dead layer due to surface spin canting has to be taken into account.

The magnetization of the particles are reduced due to the thickness of surface spin-canting determined by Mössbauer spectroscopy in chapter I. The magnetizations of the particle core are hence slightly higher and can be retrieved with the following formula:

$$M = M_{shell} + (M_{core} - M_{shell}) \left(1 - \frac{2e}{D}\right) \quad \text{IV-15}$$

with  $e$  the thickness of surface spin-canting,  $D$  the particle diameter and by taking  $M_{shell} = 0$ . It gives the following saturation magnetizations (Figure IV-32):

Particle	e shell (nm)	Particle diameter (nm)	$M_{particle}$ ( $\mu_B$ )	$M_{core}$ ( $\mu_B$ )
SP(F)M	0.10	6.2	3.59	<b>3.71</b>
FM (0.2)	0.38	22.4	2.62	<b>2.71</b>
FM (0.4)	0.60	22.4	3.94	<b>4.16</b>

Figure IV-32. Magnetization of SP(F)M and FM particles after removal of the contribution of surface spin-canting.

This correction has a stronger effect on the larger nanoparticles.

Then, the magnetization of the core depends on which structural phase it is constituted of: magnetite spinel or oxidized spinel (maghemite) with vacancies. Several cases are examined:

- Case 1: ideal case with no oxidation of the spinel and all Zn in tetrahedral sites: application of a corrected Bercoff model from Figure IV-24.
- Case 2: no oxidization of the spinel and a fraction of Zn in octahedral sites:
  - Case 2A: as retrieved from Rietveld analysis of XRD diffractometer (Chapter I).
  - Case 2B: as retrieved from Mössbauer spectroscopy (Chapter I).
  - Case 2C: a fraction of Zn in octahedral sites deduced from the extended Bercoff model of Figure IV-27 in order to retrieve the measured magnetization (Figure IV-32).
- Case 3: a mix of Zn<sup>2+</sup> substituted maghemite and Zn<sup>2+</sup> substituted magnetite determined from Mössbauer spectroscopy. The magnetization becomes:

$$M = x \times M_{Zn\ maghemite} + y \times M_{Zn\ magnetite} \quad \text{IV-16}$$

with  $x$  and  $y$  the fractions of Zn<sup>2+</sup> substituted maghemite and Zn<sup>2+</sup> substituted magnetite, respectively. As the predicted values for substituted maghemite are spread on a wide range depending on the repartition of cations on both sites, the computed moments for Zn<sup>2+</sup> substituted magnetite calculated in the previous cases are used to retrieve a value for the substituted maghemite from equation IV-16 and compare it to the predicted range in Figure IV-28.

- Case 4: using the predicted repartition of  $\text{Fe}^{3+}$  and  $\text{Fe}^{2+}$  on  $A$  and  $B$  sites estimated from Mössbauer spectroscopy (Chapter I), but taking into account the oxidation of magnetite into maghemite:  $\text{Fe}^{2+} \rightarrow \frac{2}{3} \text{Fe}^{3+} + \frac{1}{3} \square$

In this case the magnetic moment is expressed by:

$$\begin{aligned}
 M &= M_B - M_A \\
 &= g_{\text{Fe}^{3+}} S_{\text{Fe}^{3+}} x_{\text{Fe}^{3+}}^B \frac{t_{\text{Fe}}}{1+r} + g_{\text{Fe}^{2+}} S_{\text{Fe}^{2+}} x_{\text{Fe}^{2+}}^B \left( t_{\text{Fe}} - \frac{t_{\text{Fe}}}{1+r} \right) \\
 &\quad - g_{\text{Fe}^{3+}} S_{\text{Fe}^{3+}} x_{\text{Fe}^{3+}}^A \frac{t_{\text{Fe}}}{1+r}
 \end{aligned} \tag{IV-17}$$

where  $x_{\text{Fe}^{3+}}^B$  and  $x_{\text{Fe}^{3+}}^A$  stands for the measured fraction of  $\text{Fe}^{3+}$  in  $B$  and  $A$  sites deduced for Mössbauer spectroscopy,  $t_{\text{Fe}}$  the total amount of iron cations, and  $r$  the  $\text{Fe}^{2+}/\text{Fe}^{3+}$  ratio value.

The values of the magnetic moment are calculated for each cases and summarized in Figure IV-33:

Case		SP(F)M	FM (0.2)	FM (0.4)
<b>Experimental moment corrected from surface spin-canting</b>		3.71 $\mu_B$	2.71 $\mu_B$	4.16 $\mu_B$
<b>Case 1</b>		$(Zn_{0.4}^{2+}Fe_{0.6}^{3+})[Fe_{1.4}^{3+}Fe_{0.6}^{2+}]O_4$ 5.78 $\mu_B$	$(Zn_{0.2}^{2+}Fe_{0.8}^{3+})[Fe_{1.2}^{3+}Fe_{0.8}^{2+}]O_4$ 5.00 $\mu_B$	$(Zn_{0.4}^{2+}Fe_{0.6}^{3+})[Fe_{1.4}^{3+}Fe_{0.6}^{2+}]O_4$ 5.78 $\mu_B$
<b>Case 2</b>	2A	$(Zn_{0.4}^{2+}Fe_{0.6}^{3+})[Fe_{1.4}^{3+}Fe_{0.6}^{2+}]O_4$ 5.78 $\mu_B$	$(Zn_{0.2}^{2+}Fe_{0.8}^{3+})[Fe_{1.2}^{3+}Fe_{0.8}^{2+}]O_4$ 5.00 $\mu_B$	$(Zn_{0.26}^{2+}Fe_{0.74}^{3+})$ $[Zn_{0.14}^{2+}Fe_{1.26}^{3+}Fe_{0.6}^{2+}]O_4$ 4.85 $\mu_B$
		random Zn distribution	$(Zn_{0.2}^{2+}Fe_{0.8}^{3+})[Fe_{1.2}^{3+}Fe_{0.8}^{2+}]O_4$ 5.00 $\mu_B$	$(Zn_{0.3}^{2+}Fe_{0.7}^{3+})$ $[Zn_{0.10}^{2+}Fe_{1.3}^{3+}Fe_{0.6}^{2+}]O_4$ 5.16 $\mu_B$
	2C	$(Zn_{0.13}^{2+}Fe_{0.87}^{3+})$ $[Zn_{0.27}^{2+}Fe_{1.13}^{3+}Fe_{0.6}^{2+}]O_4$ 3.71 $\mu_B$	$(Zn_{0.02}^{2+}Fe_{0.98}^{3+})$ $[Zn_{0.18}^{2+}Fe_{1.02}^{3+}Fe_{0.8}^{2+}]O_4$ 3.48 $\mu_B$	$(Zn_{0.18}^{2+}Fe_{0.82}^{3+})$ $[Zn_{0.22}^{2+}Fe_{1.18}^{3+}Fe_{0.6}^{2+}]O_4$ 4.16 $\mu_B$
<b>Case 3</b>		100 % Zn <sup>2+</sup> maghemite	50.5 % Zn <sup>2+</sup> maghemite + 49.5 % Zn <sup>2+</sup> magnetite	45.2 Zn <sup>2+</sup> maghemite + 54.8 Zn <sup>2+</sup> magnetite with 5.78 $\mu_B$ for the magnetite phase: 2.2 $\mu_B$ for the maghemite close to value predicted with random distribution of Zn (2 $\mu_B$ ) with 4.85 $\mu_B$ for the magnetite phase: 3.32 $\mu_B$ for the maghemite between the value predicted with Zn on both T and O sites (4 $\mu_B$ ) and random repartition (2 $\mu_B$ ) with 5.16 $\mu_B$ for the magnetite phase: 2.95 $\mu_B$ for the maghemite between the value predicted with Zn on both T and O sites (4 $\mu_B$ ) and random repartition (2 $\mu_B$ )
<b>Case 4</b>		35.6 % Fe <sup>3+</sup> (A) 64.4 % Fe <sup>3+</sup> (B) 3.74 $\mu_B$ 1 % of gap with exp	32.5 % Fe <sup>3+</sup> (A) 49.1 % Fe <sup>3+</sup> (B) 18.4 % Fe <sup>2+</sup> (B) 2.29 $\mu_B$ 15% of gap with exp	29.4 % Fe <sup>3+</sup> (A) 59.7 % Fe <sup>3+</sup> (B) 10.9 % Fe <sup>2+</sup> (B) 3.64 $\mu_B$ 12 % of gap with exp

**Figure IV-33. Magnetic moments predicted from various models for SP(F)M and FM particles with different Zn contents (0.2 and 0.4) in different configurations (Cases 1 to 3).**

The ideal case of nanoparticles of pure spinel composition without surface oxidation and with all of the zinc located at the tetrahedral positions (Case 1) gives values of magnetic moments (Figure IV-33) in the same order of the experimental one at 2 K, but with a significant gap. Thus, FM and SP(F)M particles do not correspond to the ideal case.

Considering the presence of Zn cations on both tetrahedral and octahedral sites, similar values of theoretical magnetic moments with the experimental ones are computed for SP(F)M

and FM (0.4) particles with inversion degrees of 0.27 and 0.22, respectively (Figure IV-33). The value of 0.22 being different of the value of inversion degrees retrieved from XRD or Mössbauer data (0.14 and 0.10), the value of the magnetic moment is not only influenced by the presence of Zn cations at the octahedral sites. In the case of SP(F)M particles, XRD analysis does not predict an inversion degree, and the Mössbauer spectroscopy has shown a repartition of  $\text{Fe}^{3+}$  between tetrahedral and octahedral sites with the absence of  $\text{Fe}^{2+}$ , meaning the particles are almost completely oxidized. The Mössbauer data are not consistent with the location of Zn cations only at the tetrahedral sites, or in an equal distribution between both sites. A random distribution is thus supposed.

The oxidation of particles leading to a substituted maghemite type spinel should also be considered (Case 3). If for SP(F)M particles and FM (0.4) particles, this last assumption leads to a possible agreement between experimental and predicted value, it fails in the case of FM (0.2) particles for which a 100 % oxidation assumption is necessary to retrieve the magnetization, which is not in agreement with Mössbauer spectroscopy results (Chapter I).

The values of case 4 are very close to the experimental one for the SP(F)M particle. The difference between the predicted and experimental value is larger for FM (0.2) composition, but in an acceptable range considering the experimental uncertainties that have not been taken into account. In addition, the model does not consider the volume spin canting which can induce a 10% error from the dilution model for the FM (0.4) composition.

As a conclusion, the measured magnetic moments agree well with the proportion of the  $\text{Fe}^{2+}$  and  $\text{Fe}^{3+}$  that have been measured on the A and B sites, which makes Mössbauer spectroscopy a trustworthy characterization technique.



### II.2.6. Conclusion

*The static magnetic properties of FM and SP(F)M particles have been compared. The shape of their hysteresis cycles is different and depends on the particle size:*

- *The magnetization signal of FM particles saturates with a saturation magnetization  $M_S$  of 80.6 emu/g ( $A.m^2/kg$ ).*
- *On the contrary, SP(F)M particles are superparamagnetic and the magnetization curve does not saturate. A fit of the curve based on a Langevin function gives a crystallite size of 5 nm and a saturation magnetization  $M_S$  of 85.6 emu/g ( $A.m^2/kg$ ), close to the one of FM particles.*

*The saturation magnetizations  $M_S$  of FM and SP(F)M particles are lower than the one of the  $Zn_{0.4}Fe_{2.6}O_4$  bulk (98.8 emu/g or  $A.m^2/kg$  [3]). This difference can be explained by:*

- *the volume oxidation of the particles with the presence of an amount of  $Zn^{2+}$  substituted maghemite in the particle probably near the surface,*
- *an inversion degree in the spinel structure,*
- *and by the spin-canting effect at the nanoparticle surface, exalted in smaller SP(F)M particles.*

*The synthesis route and its parameters influence the magnetic properties of particles, as they directly impact the microstructure through phase purity, cationic redistribution in the sub-lattices of the spinel, spin-canting effect, gradient of doping inside particles...*

*The variation of magnetization of FM particles through the annealing temperature has been studied. A sharp decrease of the saturation magnetization  $M_S$  from 300 to 770 °C (the sintering temperature) is observed and can be caused by one or a combination of the following explanations:*

- *the presence of a secondary phase of  $Zn^{2+}$  substituted wüstite ( $Zn_xFe_{1-x}O$  phase) from 400 °C,*
- *a  $Zn^{2+}$  redistribution in the spinel sites,*
- *and spin disorder at the particle surface.*

*Above the sintering temperature (770 °C), the saturation magnetization  $M_S$  slightly increases at 800 °C and remains constant until 1000 °C. It could be due to an effect of sintering, observed when the reduction of the material, induced by the degradation of the organics, is finished, all of the reactants being consumed.*

*Models have been built from molecular field theory in order to predict the magnetic moment of the different magnetic phases considered ( $Zn^{2+}$  substituted pure magnetite or maghemite type). This attempt has been successful for SP(F)M and FM particles in accordance with Mössbauer spectroscopy results (Chapter I). It highlights the fact that deep structural characterizations are needed to fully described the magnetic behavior of material*

*and the Mössbauer spectroscopy has been a wonderful tool. To go further, here are some ways to explore:*

- *predict the temperature magnetization dependence to improve the molecular fields models,*
- *to have a better description of the magnetic moment in the whole range of composition, a model starting from the  $ZnFe_2O_4$  point could be written and a bridge between the corrected Bercoff model and the  $ZnFe_2O_4$  based model could be built,*
- *for Rietveld analysis, the oxidation (or vacancies in the spinel) have been neglected: with this information, what would be the predicted inversion of the spinel ?*
- *Mössbauer spectroscopy and Rietveld analysis being global but not local techniques, an analysis of the local composition inside the particle should be performed through a X-ray magnetic circular dichroism technique (XMCD) [48] or small-angle neutron-scattering (SANS) [49].*

*For the effect of annealing temperature on the nanoparticle magnetization, these models could shed light on the associated decrease of room temperature magnetization (neglecting the thermal dependence of magnetization for a given composition) before the  $Zn^{2+}$  wüstite precipitation at  $600^\circ C$ . As the cooling of the particles is slow, the Zn amount into the octahedral sites is not expected to increase but to decrease in a pure spinel case. This would result in an increase of the magnetization and not to a decrease. In addition, a reordering of the proportions between Zn magnetite and Zn maghemite induced by annealing can be considered, and has a great impact on magnetization as it has been shown for substituted maghemite models. To assess this assumption, the annealed powders should be characterized by Mössbauer spectroscopy in order to measure the  $Fe^{2+}/Fe^{3+}$  ratio.*

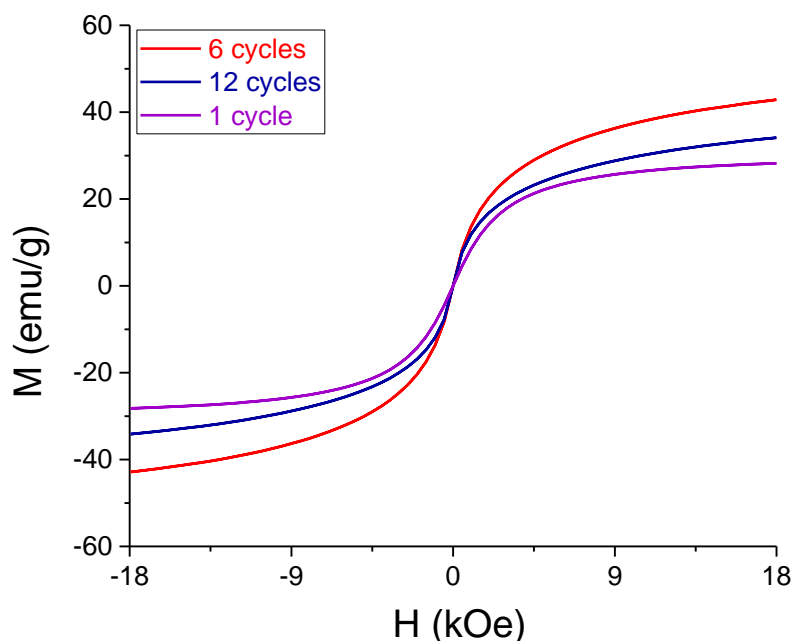
*After studying the static magnetic properties at the nanoparticle scale, the properties of coatings are examined.*

### II.3. Static magnetic properties of continuous coatings

The magnetic properties of continuous films are studied as a function of the number of particle cleanings, and of the thermal treatment. For superparamagnetic particles, the sintering may result in a decrease of particles distances, hence an increase of their dipolar interaction which lastly may overcome the demagnetizing field and suppress the superparamagnetic state [327]. It is referred to the “superferromagnetic transition”. In this case, the measured saturation magnetization could be increased by the sintering in comparison with the untreated SP(F)M ones which are in the superparamagnetic state.

#### II.3.1. Influence of the number of particle cleanings

In chapter II, the particle cleaning has been investigated through the number of centrifugation cycles  $N$ , and especially the behavior of these coatings once dried on a substrate after annealing at 300 °C during 30 minutes under argon atmosphere. The magnetic properties of these coatings are inspected in Figure IV-34 in order to discern in which case the magnetization is enhanced and to compare the results with the observations made in chapter II. One, six and twelve cycles of centrifugations have been realized on SP(F)M particles. The magnetization curves have not been corrected from the residual organic amount at 300°C to highlight the effect of the organic amount in the hysteresis cycles.



**Figure IV-34.** Measured magnetization curves of SP(F)M coatings after annealing at 300 °C as a function of the number of centrifugation cycles  $N$ . Mass magnetization  $M$  versus the applied field  $H$ .

The magnetization of the coatings displays superparamagnetic behaviors, due to the use of superparamagnetic SP(F)M particles. The magnetization firstly increases between 1 and 6 cycles of cleanings, which can be easily explained by the decrease of the organic amount surrounding particles (Figure IV-34). It is in agreement with the conclusions observed in chapter II. After one cleaning, the coating was oily in appearance and cracked due to the poorly

washing of particles, and the removal of a large quantity of organics during thermal treatment, occurring debonding. The surface of coatings was less oily after six cleanings and no cracks were noticed, indicating a better washing of particles.

However, a decrease of the magnetization is shown after twelve cycles of centrifugation (Figure IV-34), but by keeping a value higher than the coating obtained after one cycle of cleaning. This result is surprising because the particle cleaning is supposed to be enhanced by increasing the number of cycles of centrifugation  $N$  (Chapter II). It was confirmed by the powdery look of the corresponding surface of coatings in chapter II. The explanation of such a phenomenon is tricky. An hypothesis could be that from a certain number of cycles of centrifugation, all of the organics are removed from the particle surface, which will be then not anymore protected. From there, the particles could be more sensitive to oxidation. Or the samples could have different Zn cations distribution between A and B sites inside  $Zn^{2+}$  substituted maghemite and magnetite which may explain the lower magnetization.

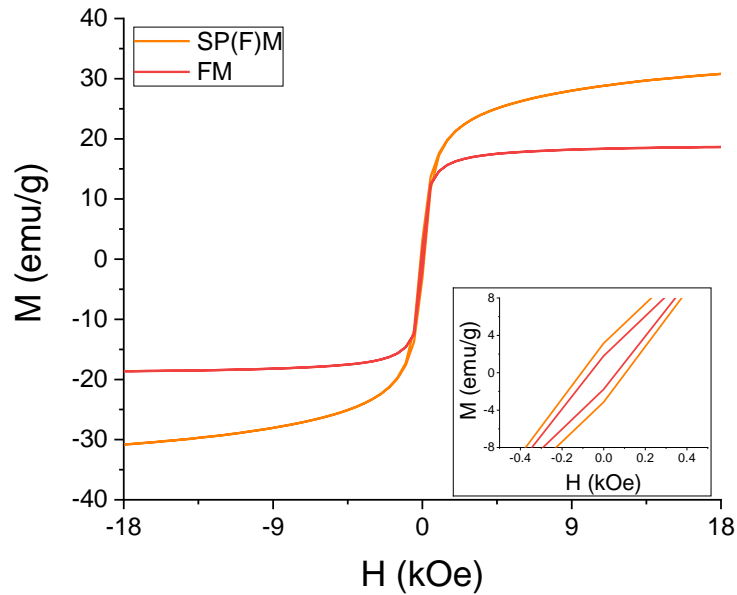
In this respect, this result corroborates the fact that the number of cleanings  $N$  has to be carefully chosen, the objective being to combine a low organic quantity, a high saturation magnetization  $M_S$  and a good adherence of the material on the substrate. The more adapted number of cycles is of six cleanings. It is a good compromise as it allows to considerably reduce the amount of organics at the particle surface, to keep a good adhesion of the particle layer on a substrate after thermal treatment (Chapter II), as well as to exhibit the highest saturation magnetization  $M_S$ .

The level of magnetization of SP(F)M coatings after thermal treatment at 300 °C is reduced in comparison with the saturation magnetization  $M_S$  of the same particles washed 6 times (65.6 emu/g or A.m<sup>2</sup>/kg, Figure IV-4). The variation of magnetization in coatings as a function of the annealing temperature seems to follow the same trend as the one described in part II.2.4 in the case of nanoparticles.

### II.3.2. Effect of the thermal treatment

Figure IV-35 compares the hysteresis cycles of SP(F)M and FM coatings after debinding at 450 °C. The values of coercivity  $H_C$  are still low and do not exceed the values obtained for nanoparticles (part II.2.4). Surprisingly, the magnetization of debinded SP(F)M coatings is stronger than for FM ones. This is in part explained from the magnetic moment at 0 K, the one of the SP(F)M particles being larger than the one of the FM particles, but also by differences induced by the debinding in the  $Zn^{2+}$  distribution inside the sub-lattices of the maghemite spinel.

Moreover, the hysteresis loop of the SP(F)M coating has features from a paramagnetic state.



**Figure IV-35.** Effect on the debinding (450 °C) on the measured magnetization of SP(F)M and FM coatings. Mass magnetization  $M$  versus the applied field  $H$ .

Moreover, the saturation magnetization  $M_S$  of FM coatings annealed at 450 °C (20 emu/g or A.m<sup>2</sup>/kg) is lower than the one corresponding to the FM particles at 450 °C (70 emu/g or A.m<sup>2</sup>/kg) (Figure IV-35). This information suggests that the variation of the magnetization as a function of the annealing temperature is different depending on the measured sample: particles or coatings.

This hypothesis is verified in Figure IV-36 and Figure IV-37. At first, the saturation magnetization  $M_S$  decreases from room temperature to 450 °C (the debinding temperature) in both cases. Nevertheless, this decrease is sharp in the case of coatings and the magnetization value attained at 450 °C is 3.5 times reduced in comparison with the particles. Then, the saturation magnetization  $M_S$  of coatings increases fastly from 450 to 770 °C (the sintering temperature), whereas it is still decreasing in the case of nanoparticles. Thus, the trend is reversed at 770 °C with the saturation magnetization  $M_S$  of coatings equal to 3 times the one of particles.

On the one hand, such a difference of magnetization between coatings and particles at 770 °C could be explained by a difference of reactivity between the powder and a film of approximately 6 μm of thickness. Indeed, as mentioned in chapter II, the secondary phase of Zn<sup>2+</sup> substituted wüstite (Zn<sub>x</sub>Fe<sub>1-x</sub>O phase) emerges at 625 °C in the XRD diffractometer of coatings, hence at a higher temperature than particles (400 °C). The secondary phase of wüstite appears with an offset. It is also confirmed by the fact the magnetization are almost similar for FM coatings at 770 °C and FM particles at 400 °C (Figure IV-37).

The difference of reactivity between the powder and the coating can be due to the fact that the powder is annealed without any shaping process, just by introducing powder in a crucible. As a consequence, the powder reacts rapidly, while the formation of a secondary phase is delayed for coatings, because of the higher compactness due to the layer stacking. Furthermore, the point at 1000 °C in the case of FM particles is obtained from a pellet of particles. Thus, its

low magnetization is due to the complete formation of the wüstite at this temperature, which is delayed in comparison with the other points. The authenticity of this point may be weakened if the magnetization value at 800 °C had not increased in comparison to the value at 770 °C. The magnetization at 1000 °C of a small amount of powder introduced in a crucible should therefore be close to the actual point.

On the other hand, the difference of reactivity does not explain the saturation magnetization  $M_S$  of FM coatings at 450 °C. The measurement has been repeated and gives the same result. Unfortunately, this phenomenon remains non-understood. This could be explained by the fact the annealing could induce different proportions of  $Zn^{2+}$  maghemite and magnetite in the particles. An increase of the proportion of  $Zn^{2+}$  maghemite could occur, but is difficult to observe with XRD since lattice parameters are close. It could be checked by Mössbauer spectroscopy by the  $Fe^{2+}/Fe^{3+}$  ratio. The recovering of almost the FM coating magnetization at 770 °C can be understood by a change in the repartition of the Zn cations in both magnetite and maghemite phases to a normal case with Zn in tetrahedral sites which maximize the magnetic moment.

The saturation magnetization  $M_S$  of a coating elaborated in chapter II with a mixture of FM (60 wt%) and SP(F)M (40 wt%) particles is analyzed. This strategy does not enable to produce a film with a higher magnetization than FM ones after sintering (Figure IV-37).

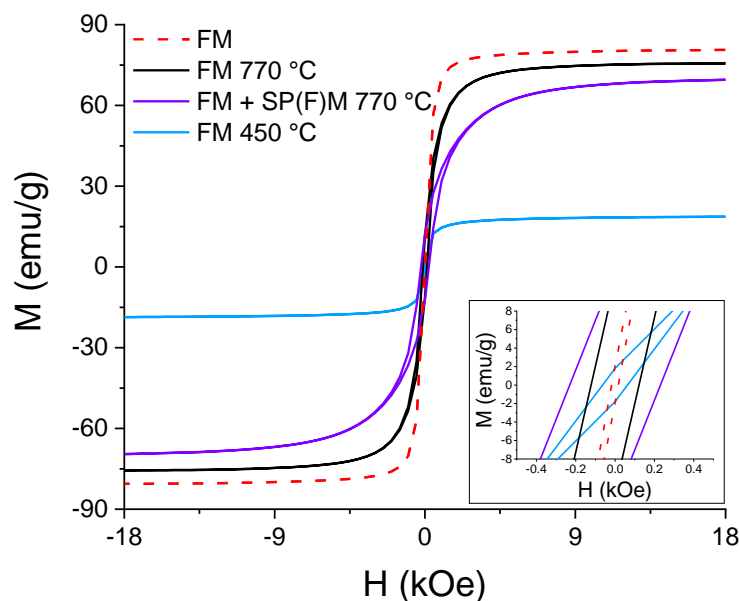
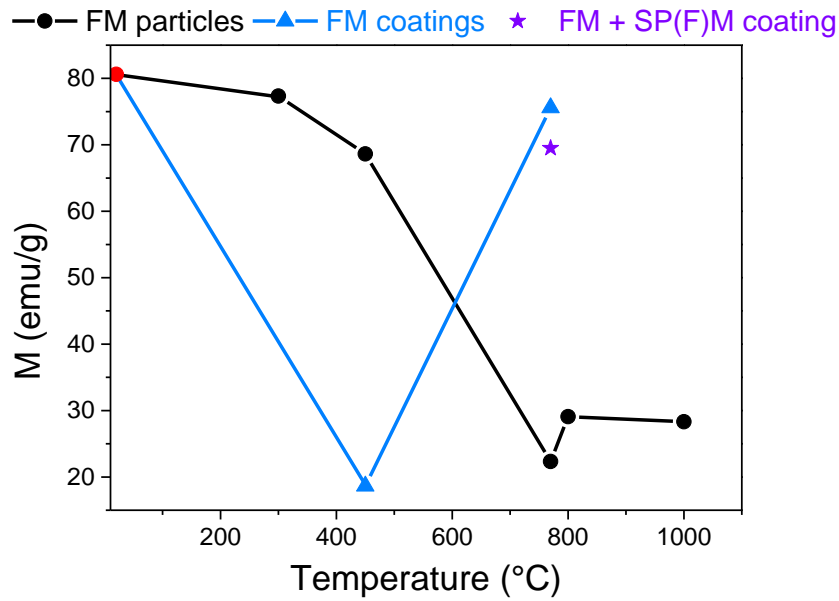


Figure IV-36. Effect on the debinding (450 °C) and sintering (770 °C) on the measured magnetization of FM coatings. Mass magnetization  $M$  versus the applied field  $H$ .



**Figure IV-37.** Evolution of the saturation magnetization  $M_S$  of FM particles and coatings as a function of the temperature.

The superferromagnetic transition has not been observed in the SP(F)M coatings, since the density is too low and the coupling too weak. Nevertheless, the saturation magnetization  $M_S$  of a cracked FM coating exhibiting 50% of porosity (Chapter II) after sintering is of 76 emu/g ( $\text{A}\cdot\text{m}^2/\text{kg}$ ), which is a promising result when compared to the value of 98.8 emu/g ( $\text{A}\cdot\text{m}^2/\text{kg}$ ) for a dense  $\text{Zn}_{0.4}\text{Fe}_{2.6}\text{O}_4$  film [3].

### II.3.3. Conclusion

*The static magnetic properties of continuous films have been studied as a function of the number of particle cleanings, and of the thermal treatment:*

- *On the one hand, concerning the number of cycle of particle cleanings  $N$ , the magnetization curves confirm the conclusions established in chapter II. The number of cycle  $N$  is fixed at 6 because it allows to combine the following properties: a reduction of the organic quantity at the particle surface, a high saturation magnetization  $M_S$  and a good adherence of the material on the substrate.*
- *On the other hand, the variation of the magnetization as a function of the annealing temperature is different between particles and coatings. This discrepancy is explained by a difference of reactivity between particles and coatings during annealing. The formation of  $Zn^{2+}$  substituted wüstite ( $Zn_xFe_{1-x}O$  phase) is thus delayed in coatings, and a high temperature followed by a slow cooling may order the Zn in tetrahedral sites which leads to a higher magnetization of sintered coatings (76 emu/g or  $A.m^2/kg$ ) in comparison with sintered nanoparticles (22 emu/g or  $A.m^2/kg$ ).*

*To conclude, the saturation magnetization  $M_S$  of a sintered FM coating with 50% of porosity (76 emu/g or  $A.m^2/kg$ ) is encouraging, as it is not so far from the value of 98.8 emu/g ( $A.m^2/kg$ ) of a dense  $Zn_{0.4}Fe_{2.6}O_4$  film [140].*

*The next part will focus on the dynamic magnetic properties of particles and continuous coatings.*



### III. Dynamic magnetic and dielectric characterizations

After the static magnetic characterizations, zero-field microwave permittivity and permeability measurements from 1 MHz up to 20 GHz are performed. The aim is to characterize the spectral response of FM and SP(F)M nanoparticles and to evidence the influence of the superparamagnetic state especially with SP(F)M ones. As previously mentioned (Chapter I), the selected chemical composition  $Zn_{0.4}Fe_{2.6}O_4$  combines a high value of the saturation magnetization with a large electrical resistivity [3].

#### III.1. Experimental techniques

Effective dielectric permittivity  $\epsilon_{eff}$  and magnetic permeability  $\mu_{eff}$  of a cell (APC7 standard) are determined by means of an APC7 coaxial line (Figure IV-38). From the measured transmission and reflection coefficients of a cell containing the nanoparticles, the  $\epsilon_{eff}$  and  $\mu_{eff}$  spectra are retrieved using the Nicolson-Ross algorithm [51]. Two vectorial network analyzers are used: a PNA N5232A from 1 MHz to 6 GHz and a PNA N5230A from 10 MHz to 20 GHz (both from Agilent Technologies) to cover a wide range of frequencies. The APC7 non-magnetic brass cell consists of two lateral plexiglass slices (Figure IV-38.B-D) spaced 3 mm apart with the following properties: a relative permittivity of 2.67 and a thickness of 2.0 mm. The powder is introduced between the two plexiglass slices by keeping one of them as the bottom of the box. The cell is then closed with the second plexiglass slice (Figure IV-38.B-D).

The particles introduced in the cell having a  $Zn_{0.4}Fe_{2.6}O_4$  magnetic core and an organic layer, the particle size and the saturation magnetization used in this section will be deduced from the magnetization curves not subtracted from the organic amount. These two parameters compensate each other in the computations.

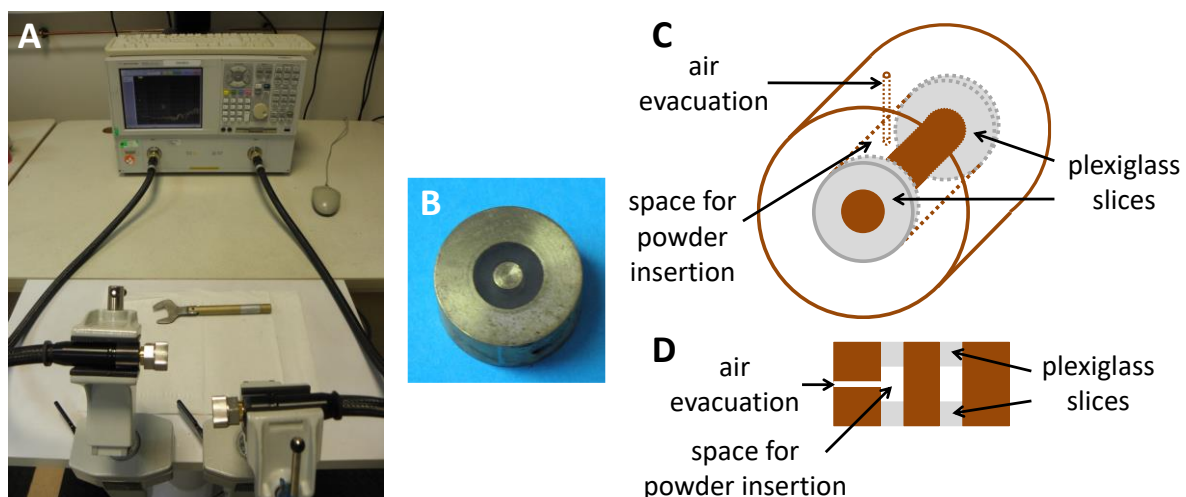


Figure IV-38. Set-up for permeability and permittivity measurements (A), APC7 cell 3D view (B-C) and cross-sectional view (D) [52].

Measurements of the permeability spectra are also conducted within the [243 K, 343 K] range by means of an HP 8720C network analyzer operating from 50 MHz up to 14 GHz. The

sample is placed in a cell (Figure IV-38.B-D) and the whole is loaded in a furnace to control the temperature. The temperature is monitored with a thermocouple sensor directly inserted inside the cell. Low temperatures are obtained by a water-cooling circuit.

Based on the volume fraction  $f_V$  of nanoparticles in the cell, the use of a mixing law is required to determine the intrinsic dynamic permeability from the effective one, considering that the cell contains a mixture of nanoparticles with air. In our case, the retained mixing law is a proportional one with the following formula:

$$\mu_{int} = 1 + \frac{3}{2 \times f_V} (\mu_{eff} - 1) \quad \text{IV-18}$$

where  $\mu_{int}$  is the intrinsic permeability. The calculation only regards the transverse dynamic susceptibility noted  $\chi_{\perp}$ , assuming that the parallel susceptibility is negligible. Thus, the relative permeability  $\mu_r$  is defined as  $\mu_r = 1 + \chi_{\perp}$ . The 3/2 prefactor comes from the randomly distributed anisotropy axes within the nanoparticles. It should be remarked that the mixing law does not consider the static and dynamic dipolar coupling between the particles (isolated particles). Taking into account these coupling effects could be achieved through an approach assuming effective demagnetizing factors [53].

Considering the low level of measured effective imaginary permeability particularly in the case of the SP(F)M particles, the uncertainty of measurement, about  $\pm 0.05$  for the cell with Plexiglas sides, has to be taken into account [54].

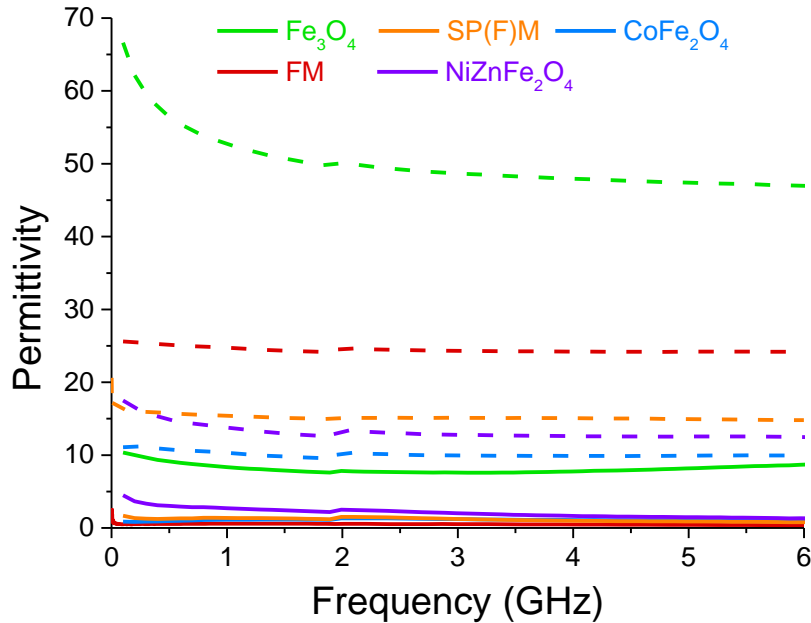
### III.2. At the nanoparticle scale

Permittivity and permeability measurements are firstly achieved at room temperature on commercial, FM and SP(F)M particles.

#### III.2.1. At room temperature

##### III.2.1.A. Permittivity measurements

The permittivity of FM and SP(F)M particles is compared to the one of commercial powders with different compositions:  $\text{Fe}_3\text{O}_4$ ,  $\text{CoFe}_2\text{O}_4$  and  $\text{NiZnFe}_2\text{O}_4$  between 1 MHz and 6 GHz (Figure IV-39).



**Figure IV-39. Real (dashed lines) and imaginary (continuous lines) part of the permittivity for FM and SP(F)M particles and commercial nanoparticles with different compositions:  $\text{Fe}_3\text{O}_4$ ,  $\text{CoFe}_2\text{O}_4$  and  $\text{NiZnFe}_2\text{O}_4$ .**

The particles can be ordered from the less to the more conductive through their real permittivities, as follows:  $\epsilon'$   $\text{CoFe}_2\text{O}_4$  ( $\sim 10$ ) <  $\epsilon'$   $\text{NiZnFe}_2\text{O}_4$  ( $\sim 14$ ) <  $\epsilon'$  SP(F)M ( $\sim 15$ ) <  $\epsilon'$  (FM) ( $\sim 25$ ) <  $\epsilon'$   $\text{Fe}_3\text{O}_4$  ( $\sim 50$ ).

The high value observed for the  $\text{Fe}_3\text{O}_4$  particles is consistent with the real permittivity of its bulk counterpart of about 45 measured in the same frequency range [55] and the relative dielectric constant of about 80 for nanoparticles with a 5 nm diameter [56] [57] [58] at other frequencies, displaying a Debye type resonance permittivity due to a polaron mode (dielectric resonance associated with the jump on an electron from  $\text{Fe}^{2+}$  to  $\text{Fe}^{3+}$ ).

The difference of real permittivity level between FM and SP(F)M particles can be explained by the slight difference of experimental chemical compositions (Figure IV-7), SP(F)M particles ( $\text{Zn}_{0.38}\text{Fe}_{2.62}\text{O}_4$ ) being closer to the theoretical composition ( $\text{Zn}_{0.4}\text{Fe}_{2.6}\text{O}_4$ ) and FM particles possessing less zinc ( $\text{Zn}_{0.31}\text{Fe}_{2.69}\text{O}_4$ ).

These measurements support the choice of the composition as  $\text{Zn}_{0.4}\text{Fe}_{2.6}\text{O}_4$  particles (FM and SP(F)M) need to combine both insulating properties with a high saturation magnetization (Chapter I). Hence, the introduction of zinc is responsible of a reduction of the permittivity when compared with pure  $\text{Fe}_3\text{O}_4$  composition.

Considering the real permittivity levels of  $\text{CoFe}_2\text{O}_4$  and  $\text{NiZnFe}_2\text{O}_4$  powders (Figure IV-39), amounts of cobalt and nickel could be introduced in the  $\text{Zn}_{0.4}\text{Fe}_{2.6}\text{O}_4$  composition in order to further decrease the permittivity.

### III.2.1.B. Permeability measurements

The permeability of commercial, FM and SP(F)M particles is studied. The influence of the composition as well as the size is investigated. Following N-N. Song *et al.* [13], the size of the

nanoparticle is believed to play a key role on the high frequency susceptibility through the superparamagnetic/ferromagnetic resonance [14].

### III.2.1.B.a. Different compositions

Commercial powders of  $\text{Fe}_3\text{O}_4$ ,  $\text{CoFe}_2\text{O}_4$ , and  $\text{NiZnFe}_2\text{O}_4$  have been purchased from Sigma Aldrich. The particle diameter provided by the supplier is controlled by TEM characterizations to verify the range of size (Figure IV-40). The supplier data underestimate the real particle diameters. Indeed,  $\text{CoFe}_2\text{O}_4$ , and  $\text{NiZnFe}_2\text{O}_4$  particles possess sizes below 100 nm, namely between 30 and 80 nm for  $\text{CoFe}_2\text{O}_4$  and between 15 and 50 for  $\text{NiZnFe}_2\text{O}_4$ .  $\text{Fe}_3\text{O}_4$  nanoparticles are larger with diameters between 50 and 200 nm (Figure IV-41). If the particle shapes are quite spherical for the  $\text{Fe}_3\text{O}_4$  composition, the other compositions display polyhedral and irregular crystallites.

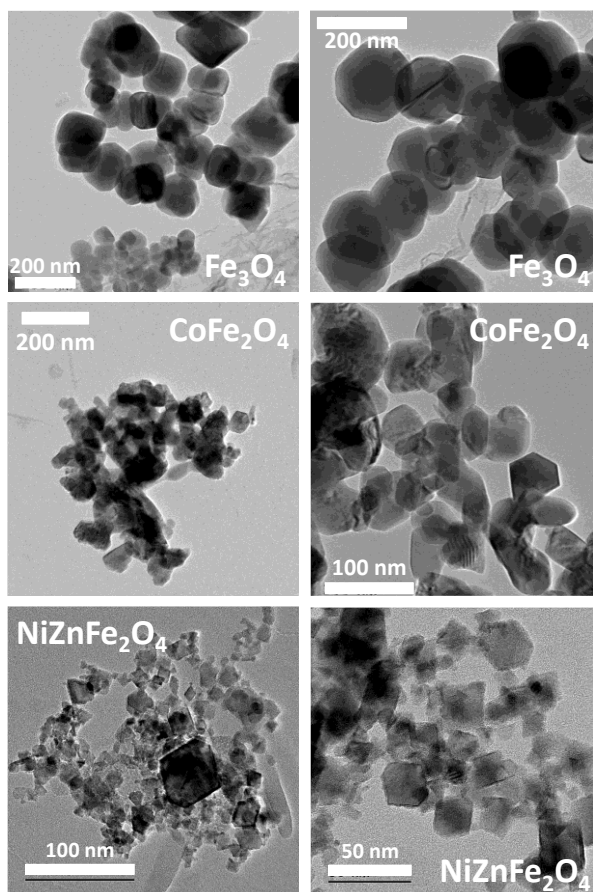
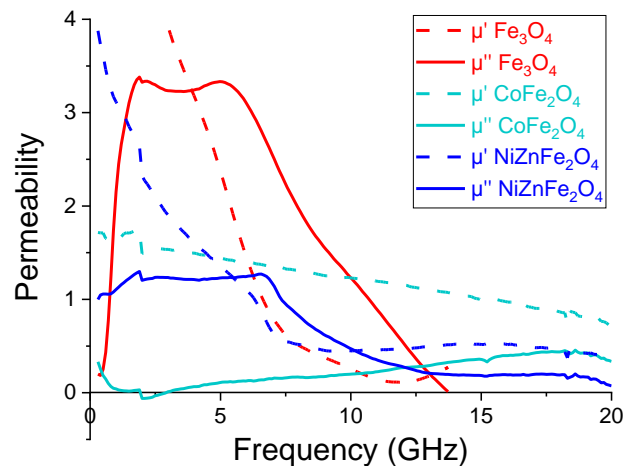


Figure IV-40. TEM images of commercial nanoparticles of  $\text{Fe}_3\text{O}_4$ ,  $\text{CoFe}_2\text{O}_4$ , and  $\text{NiZnFe}_2\text{O}_4$ .

<i>Particle diameter</i>	<i>Supplier information</i>	<i>TEM</i>
-	nm	
$\text{Fe}_3\text{O}_4$	[50 – 100]	[50 – 200]
$\text{CoFe}_2\text{O}_4$	30	[30 – 80]
$\text{NiZnFe}_2\text{O}_4$	< 100	[15 – 50]

Figure IV-41. Comparison between the particle diameter indicated by the supplier and TEM observations.

Figure IV-42 presents the effect of composition on the permeability for the commercial nanoparticles.  $\text{Fe}_3\text{O}_4$  nanoparticles permeability shows a magnetic resonance appearing in a range from 1.5 GHz to 9 GHz (full width at half maximum, FWHM) with high amplitude compared to the two other compositions. At least two peaks are discriminated in this large band width. It could be attributed to the contribution of different population of sizes in the sample, remembering that the diameters are comprised between 50 and 200 nm. Indeed, regarding the TEM images (Figure IV-40), two populations of particles are identified: one between 50 and 85 nm and another between 100 and 200 nm.

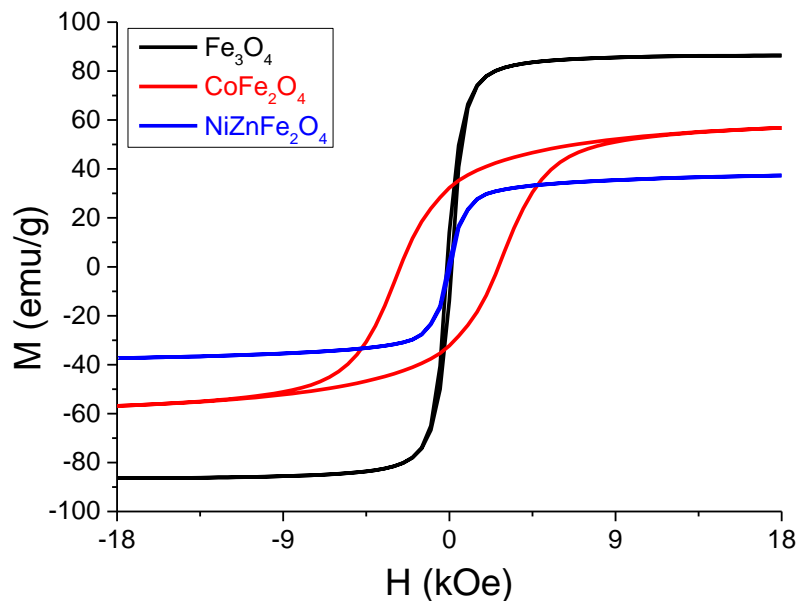


**Figure IV-42. Real and imaginary part of the permeability for nanoparticles with different compositions:  $\text{Fe}_3\text{O}_4$ ,  $\text{CoFe}_2\text{O}_4$  and  $\text{NiZnFe}_2\text{O}_4$ .**

Concerning  $\text{CoFe}_2\text{O}_4$  and  $\text{NiZnFe}_2\text{O}_4$  compositions, the level of permeability is considerably reduced due to the effect of the size (below 100 nm).  $\text{NiZnFe}_2\text{O}_4$  nanoparticles exhibit a resonance between 1 and 9 GHz (FWHM) at a low level. Unlike the other samples,  $\text{CoFe}_2\text{O}_4$  nanoparticles display a resonance at higher frequencies between 11 and 18 GHz (FWHM). This phenomenon has already been observed in the case of similar compositions [59] [60] [61] [62] [63]. Indeed, cobalt ferrite nanoparticles possess a high anisotropy due to spin-orbit coupling in Co which results in a permeability resonance at higher frequencies.

Furthermore, the hysteresis loops of these commercial samples are displayed in Figure IV-43.  $\text{Fe}_3\text{O}_4$  nanoparticles have the strongest saturation magnetization  $M_s$  (86.4 emu/g or  $\text{A}\cdot\text{m}^2/\text{kg}$ ) at 18 kOe ( $18 \times 10^3 / (4\pi)$  kA/m) close to the bulk (92 emu/g or  $\text{A}\cdot\text{m}^2/\text{kg}$ ), while  $\text{CoFe}_2\text{O}_4$  and  $\text{NiZnFe}_2\text{O}_4$  samples show 56.8 and 37.4 emu/g ( $\text{A}\cdot\text{m}^2/\text{kg}$ ) at 18 kOe ( $18 \times 10^3 / (4\pi)$  kA/m), respectively. Thus, the saturation magnetization depends on the particle composition. Indeed, bulk saturation magnetizations of nickel, zinc, manganese, and cobalt ferrites have been reported: 50 emu/g ( $\text{A}\cdot\text{m}^2/\text{kg}$ ) ( $\text{NiFe}_2\text{O}_4$ ), 5 emu/g ( $\text{A}\cdot\text{m}^2/\text{kg}$ ) ( $\text{ZnFe}_2\text{O}_4$ ), 80 emu/g ( $\text{A}\cdot\text{m}^2/\text{kg}$ ) ( $\text{MnFe}_2\text{O}_4$ ), and 80 emu/g ( $\text{A}\cdot\text{m}^2/\text{kg}$ ) ( $\text{CoFe}_2\text{O}_4$ ) [64] [65].

Moreover, cobalt ferrite particles exhibit a high coercive field of 2.6 kOe ( $2.6 \times 10^3 / (4\pi)$  kA/m) which is in agreement with the value found by A. Lopez-Ortega *et al.* for  $\text{CoFe}_2\text{O}_4$  particles with diameters between 30 and 40 nm [66]. It is well known that  $\text{CoFe}_2\text{O}_4$  particles possess a high coercive field depending on the particle size, due to the presence of cobalt ions on the octahedral sites of the spinel and to the surface anisotropy [67].



**Figure IV-43.** Measured magnetization curves of commercial nanoparticles of  $\text{Fe}_3\text{O}_4$ ,  $\text{CoFe}_2\text{O}_4$ , and  $\text{NiZnFe}_2\text{O}_4$ . Mass magnetization  $\sigma$  versus the applied field  $H$ .

As a conclusion, the frequency of the permeability resonance is linked to the nature of the doping ion and its level is affected by the particle composition and size, larger particles inducing higher permeability levels.

### III.2.1.B.b. FM and SP(F)M particles

Figure IV-44 exhibits the permeability spectra for FM and SP(F)M particles. For SP(F)M particles, the imaginary part of the permeability spectrum reveals a broad resonance spreading between 0.5 GHz and 3.5 GHz (FWHM) with a low amplitude. In the case of FM particles, the resonance amplitude is multiplied by a factor fourteen and the resonance band width extends from 0.5 GHz up to 5 GHz (FWHM). Thus, the level of permeability and the ferromagnetic resonance frequency are drastically modified by the nanoparticles size, hence the superparamagnetic state. This phenomenon could not have been reported by Y-J. Liang *et al.* [18] because these permeability measurements were performed only between 2 and 18 GHz. However, the size reduction does not result in a shift of the ferromagnetic resonance towards higher frequencies as suggested by N-N. Song *et al.* [68].

This result clearly corroborates the effect of size observed in Figure IV-42 for commercial powders.

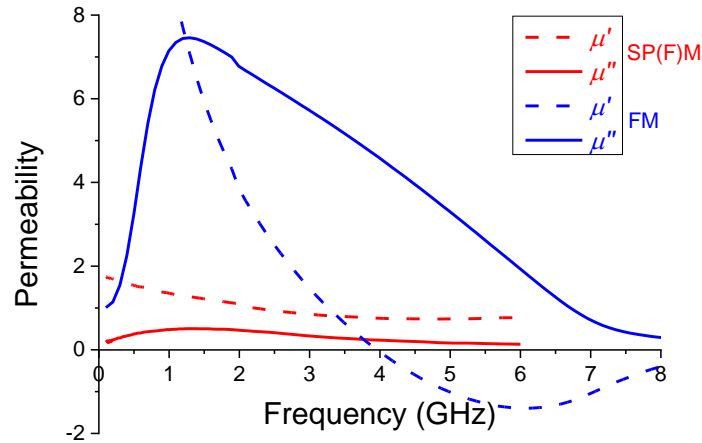


Figure IV-44. Permeability spectra for SP(F)M and FM particles. Dashed lines represent the real part of the permeability  $\mu'$ , and solid lines the imaginary part  $\mu''$ .

III.2.1.C. Conclusion

To sum up, volume fraction  $f_v$ , saturation magnetization  $M_s$ , real permittivity  $\epsilon'$  between 1 and 6 GHz and maxima at resonance frequency ( $\mu''$ ) of nanoparticles with various compositions and sizes are reported in Figure IV-45.

Composition	Size	$f_v$	$M_s$	$\epsilon'$ [1 – 6 GHz]	Maximum at resonance frequency ( $\mu''$ )
-	nm	-	emu/g	-	-
$Zn_{0.4}Fe_{2.6}O_4$	$6.2 \pm 1$	0.28	85.6	15	0.5
	$22.4 \pm 11$	0.22	80.6*	25	7.4
$Fe_3O_4$	[50 – 200]	0.22	86.4	50	3.4 (2 peaks)
$CoFe_2O_4$	[30 – 80]	0.12	56.8	10	0.5
$NiZnFe_2O_4$	[15 – 50]	0.12	37.4	14	1.2

Figure IV-45. Saturation magnetization deduced from VSM measurements for nanoparticles with different sizes and compositions. \*deduced from Langevin equation.

$Zn_{0.4}Fe_{2.6}O_4$  composition is a good compromise allowing to combine a low permittivity with a high saturation magnetization. In addition, the level of permeability and the ferromagnetic resonance frequency are drastically affected by the nanoparticles size, which evidences the superparamagnetic state. The level of permeability is thus reduced when the particle size decreases.

III.2.2. Study of the permeability at various temperatures

As the permeability is affected by the particle size, permeability measurements are carried out within the temperature range 243 K to 343 K to analyze the dependence of the dynamic permeability through the change of the energy balance between the magnetic anisotropy energy and the thermal energy. The two sizes of nanoparticles are considered in this section.



### III.2.2.A. FM particles

Figure IV-46 displays the frequency dependence of the imaginary part of the permeability for FM particles. Two measurements at 293 K are reported, to compare the results coming from the previous setup used for the measurements at room temperature and those arising from the novel one dedicated to the temperature analysis (section III.1). Keeping in mind the measurement uncertainty of about  $\pm 0.05$  for the cell with Plexiglas sides [54], the data show no clear effect of temperature (Figure IV-46).

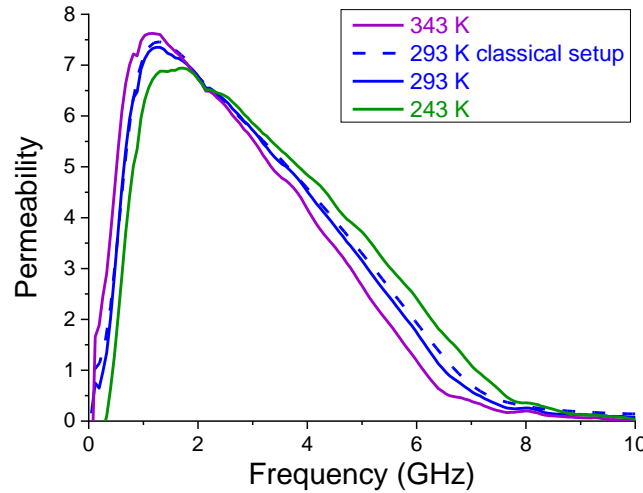


Figure IV-46. Evolution of the imaginary part of the permeability spectrum with temperature for FM particles.

### III.2.2.B. SP(F)M particles

Concerning SP(F)M particles (Figure IV-47), the imaginary part of the permeability spectrum is significantly modified when the temperature rises from 243 K to 343 K.

These results can be compared to the one obtained with FMR measurements. In FMR experiments, the frequency is fixed when sweeping the polarizing magnetic field  $H$ . The spectra commonly represent the absorbed power  $P_a$  or its derivative as a function of the magnetic field  $H$ , which is linked to the imaginary part of the permeability  $\mu''$  and expressed by:

$$P_a(H, \omega) = \frac{1}{2} \times \mu''(H, \omega) \times \omega \times h_{rf}^2 \quad \text{IV-19}$$

with  $\omega$  the angular frequency, and  $h_{rf}$  the exciting microwave magnetic field.

FMR spectra are hence characterized by the resonance field  $H_r$  defined as the field value for the maximum of the  $P_a$  curve (or zero for the derivative absorption line), the resonance linewidth  $\Delta H$  (FWHM) and the line intensity  $I$  which is the area under the absorption line. In the literature, these parameters follows some trends in the case of magnetic oxide nanoparticles dispersed in various matrices:



- the shift of  $H_r$  toward the low fields when decreasing temperature, demonstrated by N. Guskos *et al.* for magnetite nanoparticles [69], and F. Gazeau *et al.* for maghemite nanoparticles [70],
- the increase of  $\Delta H$  with the temperature decrease, observed for magnetite [69] [71] [72] and maghemite [70] nanoparticles,
- in most cases the increase of  $I$  [69] [71] or rarely its decrease [72] for decreasing temperature for magnetite nanoparticles.

In the same way, the temperature dependence of permeability spectra can be assimilated to FMR measurements by taking into account that measurements are performed at zero magnetic field when sweeping frequency. The permeability spectra are characterized by the resonance frequency  $f_r$  corresponding to the frequency value for the maximum of the  $\mu''$  curve, the frequency resonance linewidth  $\Delta f_r$  of the  $\mu''$  curve (FWHM), and the amplitude of the resonance line  $A$  defined as the maximum level of  $\mu''$  at  $f_r$ .

By analyzing the permeability spectra obtained for SP(F)M particles (Figure IV-47), a shift of the resonance frequency  $f_r$  toward the high frequencies is observed for decreasing temperature. This phenomenon is in complete agreement with the trend followed by  $H_r$  in FMR experiments as the field and the frequency act in opposite ways in relation to each other. The resonance line intensity  $A$  increases significantly for decreasing temperature, which has been not observed for FM particles (Figure IV-46) and is consistent with the FMR results regarding the line intensity  $I$ .

Moreover, the width of the resonance peak  $\Delta f_r$  (FWHM) seems to decrease for decreasing temperature which is in contrast with most of the FMR results. This point would deserve to be investigated in more depth through additional temperature dependent permeability measurements. The measurement quality is nevertheless affected by the temperature measurement set-up, especially for the lowest permeability amplitudes which are noisy, that is why the temperature curves displayed in Figure IV-47.B correspond to smoothed curves treated with the Savitzky-Golay method on Origin.

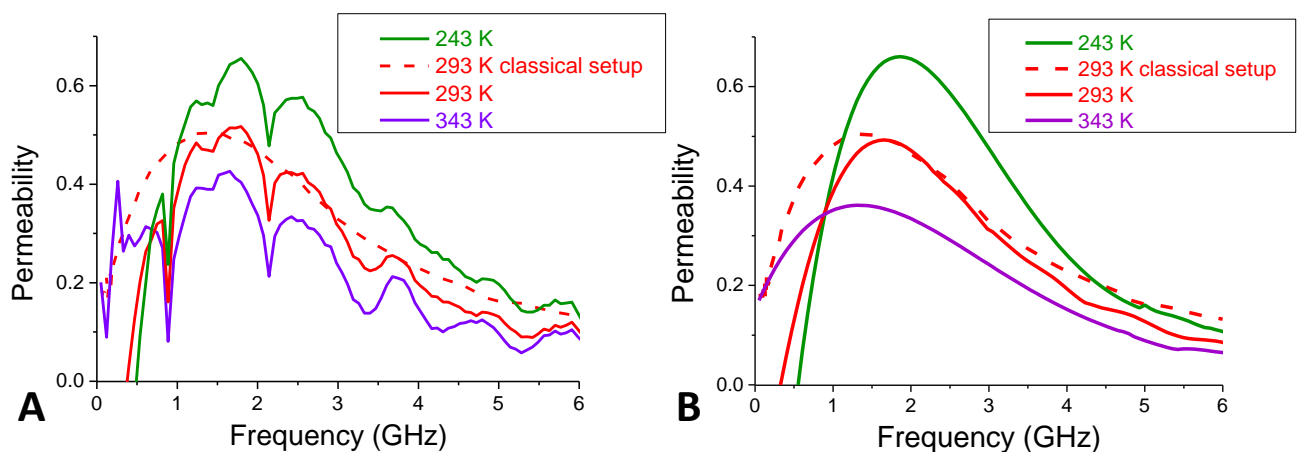


Figure IV-47. Evolution of the imaginary part of the permeability spectrum with temperature for SP(F)M particles, before (A) and after (B) smoothing treatment.

Direct comparisons between FMR data coming from literature and zero-field permeability measurements are tricky due to the various physical systems in terms of nanoparticles composition and morphology, and volume contents within the matrix.

The next objective is to find a suitable model to reproduce the temperature dependence of the permeability spectra, as well as the temperature dependences of  $f_r$ ,  $\Delta f_r$  and  $I$ .

### III.2.3. Interpretation through a dynamic susceptibility model

From the theoretical viewpoint, the high-frequency dynamics of superparamagnetic nanoparticles has been extensively studied. The general theoretical approach combines the Landau-Lifshitz-Gilbert equation (Chapter I) for the motion of magnetic moment and the Fokker-Planck continuity equation for the orientational distribution function of the magnetic moment [73] [74]. This model has been developed in the context of the FMR where the magnetic moment is subjected to a static polarizing magnetic field. In our experiments, no static magnetic field is applied and the quantity of interest is the zero-field transverse dynamic susceptibility noted  $\chi_{\perp}$ . As a first approach, the experimental data are interpreted using an approximate analytical model proposed by Y-L. Raikher and M-I. Shliomis [75], appropriate to fine ferromagnetic particles with diameters of about 100 Å. The main hypotheses are the following:

- Noninteracting randomly distributed nanoparticles are considered.
- Each particle is assumed spherical, in a single-domain state and possesses an uniaxial magnetic anisotropy.
- The ratio between the magnetic anisotropy energy  $KV$  and the thermal energy  $k_B T$  is introduced:

$$\sigma = \frac{KV}{k_B T} \quad \text{IV-20}$$

with  $K$  the anisotropy constant,  $V$  the particle volume,  $k_B$  the Boltzmann constant, and  $T$  the temperature.

From the previous hypothesis, the zero-field transverse dynamic susceptibility is expressed by:

$$\chi_{\perp}(\omega) = \frac{M_S}{H_K} \frac{\omega_0(\omega_0 R_3 + i\omega R_4)}{(\omega_0)^2 R_1 - \omega^2 + 2i\omega\omega_0 R_2} \quad \text{IV-21}$$

where  $\omega_0 = \mu_0 \gamma H_K$  is the angular resonance frequency,  $\mu_0$  the permeability of free space,  $\gamma$  the gyromagnetic factor,  $H_K$  the anisotropy field for an uniaxial particle defined as:

$$H_K = \frac{2K}{\mu_0 M_S}, \quad \text{IV-22}$$

$R_1, R_2, R_3, R_4$  coefficients [75] depending on  $\sigma$ , and  $\alpha$  the Gilbert damping parameter.

The expression of  $R_1, R_2, R_3, R_4$  coefficients to calculate the general expression of the transverse dynamic susceptibility is given by:

$$\begin{aligned}
 R_1 &= \frac{F' - F''}{F - F'} + \left(\frac{\alpha}{\sigma}\right)^2 \left(1 + \sigma \frac{F' - F''}{F - F'}\right) \left(3 - \sigma + 2\sigma \frac{F'' - F'''}{F' - F''}\right) \\
 R_2 &= \frac{\alpha}{2\sigma} \left(4 - \sigma + \sigma \frac{F' - F''}{F - F'} + 2\sigma \frac{F'' - F'''}{F' - F''}\right) \\
 R_3 &= \sigma \left(\frac{F' - F''}{F}\right) + \alpha^2 \left(\frac{F + F'}{2\sigma F}\right) \left(3 - \sigma + 2\sigma \frac{F'' - F'''}{F' - F''}\right) \\
 R_4 &= \alpha \left(\frac{F + F'}{2F}\right)
 \end{aligned} \tag{IV-23}$$

$$\text{with } F(\sigma) = \int_0^1 e^{\sigma x^2} dx, \frac{dF}{d\sigma} = \frac{e^\sigma - F}{2\sigma}, \frac{d^2F}{d\sigma^2} = \frac{2\sigma e^\sigma - 3(e^\sigma - F)}{4\sigma^2}, \frac{d^3F}{d\sigma^3} = \frac{2\sigma e^\sigma(2\sigma - 5) + 15(e^\sigma - F)}{8\sigma^3}$$

In the case of superparamagnetic particles, the fluctuations of the thermal energy become dominant in relation to the magnetic anisotropy energy ( $k_B T \gg KV$ ) (Chapter I), that is why the ratio  $\sigma$  is below one ( $\sigma \ll 1$ ) which yields to an approximate expression for the  $R_1, R_2, R_3, R_4$  coefficients:

$$\begin{aligned}
 R_1 &= 3 \left(\frac{\alpha}{\sigma}\right)^2 \left(1 + \frac{16}{105}\sigma\right) \\
 R_2 &= 2 \frac{\alpha}{\sigma} \left(1 + \frac{1}{70}\sigma\right) \\
 R_3 &= 2 \frac{\alpha^2}{\sigma} \left(1 + \frac{2}{105}\sigma\right) \\
 R_4 &= \frac{2}{3} \alpha \left(1 + \frac{1}{15}\sigma\right)
 \end{aligned} \tag{IV-24}$$

Conversely, when  $\sigma \gg 1$ , the magnetic anisotropy energy  $KV$  prevails and the motion of the magnetic moment is in the blocked state. This phenomenon occurs below the blocking temperature  $T_B$  (Chapter I), making the study of a suitable fit for the temperature-dependence permeability spectra of SP(F)M particles interesting.

### III.2.3.A. Value of the anisotropy constant $K$

The ratio  $\sigma$  between the magnetic anisotropy energy and the thermal energy being dependent on the anisotropy constant  $K$  and on the particle diameter  $\phi$  through its volume  $V$ , the order of

magnitude of these two parameters needs to be estimated to provide a suitable model. As the particle diameter  $\phi$  is already known with a value around 5.4 nm (Figure IV-4, section II.2.1), three different methods to measure an approximate value of the anisotropy constant  $K$  are studied.

The first way calculates the anisotropy constant  $K$  from the coercive field  $H_C$  of FM particles at 300 K. Indeed, the hysteresis cycle of FM particles is considered instead of the SP(F)M one, because of the superparamagnetic behavior of SP(F)M particles, which makes the estimation of the coercive field  $H_C$  more imprecise due to the shape of the magnetization curve. As a consequence, the value of  $K$  obtained through this method will just give an order of magnitude. The coercive field  $H_C = 8.2$  Oe ( $8.2 \times 10^3 / (4\pi)$  A/m) is calculated from VSM by measuring the magnetization of the sample every 5 Oe ( $5 \times 10^3 / (4\pi)$  A/m) (Figure IV-48). This technique is preferred to the VSM-SQUID magnetometer because of its lower precision with a measurement every 10 Oe ( $10 \times 10^3 / (4\pi)$  A/m) near zero field. Considering an assembly of uniaxial particles with random orientation, a Stoner-Wohlfarth model is then applied to retrieve the anisotropy field  $H_K$  [76]:

$$H_K = \frac{H_C}{0.49} \quad \text{IV-25}$$

This approach provides a  $K$  value of  $3 \times 10^3$  erg/cm<sup>3</sup> ( $3 \times 10^2$  J/m<sup>3</sup>) by taking a saturation magnetization  $M_S$  of 75.78 emu/g ( $A \cdot m^2/kg$ ) equal to 397 emu/cm<sup>3</sup> ( $d = 5.24$  g/cm<sup>3</sup>, PDF sheet 04-021-5090) in Equation IV-22. This value is one order of magnitude lower than the value of the anisotropy of Fe<sub>3</sub>O<sub>4</sub> nanoparticles ( $24.3 \times 10^4$  erg/cm<sup>3</sup>) which is close to the Fe<sub>3</sub>O<sub>4</sub> bulk anisotropy ( $18.7 \times 10^4$  erg/cm<sup>3</sup>) [77].

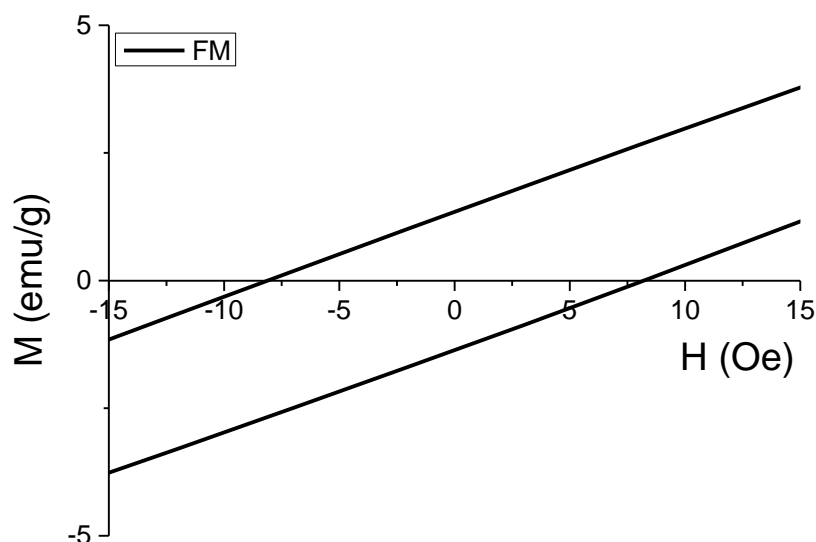


Figure IV-48. Calculation of the coercive field  $H_C$  of FM particles through VSM measurement.

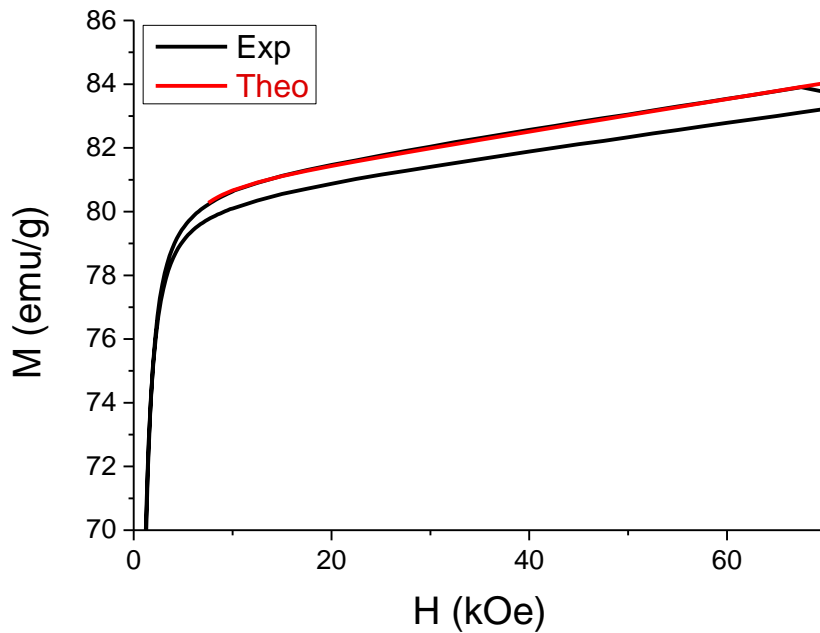
Another method is to fit the VSM-SQUID hysteresis curve of the uniaxial FM particles at 300 K with a law of approach to saturation [78] [79]. Despite the cubic structure of the spinel, the morphology of the particles does not exhibit the cubic symmetry or higher order. Thus, the

particle anisotropy can be approximated as an effective uniaxial anisotropy by taking into account shape effects. Hence, the law described by H. Duan *et al.* (Equation IV-26) [78] is preferred because it considers an uniaxial anisotropy and not a cubic one used for  $\text{Co}_x\text{Fe}_{(3-x)}\text{O}_4$  particles with a high magnetocrystalline anisotropy [79].

$$M = M_S \left[ 1 - \frac{4}{15\mu_0^2 M_S^2} \left( \frac{K_1}{H} \right)^2 \right] + \kappa H \quad \text{IV-26}$$

with  $K_1$  the anisotropy constant and  $\kappa$  the high-field susceptibility or forced magnetization.

The resulting model is shown in Figure IV-49 and gives an anisotropy value of  $K = 5.4 \times 10^5$  erg/cm<sup>3</sup> ( $5.4 \times 10^4$  J/m<sup>3</sup>). However, the corresponding  $H_K = 2558$  Oe ( $2558 \times 10^3 / (4\pi)$  A/m) and thus  $H_C = 1253$  Oe ( $1253 \times 10^3 / (4\pi)$  A/m) (Equation IV-25) are far from the experimental value of  $H_C$  of 26 Oe ( $26 \times 10^3 / (4\pi)$  A/m), measured with the VSM-SQUID magnetometer. Moreover, as seen in Figure IV-49, the curve does not saturate. It could be due to the contribution of superparamagnetic particles which are in a blocked state, or to surface or volume canted spin contribution since the applied field will reduce the canting angle and increase the magnetization. This law being not adapted for superparamagnetic particles, these contributions compromise the validity of the method in this case.



**Figure IV-49. Positive field branch of the hysteresis curve of magnetization of FM particles and fitted curve in red. The parameters are:  $\kappa = 5.05 \times 10^{-5}$ ,  $K_1 = 1.03 \times 10^5$  erg/g, and  $M_S = 80.5$  emu/g ( $\text{A}\cdot\text{m}^2/\text{kg}$ ).**

The last approach is based on the calculation of the anisotropy constant  $K$  using the blocking temperature  $T_B = 33$  K measured on the ZFC curve of SP(F)M particles (Figure IV-6.B, section II.2.1), thanks to the following formula [16]:

$$K = \frac{\ln\left(\frac{\tau_m}{\tau_0}\right) k_B T_B}{V} \quad \text{IV-27}$$

with  $\tau_m$  the measuring time,  $\tau_0$  a prefactor depicting the time of superparamagnetic relaxation ( $\sim 1 \times 10^{-9}$  s for  $\text{MnFe}_2\text{O}_4$  nanoparticles [16]),  $k_B$  the Boltzmann constant and  $V$  the particle volume.

With the measuring time  $\tau_m$  of the VSM-SQUID magnetometer of 2 s, the value of  $K$  becomes of  $7.8 \times 10^5$  erg/cm<sup>3</sup> ( $7.8 \times 10^4$  J/m<sup>3</sup>). This formula overestimates the anisotropy value because it is computed at the blocking temperature.  $\tau_0$  is also an approximation and can be defined more precisely through Mössbauer experiments which could measure a blocking temperature with another  $\tau_m$ , then reducing the indetermination on  $\tau_0$ . Nevertheless, the values calculated at 2 s is in the same range of the ones of  $\text{MnFe}_2\text{O}_4$  nanoparticles with a 7.4 nm diameter ( $5.6 \cdot 10^5$  erg/cm<sup>3</sup>) [17] and of NiZn ferrite particles of a 10.6 nm diameter ( $1.74 \cdot 10^5$  erg/cm<sup>3</sup>) with a coercive field  $H_C$  of 11 Oe ( $11 \times 10^3 / (4\pi)$  A/m) close to the one of FM particles [80]. Furthermore, the last two methods are in agreement, highlighting a value of anisotropy  $K$  around  $\sim 10^5$  erg/cm<sup>3</sup>.

As a conclusion, none of these methods is one hundred percent reliable. The values are summarized in Figure IV-50. They are in the same range of the absolute value  $2.5 \times 10^4$  erg/cm<sup>3</sup> obtained for the  $\text{Zn}_{0.4}\text{Fe}_{2.6}\text{O}_4$  composition in the study of N. Miyata [81] (Figure IV-51). Thus, the order of magnitude of the anisotropy constant  $K$  at 300 K is in the range of  $10^3$  to  $10^5$  erg/cm<sup>3</sup> ( $10^2$  to  $10^4$  J/cm<sup>3</sup>).

Method	Stoner-Wohlfarth model	Law of approach to saturation	From the blocking temperature $T_B$
			$\tau_m = 2$ s
$K$ (erg/cm <sup>3</sup> )	$3 \times 10^3$	$5.4 \times 10^5$	$7.8 \times 10^5$
$K$ (J/m <sup>3</sup> )	$3 \times 10^2$	$5.4 \times 10^4$	$7.8 \times 10^4$

Figure IV-50. Summary of the values obtained for the anisotropy constant  $K$  with different methods.

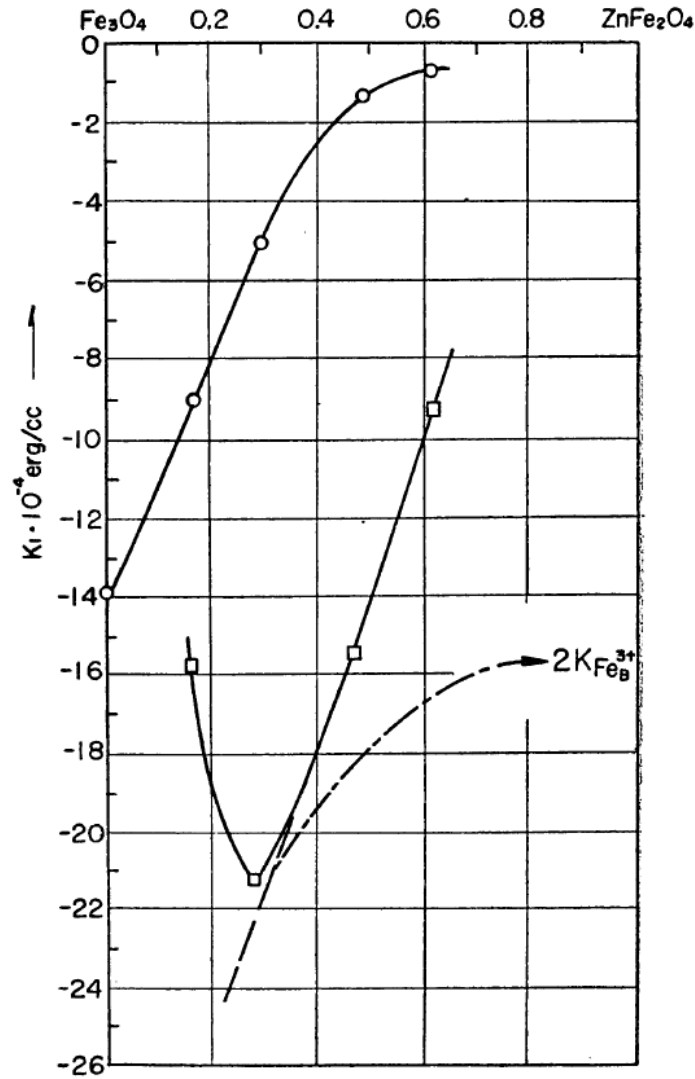
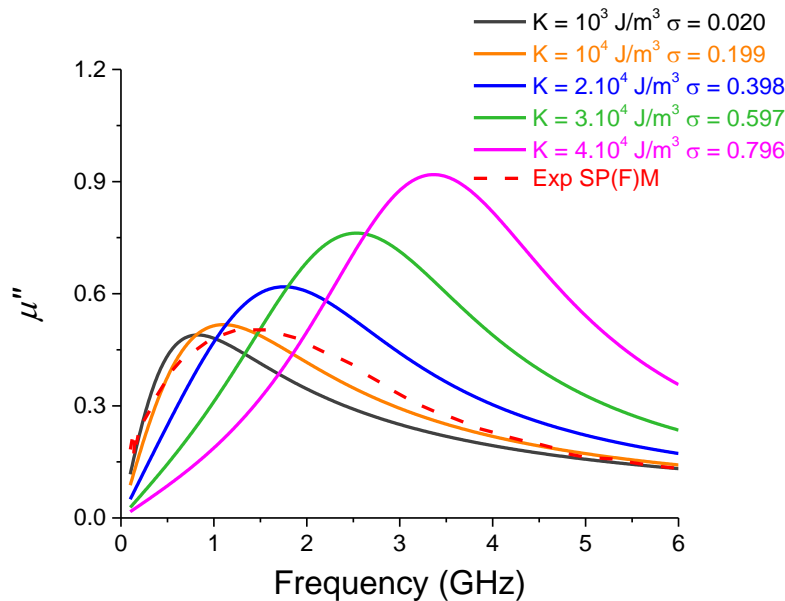


Figure IV-51. Variation of the anisotropy constant  $K$  with the zinc concentration in  $(Zn_{1-y}Fe_y)Fe_2O_4$  crystals. From N. Miyata [81].

III.2.3.B. *Influence of  $\sigma$ : the ratio between the magnetic anisotropy energy and the thermal energy*

The order of magnitude of the anisotropy  $K$  being in the range of  $10^3$  to  $10^5$  erg/cm<sup>3</sup> ( $10^2$  to  $10^4$  J/m<sup>3</sup>), the magnetic permeability of SP(F)M particles can be fitted with the model proposed by Y-L. Raikher and M-I. Shliomis [75] (Equation IV-21) at room temperature by testing different values of anisotropy  $K$  with the approximate expression (Equation IV-24), which directly impacts the ratio  $\sigma$  (Equation IV-20). The particle diameter is firstly fixed to 5.4 nm, the value computed through the Langevin function for particles surrounded by an organic layer (Figure IV-4.A, section II.2.1). In the same manner, the corresponding saturation magnetization  $M_S$  is equal to 65.6 emu/g ( $A \cdot m^2/kg$  or  $3.44 \times 10^5$  A/m by taking  $d = 5.24$  g/cm<sup>3</sup>). The result is exhibited in Figure IV-52.



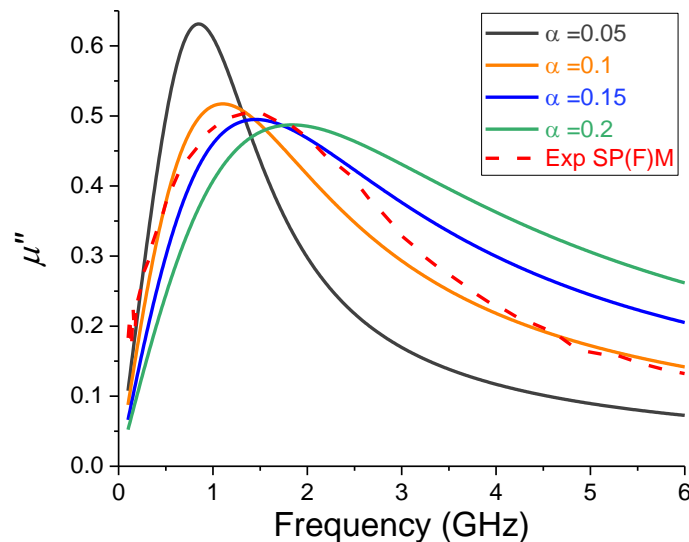
**Figure IV-52.** Computed permeability spectra (imaginary part,  $\mu''$ ) for different values of  $\sigma$  and comparison with experiment at room temperature. The parameters are:  $M_s = 3.44 \times 10^5$  A/m,  $\gamma = 1.76 \times 10^{11}$  s<sup>-1</sup>T<sup>-1</sup>,  $\alpha = 0.1$  and  $\phi = 5.4$  nm.

The model is sensitive to the value of the anisotropy constant  $K$ . A transition between a relaxant and a resonant behavior is observed from  $\sigma = 0.60$ . This value is close to the one of 0.73 obtained in the paper of Y-L. Raikher and M-I. Shliomis [75]. An anisotropy value  $K$  of  $10^4$  J/m<sup>3</sup> provides a better fit and is kept for the following study. This last value is consistent with the anisotropy constants calculated with the law of approach to saturation and from the blocked temperature (Figure IV-50).

### III.2.3.C. Influence of the damping parameter $\alpha$

Figure IV-53 shows the variation of the model results by changing the values of the damping parameter  $\alpha$  and also a comparison with the experimental spectrum. A shift of the curves towards the higher frequencies when the damping parameter increases is noticed as well as an increase of the full width at half maxima (FMWH). An adapted value for the damping parameter  $\alpha$  is around 0.15.

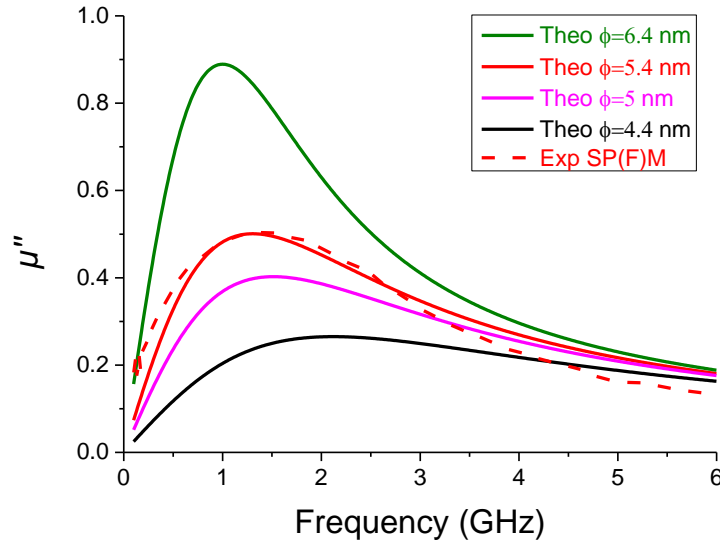




**Figure IV-53. Computed permeability spectra (imaginary part,  $\mu''$ ) for different values of  $\alpha$  and comparison with experiment at room temperature. The parameters are:  $M_S = 3.44 \times 10^5$  A/m,  $\gamma = 1.76 \times 10^{11}$  s<sup>-1</sup>T<sup>-1</sup>,  $K = 10^4$  J/m<sup>3</sup> and  $\phi = 5.4$  nm.**

#### III.2.3.D. Effect of the size distribution

As previously observed, the permeability spectra are dependent on the particle size (part III.2.1.B.b). The variation of the model is thus studied as a function of the particle diameter. Figure IV-54 shows the computed nanoparticle size dependence of the permeability spectra (imaginary part) at room temperature. A transition between a relaxant character and a resonant one is revealed for increasing the nanoparticle size. The model reproduces adequately the experimental curve for the nanoparticle diameter  $\phi = 5.4$  nm ( $\sigma \approx 0.2$ ) corresponding to the one calculated with the Langevin function for particles surrounded by an organic layer (Figure IV-4.A, section II.2.1) and  $K = 10^4$  J/m<sup>3</sup>. As the particles used for the measurement comprise a proportion of organics at an outer shell, the diameter deduced from the Langevin function of the hysteresis loop without subtraction of the organic amount from the total weight better suits. Furthermore, the damping parameter  $\alpha$  is refined with a value of 0.13.



**Figure IV-54. Computed permeability spectra (imaginary part,  $\mu''$ ) and comparison with experiment. Nanoparticle size-dependence of  $\mu''$  at room temperature. The magnetic parameters are:  $K = 10^4 \text{ J/m}^3$ ,  $M_S = 3.44 \times 10^5 \text{ A/m}$ ,  $\gamma = 1.76 \times 10^{11} \text{ s}^{-1}\text{T}^{-1}$ ,  $\alpha = 0.13$ .**

The size distribution of SP(F)M particles is centered around 6.2 nm with a standard deviation of 1 nm. Due to the gap between this range of size and the one retrieved from the Langevin function (5.4 nm) which matches well with the experimental curve (Figure IV-53), the effect of the size distribution on the shape of the model is investigated, in order to further improve the fit between the experimental and the theoretical curves.

The magnetic susceptibility can be written as a function of the distribution density in volume  $f_V$ :

$$\langle \chi_{\perp} \rangle_{\sigma}(\omega) = \int_0^{\infty} \chi_{\perp}(\omega, \sigma) f_V d\sigma \quad \text{IV-28}$$

with  $f_V$  expressed as follows in the case of spherical particles with a diameter  $\phi$  [82]:

$$f_V(\phi) = \frac{1}{6} \pi \phi^3 P(\phi) \quad \text{IV-29}$$

$P(\phi)$  is the log-normal size distribution density of the number of particles [82]:

$$P(\phi) = \frac{1}{\sqrt{2\pi}\Delta\phi} \exp\left(-\frac{1}{2} \frac{\ln^2\left(\frac{\phi}{\phi_0}\right)}{\sigma^2}\right) \quad \text{IV-30}$$

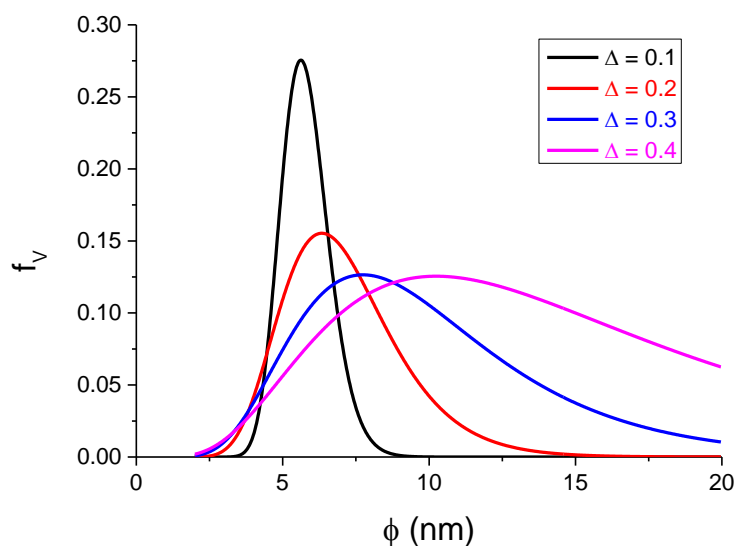
where  $\phi_0$  is the mean diameter and  $\Delta$  the standard deviation of the log-normal law.

The mean diameter in particle number  $\phi_{m,N}$  and in volume  $\phi_{m,V}$ , as well as the corresponding standard deviations  $\Delta_N$  and  $\Delta_V$  are given by:

$$\Phi_{m,N} = \langle \phi \rangle \exp\left(\frac{\Delta^2}{2}\right) \quad \Delta_N = \Phi_{m,N} \left(\sqrt{\exp(\Delta^2) - 1}\right) \quad \text{IV-31}$$

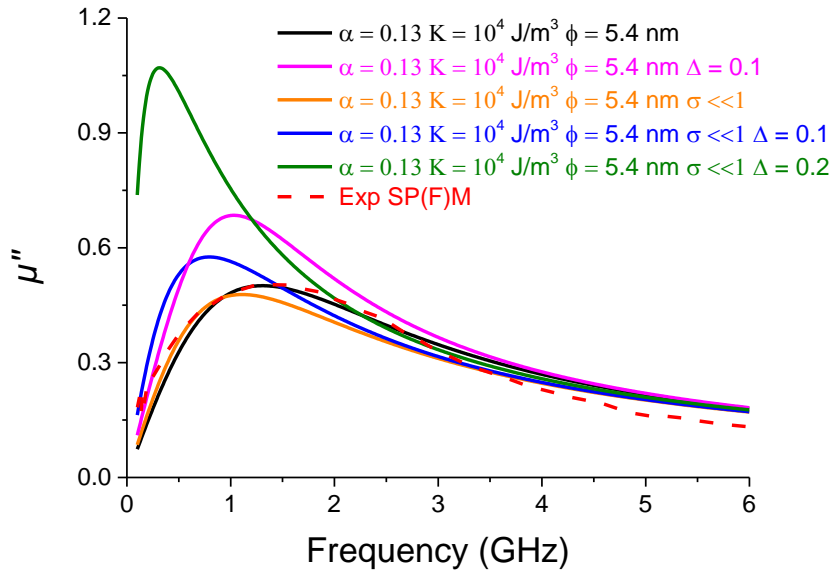
$$\Phi_{m,V} = \langle \phi \rangle \exp\left(\frac{7\Delta^2}{2}\right) \quad \Delta_V = \Delta_N \exp(3\Delta^2) \quad \text{IV-32}$$

From Equations IV-29 to IV-32, the distribution density in volume  $f_V$  can be plotted as a function of the standard deviation  $\Delta$  for a mean particle diameter of 5.4 nm (Figure IV-55). As expected, the curves become asymmetric towards the large diameters with the increase of the standard deviation  $\Delta$ . The larger the standard deviation will be, the greater impact it will have on the permeability spectra.



**Figure IV-55.** Distribution density  $f_V$  in volume for different standard deviation  $\Delta$ .

The previous formula for the susceptibility (Equation IV-28) is applied to the Raikher's model (Equation IV-21) and compared to the experimental curve in Figure IV-56. Two observations can be done. On the one hand, the curve maxima is shifted towards the low frequencies when the standard deviation  $\Delta$  increases due to the large particle diameter. The best fit (black curve) is obtained when the polydispersity is not taken into account. On the other hand, the general formula (Equation IV-23) allows to plot a theoretical curve (black curve) closer to the experimental one in comparison with the approximative formula (Equation IV-24) (yellow curve).



**Figure IV-56.** Computed permeability spectra (imaginary part,  $\mu''$ ) weighted by the size distribution and comparison with experiment.

### III.2.3.E. Effect of the anisotropy constant $K$ and the saturation magnetization $M_S$

The anisotropy constant  $K$  and the saturation magnetization  $M_S$  are two variables which evolve with the temperature. It is interesting to examine if this temperature dependence needs to be taken into account in the model to fit well the experimental curve, or if it can be neglected.

#### III.2.3.E.a. $K$ and $M_S$ independent of the temperature

In this section, the temperature dependence of the anisotropy constant  $K$  and the saturation magnetization  $M_S$  is neglected. The value of the anisotropy constant  $K$  selected in part III.2.3.A is kept constant ( $10^5 \text{ erg/cm}^3 = 10^4 \text{ J/m}^3$ ), as well as the saturation magnetization  $M_S$  of SP(F)M particles (section II.2.1) of  $3.44 \times 10^2 \text{ emu/cm}^3$ . Figure IV-57 presents the results of such a model.

The fit does not reproduce the experimental curves well. The model follows the trend of the experimental curves concerning the evolution of the amplitude of the resonance peak  $A$  and also the width of the resonance peak  $\Delta f_r$ , which respectively increases and decreases for decreasing temperature.

However, the inverse trend is observed for the resonance frequency  $f_r$ . Indeed, a shift of the resonance frequency  $f_r$  towards the low frequencies is observed for decreasing temperature, whereas this shift occurs towards the high frequencies for the experimental curves. As a consequence, the temperature dependence of the anisotropy constant  $K$  and the saturation magnetization  $M_S$  should be taken into account in the model to reproduce this effect.

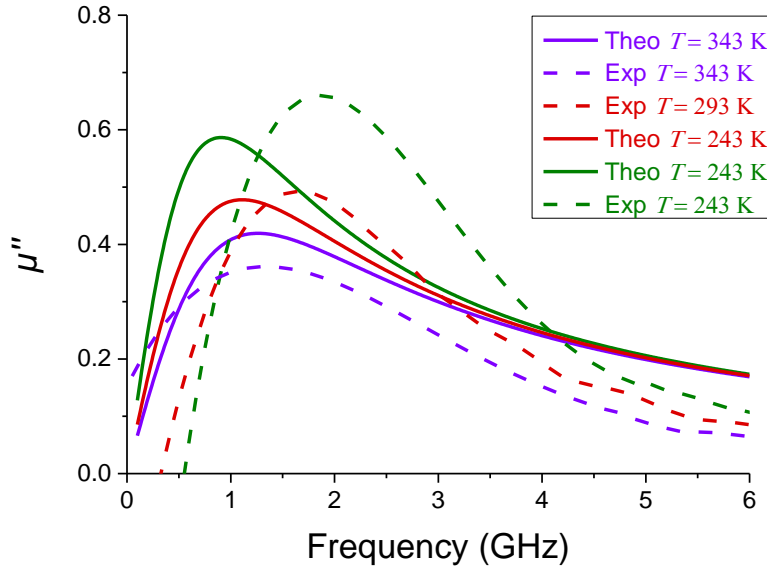


Figure IV-57. Temperature dependence of the computed permeability spectra (imaginary part,  $\mu''$ ) and comparison with experiments. The magnetic parameters are:  $K = 10^4 \text{ J/m}^3$ ,  $M_S = 3.44 \times 10^5 \text{ A/m}$ ,  $\gamma = 1.76 \times 10^{11} \text{ s}^{-1}\text{T}^{-1}$ ,  $\alpha = 0.13$ ,  $\phi = 5.4 \text{ nm}$ .

III.2.3.E.b. Temperature dependence of  $K$  and  $M_S$

Figure IV-58.A exhibits the temperature dependence of the computed imaginary permeability spectra compared to experimental curves by taking into account the variation of the anisotropy constant  $K$  and the saturation magnetization  $M_S$  with temperature.

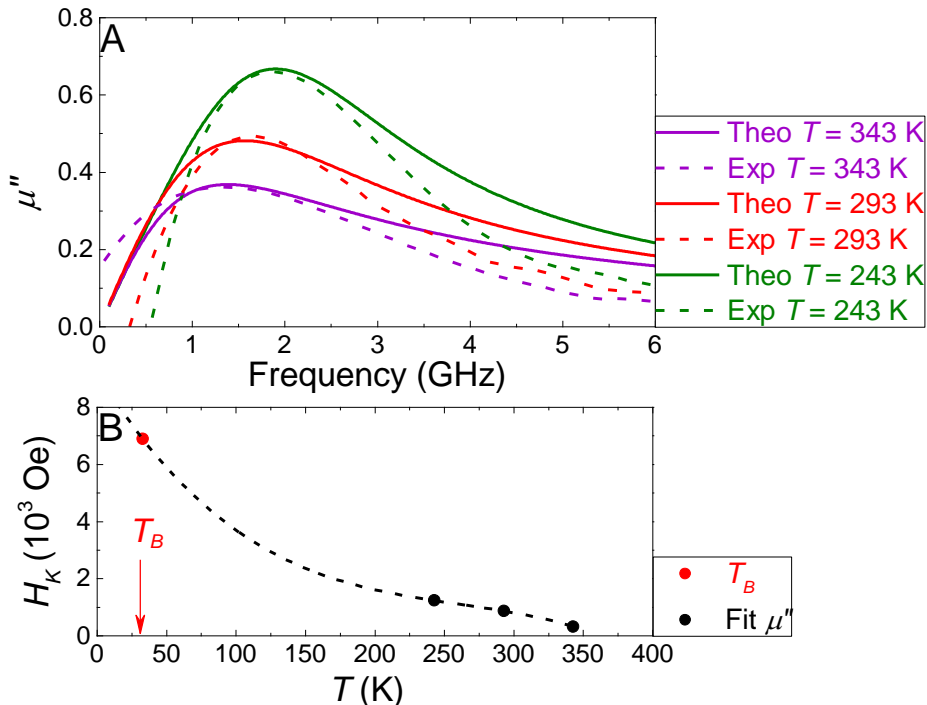


Figure IV-58. (A) Temperature dependence of the computed permeability spectra (imaginary part,  $\mu''$ ) and comparison with experiments. The parameters are:  $\gamma = 1.76 \times 10^{11} \text{ s}^{-1}\text{T}^{-1}$ ,  $\alpha = 0.13$ ,  $\phi = 5.4 \text{ nm}$ . (B) Temperature dependence of the effective anisotropy field  $H_K$  used for fitting the experimental curves (black circles) with the  $K$  value at  $T_B$  (red circle). The dashed line is a guide for eyes.

The anisotropy constant  $K$  is calculated at the blocking temperature  $T_B$  (33 K) from the VSM-SQUID measurements with  $\tau_m = 2$  s (part II.2.1). The values of anisotropy constant  $K$  and of saturation magnetization  $M_S$  at 243, 293 and 343 K are estimated from the model and summarized in Figure IV-59. From these data, the anisotropy field  $H_K$  is computed (Equation IV-22) and its evolution is plotted in Figure IV-58.B as a function of the temperature. The anisotropy field  $H_K$  decreases with increasing temperature. Such a rapidly decreasing anisotropy profile has been reported for FePt nanoparticles [83]. All of the data are summarized in Figure IV-59.

	33 K	243 K	293 K	343 K
$K$ (erg/cm <sup>3</sup> )	$1.18 \times 10^6$	$2.05 \times 10^5$	$1.40 \times 10^5$	$0.49 \times 10^5$
$M_S$ (emu/cm <sup>3</sup> )	$3.44 \times 10^2$	$3.34 \times 10^2$	$3.26 \times 10^2$	$3.10 \times 10^2$
$H_K$ (Oe)	$6.88 \times 10^3$	$1.23 \times 10^3$	$8.59 \times 10^2$	$3.16 \times 10^2$

Figure IV-59. Temperature dependence of the anisotropy constant  $K$ , the saturation magnetization  $M_S$  and the anisotropy field  $H_K$  obtained from calculation at  $T_B$  (33 K) and simulations at 243, 293 and 343 K.

Moreover, the values of anisotropy constant  $K$  in Figure IV-59 are correlated to the one of  $(Zn_{1-y}Fe_y)Fe_2O_4$  crystals studied by N. Miyata [81]. The values are taken at 90, 150, 220 and 290 K for the following compositions:  $Zn_{0.3}Fe_{2.7}O_4$  and  $Zn_{0.48}Fe_{2.52}O_4$  [81], allowing to estimate the corresponding values for the composition of interest  $Zn_{0.4}Fe_{2.6}O_4$  by interpolation. Thus, the decrease of anisotropy with temperature is also evidenced by N. Miyata [81] which is consistent with the computation for SP(F)M particles (Figure IV-60).

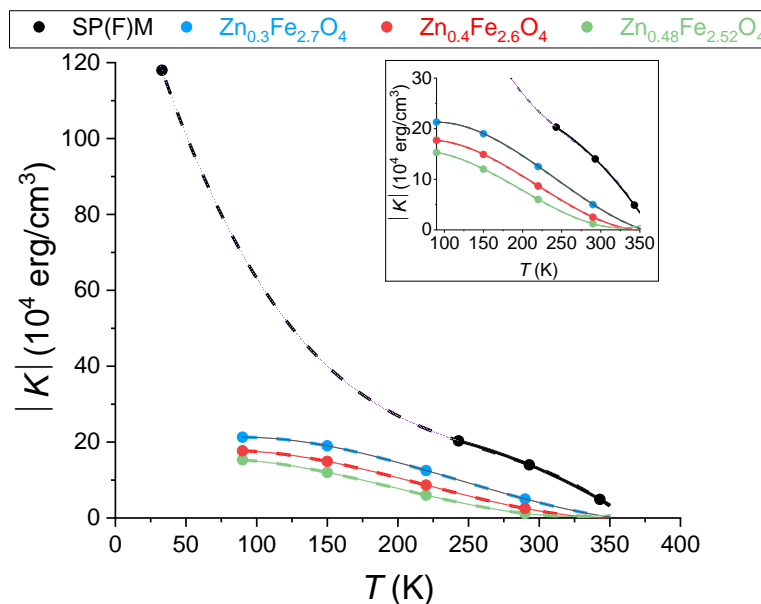


Figure IV-60. Comparison of the temperature dependence of the anisotropy of  $(Zn_{1-y}Fe_y)Fe_2O_4$  crystals from N. Miyata [81] and the computation for SP(F)M particles.

By comparing the experimental and theoretical temperature dependences of the  $\mu''$  spectra (Figure IV-58.A), the experimental evolutions are satisfactorily reproduced by the analytical model due to the introduction of a temperature dependence of the effective anisotropy field (Figure IV-58.B). This time, the temperature dependences of the resonance frequency  $f_r$ , the width of the resonance peak  $\Delta f_r$  and the amplitude of the resonance peak  $A$  are similar between

the theory and the experiment. Indeed, the shift of the resonance frequency  $f_r$  towards the high frequencies is properly observed for decreasing temperature.

Consequently, this analytical model appears relevant to capture the main features of the experimentally observed superparamagnetic resonances.

Nevertheless, a deviation of the model from the experiment is noticed especially at high frequencies (Figure IV-58.A). As including an effect of polydispersity in the particle size (part III.2.3.D) has not improved the fit, the hypothesis of the presence of dipolar interactions between SP(F)M particles could be a first explanation.

### III.2.3.F. Conclusion

*Size effects of  $Zn_{0.4}Fe_{2.6}O_4$  nanoparticles have been exhibited in the zero-field dynamic permeability spectra. Indeed, the decrease of the particle size has an influence on the motion of the particle magnetic moments, which directly impacts the magnetic susceptibility and hence the permeability. The main effect is a drastic reduction of the permeability level, whereas a shift in the resonance frequency is not clearly observed. A dynamic susceptibility model has been developed to successfully reproduce the experimental results for the superparamagnetic particles and, in particular, the trend in the temperature dependence of the permeability spectra.*

## III.3. Continuous coatings

The dynamic magnetic properties of continuous FM coatings after debinding and sintering are measured through the method of spire perturbation [84]. This method relies on the measurement of an impedance through an analyzer connected to a support constituted of a spire. Figure IV-61 displays the permeability  $\mu'$  and  $\mu''$  of FM coatings elaborated by airbrushing after debinding and sintering. Two sintered samples are compared: one realized on a silicon wafer and another on alumina.

The high level of permittivity of Si and alumina substrate reduces the precision of the measurement by a high capacitive contribution to the impedance. The measurements are then very sensitive to the positioning of the sample into the cell.

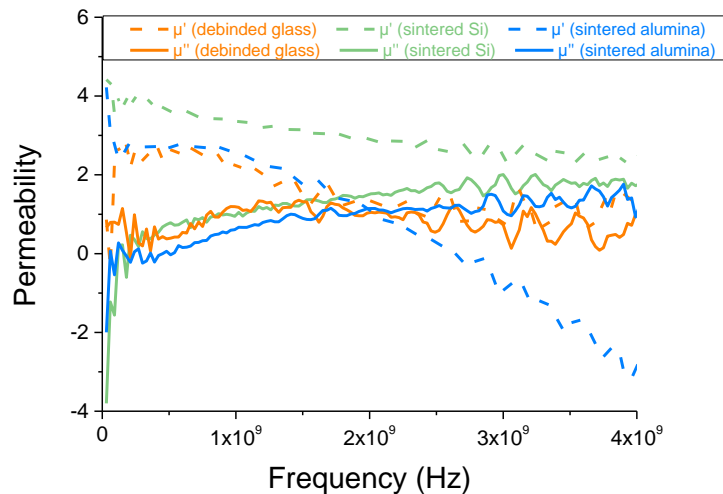


Figure IV-61. Spectra of the permeability ( $\mu'$ ,  $\mu''$ ) of FM coatings after debinding and sintering.

The resulted curves being very noisy, a smoothing treatment have been used on Origin to recover the following curves for the imaginary permeability  $\mu''$  (Figure IV-62).

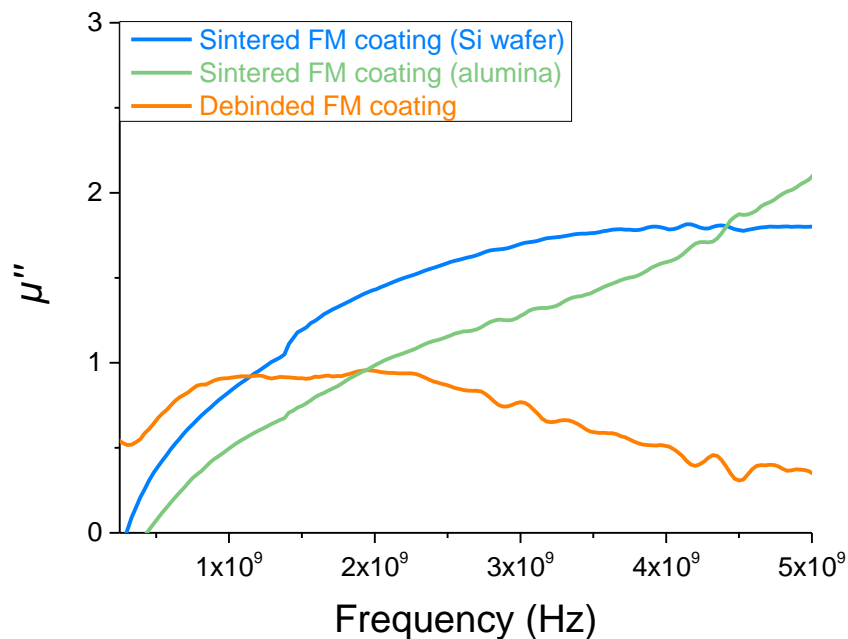


Figure IV-62. Spectra of the imaginary permeability ( $\mu''$ ) of FM coatings after debinding and sintering. The curves are smoothed on Origin.

The level of the imaginary permeability of the debinded sample is lower than after sintering. The two sintered samples exhibit similar results, which are too weak to be precisely measured by a perturbation technique.

In all cases, the dynamic magnetic response are low in comparison with dense films realized for example by spin spray [3] or inkjet printing [85]. On these samples, the effect of patterning will not modify the dynamic response, since it behaves more like a set of nanoparticles than a continuous magnetic medium with a perfect magnetic continuity.



## IV. Conclusion

*The magnetic properties of FM and SP(F)M nanoparticles and coatings have been studied through static and dynamic characterizations.*

*On the one hand, the static magnetic characterizations of FM and SP(F)M particles have demonstrated:*

- *A saturation of the magnetization signal of FM particles ( $M_S$  of 80.6 emu/g or  $A.m^2/kg$ ).*
- *A superparamagnetic behavior of SP(F)M particles with a magnetization curve which does not saturate. A fit of the curve based on a Langevin function gives a crystallite size of 5 nm and a saturation magnetization  $M_S$  of 85.6 emu/g ( $A.m^2/kg$ ), close to the one of FM particles.*
- *A sharp decrease of the saturation magnetization  $M_S$  of annealed FM particles from 400 °C, due to:*
  - *the presence of a secondary phase of  $Zn^{2+}$  substituted wüstite ( $Zn_xFe_{1-x}O$  phase)*
  - *a  $Zn^{2+}$  redistribution in the spinel sites inside both magnetite and maghemite phases,*
  - *and spin disorder at the particle surface.*

*Then, the static magnetic properties of continuous coatings have been examined as a function of the number of particle cleanings  $N$ , and of the thermal treatment:*

- *The number of cycles  $N$  is fixed at 6. It allows to combine a reduction of the organic quantity at the particle surface, a high saturation magnetization  $M_S$  and a good adherence of the material on the substrate.*
- *The different evolution of the magnetization as a function of the annealing temperature between particles and coatings can be explained by a difference of reactivity. Indeed, the formation of  $Zn^{2+}$  substituted wüstite ( $Zn_xFe_{1-x}O$  phase) is delayed in coatings, which leads to a higher magnetization of sintered coatings (76 emu/g or  $A.m^2/kg$ ) in comparison with sintered nanoparticles (22 emu/g or  $A.m^2/kg$ ).*
- *The saturation magnetization  $M_S$  of a sintered FM coating with 50% of porosity (76 emu/g or  $A.m^2/kg$ ) is encouraging, as it is not so far from the value of 98.8 emu/g ( $A.m^2/kg$ ) of a dense  $Zn_{0.4}Fe_{2.6}O_4$  film [3].*

*As a conclusion, the saturation magnetization  $M_S$  of particles and coatings is strictly related to the material microstructure and can be affected by several factors summarized in Figure IV-63:*

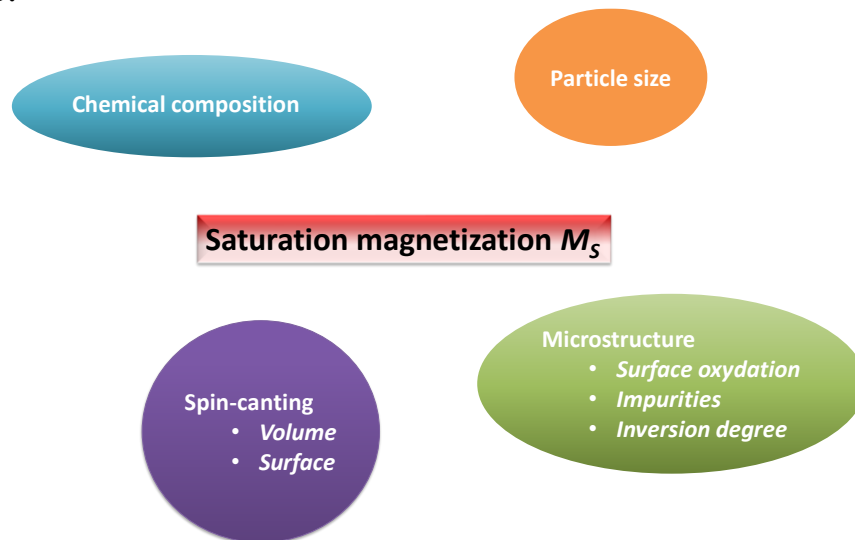


Figure IV-63. Parameters influencing the saturation magnetization  $M_S$ .

- *the chemical composition of the material, especially the quantity of doping ion,*
- *the microstructure of the material, namely the volume oxidation, the presence of secondary phases, and the cationic distribution in the structure (inversion degree),*
- *and the spin-canting effect at the nanoparticle surface and in the volume due to non-magnetic substitution, exalted for smaller particles.*

*From the main factors affecting the saturation magnetization  $M_S$ , the values of the experimental magnetic moment of FM and SP(F)M particles have been compared to the theoretical ones estimated from a corrected model with different hypotheses. This model enables to establish a link between the microstructure and the magnetic properties of particles. The best fit has been obtained by considering particles with volume surface oxidation, and various amounts of Zn cations at octahedral sites for  $Zn^{2+}$  substituted maghemite and magnetite phases.*

*On the other hand, the dynamic magnetic properties of FM and SP(F)M particles and continuous coatings have been analyzed.*

*The permittivity and permeability of FM and SP(F)M particles have been investigated and lead to the following conclusions:*

- *The introduction of zinc in the structure induces a decrease of the permittivity when compared with commercial  $Fe_3O_4$  composition.*
- *The frequency of the permeability resonance  $f_r$  is linked to the nature of the doping ion and its level is affected by the particle size, larger particles inducing higher permeability levels.*

- *Zn<sub>0.4</sub>Fe<sub>2.6</sub>O<sub>4</sub> composition is a good compromise allowing to combine a low permittivity with a high saturation magnetization. The level of permeability  $A$  and the ferromagnetic resonance frequency  $f_r$  are drastically affected by the nanoparticles size, which evidences the superparamagnetic state.*
- *A dynamic susceptibility model has been employed to successfully reproduce the experimental results for SP(F)M particles, and especially the trend in the temperature dependence of the permeability spectra, by taking into account the temperature dependence of the effective anisotropy field:*
  - *a shift of the resonance frequency  $f_r$  toward the high frequencies for decreasing temperature,*
  - *an increase of the resonance line intensity  $A$  for decreasing temperature,*
  - *and the decrease of the width of the resonance peak  $\Delta f_r$  for decreasing temperature. This point needs further investigation.*

*Finally, the dynamic magnetic properties of continuous FM coatings after debinding and sintering have been measured. The levels of the imaginary permeability are too low to realize the final application, a material with magnetic losses at desired frequencies after patterning. An enhancement of the density of coatings is the key to obtain a better dynamic magnetic response. Solutions to the improvement of the coating density have been discussed in chapter II and require the study of more adapted processing methods. Moreover, all the understanding that have been gained on this family of composition can be reused even if the process deposition of the ferrite is changed so as to elaborate dense thin films.*

**Chapter IV references:**

- [1] M. Schott, "Propriétés magnétiques du système Pt/Co/AlOx et ses variations sous champ électrique.," Grenoble Alpes, thèse, 2017.
- [2] Sapna, N. Budhiraja, V. Kumar, and S. K. Singh, "Shape-controlled synthesis of superparamagnetic ZnFe<sub>2</sub>O<sub>4</sub> hierarchical structures and their comparative structural, optical and magnetic properties," *Ceram. Int.*, vol. 45, no. 1, pp. 1067–1076, Jan. 2019, doi: 10.1016/j.ceramint.2018.09.286.
- [3] A. Fujiwara, M. Tada, T. Nakagawa, and M. Abe, "Permeability and electric resistivity of spin-sprayed Zn ferrite films for high-frequency device applications," *J. Magn. Magn. Mater.*, vol. 320, no. 8, pp. L67–L69, Apr. 2008, doi: 10.1016/j.jmmm.2007.11.026.
- [4] H. Shokrollahi, "A review of the magnetic properties, synthesis methods and applications of maghemite," *J. Magn. Magn. Mater.*, vol. 426, pp. 74–81, Mar. 2017, doi: 10.1016/j.jmmm.2016.11.033.
- [5] S. Yoon, "Preparation and Physical Characterizations of Superparamagnetic Maghemite Nanoparticles," *J. Magn.*, vol. 19, no. 4, pp. 323–326, Dec. 2014, doi: 10.4283/JMAG.2014.19.4.323.
- [6] A. Demortière *et al.*, "Size-dependent properties of magnetic iron oxidenanocrystals," *Nanoscale*, vol. 3, no. 1, pp. 225–232, 2011, doi: 10.1039/C0NR00521E.
- [7] M. Mozaffari, M. Eghbali Arani, and J. Amighian, "The effect of cation distribution on magnetization of ZnFe<sub>2</sub>O<sub>4</sub> nanoparticles," *J. Magn. Magn. Mater.*, vol. 322, no. 21, pp. 3240–3244, Nov. 2010, doi: 10.1016/j.jmmm.2010.05.053.
- [8] J. Marx, H. Huang, K. S. M. Salih, W. R. Thiel, and V. Schünemann, "Spin canting in ferrite nanoparticles," *Hyperfine Interact.*, vol. 237, no. 1, Dec. 2016, doi: 10.1007/s10751-016-1241-5.
- [9] M. P. Morales *et al.*, "Surface and Internal Spin Canting in  $\gamma$ -Fe<sub>2</sub>O<sub>3</sub> Nanoparticles," *Chem. Mater.*, vol. 11, no. 11, pp. 3058–3064, Nov. 1999, doi: 10.1021/cm991018f.
- [10] R. H. Kodama, A. E. Berkowitz, E. J. McNiff, and S. Foner, "Surface spin disorder in ferrite nanoparticles (invited)," *J. Appl. Phys.*, vol. 81, no. 8, pp. 5552–5557, Apr. 1997, doi: 10.1063/1.364659.
- [11] J. M. D. Coey, "Noncollinear Spin Arrangement in Ultrafine Ferrimagnetic Crystallites," *Phys. Rev. Lett.*, vol. 27, no. 17, pp. 1140–1142, Oct. 1971, doi: 10.1103/PhysRevLett.27.1140.
- [12] S. Noh *et al.*, "Nanoscale Magnetism Control via Surface and Exchange Anisotropy for Optimized Ferrimagnetic Hysteresis," *Nano Lett.*, vol. 12, no. 7, pp. 3716–3721, Jul. 2012, doi: 10.1021/nl301499u.
- [13] J. L. Dormann, "Le phénomène de superparamagnétisme," *Rev. Phys. Appliquée*, vol. 16, no. 6, pp. 275–301, 1981, doi: 10.1051/rphysap:01981001606027500.
- [14] J. L. Dormann, "Le phénomène de superparamagnétisme," *Rev. Phys. Appliquée*, vol. 16, no. 6, pp. 275–301, 1981, doi: 10.1051/rphysap:01981001606027500.
- [15] A. Demortière *et al.*, "Size-dependent properties of magnetic iron oxidenanocrystals," *Nanoscale*, vol. 3, no. 1, pp. 225–232, 2011, doi: 10.1039/C0NR00521E.
- [16] X. Battle, M. García del Muro, J. Tejada, H. Pfeiffer, P. Görnert, and E. Sinn, "Magnetic study of Mtype doped barium ferrite nanocrystalline powders," *J. Appl. Phys.*, vol. 74, no. 5, pp. 3333–3340, Sep. 1993, doi: 10.1063/1.354558.
- [17] A. J. Rondinone, C. Liu, and Z. J. Zhang, "Determination of Magnetic Anisotropy Distribution and Anisotropy Constant of Manganese Spinel Ferrite Nanoparticles," *J. Phys. Chem. B*, vol. 105, no. 33, pp. 7967–7971, Aug. 2001, doi: 10.1021/jp011183u.
- [18] Y.-J. Liang *et al.*, "Size-dependent electromagnetic properties and the related simulations of Fe<sub>3</sub>O<sub>4</sub> nanoparticles made by microwave-assisted thermal decomposition," *Colloids Surf. Physicochem. Eng. Asp.*, vol. 530, pp. 191–199, Oct. 2017, doi: 10.1016/j.colsurfa.2017.06.059.
- [19] Y. Yang *et al.*, "Synthesis of nonstoichiometric zinc ferrite nanoparticles with extraordinary room temperature magnetism and their diverse applications," *J. Mater. Chem. C*, vol. 1, no. 16, p. 2875, 2013, doi: 10.1039/c3tc00790a.
- [20] F. Perton, "Architecturation de nanoparticules hybrides pour une imagerie et thérapie multimodales," 2019.

- [21] J. Jang, H. Nah, J.-H. Lee, S. H. Moon, M. G. Kim, and J. Cheon, "Critical Enhancements of MRI Contrast and Hyperthermic Effects by Dopant-Controlled Magnetic Nanoparticles," *Angew. Chem.*, vol. 121, no. 7, pp. 1260–1264, Feb. 2009, doi: 10.1002/ange.200805149.
- [22] L. M. Bauer, S. F. Situ, M. A. Griswold, and A. C. S. Samia, "High-performance iron oxide nanoparticles for magnetic particle imaging – guided hyperthermia (hMPI)," *Nanoscale*, vol. 8, no. 24, pp. 12162–12169, 2016, doi: 10.1039/C6NR01877G.
- [23] C. Yao *et al.*, "ZnFe<sub>2</sub>O<sub>4</sub> Nanocrystals: Synthesis and Magnetic Properties," *J. Phys. Chem. C*, vol. 111, no. 33, pp. 12274–12278, Aug. 2007, doi: 10.1021/jp0732763.
- [24] F. Li, H. Wang, L. Wang, and J. Wang, "Magnetic properties of ZnFe<sub>2</sub>O<sub>4</sub> nanoparticles produced by a low-temperature solid-state reaction method," *J. Magn. Magn. Mater.*, vol. 309, no. 2, pp. 295–299, Feb. 2007, doi: 10.1016/j.jmmm.2006.07.012.
- [25] N. M. Belozerova *et al.*, "Neutron diffraction study of the crystal and magnetic structures of nanostructured Zn<sub>0.34</sub>Fe<sub>2.53</sub>O<sub>4</sub> ferrite," *J. Nanoparticle Res.*, vol. 22, no. 5, p. 121, May 2020, doi: 10.1007/s11051-020-04852-4.
- [26] N. Modaresi *et al.*, "Magnetic properties of Zn<sub>x</sub>Fe<sub>3-x</sub>O<sub>4</sub> nanoparticles: A competition between the effects of size and Zn doping level," *J. Magn. Magn. Mater.*, vol. 482, pp. 206–218, Jul. 2019, doi: 10.1016/j.jmmm.2019.03.060.
- [27] X. Li, E. Liu, Z. Zhang, Z. Xu, and F. Xu, "Solvothermal synthesis, characterization and magnetic properties of nearly superparamagnetic Zn-doped Fe<sub>3</sub>O<sub>4</sub> nanoparticles," *J. Mater. Sci. Mater. Electron.*, vol. 30, no. 4, pp. 3177–3185, Feb. 2019, doi: 10.1007/s10854-018-00640-y.
- [28] M. Rivero, A. del Campo, Á. Mayoral, E. Mazario, J. Sánchez-Marcos, and A. Muñoz-Bonilla, "Synthesis and structural characterization of Zn<sub>x</sub>Fe<sub>3-x</sub>O<sub>4</sub> ferrite nanoparticles obtained by an electrochemical method," *RSC Adv.*, vol. 6, no. 46, pp. 40067–40076, 2016, doi: 10.1039/C6RA04145K.
- [29] D. Kotsikau, V. Pankov, E. Petrova, V. Natarov, D. Filimonov, and K. Pokholok, "Structural, magnetic and hyperfine characterization of Zn<sub>x</sub>Fe<sub>3-x</sub>O<sub>4</sub> nanoparticles prepared by sol-gel approach via inorganic precursors," *J. Phys. Chem. Solids*, vol. 114, pp. 64–70, Mar. 2018, doi: 10.1016/j.jpcs.2017.11.004.
- [30] D. Venkateshvaran, "Fabrication and characterization of Zn<sub>x</sub>Fe<sub>3-x</sub>O<sub>4</sub> Epitaxial Films," Technical University of Munich Thesis, 2008.
- [31] R. Sai, S. D. Kulkarni, S. S. M. Bhat, N. G. Sundaram, N. Bhat, and S. A. Shivashankar, "Controlled inversion and surface disorder in zinc ferrite nanocrystallites and their effects on magnetic properties," *RSC Adv.*, no. 5, p. 10267\_10274, 2015.
- [32] P. Saha, R. Rakshit, M. Alam, and K. Mandal, "Magnetic and Electronic Properties of Zn -Doped Fe<sub>3</sub>O<sub>4</sub> Hollow Nanospheres," *Phys. Rev. Appl.*, vol. 11, no. 2, p. 024059, Feb. 2019, doi: 10.1103/PhysRevApplied.11.024059.
- [33] M. Srivastava, S. K. Alla, S. S. Meena, N. Gupta, R. K. Mandal, and N. K. Prasad, "Zn<sub>x</sub>Fe<sub>3-x</sub>O<sub>4</sub> (0.01 ≤ x < 0.8) nanoparticles for controlled magnetic hyperthermia application," *New J. Chem.*, vol. 42, no. 9, pp. 7144–7153, 2018, doi: 10.1039/C8NJ00547H.
- [34] S. Ayyappan, G. Gnanaprakash, G. Panneerselvam, M. P. Antony, and J. Philip, "Effect of Surfactant Monolayer on Reduction of Fe<sub>3</sub>O<sub>4</sub> Nanoparticles under Vacuum," *J. Phys. Chem. C*, vol. 112, no. 47, pp. 18376–18383, Nov. 2008, doi: 10.1021/jp8052899.
- [35] W. L. Roth, "Defects in the crystal and magnetic structures of ferrous oxide," *Acta Crystallogr.*, vol. 13, no. 2, pp. 140–149, Feb. 1960, doi: 10.1107/S0365110X60000297.
- [36] T. Sano, "Effect of foreign cation of Zn(II) or Mn(II) ion in FeO-wüstite on its disproportionation reaction below 575°C," *Solid State Ion.*, vol. 104, no. 3–4, pp. 311–317, Dec. 1997, doi: 10.1016/S0167-2738(97)00432-3.
- [37] M. A. Cobos *et al.*, "Magnetic Phase Diagram of Nanostructured Zinc Ferrite as a Function of Inversion Degree δ," *J. Phys. Chem. C*, vol. 123, no. 28, pp. 17472–17482, Jul. 2019, doi: 10.1021/acs.jpcc.9b02180.

- [38] E. Petrova, D. Kotsikau, and V. Pankov, "Structural characterization and magnetic properties of sol-gel derived  $Zn_x Fe_{3-x} O_4$  nanoparticles," *J. Magn. Magn. Mater.*, vol. 378, pp. 429–435, Mar. 2015, doi: 10.1016/j.jmmm.2014.11.076.
- [39] E. W. Gorter, "SATURATION MAGNETIZATION AND CRYSTAL CHEMISTRY OF FERRIMAGNETIC OXIDES," *Philips Res Rep*, no. 9, pp. 321–365, 1954.
- [40] P. G. Bercoff and H. R. Bertorello, "Localized canting elect in Zn-substituted Ni ferrites," *J. Magn. Magn. Mater.*, vol. 213, pp. 56–62, 2000.
- [41] C. E. Patton and Y. Liu, "Localised canting models for substituted magnetic oxides," *J. Phys. C Solid State Phys.*, vol. 16, no. 31, pp. 5995–6010, Nov. 1983, doi: 10.1088/0022-3719/16/31/014.
- [42] G. F. Dionne, *Magnetic Oxides*, Springer. 2009.
- [43] P. G. Bercoff and H. R. Bertorello, "Exchange constants and transfer integrals of spinel ferrites.," *J. Magn. Magn. Mater.*, no. 169, pp. 314–322, 1997.
- [44] G. F. Dionne, "Molecular-field coefficients of  $MnFe_2O_4$  and  $NiFe_2O_4$  spinel ferrite systems," *J. Appl. Phys.*, no. 63, p. 3777, 1988.
- [45] D. J. Dunlop and Ö. Özdemir, *Rock Magnetism: Fundamentals and Frontiers*, vol. 3. Cambridge University Press: Cambridge, 1997.
- [46] C. J. Goss, "Saturation Magnetisation, Coercivity and Lattice Parameter Changes in the System  $Fe_{304-y}Fe_2O_3$ , and Their Relationship to Structure," *Phys. Chem. Miner.*, p. 8, 1988.
- [47] Y. Khan and E. Kneller, "STRUCTURE AND MAGNETIC MOMENT OF ZINC-SUBSTITUTED  $\gamma$  IRON OXIDE," *J. Magn. Magn. Mater.*, vol. 7, pp. 9–11, 1978.
- [48] S. Brice-Profeta *et al.*, "Magnetic order in  $\gamma$ -nanoparticles: a XMCD study," *J. Magn. Magn. Mater.*, vol. 288, pp. 354–365, Mar. 2005, doi: 10.1016/j.jmmm.2004.09.120.
- [49] M. Bersweiler *et al.*, "Size-dependent spatial magnetization profile of manganese-zinc ferrite  $Mn_{0.2}Zn_{0.2}Fe_{2.6}O_4$  nanoparticles," *Phys. Rev. B*, vol. 100, no. 14, p. 144434, Oct. 2019, doi: 10.1103/PhysRevB.100.144434.
- [50] S. Bedanta *et al.*, "Overcoming the Dipolar Disorder in Dense CoFe Nanoparticle Ensembles: Superferromagnetism," *Phys. Rev. Lett.*, vol. 98, no. 17, p. 176601, Apr. 2007, doi: 10.1103/PhysRevLett.98.176601.
- [51] J.-H. Le Gallou, M. Ledieu, V. Grimal, and O. Acher, "Technique under compressive stress for determining the magneto-elastic effects in ferrites," *J. Magn. Magn. Mater.*, vol. 320, no. 14, pp. e172–e174, Jul. 2008, doi: 10.1016/j.jmmm.2008.02.041.
- [52] M. Darcheville *et al.*, "Evidence of the Superparamagnetic State in the Zero-Field Microwave Susceptibility Spectra of Ferrimagnetic Nanoparticles," *IEEE Magn. Lett.*, vol. 11, pp. 1–5, 2020, doi: 10.1109/LMAG.2020.3026228.
- [53] R. Ramprasad, P. Zurcher, M. Petras, M. Miller, and P. Renaud, "Magnetic properties of metallic ferromagnetic nanoparticle composites," *J. Appl. Phys.*, vol. 96, no. 1, pp. 519–529, Jul. 2004, doi: 10.1063/1.1759073.
- [54] N. Bardy, G. Leblevenec, D. Le Potier, and J. Authesserre, "Control of Ferrites Microwave Properties at the French Atomic Energy Commission - Manufacturing Process and Characterization," *J. Phys. IV*, vol. 07, no. C1, pp. C1-417-C1-418, Mar. 1997, doi: 10.1051/jp4:19971168.
- [55] M. Hotta, M. Hayashi, and K. Nagata, "High Temperature Measurement of Complex Permittivity and Permeability of  $Fe_3O_4$  Powders in the Frequency Range of 0.2 to 13.5 GHz," *ISIJ Int.*, vol. 51, no. 3, pp. 491–497, 2011, doi: 10.2355/isijinternational.51.491.
- [56] J. G. Hwang, M. Zahn, F. M. O'Sullivan, L. A. A. Pettersson, O. Hjortstam, and R. Liu, "Effects of nanoparticle charging on streamer development in transformer oil-based nanofluids," *J. Appl. Phys.*, vol. 107, no. 1, p. 014310, Jan. 2010, doi: 10.1063/1.3267474.
- [57] B. Du, Q. Liu, Y. Shi, and Y. Zhao, "The Effect of  $Fe_3O_4$  Nanoparticle Size on Electrical Properties of Nanofluid Impregnated Paper and Trapping Analysis," *Molecules*, vol. 25, no. 16, p. 3566, Aug. 2020, doi: 10.3390/molecules25163566.

- [58] A. Dey, A. De, and S. K. De, "Electrical transport and dielectric relaxation in Fe<sub>3</sub>O<sub>4</sub>-polypyrrole hybrid nanocomposites," *J. Phys. Condens. Matter*, vol. 17, no. 37, pp. 5895–5910, Sep. 2005, doi: 10.1088/0953-8984/17/37/025.
- [59] G. Li, L. Sheng, L. Yu, K. An, W. Ren, and X. Zhao, "Electromagnetic and microwave absorption properties of single-walled carbon nanotubes and CoFe<sub>2</sub>O<sub>4</sub> nanocomposites," *Mater. Sci. Eng. B*, vol. 193, pp. 153–159, Mar. 2015, doi: 10.1016/j.mseb.2014.12.008.
- [60] Y. Liu, X. Liu, and X. Wang, "Double-layer microwave absorber based on CoFe<sub>2</sub>O<sub>4</sub> ferrite and carbonyl iron composites," *J. Alloys Compd.*, vol. 584, pp. 249–253, Jan. 2014, doi: 10.1016/j.jallcom.2013.09.049.
- [61] S. Golchinvafa, S. M. Masoudpanah, and M. Jazirehpour, "Magnetic and microwave absorption properties of FeCo/CoFe<sub>2</sub>O<sub>4</sub> composite powders," *J. Alloys Compd.*, vol. 809, p. 151746, Nov. 2019, doi: 10.1016/j.jallcom.2019.151746.
- [62] M. Zong, Y. Huang, H. Wu, Y. Zhao, Q. Wang, and X. Sun, "One-pot hydrothermal synthesis of RGO/CoFe<sub>2</sub>O<sub>4</sub> composite and its excellent microwave absorption properties," *Mater. Lett.*, vol. 114, pp. 52–55, Jan. 2014, doi: 10.1016/j.matlet.2013.09.113.
- [63] J. Zheng, X. Song, X. Liu, W. Chen, Y. Li, and J. Guo, "Synthesis of hexagonal CoFe<sub>2</sub>O<sub>4</sub>/ZnO nanoparticles and their electromagnetic properties," *Mater. Lett.*, vol. 73, pp. 143–146, Apr. 2012, doi: 10.1016/j.matlet.2012.01.035.
- [64] R. D. K. Misra, S. Gubbala, A. Kale, and W. F. E. Jr, "A comparison of the magnetic characteristics of nanocrystalline nickel, zinc, and manganese ferrites synthesized by reverse micelle technique," *Mater. Sci. Eng. B*, p. 11, 2004.
- [65] Y. Shi, J. Ding, and H. Yin, "CoFe<sub>2</sub>O<sub>4</sub> nanoparticles prepared by the mechanochemical method," *J. Alloys Compd.*, vol. 308, no. 1–2, pp. 290–295, Aug. 2000, doi: 10.1016/S0925-8388(00)00921-X.
- [66] A. López-Ortega, E. Lottini, C. de J. Fernández, and C. Sangregorio, "Exploring the Magnetic Properties of Cobalt-Ferrite Nanoparticles for the Development of a Rare-Earth-Free Permanent Magnet," *Chem. Mater.*, vol. 27, no. 11, pp. 4048–4056, Jun. 2015, doi: 10.1021/acs.chemmater.5b01034.
- [67] P. Tancredi, P. C. Rivas-Rojas, O. Moscoso-Londoño, D. Muraca, M. Knobel, and L. M. Socolovsky, "Significant coercivity enhancement at low temperatures in magnetically oriented cobalt ferrite nanoparticles," *Appl. Phys. Lett.*, vol. 115, no. 26, p. 263104, Dec. 2019, doi: 10.1063/1.5131259.
- [68] N.-N. Song *et al.*, "Exceeding natural resonance frequency limit of monodisperse Fe<sub>3</sub>O<sub>4</sub> nanoparticles via superparamagnetic relaxation," *Sci. Rep.*, vol. 3, no. 1, p. 3161, Dec. 2013, doi: 10.1038/srep03161.
- [69] N. Guskos *et al.*, "Ferromagnetic resonance and ac conductivity of a polymer composite of Fe<sub>3</sub>O<sub>4</sub> and Fe<sub>3</sub>C nanoparticles dispersed in a graphite matrix," *J. Appl. Phys.*, vol. 97, no. 2, p. 024304, Jan. 2005, doi: 10.1063/1.1836855.
- [70] F. Gazeau *et al.*, "Magnetic resonance of ferrite nanoparticles: evidence of surface effects," *J. Magn. Magn. Mater.*, p. 13, 1998.
- [71] D. Griscom, "Particle size effects in the FMR spectra of fine-grained precipitates in glass," *IEEE Trans. Magn.*, vol. 17, no. 6, pp. 2718–2720, Nov. 1981, doi: 10.1109/TMAG.1981.1061662.
- [72] T. Bodziony *et al.*, "Temperature dependence of the FMR spectra of Fe<sub>3</sub>O<sub>4</sub> and Fe<sub>3</sub>C nanoparticle magnetic systems in copolymer matrices," *Mater. Sci.-Pol.*, vol. 23, no. 4, 2005.
- [73] Yu. L. Raikher and V. I. Stepanov, "Magnetization dynamics of single-domain particles by superparamagnetic theory," *J. Magn. Magn. Mater.*, vol. 316, no. 2, pp. 417–421, Sep. 2007, doi: 10.1016/j.jmmm.2007.03.090.
- [74] I. S. Poperechny and Yu. L. Raikher, "Ferromagnetic resonance in uniaxial superparamagnetic particles," *Phys. Rev. B*, vol. 93, no. 1, Jan. 2016, doi: 10.1103/PhysRevB.93.014441.
- [75] Yu. L. Raikher and M. I. Shliomis, "Theory of dispersion of the magnetic susceptibility of fine ferromagnetic particles," *Sov. Phys.-JETP*, vol. 40, no. 3, 1974.
- [76] E. Du Trémolet de Lacheisserie, *Magnétisme-Fondements*, EDP Sciences. EDP Sciences, 2000.

- [77] E. Lima, A. L. Brandl, A. D. Arelaro, and G. F. Goya, "Spin disorder and magnetic anisotropy in Fe<sub>3</sub>O<sub>4</sub> nanoparticles," *J. Appl. Phys.*, vol. 99, no. 8, p. 083908, Apr. 2006, doi: 10.1063/1.2191471.
- [78] H. Duan, J. Wang, L. Li, V. Aguilar, and G. Zhao, "Magnetic properties of barium ferrite nanoparticles: Quantitative test of the Stoner–Wohlfarth theory for uniaxial single-domain magnetic particles," *Phys. Lett. A*, vol. 377, no. 38, pp. 2659–2662, Nov. 2013, doi: 10.1016/j.physleta.2013.07.050.
- [79] A. F. Jr and V. Zapf, "Temperature dependence of magnetic anisotropy in nanoparticles of Co<sub>x</sub>Fe<sub>(3-x)</sub>O<sub>4</sub>," *J. Magn. Magn. Mater.*, p. 5, 2008.
- [80] Ch. Srinivas, B. V. Tirupanyam, A. Satish, V. Seshubai, D. L. Sastry, and O. F. Caltun, "Effect of Ni<sup>2+</sup> substitution on structural and magnetic properties of Ni–Zn ferrite nanoparticles," *J. Magn. Magn. Mater.*, vol. 382, pp. 15–19, May 2015, doi: 10.1016/j.jmmm.2015.01.008.
- [81] N. Miyata, "Ferromagnetic Crystalline Anisotropy of MeFe<sub>2</sub>O<sub>4</sub>-Fe<sub>3</sub>O<sub>4</sub> Ferrite Solid Solutions," *J. Phys. Soc. Jpn.*, vol. 16, no. 7, 1961.
- [82] Gubin, *Magnetic Nanoparticles*, Wiley-VCH. 2009.
- [83] C. Antoniak, J. Lindner, and M. Farle, "Magnetic anisotropy and its temperature dependence in iron-rich Fe<sub>x</sub>Pt<sub>1-x</sub> nanoparticles," *Europhys. Lett. EPL*, vol. 70, no. 2, pp. 250–256, Apr. 2005, doi: 10.1209/epl/i2004-10485-9.
- [84] J. Neige, "Élaboration, caractérisation et modélisation d'un composite à base de pétales ferromagnétiques pour des applications hyperfréquences," Thesis, Tours, 2013.
- [85] M. Bissannagari, W. Lee, W. Y. Lee, J. H. Jeong, and J. Kim, "Fully-Inkjet-Printed Ag-Coil/NiZn-Ferrite for Flexible Wireless Power Transfer Module: Rigid Sintered Ceramic Body into Flexible Form," *Adv. Funct. Mater.*, vol. 27, no. 31, p. 1701766, Aug. 2017, doi: 10.1002/adfm.201701766.





# General conclusion

The prospects of the project are written in italics.

The objective of this study was to elaborate a patterned magnetic material with a texturization in domains from which the magnetic losses would be controlled through their geometric characteristics (size, shape, thickness and spacing). The expected magnetic behavior is called a “multi-band” behavior since the magnetic losses are controlled at desired frequencies, and it has an interest in electromagnetic applications like power transformers in electronics and telecommunications, information storage, wireless power transfer (WPT), radar absorption. Such frameworks require the development of dense coatings in order to be able to tune the magnetic response of the material only through the microstructure at the scale of patterns, not disturbed by the presence of defects at the microscopic scale generated by porosity. For this purpose, the viability and suitability of an overall process of coating has been studied, from the nanoparticle synthesis to the film. A  $\text{Zn}_{0.4}\text{Fe}_{2.6}\text{O}_4$  composition has been chosen to combine a high value of saturation magnetization with an electrical resistivity sufficient to ensure the penetration of the electromagnetic wave.

First of all,  $\text{Zn}_{0.4}\text{Fe}_{2.6}\text{O}_4$  nanoparticles have been synthesized by microwave-assisted thermal decomposition. This synthesis route provides a fast and uniform heating, leading to reproducible results and homogeneous particles in size and shape. The synthesis has been performed in an organic medium with a mixture of oleylamine (OAm) and oleic acid (OA), used as surfactants, in octadecene. OAm and OA have separate and complementary roles. On the one hand, they allow to control the particle morphology. Indeed, OA favors the particle growth along a preferential axis and OAm inhibits its growth. Spherical particles have been obtained using equal quantities of OAm and OA. On the other hand, OAm also serves as a pH regulator since OAm absorbs the protons generated during the grafting of OA molecules at the particle surface. The particles are thus essentially surrounded by OA molecules through the carboxylic groups chemically adsorbed onto the particle surface. Ethylene glycol has been shown to increase the nanoparticle size as found in other oxides with an atypical “raspberry” morphology [1], and as observed with diethylene glycol too [2]. The mechanism of this peculiar growth has not been elucidated.

Two types of particles have been elaborated: spherical superparamagnetic particles (SP(F)M) with a diameter of  $6.2 \pm 1$  nm and ferrimagnetic ones (FM) with a diameter of  $22.4 \pm 11$  nm. In order to avoid parasitic signals from particle domains or walls, the size of the particles should be smaller than 1  $\mu\text{m}$ .

The chemical composition and microstructure of particles have been deeply investigated. The measured chemical composition is consistent with the theoretical one and is homogeneous at global (ICP-AES) and local scales (SEM-EDX). The combination of four means of characterization has provided a good knowledge of the microstructure of particles through Fourier transform infrared spectroscopy (FTIR), X-ray diffraction with a Rietveld analysis, high resolution microscopy HAADF-STEM coupled to EELS, and Mössbauer spectroscopy. The

results are in agreement and have evidenced: the core/shell structure of particles due to surface oxidation amplified for SP(F)M particles, a partial inversion of the spinel structure for FM particles and the presence of a surface spin-canting on the outer shell of the particle surface. The particles can be split in three layers from the outer to the inner: a canted layer, an oxidized layer, and a core displaying the zinc iron oxide spinel phase.

*In this work, the chemical composition has been restricted to doped zinc iron oxide spinel particles. Nevertheless, the microwave route could be adapted for the synthesis of other interesting compositions, like  $(\text{ZnMn})\text{Fe}_2\text{O}_4$  or  $(\text{NiZn})\text{Fe}_2\text{O}_4$ . The idea of a microwave-assisted thermal decomposition by adding other metallic precursors may be further considered. Indeed, additional doping ions in the structure of the ferrite might potentially be attractive to tune the electrical and magnetic properties as different cationic distributions will occur. The material behavior will differ with responses on different frequency ranges, leading to different types of applications.*

Once elaborated, the particles have been cleaned through centrifugations before being dispersed in hexane. The successful dispersion of particles in hexane is due to the affinity with hexane of the nonpolar hydrocarbon chains of OA molecules grafted onto the particle surface through their carboxylates groups. A compromise regarding the residual organics surrounding particles after synthesis has been found. Due to the fact that they affect the magnetic properties of the particles, the organics have to be removed as much as possible, keeping in mind that some are needed to maintain a good stability of the particles in solution. Continuous layers have been then deposited onto silicon wafer and alumina substrates by airbrushing. Finally, the coatings have been annealed under argon to prevent oxidation through a procedure in two stages: a debinding step at 450 °C to remove the organic residues coming from the dispersion, and a sintering one at 770 °C to densify the layer after the organics removal, and also ensure a good adhesion of the layer to the substrate.

The generated coatings are cracked due to the progressive departure of organics. Indeed, OA molecules are thermally decomposed in two stages. The hydrocarbon chains are firstly removed from 300 °C due to their weak bonding with the particle, while the carboxylates groups are decomposed at higher temperatures because they are chemically adsorbed onto the particle surface. A second reason to explain the cracking is the reduction of the particles into  $\text{Zn}^{2+}$  substituted wüstite caused by the degradation of the carbon residues. After annealing at 770 °C, the particles can be assimilated to core/shell structures with  $\text{Zn}_{0.4}\text{Fe}_{2.6}\text{O}_4$  composition at the core and  $\text{Zn}^{2+}$  substituted wüstite at the outer.

Different strategies have been tested to reduce the cracking. However, the coating density has not been improved and the best coating is approximately half porous. With such values of porosity, the aimed magnetic response is not expected. Nevertheless, a test of patterning through laser etching has been successful on a sintered sample, which demonstrates the feasibility of the processing method.

A transfer of the airbrushing towards an innovative and automatized process has been studied. The inkjet printing allows the realization of patterned coatings in a single step without post-processing. The dispersion of particles previously optimized has been reformulated to

meet the criteria imposed by the printer, and especially the respect of a dimensionless ejection ratio, linked to the viscosity and surface tension of the fluid. Two compatible inks have been formulated from the particle dispersion: a polymer-based formulation (PF) with a mixture of poly(1-decene) and hexane, and a solvent-based (SF) one with a mixture of octanol and hexane.

Both inks have exhibited a good jet-ability and led to the elaboration of well-defined squares of 500  $\mu\text{m}$  of length. Nevertheless, the major drawback of the PF formulation is the use of a large quantity of polymers which requires the optimization of a novel thermal treatment at elevated temperature to be removed from coatings. Moreover, it may induce a lot of porosity inside coatings. In this respect, the SF formulation has been preferred, even if the fast drying of this composition generates a “coffee-ring” effect during the evaporation of solvents. This phenomenon could be avoided or reduced by heating the substrate. Thus, the results are promising but the quality of printing, as well as the drying could be improved by further investigations.

*Similarly to the airbrushing, inkjet printed coatings also need a thermal post treatment through debinding and sintering. The same problem of cracking will be encountered. Thus, a modification of the processing method and/or another thermal densification technique could help to overcome this issue. On the one hand, the laser sintering of coatings after airbrushing or printing could be a solution. It induces local heating through laser irradiation on the coating surface, and hence causes less cracking since stress relief can occur in the non-sintered part of the film. The possibility to create a patterned network by managing the cracks is also feasible. For this purpose, a laser sintering module could be installed in the printer.*

*On the other hand, the elaboration of continuous films through precursor solutions directly on the substrate through low temperature processes like a microwave-assisted solvothermal method, or the spraying of a solution on a heating spinner with a moderate temperature of 80  $^{\circ}\text{C}$ , could be considered. No further post annealing treatment is required to densify the films. However, a laser etching will be necessary for patterning. A solution to obtain direct patterns could be to transfer the spraying technique to the inkjet printing with the possibility to heat the substrate during printing.*

*Other alternatives could be mentioned as the introduction of a flexible intermediate layer on the substrate, easy to remove in order to reduce stresses between the deposited layer and the substrate, and hence less cracking. A network of patterns could be realized from a printed hydrophobic negative template inserted in a microwave filled with a precursor solution. The formation of an adhesive layer from hydrophilic precursors will occur only in the holes of the grid due to the different affinity of the precursors, hence a structured coating. Lastly, an aqueous dispersion of particles, which has been formulated in this study by transferring the organic dispersion in water through the addition of a transferring agent, could be applied to a crack patterning method. The principle is to control the solvent evaporation to generate periodic cracks in a film deposited by dip-coating.*

The magnetic properties of particles and continuous coatings elaborated by airbrushing have been explored. The static magnetic properties have evidenced different magnetic behaviors at the particle scale. The magnetization cycle of SP(F)M particles does not saturate at high fields, whereas it saturates for FM particles. The SP(F)M particles are therefore superparamagnetic.

In addition, the saturation magnetizations of SP(F)M (85.6 emu/g or A.m<sup>2</sup>/kg) and FM (80.6 emu/g or A.m<sup>2</sup>/kg) particles are lower than the one of the bulk for the same composition (98.8 emu/g or A.m<sup>2</sup>/kg). This reduction of magnetization could come from multiple reasons: a surface oxidation of particles, an inversion degree of the spinel structure and surface spin-canting. The magnetization loops have been also measured for annealed particles at different temperatures. A decrease of the magnetization between 300 and 770 °C, attributed to the formation of zinc substituted wüstite has been observed.

A corrected Bercoff model based on the molecular field theory enables to calculate the magnetic moments of particles and to compare the results to the experiment. Many hypotheses have been tested to compute these magnetic moments: surface oxidation, inversion degree and surface spin-canting.

The trend noticed for particles regarding the magnetization as a function of the annealing temperature is different than the one of coatings. A difference of reactivity between particles and coatings has been thus highlighted. The formation of zinc substituted wüstite is delayed in coatings, which leads to a higher magnetization of sintered coatings (76 emu/g or A.m<sup>2</sup>/kg) in comparison with sintered nanoparticles (22 emu/g or A.m<sup>2</sup>/kg). Furthermore, a saturation magnetization of 76 emu/g (A.m<sup>2</sup>/kg) for a sintered FM coating with 50 % of porosity is encouraging, compared to the bulk value (98.8 emu/g or A.m<sup>2</sup>/kg).

Permittivity and permeability of particles have been compared to commercial particles of Fe<sub>3</sub>O<sub>4</sub>, CoFe<sub>2</sub>O<sub>4</sub> and NiZnFe<sub>2</sub>O<sub>4</sub>. The zinc doping allows to reduce the permittivity of the material when compared to Fe<sub>3</sub>O<sub>4</sub> commercial powder, which is in agreement with the composition choice.

The level of the complex-permeability is affected by the particle size, FM particles demonstrating higher levels than SP(F)M ones. A model written by Y. Raikher for the dynamic susceptibility has been applied and it has successfully reproduced the permeability spectra of SP(F)M particles, as well as their temperature dependence. Concerning in-temperature measurements, the temperature dependence of the anisotropy field has to be taken into account. The experimental trends are perfectly recovered by the model, namely a shift of the resonance frequency towards high frequencies as well as an increase of the permeability level when the temperature decreases, and a decrease of the full width at half maximum for decreasing temperatures. This last observation needs further study.

The measured permeabilities of FM continuous coatings after debinding and sintering have displayed too weak levels to expect a control of the magnetic losses of the material through its structuration in domains, the coating being already cracked.

*An enhancement of the density of coatings is the key to obtain a better dynamic magnetic response. This could be realized through the different alternatives previously exposed about more adapted processing methods for coatings made from precursor solutions, and/or other sintering methods.*

## General conclusion references

- [1] O. Gerber *et al.*, "Low Oxidation State and Enhanced Magnetic Properties Induced by Raspberry Shaped Nanostructures of Iron Oxide," *J. Phys. Chem. C*, vol. 119, no. 43, pp. 24665–24673, Oct. 2015, doi: 10.1021/acs.jpcc.5b08164.
- [2] S. Xuan, F. Wang, Y.-X. J. Wang, J. C. Yu, and K. C.-F. Leung, "Facile synthesis of size-controllable monodispersed ferrite nanospheres," *J. Mater. Chem.*, vol. 20, no. 24, p. 5086, 2010, doi: 10.1039/c0jm00159g.

# Table of Figures

FIGURE 1. EXAMPLES OF A WIDE BAND TYPE MAGNETIC BEHAVIOR OF A POLYCRYSTALLINE FERRITE (A [9], C), AND A MULTIBAND ONE (D) IN THE CASE OF A STRUCTURE CONSTITUTED OF SQUARES OF PERMALLOY (B) [10]. PERMEABILITY VERSUS LOG(FREQUENCY) FOR A POLYCRYSTALLINE BULK $\text{Ni}_{0.5}\text{Zn}_{0.5}\text{Fe}_2\text{O}_4$ (C) AND A PERFECT SQUARE OF PERMALLOY ( $150 \times 150 \text{ mm}^2$ ) (D) [11].	10
FIGURE I-1. BASIC MESH FOR THE SPINEL STRUCTURE [1] [2].	15
FIGURE I-2. MOST COMMONLY CRYSTAL SHAPES ENCOUNTERED FOR MAGNETITE PHASE: OCTAHEDRAL (A-C), AND TWINNED (D) [3].	16
FIGURE I-3. ARRANGEMENTS OF MAGNETIC MOMENTS FOR MATERIALS WITH MAGNETIC ORDER	18
FIGURE I-4. SKETCH OF THE MAGNETIC DOMAINS ARRANGEMENT IN A SINGLE CRYSTAL (A) AND IN A POLYCRYSTAL (B) [14].	19
FIGURE I-5. REORGANIZATION OF THE MAGNETIC DOMAINS UNDER MAGNETIC FIELD. ARRANGEMENTS WITHOUT APPLIED FIELD (A), DOMAINS GROWTH UNDER FIELD (B) AND DOMAINS ROTATIONS UNDER FIELD (C) [14].	20
FIGURE I-6. TRANSITION AREA BETWEEN TWO DOMAINS: SHARPLY CONFIGURATION WHICH NEVER HAPPENS (A) AND PROGRESSIVELY CONFIGURATION WHICH IS CALLED A BLOCH WALL (B).	20
FIGURE I-7. BLOCH WALL (A) AND NÉEL WALL (B) WITHIN A FILM THICKNESS D.	20
FIGURE I-8. PICTURES OF A POLYCRYSTALLINE FERRITE (A) [34] AND SQUARES OF PERMALLOY ( $2 \times 2 \text{ }\mu\text{m}^2$ ) (B) [35]. DIFFERENCE OF PERMEABILITY BEHAVIOR BETWEEN A WIDE BAND (C) AND A MULTIBAND MATERIAL (D). PERMEABILITY VERSUS LOG(FREQUENCY) FOR A POLYCRYSTALLINE BULK $\text{Ni}_{0.5}\text{Zn}_{0.5}\text{Fe}_2\text{O}_4$ (C) AND A PERFECT SQUARE OF PERMALLOY ( $150 \times 150 \text{ }\mu\text{m}^2$ ) (D) [33].	24
FIGURE I-9. ORGANIZATION OF MAGNETIC MOMENTS IN A AND B SUBLATTICES FOR MAGNETITE CASE.	28
FIGURE I-10. SUMMARY TABLE OF THE GENERAL INFORMATION (PER FORMULA UNIT), ABOUT SPIN MAGNETIC MOMENT AND MAGNETIZATION OF MAGNETITE AND MAGHEMITE, FROM DUNLOP <i>ET AL.</i> [21] [42]. $M_s$ IS ABOUT 95 EMU/G FOR $\text{Fe}_3\text{O}_4$ ABOVE THE VERWEY TEMPERATURE.	29
FIGURE I-11. GENERAL DATA ABOUT $\text{Fe}^{3+}$ , $\text{Fe}^{2+}$ AND $\text{Zn}^{2+}$ IONS. HIGH SPIN NOTED HS AND LOW SPIN LS. INFORMATION FROM R.D. SHANNON [56].	30
FIGURE I-12. MEASUREMENTS OF $M_s$ AND $H_c$ AS A FUNCTION OF THE ZN AMOUNT IN $\text{Zn}_x\text{Fe}_{3-x}\text{O}_4$ FILMS [30] (A) (THE RED ARROW POINTS THE INTERESTING COMPOSITION FOR THE STUDY) AND A SCHEME OF THE YAFET-KITTEL-TYPE CANTING EFFECT (B).	31
FIGURE I-13. SATURATION MAGNETIC MOMENT IN $\mu_B$ OF VARIOUS FERRITES WITH ZN CONTENT, INCLUDING $\text{Zn}_x\text{Fe}_{3-x}\text{O}_4$ . FROM GORTER [42].	32
FIGURE I-14. CATION DISTRIBUTION ON A AND B SITES FOR $\text{Zn}_x\text{Fe}_{3-x}\text{O}_4$ COMPOSITION IN A "NORMAL" (A) AND "INVERSE" (B) SPINEL STRUCTURE.	33
FIGURE I-15. CATION DISTRIBUTION ON A AND B SITES FOR $\text{ZnFe}_2\text{O}_4$ COMPOSITION IN A "NORMAL" (A) AND "INVERSE" (B) SPINEL STRUCTURE.	34
FIGURE I-16. EVOLUTION OF THE RESISTIVITY VERSUS THE ZN CONTENT IN $\text{Zn}_x\text{Fe}_{3-x}\text{O}_4$ FILMS [30].	34
FIGURE I-17. RELATION BETWEEN THE COERCIVE FIELD AND THE PARTICLE SIZE (SOLID AND DASHED LINES FOR PARTICLES WITHOUT AND WITH INTERACTIONS, RESPECTIVELY). FROM U. JEONG <i>ET AL.</i> [67].	35
FIGURE I-18. COMPARISON BETWEEN THE DIFFERENT CHEMICAL SYNTHESIS METHODS TO ELABORATE MAGNETIC NANOPARTICLES [2] [78] [84] [104].	44
FIGURE I-19. LAMER'S DIAGRAM: MONOMER CONCENTRATION VERSUS TIME OF REACTION [114]. FROM L. WU <i>ET AL.</i> [115].	45
FIGURE I-20. (A,F) 5 (B,G) 9 (C,H) 12 (D,I) 16 AND (E,J) 22 NM NANOPARTICLES OBTAINED BY INCREASING THE BOILING POINT OF THE SOLVENT. FROM J. PARK <i>ET AL.</i> [26].	47
FIGURE I-21. A) 6 B) 7 C) 8 D) 9 E) 10 F) 11 G) 12 AND H) 13 NM NANOPARTICLES OBTAINED BY A SEED-MEDIATED GROWTH METHOD. FROM J. PARK <i>ET AL.</i> [116].	48
FIGURE I-22. EFFECT OF THE MOLAR RATIO BETWEEN SURFACTANT AND PRECURSOR AND THE SOLVENT BOILING POINT ON THE NANOPARTICLE SIZE. FROM DEMORTIÈRE <i>ET AL.</i> [27].	48
FIGURE I-23. 16 NM $\text{Fe}_3\text{O}_4$ NANOPARTICLES (TEM BRIGHT FIELD IMAGES. FROM S. SUN AND H. ZENG [119].	49
FIGURE I-24. TEM IMAGES OF A) SPHERICAL AND B) CUBIC $\gamma\text{-Fe}_2\text{O}_3$ NANOPARTICLES. FROM G. SALAZAR-ALVAREZ <i>ET AL.</i> [121].	49
FIGURE I-25. $\text{Fe}_3\text{O}_4$ NANOPARTICLES SYNTHESIS BY THERMAL DECOMPOSITION IN OCTADECENE. FROM N. R. JANA'S GROUP [122].	50
FIGURE I-26. B) TEM IMAGE AND E) HRTEM MICROGRAPH OF 19 NM NANOPARTICLES WITH CUBIC SHAPE. FROM W. BAAZIZ <i>ET AL.</i> [123].	50
FIGURE I-27. SCHEME OF A MICROWAVE REACTOR WITH A TEMPERATURE PROBE. FROM GAWANDE <i>ET AL.</i> [128].	52

FIGURE I-28. MECHANISMS OF HEATING FOR MICROWAVE AND CLASSICAL CONFIGURATIONS. FROM PERINO <i>ET AL.</i> [130].	53
FIGURE I-29. DIFFERENCE OF REACTIONAL MECHANISM FOR THE PARTICLE FORMATION FOR CLASSICAL AND MICROWAVE THERMAL DECOMPOSITION. FROM BROLLO <i>ET AL.</i> [129].	53
FIGURE I-30. LOSS TANGENT $\Delta$ FOR THE MOST COMMON SOLVENTS (2.45 GHz, 20°C). FROM GAWANDE <i>ET AL.</i> [128].	53
FIGURE I-31. SETUP SKETCH (A) AND TEMPERATURE PROFILE (B) FOR CLASSICAL THERMAL DECOMPOSITION.	56
FIGURE I-32. TG-DTA CURVES OF ACID OLEIC (90% PURITY)	57
FIGURE I-33. SUMMARY TABLE OF THE EXPERIMENTS WITH VARIATION OF SOME PARAMETERS: MOLAR RATIOS OF ZN, SOLVENT AND SURFACTANT COMPARED TO FE, MOLAR RATIO OF SOLVENT VERSUS SURFACTANT, AND ALSO A AND T <sub>3</sub> .	58
FIGURE I-34. X-RAY DIFFRACTION PATTERNS FOR THE EXPERIMENTS 1 TO 4 SUMMARIZED IN FIGURE I-33.	59
FIGURE I-35. TEM PICTURES FOR THE EXPERIMENTS 1 TO 5 SUMMARIZED IN FIGURE I-33.	60
FIGURE I-36. OCTAHEDRAL (A), POLYHEDRAL (TRUNCATED OCTAHEDRAL) (B) AND CUBIC (C) MORPHOLOGY WITH A PRECURSOR/SURFACTANT RATIO BELOW 0.58 (A), BETWEEN 0.58 AND 0.72 (B) AND BETWEEN 0.72 AND 0.78 (C). AT HIGHER RATIO, IRREGULAR PARTICLES ARE FORMED. FROM Y. YANG <i>ET AL.</i> [32].	61
FIGURE I-37. SETUP SKETCH (A) AND TEMPERATURE PROFILE (B) FOR MICROWAVE-ASSISTED THERMAL DECOMPOSITION.	62
FIGURE I-38. BOILING POINT (FROM THE SAFETY DATA SHEETS) AND THE MEASURED DIELECTRIC CONSTANT, LOSS AND LOSS TANGENT AT 2.45 GHz OF THE SOLVENTS USED. COMPARISON OF THE DIELECTRIC CONSTANTS WITH THE LITERATURE [150] [151] [152].	63
FIGURE I-39. NANOPARTICLES OBTAINED BY THERMAL DECOMPOSITION. (A) CLASSICAL AND (B) MICROWAVE HEATING.	64
FIGURE I-40. Zn <sub>0.4</sub> Fe <sub>2.6</sub> O <sub>4</sub> MICROWAVE HEATING. (A) SP(F)M AND (B) FM PARTICLES.	65
FIGURE I-41. (A) TEM AND (B-E) HRTEM IN GRAND ARM IMAGES OF THE “RASPBERRY” STRUCTURE (FM PARTICLES).	66
FIGURE I-42. VALUES OF SPECIFIC SURFACES, CUMULATIVE VOLUME TO DESORPTION AND PORE DIAMETERS ESTIMATED BY BET FOR NANOPARTICLES OBTAINED BY CLASSICAL AND MICROWAVE HEATING.	67
FIGURE I-43. EVOLUTION OF PORE DIAMETERS AND CUMULATIVE VOLUME TO DESORPTION VERSUS THE SPECIFIC SURFACE FOR CLASSICAL AND MICROWAVE SAMPLES (FIGURE I-42). DASHED LINES ARE JUST GUIDES FOR EYES.	67
FIGURE I-44. X-RAY DIFFRACTION PATTERNS OF Zn <sub>0.48</sub> Fe <sub>2.52</sub> O <sub>4</sub> (BLUE CURVE) AND Zn <sub>0.4</sub> Fe <sub>2.6</sub> O <sub>4</sub> NANOPARTICLES (FM IN RED AND SP(F)M IN ORANGE) FOR CLASSICAL AND MICROWAVE HEATING RESPECTIVELY.	68
FIGURE I-45. FREQUENCY DISTRIBUTION IN PERCENTAGE OF THE DIAMETERS OF 7 SAMPLES OF SP(F)M NANOPARTICLES.	69
FIGURE I-46. FREQUENCY DISTRIBUTION IN PERCENTAGE OF THE DIAMETERS OF 4 SAMPLES OF FM NANOPARTICLES.	70
FIGURE I-47. HIGHLIGHTING OF TWO POPULATIONS OF SIZE IN THE FREQUENCY DISTRIBUTION OF DIAMETERS FOR FM PARTICLES.	70
FIGURE I-48. HISTOGRAM DISTRIBUTIONS FITTED WITH A LOGNORMAL FUNCTION IN DARK LINES OF Zn <sub>0.4</sub> Fe <sub>2.6</sub> O <sub>4</sub> (A) SP(F)M AND (B) FM WITH SIZES OF 6.2 ± 1 nm AND 22.4 ± 11 nm RESPECTIVELY. STATISTIC MADE WITH A SET OF 1000 TO 2500 PARTICLES.	71
FIGURE I-49. SUMMARY TABLE OF THE TWO HEATING WAYS WITH ADVANTAGES AND DRAWBACKS.	72
FIGURE I-50. DISCREPANCIES BETWEEN THEORETICAL AND EXPERIMENTAL CHEMICAL COMPOSITION FOR CLASSICAL THERMAL DECOMPOSITION. X GIVEN FOR THE MOLAR QUANTITY OF ZN IN THE FORMULA Zn <sub>x</sub> Fe <sub>3-x</sub> O <sub>4</sub> . SAMPLES 1, 2, 4, 5 ADDED (FIGURE I-33).	72
FIGURE I-51. SUMMARY OF THE THEORETICAL AND EXPERIMENTAL CHEMICAL COMPOSITIONS FOR CLASSICAL AND MICROWAVE-ASSISTED THERMAL DECOMPOSITION. THE THREE EXPERIMENTAL COMPOSITIONS CORRESPONDS TO THREE MEASURES REALIZED IN THE SAME BATCH.	73
FIGURE I-52. MICROWAVE-ASSISTED THERMAL DECOMPOSITION WITH CHANGE OF ZN PRECURSOR: (A) Zn(ACAC) <sub>2</sub> AND (B) ZnCl <sub>2</sub> .	75
FIGURE I-53. X-RAY DIFFRACTION PATTERNS OF TWO DISSOCIATED EXPERIMENTS REALIZED WITH Zn(ACAC) <sub>2</sub> AND ZnCl <sub>2</sub> .	75
FIGURE I-54. COMPARISON OF CHEMICAL COMPOSITIONS FROM ICP-AES AND NANOPARTICLE SIZES WITH THE CHANGE OF ZN PRECURSOR.	76
FIGURE I-55. EFFECT OF ETHYLENE GLYCOL QUANTITY IN THE MICROWAVE SYNTHESIS. A IS THE REFERENCE CORRESPONDING TO FM PARTICLES.	77
FIGURE I-56. X-RAY DIFFRACTION PATTERNS EVIDENCING THE INFLUENCE OF EG ADDITION THROUGH A TO E EXPERIMENTS.	78
FIGURE I-57. EVOLUTION OF THE PARTICLE DIAMETER WITH THE INCREASE OF EG CONTENT (DERIVED FROM XRD) THE BLUE DASHED LINE IS JUST A GUIDE FOR THE EYES.	79
FIGURE I-58. OVERVIEW OF THE PARTICLE SIZE (FROM XRD) IN RELATION TO THE EG AMOUNT.	79
FIGURE I-59. MOLECULAR WEIGHT OF ETHYLENE GLYCOL (EG), TRIETHYLENE GLYCOL (TREG) AND POLYTETHYLENE GLYCOL (PEG).	79
FIGURE I-60. NANOPARTICLES OBTAINED BY MICROWAVE-ASSISTED THERMAL DECOMPOSITION WITH EG (A), TREG (B), AND A MIX OF EG AND TREG (C). SEE FIGURE I-61 FOR RATIOS.	80



FIGURE I-61. VOLUME QUANTITIES OF SOLVENTS AND XRD SIZES OF NANOPARTICLES SYNTHESIZED WITH EG (A), TREG (B), AND A MIX OF EG AND TREG (C).....	80
FIGURE I-62. X-RAY DIFFRACTION PATTERNS OF NANOPARTICLES SYNTHESIZED WITH EG (A), TREG (B), AND A MIX OF EG AND TREG (C).....	81
FIGURE I-63. NANOPARTICLES OBTAINED BY MICROWAVE-ASSISTED THERMAL DECOMPOSITION WITH EG (A) AND PEG (B). SEE FIGURE I-64 FOR RATIOS. ....	82
FIGURE I-64. VOLUME QUANTITIES OF SOLVENTS AND XRD SIZES OF NANOPARTICLES SYNTHESIZED WITH EG (A), AND PEG (B). ...	82
FIGURE I-65. X-RAY DIFFRACTION PATTERNS OF NANOPARTICLES SYNTHESIZED WITH EG (A), AND PEG (B). ....	82
FIGURE I-66. NANOPARTICLES OBTAINED BY MICROWAVE-ASSISTED THERMAL DECOMPOSITION WITH PEG (A) AND A COMBINATION OF PEG AND EG (B-C). SEE FIGURE I-68 FOR RATIOS. ....	83
FIGURE I-67. X-RAY DIFFRACTION PATTERNS OF NANOPARTICLES SYNTHESIZED WITH PEG (A) AND A COMBINATION OF PEG AND EG (B-C). SEE FIGURE I-68 FOR RATIOS. ....	83
FIGURE I-68. MOLAR RATIO OF SOLVENTS AND XRD SIZES OF NANOPARTICLES SYNTHESIZED WITH PEG (A) AND A COMBINATION OF PEG AND EG (B-C). ....	84
FIGURE I-69. COMPARISON OF RASPBERRY NANOPARTICLES ELABORATED IN THIS STUDY (BLUE BOX), BY XUAN <i>ET AL.</i> [165] (VIOLET BOX) AND BY GERBER <i>ET AL.</i> [158] (ORANGE BOX). ....	84
FIGURE I-70. MICROWAVE-ASSISTED THERMAL DECOMPOSITION COMPLETED UNTIL THE FIRST TEMPERATURE LEVEL ( $T_1$ , $T_1$ , FIGURE I-37.B) (A) IN COMPARISON WITH THE FULL PROTOCOL (B). ....	85
FIGURE I-71. X-RAY DIFFRACTION PATTERNS OF NANOPARTICLES REPRESENTED IN FIGURE I-70, SYNTHESIZED WITH PEG. ....	86
FIGURE I-72. MOLAR RATIO OF PEG WITH IRON PRECURSOR AND XRD SIZES OF NANOPARTICLES (A) AND (B) OF FIGURE I-70. ....	86
FIGURE I-73. REACTION STEPS DURING THERMAL PROCEDURE. ....	87
FIGURE I-74. INFLUENCE OF THE SURFACTANTS: OLEYLAMINE (OAM) AND OLEIC ACID (OA) IN THE MICROWAVE SYNTHESIS. FIGURE I-75 FOR RATIOS. ....	88
FIGURE I-75. VOLUMETRIC RATIO OF OAM VERSUS OA AND XRD SIZES OF NANOPARTICLES (A) TO (D) OF FIGURE I-74. ....	88
FIGURE I-76. NANOPARTICLES SYNTHESIZED WITH A SURFACTANT VOLUMETRIC RATIO OF 2.5 AND BY DECREASING THE VOLUME OF ODE (2 INSTEAD OF 6 ML). ....	89
FIGURE I-77. NANOPARTICLES SYNTHESIZED WITHOUT ODE EVIDENCING THE INFLUENCE OF OAM AND EG. ....	90
FIGURE I-78. COMPARISON OF THE THEORETICAL ZN/FE RATIO OF TWO SAMPLES WITH THE ONE ESTIMATED BY STEM-EDX. ....	90
FIGURE I-79. ESTIMATED ZN/FE RATIOS OF FOUR DIFFERENT NANOPARTICLES IN SAMPLE A (FIGURE I-74, FIGURE I-75). ....	92
FIGURE I-80. INFRARED SPECTRUM OF THE SP(F)M AND FM NANOPARTICLES AFTER 4 AND 6 CLEANING STEPS RESPECTIVELY. ....	94
FIGURE I-81. INFRARED SPECTRUM OF THE SP(F)M (4 CLEANING STEPS) (A) AND FM (6 CLEANING STEPS) (B) NANOPARTICLES (ZOOM ON THE FE-O VIBRATIONAL BAND). ....	94
FIGURE I-82. INFRARED SPECTRUM OF IRON OXIDE NANOPARTICLES WITH 5 (NP5), 12 (NP12) AND 16 (NP16) NM DIAMETER, CORRELATED TO PURE MAGNETITE AND MAGHEMITE. FROM M. PAULY [2]. ....	95
FIGURE I-83. ESTIMATED CRYSTALLITE SIZE OF $Zn_xFe_{3-x}O_4$ PARTICLES THROUGH TEM, SCHERRER AND RIETVELD ANALYSIS. INFORMATION ABOUT ZN CATIONS POSITIONS ON THE TETRAHEDRAL AND OCTAHEDRAL SITES. ....	97
FIGURE I-84. EVOLUTION OF THE EXPERIMENTAL LATTICE PARAMETERS AS A FUNCTION OF THE ZN CONTENT IN THE CASE OF $Zn^{2+}$ SUBSTITUTED MAGHEMITE (A) AND MAGNETITE COMPOSITION (B). THE POINTS ARE CORRELATED TO A FIT FROM BATISTA <i>ET AL.</i> [176] (A) AND WITH THE PAUL POIX'S METHOD. ....	98
FIGURE I-85. TYPICAL ATOMIC RESOLVED HAADF IMAGES OF AN AREA OF AN ORIENTATED PARTICLE ALONG [211] (A) AND [100] (B).....	100
FIGURE I-86. (A) TYPICAL ATOMIC RESOLVED HAADF IMAGE OF AN AREA OF AN ORIENTATED PARTICLE ALONG [101], (B) POSITION OF FE AND ZN CATIONS IN THE SPINEL STRUCTURE, (C) SPINEL STRUCTURE IN 3D. ....	100
FIGURE I-87. (A) HAADF IMAGE OF A PARTICLE ORIENTED ALONG [101] WITH THE FOLLOWING HAADF-EELS CHEMICAL MAPPING (B), Fe (C) AND Zn (D) $L_{2,3}$ EELS SPECTRA. ....	101
FIGURE I-88. HAADF-EELS CHEMICAL MAPPINGS OF A PARTICLE ORIENTED ALONG [101]. ....	101
FIGURE I-89. MÖSSBAUER SPECTRA OF $Zn_{0.2}Fe_{2.6}O_4$ AND FM PARTICLES AT 77 AND 300 K. ....	102
FIGURE I-90. MEAN VALUES OF ISOMER SHIFT AND THE CORRESPONDING PROPORTIONS OF $Zn^{2+}$ SUBSTITUTED MAGNETITE AND MAGHEMITE FOR $Zn_{0.2}Fe_{2.6}O_4$ AND FM PARTICLES. ....	103
FIGURE I-91. MÖSSBAUER SPECTRA OF SP(F)M PARTICLES AT 77 AND 300 K. ....	104
FIGURE I-92. MEAN VALUE OF ISOMER SHIFT OF SP(F)M PARTICLES AT 300 K. ....	104
FIGURE I-93. REFINED VALUES OF THE HYPERFINE PARAMETERS ESTIMATED FROM THE IN-FIELD MÖSSBAUER SPECTRA (SEE FIGURE I-94) OBTAINED ON SP(F)M, $Zn_{0.2}Fe_{2.6}O_4$ AND FM PARTICLES. ....	106

FIGURE I-94. MÖSSBAUER SPECTRA OF SP(F)M (TOP), $Zn_{0.2}Fe_{2.6}O_4$ (MIDDLE )AND FM (BOTTOM) PARTICLES AT 14K UNDER AN EXTERNAL MAGNETIC FIELD OF 8T APPLIED PARALLEL TO THE $\gamma$ -BEAM. ....	106
FIGURE I-95. COMPARISON BETWEEN THEORETICAL CHEMICAL COMPOSITION AND THE ONE DETERMINED BY ICP-AES AT THE GLOBAL SCALE. ....	107
FIGURE I-96. SEM-FEG OF SP(F)M (A) AND FM PARTICLES (B-D) PRESSED IN PELLETS. ....	107
FIGURE I-97. CHEMICAL MAPPING OF SP(F)M PARTICLES. ....	108
FIGURE I-98. CHEMICAL COMPOSITION DETAILS OF SP(F)M PARTICLES AT THE LOCAL SCALE (FIGURE I-97). ....	108
FIGURE I-99. CHEMICAL MAPPING OF FM PARTICLES. ....	109
FIGURE I-100. CHEMICAL COMPOSITION DETAILS OF FM PARTICLES AT THE LOCAL SCALE IN TWO DIFFERENT AREAS. ....	109
FIGURE I-101. SUMMARY TABLE OF THE GLOBAL AND LOCAL CHEMICAL COMPOSITION FOR SP(F)M AND FM PARTICLES. ....	109
FIGURE II-1. ELABORATION OF COATINGS THROUGH AIRBRUSHING AND THERMAL TREATMENTS. ....	125
FIGURE II-2. SKETCHES OF PARTICLE ATTRACTION INTERACTIONS: VAN DER WAALS FORCES (A), ELECTROSTATIC FORCES (B) AND MAGNETIC FORCES (C) [1]. ....	126
FIGURE II-3. SCHEME OF THE ELECTRICAL DOUBLE LAYER (PARTICLES WITH POSITIVE CHARGE SURFACES) AND RELATION BETWEEN ELECTROSTATIC POTENTIAL AND DISTANCE FROM THE SURFACE PROPOSED BY STERN [4]. ....	127
FIGURE II-4. INFLUENCE OF HÜCKEL AND SMOLUCHOWSKI APPROACH IN THE ELECTROPHORETIC MOBILITY $M$ OF PARTICLES. ....	128
FIGURE II-5. INDICATION OF THE DISPERSION STABILITY AS A FUNCTION OF THE ZETA POTENTIAL. FROM VALLAR ET AL. [7]. ....	129
FIGURE II-6. ZETA POTENTIAL BEHAVIOR AS A FUNCTION OF PH. ....	129
FIGURE II-7. TOTAL POTENTIAL ENERGY AS A FUNCTION OF THE DISTANCE FOLLOWING THE DLVO THEORY. FROM DICKERSON ET AL. [5]. ....	130
FIGURE II-8. SHORT AND LONG RANGE ARRANGEMENTS OF CO NANOPARTICLES WITHOUT (A) AND WITH (B) EXTERNAL FIELD. FROM TRIPP ET AL. [22]. ....	131
FIGURE II-9. STERIC HINDRANCE PRINCIPLE. ....	132
FIGURE II-10. SUMMARY OF THE EFFECT ENGENDERED BY THE STABILIZATION METHODS. ....	133
FIGURE II-11. ADVANTAGES AND DRAWBACKS OF ELECTROSTATIC AND STERIC STABILIZATION. FROM HUNTER ET AL. [25]. ....	133
FIGURE II-12. SCHEME OF A SURFACTANT MOLECULE. ....	133
FIGURE II-13. SURFACE TENSION AS A FUNCTION OF THE SURFACTANT CONCENTRATION IN LOGARITHMIC SCALE. ....	135
FIGURE II-14. DISPERSION OF FERRITE PARTICLES SYNTHESIZED BY THERMAL DECOMPOSITION IN ORGANIC SOLVENTS. ....	136
FIGURE II-15. INFRARED SPECTRUM OF THE EVOLUTION OF NANOPARTICLE CLEANINGS BY CENTRIFUGATION. ....	139
FIGURE II-16. AREA UNDER CURVE (AUC) OF THE CHARACTERISTIC BANDS OBSERVED BY FTIR (FIGURE II-15) DURING CLEANINGS BY CENTRIFUGATION. AUC ARE CALCULATED WITH ORIGIN. ....	139
FIGURE II-17. RATIOS OF THE AUC OF THE BANDS CHARACTERISTIC OF THE ORGANICS TO THE ONE OF THE MATERIAL AS A FUNCTION OF THE NUMBER OF CLEANINGS. ....	140
FIGURE II-18. CONCENTRATIONS (WT%) IN Fe, Zn, C AND N IN FM PARTICLES, WASHED 2 AND 6 TIMES. ....	140
FIGURE II-19. SET-UP FOR CLEANING IN A HEATING MANTLE. ....	141
FIGURE II-20. INFRARED SPECTRUM OF THE EVOLUTION OF NANOPARTICLE CLEANING BY REFLUX. ....	141
FIGURE II-21. AREA UNDER CURVE (AUC) OF THE CHARACTERISTIC BANDS OBSERVED BY FTIR (FIGURE II-20) DURING CLEANING BY REFLUX. AUC ARE CALCULATED WITH ORIGIN. ....	142
FIGURE II-22. RATIOS OF THE AUC OF THE BANDS CHARACTERISTIC OF THE ORGANICS TO THE ONE OF THE MATERIAL AS A FUNCTION OF THE REFLUX DURATION. ....	142
II-5 143	
FIGURE II-23. MIXTURE OF PARTICLES WITH TOLUENE AND ETHANOL. ....	143
FIGURE II-24. SIZE DISTRIBUTION IN NUMBER BY DLS. ....	144
FIGURE II-25. INFRARED SPECTRUM OF THE EVOLUTION OF NANOPARTICLE CLEANING BY ESTERIFICATION. ....	145
FIGURE II-26. SOXHLET EXTRACTION SET-UP. ....	146
FIGURE II-27. COMPARISON BETWEEN THE CENTRIFUGATIONS AND THE SOXHLET METHOD BY FTIR. ....	146
FIGURE II-28. AREA UNDER CURVE (AUC) OF THE CHARACTERISTIC BANDS OBSERVED BY FTIR (FIGURE II-27) WITH THE SOXHLET METHOD. AUC ARE CALCULATED WITH ORIGIN. ....	147
FIGURE II-29. OVERVIEW OF THE DIFFERENT CLEANINGS METHODS TESTED WITH THE CORRESPONDING ORGANIC/INORGANIC RATIOS AND THE CLEANING EFFICIENCY. ....	147
FIGURE II-30. SURFACE TENSION VERSUS THE CONCENTRATION OF DISPERBYK 180 IN LOGARITHMIC SCALE. ....	148
FIGURE II-31. DISPERSION TESTS WITH A NiZnFeO COMMERCIAL POWDER, (A) AFTER ULTRASONICATION (B) AFTER BEING LEFT FOR A FEW MINUTES. ....	149

FIGURE II-32. AQUEOUS DISPERSION OF SP(F)M PARTICLES (3 WT%) WITH TMAOH. ....	149
FIGURE II-33. SP(F)M PARTICLES BEFORE (A) AND AFTER (B) AQUEOUS DISPERSION WITH TMAOH. ....	150
FIGURE II-34. FTIR SPECTRA OF THE SP(F)M PARTICLES BEFORE AND AFTER DISPERSION WITH TMAOH. ....	150
FIGURE II-35. DTA-TGA OF AN AQUEOUS DISPERSION OF SP(F)M PARTICLES (3 WT%) WITH TMAOH. ....	151
FIGURE II-36. X-RAY DIFFRACTION PATTERN OF SP(F)M PARTICLES BEFORE DISPERSION AND ANNEALED AT 200 °C AFTER DISPERSION. ....	151
FIGURE II-37. SUMMARY OF THE DISPERSION TESTS IN POLAR MEDIA. ....	152
FIGURE II-38. TEST OF PEPTIZATION OF SP(F)M PARTICLES IN ETHANOL WITH HCL. ....	153
FIGURE II-39. NEW STRATEGIES OF DISPERSION. ....	153
FIGURE II-40. DISPERSION OF SP(F)M PARTICLES IN HEXANE. ....	153
FIGURE II-41. PROCESS OF DISPERSION IN HEXANE STARTING FROM THE SYNTHESIS. ....	154
FIGURE II-42. SIZE DISTRIBUTIONS IN NUMBER BY DLS FOR SP(F)M (A) AND FM (B) PARTICLES. TABLE RELATED TO THE MEAN SIZE CALCULATED FROM DLS MEASUREMENTS (C). ....	155
FIGURE II-43. INFLUENCE OF THE NUMBER OF CLEANING <i>N</i> ON THE PRESENCE OF ORGANICS AROUND PARTICLES BY FTIR. ....	156
FIGURE II-44. AREA UNDER CURVE (AUC) OF THE CHARACTERISTIC BANDS OBSERVED BY FTIR (FIGURE II-43). AUC ARE CALCULATED WITH ORIGIN. ....	156
FIGURE II-45. RATIOS OF THE AUC OF THE BANDS CHARACTERISTIC OF THE ORGANICS TO THE ONE OF THE MATERIAL AS A FUNCTION OF THE NUMBER OF CLEANINGS <i>N</i> . ....	157
FIGURE II-46. VISUAL APPEARANCE OF COATINGS AFTER ANNEALING AT 300 °C DURING 30 MINUTES UNDER ARGON ATMOSPHERE AS A FUNCTION OF THE NUMBER OF CLEANINGS <i>N</i> . ....	157
FIGURE II-47. TRANSFER OF THE ORGANIC DISPERSION TO AN AQUEOUS MEDIUM. ....	158
FIGURE II-48. SIZE DISTRIBUTIONS IN NUMBER BY DLS FOR SP(F)M PARTICLES DISPERSED IN WATER. ....	159
FIGURE II-49. TABLE RELATED TO THE MEAN SIZE CALCULATED FROM DLS MEASUREMENTS (FIGURE II-48). ....	159
FIGURE II-50. DISPERSION OF SP(F)M PARTICLES IN WATER. ....	159
FIGURE II-51. EXPERIMENTAL SET-UP. ....	163
FIGURE II-52. COATINGS OBTAINED WITH A DISPERSION OF SP(F)M PARTICLES IN HEXANE (3 WT%). ....	164
FIGURE II-53. COATINGS WITH A DISPERSION OF FM PARTICLES IN HEXANE (8 WT%) ON ALUMINE (A) AND SILICON WAFERS (B). .	164
FIGURE II-54. FE-O PHASE DIAGRAM WITH FeO FOR WÜSTITE AND A-Fe <sub>2</sub> O <sub>3</sub> FOR HEMATITE. FROM A. RANZANI DA COSTA [40] [41] [42]. ....	165
FIGURE II-55. ZN-FE-O PHASE DIAGRAM IN AIR. FROM A. SERGEI <i>ET AL.</i> [43]. ....	165
FIGURE II-56. EFFECT OF A SINTERING AT 950 °C ON NiZn FERRITE FILMS (A) AND ITS CORRESPONDING PERMEABILITY SPECTRA. FROM M. BISSANNAGARI <i>ET AL.</i> [30]. ....	166
FIGURE II-57. OBSERVATION OF A COLOR CHANGE BETWEEN A SP(F)M COATING ANNEALED UNDER AIR AND ARGON ATMOSPHERE DURING 24H AT ~100 °C. ....	167
FIGURE II-58. EFFECT OF THE ANNEALING ATMOSPHERE ON THE DEBINDING OF SP(F)M (A) AND FM (B) POWDERS AT 450 °C. THE TABLE SUMMARIZES THE CRYSTALLITE SIZES BEFORE AND AFTER DEBINDING FROM SCHERRER EQUATION. ....	168
FIGURE II-59. TG-DTA AND MASS SPECTROSCOPY CURVES OF OAM AND OA UNDER HELIUM. ....	169
FIGURE II-60. TG-DTA AND MASS SPECTROSCOPY CURVES OF SP(F)M AND FM PARTICLES UNDER HELIUM UNTIL 600 °C. ....	170
FIGURE II-61. SCHEME OF THE INTERACTION BETWEEN CARBOXYLATE GROUP AND PARTICLE SURFACE. FROM ZHANG <i>ET AL.</i> [49]. .	171
FIGURE II-62. DERIVATIVE OF THE WEIGHT LOSS FOR SP(F)M AND FM PARTICLES UNDER HELIUM. ....	171
FIGURE II-63. INTERACTION OF OLEIC ACID (COOH) WITH PARTICLES THROUGH MONODENTATE (A), BRIDGED (B) AND CHELATING (C) CONFIGURATIONS. ....	172
FIGURE II-64. FOCUS ON THE 1300-1700 CM <sup>-1</sup> AREA OF FTIR SPECTRA FOR SP(F)M AND FM PARTICLES DIRECTLY AFTER SYNTHESIS. ....	173
FIGURE II-65. COMPARISON OF TG CURVES OF OAM, OA, SP(F)M AND FM PARTICLES UNDER HELIUM. ....	174
FIGURE II-66. CALCULATION OF THE NUMBER OF OA LAYER (N <sub>OA LAYER</sub> ) AROUND PARTICLES. ....	175
FIGURE II-67. EXPERIMENTAL SCHEME OF THE SET-UP OF THE TUBE OVEN UNDER AN ARGON FLOW OF 2.5 L/MIN. ....	176
FIGURE II-68. TEMPERATURE PROFILE OF THE DEBINDING STEP. ....	176
FIGURE II-69. EXAMPLES OF CRACKS (A, B) AND BUBBLING (C, D) AT THE SURFACE OF SP(F)M COATINGS (SEM-FEG). ....	177
FIGURE II-70. INCIDENCE OF A FAST TEMPERATURE RAMP (300 °C/H) ON COATINGS. ....	177
FIGURE II-71. OPTICAL MICROSCOPY OF FM COATINGS BEFORE ANNEALING (4 APPLICATIONS BY AIRBRUSHING). ....	178
FIGURE II-72. OPTICAL MICROSCOPY OF SP(F)M (A, B) AND FM (C, D) COATINGS AFTER DEBINDING UNDER ARGON. ....	178
FIGURE II-73. CHEMICAL MAPPINGS OF A SP(F)M COATING ON A GLASS SUBSTRATE AFTER DEBINDING. ....	179

FIGURE II-74. DILATOMETRY CURVE OF A PELLET OF FM PARTICLES HEATED FROM ROOM TEMPERATURE TO 1000 °C UNDER ARGON.	180
.....	180
FIGURE II-75. SEM IMAGES OF A PELLET OF FM PARTICLES ANNEALED AT 1000 °C.	180
FIGURE II-76. TEMPERATURE PROFILE OF THERMAL TREATMENTS INCLUDING A DEBINDING AND A SINTERING STEP.	181
FIGURE II-77. SEM-FEG AT VARIOUS MAGNIFICATIONS OF SP(F)M (A-D) AND FM (E-H) COATINGS AFTER SINTERING UNDER ARGON.	182
FIGURE II-78. CROSS-SECTION VIEW OF AN EPOXY-COATED FM FILM (SEM-FEG).	183
FIGURE II-79. COMPARISON OF FM COATINGS ON SILICON WAFERS AFTER DEBINDING (A, B) AND SINTERING (C, D) UNDER ARGON (OPTICAL MICROSCOPY).	183
FIGURE II-80. COMPARISON BETWEEN FM PARTICLES SPRAYED ON A SILICON WAFER (A, B) AND ON ALUMINA (C, D) AFTER SINTERING UNDER ARGON (OPTICAL MICROSCOPY).	184
FIGURE II-81. PICTURES OF THE COATING SURFACE AFTER ANNEALING OF ADDITIONAL LAYERS IN COMPARISON WITH THE COATING REFERENCE (RED BOX). N IS THE NUMBER OF APPLICATIONS.	185
FIGURE II-82. EFFECT OF THE NUMBER OF LAYERS ON COATING SURFACE IN COMPARISON WITH THE COATING REFERENCE (RED BOX). N IS THE NUMBER OF APPLICATIONS.	187
FIGURE II-83. EFFECT OF THE PARTICLE CONCENTRATION ON COATING SURFACE IN COMPARISON WITH THE COATING REFERENCE (RED BOX). N IS THE NUMBER OF APPLICATIONS.	188
FIGURE II-84. EFFECT OF A SLOWER TEMPERATURE RAMP ON COATING SURFACE IN COMPARISON WITH THE COATING REFERENCE (RED BOX). N IS THE NUMBER OF APPLICATIONS.	189
FIGURE II-85. EFFECT OF THE USE OF TWO RANGES OF PARTICLE SIZE ON COATING SURFACE IN COMPARISON WITH THE COATING REFERENCE (RED BOX). N IS THE NUMBER OF APPLICATIONS.	190
FIGURE II-86. CROSSECTIONAL VIEW OF A NiZn FERRITE FILM AEROJET-PRINTED (A) AND INFLUENCE OF THE LASER FLUENCE ON THE SURFACE CONDITIONS OF COATINGS AFTER LASER SINTERING (B). FROM K. RAJARAM [59].	191
FIGURE II-87. OPTICAL IMAGES OF SURFACES OF SINTERED SILICA FILMS AFTER LASER SINTERING AND FURNACE HEATING. FROM J. LEI ET AL. [61].	192
FIGURE II-88. (A) CROSS-SECTIONAL VIEW OF A SPRAYED FERRITE FILM. FROM J. MIYASAKA ET AL. [62]. AND (B) OF A MICROWAVE-DEPOSITED NiFe <sub>2</sub> O <sub>4</sub> FILM. FROM R.D. RALANDINLIU KAHMEI ET AL. [64].	193
FIGURE II-89. EFFECT OF THE TEMPERATURE ON THE X-RAY DIFFRACTION PATTERNS OF FM POWDER FROM 30 TO 1000 °C UNDER ARGON.	194
FIGURE II-90. VARIATION OF THE LATTICE PARAMETER AND OF THE PARTICLE DIAMETER AS A FUNCTION OF THE TEMPERATURE FOR THE PRINCIPAL PHASE OF ZINC IRON OXIDE SPINEL IN THE CASE OF POWDER. OBTAINED FROM THE DIFFRACTOMETERS IN FIGURE II-89. THE CONFIDENCE INTERVAL (IN LIGHT RED FOR THE LATTICE PARAMETER AND LIGHT BLUE FOR THE PARTICLE DIAMETER) IS EQUAL TO THREE TIMES THE STANDARD DEVIATION. THE LAST POINT AT 30 °C IS MEASURED AFTER DECREASING TEMPERATURE.	194
FIGURE II-91. EFFECT OF THE TEMPERATURE ON THE X-RAY DIFFRACTION PATTERNS OF FM COATINGS FROM 30 TO 1000 °C UNDER ARGON.	195
FIGURE II-92. TG-DTA AND MASS SPECTROSCOPY CURVES OF SP(F)M AND FM PARTICLES UNDER HELIUM UNTIL 800 °C.	195
FIGURE II-93. THICKNESS OF THE LAYER VERSUS ITS LENGTH (C), AFTER DEBINDING (A) AND SINTERING (B).	197
FIGURE II-94. OPTICAL MICROSCOPY OF PATTERNED COATINGS AFTER DEBINDING (A IN BRIGHT FIELD, B IN DARK FIELD) AND AFTER SINTERING (C IN BRIGHT FIELD, D IN DARK FIELD).	198
FIGURE II-95. DEVELOPMENT OF MAGNETIC COATINGS BY AIRBRUSHING.	199
FIGURE III-1. TRANSFER OF THE AIRBRUSHING TOWARDS THE INKJET PRINTING.	207
FIGURE III-2. PICTURE OF THE DEVICE OF INKJET PRINTING DEVELOPED BY CERADROP (A) AND SCHEMATIC VIEW (B).	209
FIGURE III-3. EJECTION REQUIREMENTS OF AN INK.	210
FIGURE III-4. COMPARISON OF HEXANE, OCTANE AND OCTANOL IN TERMS OF BOILING POINT AND DYNAMIC VISCOSITY.	212
FIGURE III-5. VARIATION OF THE VISCOSITY (A) AND THE SHEAR STRESS (B) AS A FUNCTION OF THE SHEAR RATE FOR DIFFERENT WT% PROPORTION OF POLY(1-DECENE) IN HEXANE. THE SHEAR RATE IS IN A LOGARITHMIC SCALE IN THE A INSET.	213
FIGURE III-6. PHYSICO-CHEMICAL CHARACTERISTICS OF INK MEDIA WITH DIFFERENT WT% PROPORTION OF POLY(1-DECENE) IN HEXANE.	214
FIGURE III-7. EVOLUTION OF THE VISCOSITY AS A FUNCTION OF WEIGHT POURCENT OF PROPORTION OF DIFFERENT POLYMERS OR SOLVENTS IN HEXANE. THE BLUE BOX INDICATES THE ACCEPTED VALUES FOR COMPATIBILITY WITH THE PRINTING DEVICE.	215
FIGURE III-8. BOILING POINTS OF DIFFERENT POLYMERS OR SOLVENTS USED IN THE INK FORMULATION.	215
FIGURE III-9. PHYSICO-CHEMICAL CHARACTERISTICS OF INK MEDIA WITH 50 WT% OF POLYBUTENE 2300 AND 80 WT% OF OCTANOL IN HEXANE.	216

FIGURE III-10. VARIATION OF THE VISCOSITY AS A FUNCTION OF THE SHEAR RATE FOR THE PF MEDIUM WITHOUT AND WITH ADDITION OF SP(F)M PARTICLES IN A LOGARITHMIC SCALE. ....	217
FIGURE III-11. PHYSICO-CHEMICAL CHARACTERISTICS OF THE PF MEDIUM WITHOUT AND WITH ADDITION OF SP(F)M PARTICLES. .	217
FIGURE III-12. VARIATION OF THE VISCOSITY AS A FUNCTION OF THE SHEAR RATE FOR THE SF MEDIUM WITHOUT AND WITH ADDITION OF 8 WT% OF SP(F)M PARTICLES IN A LOGARITHMIC SCALE. ....	217
FIGURE III-13. PHYSICO-CHEMICAL CHARACTERISTICS OF THE SF MEDIUM WITHOUT AND WITH ADDITION OF 8 WT% OF SP(F)M PARTICLES. ....	218
FIGURE III-14. PHYSICO-CHEMICAL CHARACTERISTICS OF PF AND SF FORMULATIONS OF INK WITH 0.2 AND 8 WT% OF SP(F)M PARTICLES. ....	219
FIGURE III-15. PERMALLOY DISKS WITH A 500 NM RADIUS ON A SCANNING-ELECTRON MICROGRAPH (A), AND MAGNETIC FORCE MICROGRAPHS UNDER A FIELD OF 0 (B) AND 70 mT (C). FROM A. VOGEL <i>ET AL.</i> [19]. SEM IMAGE OF SILICA MICRODOTS ON A SILICON WAFER OBTAINED BY INKJET PRINTING (D). FROM O. DE LOS COBOS <i>ET AL.</i> [20]. ....	221
FIGURE III-16. PRINCIPLE SCHEME OF WORKING OF INKJET PRINTING [1]. ....	222
FIGURE III-17. SCHEME OF DROPLET EJECTION THROUGH A PIEZOELECTRIC NOZZLE. FROM J-J. ELTGEN [21]. ....	223
FIGURE III-18. ELECTRICAL PULSE APPLIED TO PIEZOELECTRIC NOZZLES. ....	223
FIGURE III-19. OBSERVATION BY A CCD CAMERA OF AN INK FILAMENT IN A COLUMNAR SHAPE (A), GENERATING PERFECT (B), OR SATELLITE (C) DROPLETS (PF FORMULATION). (EXPOSURE TIME = 200 $\mu$ s). ....	224
FIGURE III-20. SQUARE (A), CENTERED SQUARE (B) AND HEXAGONAL (C) MESH TYPES. ....	224
FIGURE III-21. FILLING OF A SQUARE PATTERN USING A SQUARE MESH TYPE WITH SPACED (A), IN CONTACT (B) AND OVERLAPPED (C) SPLATS. ....	225
FIGURE III-22. INCLINATION OF THE PRINTHEAD TO ALLOW THE OVERLAPPING OF DROPLETS. ....	225
FIGURE III-23. TOP VIEW OF THE CONFIGURATION OF THE PRINTING HEAD DURING PROCESSING WITH A TILT ANGLE [22]. ....	226
FIGURE III-24. PRINTING STRATEGIES WITH THE SQUARE MESH: FREE (A) AND TRAPEZE (B) MODES. ....	227
FIGURE III-25. PICTURES OF THE EJECTION OF DROPLETS AT 60 V WITH PF (A) AND SF (B) FORMULATIONS. THE RED LINE PINPOINTS THE BOTTOM OF THE NOZZLE PLATE. ....	229
FIGURE III-26. EXAMPLE OF PRINTED SPLATS WITH THE PF FORMULATION WITH 0.2 WT% OF SP(F)M PARTICLES. ....	229
FIGURE III-27. SQUARE PATTERNS PRINTED WITH PERFECT (A) AND COLUMNAR (B) DROPLETS WITH THE PF FORMULATION (0.2 WT% PARTICLES). ....	230
FIGURE III-28. EVOLUTION OF THE DESIGN OF THE SQUARES PRINTED AT DIFFERENT LOCATIONS OF THE SUBSTRATE WITH THE PF FORMULATION (0.2 WT% OF SP(F)M PARTICLES): AT THE BEGINNING OF A LINE (RED BOX) AND AT THE END OF A LINE (BLUE BOX). ....	231
FIGURE III-29. ENHANCEMENT OF THE PRINTING QUALITY BY USING ONLY ONE IN FOUR NOZZLES (PF FORMULATION WITH 0.4 WT% OF SP(F)M PARTICLES). ....	232
FIGURE III-30. ENHANCEMENT OF THE PRINTING QUALITY OF SWISS CROSS PATTERNS PRINTED WITH THE PF FORMULATION (0.4 %WT PARTICLES). ....	233
FIGURE III-31. OBSERVATION OF THE FAMOUS "COFFEE-RING" EFFECT DURING THE DRYING OF SPLATS WITH THE SF FORMULATION WITH 0.2 WT% OF SP(F)M PARTICLES. ....	234
FIGURE III-32. « COFFEE-RING EFFECT » OBSERVED IN THE CASE OF DEPOSITION OF SPHERICAL PARTICLES OF POLYSTYRENE IN WATER (A) AND NOT WITH ELLIPSOIDAL ONES (B). FROM P. J. YUNKER <i>ET AL.</i> [26]. ....	235
FIGURE III-33. SCHEME OF THE EFFECT OF CAPILLARY FLUX (A) AND MARANGONI FLUX (B) ON THE DRYING OF A DROPLET ON A SUBSTRATE. ....	235
FIGURE III-34. BINARY PHASE DIAGRAM OF AN HEXANE IN OCTANOL MIXTURE. FROM [30]. ....	236
FIGURE III-35. DRYING OF A SQUARE PATTERN FROM A TO B PRINTED WITH THE SF FORMULATION 2 WITHOUT PARTICLES. ....	236
FIGURE III-36. TESTS OF PRINTING OF SQUARE PATTERNS WITH THE SF FORMULATION (0.2 WT% OF SP(F)M PARTICLES). ....	237
FIGURE III-37. IMPROVEMENT OF THE SQUARE SHAPE FROM A TO B BY CHANGING THE MESH FILLING IN CERASLICE (SF FORMULATION WITH 0.2 WT% OF SP(F)M PARTICLES). ....	237
FIGURE III-38. ADDITION OF DROPS IN THE MESH FILLING OF PATTERNS IN THE SIMULATOR IN CERASLICE. ....	238
FIGURE III-39. NETWORK OF SPHERICAL PATTERNS PRINTED WITH THE SF FORMULATION WITH 0.2 WT% OF SP(F)M PARTICLES. .	238
FIGURE III-40. COMPARISON OF SQUARE PATTERNS DEPOSITED WITH THE PF (A) AND SF (B) FORMULATION WITH LESS THAN 1 WT% OF SP(F)M PARTICLES. ....	239
FIGURE III-41. PRINTING OF SQUARE PATTERNS (1x1 cm <sup>2</sup> ) WITH SF FORMALTION (8 WT% SP(F)M PARTICLES) AS A FUNCTION OF THE NUMBER OF LAYER ET THE SPLAT OVERLAPPING. ....	239
FIGURE III-42. DIFFERENT STEPS OF DEVELOPMENT OF NETWORK OF PATTERNS THROUGH THE INKJET PRINTING PROCESS. ....	241

FIGURE III-43. PRINTING OF PATTERNS WITH PF AND SF FORMULATIONS OF INK.....	242
FIGURE III-44. COMPARISON BETWEEN AIRBRUSHING AND INKJET PRINTING.....	243
FIGURE IV-1. SCHEME OF THE OVERALL PROCESS FROM THE NANOPARTICLE SYNTHESIS TO THE ELABORATION OF COATINGS THROUGH AIRBRUSHING AND INKJET PRINTING. ....	248
FIGURE IV-2. SCHEME OF A MAGNETIZATION CURVE WITH AN HYSTERESIS CYCLE (DASHED LINE) AND CURVE OF FIRST MAGNETIZATION (CONTINUOUS LINE). FROM M. SCHOTT [1]. ....	249
FIGURE IV-3. MEASURED MAGNETIZATION CURVES OF FM AND SP(F)M PARTICLES. MASS MAGNETIZATION VERSUS THE APPLIED FIELD. ....	251
FIGURE IV-4. MEASURED AND FITTED MAGNETIZATION CURVES OF SP(F)M PARTICLES WITH (A) AND WITHOUT (B) ORGANICS. MASS MAGNETIZATION $M$ VERSUS THE APPLIED FIELD $H$ . ....	252
FIGURE IV-5. HYSTERESIS LOOP AT 2 K OF SP(F)M PARTICLES. MASS MAGNETIZATION $M$ VERSUS THE APPLIED FIELD $H$ . ....	253
FIGURE IV-6. ZFC/FC MEASUREMENTS FOR FM (A) AND SP(F)M (B) PARTICLES.....	253
FIGURE IV-7. SATURATION MAGNETIZATIONS $M_S$ OF ZINC IRON OXIDE NANOPARTICLES WITH A COMPOSITION CLOSE TO THE ONE OF FM AND SP(F)M PARTICLES. ....	254
FIGURE IV-8. HYSTERESIS LOOP AT 300 K OF FM PARTICLES WITH DIFFERENT COMPOSITIONS: $Zn_{0.2}Fe_{2.8}O_4$ AND $Zn_{0.4}Fe_{2.6}O_4$ MEASURED WITH A VSM-SQUID MAGNETOMETER. MASS MAGNETIZATION $M$ VERSUS THE APPLIED FIELD $H$ . ....	255
FIGURE IV-9. TEM PICTURES OF $ZnFe_2O_4$ SPHERICAL PARTICLES WITH DIAMETERS COMPRISED BETWEEN 5 AND 7 NM. ....	257
FIGURE IV-10. CHEMICAL PROPORTIONS BETWEEN REACTANTS FOR THE SYNTHESIS OF SP(F)M AND $ZnFe_2O_4$ PARTICLES.....	257
FIGURE IV-11. MEASURED AND FITTED MAGNETIZATION CURVES OF $ZnFe_2O_4$ PARTICLES WITH DIAMETERS COMPRISED BETWEEN 5 AND 7 NM. MASS MAGNETIZATION $M$ VERSUS THE APPLIED FIELD $H$ . ....	258
FIGURE IV-12. CATION DISTRIBUTION ON TETRAHEDRAL AND OCTAHEDRAL SITES FOR $ZnFe_2O_4$ COMPOSITION AT THE BULK (LEFT) AND NANOPARTICLE (RIGHT) SCALE. ....	258
FIGURE IV-13. MEASURED MAGNETIZATION CURVES OF FM PARTICLES ANNEALED AT DIFFERENT TEMPERATURES. MASS MAGNETIZATION $M$ VERSUS THE APPLIED FIELD $H$ . ....	259
FIGURE IV-14. EVOLUTION OF THE SATURATION MAGNETIZATION $M_S$ AND OF THE PARTICLE DIAMETER OF FM PARTICLES AS A FUNCTION OF THE TEMPERATURE. ....	260
FIGURE IV-15. MOMENT $N_B$ PER FORMULA UNIT AS A FUNCTION OF THE MOLAR QUANTITY $x$ IN THE FOLLOWING FORMULA ( $Zn_xFe_{1-x}[Li_{0.5-x/2}Fe_{1.5-x/2}]O_4$ ) AND COMPARISON WITH THEORETICAL PREDICTIONS. FROM C. E. PATTON AND Y-H. LIU [41]. ....	262
FIGURE IV-16. SCHEME OF THE CONFIGURATIONS OF SPINS IN ZN SUBSTITUTED FERRITES. FROM P.G. BERCOFF AND H.R. BERTORELLO [40]. ....	263
FIGURE IV-17. MOMENT $N_B$ PER FORMULA UNIT AS A FUNCTION OF THE ZN MOLAR QUANTITY $x$ . COMPARISON BETWEEN MODEL AND EXPERIMENTS. FROM P.G. BERCOFF AND H.R. BERTORELLO [40]. ....	264
FIGURE IV-18. SCHEME OF THE SPIN-CANTING OF $I$ SITES SURROUNDING A VACANCY IN A $J$ SITE. FROM G.F. DIONNE [42]. ....	265
FIGURE IV-19. COMPARISON OF THE THREE MOLECULAR FIELDS OF C.E. PATTON AND Y-H. LIU, P.G. BERCOFF AND H.R. BERTORELLO, AND G.F. DIONNE. ....	266
FIGURE IV-20. CORRECTIONS OF THE BERCOFF MODEL. ....	267
FIGURE IV-21. FIT OF THE EXPERIMENTAL DATA FOR $Ni_{(1-z)}Zn_zFe_2O_4$ FERRITE FROM E.W. GORTER [39] WITH THE UNCORRECTED AND CORRECTED BERCOFF MODEL AND COMPARISON WITH THE NÉEL MODEL. ....	267
FIGURE IV-22. VALUES OF EXCHANGE CONSTANTS FOR VARIOUS INTERACTIONS OF CATIONS. FROM P.G. BERCOFF AND H.R. BERTORELLO [43]. ....	268
FIGURE IV-23. PARAMETERS USED IN THE CORRECTED FIT PLOTTED IN FIGURE IV-24. ....	268
FIGURE IV-24. FIT OF THE EXPERIMENTAL DATA FOR $Zn_zFe_{3-2z}O_4$ FERRITE FROM E.W. GORTER [39] WITH THE CORRECTED BERCOFF MODEL AND COMPARISON WITH THE NÉEL MODEL (ALL OF THE ZINC IS LOCATED AT THE TETRAHEDRAL SITES). ....	269
FIGURE IV-25. EXCHANGE CONSTANTS $JAB'$ AND $JBB'$ FOR THE INTER AND INTRASUBLATTICE INTERACTIONS IN THE CASE OF THE $NiZn$ AND $FeZn$ COMPOSITIONS. ....	270
FIGURE IV-26. PARAMETERS USED IN THE CORRECTED FIT PLOTTED IN FIGURE IV-27. ....	271
FIGURE IV-27. COMPARISON BETWEEN NÉEL AND BERCOFF MODELS AS A FUNCTION OF THE ZN ATOMIC FRACTION IN OCTAHEDRAL SITES FOR A ZN TOTAL CONTENT OF 0.2 (A) AND 0.4 (B). ....	271
FIGURE IV-28. MAGNETIC MOMENT AS A FUNCTION OF ZINC ATOMIC FRACTION WITH THREE DIFFERENT CONFIGURATIONS DEPENDING ON THE LOCATION OF IRON AND ZINC IN MAGHEMITE. COMPARISON WITH THE EXPERIMENTAL POINT AT 0 K. ....	273
FIGURE IV-29. MAGNETIC MOMENT AND LATTICE CONSTANT OF ZINC SUBSTITUTED SPINEL AND MAGHEMITE AS A FUNCTION OF THE ZINC MOLAR FRACTION. FROM Y. KHAN AND E. KNELLER [47]. ....	274
FIGURE IV-30. PREDICTED MAGNETIC MOMENTS FOR FM PARTICLES WITH DIFFERENT ZN CONTENTS (0.2 AND 0.4). ....	274

FIGURE IV-31. MEASURED MAGNETIC MOMENTS AT 2 K OF SP(F)M AND FM PARTICLES WITH DIFFERENT ZN CONTENTS (0.2 AND 0.4).	274
FIGURE IV-32. MAGNETIZATION OF SP(F)M AND FM PARTICLES AFTER REMOVAL OF THE CONTRIBUTION OF SURFACE SPIN-CANTING.	275
FIGURE IV-33. MAGNETIC MOMENTS PREDICTED FROM VARIOUS MODELS FOR SP(F)M AND FM PARTICLES WITH DIFFERENT ZN CONTENTS (0.2 AND 0.4) IN DIFFERENT CONFIGURATIONS (CASES 1 TO 3).	277
FIGURE IV-34. MEASURED MAGNETIZATION CURVES OF SP(F)M COATINGS AFTER ANNEALING AT 300 °C AS A FUNCTION OF THE NUMBER OF CENTRIFUGATION CYCLES $N$ . MASS MAGNETIZATION $M$ VERSUS THE APPLIED FIELD $H$ .	281
FIGURE IV-35. EFFECT ON THE DEBINDING (450 °C) ON THE MEASURED MAGNETIZATION OF SP(F)M AND FM COATINGS. MASS MAGNETIZATION $M$ VERSUS THE APPLIED FIELD $H$ .	283
FIGURE IV-36. EFFECT ON THE DEBINDING (450 °C) AND SINTERING (770 °C) ON THE MEASURED MAGNETIZATION OF FM COATINGS. MASS MAGNETIZATION $M$ VERSUS THE APPLIED FIELD $H$ .	284
FIGURE IV-37. EVOLUTION OF THE SATURATION MAGNETIZATION $M_S$ OF FM PARTICLES AND COATINGS AS A FUNCTION OF THE TEMPERATURE.	285
FIGURE IV-38. SET-UP FOR PERMEABILITY AND PERMITTIVITY MEASUREMENTS (A), APC7 CELL 3D VIEW (B-C) AND CROSS-SECTIONAL VIEW (D) [52].	287
FIGURE IV-39. REAL (DASHED LINES) AND IMAGINARY (CONTINUOUS LINES) PART OF THE PERMITTIVITY FOR FM AND SP(F)M PARTICLES AND COMMERCIAL NANOPARTICLES WITH DIFFERENT COMPOSITIONS: $Fe_3O_4$ , $CoFe_2O_4$ AND $NiZnFe_2O_4$ .	289
FIGURE IV-40. TEM IMAGES OF COMMERCIAL NANOPARTICLES OF $Fe_3O_4$ , $CoFe_2O_4$ , AND $NiZnFe_2O_4$ .	290
FIGURE IV-41. COMPARISON BETWEEN THE PARTICLE DIAMETER INDICATED BY THE SUPPLIER AND TEM OBSERVATIONS.	290
FIGURE IV-42. REAL AND IMAGINARY PART OF THE PERMEABILITY FOR NANOPARTICLES WITH DIFFERENT COMPOSITIONS: $Fe_3O_4$ , $CoFe_2O_4$ AND $NiZnFe_2O_4$ .	291
FIGURE IV-43. MEASURED MAGNETIZATION CURVES OF COMMERCIAL NANOPARTICLES OF $Fe_3O_4$ , $CoFe_2O_4$ , AND $NiZnFe_2O_4$ . MASS MAGNETIZATION $\Sigma$ VERSUS THE APPLIED FIELD $H$ .	292
FIGURE IV-44. PERMEABILITY SPECTRA FOR SP(F)M AND FM PARTICLES. DASHED LINES REPRESENT THE REAL PART OF THE PERMEABILITY $\mu'$ , AND SOLID LINES THE IMAGINARY PART $\mu''$ .	293
FIGURE IV-45. SATURATION MAGNETIZATION DEDUCED FROM VSM MEASUREMENTS FOR NANOPARTICLES WITH DIFFERENT SIZES AND COMPOSITIONS. *DEDUCED FROM LANGEVIN EQUATION.	293
FIGURE IV-46. EVOLUTION OF THE IMAGINARY PART OF THE PERMEABILITY SPECTRUM WITH TEMPERATURE FOR FM PARTICLES.	294
FIGURE IV-47. EVOLUTION OF THE IMAGINARY PART OF THE PERMEABILITY SPECTRUM WITH TEMPERATURE FOR SP(F)M PARTICLES, BEFORE (A) AND AFTER (B) SMOOTHING TREATMENT.	295
FIGURE IV-48. CALCULATION OF THE COERCIVE FIELD $H_C$ OF FM PARTICLES THROUGH VSM MEASUREMENT.	298
IV-26	299
FIGURE IV-49. POSITIVE FIELD BRANCH OF THE HYSTERESIS CURVE OF MAGNETIZATION OF FM PARTICLES AND FITTED CURVE IN RED. THE PARAMETERS ARE: $k=5.05 \times 10^{-5}$ , $K_1=1.03 \times 10^5$ ERG/G, AND $M_S=80.5$ EMU/G.	299
FIGURE IV-50. SUMMARY OF THE VALUES OBTAINED FOR THE ANISOTROPY CONSTANT $K$ WITH DIFFERENT METHODS.	300
FIGURE IV-51. VARIATION OF THE ANISOTROPY CONSTANT $K$ WITH THE ZINC CONCENTRATION IN $(Zn_{1-y}Fe_y)Fe_2O_4$ CRYSTALS. FROM N. MIYATA [81].	301
FIGURE IV-52. COMPUTED PERMEABILITY SPECTRA (IMAGINARY PART, $\mu''$ ) FOR DIFFERENT VALUES OF $\Sigma$ AND COMPARISON WITH EXPERIMENT AT ROOM TEMPERATURE. THE PARAMETERS ARE: $M_S=3.44 \times 10^5$ A/M, $\Gamma=1.76 \times 10^{11}$ S <sup>-1</sup> T <sup>-1</sup> , $A=0.1$ AND $\phi=5.4$ NM.	302
FIGURE IV-53. COMPUTED PERMEABILITY SPECTRA (IMAGINARY PART, $\mu''$ ) FOR DIFFERENT VALUES OF $A$ AND COMPARISON WITH EXPERIMENT AT ROOM TEMPERATURE. THE PARAMETERS ARE: $M_S=3.44 \times 10^5$ A/M, $\Gamma=1.76 \times 10^{11}$ S <sup>-1</sup> T <sup>-1</sup> , $K=10^4$ J/M <sup>3</sup> AND $\phi=5.4$ NM.	303
FIGURE IV-54. COMPUTED PERMEABILITY SPECTRA (IMAGINARY PART, $\mu''$ ) AND COMPARISON WITH EXPERIMENT. NANOPARTICLE SIZE-DEPENDENCE OF $\mu''$ AT ROOM TEMPERATURE. THE MAGNETIC PARAMETERS ARE: $K=10^4$ J/M <sup>3</sup> , $M_S=3.44 \times 10^5$ A/M, $\Gamma=1.76 \times 10^{11}$ S <sup>-1</sup> T <sup>-1</sup> , $A=0.13$ .	304
IV-31	305
IV-32	305
FIGURE IV-55. DISTRIBUTION DENSITY $F_V$ IN VOLUME FOR DIFFERENT STANDARD DEVIATION $\Delta$ .	305
FIGURE IV-56. COMPUTED PERMEABILITY SPECTRA (IMAGINARY PART, $\mu''$ ) WEIGHTED BY THE SIZE DISTRIBUTION AND COMPARISON WITH EXPERIMENT.	306

FIGURE IV-57. TEMPERATURE DEPENDENCE OF THE COMPUTED PERMEABILITY SPECTRA (IMAGINARY PART, $\mu''$ ) AND COMPARISON WITH EXPERIMENTS. THE MAGNETIC PARAMETERS ARE: $K = 10^4 \text{ J/M}^3$ , $M_S = 3.44 \times 10^5 \text{ A/M}$ , $r = 1.76 \times 10^{11} \text{ s}^{-1}\text{T}^{-1}$ , $A = 0.13$ , $\phi = 5.4 \text{ NM}$ . .....	307
FIGURE IV-58. (A) TEMPERATURE DEPENDENCE OF THE COMPUTED PERMEABILITY SPECTRA (IMAGINARY PART, $\mu''$ ) AND COMPARISON WITH EXPERIMENTS. THE PARAMETERS ARE: $r = 1.76 \times 10^{11} \text{ s}^{-1}\text{T}^{-1}$ , $A = 0.13$ , $\phi = 5.4 \text{ NM}$ . (B) TEMPERATURE DEPENDENCE OF THE EFFECTIVE ANISOTROPY FIELD $H_K$ USED FOR FITTING THE EXPERIMENTAL CURVES (BLACK CIRCLES) WITH THE $K$ VALUE AT $T_B$ (RED CIRCLE). THE DASHED LINE IS A GUIDE FOR EYES.....	307
FIGURE IV-59. TEMPERATURE DEPENDENCE OF THE ANISOTROPY CONSTANT $K$ , THE SATURATION MAGNETIZATION $M_S$ AND THE ANISOTROPY FIELD $H_K$ OBTAINED FROM CALCULATION AT $T_B$ (33 K) AND SIMULATIONS AT 243, 293 AND 343 K. ....	308
FIGURE IV-60. COMPARISON OF THE TEMPERATURE DEPENDENCE OF THE ANISOTROPY OF $(\text{Zn}_{1-x}\text{Fe}_x)\text{Fe}_2\text{O}_4$ CRYSTALS FROM N. MIYATA [81] AND THE COMPUTATION FOR SP(F)M PARTICLES. ....	308
FIGURE IV-61. SPECTRA OF THE PERMEABILITY ( $\mu'$ , $\mu''$ ) OF FM COATINGS AFTER DEBINDING AND SINTERING.....	310
FIGURE IV-62. SPECTRA OF THE IMAGINARY PERMEABILITY ( $\mu''$ ) OF FM COATINGS AFTER DEBINDING AND SINTERING. THE CURVES ARE SMOOTHED ON ORIGIN. ....	310
FIGURE IV-63. PARAMETERS INFLUENCING THE SATURATION MAGNETIZATION $M_S$ . ....	312



**Titre :** Synthèse de nanoparticules d'oxydes de fer et élaboration de dépôts magnétiques par voie liquide

**Mots clés :** nanoparticules, oxyde de fer, dépôts, impression jet d'encre, propriétés magnétiques

**Résumé :** Ce projet porte sur la réalisation de nouveaux matériaux aux propriétés magnétiques parfaitement contrôlées pour des applications électromagnétiques de types antennes RFID, transmission de puissance sans fil, absorbants radars... Le principe repose sur l'élaboration d'une structure organisée en motifs ou domaines magnétiques définie par des caractéristiques géométriques (taille des motifs, épaisseur, distance entre motifs). La réponse magnétique en perméabilité de tels matériaux est liée aux contributions des domaines et des parois formés, donnant naissance à un matériau dit « multi-bandes » au regard des pics distincts et séparés observés sur son spectre de perméabilité. L'élaboration d'un tel matériau est étudiée par dépôt en voie liquide de nanoparticules d'oxyde de fer. La composition du matériau est fixée à  $Zn_{0.4}Fe_{2.6}O_4$  afin de combiner une aimantation à saturation forte, et une permittivité diélectrique faible pour une bonne pénétration de l'onde électromagnétique dans le

dépôt. Les nanoparticules sont synthétisées par décomposition thermique en voie micro-ondes. Deux gammes de tailles de nanoparticules sont visées : des nanoparticules superparamagnétiques (diamètre inférieur à 20 nm) et ferrimagnétiques. Deux techniques de réalisation de dépôts structurés à partir de suspensions stables de nanoparticules sont discutées : l'aérogographie suivie d'une gravure laser, et l'impression jet d'encre. De nombreuses caractérisations physico-chimiques, locales ou globales, ont été effectuées. Un traitement thermique est requis pour la densification du matériau, mais ne permet pas d'obtenir une densité suffisante pour l'application envisagée. Une étude approfondie des propriétés magnétiques statiques et dynamiques des particules et des dépôts est réalisée, et corrélée à leurs caractéristiques structurales par le biais de modèles de champ moléculaire. Des pistes sont ouvertes pour l'élaboration d'un matériau magnétique multi-bandes.

**Title:** Synthesis of iron oxide nanoparticles and development of magnetic coatings by fluid processing

**Keywords:** nanoparticles, iron oxide, coatings, inkjet printing, magnetic properties

**Abstract:** The aim of the study is to develop novel materials with well-controlled magnetic properties for electromagnetic applications like RFID antennas, wireless power transmission, radar absorption... The principle is based on the development of an organized framework in patterns or magnetic domains, defined by their geometry (pattern size, thickness, spacing). The permeability response of such materials is linked to the contributions of created domains and walls, giving rise to a "multi-band" material with separate and distinct peaks on its permeability spectrum. The development of such material is studied through fluid processing from iron oxide nanoparticles. The  $Zn_{0.4}Fe_{2.6}O_4$  material composition is selected in order to provide a high saturation magnetization and a low dielectric permittivity to ensure the penetration of the electromagnetic wave in the coating.

The nanoparticles are synthesized by microwave-assisted thermal decomposition. Two ranges of sizes are chosen: superparamagnetic particles (diameter below 20 nm) and ferrimagnetic ones. Two processing methods from stable particle dispersions are discussed: airbrushing followed by a laser etching, and inkjet printing. Several physico-chemical characterizations, at local and global scales, have been performed. An annealing is required to densify the material, but does not provide a suitable density for the desired application. An in-depth study of the static and dynamic magnetic properties of nanoparticles and coatings is done, and correlated to their microstructure through modeling from the molecular field theory. Many guidelines are suggested for the development of a multiband magnetic material.